Journal of Applied Mechanics

Published Bimonthly by ASME

VOLUME 72 • NUMBER 6 • NOVEMBER 2005

TECHNICAL PAPERS

TECHNICAL BRIEFS

(Contents continued on inside back cover)

This journal is printed on acid-free paper, which exceeds the ANSI Z39.48-1992 specification for permanence of paper and library materials. ♾™
♲ 85% recycled content, including 10% post-consumer fibers.

Editor
ROBERT M. McMEEKING

Assistant to the Editor
LIZ MONTANA

APPLIED MECHANICS DIVISION

Executive Committee
(Chair) **W.-K. LIU**
T. N. FARRIS
K. RAVI-CHANDAR
D. J. INMAN
Z. SUO

Associate Editors
E. ARRUDA (2007)
H. ESPINOSA (2007)
H. GAO (2006)
S. GOVINDJEE (2006)
D. A. KOURIS (2005)
K. M. LIECHTI (2006)
A. M. MANIATTY (2007)
I. MEZIC (2006)
M. P. MIGNOLET (2006)
S. MUKHERJEE (2006)
O. O'REILLY (2007)
K. RAVI-CHANDAR (2006)
N. SRI NAMACHCHIVAYA (2006)
Z. SUO (2006)
T. E. TEZDUYAR (2006)
N. TRIANTAFYLLIDIS (2006)
B. A. YOUNIS (2006)

PUBLICATIONS DIRECTORATE

Chair, **ARTHUR G. ERDMAN**

OFFICERS OF THE ASME

President, **RICHARD E. FEIGEL**
Executive Director, **V. R. CARTER**
Treasurer, **T. PESTORIUS**

PUBLISHING STAFF

Managing Director, Publishing
PHILIP DI VIETRO

Production Coordinator
JUDITH SIERANT

Production Assistant
MARISOL ANDINO

Transactions of the ASME, Journal of Applied Mechanics (ISSN 0021-8936) is published bimonthly (Jan., Mar., May, July, Sept., Nov.) by The American Society of Mechanical Engineers, Three Park Avenue, New York, NY 10016. Periodicals postage paid at New York, NY and additional mailing offices. POSTMASTER: Send address changes to Transactions of the ASME, Journal of Applied Mechanics, c/o THE AMERICAN SOCIETY OF MECHANICAL ENGINEERS, 22 Law Drive, Box 2300, Fairfield, NJ 07007-2300.
CHANGES OF ADDRESS must be received at Society headquarters seven weeks before they are to be effective. Please send old label and new address.
STATEMENT from By-Laws. The Society shall not be responsible for statements or opinions advanced in papers or . . . printed in its publications (B7.1, Para. 3).
COPYRIGHT © 2005 by The American Society of Mechanical Engineers. For authorization to photocopy material for internal or personal use under those circumstances not falling within the fair use provisions of the Copyright Act, contact the Copyright Clearance Center (CCC), 222 Rosewood Drive, Danvers, MA 01923, tel: 978-750-8400, www.copyright.com. Request for special permission or bulk copying should be addressed to Reprints/Permission Department.
Canadian Goods & Services Tax Registration #126148048.

(Contents continued)

Journal of Applied Mechanics **Volume 72, Number 6** **NOVEMBER 2005**

DISCUSSION

The ASME Journal of Applied Mechanics is abstracted and indexed in the following:

Alloys Index, Aluminum Industry Abstracts, Applied Science & Technology Index, Ceramic Abstracts, Chemical Abstracts, Civil Engineering Abstracts, Compendex (The electronic equivalent of Engineering Index), Computer & Information Systems Abstracts, Corrosion Abstracts, Current Contents, EEA (Earthquake Engineering Abstracts Database), Electronics & Communications Abstracts Journal, Engineered Materials Abstracts, Engineering Index, Environmental Engineering Abstracts, Environmental Science and Pollution Management, Fluidex, Fuel & Energy Abstracts, GeoRef, Geotechnical Abstracts, INSPEC, International Aerospace Abstracts, Journal of Ferrocement, Materials Science Citation Index, Mechanical Engineering Abstracts, METADEX (The electronic equivalent of Metals Abstracts and Alloys Index), Metals Abstracts, Nonferrous Metals Alert, Polymers Ceramics Composites Alert, Referativnyi Zhurnal, Science Citation Index, SciSearch (Electronic equivalent of Science Citation Index), Shock and Vibration Digest, Solid State and Superconductivity Abstracts, Steels Alert, Zentralblatt MATH

Enhanced First-Order Shear Deformation Theory for Laminated and Sandwich Plates

Jun-Sik Kim
Department of Aerospace Engineering,
The Pennsylvania State University,
University Park, PA 16802

Maenghyo Cho[1]
School of Mechanical and Aerospace
Engineering,
Seoul National University,
Seoul 151-742, Korea
e-mail: mhcho@snu.ac.kr

A new first-order shear deformation theory (FSDT) has been developed and verified for laminated plates and sandwich plates. Based on the definition of Reissener–Mindlin's plate theory, the average transverse shear strains, which are constant through the thickness, are improved to vary through the thickness. It is assumed that the displacement and in-plane strain fields of FSDT can approximate, in an average sense, those of three-dimensional theory. Relationship between FSDT and three-dimensional theory has been systematically established in the averaged least-square sense. This relationship provides the closed-form recovering relations for three-dimensional variables expressed in terms of FSDT variables as well as the improved transverse shear strains. This paper makes two main contributions. First an enhanced first-order shear deformation theory (EFSDT) has been developed using an available higher-order plate theory. Second, it is shown that the displacement fields of any higher-order plate theories can be recovered by EFSDT variables. The present approach is applied to an efficient higher-order plate theory. Comparisons of deflection and stresses of the laminated plates and sandwich plates using present theory are made with the original FSDT and three-dimensional exact solutions. [DOI: 10.1115/1.2041657]

1 Introduction

Increasingly in modern aerospace industry, composite materials are being used in primary load structures. Laminated composite materials provide excellent opportunities for lightweight and high stiffness structures as well as elastic couplings for potential optimization of design criteria. In the analysis of laminated composites, a first-order shear deformation theory is adequate to estimate the global behavior. But for high accuracy and fidelity of strength analysis, accurate prediction of stresses is required as well. Various analysis techniques have been developed for predicting the behavior of laminated plates. However, simple methods which can accurately predict not only the global behavior but also the through-the-thickness stress distribution are rare.

Since the first-order shear deformation theory (FSDT) was proposed by Reissner [1] and Mindlin [2], many plate theories have been developed to overcome the deficiency of FSDT. Historically, smeared displacement based higher order theories were developed first ([3–5]). The assumed in-plane displacement of these higher order theories is expressed as polynomial form. The degree of assumed polynomial decides the order of the plate theory. The polynomial-based in-plane displacement field is at variance with the three-dimensional elasticity displacement field because it does not satisfy interface stress continuity and top and bottom surface static boundary conditions. To obtain improved results, layerwise theories have been developed [6]. These are known to be fairly accurate since at each interface between layers, they allow a kink in the slope of deflection. Nevertheless, these theories have the drawback of requiring many degrees of freedom, which depend upon the number of layers. Simplified zigzag theories have gained attention because of their accuracy and efficiency in the ply-level analysis [7–9]. One of them is an efficient higher plate theory (EHOPT) developed by Cho and Parameter ([8]), which satisfies not only the traction free conditions at the top and bottom surface but also the traction continuity conditions at the interface, and has only five degrees of freedom. Extensive reviews up to date can be found in the review papers of Noor and Burton ([10]), Kapania and Raciti ([11]), and Reddy and Robbins, Jr. ([12]).

On the other hand, the efforts to improve the original first-order shear deformation theory have been made because FSDT is still the most attractive approach due to its simplicity and low computational cost. One of them is to find an accurate shear correction factor (SCF) for laminated composites [13,14]. As is well known, the global response by FSDT with an appropriate SCF is fairly good, even for thick laminated plates. However, it is also difficult to determine properly the shear correction factor of laminates, upon which the accuracy of the prediction of FSDT is strongly dependent. Qi and Knight have developed a refined first-order shear deformation theory [15,16]. They introduced the effective shear stress and strain so that the actual shear stress and strain are expressed in terms of the averaged shear strain of the original FSDT. The resulting effective shear stiffness plays a role of the SCF. This method, however, is limited to cylindrical bending problem and thus it is not adequate for angle-ply laminates that have the transverse shear coupling. Noor and Burton proposed a predictor-corrector method [17]. The displacement fields have been calculated by integrating the equilibrium equation of the FSDT with an appropriate SCF through the thickness. A postprocess method has been developed by Cho and Kim [18]. An EHOPT developed by Cho and Parameter ([8]) is utilized as a postprocessor. They found the relationship between FSDT with SCF and EHOPT under the assumption of the transverse shear energy equivalence. This method has been extended to general lamination configuration [19]. Accuracy of both predictor-corrector and postprocess methods is strongly dependent upon the SCF. The problem that has arisen in both methods is complexity due to the transverse shear coupling.

Hodges et al. ([20]) have developed the neo-classical plate theory (NCPT) that was derived using the variational-asymptotic method originally proposed by Berdichevsky ([21]). It provides

---

[1] To whom correspondence should be addressed.

Contributed by the Applied Mechanics Division of THE AMERICAN SOCIETY OF MECHANICAL ENGINEERS for publication in the ASME JOURNAL OF APPLIED MECHANICS. Manuscript received by the Applied Mechanics Division, May 25, 2004; final revision, May 22, 2005. Associate Editor: R. C. Benson. Discussion of the paper should be addressed to the Editor, Prof. Robert M. McMeeking, Journal of Applied Mechanics, Department of Mechanical and Environmental Engineering, University of California-Santa Barbara, Santa Barbara, CA 93106-5070, and will be accepted until four months after final publication in the paper itself in the ASME JOURNAL OF APPLIED MECHANICS.

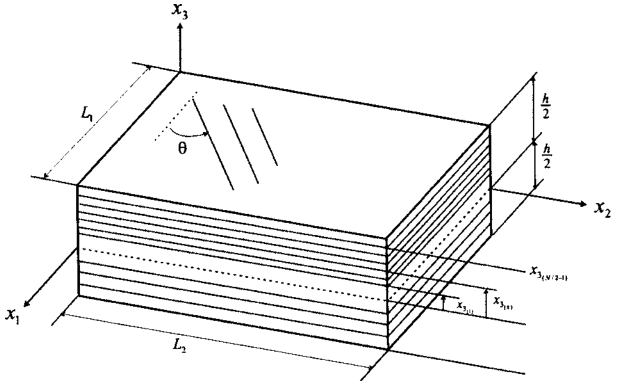

Fig. 1 Geometry and coordinates of laminated plate

the refined transverse shear stiffness as well as recovering relations to three-dimensional (3D) displacement fields. Although it is variational-asymptotically correct, results reported for that correlation of NCPT with the exact solution is not good for thick composites. A more accurate asymptotically correct shear deformation theory is proposed by Sutyrin ([22]). As he pointed out, however, the variational-asymptotic technique leads to a theory with higher derivatives, which is asymptotically correct but not useful because of its being overly complex.

In this paper, an enhanced first-order shear deformation theory (EFSDT) is presented and used to solve the laminated plates and sandwich plates as a justification. The present theory is based on the definition of Reissener-Mindlin's plate theory. It is assumed that the displacements of FSDT can approximate, in an average sense, three-dimensional displacements or those of higher-order theories. Relationship between FSDT and a higher-order theory has been systematically established using the definition of the FSDT variables. This relationship provides the closed-form recovering relations for higher-order theory variables expressed in terms of FSDT variables as well as the improved transverse shear strains. There are many higher-order theories. One of them, EHOPT developed by Cho and Parameter ([8]), is selected because it can describe an accurate transverse shear distribution and has the same number of variables as the FSDT. The transverse shear strains of the original FSDT, which are constant through the thickness, are improved to vary through the thickness.

This paper makes two main contributions. First, an enhanced first-order shear deformation theory (EFSDT) has been developed. Second, it is shown that the displacement fields of a higher-order theory can be recovered by EFSDT variables, in the averaged least-square sense. Comparisons of deflection and stresses of the laminated plates and sandwich plates using the present theory are made with the original FSDT and three-dimensional exact solutions.

2 Three-Dimensional Displacement and Strain Fields

In this paper we consider only linear plate theory. A laminated plate of thickness h made of a monoclinic material is considered. Geometry and coordinates of a laminated plate are shown in Fig. 1. Greek indices will take values in the set 1,2, whereas Latin indices will take values in 1,2,3. The summation convention on repeated indices will also be used.

The reference two-dimensional plane is represented by x_α and the through-the-thickness position is denoted by x_3, where $x_3 \in [-h/2, h/2]$ and h is the thickness of the plate. The deformed state of plate is described by three spatial displacements, u_i, as functions of x_i. According to the asymptotic analysis ([23]), the general form of displacement fields of the interior solution can be expressed by

$$u_\alpha(x_i) = u_\alpha^o(x_\alpha) - u_{3,\alpha}^o(x_\alpha)x_3 + W_\alpha(x_i) \tag{1}$$

$$u_3(x_i) = u_3^o(x_\alpha) + W_3(x_i) \tag{2}$$

in which W_i are through-the-thickness warping functions, and in-plane warping function W_α can be expanded in terms of the *effective transverse shear strain* $\phi_\alpha^{(k)}$

$$W_\alpha(x_i) = \sum_{k=1}^{N_\phi} \Phi_{\alpha\gamma}^{(k)}(x_3)\phi_\gamma^{(k)}(x_\alpha), \quad (k=1,2,\ldots,N_\phi) \tag{3}$$

so that in-plane displacement converges to *Kirchhoff-Love* displacement as the transverse shear strain vanishes.

From definition of the mean displacement through the thickness of the plate u_i^o, the kinematical constraints on the warping functions are given

$$\langle W_i(x_\alpha,x_3)\rangle = 0 \rightarrow \langle \Phi_{\alpha\gamma}^{(k)}(x_3)\rangle = 0, \quad (k=1,2,\ldots,N_\phi) \tag{4}$$

so that

$$u_\alpha^o = \frac{1}{h}\langle u_\alpha(x_i)\rangle, \quad u_3^o(x_\alpha) = \frac{1}{h}\langle u_3(x_i)\rangle, \tag{5}$$

where $\langle \bullet \rangle$ is defined by

$$\langle \bullet \rangle \equiv \int_{-h/2}^{h/2} \bullet \, dx_3. \tag{6}$$

Note that u_i^o, which is the averaged displacement through the thickness of the deformed middle surface, may or may not be the displacement at the undeformed middle surface, $x_3=0$ [21].

The strains associated with the small displacement theory of elasticity are given by

$$\varepsilon_{\alpha\beta}(x_i) = \varepsilon_{\alpha\beta}^{(o)}(x_\alpha) + x_3\varepsilon_{\alpha\beta}^{(1)}(x_\alpha) + \varepsilon_{\alpha\beta}^{(w)}(x_i), \tag{7}$$

$$\gamma_{3\alpha}(x_i) = W_\alpha(x_i)_{,3} + W_3(x_i)_{,\alpha} = \sum_{k=1}^{N_\phi} \Phi_{\alpha\gamma,3}^{(k)}\phi_\gamma^{(k)} + W_{3,\alpha}, \tag{8}$$

where

$$\varepsilon_{\alpha\beta}^{(0)} = \frac{1}{2}(u_{\alpha,\beta}^o + u_{\beta,\alpha}^o), \quad \varepsilon_{\alpha\beta}^{(1)} = -\frac{1}{2}(u_{3,\alpha\beta}^o + u_{3,\beta\alpha}^o), \quad \varepsilon_{\alpha\beta}^{(w)} = \frac{1}{2}(W_{\alpha,\beta} + W_{\beta,\alpha}). \tag{9}$$

The three-dimensional strain energy per unit area $U^{3\text{D}}$ is given by

$$U^{3\text{D}} = \frac{1}{2}\langle C_{\alpha\beta\lambda\mu}\varepsilon_{\alpha\beta}\varepsilon_{\lambda\mu} + C_{\alpha3\beta3}\gamma_{\alpha3}\gamma_{\beta3} + 2C_{33\alpha\beta}\varepsilon_{\alpha\beta}\varepsilon_{33} + C_{3333}\varepsilon_{33}\varepsilon_{33}\rangle, \tag{10}$$

where C_{ijkl} are components of the elasticity tensor with monoclinic symmetry properties.

Under the assumption of a negligible transverse normal stress $\sigma_{33} \simeq 0$, which is equivalent to minimize the strain energy with respect to ε_{33}, the reduced strain energy U is given as

$$U = \min_{\varepsilon_{33}} U^{3\text{D}} = \frac{1}{2}\langle E_{\alpha\beta\lambda\mu}\varepsilon_{\alpha\beta}\varepsilon_{\lambda\mu} + E_{\alpha3\beta3}\gamma_{\alpha3}\gamma_{\beta3}\rangle, \tag{11}$$

where

$$E_{\alpha\beta\lambda\mu} \equiv C_{\alpha\beta\lambda\mu} - \frac{C_{\alpha\beta33}C_{\lambda\mu33}}{C_{3333}}, \quad E_{\alpha3\beta3} \equiv C_{\alpha3\beta3} \tag{12}$$

and corresponding condition is

$$\varepsilon_{33} = -\frac{C_{\alpha\beta33}}{C_{3333}}\varepsilon_{\alpha\beta}. \tag{13}$$

From this condition, we can obtain the out-of-plane warping function W_3 with a geometric constraint of Eq. (4) and a kinematic continuity condition. That is,

$$W_3 = -\int \frac{C_{\alpha\beta 33}}{C_{3333}}\varepsilon_{\alpha\beta}dx_3, \quad \text{s.t. } \langle W_3\rangle = 0. \tag{14}$$

3 Averaged Displacement and Strain Fields in Least-Square Sense

In Reissner-Mindlin's plate theory, the displacement field assumptions include a linear in-plane displacement and a constant transverse deflection. These assumptions are retained in the present approach so that extensional and bending strain energy expression are the same as FSDT. However, the transverse shear strain energy will be derived from three-dimensional strain energy by introducing the averaged extensional and bending strain concept in this section.

Complexities in three-dimensional analysis come from warping function W_i. In order to approximate the warping function, we introduce the averaged in-plane strain $\bar{\varepsilon}_{\alpha\beta}$ such that

$$\bar{\varepsilon}_{\alpha\beta} = \bar{\varepsilon}^o_{\alpha\beta} + x_3\kappa_{\alpha\beta}, \tag{15}$$

where $\bar{\varepsilon}^o_{\alpha\beta}$ and $\kappa_{\alpha\beta}$ are obtained by minimizing the error of averaged strain in the least-square sense

$$\min_{\bar{\varepsilon}^o_{\alpha\beta}}\langle\|\varepsilon_{\alpha\beta} - \bar{\varepsilon}_{\alpha\beta}\|_2\rangle = 0 \rightarrow \bar{\varepsilon}^o_{\alpha\beta} = \varepsilon^{(o)}_{\alpha\beta}, \tag{16}$$

$$\min_{\kappa_{\alpha\beta}}\langle\|\varepsilon_{\alpha\beta} - \bar{\varepsilon}_{\alpha\beta}\|_2\rangle = 0 \rightarrow \kappa_{\alpha\beta} = \varepsilon^{(1)}_{\alpha\beta} + \frac{12}{h^3}\langle x_3\varepsilon^{(w)}_{\alpha\beta}\rangle. \tag{17}$$

It has turned out that minimizing the error of averaged in-plane strain is equivalent to minimizing the error of averaged in-plane displacement. The averaged displacement fields are defined by

$$\bar{u}_\alpha = \bar{u}^o_\alpha + x_3\theta_\alpha, \quad \bar{u}_3 = \bar{u}^o_3, \tag{18}$$

where

$$\min_{\bar{u}^o_\alpha}\langle\|u_\alpha - \bar{u}_\alpha\|_2\rangle = 0 \rightarrow \bar{u}^o_\alpha = u^o_\alpha, \tag{19}$$

$$\min_{\theta_\alpha}\langle\|u_\alpha - \bar{u}_\alpha\|_2\rangle = 0 \rightarrow \theta_\alpha = -u^o_{3,\alpha} + \frac{12}{h^3}\langle x_3W_\alpha\rangle, \tag{20}$$

$$\min_{\bar{u}^o_3}\langle\|u_3 - \bar{u}_3\|_2\rangle = 0 \rightarrow \bar{u}^o_3 = u^o_3, \tag{21}$$

which are the same results as Reissner's definition ([1]), that is,

$$\bar{u}^o_\alpha \equiv \frac{1}{h}\langle u_\alpha\rangle, \quad \theta_\alpha \equiv \frac{12}{h^3}\langle x_3u_\alpha\rangle. \tag{22}$$

From Eqs. (20) and (21), the averaged displacement term $\theta_\alpha + \bar{u}^o_{3,\alpha}$, which is the transverse shear strain from Eq. (18), can be expressed in terms of the effective transverse shear strain $\phi^{(k)}_\alpha$. Namely

$$\bar{\gamma}_{3\alpha} = \sum_{k=1}^{N_\phi}\Gamma^{(k)}_{\alpha\gamma}\phi^{(k)}_\gamma \tag{23}$$

where

$$\bar{\gamma}_{3\alpha} \equiv \theta_\alpha + \bar{u}^o_{3,\alpha}, \quad \Gamma^{(k)}_{\alpha\gamma} \equiv \frac{12}{h^3}\langle x_3\Phi^{(k)}_{\alpha\gamma}\rangle. \tag{24}$$

It is assumed that the out-of-plane warping function W_3 is negligible in the actual transverse shear strain $\gamma_{3\alpha}$ of Eq. (8), in the variational-asymptotic sense ([20]). Then the transverse shear strain can be expressed in terms of the effective shear strain $\phi^{(k)}_\alpha$

$$\gamma_{3\alpha} \simeq \sum_{k=1}^{N_\phi}\Phi^{(k)}_{\alpha\gamma,3}\phi^{(k)}_\gamma. \tag{25}$$

In order to rewrite the reduced strain energy of Eq. (11) in terms of the averaged strain, it is required to express the effective transverse shear strain $\phi^{(k)}_\alpha$ in terms of the averaged transverse shear strain $\bar{\gamma}_{3\alpha}$. However, the number of equations for the relations between $\bar{\gamma}_{3\alpha}$ and $\phi^{(k)}_\alpha$ is less than the number of the effective shear strain $\phi^{(k)}_\alpha$. The required additional equations are obtained by introducing the weighted least-square approximation. By applying the weighting function that is a function of the through-the-thickness coordinate x^k_3 to Eq. (20), it can be rewritten by

$$\min_{\theta_\alpha}\langle\|\mathcal{W}_{k-1}(x_3)(u_\alpha - \bar{u}_\alpha)\|_2\rangle = 0 \quad (k = 1,2,\ldots,N_\phi), \tag{26}$$

where weighting function $\mathcal{W}_{k-1}$ can be chosen from the various function sets such as Legendre polynomials, power form, and trigonometric functions. In the present study, we pick up power form x^{k-1} as a weighting function. Then

$$\min_{\theta_\alpha}\langle\|x_3^{k-1}(u_\alpha - \bar{u}_\alpha)\|_2\rangle = 0 \quad (k = 1,2,\ldots,N_\phi), \tag{27}$$

which renders

$$\begin{Bmatrix}\bar{\gamma}_{31}\\ \vdots\\ \bar{\gamma}_{31}\\ \bar{\gamma}_{32}\\ \vdots\\ \bar{\gamma}_{32}\end{Bmatrix} = \begin{bmatrix}\Gamma^{(1,1)}_{11} & \Gamma^{(1,1)}_{12} & \cdots & \Gamma^{(1,N_\phi)}_{11} & \Gamma^{(1,N_\phi)}_{12}\\ \vdots & \vdots & \ddots & \vdots & \vdots\\ \Gamma^{(N_\phi,1)}_{11} & \Gamma^{(N_\phi,1)}_{12} & \cdots & \Gamma^{(N_\phi,N_\phi)}_{11} & \Gamma^{(N_\phi,N_\phi)}_{12}\\ \Gamma^{(1,1)}_{21} & \Gamma^{(1,1)}_{22} & \cdots & \Gamma^{(1,N_\phi)}_{21} & \Gamma^{(1,N_\phi)}_{22}\\ \vdots & \vdots & \ddots & \vdots & \vdots\\ \Gamma^{(N_\phi,1)}_{21} & \Gamma^{(N_\phi,1)}_{22} & \cdots & \Gamma^{(N_\phi,N_\phi)}_{21} & \Gamma^{(N_\phi,N_\phi)}_{22}\end{bmatrix}\begin{Bmatrix}\phi^{(1)}_1\\ \phi^{(1)}_2\\ \vdots\\ \phi^{(N_\phi)}_1\\ \phi^{(N_\phi)}_2\end{Bmatrix}, \tag{28}$$

where

$$\Gamma^{(i,j)}_{\alpha\beta} = \frac{\langle x_3^{2i-1}\Phi^{(j)}_{\alpha\beta}\rangle}{\langle x_3^{2i}\rangle}, \quad (i,j = 1,2,\ldots,N_\phi). \tag{29}$$

Thus the effective shear strain $\phi^{(k)}_\alpha$ is expressed in terms of the averaged shear strain $\bar{\gamma}_{3\alpha}$ only

$$\phi^{(k)}_\alpha = \hat{\Gamma}^{(k)}_{\alpha\mu}\bar{\gamma}_{3\mu}, \quad (k = 1,2,\ldots,N_\phi), \tag{30}$$

where $\hat{\Gamma}^{(k)}_{\alpha\mu}$ is obtained from the inverse of the matrix that retains $\Gamma^{(i,j)}_{\alpha\beta}$ in Eq. (28).

This expression in Eq. (28) is the major contribution of the present study.

4 Enhanced First-Order Shear Deformation Theory

In this section we present an enhanced first-order shear deformation theory for laminated plate using an efficient higher-order plate theory [8]. Three-dimensional strain energy per unit area is restated in terms of the averaged strain. Explicit relations between three-dimensional and averaged displacement fields are given through the least-square approximation of in-plane strains that are presented in the previous section.

The reduced strain energy per unit area of the plate in terms of the effective shear strain is obtained by substituting Eq. (25) into Eq. (11)

$$U = \frac{1}{2}\left\langle E_{\alpha\beta\lambda\mu}\varepsilon_{\alpha\beta}\varepsilon_{\lambda\mu} + E_{\alpha3\beta3}\sum_{i=1}^{N_\phi}\sum_{j=1}^{N_\phi}\Phi^{(i)}_{\alpha\lambda,3}\Phi^{(j)}_{\beta\mu,3}\phi^{(i)}_\lambda\phi^{(j)}_\mu\right\rangle. \tag{31}$$

To minimize the error of the averaged in-plane strains, the relation of Eq. (23) should be satisfied. However, as mentioned before, we cannot uniquely determine the relation between the averaged shear strain and the effective shear strain. Thus we use the approximated relation of Eq. (30). By imposing this relation to the reduced total strain energy expression, the approximated strain energy in the least-square sense is given as follows:

$$U \approx \frac{1}{2}\left\langle E_{\alpha\beta\lambda\mu}\bar{\varepsilon}_{\alpha\beta}\bar{\varepsilon}_{\lambda\mu} + E_{\alpha 3\beta 3}\sum_{i=1}^{N_\phi}\sum_{j=1}^{N_\phi}\Phi^{(i)}_{\alpha\lambda,3}\Phi^{(j)}_{\beta\mu,3}\hat{\Gamma}^{(i)}_{\lambda\nu}\hat{\Gamma}^{(j)}_{\mu\omega}\bar{\gamma}_{3\nu}\bar{\gamma}_{3\omega}\right\rangle. \tag{32}$$

Substituting Eq. (15) into Eq. (32) and integrating the strain energy through the thickness yields

$$U = \frac{1}{2}(A_{\alpha\beta\lambda\mu}\bar{\varepsilon}^o_{\alpha\beta}\bar{\varepsilon}^o_{\lambda\mu} + 2B_{\alpha\beta\lambda\mu}\bar{\varepsilon}^o_{\alpha\beta}\kappa_{\lambda\mu} + D_{\alpha\beta\lambda\mu}\kappa_{\alpha\beta}\kappa_{\lambda\mu} + G_{\alpha 3\beta 3}\bar{\gamma}_{3\alpha}\bar{\gamma}_{3\beta}), \tag{33}$$

where

$$A_{\alpha\beta\lambda\mu} = \langle E_{\alpha\beta\lambda\mu}\rangle, \quad B_{\alpha\beta\lambda\mu} = \langle x_3 E_{\alpha\beta\lambda\mu}\rangle, \quad D_{\alpha\beta\lambda\mu} = \langle x_3^2 E_{\alpha\beta\lambda\mu}\rangle,$$

$$G_{\alpha 3\beta 3} = \left\langle E_{\nu 3\omega 3}\sum_{i=1}^{N_\phi}\sum_{j=1}^{N_\phi}\Phi^{(i)}_{\nu\lambda,3}\Phi^{(j)}_{\omega\mu,3}\hat{\Gamma}^{(i)}_{\lambda\alpha}\hat{\Gamma}^{(j)}_{\mu\beta}\right\rangle \tag{34}$$

and the averaged strain-displacement relations are given by

$$\bar{\varepsilon}^o_{\alpha\beta} = \frac{1}{2}(\bar{u}^o_{\alpha,\beta} + \bar{u}^o_{\beta,\alpha}), \quad \kappa_{\alpha\beta} = \frac{1}{2}(\theta_{\alpha,\beta} + \theta_{\beta,\alpha}), \quad \bar{\gamma}_{3\alpha} = \theta_\alpha + \bar{u}^o_{3,\alpha}. \tag{35}$$

Note that the strain energy expression except the transverse shear energy coincides with that of FSDT. Matrices A, B and D are the well known transformed reduced stiffness in both classical laminated plate theory (CLPT) and FSDT ([24]).

Three-dimensional displacement fields can also be expressed in terms of the averaged displacement variables as

$$u_\alpha = \bar{u}^o_\alpha - x_3\bar{u}^o_{3,\alpha} + \sum_{k=1}^{N_\phi}\Phi^{(k)}_{\alpha\gamma}\hat{\Gamma}^{(k)}_{\gamma\lambda}\bar{\gamma}_{3\lambda},$$

$$u_3 = \bar{u}^o_3 + W_3, \tag{36}$$

where W_3 is determined by Eq. (14), and in-plane warping function $\Phi^{(k)}_{\alpha\gamma}$ is not determined yet. In general, it is hard to determine an appropriate warping function $\Phi^{(k)}_{\alpha\gamma}$ for laminated composites. Thus we utilize a refined plate theory to obtain the in-plane warping function. Many higher order theories have been reported in the literature. An efficient higher order plate theory (EHOPT) among others, is selected due to its simplicity and accuracy.

In EHOPT, zigzag linear function is superimposed to the globally cubic varying displacement field to satisfy the static continuity as well as the geometric continuity conditions. Thus the EHOPT displacement field for symmetric lamination configurations is given as follows:

$$u_\alpha(x_i) = u^o_\alpha(x_\alpha) - u^o_{3,\alpha}(x_\alpha)x_3 + \Phi_{\alpha\gamma}(x_3)\phi_\gamma(x_\alpha), \quad u_3(x_i) = u^o_3(x_\alpha) \tag{37}$$

in which

$$\Phi_{\alpha\gamma} \equiv \delta_{\alpha\gamma}x_3 - \frac{4}{3h^2}\left(\delta_{\alpha\gamma} + \sum_{k=1}^{N/2-1} a^k_{\alpha\gamma}\right)x_3^3 + \sum_{k=1}^{N/2-1} a^k_{\alpha\gamma}[(x_3 - x_{3_{(k)}})H(x_3 - x_{3_{(k)}}) - (-x_3 - x_{3_{(k)}})H(-x_3 - x_{3_{(k)}})] \tag{38}$$

where $\delta_{\alpha\gamma}$ is the Kronecker delta function, N is the number of layers, and $H(x_3 - x_{3_{(k)}})$ is the Heaviside unit step function. The coefficient $a^k_{\alpha\gamma}$ represents the change in slope at each interface, and depends only upon the material properties of each layer. The explicit expression of $a^k_{\alpha\gamma}$ can be found in Ref. [8].

From Eqs. (24) and (38), the 2 by 2 matrix $\Gamma_{\alpha\gamma}$ can be obtained as follows:

$$\Gamma_{\alpha\gamma} = \frac{4}{5}\delta_{\alpha\gamma} - \frac{1}{5}\sum_{k=1}^{N/2-1} a^k_{\alpha\gamma} + \frac{h^3}{6}\sum_{n=1}^{N/2-1}\left\{\frac{1}{3}(x^3_{3_{(n+1)}} - x^3_{3_{(n)}})\sum_{k=1}^{n} a^k_{\alpha\gamma}\right\} \tag{39}$$

For isotropic plates, the diagonal components of the inverse matrix of $\Gamma_{\alpha\gamma}$ can be easily shown to be 4/5, which coincides with Qi and Knight's ([15,16]) result. This result is equivalent to the case of the shear correction factor equal to be 5/6. The transverse shear strains of the EHOPT can be expressed in terms of the averaged transverse shear strain $\bar{\gamma}_{3\alpha}$ from Eqs. (30) and (39). Namely,

$$\gamma_{3\alpha} = \Phi_{\alpha\gamma,3}\phi_\gamma = \Phi_{\alpha\gamma,3}\hat{\Gamma}_{\gamma\mu}\bar{\gamma}_{3\mu}, \quad \bar{\gamma}_{3\mu} \equiv \theta_\mu + u^o_{3,\mu}, \tag{40}$$

where $\hat{\Gamma}_{\alpha\gamma}$ is the inverse of $\Gamma_{\alpha\gamma}$, and

$$\Phi_{\alpha\gamma,3} = \left(1 - \frac{4}{h^2}x_3^2\right)\delta_{\alpha\gamma} + \sum_{k=1}^{N/2-1} a^k_{\alpha\gamma}\left[-\frac{4}{h^2}x_3^2 + H(x_3 - x_{3_{(k)}}) + H(-x_3 - x_{3_{(k)}})\right]. \tag{41}$$

The new transverse shear stiffness $G_{\alpha 3\beta 3}$, which is the so-called *effective transverse shear stiffness*, using EHOPT and the nominal shear stiffness in FSDT is given by

$$G_{\alpha 3\beta 3} = \langle E_{\nu 3\omega 3}\Phi_{\nu\lambda,3}\Phi_{\omega\mu,3}\hat{\Gamma}_{\lambda\alpha}\hat{\Gamma}_{\mu\beta}\rangle, \quad \bar{G}_{\alpha 3\beta 3} = \langle E_{\alpha 3\beta 3}\rangle. \tag{42}$$

Note that the effective shear stiffness $G_{\alpha 3\beta 3}$ comes to be $\frac{5}{6}\bar{G}_{\alpha 3\beta 3}$ for isotropic material. Finally, the following displacement fields are used to predict the stresses:

$$u_\alpha = \bar{u}^0_\alpha - \bar{u}^o_{3,\alpha}x_3 + \Phi_{\alpha\gamma}\hat{\Gamma}_{\gamma\mu}\bar{\gamma}_{3\mu}, \quad u_3 = \bar{u}^o_3, \tag{43}$$

where overbar $\overline{(\ )}$ variables are obtained from the traditional FSDT with the *effective transverse shear stiffness* instead of the *nominal transverse shear stiffness*, without SCF.

The present approach is analogous to Qi and Knight's ([15,16]) treatment of effective transverse shear strain, which takes the form

$$\bar{\gamma}_{xz} = \frac{\langle\sigma_{xz}\gamma_{xz}\rangle}{\langle\sigma_{xz}\rangle} = \frac{\langle H_\sigma H_\gamma\rangle}{\langle H_\sigma\rangle}\phi_{xz}, \quad \gamma_{xz} \equiv H_\gamma(z)\phi_{xz} \tag{44}$$

However, their approach was limited by the one-dimensional case. The transverse shear stress and strain distribution shape function H_σ, H_γ could not be calculated by such a manner, especially for the angle-ply laminated plates that include the transverse shear coupling. The present approach does not require the shear correction factors, and can also be applied for general lamination configuration.

5 Numerical Results and Discussion

To examine the accuracy of the present theory, a simply supported laminated plate has been considered. The exact solution for bending problem of cross-ply laminated plates and sandwich plates proposed by Pagano ([25]) is used as the benchmark solution for the present theory, and the results presented herein labeled as "exact" generated from his equations.

The ply material properties in cross-ply laminated plates are given as

$$E_L = 25 \times 10^6 \text{ psi}, \quad E_T = 1.0 \times 10^6 \text{ psi},$$

$$G_{LT} = 0.5 \times 10^6 \text{ psi}, \quad G_{TT} = 0.2 \times 10^6 \text{ psi},$$

$$\nu_{LT} = \nu_{TT} = 0.25, \tag{45}$$

where L denotes a fiber direction and T denotes a perpendicular direction to the fiber. For a sandwich plate, the material properties of face sheet are given by Eq. (45), and the core material properties are taken as

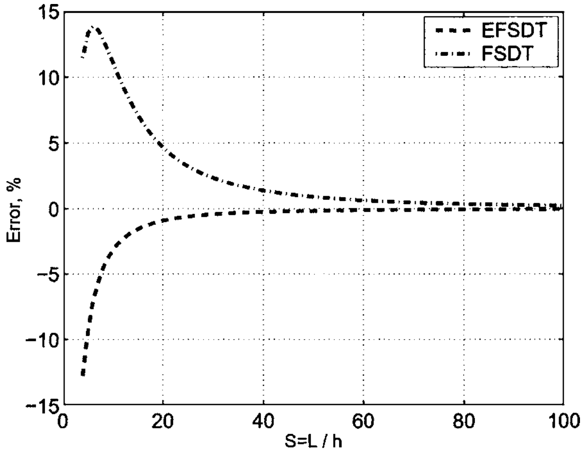

Fig. 2 Transverse displacement error for [0°/90°/0°] laminated plate

$$E_x = 0.145 \times 10^5 \text{ psi}, \quad E_y = E_x,$$

$$G_{xz} = 0.58 \times 10^4 \text{ psi}, \quad G_{yz} = G_{xy} = G_{xz}, \quad \nu_{xy} = 0.25. \quad (46)$$

We have chosen to present most of our results for the length-to-thickness ratio, L_1/h, values of 4 and 20, which are selected for laminated plates and sandwich plates, respectively. We also look at the plate transverse displacement as a function of L_1/h.

Non-dimensionalized displacement and stresses reported in Figs. 2–12 are defined by

$$\bar{u}_\alpha = \frac{E_T u_\alpha}{p_o h S^3}, \quad \bar{u}_3 = \frac{100 E_T u_3}{p_o h S^4}, \quad \bar{\sigma}_{\alpha\beta} = \frac{\sigma_{\alpha\beta}}{p_o S^2}, \quad \bar{\sigma}_{3\alpha} = \frac{\sigma_{3\alpha}}{p_o S},$$

$$S \equiv \frac{L_1}{h}, \quad (47)$$

where $\overline{(\;)}$ denotes the normalized quantities. The through-the-thickness distributions of in-plane displacement, in-plane stresses, and transverse shear stresses are evaluated at which their maximum occurs.

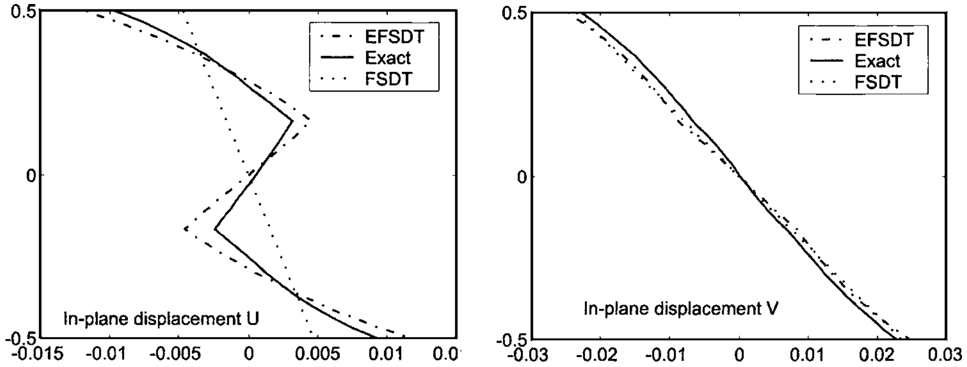

Fig. 3 In-plane displacements for [0°/90°/0°] laminated plate

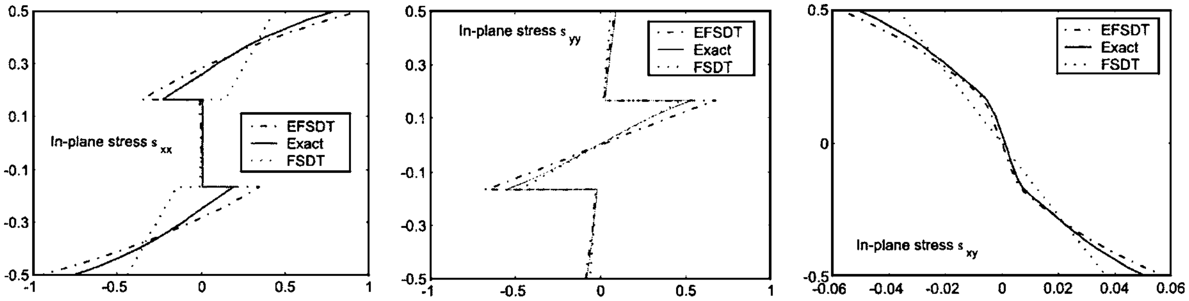

Fig. 4 In-plane stresses for [0°/90°/0°] laminated plate

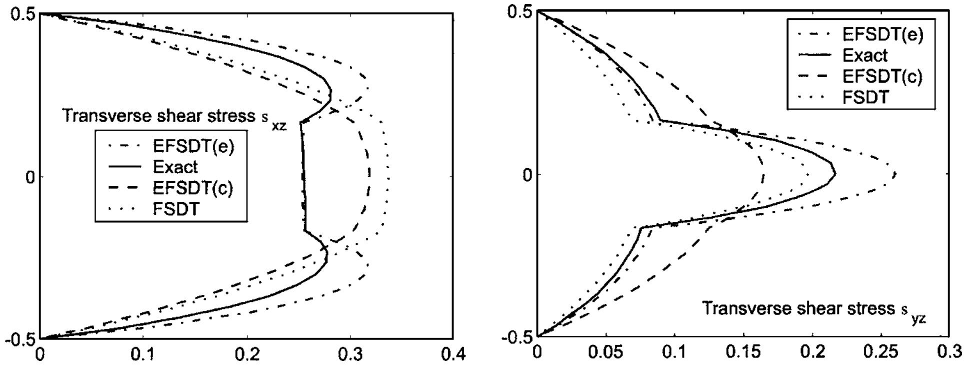

Fig. 5 Transverse shear stresses for [0°/90°/0°] laminated plate

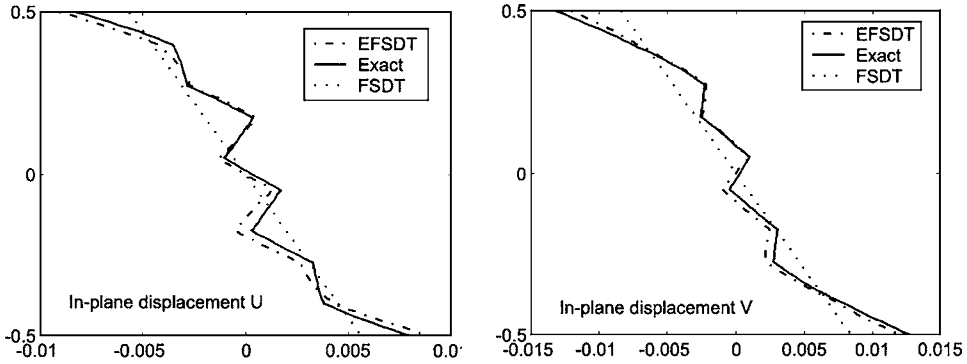

Fig. 6 In-plane displacements for $[0°/90°/0°/90°/0°]_s$ laminated plate

The calculated results are compared to the elasticity solutions. For all the problems, a simply supported boundary condition is applied. The transverse load is assumed to have the form

$$p(x_\alpha,0.5h) = p_o \sin\left(\frac{\pi x_1}{L_1}\right)\sin\left(\frac{\pi x_2}{L_2}\right). \tag{48}$$

The following three cases are considered to demonstrate the accuracy of the present theory.

- Case 1: A three-layered symmetric cross-ply [0°/90°/0°] square plate. Each layer has the same thickness $h/3$ [25].
- Case 2: A nine-layered symmetric cross-ply $[0°/90°/0°/90°/0°]_s$ square plate [26].
- Case 3: A sandwich [0°/Core/0°] square plate [27]. The thickness of each face sheet is equal to $h/10$.

In all the results below, solid lines represent the exact solution, while dashed lines represent the present enhanced first-order shear deformation theory (EFSDT) results. Results from Reissner-Mindlin's FSDT with SCF of 5/6 are shown in dash-dotted line. Transverse shear stresses by FSDT are obtained from the equilibrium equations through integration of the in-plane stresses. We present the transverse shear stresses from the present EFSDT by two different ways that are the constitutive and equilibrium approaches, denoted by (c) and (e), respectively.

5.1 Comparison of Shear Correction Factor (SCF). There are two ways to obtain the shear correction factor. Whitney [13,14] calculated the SCF using the closed form solution for the cylindrical bending problem. Noor and Burton [17] obtained the SCF by an iterative manner. In any case, the SCF is obtained through the comparison between the transverse shear strain energies that are estimated by constitutive and equilibrium equations. Their results are quite good for cross-ply laminated and sandwich plates, as presented in Ref. [28]. However, it is not natural to apply these methods to general layup configurations.

The present EFSDT does not require shear correction factor explicitly and the conventional "equivalent" shear correction factors can be defined from the present EFSDT as follows:

$$k_\alpha^2 \equiv G_{\alpha 3\alpha 3}/\bar{G}_{\alpha 3\alpha 3}, \quad k_3^2 \equiv G_{1323}/\bar{G}_{1323}, \tag{49}$$

where $\overline{(\ )}$ denotes the nominal shear stiffness, and k_3^2 represents

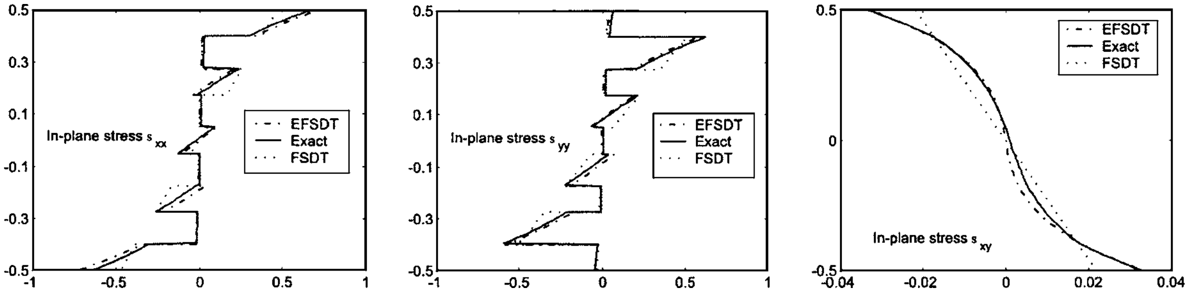

Fig. 7 In-plane stresses for $[0°/90°/0°/90°/0°]_s$ laminated plate

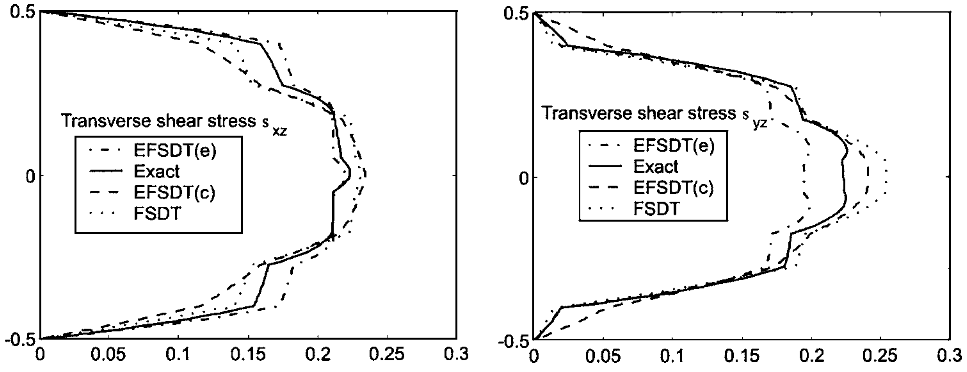

Fig. 8 Transverse shear stresses for $[0°/90°/0°/90°/0°]_s$ laminated plate

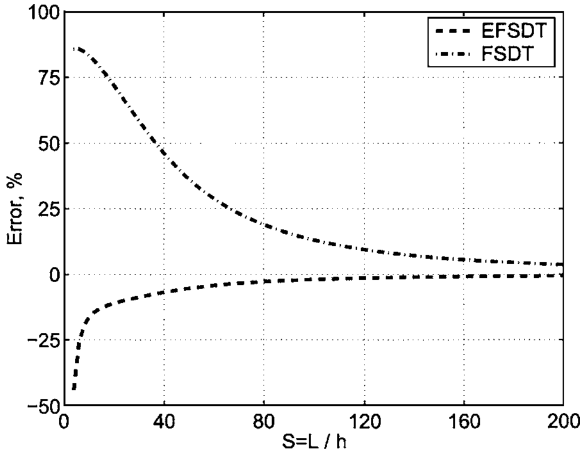

Fig. 9 Transverse displacement error for [0°/Core/0°] sandwich plate

the SCF due to the transverse shear coupling.

Shear correction factors obtained from present theory for three-layered laminated plates and sandwich plates are compared in Table 1 with the results obtained by the methods of Whitney and Noor and Burton [14,17]. The SCF obtained from present theory shows a good agreement with the others for each case. In three-layer laminated plate case, the shear correction factor is close to SCF of 5/6 for isotropic material. However, it is significantly changed in the sandwich plate. The difference between SCF presented in Table 1 and a typical value of 5/6 is about 90%. Therefore, an appropriate transverse shear stiffness is required to estimate an accurate global response, such as deflection, particularly for a sandwich plate that experiences a significant shear deformation due to core material.

5.2 Displacement and Stress Distributions in Cross-Ply Laminated Plates. Results for the three-layered laminated plate with $S=4$ are shown in Figs. 2–5. The transverse displacement of the plate reference surface as a function of length-to-thickness ratio $S=L_1/h$ is presented in Fig. 2. The percentage error of FSDT and EFSDT solution with respect to the exact solution are shown. Results from EFSDT solution converge rapidly to those of the

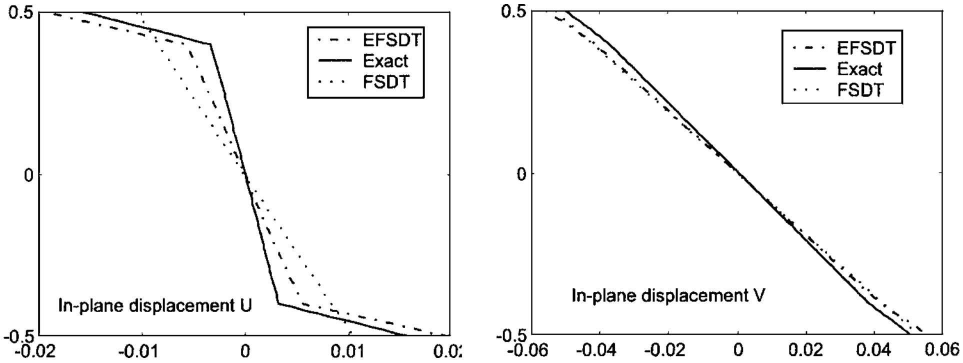

Fig. 10 In-plane displacements for [0°/Core/0°] sandwich plate

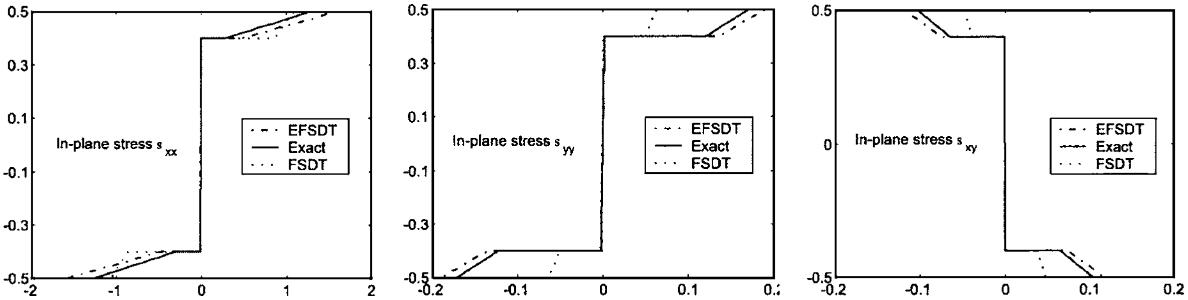

Fig. 11 In-plane stresses for [0°/Core/0°] sandwich plate

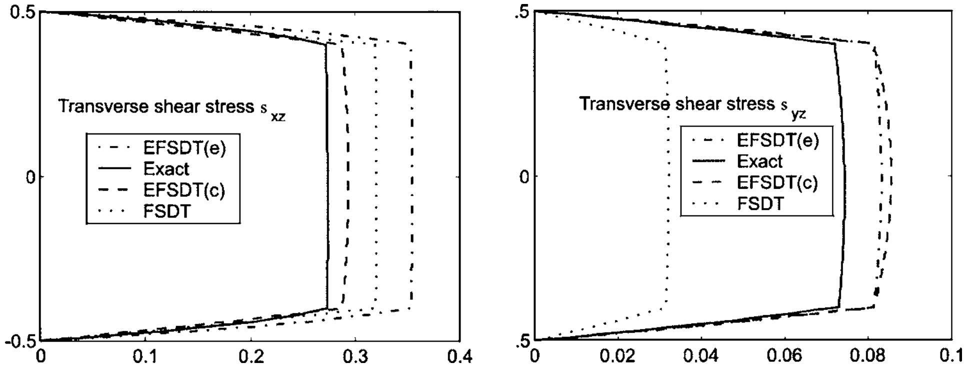

Fig. 12 Transverse shear stresses for [0°/Core/0°] sandwich plate

Table 1 Comparison of shear correction factor

	Three layer			Sandwich		
SCF	Whitney	Noor and Burton	Present	Whitney	Noor and Burton	Present
k_1^2	0.582 78	0.579 92	0.557 33	0.056 545	0.056 496	0.049 62
k_2^2	0.802 78	0.865 00	0.855 37	0.131 918	0.131 808	0.115 85

exact for thin plates, while FSDT solution converge slowly to the exact solution as the thickness becomes smaller. The difference between EFSDT and FSDT is very small, over $S=40-100$, but rapidly grows up as length-to-thickness ratio approaches $S=4$.

Figures 3 and 4 show the through-the-thickness variation of non-dimensionalized in-plane displacements and stresses, respectively. It is observed that the present results for $\bar{u}_\alpha$ and $\bar{\sigma}_{\alpha\beta}$ are in good agreement with the exact solution for thick plate with $S=4$. The nonlinear through-the-thickness distributions of $\bar{u}_1$ and $\bar{\sigma}_{11}$ with slope discontinuities at interfaces have been very well captured by the present EFSDT. The transverse shear stresses are presented in Fig. 5. The direct constitutive approach yields comparatively less accurate shear distribution, but predicts the qualitative through-the-thickness distribution quite accurately. It is shown that present EFSDT is capable of producing good transverse shear stresses using constitutive equations. But, as expected, the equilibrium approach gives much better results. The constitutive approach is, however, more attractive because the equilibrium approach requires the higher derivatives of deflection $\bar{u}_3^o$ that causes a numerical problem in practice [28].

Results for the nine-layered laminated plate with $S=4$ are shown in Figs. 6–8. Results from EFSDT in this example show more close to exact solution than those in previous example. Once more, Fig. 8 shows reasonable agreement by transverse shear stress calculated by the present theory using constitutive relations and the exact solution. The constitutive approach in EFSDT produces even better results than the equilibrium approach in FSDT in predicting the maximum shear stress.

5.3 Displacement and Stress Distributions in a Sandwich Plate. In order to study a significant transverse shear deformation effect, a simply supported [0°/Core/0°] sandwich plate with the thickness of each face sheet equal to $h/10$ is considered (Case 3). The percentage error of non-dimensionalized transverse displacement is shown in Fig. 9. The results from EFSDT clearly indicate that the percentage error with respect to the exact solution in predicting the transverse displacement is much less than in the case of FSDT. For a moderately thick sandwich plate with $S=20$, the deflection error of EFSDT is 11.0% while that of FSDT shows a significant deviation of 71.9% from the exact solution. Even for a very thin plate with $S=200$, the transverse displacement error of FSDT shows a deviation of 3.7%.

For the length-to-thickness ratio of $S=20$, in-plane displacements and stresses are presented in Figs. 10 and 11, and results are also compared with the exact and FSDT solutions. The slope discontinuities of in-plane displacement at interface are well predicted by present EFSDT. In the in-plane stress distributions the present results are in good agreement with those of the exact solution. It is shown that the predicted in-plane stresses using FSDT are very poor, especially for σ_{22}. The transverse shear stresses of sandwich plate with $S=20$ are shown in Fig. 12. The transverse shear stress σ_{23} is severely underestimated by FSDT. It is observed that the constitutive approach gives better results than the equilibrium approach in EFSDT, which results from inaccurate in-plane warping function W_α.

For an accurate prediction of the transverse shear stresses in sandwich plates, it is required to utilize more accurate refined displacement field of higher order theory rather than EHOPT, which may require the effect of transverse normal deformation. However, the present theory has a merit in that it always gives better results than the FSDT while it retains the same computational cost.

6 Conclusions

An enhanced first order shear deformation theory, we call it EFSDT, is developed, which is based on the weighted least-square approximation for three-dimensional in-plane strain fields. The appropriate two-dimensional stiffness model for the laminated plates is derived from a three-dimensional theory through a systematic approach. It is shown that the definition for displacement variables of traditional FSDT ([1]) can be derived from the condition that in-plane strains of FSDT approximate those of a three-dimensional theory in the least-square sense. From this condition, the relationship between variables of FSDT and a three-dimensional theory is constructed, which yields the *effective transverse shear stiffness* and recovering relationships from two-dimensional FSDT displacement to three-dimensional one.

The averaged displacement fields are the same as those of FSDT. Thus the present theory preserves the computational advantage of FSDT while allowing for important local through-the-thickness variations of displacements and stresses. An efficient higher order theory (EHOPT) is utilized to obtain the in-plane warping function, but the proposed approach can also be applied to any higher order theories.

The accuracy, applicability, and robustness of the present theory have been demonstrated by obtaining an analytical solution for simply supported laminated plates and sandwich plates and comparing the results with the 3D exact solution and the FSDT solution with SCF of $5/6$. The accuracy level increases drastically with the increase of length-to-thickness ratio. The transverse shear stress in a sandwich plate, however, is not as accurately predicted as that of composite laminates although it is better than FSDT. The error is due to the inaccurate in-plane warping function and the neglect of out-of-plane warping effect affect, the *effective transverse shear stiffness*.

Work is in progress to extend the present theory to the dynamics and more general classes of laminated plates.

References

[1] Reissner, E., 1950, "On a Variational Theorem in Elasticity," J. Math. Phys. (Cambridge, Mass.), **29**, pp. 90–95.

[2] Mindlin, R. D., 1951, "Influence of Rotary Inertia and Shear on Flexural Motions of Isotropic, Elastic Plates," ASME J. Appl. Mech., **18**, pp. 31–38.

[3] Lo, K. H., Christensen, R. M., and Wu, F. M., 1977, "A Higher-Order Theory of Plate Deformation Part 2: Laminated Plates," ASME J. Appl. Mech., **44**, pp. 669–676.

[4] Levinson, M., 1980, "An Accurate Simple Theory of the Statics and Dynamics of Elastic Plates," Mech. Res. Commun., **7**, pp. 343–350.

[5] Reddy, J. N., 1984, "A Simple Higher-Order Theory for Laminated Composite Plates," ASME J. Appl. Mech., **51**, pp. 745–752.

[6] Reddy, J. N., 1987, "A Generalization of Two-Dimensional Theories of Laminated Plates," Commun. Appl. Numer. Methods, **3**, pp. 173–180.

[7] Di Sciuva, M., 1986, "Vibration and Buckling of Simply Supported Thick Multilayered Orthotropic Plates: An Evaluation of a New Displacement Model," J. Sound Vib., **105**, pp. 425–442.

[8] Cho, M., and Parmerter, R. R., 1992, "An Efficient Higher Order Plate Theory for Laminated Composites," Compos. Struct., **20**, pp. 113–123.

[9] Cho, M., and Parmerter, R. R., 1993, "Efficient Higher Order Composite Plate Theory for General Lamination Configurations," AIAA J., **31**, pp. 1299–1306.

[10] Noor, A. K., and Burton, W. S., 1989, "Assessment of Shear Deformation Theories for Multilayered Composite Plates," Appl. Mech. Rev., **42**, pp. 1–13.

[11] Kapania, R. K., and Raciti, S., 1989, "Recent Advances in Analysis of Lami-

nated Beams and Plates," AIAA J., **27**, pp. 923–946.

[12] Reddy, J. N., and Robbins, Jr., D. H., 1994, "Theories and Computational Models for Composite Laminates," Appl. Mech. Rev., **47**, pp. 147–169.

[13] Whitney, J. M., 1972, "Stress Analysis of Thick Laminated Composites and Sandwich Plates," J. Compos. Mater., **6**, pp. 426–440.

[14] Whitney, J. M., 1973, "Shear Correction Factors for Orthotropic Laminates Under Static Load," ASME J. Appl. Mech., **40**, pp. 302–304.

[15] Qi, Y., and Knight, Jr., N. F., 1996, "A Refined First-Order Shear-Deformation Theory and Its Justification by Plate-Strain Bending Problem of Laminated Plates," Int. J. Solids Struct., **33**, pp. 49–64.

[16] Knight, Jr., N. F., and Qi, Y., 1997, "Restatement of First-Order Shear-Deformation Theory for Laminated Plates," Int. J. Solids Struct., **34**(4), pp. 481–492.

[17] Noor, A. K., and Burton, W. S., 1990, "Stress and Free Vibration Analysis of Multilayered Composite Plates," Compos. Struct., **14**, pp. 233–265.

[18] Cho, M., and Kim, J.-H., 1996, "Postprocess Method Using Displacement Field of Higher Order Laminated Composite Plate Theory," AIAA J., **34**, pp. 362–368.

[19] Cho, M., and Choi, Y. J., 2001, "A New Postprocessing Method for Laminated Composites of General Lamination Configurations," Compos. Struct., **54**, pp. 397–406.

[20] Hodges, D. H., Lee, B. W., and Atilgan, A. R., 1993, "Application of the Variational-Asymptotic Method to Laminated Composite Plates," AIAA J., **31**, pp. 1674–1683.

[21] Berdichevsky, V. L., 1979, "Variational-Asymptotic Method of Construction a Theory of Shell," PMM, **43**, pp. 664–687.

[22] Sutyrin, V. G., 1997, "Derivation of Plate Theory Accounting Asymptotically Correct Shear Deformation," ASME J. Appl. Mech., **64**, pp. 905–915.

[23] Dauge, M., and Gruais, I., 1996, "Asymptotics of Arbitrary Order for a Thin Elastic Clamped Plate, I. Optimal Error Estimates," Asymptotic Anal., **13**, pp. 167–197.

[24] Reddy, J. N., 1997, *Mechanics of Laminated Composite Plates, Theory and Analysis*, CRC, Boca Raton, FL.

[25] Pagano, N. J., 1970, "Exact Solutions for Rectangular Bidirectional Composites and Sandwich Plates," J. Compos. Mater., **3**, pp. 398–441.

[26] Pagano, N. J., 1972, "Elastic Behavior of Multilayered Bidirectional Composites," AIAA J., **10**, pp. 931–933.

[27] Rao, K. M., and Meyer-Piening, H.-R., 1991, "Analysis of Sandwich Plates Using a Hybrid-Stress Finite Element," AIAA J., **29**, pp. 1498–1506.

[28] Cho, M., and Kim, J.-S., 1997, "Improved Mindlin Plate Stress Analysis for Laminated Composites in Finite Element Method," AIAA J., **35**, pp. 587–590.

Wrinkling of Wide Sandwich Panels/Beams With Orthotropic Phases by an Elasticity Approach

G. A. Kardomateas
Professor of Aerospace Engineering
Fellow ASME
Georgia Institute of Technology,
Atlanta, GA 30332-0150

There exist many formulas for the critical compression of sandwich plates, each based on a specific set of assumptions and a specific plate or beam model. It is not easy to determine the accuracy and range of validity of these rather simple formulas unless an elasticity solution exists. In this paper, we present an elasticity solution to the problem of buckling of sandwich beams or wide sandwich panels subjected to axially compressive loading (along the short side). The emphasis on this study is on the wrinkling (multi-wave) mode. The sandwich section is symmetric and all constituent phases, i.e., the facings and the core, are assumed to be orthotropic. First, the pre-buckling elasticity solution for the compressed sandwich structure is derived. Subsequently, the buckling problem is formulated as an eigen-boundary-value problem for differential equations, with the axial load being the eigenvalue. For a given configuration, two cases, namely symmetric and anti-symmetric buckling, are considered separately, and the one that dominates is accordingly determined. The complication in the sandwich construction arises due to the existence of additional "internal" conditions at the face sheet/core interfaces. Results are produced first for isotropic phases (for which the simple formulas in the literature hold) and for different ratios of face-sheet vs core modulus and face-sheet vs core thickness. The results are compared with the different wrinkling formulas in the literature, as well as with the Euler buckling load and the Euler buckling load with transverse shear correction. Subsequently, results are produced for one or both phases being orthotropic, namely a typical sandwich made of glass/polyester or graphite/epoxy faces and polymeric foam or glass/phenolic honeycomb core. The solution presented herein provides a means of accurately assessing the limitations of simplifying analyses in predicting wrinkling and global buckling in wide sandwich panels/beams.

[DOI: 10.1115/1.1978919]

1 Introduction

The compressive strength of thin sheets can be realized only if they are stabilized against buckling. In sandwich construction, two such sheets (face-sheets) are bonded to a core slab of different (light) material. Both the core and the face-sheets can be isotropic or anisotropic.

Panels of this construction give rise to a set of problems of strength, stiffness, and stability analogous to, but by no means identical with, the well-known problems of ordinary homogeneous elastic beam/plates. One of these is "cylindrical buckling." Referring to Fig. 1, the panel is so wide that lines along the y axis can be taken as uncarved. Therefore, a unit width can be treated as an Euler column. Buckling is either like column buckling (Euler buckling) or a short wave "wrinkling" of the face sheets. In the former, the core may exhibit a substantial shearing deformation; in the latter, it acts like an elastic foundation and the buckling deformation is mainly confined to the layers adjacent to the face sheets.

Wrinkling of a symmetric configuration can occur in a symmetric mode or an antisymmetric one (Fig. 2). The initial investigations of this mode of buckling were by Hoff and Mautner [1], Goodier and Neou [2] and Gough, Elam, and de Bruyne [3]. Based on these early investigations, a whole chapter is devoted to wrinkling in Allen's book [4]. Recently, interest has also been in wrinkling under biaxial loading (Birman and Bert [5]).

The existence of different wrinkling formulas based on various beam or plate models underscores the need for an elasticity solution, in order to compare the accuracy of the predictions from the simple beam/plate formulas. Elasticity solutions for buckling have become available mainly for the axisymmetric cylindrical shell geometry, due to the availability of three-dimensional elasticity solutions for the pre-buckling state and the ease of formulation afforded by the axisymmetry. In particular, Kardomateas [6] and Kardomateas and Chung [7] formulated and solved the problem for the case of uniform external pressure and orthotropic homogeneous material (a two-dimensional "ring" assumption was made in the first paper). Homogeneous cylindrical shells under axial compression were studied by Kardomateas [8,9] and by Soldatos and Ye [10] for combined axial compression and uniform external pressure (the latter was based on a successive approximation method).

As far as sandwich structures, a three-dimensional elasticity solution for the buckling of a sandwich long shell under external pressure (again, "ring" assumption) was recently done by Kardomateas and Simitses [11]. In all these studies, a pre-requisite to obtaining elasticity solutions for shell buckling is the existence of three-dimensional elasticity solutions to the pre-buckling problem. For the monolithic homogeneous cylindrical shells, the elasticity solutions for orthotropy provided by Lekhnitskii [12] were used, whereas for the sandwich shells, the elasticity solution of Kardomateas [13] was used.

In this paper we again make the simplifying assumption of a two-dimensional problem by considering a wide plate. Because the plate is wide, lines along the long dimension can be taken as uncurved during buckling and the problem reduces to two-

---

Contributed by the Applied Mechanics Division of THE AMERICAN SOCIETY OF MECHANICAL ENGINEERS for publication in the ASME JOURNAL OF APPLIED MECHANICS. Manuscript received by the Applied Mechanics Division, February 11, 2003; final revision, November 4, 2004. Associate Editor. K. Ravi-Chandar. Discussion on the paper should be addressed to the Editor, Prof. Robert M. McMeeking, Journal of Applied Mechanics, Department of Mechanical and Environmental Engineering, University of California - Santa Barbara, Santa Barbara, CA 93106-5070, and will be accepted until four months after final publication in the paper itself in the ASME JOURNAL OF APPLIED MECHANICS.

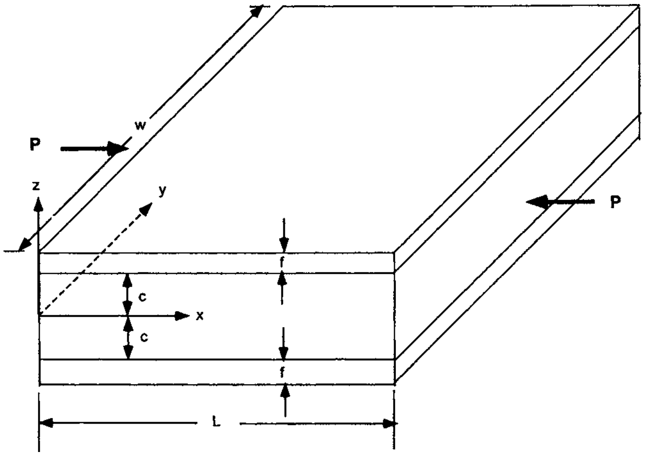

Fig. 1 Definition of the geometry for a sandwich wide panel/ beam under axial compression

dimensional (equivalent to a beam rather than a plate assumption). This assumption would also allow for a direct comparison with the wrinkling formulas that exist in the literature.

In the beginning, the elasticity solution for the pre-buckling state is derived for the case of a sandwich plate with generally orthotropic phases under axial loading. Subsequently, the governing buckling equations along with the corresponding boundary conditions are derived. These reduce to an eigen-boundary value problem for differential equations with the axial load being the eigenvalue. The complication in the sandwich construction arises due to the existence of additional "internal" conditions at the face sheet/core interfaces. The shooting method is used to solve the problem thus formulated.

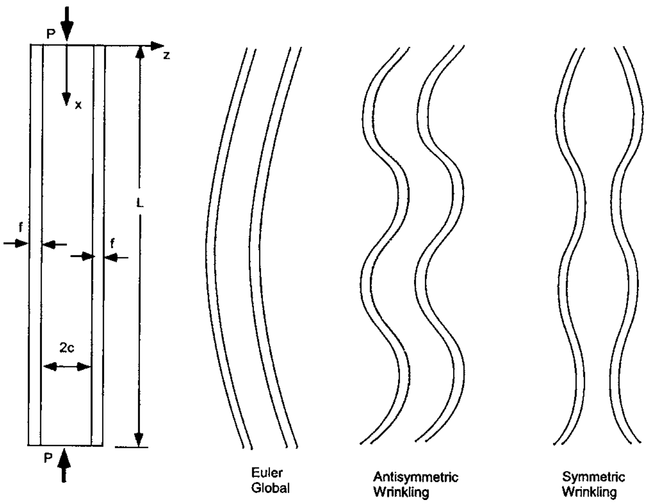

Fig. 2 Buckling modes

2 Formulation

By considering the equations of equilibrium in terms of the second Piola-Kirchhoff stress tensor, subtracting these at the perturbed and initial conditions, and making order of magnitude assumptions on the products of stresses and strains/rotations, based on the fact that a characteristic feature of stability problems is the shift from positions with small rotations to positions with rotations substantially exceeding the strains, the buckling equations for a Cartesian coordinate system can be obtained (Novozhilov [14]):

$$\frac{\partial}{\partial x}(\sigma_{xx} - \tau^0_{xy}\omega_z + \tau^0_{xz}\omega_y) + \frac{\partial}{\partial y}(\tau_{xy} - \sigma^0_{yy}\omega_z + \tau^0_{yz}\omega_y) + \frac{\partial}{\partial z}(\tau_{xz} + \sigma^0_{zz}\omega_y - \tau^0_{yz}\omega_z) = 0, \qquad (1a)$$

$$\frac{\partial}{\partial x}(\tau_{xy} + \sigma^0_{xx}\omega_z - \tau^0_{xz}\omega_x) + \frac{\partial}{\partial y}(\sigma_{yy} - \tau^0_{yz}\omega_x + \tau^0_{xy}\omega_z) + \frac{\partial}{\partial z}(\tau_{yz} - \sigma^0_{zz}\omega_x + \tau^0_{xz}\omega_z) = 0, \qquad (1b)$$

$$\frac{\partial}{\partial x}(\tau_{xz} - \sigma^0_{xx}\omega_y + \tau^0_{xy}\omega_x) + \frac{\partial}{\partial y}(\tau_{yz} + \sigma^0_{yy}\omega_x - \tau^0_{xy}\omega_y) + \frac{\partial}{\partial z}(\sigma_{zz} - \tau^0_{xz}\omega_y + \tau^0_{yz}\omega_x) = 0. \qquad (1c)$$

In the previous equations, σ^0_{ij} are the values of stresses at the initial equilibrium position (pre-buckling state), and σ_{ij} and ω_j are the values of stresses and rotations at the perturbed position (buckled state).

The boundary conditions associated with Eq. (1) can be obtained from the traction (stress resultant) relationships in terms of the second Piola-Kirchhoff stress tensor, and in the general case of an external hydrostatic pressure loading (in which case the magnitude of the surface load remains invariant under deformation, but its direction changes). By writing these equations for the initial and the perturbed equilibrium position and then subtracting them and using the previous arguments on the relative magnitudes of the rotations, the following boundary conditions on a surface which has outward unit normal $(\hat{l},\hat{m},\hat{n})$ and is under the action of a hydrostatic pressure, p, are obtained [14]:

$$(\sigma_{xx} - \tau^0_{xy}\omega_z + \tau^0_{xz}\omega_y)\hat{l} + (\tau_{xy} - \sigma^0_{yy}\omega_z + \tau^0_{yz}\omega_y)\hat{m} + (\tau_{xz} + \sigma^0_{zz}\omega_y - \tau^0_{yz}\omega_z)\hat{n} = p(\omega_z\hat{m} - \omega_y\hat{n}), \qquad (2a)$$

$$(\tau_{xy} + \sigma^0_{xx}\omega_z - \tau^0_{xz}\omega_x)\hat{l} + (\sigma_{yy} - \tau^0_{yz}\omega_x + \tau^0_{xy}\omega_z)\hat{m} + (\tau_{yz} - \sigma^0_{zz}\omega_x + \tau^0_{xz}\omega_z)\hat{n} = p(\omega_x\hat{n} - \omega_z\hat{l}), \qquad (2b)$$

$$(\tau_{xz} - \sigma^0_{xx}\omega_y + \tau^0_{xy}\omega_x)\hat{l} + (\tau_{yz} + \sigma^0_{yy}\omega_x - \tau^0_{xy}\omega_y)\hat{m} + (\sigma_{zz} - \tau^0_{xz}\omega_y + \tau^0_{yz}\omega_x)\hat{n} = p(\omega_y\hat{l} - \omega_x\hat{m}). \qquad (2c)$$

For the bounding surfaces, $\hat{l}=\hat{m}=0$ and $\hat{n}=\pm 1$. These conditions will also be used when we impose traction continuity at the core/face sheet interfaces.

2.1 Pre-buckling State. Let us assume general orthotropy for the face sheet, $i=f$, or the core, $i=c$:

$$\begin{bmatrix} \sigma^{(i)}_{xx} \\ \sigma^{(i)}_{yy} \\ \sigma^{(i)}_{zz} \\ \tau^{(i)}_{yz} \\ \tau^{(i)}_{xz} \\ \tau^{(i)}_{xy} \end{bmatrix} = \begin{bmatrix} c^i_{11} & c^i_{12} & c^i_{13} & 0 & 0 & 0 \\ c^i_{12} & c^i_{22} & c^i_{23} & 0 & 0 & 0 \\ c^i_{13} & c^i_{23} & c^i_{33} & 0 & 0 & 0 \\ 0 & 0 & 0 & c^i_{44} & 0 & 0 \\ 0 & 0 & 0 & 0 & c^i_{55} & 0 \\ 0 & 0 & 0 & 0 & 0 & c^i_{66} \end{bmatrix} \begin{bmatrix} \epsilon^{(i)}_{xx} \\ \epsilon^{(i)}_{yy} \\ \epsilon^{(i)}_{zz} \\ \gamma^{(i)}_{yz} \\ \gamma^{(i)}_{xz} \\ \gamma^{(i)}_{xy} \end{bmatrix} \quad (i=f,c) \qquad (3)$$

where c^i_{kl} are the stiffness constants (we have used the notation $1\equiv x, 2\equiv y, 3\equiv z$, see Fig. 1).

Assuming a pre-buckling displacement field in the form:

$$u_0 = Pd_1x; \quad v_0 = Pd_2y; \quad w_0 = P\left(d_3\frac{z^3}{3} + d_4z\right), \qquad (4a)$$

would satisfy the displacement continuity conditions at face-sheet/ core interfaces and the symmetry conditions.

Substituting into the strain-displacement and then stress-strain relations (3), leads to zero shear strains and stresses:

$$\tau^0_{xy}=\tau^0_{xz}=\tau^0_{yz}=0, \tag{4b}$$

and normal pre-buckling stresses in the form (for $i=f,c$):

$$\sigma^{0(i)}_{xx}=P[c^i_{11}d_1+c^i_{12}d_2+c^i_{13}(d_3z^2+d_4)], \tag{4c}$$

$$\sigma^{0(i)}_{yy}=P[c^i_{12}d_1+c^i_{22}d_2+c^i_{23}(d_3z^2+d_4)], \tag{4d}$$

$$\sigma^{0(i)}_{zz}=P[c^i_{13}d_1+c^i_{23}d_2+c^i_{33}(d_3z^2+d_4)]. \tag{4e}$$

Notice that it is easily seen that the stresses in Eqs. (4*b*)–(4*e*) produce no resultant moment. The constants d_1,d_2,d_3, and d_4 can be found as follows.

First, the condition of zero tractions at the bounding surfaces, $\sigma_{zz}=0$, i.e., at $z=\pm(c+f)$, gives

$$c^f_{13}d_1+c^f_{23}d_2+c^f_{33}[d_3(c+f)^2+d_4]=0. \tag{4f}$$

Second, the condition of zero resultant force on the bounding sides normal to the y axis, $\int\sigma_{yy}wdz=0$, at $y=0,w$, gives

$$\left(c^f_{12}f+c^c_{12}c\right)d_1+\left(c^f_{22}f+c^c_{22}c\right)d_2+\left\{c^f_{23}[(c+f)^3-c^3]+c^c_{23}c^3\right\}\frac{d_3}{3} + \left(c^f_{23}f+c^c_{23}c\right)d_4=0. \tag{4g}$$

Third, the condition of the resultant applied compressive load, P, on the bounding sides normal to the x axis, $\int\sigma_{xx}wdz=-P$, i.e., at $x=0,L$, gives

$$\left(c^f_{11}f+c^c_{11}c\right)d_1+\left(c^f_{12}f+c^c_{12}c\right)d_2+\left\{c^f_{13}[(c+f)^3-c^3]+c^c_{13}c^3\right\}\frac{d_3}{3} + \left(c^f_{13}f+c^c_{13}c\right)d_4=-\frac{1}{2w}. \tag{4h}$$

Finally, traction continuity at the face-sheet/core interface, i.e., at $z=\pm c$, requires $\sigma^c_{zz}=\sigma^f_{zz}$, i.e., the fourth condition:

$$c^f_{13}d_1+c^f_{23}d_2+c^f_{33}(d_3c^2+d_4)=c^c_{13}d_1+c^c_{23}d_2+c^c_{33}(d_3c^2+d_4). \tag{4i}$$

Therefore, there are four linear algebraic equations, Eqs. (4*f*)–(4*i*), which can be used to determine the four unknowns, d_1,d_2,d_3, and d_4.

Notice that if the phases are isotropic, with Young's modulus, E_i and Poisson's ratio ν_i then,

$$c^i_{11}=c^i_{22}=c^i_{33}=\frac{1-\nu_i}{(1-2\nu_i)(1+\nu_i)}E_i, \tag{4j}$$

$$c^i_{12}=c^i_{13}=c^i_{23}=\frac{\nu_i}{(1-2\nu_i)(1+\nu_i)}E_i \tag{4k}$$

2.2 Perturbed State. The buckling equations (1) can be written in terms of the buckling displacemenis u,v, and w by using the strain vs displacement relations:

$$\epsilon_{xx}=u_{,x},\quad \epsilon_{yy}=v_{,y},\quad \epsilon_{zz}=w_{,z}, \tag{5a}$$

$$\gamma_{xy}=u_{,y}+v_{,x},\quad \gamma_{xz}=u_{,z}+w_{,x},\quad \gamma_{yz}=v_{,z}+w_{,y}, \tag{5b}$$

and rotation vs displacement relations:

$$2\omega_x=w_{,y}-v_{,z},\quad 2\omega_y=u_{,z}-w_{,x},\quad 2\omega_z=v_{,x}-u_{,y}, \tag{5c}$$

and then using the stress-strain relations (3). The following three equations are obtained for zero pre-buckling shear stresses. These equations apply at every point through the thickness, but for convenience we have dropped the superscript i,

$$c_{11}u_{,xx}+\left(c_{66}-\frac{\sigma^0_{yy}}{2}\right)u_{,yy}+\left(c_{55}+\frac{\sigma^0_{zz}}{2}\right)u_{,zz}+\left(c_{12}+c_{66}-\frac{\sigma^0_{yy}}{2}\right)v_{,xy} + \left(c_{13}+c_{55}-\frac{\sigma^0_{zz}}{2}\right)w_{,xz}+\frac{\sigma^0_{zz,z}}{2}(u_{,z}-w_{,x})=0, \tag{6a}$$

$$c_{22}v_{,yy}+\left(c_{66}+\frac{\sigma^0_{xx}}{2}\right)v_{,xx}+\left(c_{44}+\frac{\sigma^0_{zz}}{2}\right)v_{,zz}+\left(c_{12}+c_{66}-\frac{\sigma^0_{xx}}{2}\right)u_{,xy} + \left(c_{44}+c_{23}-\frac{\sigma^0_{zz}}{2}\right)w_{,yz}+\frac{\sigma^0_{zz,z}}{2}(v_{,z}-w_{,y})=0, \tag{6b}$$

$$c_{33}w_{,zz}+\left(c_{55}+\frac{\sigma^0_{xx}}{2}\right)w_{,xx}+\left(c_{44}+\frac{\sigma^0_{yy}}{2}\right)w_{,yy}+\left(c_{13}+c_{55}-\frac{\sigma^0_{xx}}{2}\right)u_{,xz} + \left(c_{44}+c_{23}-\frac{\sigma^0_{yy}}{2}\right)v_{,yz}=0. \tag{6c}$$

The corresponding from Eqs. (2*a*)–(2*c*) traction boundary conditions at the bounding surfaces for $\hat{l}=\hat{m}=0$ and $\hat{n}=1$ are

$$\left(c_{55}+\frac{\sigma^0_{zz}}{2}\right)u_{,z}+\left(c_{55}-\frac{\sigma^0_{zz}}{2}\right)w_{,x}=0, \tag{7a}$$

$$\left(c_{44}-\frac{\sigma^0_{zz}}{2}\right)w_{,y}+\left(c_{44}+\frac{\sigma^0_{zz}}{2}\right)v_{,z}=0, \tag{7b}$$

$$c_{13}u_{,x}+c_{23}v_{,y}+c_{33}w_{,z}=0 \tag{7c}$$

In the petrurbed position we seek two-dimensional equilibrium modes as follows:

$$u_i=U_i(z)\cos\lambda x;\quad v_i=0;\quad w_i=W_i(z)\sin\lambda x,\quad \lambda=\frac{m\pi}{L}\quad i=f,c \tag{8}$$

Substituting into Eq. (7), results in the following two linear homogeneous ordinary differential equations of the second order for $U_i(z),W_i(z)$, where $i=c$ for $0\leqslant z\leqslant c$ and $i=f$ for $c\leqslant z\leqslant(c+f)$:

$$\left(c^{(i)}_{55}+\frac{\sigma^{0(i)}_{zz}}{2}\right)U_i''+\frac{\sigma^{0(i)}_{zz,z}}{2}U_i'-c^{(i)}_{11}\lambda^2U_i+\left(c^{(i)}_{13}+c^{(i)}_{55}-\frac{\sigma^{0(i)}_{zz}}{2}\right)\lambda W_i' - \frac{\sigma^{0(i)}_{zz,z}}{2}\lambda W_i=0, \tag{9a}$$

and

$$c^{(i)}_{33}W_i''-\left(c^{(i)}_{55}+\frac{\sigma^{0(i)}_{xx}}{2}\right)\lambda^2W_i-\left(c^{(i)}_{13}+c^{(i)}_{55}-\frac{\sigma^{0(i)}_{xx}}{2}\right)\lambda U_i'=0. \tag{9b}$$

The associated boundary conditions are as follows.

(a) At the bounding surfaces, $z=c+f$, we have the following two traction-free conditions:

$$c^{(f)}_{55}U_f'+c^{(f)}_{55}\lambda W_f=0, \tag{10a}$$

$$c^{(f)}_{33}W_f'-c^{(f)}_{13}\lambda U_f=0 \tag{10b}$$

(b) At the face-sheet/core interface, $z=c$, we have the following four conditions at each of the interfaces.

Displacement continuity:

$$U_f=U_c;\quad W_f=W_c. \tag{10c}$$

Traction continuity:

$$\left(c^{(f)}_{55}+\frac{\sigma^0_{zz}}{2}\right)U_f'+\left(c^{(f)}_{55}-\frac{\sigma^0_{zz}}{2}\right)\lambda W_f = \left(c^{(c)}_{55}+\frac{\sigma^0_{zz}}{2}\right)U_c'+\left(c^{(c)}_{55}-\frac{\sigma^0_{zz}}{2}\right)\lambda W_c, \tag{10d}$$

$$c_{33}^{(f)}W_f' - c_{13}^{(f)}\lambda U_f = c_{33}^{(c)}W_c' - c_{13}^{(c)}\lambda U_c. \qquad (10e)$$

(c) At the axis of symmetry, $z=0$, we have the following conditions.

For symmetric wrinkling:

$$U_c' = W_c = 0, \text{ symmetric wrinkling} \qquad (10f)$$

For antisymmetric wrinkling:

$$U_c = W_c' = 0, \text{ antisymmetric wrinkling} \qquad (10g)$$

Notice that since the construction is assumed to be symmetric, only half of the sandwich needs to be considered.

Solution of the eigen-boundary-value problem for differential equations. Equations (9) and (10) constitute an eigenvalue problem for differential equations, with the axial load, P, the parameter (two point boundary value problem). An important point is that the pre-buckling stresses $\sigma_{jj}^{0(i)}(z)$, depend *linearly* on the applied axial load, P (the parameter), through expressions in the form of Eq. (4) and this makes possible the direct application of standard solution techniques.

With respect to the method used there is a difference between the present problem and the homogeneous orthotropic body (apart from being shell geometry) solved by Kardomateas [6]. The complication in the present problem is due to the fact that the displacement field is continuous but has a slope discontinuity at the face-sheet/core interfaces. This is the reason that the displacement field was not defined as one function but as two distinct functions for $i=f$, and $i=c$, i.e., the face sheet and the core. Our formulation of the problem employs, hence, "internal" boundary conditions at the face-sheet/core interface, as outlined earlier. Due to this complication, the shooting method (Press et al. [15]) was deemed to be the best way to solve this eigen-boundary-value problem for differential equations. A special version of the shooting method was formulated and programmed for this problem. In fact, for each of the two constituent phases of the sandwich structure, we have five variables: $y_1=U_i, y_2=U_i', y_3=W_i, y_4=W_i'$, and $y_5=P$. The five differential equations are: $y_1'=y_2$, the first equilibrium equation (9*a*), $y_3'=y_4$, the second equilibrium equation (9*b*) and $y_5'=0$.

The method starts from the middle of the core, $z=0$ and integrates the five first-order differential equations from $z=0$ to the face-sheet/core interface $z=c$ (i.e., through the core). At the start point, $z=0$, we have three conditions as follows:

(a) for symmetric wrinkling: $U_c'=y_2=0, W_c=y_3=0$ and a third condition of (abritrarily) setting $U_c=y_1=1.0$, therefore we have two freely specifiable variables, the $P=y_5$ and the $W_c'=y_4$.

(b) for antisymmetric wrinkling: $U_c=y_1=0, W_c'=y_4=0$ and a third condition of (abritrarily) setting $W_c=y_3=1.0$, therefore we have two freely specifiable variables, the $P=y_5$ and the $U_c'=y_2$.

The freely specifiable starting values at $z=0$ are taken as the values from the simple plate/beam theory solutions available in the literature (described later).

Once we reach the face-sheet/core interface, $z=c$, the tractions from the core side are calculated; these should equal the tractions from the face-sheet side, according to the internal boundary conditions on the face-sheet/core interface, Eqs. (10*d*) and (10*e*). This allows finding the slopes of the displacements, $y_2=U_f'$ and $y_4=W_f'$ for starting the shooting into the face-sheet [notice that the other three functions, $y_1=U_f, y_3=W_f$ and $y_5=P$ are continuous according to Eq. (10*c*), and their values at $z=c$ have already been found at the end of the integration step through the core]. The next step is integrating the five differential equations from $z=c$ to $z=c+f$, i.e., through the face-sheet. Once the outer bounding surface, $z=c+f$, is reached, the traction boundary conditions, Eqs. (10*a*) and (10*b*), are imposed. Multi-dimensional Newton-Raphson is then used to develop a linear matrix equation for the two increments to the adjustable parameters, which are the y_5 and y_4 at $z=0$ for the case of symmetric wrinkling, and the the y_5 and y_2 at $z=0$ for the case of antisymmetric wrinkling. These increments are solved for and added and the shooting repeats until convergence. For the integration phase, we used a Runge-Kutta driver with adaptive step size control. The method produced results very fast and without any numerical complication.

As has already been stated, in the numerical scheme, the starting point (guess) is one of the simple formulas in the literature; in particular, we have used Allen's [4] solution; therefore, we input the Allen's [4] solution as a guess and then obtain the elasticity solution by the shooting method described; this is done for a range of m's, around Allen's critical m. Therefore, we vary m in the range of ±20 of the Allen's critical m (of course, the lower bound for m is $m=1$) and obtain the corresponding load; the critical m is the one that results in the lowest load (critical value).

Furthermore, for the integration phase we use a Runge-Kutta driver with monitoring of local truncation error to ensure accuracy and adjust step size; the initial step size to be attempted is 1/20th of the corresponding thickness (core or face sheet) and the numerical tolerance is 5×10^{-6}. A finer initial step size or tolerance has indicated absolutely no effect on the solution.

3 Plate/Beam Wrinkling Formulas in the Literature, Results and Discussion

Several formulas can be found in the literature for the critical wrinkling load. Allen's book [4] devotes a whole chapter on the problem. A simple formula can be found in this book for the critical stress for isotropic core and face-sheet. Allen's formula [4] is based on a beam differential equation for the face sheet, assumed to be supported by an elastic medium (the core), which extends infinitely on one side of the beam (hence the face is unaffected by the opposing face):

$$\sigma_{f,cr} = B_1 E_f^{1/3} E_c^{2/3}; \text{ where } B_1 = 3[12(3-\nu_c)^2(1+\nu_c)^2]^{-1/3}, \qquad (11a)$$

$$\left(\frac{m\pi f}{L}\right)_{cr} = \frac{\pi}{C}\left(\frac{E_f}{E_c}\right)^{-1/3}; \quad \text{where } C = \pi[(3-\nu_c)(1+\nu_c)/12]^{1/3}. \qquad (11b)$$

Goodier and Neou [2] give the following formula for isotropic core with $\nu_c=0$ and face-sheet with $\nu_f=1/3$, where $\rho=E_f/E_c$.

$$\frac{\sigma_{f,cr}}{E_f} = 0.655\rho^{-2/3}\left(1 + \frac{0.51\rho^{1/3}+0.32}{\rho^{2/3}+0.39}\right), \quad \text{and } \left(\frac{m\pi f}{2L}\right)_{cr} = 0.726\rho^{-1/3}. \qquad (11c)$$

Hoff and Mautner [1] give the following simple formula:

$$\sigma_{f,cr} = 0.91(E_f E_c G_c)^{1/3}; \quad \left(\frac{m\pi f}{L}\right)_{cr} = \frac{\pi}{1.65}E_f^{-1/3}(E_c G_c)^{1/6}. \qquad (11d)$$

Although variations of this formula can be developed depending on symmetric or antisymmetric cases and also for thinner cores, Hoff and Mautner [1] concluded from their analysis that the very simple formula of Eq. (11*d*) is a conservative estimate of the critical load for all cases.

Although there are other formulas in the literature, such as Plantema's [16], there seem to introduce only small variations and the aforementioned three formulas will be taken herein as representative and compared with. In particular, Plantema's [16] critical load is:

$$\sigma_{f,cr} = \frac{0.825}{\sqrt[3]{1-\nu_f^2}}\sqrt[3]{E_f E_c G_c}. \qquad (11e)$$

Table 1 Critical loads for E_f/E_c=1,000. Loads normalized with the Euler load (w/o shear), Eq. (12*a*) *W*=wrinkling (multi-wave); *GL*=global (Euler).

f/h	$\tilde{P}_{Elast}$ (m) (% difference from elasticity)	$\tilde{P}^{W}_{Allen}$ (m)	$\tilde{P}^{W}_{Goodier}$ (m)	$\tilde{P}^{W}_{Hoff}$ (m)	$\tilde{P}^{GL}_{Allen}$
0.01 Antisymm	0.07381 (24) (W)	0.06724 (25) (−8.9%)	0.07368 (23) (−0.2%)	0.07709 (27) (+4.4%)	0.2021 (+173.8%)
0.02 Antisymm	0.07393 (12) (W)	0.06753 (13) (−8.7%)	0.07400 (12) (+0.1%)	0.07742 (13) (+4.7%)	0.1156 (+56.4%)
0.03 Antisymm	0.07288 (7) (W)	0.06854 (8) (−6.0%)	0.07511 (8) (+3.1%)	0.07859 (9) (+7.8%)	0.08199 (+12.5%)
0.04 Antisymm	0.06489 (1) (GL)	0.06977 (6) (+7.5%)	0.07646 (6) (+17.8%)	0.07999 (7) (+23.3%)	0.06414 (−1.2%)
0.05 Antisymm	0.05411 (1) (GL)	0.07110 (5) (+31.4%)	0.07792 (5) (+44.0%)	0.08152 (5) (+50.7%)	0.05310 (−1.9%)

Table 2 Critical loads for E_f/E_c=500. Loads normalized with the Euler load (w/o shear), Eq. (12*a*) *W*=wrinkling (multi-wave); *GL*=global (Euler).

f/h	$\tilde{P}_{Elast}$ (m) (% difference from elasticity)	$\tilde{P}^{W}_{Allen}$ (m)	$\tilde{P}^{W}_{Goodier}$ (m)	$\tilde{P}^{W}_{Hoff}$ (m)	$\tilde{P}^{GL}_{Allen}$
0.01 Antisymm	0.1222 (30) (W)	0.1100 (32) (−10.0%)	0.1222 (29) (0%)	0.1261 (34) (+3.2%)	0.3302 (+170.2%)
0.02 Antisymm	0.1210 (15) (W)	0.1089 (16) (−10.0%)	0.1210 (15) (0%)	0.1248 (17) (+3.1%)	0.2056 (+69.4%)
0.03 Antisymm	0.1211 (10) (W)	0.1099 (11) (−9.2%)	0.1222 (10) (+0.9%)	0.1261 (11) (+4.1%)	0.1508 (+24.5%)
0.04 Antisymm	0.1188 (6) (W)	0.1116 (8) (−6.1%)	0.1241 (7) (+4.5%)	0.1280 (9) (+7.7%)	0.1201 (+1.1%)
0.05 Antisymm	0.1027 (1) (GL)	0.1136 (6) (+10.6%)	0.1262 (6) (+22.9%)	0.1302 (7) (+26.8%)	0.1006 (−2.0%)

For $\nu_f=0.35$ (the value used for the isotropic results), the factor before the moduli product term becomes 0.862, which, when compared with the value 0.91 of the Hoff and Mautner [1] formula, would give a critical load 5.3% lower. For the orthotropic face sheet with $\nu_f=0.26$, the factor becomes 0.844, which would give a critical load 7.2% lower than the Hoff and Mautner [1] formula.

A few recent related studies will be mentioned at this point. Vonach and Rammerstorfer [17] have also addressed the problem of wrinkling of orthotropic sandwich plates under general loading. They tackle the problem by assuming the core to be infinitely thick and transversely isotropic and the wrinkling wave at the interface between the face sheet and the core to be sinusoidal. Thereafter they are able to solve the governing differential equation (based on plate theory) describing the face sheets deformation. Another related study is that by Grenestedt and Olsson [18], which assumes two layers of different materials attached to a semi-infinite substrate of a third material and treats the problem from an elasticity theory. These studies make in general less restrictive assumptions than the old formulas and utilize more advanced methods of analysis but, nevertheless, they still do not correspond to the configuration of a finitely thick core between two finitely thick face sheets, which is studied in this paper.

As far as global buckling, the Euler load is simply

$$P_{Eul}=\frac{\pi^2(EI)_{eq}}{L^2}\quad (EI)_{eq}=2w\left[E_f\frac{f^3}{12}+E_f f\left(\frac{f}{2}+c\right)^2+E_c\frac{c^3}{3}\right]. \tag{12a}$$

A formula correcting for transverse shear is in Allen's book [4] as follows:

$$P_{gl}=\frac{P_E}{1+[P_E 2c/G_c w(2c+f)^2]};\quad P_E=E_f w f(2c+f)^2\frac{\pi^2}{2L^2}. \tag{12b}$$

Results are produced for the following configuration: $L/h=5$ where $h=2(f+c)$ is the total plate thickness and $f/h=0.01$ to 0.05 (we also assigned the width $w/L=2$).

First, the case of both faces being isotropic, is examined. Therefore, we first consider isotropic phases, $E_f/E_c=1000$ and 500, $\nu_f=0.35$ and $\nu_c=0$.

Table 1 shows the critical load for $E_f/E_c=1{,}000$ and Table 2 for $E_f/E_c=500$. Before discussing the results, it should be noticed that these results have been derived for the isotropic phases with $\nu_c=0$, because this has been historically emphasized.

In general, we can make the following conclusions for the isotropic case:

(1) The Goodier and Neou [2] formula is the most accurate; next in accuracy is Hoff and Mautner [1]. In both cases the accuracy is improved for the thinner face sheets, i.e., for the smaller f/h ratios.
(2) For the cases considered where wrinkling dominates, the Goodier and Neou [2] formula is within 5% of the elasticity value.
(3) For the cases considered, and whenever global buckling dominates, the Allen's global buckling formula [4] which corrects for transverse shear, performs very well, being within 2% of the elasticity critical load.
(4) It is possible that the global buckling load is less than the wrinkling formulas, as in the case of $E_f/E_c=500, f/h=0.04$, in which P^{GL}_{Allen} is less than $P^{W}_{Goodier}$; yet wrinkling dominates according to the elasticity solution. Although the exact mode of buckling may not be the most important issue, this indicates the complexity and the difficulty of drawing the right conclusions when only simple formulas are employed.
(5) Allen's [4] formula is conservative whenever wrinkling dominates. On the contrary, Hoff and Mautner's [1] formula is non-conservative whenever wrinkling dominates. But the amount of non-conservatism is quite moderate.
(6) Whenever global buckling dominates, Allen's [4] formula which corrects the Euler load for transverse shear, is conservative.
(7) Whenever global buckling dominates, the critical load being only 5%–10% of the Euler load (w/o shear) indicates the very strong influence of transverse shear effects on sandwich buckling.
(8) Antisymmetric buckling seems to dominate in the cases considered.

Next, the case of either or both phases being orthotropic is examined.

Table 3 gives results for E-glass/polyester unidirectional facings and R75 cross-linked PVC foam core. E-glass/polyester facings moduli are (in GPa): $E_1^f=40, E_2^f=E_3^f=10, G_{23}^f=3.5, G_{12}^f=G_{31}^f=4.5$; and the facings Poisson's ratios: $\nu_{12}^f=0.26, \nu_{23}^f=0.40$, and $\nu_{31}^f=0.065$. The PVC core is isotropic with modulus $E^c=0.075$ GPa and Poisson's ratio $\nu^c=0.30$.

Since the axial modulus ratio of the facings and the core is close to 500, the results of Table 3 can be compared with the results of Table 1. In Table 3, the facings are orthotropic rather than isotropic and the core, although isotropic, does not have zero Poisson's ratio. We can conclude that:

Table 3 Critical loads for E-glass/polyester faces and PVC/R75 foam core. Loads normalized with the Euler load (w/o shear), Eq. (12*a*) *W*=wrinkling (multi-wave); *GL*=global (Euler)

f/h	$\tilde{P}_{Elast}$ (m)	$\tilde{P}^{W}_{Allen}$ (m)	$\tilde{P}^{W}_{Goodier}$ (m)	$\tilde{P}^{W}_{Hoff}$ (m)	$\tilde{P}^{GL}_{Allen}$
	(% difference from Elasticity)				
0.01 Antisymm	0.1023 (30) (W)	0.09454 (30) (−7.6%)	0.1165 (28) (+13.9%)	0.1103 (32) (+7.8%)	0.2636 (+157.7%)
0.02 Antisymm	0.1012 (15) (W)	0.09375 (15) (−7.4%)	0.1155 (14) (+14.1%)	0.1093 (16) (+8.0%)	0.1576 (+55.7%)
0.03 Antisymm	0.1008 (9) (W)	0.09473 (10) (−6.0%)	0.1167 (9) (+15.8%)	0.1105 (11) (+9.6%)	0.1136 (+12.7%)
0.04 Antisymm	0.09096 (1) (GL)	0.09620 (7) (+5.8%)	0.1185 (7) (+30.3%)	0.1122 (8) (+23.4%)	0.08967 (−1.4%)
0.05 Antisymm	0.07596 (1) (GL)	0.09790 (6) (+28.9%)	0.1206 (6) (+58.8%)	0.1142 (6) (+50.3%)	0.07464 (−1.7%)

(9) The Goodier and Neou [2] formula no longer exhibits the excellent accuracy that was shown in Table 1. Notice, though, that this formula was derived for isotropic phases with $\nu_c=0$. In fact, in Table 3, this formula has the worst performance although in Table 1 it had the best performance whenever wrinkling occurred.
(10) Allen's [4] formula is still conservative whenever wrinkling dominates. On the contrary, all other wrinkling formulas are non-conservative (again, whenever wrinkling dominates).
(11) Global buckling occurs sooner now, even for $f/h=0.04$.
(12) Whenever global buckling dominates, Allen's [4] formula, which corrects the Euler load for transverse shear, is still conservative.

Table 4 gives results for graphite/epoxy unidirectional facings and hexagonal glass/phenolic honeycomb core. The graphite/epoxy facings moduli are (in GPa): $E_1^f=181, E_2^f=E_3^f=10.3, G_{23}^f=5.96, G_{12}^f=G_{31}^f=7.17$; and the facings Poisson's ratios: $\nu_{12}^f=0.28, \nu_{23}^f=0.49$, and $\nu_{31}^f=0.0159$. The honeycomb core moduli are (in GPa): $E_1^c=E_2^c=0.032, E_3^c=0.390, G_{23}^c=G_{31}^c=0.048, G_{12}^c=0.013$; and the core Poisson's ratios: $\nu_{31}^c=\nu_{32}^c=\nu_{21}^c=0.25$.

Table 4 Critical loads for graphite/epoxy faces and glass/phenolic honeycomb core. Loads normalized with the Euler load (w/o shear), Eq. (12*a*) *W*=wrinkling (multi-wave); *GL*=global (Euler).

f/h	$\tilde{P}_{Elast}$ (m)	$\tilde{P}^{W}_{Allen}$ (m)	$\tilde{P}^{W}_{Goodier}$ (m)	$\tilde{P}^{W}_{Hoff}$ (m)	$\tilde{P}^{GL}_{Allen}$
	(% difference from Elasticity)				
0.01 Antisymm	0.07037 (26) (W)	0.01884 (14) (−73.2%)	0.02209 (13) (−68.6%)	0.02196 (15) (−68.8%)	0.03517 (−50.0%)
0.02 Antisymm	0.06552 (1) (GL)	0.01917 (7) (−70.7%)	0.02247 (6) (−65.7%)	0.02234 (7) (−65.9%)	0.01826 (−72.1%)
0.03 Antisymm	0.04576 (1) (GL)	0.01955 (5) (−57.3%)	0.02291 (4) (−49.9%)	0.02278 (5) (−50.2%)	0.01253 (−72.6%)
0.04 Antisymm	0.03577 (1) (GL)	0.01994 (3) (−44.3%)	0.02337 (3) (−34.7%)	0.02324 (4) (−35.0%)	0.00963 (−73.1%)
0.05 Antisymm	0.02988 (1) (GL)	0.02035 (3) (−31.9%)	0.02385 (3) (−20.2%)	0.02372 (3) (−20.6%)	0.00789 (−73.6%)

In this case the axial modulus ratio of the facings and the core is very large, close to 5,000. Notice also that in Table 4 both facings and the core are orthotropic. The results show clearly the inadequacy of the simple wrinkling formulas and even the global buckling formula whenever a strongly orthotropic construction is made. In particular we can conclude that:

(13) Global buckling occurs even sooner now, even for $f/h=0.02$. Actually, only in the $f/h=0.01$ case, wrinkling dominates.
(14) All formulas are strongly conservative. Whenever global buckling dominates, Allen's [4] formula shows a very large degree of conservatism, being almost one quarter of the elasticity critical load. The same is true whenever wrinkling dominates, the wrinkling formulas show a very large degree of conservatism, being almost a quarter of the elasticity critical wrinkling load.

The thickness-wise variation of the displacements has been a matter of great interest. Hoff and Mautner [1] based their analysis on a linear decay of the transverse displacement, $W(z)$, whereas Plantema [16] based his analysis on an exponential decay. Figure 3(*a*) shows the transverse displacement, $W(z)$ and Fig. 3(*b*) shows the axial displacement, $U(z)$, for the two cases of isotropic phases, $f/h=0.02$ and at the critical point. Since the modes are derived by setting the core displacement at the middle, $W_c=1$, the displacements are normalized with the corresponding mid-point ($z=0$) transverse displacement of the core, W_{c0}. We see that the variation is certainly nonlinear through the core in both $W(z)$ and $U(z)$. The $W(z)$ has a high slope gradient near the core mid-line, $z=0$.

Figures 4(*a*) and 4(*b*) show the same displacements for the two cases of orthotropic phases examined and $f/h=0.01$ and at the critical point. Double *y*-axis plots were used in this case because the scales for the two material systems are very much apart. The displacements are again normalized with the corresponding mid-point ($z=0$) transverse displacement of the core, W_{c0}. We see that, again, the variation is nonlinear through the core, in both $W(z)$ and $U(z)$ and the $W(z)$ has again a high slope gradient near the core mid-line, $z=0$. A comparison of the isotropic and the orthotropic plots shows that the nonlinearities are more pronounced in the latter case.

A literature search has not revealed detailed finite element data on the wrinkling of sandwich plates (based on solid elements), which can be used to compare with the present solution. This indicates that there is a need for numerical studies of wrinkling, based on various finite element (or other numerical) formulations. In this regard, the present elasticity solution will serve to compare the accuracy of the various numerical approaches. We can, however, obtain a validation of the solution developed in this paper by comparing with the early buckling experiments performed in 1945 by Hoff and Mautner [1]. In these experiments, the face sheet material was a high strength paper plastic (papreg, isotropic with Young's modulus 3×10^6 lb per in.^{2}). The sandwich specimens had a cellular acetate core, also isotropic with Young's modulus 1,500 lb per in.^{2} (for both the face sheet and the core, the Poisson's ratio used in the analysis was 0.30). The length of all the specimens in the direction of the applied load, L, was 10.5 in. The width of the specimens perpendicular to the direction of the applied load, w, varied as well as the thickness of the face sheet and that of the core. Table 5 shows the critical load, as predicted from Hoff's formula (Eq. (11*d*)) and from the present elasticity formulation for the observed mode of buckling. We can conclude that, in general, the present elasticity solution predicts loads closer to the experimentally measured values. In some cases, where the critical half-wave numbers, m, are high and close to each other, the elasticity and the Hoff's solution do not differ practically (as in the third and fourth cases in Table 5). In other cases, the Hoff's solution would be very non-conservative (as in the fifth and seventh cases in Table 5) and it would predict wrinkling at half-wave

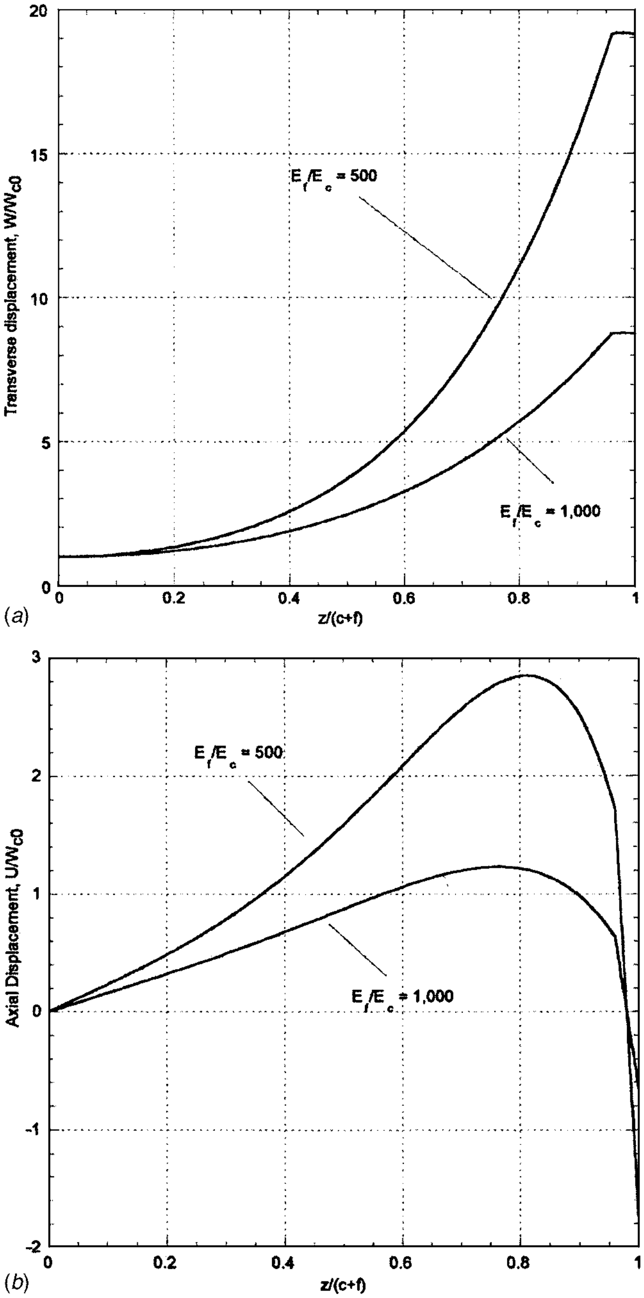

Fig. 3 (*a*) Thickness-wise variation of the transverse displacement, W, for isotropic phases and $f/h=0.02$ (at the critical point). The displacement is normalized with the mid-point ($z=0$) transverse displacement of the core, W_{c0}. (*b*) Thickness-wise variation of the axial displacement, U, for isotropic phases and $f/h=0.02$ (at the critical point). The displacement is normalized with the mid-point ($z=0$) transverse displacement of the core, W_{c0}.

numbers, m, which are much higher than the elasticity solution; the latter being much closer to the experiments. Note that Hoff and Mautner's paper [1] does not report data on the experimental half wave numbers. The data in Table 5 can be considered as offering a validation of the accuracy of the present solution.

The intent of this study was to focus on the wrinkling behavior of sandwich beams (or wide plates), hence the illustrative examples were for very thin facings. Future elasticity studies will focus on the global buckling behavior which is expected to dominate with thicker facings.

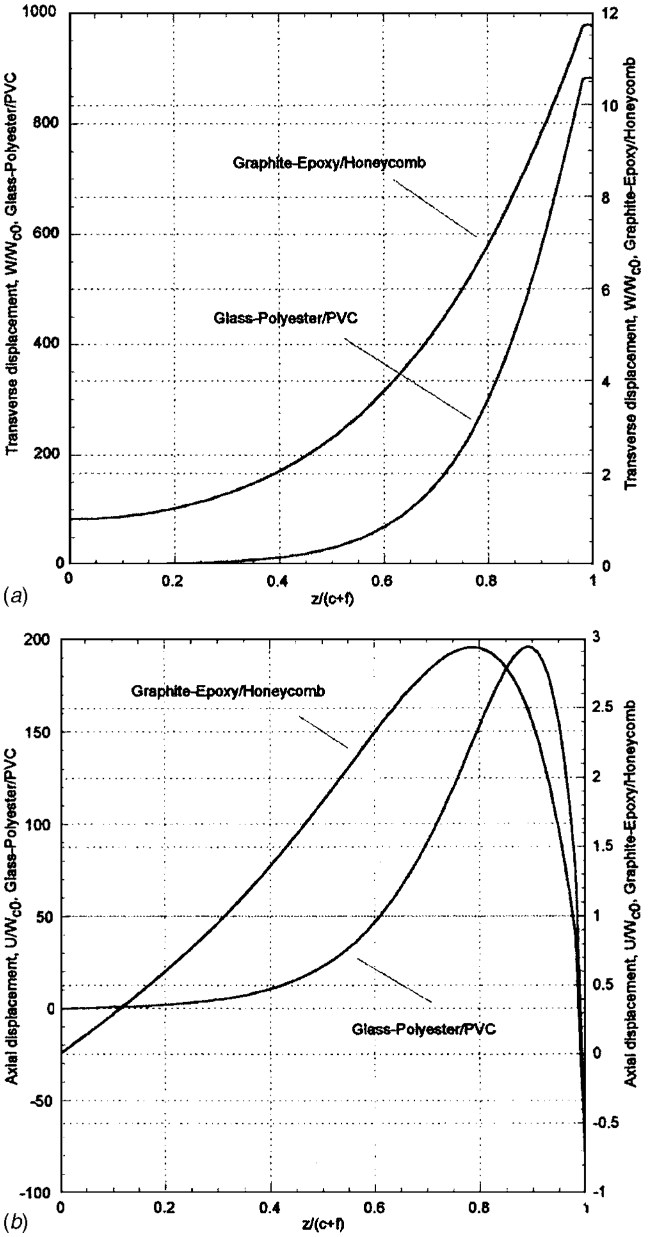

Fig. 4 (*a*) Thickness-wise variation of the transverse displacement, W, for the orthotropic phases examined and $f/h=0.01$ (at the critical point). The displacement is normalized with the corresponding mid-point ($z=0$) transverse displacement of the core, W_{c0}. (*b*) Thickness-wise variation of the axial displacement, U, for the orthotropic phases examined and $f/h=0.01$ (at the critical point). The displacement is normalized with the corresponding mid-point ($z=0$) transverse displacement of the core, W_{c0}.

4 Conclusions

An elasticity solution to the problem of buckling of sandwich beams or wide sandwich panels subjected to axially compressive loading is presented. A symmetric section is considered with all constituent phases, i.e., the facings and the core, being in general orthotropic. For the configurations considered with both phases isotropic, the Goodier and Neou [2] wrinkling formula is the most accurate, next in accuracy being the Hoff and Mautner [1] and in both cases the accuracy improved for the thinner face sheets. Furthermore, whenever wrinkling dominates, Allen's [4] formula is always conservative but the Hoff and Mautner's [1] wrinkling

Table 5 Comparison with experimental data from Hoff and Mautner [1]

Width, thick ness, w (in.)	Face thick ness, f (in.)	Core thick ness, $2c$ (in.)	Observed mode of buckling	Critical load lb from Hoff Eq. (11d) (m)	Critical load lb from present elasticity (m)	Buckling load lb from experiments (Hoff and Mautner [1])
4	0.02025	0.441	Sym	2035.8 (21)	2273.9 (24)	2240
4	0.02025	0.434	Sym	2035.7 (21)	2284.5 (24)	2220
4	0.00675	0.458	Sym	686.4 (64)	690.7 (60)	750
4	0.00675	0.448	Sym	686.1 (64)	690.4 (60)	700
11	0.02025	0.230	Anti-Sym	5584.1 (21)	1079.3 (1)	1600
4	0.01125	0.725	Sym	1143.0 (38)	1150.2 (36)	1455
4	0.01125	0.076	Anti-Sym	1126.8 (38)	435.4 (1)	350

formula is slightly non-conservative. Whenever global buckling dominates, Allen's [4] global buckling formula, which corrects the Euler load for transverse shear, is conservative and moreover, the critical load is only 5%–10% of the Euler load (w/o shear), indicating the very strong influence of transverse shear effects on sandwich buckling. Antisymmetric buckling seems to be dominant in the cases considered. With the ortotropic (rather than isotropic) phases examined, wrinkling is harder to occur, global buckling taking place for even thinner face sheets. But now the accuracy of the simple wrinkling and global buckling formulas is seriously compromised, and there are large deviations from the elasticity solution. In particular, for the graphite/epoxy facings and glass/phenolic honeycomb core, whenever global buckling dominates, Allen's [4] global buckling formula shows a very large degree of conservatism, being almost one quarter of the elasticity critical load. The same is true for this material system whenever wrinkling dominates, the simple wrinkling formulas show a very large degree of conservatism, being almost a quarter of the elasticity critical wrinkling load. In addition, the results show that the variation of both the transverse and axial displacement through the core is nonlinear, more so with the orthotropic phases, and with the transverse displacement exhibiting a high slope gradient near the core mid-line. The solution presented herein provides a means of accurately assessing the limitations of simplifying analyses in predicting wrinkling and global buckling in wide sandwich panels/beams.

Acknowledgment

Financial support of the Office of Naval Research, Ship Structures and Systems, S& T Division, Grant Nos. N00014-90-J-1995 and N00014-0010323, and the interest and encouragement of the Grant Monitor, Dr. Y.D.S. Rajapakse, are both gratefully acknowledged.

References

[1] Hoff, N. J., and Mautner, S. F., 1945, "The Buckling of Sandwich-Type Panels," J. Aeronaut. Sci., **12**, pp. 285–297.

[2] Goodier J. N., and Neou I. M., 1951, "The Evaluation of Theoretical Compression in Sandwich Plates," J. Aeronaut. Sci., **18**, pp. 649–657.

[3] Gough, G. S., Elam, C. F., and de Bruyne, N. A., 1940, "The Stabilization of a Thin Sheet by a Continuous Supporting Medium," J. R. Aeronaut. Soc., **44**, pp. 12–43.

[4] Allen, H. G., 1969, *Analysis and Design of Structural Sandwich Panels*, Pergamon, Oxford, UK, Chap. 8.

[5] Birman, V., and Bert, C. W., 2002, "Wrinkling of Composite-Facing Sandwich Panels Under Biaxial Loading," IMECE 02, the 2002 International Mechanical Engineering Congress & Exposition, November 17–22, New Orleans, LA.

[6] Kardomateas, G. A., 1993, "Buckling of Thick Orthotropic Cylindrical Shells Under External Pressure," ASME J. Appl. Mech., **60**, pp. 195–202.

[7] Kardomateas, G. A., and Chung, C. B., 1994, "Buckling of Thick Orthotropic Cylindrical Shells Under External Pressure Based on Non-Planar Equilibrium Modes," Int. J. Solids Struct. **31**, pp. 2195–2210.

[8] Kardomateas, G. A., 1993, "Stability Loss in Thick Transversely Isotropic Cylindrical Shells Under Axial Compression," ASME J. Appl. Mech., **60**, pp. 506–513.

[9] Kardomateas, G. A., 1995, "Bifurcation of Equilibrium in Thick Orthotropic Cylindrical Shells Under Axial Compression," ASME J. Appl. Mech., **62**, pp. 43–52.

[10] Soldatos, K. P., and Ye, J-Q., 1994, "Three-Dimensional Static, Dynamic, Thermoelastic and Buckling Analysis of Homogeneous and Laminated Composite Cylinders," Compos. Struct., **29**, pp. 131-143.

[11] Kardomateas, G. A., and Simitses, G. J., 2005, "Elasticity Solution for the Bucking of Long Sandwich Cylindrical Shells Under External Pressure," ASME J. Appl. Mech., **72**, pp. 493–499.

[12] Lekhnitskii, S. G., 1963, *Theory of Elasticity of an Anisotropic Elastic Body*, Holden Day, San Francisco (also Mir Publishers, Moscow, 1981).

[13] Kardomateas, G. A., 2001, "Elasticity Solutions for a Sandwich Orthotropic Cylindrical Shell Under External Pressure, Internal Pressure and Axial Force," AIAA J. **39**, pp. 713–719.

[14] Novozhilov, V. V., 1953, *Foundations of the Nonlinear Theory of Elasticity*, Graylock, Rochester, NY.

[15] Press, W. H., Flannery, B. P., Teukolsky, S. A., and Vetterling, W. T., 1989, *Numerical Recipes*, Cambridge University Press, Cambridge.

[16] Plantema, F. J., 1966, *Sandwich Construction*, John Wiley & Sons, New York.

[17] Vonach, W. K., and Rammerstorfer, F. G., 2000, "Wrinkling of Thick Orthotropic Sandwich Plates under General Loading Conditions," Arch. Appl. Mech. **70**, pp. 338–348.

[18] Grenestedt, J. L., and Olsson, K.-A., 1995, *Proc., Third International Conference on Sandwich Construction*, Southampton, U.K., 12–15 September.

Dynamic Analysis of the Optical Disk Drives Equipped with an Automatic Ball Balancer with Consideration of Torsional Motions

Paul C. P. Chao[1]
Department of Mechanical Engineering,
Chung-Yuan Christian University,
Chung-Li, Taiwan 320
e-mail: pchao@cycu.edu.tw

Cheng-Kuo Sung
e-mail: cksung@pme.nthu.edu.tw

Chun-Chieh Wang

Department of Power Mechanical Engineering,
National Tsing Hua University,
Hsinchu, Taiwan 300

This study is dedicated to evaluate the performance of an automatic ball-type balancer system (ABS) installed in optical disk drives (ODDs) with consideration of the relative torsional motion between the ODD case and the spindle-disk-ABS-turntable system, noting that the turntable is the supporting plate structure for disk, pickup, and spindle motor inside the ODD. To this end, a complete dynamic model of the ABS considering the torsional motion is established with assuming finite torsional stiffness of the damping washers, which provides suspension of the spindle-disk-ABS-turntable system to the ODD case. Considering the benchmark case of a pair of balancing balls in an ABS, the method of multiple scales is then applied to formulate a scaled model for finding all possible steady-state solutions of ball positions and analyzing corresponding stabilities. The results are used to predict the levels of residual vibration, with which the performance of the ABS can then be reevaluated. Numerical simulations are conducted to verify theoretical results. It is deduced from both analytical and numerical results that the spindle speed of an ODD could be operated above both primary translational and secondary torsional resonances in order to guarantee stabilization of the desired balanced solution for a substantial vibration reduction. [DOI: 10.1115/1.2041659]

1 Introduction

In optical disk drives (ODDs), substantial radial vibrations often occur due to the inherent imbalance of the rotating rotor-disk assembly at high speeds. These vibrations would cause excessive oscillatory vibrations of the objective lens suspended by four wires inside the pickup, leading to great difficulty in data reading. Common remedies for these vibrations are the installation of the damping washers between inner electromechanical components and the outer case of an ODD. With the washers, residual vibrations can be reduced and/or isolated, but not eliminated, from the outer case of ODDs. Contrary to the dampers, the automatic balancer system (ABS), consisting physically of free-running balls inside races, is a device capable of almost eliminating radial vibrations by a different concept of counter-balance. This is based on the fact that as the operating speed of the ODD spindle exceeds the translational resonant frequency of damping washers, the balls inside the race could reside at appropriate positions due to the centrifugal field induced by rotor rotation such that a significant counter-balancing effect is achieved [1].

Some studies were conducted to explore the capability of ball balancers. Thearle [2,3] showed the excellence of ball balancers in vibration reduction. Inoue et al. [4] utilized numerical methods to analyze the dynamics of a rotor/balancer system assuming a constant speed. Bövik and Högfors [5] showed that the auto-balancers were applicable to planar and nonplanar vibrating rotors. Jinnouchi et al. [6] concluded that ball balancers provide excellent balancing above the critical speed, but lead to moderate vibrations at low speeds. Majewski [7] found the negative effects of ball rolling resistance, race eccentricity, and external vibrations on the rotor/balancer system at steady state. Rajalingham and Rakheja [8] first considered the contact friction of balancing balls in the model for analysis. Hwang and Chung [9] used the variational method to derive equations of motion in polar coordinate. Huang et al. [10] successfully conducted dynamics analysis on the ball balancer and computed corresponding residual vibrations based on steady-state solutions solved. Kang et al. [1] utilized methods of perturbation and multiple scales to find steady-state solutions and determine their stabilities for the ABS equipped with a pair of balancing balls. Sung et al. [11] presented a nonplanar dynamic model of the ABS along with experimental data in order to conduct a more realistic analysis on ABS performance.

Despite a number of researches having been conducted for a better understanding of the ABS dynamics in an ODD, the torsional motion of the turntable—a plate supporting the spindle, disk, and ABS through damping washers—was not considered until Kim and Chung [12] reported related analytical work and Sung et al. [11] evidenced the secondary torsional resonance along with the first translational one in experiment. Note that since the supporting plate (the turntable) is seldom seen in other spindle applications of an ABS, such as machine tools and a washing machine, the torsional motion considered in this study is a unique dynamic feature of optical disk drives. In [12], a dynamic model concerning torsion was established with focus only on the desired balanced solution and its stability is determined based on a numerical method to distill favorable operation guidelines for substantial vibration reduction. However, due to the nonlinear nature of the system that multiple stable solutions might coexist, the method of multiple scales along with modal transformation is adopted herein to find all possible steady-state solutions of ball

---

[1] To whom correspondence should be addressed.

Contributed by the Applied Mechanics Division of THE AMERICAN SOCIETY OF MECHANICAL ENGINEERS for publication in the ASME JOURNAL OF APPLIED MECHANICS. Manuscript received by the Applied Mechanics Division, May 23, 2003; final revision; March 24, 2005. Associate Editor: A. A. Ferri. Discussion on the paper should be addressed to the Editor, Prof. Robert M. McMeeking, Journal of Applied Mechanics, Department of Mechanical and Environmental Engineering, University of California—Santa Barbara, Santa Barbara, CA 93106-5070, and will be accepted until four months after final publication in the paper itself in the ASME JOURNAL OF APPLIED MECHANICS.

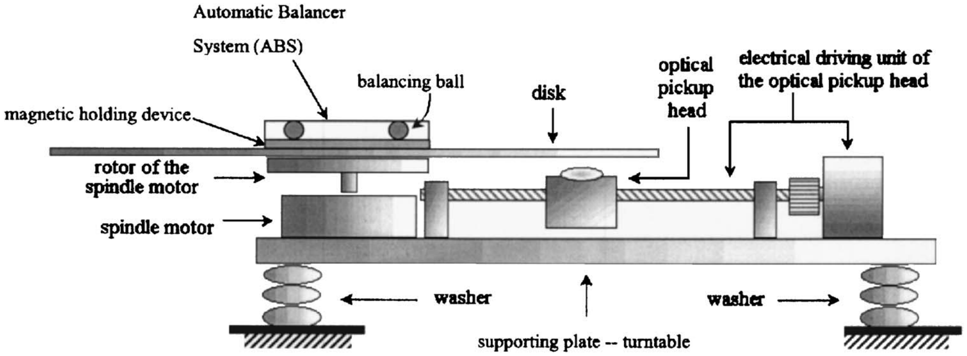

Fig. 1 Schematic of the optical pickup assembly including rotating and nonrotating parts

residing positions and analyzing corresponding stability. The benchmark case of a pair of balancing balls is considered. Numerical simulations are conducted to verify the corresponding theoretical results. It is found from analytical and numerical results that the torsional dynamics of the turntable introduces a secondary resonance above the original translational one. This torsional resonance creates additional narrow unstable region and turns some original stable region of the balanced solution between two resonances into the one where multiple stable solutions exist. One of these stable solutions leads to a balanced system while the other leads to an unbalanced one. To remedy the problem, the spindle speed could be operated conservatively above both primary translational and secondary torsional resonances to stabilize the desired steady-state solutions for expected reduction in radial and torsional vibrations.

The paper is organized as follows. The dynamical model is first established in Sec. 2, which is followed by searching for desired stead-state solutions via a method of multiple scales in Secs. 3 and 4. The corresponding stabilities are analyzed in Sec. 5. Section 6 presents numerical results to validate the analytic findings. Section 7 gives conclusions.

2 Mathematical Model

The data-reading electromechanical system of a typical ODD is schematically shown in Fig. 1, which consists of the components that can be classified into two categories: rotating and nonrotating parts. The assembly of rotating parts, named the equivalent rotor, contains a disk, the ABS circular race enclosing balancing balls, a magnetic device for holding the ABS race case to the spindle, and the rotor of the spindle motor. The assembly of nonrotating parts, named the equivalent stator, contains the supporting plate structure (the turntable in the ODD industry), the stator of the spindle motor, the optical pick-up head, and its electrical driving units. The motion of the unbalanced rotor is mainly in radial directions due to the horizontal flexibility of the damping washers that constitute the suspension system for the turntable. To facilitate derivation of the mathematical model, the following assumptions are made.

1. The rotor shaft is treated as a rigid body, leading to no lateral flexural vibrations while in rotation.
2. The equivalent rotor is treated as a single rigid body, i.e., the disk and its magnetic holding device are fixed to each other, exhibiting no relative motion while in high-speed rotations.
3. After the optical pick-up head unit completes a single seeking process, the stator of the spindle motor, the optical pick-up head, the turntable, and its drive unit are considered as a single rigid body; that is, the equivalent stator is treated as a rigid body.
4. The flexibilities of the washers are assumed to be well captured by linear springs and dampers, denoted by K's and C's, respectively.
5. Since the suspensions constituted by washers are much more flexible than spindle bearings, bearing dynamics is neglected.
6. The races in various radii containing the rolling balls of the ABS shape as perfect circles. The balls are assumed perfect spheres, moving along their respective races. Due to the centrifugal field generated by the rotor rotation, the rolling balls always keep contact with the outer flange of their race. Furthermore, no slip occurs between the rolling balls and the race flanges.
7. Due to the possible assembling error caused by magnetic attachment of the race onto the spindle rotor, the center of the circular races deviates from the rotating center of the rotor by a small distance, ρ.

With the above assumptions made, the stator-rotor-balls system mainly undergoes planar motion under the centrifugal force induced by the inherent imbalance of the rotating disk. The planar motion consists of persistent high-speed rotations of the rotor and reciprocating torsions of the stator, including the turntable. Figure 2 shows the schematic physical configuration of the system, where the ith ball with mass m_i and radius r_i is illustrated. The race radius for the ith ball is R_i. To perform the ensuing analysis, the following notations and coordinates are defined. G_r and G_s denote the mass centers of the equivalent rotor and stator, respectively, while M_r and M_s denote the corresponding masses. O_{Bi} is the center of the ith ball. O_R denotes the origin of the ground coordinate frame $O_R X_R Y_R$, while O_s, coinciding with G_s, is designated as the origin of a rotating frame $O_s X_s Y_s$ which is fixed to the stator (or turntable). Note that when the rotor is at rest; i.e., no radial/torsional vibration caused by the inherent imbalance of the equivalent rotor, O_R coincides with O_s. Also when the rotor is at rest before rotation, γ, defined in frame $O_R X_R Y_R$, denotes the fixed, initial angle between $O_R X_R$ and $O_s X_s$. As the rotor is rotating, the torsional angle of the turntable or the stator can be captured by the one between $O_R X_R$ and $O_S X_S$, which is denoted by $[\gamma + \varphi(t)]$ with $\varphi(t)$ defined as the time-varying part of the torsional angle of the turntable. Furthermore, O_m is designated as the rotational center of the equivalent rotor, also serving as the origin of the rotating frame $O_m X_m Y_m$, which is fixed to the rotor. The rotating angle of the disk is in fact the rotating angle of $O_m X_m$ relative to the $O_s X_s$, which is captured by $\theta(t)$. Considering the rotating angle of the stator (or turntable), the angle of the disc (or $O_m X_m Y_m$) to the ground frame $O_R X_R Y_R$ is then $\lambda + \theta(t) + \varphi(t)$. Finally, O_r is the center of the ball race, also designated as the origin of frame $O_r X_r Y_r$, which is rotated with the same angle as $O_m X_m Y_m$ relative to ground. The deviation of O_r from O_m is due to the prescribed race eccentricity ρ. Note in Fig. 2 that $\overline{O_R O_s}$ and $\overline{O_m O_r}$ are greatly exaggerated for a clear visualization.

Other dynamic variables and parameters are next defined. e captures the mass eccentricity of the equivalent rotor relative to

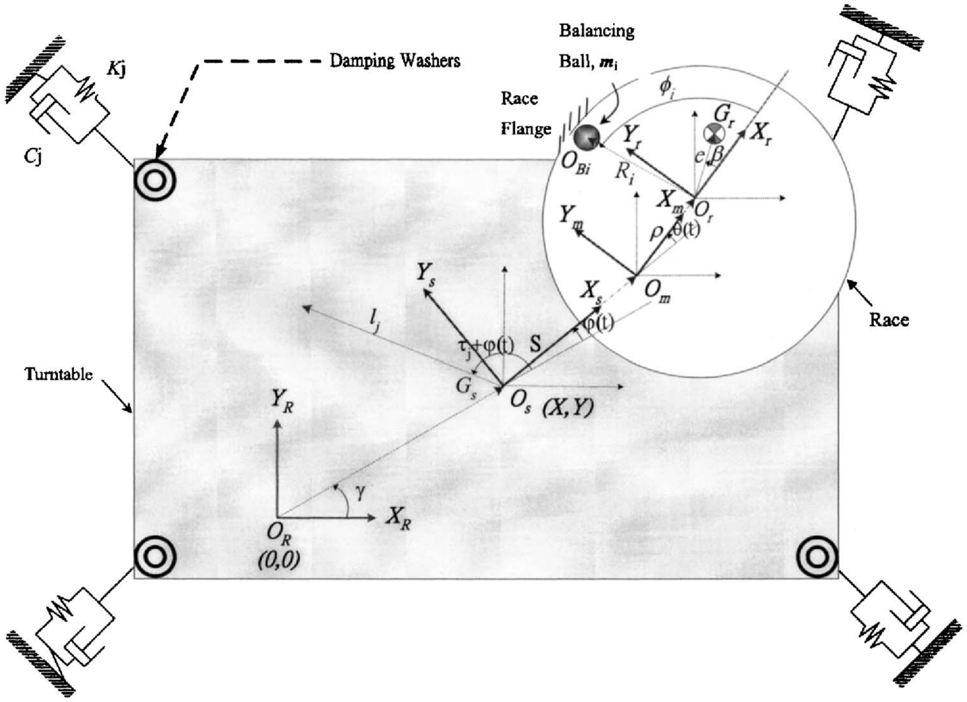

Fig. 2 Mathematical model

O_r (not including the inertial effect from balancing balls of the ABS), i.e., $e=\overline{O_rG_r}$. β, defined in frame $O_rX_rY_r$, denotes the lead angle of the rotor's mass center location with respect to the current angular position of the rotor, $\lambda+\theta(t)+\varphi(t)$. $\phi_i(t)$, defined in frame $O_rX_rY_r$, denotes the lead angle of the ith ball position with respect to the current angular position of rotor. S, defined in frame $O_rX_rY_r$, denotes the distance between the mass center of the stator and the rotation center of rotor, i.e., $S=\overline{O_sO_m}$. l_j denotes the distance between the stator center and the jth washer. τ_j, defined in frame $O_sX_sY_s$, denotes the azimuth angles toward the jth washer from the stator center.

All dynamic degrees of freedom can be identified based on the aforementioned system description and definitions to characterize system dynamics. The displacements of O_R from O_s along axes O_RX_R and O_RY_R, respectively, as shown in Fig. 2, can be captured by $(X(t),Y(t))$, which prescribes the degrees of freedom of the rotor/turntable in two horizontal directions. Thus, the magnitude of the residual radial vibration of the rotor and turntable can be captured by $A(t)=\overline{O_RO_s}=\sqrt{X(t)^2+Y(t)^2}$. On the other hand, the rotational angle of the stator, $\varphi(t)$, provides another degree of freedom describing torsional motions or vibrations of the stator or turntable. Finally, the remaining degrees of freedom are the angular positions of the balancing balls, which as stated are prescribed by the lead angles $\phi_i(t)$'s. With notations and coordinates defined, in the following subsections the kinetic, potential, and generalized forces are formulated for application of Larganege's equations to derive equations of motion.

2.1 Formulation of Kinetic Energy. The formulation of kinetic energy is started with expression of system motions in terms of the notations defined, yielding

$$\vec{R}_s=\begin{bmatrix}X_s\\Y_s\end{bmatrix}=\begin{bmatrix}X\\Y\end{bmatrix},$$

$$\vec{R}_r=\begin{bmatrix}X_r\\Y_r\end{bmatrix}=\begin{bmatrix}X\\Y\end{bmatrix}+S\begin{bmatrix}\cos(\gamma+\varphi)-\cos\gamma\\\sin(\gamma+\varphi)-\sin\gamma\end{bmatrix}+\rho\begin{bmatrix}\cos(\theta+\varphi)-1\\\sin(\theta+\varphi)\end{bmatrix}+e\begin{bmatrix}\cos(\theta+\varphi+\beta)-\cos\beta\\\sin(\theta+\varphi+\beta)-\sin\beta\end{bmatrix},$$

$$\vec{R}_{bi}=\begin{bmatrix}X_{bi}\\Y_{bi}\end{bmatrix}=\begin{bmatrix}X\\Y\end{bmatrix}+S\begin{bmatrix}\cos(\gamma+\varphi)-\cos\gamma\\\sin(\gamma+\varphi)-\sin\gamma\end{bmatrix}+\rho\begin{bmatrix}\cos(\theta+\varphi)-1\\\sin(\theta+\varphi)\end{bmatrix}+R_i\begin{bmatrix}\cos(\theta+\varphi+\phi_i)-1\\\sin(\theta+\varphi+\phi_i)\end{bmatrix},\tag{1}$$

$$\vec{R}_{kj}=\begin{bmatrix}X_{kj}\\Y_{kj}\end{bmatrix}=\begin{bmatrix}X\\Y\end{bmatrix}+l_j\begin{bmatrix}\cos(\tau_j+\varphi)-\cos\tau_j\\\sin(\tau_j+\varphi)-\sin\tau_j\end{bmatrix},$$

where $\bar{R}_s$, $\bar{R}_r$, and $\bar{R}_{bi}$ denote the displacement vectors of the equivalent stator, rotor, and the ith ball, respectively, while $\bar{R}_{kj}$'s denote those of four supporting points of the turntable by washers. The kinetic energy for the system consists of three parts, stators, rotors, and balls. Each part includes translational and rotational kinetics. Based on Eqs. (1), the kinetic energies of the equivalent stator and rotor can be derived as

$$\begin{aligned}T_{ss}&=\tfrac{1}{2}M_s\cdot|\dot{\vec{R}}_s|^2,\\T_{sr}&=\tfrac{1}{2}I_s\cdot\dot{\varphi}^2,\\T_{rs}&=\tfrac{1}{2}M_r\cdot|\dot{\vec{R}}_r|^2,\\T_{rr}&=\tfrac{1}{2}I_r\cdot\dot{\theta}^2,\end{aligned}\tag{2}$$

where I_s and I_r are the moments of inertia of the stator and rotor, respectively. Note also in Eqs. (2) that the first subscripts of s and r under T denote stator and rotor, respectively, while the second subscripts of s and r denotes the types of the kinetic energy T in translational and rotational, respectively. The energies of the balancing ball are formulated next with assumptions of no slip between the balls and races and the perpendicularity of the ball's spinning axis to the ABS circular bottom plane. These assumptions enable one to express the angular velocity of ball self-spinning: $\dot{\alpha}_{Bi}$, in terms of center velocity of the ball, V_{bti}, and circumferential velocity of the race wall, V_{wti}, by $\dot{\alpha}_{Bi}=(V_{wti}-V_{bt1})/r_i$. With this expression, the rotational energy of the ball becomes

$$T_{bri}=\frac{1}{2}I_{bi}\dot{\alpha}_{Bi}^2=\frac{1}{2}I_{bi}\left(\frac{V_{wti}-V_{bti}}{r_i}\right)^2=\frac{1}{2}\frac{I_{bi}}{r_i^2}(V_{wti}-V_{bti})^2, \quad (3a)$$

where I_{bi} is the moment of inertia of the ith ball. The translational energy is

$$T_{bsi}=\tfrac{1}{2}m_i\cdot\dot{\vec{R}}_{bi}^2. \quad (3b)$$

Considering n balls in the ABS, then the total kinetic energy of the system is

$$T=T_{ss}+T_{sr}+T_{rs}+T_{rr}+\sum_{i=1}^{n}(T_{bsi}+T_{bri}). \quad (4)$$

2.2 Formulation of Potential Energy. The total potential energy of the system is induced by the deflections of damping washers in the X and Y directions. Considering N isotropic damping washers, the total potential can be derived by

$$V=\sum_{j=1}^{N}\frac{1}{2}K_j(X_{kj}^2+Y_{kj}^2) \quad (5)$$

$$=\frac{1}{2}\sum_{j=1}^{N}K_j\{X+l_j[\cos(\tau_j+\varphi)-\cos\tau_j]\}^2+\frac{1}{2}\sum_{j=1}^{N}K_j\{Y+l_j[\sin(\tau_j+\varphi)-\sin\tau_j]\}^2, \quad (6)$$

where K_j is the stiffness of the jth washers in both X and Y directions.

2.3 Formulation of Generalized Forces. The generalized forces of the system can be categorized into two kinds, acting on the stator and acting on the balls. Those on the stator are the damping forces exerted by the washers. Due to the dynamic proportionality of these damping forces to the stator's moving speed, the generalized forces due to damping washers can simply be captured by

$$f_x=-\sum_{j=1}^{N}C_j[\dot{X}-l_j\dot{\varphi}\sin(\tau_j+\varphi)], \quad (7a)$$

$$f_y=-\sum_{j=1}^{N}C_j[\dot{Y}+l_j\dot{\varphi}\cos(\tau_j+\varphi)], \quad (7b)$$

$$f_\varphi=-\sum_{j=1}^{N}\{C_j[\dot{X}l_j\sin(\tau_j+\varphi)-\dot{Y}l_j\cos(\tau_j+\varphi)-l_j^2\dot{\varphi}]\}, \quad (7c)$$

where f_x, f_y, and f_φ denote the generalized damping forces acting on the X, Y, and φ directions, respectively.

For those acting on the balls rolling inside the race, as shown in Fig. 3, each ball bears a viscous drag D and a rolling resistant moment M_f due to the contact with race wall. The generalized force acting on the ball can be described by

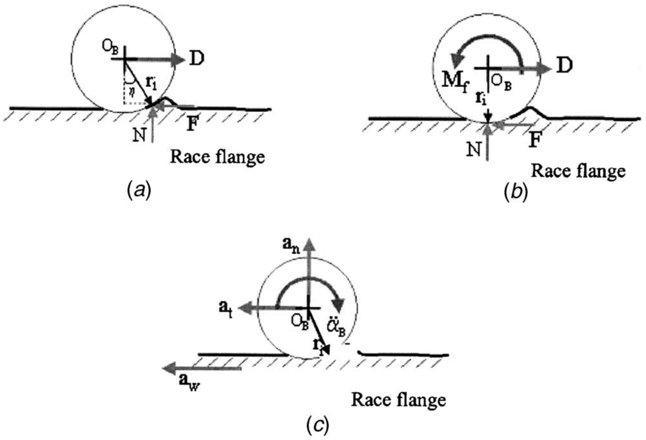

Fig. 3 Actions of forces and acceleration on the balancing balls. (*a*) Free-body diagram; (*b*) equivalent free body diagram; and (*c*) accelerations.

$$f_{\phi i}=-D_i-\frac{M_{fi}}{r_i}\operatorname{sgn}(\dot{\phi}_i) \quad (8a)$$

where the second term results from the rolling resistant moment, while the first term, the viscous drag due to the lubricant between ball and race, D_i, can be assumed in the form of

$$D_i=\alpha_i R_i\dot{\phi}_i \quad (8b)$$

which is the product of the adhesive coefficient α_1 and the relative velocity of the ith ball to the race flange.

Based on the basics of contact theory, the rolling resistant moment M_{fi} in the second term of Eq. (8*a*) can be derived by first constructing the free-body diagram of the rolling ball as shown in Fig. 3(*a*). With the assumption that the ball material is much stiffer than the race, it results in a small bump deformation in the frontal area of the rolling ball. However, one needs to note that the geometry change due to this bump in the circular shape of the race is negligible from the macroscopic point of view, thus resulting in almost no strain energy change of the race, as compared to the total system potential. The bump deformation in fact shifts the contact point between the ball and race flange from a downright position to the one with a corresponding angle η, deviating from the downright direction. In order to capture the generalized forces that are described in the frames previously defined, the acting points of the forces in the original free-body diagram are translated to the downright position as shown in Fig. 3(*b*) with an additional moment generated as

$$M_{fi}=Nr_i\sin\eta+Fr_i(1-\cos\eta), \quad (9a)$$

which in fact deters the ball rolling forward, thus named the "rolling resistance moment." Incorporating the friction effect by surface roughness, the resistance is modified as

$$M_{fi}=Nr_i\sin\eta+Fr_i(1-\cos\eta)+\mu Nr_i \quad (9b)$$

where η, in practice, can be assumed very small, thus, $M_{fi}\approx r_iN(\eta+\mu)$. Note also in Eq. (9*b*) that N is the reaction force which is, by Newton's third law, equivalent to the inertial force generated by the ball in the centrifugal field, i.e., $N=m_ia_n$, where a_n represents the inertial acceleration of the ball induced by the centrifugal field. a_n can be formulated in terms of system variables and parameters by

$$a_n=-\ddot{X}\cos(\theta+\varphi+\phi_i)-\ddot{Y}\sin(\theta+\varphi+\phi_i)-S[\ddot{\varphi}\sin(\theta+\phi_i-\gamma)-\dot{\varphi}^2\cos(\theta+\phi_i-\gamma)]-\rho[(\ddot{\theta}+\ddot{\varphi})\sin\phi_i-(\dot{\theta}+\dot{\varphi})^2\cos\phi_i]+R_i(\dot{\theta}+\dot{\varphi}+\dot{\phi}_i)^2. \quad (10)$$

For simplicity, the definition $\alpha_0 \equiv \eta + \mu$ is introduced. With the derivation of M_{fi} in Eq. (9*b*), the assumption of the smallness of η, and the expression of a_n given in Eq. (10), the rolling resistance moment M_{fi} on the ith ball can finally be approximated by

$$
\begin{aligned}
M_{fi} = r_i \alpha_0 m_i \{ & - \ddot{X}\cos(\theta + \dot{\varphi} + \phi_i) - \ddot{Y}\sin(\theta + \varphi + \phi_i) \\
& - S[\ddot{\varphi}\sin(\theta + \phi_i - \gamma) - \dot{\varphi}^2\cos(\theta + \phi_i - \gamma)] \\
& - \rho[(\ddot{\theta} + \ddot{\varphi})\sin\phi_i - (\dot{\theta} + \dot{\varphi})^2\cos\phi_i] + R_i(\dot{\theta} + \dot{\varphi} + \dot{\phi}_i)^2 \}.
\end{aligned}
\tag{11}
$$

2.4 Application of Lagrange's Equations. With potentials, kinetic energies, and generalized forces derived, the equations of motion for the system can be derived by applying Lagrange's equations

$$
\frac{d}{dt}\left(\frac{\partial L}{\partial \dot{\tilde{q}}_k}\right) - \frac{\partial L}{\partial \tilde{q}_k} = F_{q_k},
\tag{12}
$$

where $L = T - V$, T is the total kinetic energy, V is the total potentials, F_{qk}'s are generalized forces, and $\tilde{q}_k$'s are the generalized coordinates incorporating all dynamic variables of the system; i.e., $\tilde{\mathbf{q}} = [X\ Y\ \varphi\ \phi_1 \cdots \phi_n]$. Application of Lagrange's equation (12) gives differential equations governing the translational and torsional motions of the rotor-stator assembly in X, Y, and φ, respectively, and the motions of balancing balls in ϕ_i's, which are expressed by

$$
\begin{aligned}
M\ddot{X} + \sum_{j=1}^{N} C_j \dot{X} + \sum_{j=1}^{N} K_j X = {} & \left(M_r + \sum_{i=1}^{n} m_i\right) S[\ddot{\varphi}\sin(\gamma + \varphi) + \dot{\varphi}^2\cos(\gamma + \varphi)] + \left(M_r + \sum_{i=1}^{n} m_i\right)\rho[(\ddot{\theta} + \ddot{\varphi})\sin(\theta + \varphi) + (\dot{\theta} + \dot{\varphi})^2\cos(\theta + \varphi)] \\
& + M_r e[(\ddot{\theta} + \ddot{\varphi})\sin(\theta + \beta + \varphi) + (\dot{\theta} + \dot{\varphi})^2\cos(\theta + \beta + \varphi)] + \sum_{i=1}^{n} m_i R_i[(\ddot{\theta} + \ddot{\phi}_i + \ddot{\varphi})\sin(\theta + \phi_i + \varphi) \\
& + (\dot{\theta} + \dot{\phi}_i + \dot{\varphi})^2\cos(\theta + \phi_i + \varphi)] - \sum_{j=-1}^{N} K_j l_j[\cos(\tau_j + \varphi) - \cos\tau_j] + \sum_{i=1}^{N} C_j l_j \dot{\varphi}\sin(\tau_j + \varphi),
\end{aligned}
\tag{13a}
$$

$$
\begin{aligned}
M\ddot{Y} + \sum_{j=1}^{N} C_j \dot{Y} + \sum_{j=1}^{N} K_j Y = {} & \left(M_r + \sum_{i=1}^{n} m_i\right) S[-\ddot{\varphi}\cos(\gamma + \varphi) + \dot{\varphi}^2\sin(\gamma + \varphi)] + \left(M_r + \sum_{i=1}^{n} m_i\right)\rho[-(\ddot{\theta} + \ddot{\varphi})\cos(\theta + \varphi) + (\dot{\theta} + \dot{\varphi})^2\sin(\theta + \varphi)] \\
& + M_r e[-(\ddot{\theta} + \ddot{\varphi})\cos(\theta + \beta + \varphi) + (\dot{\theta} + \dot{\varphi})^2\sin(\theta + \beta + \varphi)] + \sum_{i=1}^{n} m_i R_i[-(\ddot{\theta} + \ddot{\phi}_i + \ddot{\varphi})\cos(\theta + \phi_i + \varphi) \\
& + (\dot{\theta} + \dot{\phi}_i + \dot{\varphi})^2\sin(\theta + \phi_i + \varphi)] - \sum_{j=-1}^{N} K_j l_j[\sin(\tau_j + \varphi) - \sin\tau_j] - \sum_{j=1}^{N} C_j l_j \dot{\varphi}\cos(\tau_j + \varphi),
\end{aligned}
\tag{13b}
$$

$$
\begin{aligned}
& \Bigg(M_r[S^2 + \rho^2 + e^2 + 2\rho S\cos(\gamma - \theta) + 2Se\cos(\gamma - \theta - \beta) + 2\rho e\cos\beta] + I_s + \sum_{i=1}^{n} I_{bi} + \sum_{i=1}^{n} m_i[S^2 + \rho^2 + R_i^2 + 2\rho S\cos(\gamma - \theta) + 2SR_i\cos(\gamma \\
& \quad - \theta - \phi_i) + 2\rho R_i\cos\phi_i] \Bigg)\ddot{\varphi} + \sum_{j=1}^{N} C_j l_j[-\dot{X}\sin(\tau_j + \varphi) + \dot{Y}\cos(\tau_j + \varphi) + l_j\dot{\varphi}] + \sum_{j=1}^{N} K_j l_j[-X\sin(\tau_j + \varphi) + Y\cos(\tau_j + \varphi) + l_j\sin\varphi] \\
& = -\Bigg(M_r[\rho^2 + e^2 + \rho S\cos(\gamma - \theta) + Se\cos(\gamma - \theta - \beta) + 2\rho e\cos\beta] + \sum_{i=1}^{n} I_{bi} + \sum_{i=1}^{n} m_i[\rho^2 + R_i^2 + \rho S\cos(\gamma - \theta) + SR_i\cos(\gamma - \theta - \phi_i) \\
& \quad + 2\rho R_i\cos\phi_i] \Bigg)\ddot{\theta} - \sum_{i=1}^{n} m_i[R_i^2 + SR_i\cos(\gamma - \theta - \phi_i) + \rho R_i\cos\phi_i]\ddot{\phi}_i + \sum_{i=1}^{n} I_{bi}\frac{R_i}{r_i}\ddot{\phi}_i - \left(M_r + \sum_{i=1}^{n} m_i\right)\rho S\dot{\theta}[(\dot{\theta} + 2\dot{\varphi})\sin(\gamma - \theta)] \\
& \quad - M_r Se\dot{\theta}(\dot{\theta} + 2\dot{\varphi})\sin(\gamma - \theta - \beta) - \sum_{i=1}^{n} m_i R_i[S(\dot{\theta} + \dot{\phi}_i + 2\dot{\varphi})(\dot{\theta} + \dot{\phi}_i)\sin(\gamma - \theta - \phi_i) - \rho(2\dot{\theta} + \dot{\phi}_i + 2\dot{\varphi})\dot{\phi}_i\sin\phi_i] \\
& \quad + \left(M_r + \sum_{i=1}^{n} m_i\right)\{[S\sin(\gamma + \varphi) + \rho\sin(\theta + \varphi)]\ddot{X} - [S\cos(\gamma + \varphi) + \rho\cos(\theta + \varphi)]\ddot{Y}\} + M_r e[\ddot{X}\sin(\theta + \beta + \varphi) - \ddot{Y}\cos(\theta + \beta + \varphi)] \\
& \quad + \sum_{i=1}^{n} m_i R_i[\ddot{X}\sin(\theta + \phi_i + \varphi) - \ddot{Y}\cos(\theta + \phi_i + \varphi)],
\end{aligned}
\tag{13c}
$$

$$\left(m_i+\frac{I_{bi}}{r_i^2}\right)R_i\ddot{\phi}_i=\left(\frac{I_{bi}}{r_i}-m_iR_i\right)(\ddot{\theta}+\ddot{\varphi})-D_i-\frac{M_{fi}}{r_i}\operatorname{sgn}(\dot{\phi}_i)+m_i[\ddot{X}\sin(\theta+\phi_i+\varphi)-\ddot{Y}\cos(\theta+\phi_i+\varphi)]+m_i\{S[-\ddot{\varphi}\cos(\theta+\phi_i-\gamma)$$
$$-\dot{\varphi}^2\sin(\theta+\phi_i-\gamma)]+\rho[-(\ddot{\theta}+\ddot{\varphi})\cos\phi_i-(\dot{\theta}+\dot{\varphi})^2\sin\phi_i]\}. \quad (13d)$$

3 Asymptotic Analysis

To understand the dynamic characteristics of the system and further evaluate performance of the ABS in vibration reduction, approximate steady-state solutions are next sought by first making some scaling assumptions to manipulate equations of motion and then employing the asymptotic analysis techniques, the method of multiple time scales. To this end, stiffnesses and dampings of four washers are first assumed identical for simplicity, that is, $K_i=K$ and $C_i=C$ for all i, which is followed by assuming all balls are inside a single race with $R_i=R$ for all i. Furthermore, the installing positions of the four washers are assumed symmetrical to the mass center of the stator, i.e., $l_1=l_2=l_3=l_4=l$ and $\tau_1=\pi-\tau_2=\tau_3-\pi=2\pi-\tau_4=\tau$. Finally, the practice that the mass of the balancing ball m is much smaller than that of the net system M facilitates a small parameter to be defined by

$$\varepsilon=\sqrt{m/M}. \quad (14)$$

With the scaling parameter defined in the above, the following are made based on practice to rearrange the system equations into an amenable form for multiple time scale analysis:

$$\tau=\omega_n t, \quad \mu_i=I_b/mRr, \quad \varepsilon x=X/R,$$
$$\omega_n=\sqrt{4K/M}, \quad \kappa=l/R, \quad \varepsilon y=Y/R,$$
$$\mu_0=m/(m+I_b/r^2), \quad \lambda=S/R, \quad \varepsilon q=\varphi,$$
$$\bar{M}=M_r/M, \quad \varepsilon^2\lambda_1=\rho/R, \quad \varepsilon\varsigma=C/M\omega_n, \quad (15)$$
$$\bar{I}=\frac{I_s+2I_b}{MR^2}, \quad \varepsilon^2\lambda_2=e/R, \quad \varepsilon\varsigma_1=\alpha_1/m\omega_n,$$
$$\varepsilon\varsigma_0=\alpha_0,$$

where λ_1 and λ_2 are nondimensionalized race and rotor mass eccentricities, respectively. In practice, radial vibrations of spindle, disk, and turntable are normally within the range of 1–10 μm, while the torsional angle φ is within the range of 10^{-4} to 10^{-3} degrees. Therefore, as nondimensionalized by the race radius R, normally around 1 cm, X/R and Y/R can be scaled as small numbers, while φ can be scaled as a small quantity. On the other hand, two eccentricities of ρ and e are assumed to be in levels of ε^2, which indicates that, compared to scaled responses in x, y, and q defined in the above, the system is under weak excitations. Substituting the definition of ε in Eq. (14) and definitions/scalings in Eqs. (15) into system of equations (13) with the assumption that the rotor undergoes a constant speed, i.e., $d\theta/d\tau=p(\theta=p\tau)$, the following nondimensionalized equations of motion in terms of scaled system variables can be obtained:

$$\ddot{x}+\varsigma\varepsilon\dot{x}+x=\bar{M}\{\lambda[\varepsilon\ddot{q}\sin(\gamma+\varphi)+\varepsilon^2\dot{q}^2\cos(\gamma+\varphi)]+\varepsilon\lambda_1[\varepsilon\ddot{q}\sin(\theta+\varphi)+(p+\varepsilon\dot{q})^2\cos(\theta+\varphi)]+\varepsilon\lambda_2[\varepsilon\ddot{q}\sin(\theta+\varphi+\beta)$$
$$+(p+\varepsilon\dot{q})^2\cos(\theta+\varphi+\beta)]\}+\varepsilon\sum_{i=1}^{n}\{\varepsilon\lambda[\varepsilon\ddot{q}\sin(\gamma+\varphi)+\varepsilon^2\dot{q}^2\cos(\gamma+\varphi)]+\varepsilon^2\lambda_1[\varepsilon\ddot{q}\sin(\theta+\varphi)+(p+\varepsilon\dot{q})^2\cos(\theta+\varphi)]$$
$$+[(\varepsilon\ddot{q}+\ddot{\phi}_i)\sin(\theta+\varphi+\phi_i)+(p+\varepsilon\dot{q}+\dot{\phi}_i)^2\cos(\theta+\varphi+\phi_i)]\}, \quad (16a)$$

$$\ddot{y}+\varsigma\varepsilon\dot{y}+y=\bar{M}\{\lambda[-\varepsilon\ddot{q}\cos(\gamma+\varphi)+\varepsilon^2\dot{q}^2\sin(\gamma+\varphi)]+\varepsilon\lambda_1[-\varepsilon\ddot{q}\cos(\theta+\varphi)+(p+\varepsilon\dot{q})^2\sin(\theta+\varphi)]+\varepsilon\lambda_2[-\varepsilon\ddot{q}\cos(\theta+\varphi+\beta)$$
$$+(p+\varepsilon\dot{q})^2\sin(\theta+\varphi+\beta)]\}+\varepsilon\sum_{i=1}^{n}\{\varepsilon\lambda[-\varepsilon\ddot{q}\cos(\gamma+\varphi)+\varepsilon^2\dot{q}^2\sin(\gamma+\varphi)]+\varepsilon^2\lambda_1[-\varepsilon\ddot{q}\cos(\theta+\varphi)+(p+\varepsilon\dot{q})^2\sin(\theta+\varphi)]$$
$$+[-(\varepsilon\ddot{q}+\ddot{\phi}_i)\cos(\theta+\varphi+\phi_i)+(p+\varepsilon\dot{q}+\dot{\phi}_i)^2\sin(\theta+\varphi+\phi_i)]\}, \quad (16b)$$

$$\Bigg(\bar{M}[(\varepsilon\lambda)^2+(\varepsilon^2\lambda_1)^2+(\varepsilon^2\lambda_2)^2+2\varepsilon^2\lambda_1\varepsilon\lambda\cos(\gamma-\theta)+2\varepsilon\lambda\varepsilon^2\lambda_2\cos(\gamma-\theta-\beta)+2\varepsilon^2\lambda_1\varepsilon^2\lambda_2\cos\beta]+\bar{I}+\varepsilon^2\sum_{i=1}^{n}[(\varepsilon\lambda)^2+(\varepsilon^2\lambda_1)^2$$
$$+1+2\varepsilon^2\lambda_1\varepsilon\lambda\cos(\gamma-\theta)+2\varepsilon\lambda\cos(\gamma-\theta-\phi_i)+2\varepsilon^2\lambda_1\cos\phi_i]\Bigg)\ddot{q}+\varsigma\kappa^2\varepsilon\dot{q}+\kappa^2 q$$
$$=-\varepsilon\sum_{i=1}^{n}[1+\varepsilon\lambda\cos(\gamma-\theta-\phi_i)+\varepsilon^2\lambda_1\cos\phi_i-\mu_1]\ddot{\phi}_i-(\bar{M}+n\varepsilon^2)\varepsilon^2\lambda_1\lambda p(p+2\varepsilon\dot{q})\sin(\gamma-\theta)-\bar{M}\lambda\varepsilon^2\lambda_2 p(p+2\varepsilon\dot{q})\sin(\gamma-\theta-\beta)$$
$$-\varepsilon^2\sum_{i=1}^{n}[\lambda(p+2\varepsilon\dot{q}+\dot{\phi}_i)(p+\dot{\phi}_i)\sin(\gamma-\theta-\phi_i)-\varepsilon\lambda_1(2p+2\varepsilon\dot{q}+\dot{\phi}_i)\dot{\phi}_i\sin\phi_i]+(\bar{M}+n\varepsilon^2)\{[\varepsilon\lambda\sin(\gamma+\varphi)+\varepsilon^2\lambda_1\sin(\theta+\varphi)]\ddot{x}$$
$$-[\varepsilon\lambda\cos(\gamma+\varphi)+\varepsilon^2\lambda_1\cos(\theta+\varphi)]\ddot{y}\}+\bar{M}\varepsilon^2\lambda_2[\ddot{x}\sin(\theta+\varphi+\beta)-\ddot{y}\cos(\theta+\varphi+\beta)]$$

$$+\varepsilon^2\sum_{i=1}^{n}[\ddot{x}\sin(\theta+\varphi+\phi_i)-\ddot{y}\cos(\theta+\varphi+\phi_i)], \tag{16c}$$

$$\begin{aligned}\ddot{\phi}_i={}&-\mu_0(1-\mu_1)\varepsilon\ddot{q}-\mu_0\varepsilon\varsigma_1\dot{\phi}_i+\mu_0[\varepsilon\ddot{x}\sin(\theta+\varphi+\phi_i)-\varepsilon\ddot{y}\cos(\theta+\varphi+\phi_i)]+\mu_0\{\lambda[-\varepsilon\ddot{q}\cos(\theta+\phi_i-\gamma)-\varepsilon^2\dot{q}^2\sin(\theta+\phi_i-\gamma)]\\&+\varepsilon^2\lambda_1[-\varepsilon\ddot{q}\cos\phi_i-(\dot{\theta}+\varepsilon\dot{q})^2\sin\phi_i]\}-\mu_0\varepsilon\varsigma_0\{-\varepsilon\ddot{x}\cos(\theta+\varphi+\phi_i)-\varepsilon\ddot{y}\sin(\theta+\varphi+\phi_i)\\&-\lambda[\varepsilon\ddot{q}\sin(\theta+\phi_i-\gamma)-\varepsilon^2\dot{q}^2\cos(\theta+\phi_i-\gamma)]-\varepsilon^2\lambda_1[\varepsilon\ddot{q}\sin\phi_i-(\dot{\theta}+\varepsilon\dot{q})^2\cos\phi_i]+(\dot{\theta}+\dot{\phi}_i+\varepsilon\dot{q})^2\}\mathrm{sgn}(\phi_i),\end{aligned} \tag{16d}$$

where single and double overdots denote single and double differentiations with respect to new time scale τ, respectively. Equations (16) are ready for application of the multiple-scale method to find approximate steady-state solutions and analyze their stabilities. Assume

$$x(\tau,\varepsilon)=x_0(T_0,T_1)+\varepsilon x_1(T_0,T_1)+O(\varepsilon^2), \tag{17a}$$

$$y(\tau,\varepsilon)=y_0(T_0,T_1)+\varepsilon y_1(T_0,T_1)+O(\varepsilon^2), \tag{17b}$$

$$q(\tau,\varepsilon)=q_0(T_0,T_1)+\varepsilon q_1(T_0,T_1)+O(\varepsilon^2), \tag{17c}$$

$$\phi_i(\tau,\varepsilon)=\phi_{i0}(T_0,T_1)+\varepsilon\phi_{i1}(T_0,T_1)+O(\varepsilon^2), \tag{17d}$$

where $T_0=\tau$ is the fast time scale and $T_1=\varepsilon\tau$ is the slow time scale. The introduction of T_0 and T_1 renders

$$\frac{d}{d\tau}=D_0+\varepsilon D_1+O(\varepsilon^2)\quad\text{and}\quad\frac{d^2}{d\tau^2}=D_0^2+2\varepsilon D_0D_1+O(\varepsilon^2), \tag{18}$$

where $D_n=\partial/\partial T_n$ for $n=0,1$. Substituting Eqs. (17) and (18) into Eq. (16) and ignoring $O(\varepsilon^2)$ terms give

$$\begin{aligned}&\varepsilon^0(D_0^2x_0+x_0)+\varepsilon^1\Bigg(D_0^2x_1+x_1-\bar{M}[\lambda D_0^2q_0\sin\gamma+\lambda_1p^2\cos\theta\\&\quad+\lambda_2p^2\cos(\theta+\beta)]+\varsigma D_0x_0+2D_0D_1x_0\\&\quad-\sum_{i=1}^{n}[D_0^2\phi_{i0}\sin(\theta+\phi_i)+(p+D_0\phi_{i0})^2\cos(\theta+\phi_i)]\Bigg)=0,\end{aligned} \tag{19a}$$

$$\begin{aligned}&\varepsilon^0(D_0^2y_0+y_0)+\varepsilon^1\Bigg(D_0^2y_1+y_1-\bar{M}[-\lambda D_0^2q_0\cos\gamma+\lambda_1p^2\sin\theta\\&\quad+\lambda_2p^2\sin(\theta+\beta)]+\varsigma D_0y_0+2D_0D_1y_0\\&\quad-\sum_{i=1}^{n}[-D_0^2\phi_{i0}\cos(\theta+\phi_i)+(p+D_0\phi_{i0})^2\sin(\theta+\phi_i)]\Bigg)=0,\end{aligned} \tag{19b}$$

$$\begin{aligned}&\varepsilon^0(\bar{I}D_0^2q_0+\kappa^2q_0)+\varepsilon^1\Big(\bar{I}D_0^2q_1+\kappa^2q_1+(1-\mu_1)\sum D_0^2\phi_{i0}\\&\quad-\bar{M}\lambda(\sin\gamma D_0^2x_0-\cos\gamma D_0^2y_0)+\varsigma\kappa^2D_0q_0+2\bar{I}D_0D_1q_0\Big)=0,\end{aligned} \tag{19c}$$

$$\begin{aligned}&\varepsilon^0(D_0^2\phi_{i0})+\varepsilon^1\{D_0^2\phi_{i1}+2D_0D_1\phi_{i0}+\mu_0(1-\mu_1)D_0^2q_0+\mu_0\varsigma_1D_0\phi_{i0}\\&\quad+\mu_0\varsigma_0(p+D_0\phi_{i0})^2\,\mathrm{sgn}(D_0\phi_{i0})+\mu_0\varsigma_0(p+D_0\phi_{i0})^2\\&\quad-\mu_0[D_0^2x_0\sin(\theta+\phi_i)-D_0^2y_0\cos(\theta+\phi_i)]\}=0.\end{aligned} \tag{19d}$$

Forcing the $O(\varepsilon^0)$ terms in Eq. (19) equal to zeros renders

$$\begin{bmatrix}1 & 0 & -\bar{M}\lambda\sin\gamma\\ 0 & 1 & \bar{M}\lambda\cos\gamma\\ -\bar{M}\lambda\sin\gamma & \bar{M}\lambda\cos\gamma & \bar{M}\lambda^2+\bar{I}\end{bmatrix}\begin{bmatrix}\ddot{x}_0\\ \ddot{y}_0\\ \ddot{q}_0\end{bmatrix}+\begin{bmatrix}1 & 0 & 0\\ 0 & 1 & 0\\ 0 & 0 & \kappa^2\end{bmatrix}\begin{bmatrix}x_0\\ y_0\\ q_0\end{bmatrix}=0, \tag{20a}$$

$$D_0^2\phi_{i0}=0. \tag{20b}$$

Using the framework of fundamental modal transformation, the nontrivial solutions of Eq. (20) can be captured as the sum of subsolutions in three modal spaces, yielding

$$\begin{bmatrix}x_0\\ y_0\\ q_0\end{bmatrix}=A_0(T_1)[U_1]e^{i\omega_1T_0}+B_0(T_1)[U_2]e^{i\omega_2T_0}+C_0(T_1)[U_3]e^{i\omega_3T_0}+\text{c.c.}, \tag{21a}$$

$$\phi_{i0}=\psi_{i0}(T_1)T_0+\varphi_{i0}(T_1), \tag{21b}$$

where ω_i's are three modal frequencies (resonance frequencies), U_i's are the corresponding eigenvectors spanning a modal subspace, c.c. represents the complex conjugates of preceding terms, and finally $[A_0\ B_0\ C_0\ \psi_{i0}\ \varphi_{i0}]$ are to be determined in later analysis. ω_i's and U_i can first be easily derived from Eqs. (20) based on simple vibration analysis, yielding

$$\begin{aligned}&\omega_1=1,\quad U_1=\begin{bmatrix}\cos\gamma\\ \sin\gamma\\ 0\end{bmatrix};\\&\omega_2=\frac{(\bar{M}\lambda^2+\bar{I}+\kappa^2)-\sqrt{(\bar{M}\lambda^2+\bar{I}-\kappa^2)^2+4\kappa^2\bar{M}^2\lambda^2}}{2(\bar{M}\lambda^2+\bar{I}-\bar{M}^2\lambda^2)},\\&U_2=\begin{bmatrix}-\dfrac{\omega_2}{1-\omega_2}\bar{M}\lambda\sin\gamma\\ \dfrac{\omega_2}{1-\omega_2}\bar{M}\lambda\cos\gamma\\ 1\end{bmatrix};\\&\omega_3=\frac{(\bar{M}\lambda^2+\bar{I}+\kappa^2)+\sqrt{(\bar{M}\lambda^2+\bar{I}-\kappa^2)^2+4\kappa^2\bar{M}^2\lambda^2}}{2(\bar{M}\lambda^2+\bar{I}-\bar{M}^2\lambda^2)},\\&U_3=\begin{bmatrix}\dfrac{\omega_3}{1-\omega_3}\bar{M}\lambda\sin\gamma\\ -\dfrac{\omega_3}{1-\omega_3}\bar{M}\lambda\cos\gamma\\ -1\end{bmatrix}.\end{aligned} \tag{22}$$

It can be shown with S approaching zero, i.e., the spindle installed at the position close to the geometric center of the turntable, that the space spanned by U_1 and U_2 is the one that corresponds to the translational motion of the stator/rotor in the x and y directions and the space by U_3 corresponds to torsional motion in φ. Furthermore, with the washers assumed isotropic in dampings/stiffnesses and installed symmetric to the mass center of the stator, one can show that ω_1 and ω_2 calculated by Eqs. (22) are close but not equal to each other due to the coupling effect between translational and torsional motions.

In Eqs. (21), A_0, B_0, C_0, ψ_{i0}, and φ_{i0} are unknown parameters varied in slow time scale T_1, which are, in a standard procedure of multiple-scale analysis, to be determined in the next stage of analysis, i.e., in the $O(\varepsilon^1)$ analysis. This is started with expressing $\{A_0, B_0, C_0\}$ by

$$A_0 = A_1 e^{i\sigma T_1}, \quad B_0 = B_1 e^{i\sigma T_1}, \quad \text{and } C_0 = C_1 e^{i\sigma T_1}, \tag{23}$$

and then performing the asymptotic analysis with the assumption that the rotation of the system-equivalent rotor is operated near one of the resonances, ω_i, given in Eqs. (22), that is,

$$p = \omega_i + \varepsilon\sigma \quad \text{for } i = 1,2,3. \tag{24}$$

Incorporating the expressions (23) and the assumption (24) into Eqs. (19), the equations governing the $O(\varepsilon^1)$ dynamics can be obtained as below,

$$\begin{aligned} D_0^2 x_1 + x_1 - \bar{M}\lambda \sin\gamma D_0^2 q_1 = {} & - i\omega_1 e^{i\omega_1 T_0}\left[\varsigma A_1 + 2\left(\frac{\partial A_1}{\partial T_1} + i\sigma A_1\right)\right]\cos\gamma + i\omega_2 e^{i\omega_2 T_0}\left[\varsigma B_1 + \frac{2}{\Omega_2}\left(\frac{\partial B_1}{\partial T_1} + i\sigma B_1\right)\right]\frac{\Omega_2}{1-\Omega_2}\bar{M}\lambda\sin\gamma \\ & + i\omega_3 e^{i\omega_3 T_0}\left[\varsigma C_1 + \frac{2}{\Omega_3}\left(\frac{\partial C_1}{\partial T_1} + i\sigma C_1\right)\right]\frac{\Omega_3}{1-\Omega_3}\bar{M}\lambda\sin\gamma + i\omega_i e^{i\omega_i T_0}\left(\frac{1}{2i\omega_i}\bar{M}p^2\lambda_1 + \frac{1}{2i\omega_i}\bar{M}p^2\lambda_2 e^{i\beta}\right. \\ & \left. + \frac{1}{2i\omega_i}\sum_{i=1}^{n}\left[(p+\psi_{i0})^2 e^{i\phi_{i0}}\right]\right) + \text{c.c.} + \text{N.S.T.}, \end{aligned} \tag{25a}$$

$$\begin{aligned} D_0^2 y_1 + y_1 + \bar{M}\lambda \cos\gamma D_0^2 q_1 = {} & - i\omega_1 e^{i\omega_1 T_0}\left[\varsigma A_1 + 2\left(\frac{\partial A_1}{\partial T_1} + i\sigma A_1\right)\right]\sin\gamma - i\omega_2 e^{i\omega_2 T_0}\left[\varsigma B_1 + \frac{2}{\Omega_2}\left(\frac{\partial B_1}{\partial T_1} + i\sigma B_1\right)\right]\frac{\Omega_2}{1-\Omega_2}\bar{M}\lambda\cos\gamma \\ & - i\omega_3 e^{i\omega_3 T_0}\left[\varsigma C_1 + \frac{2}{\Omega_3}\left(\frac{\partial C_1}{\partial T_1} + i\sigma C_1\right)\right]\frac{\Omega_3}{1-\Omega_3}\bar{M}\lambda\cos\gamma - i\omega_i e^{i\omega_i T_0}\left(\frac{1}{2\omega_i}\bar{M}p^2\lambda_1 + \frac{1}{2\omega_i}\bar{M}p^2\lambda_2 e^{i\beta}\right. \\ & \left. + \frac{1}{2\omega_i}\sum_{i=1}^{n}\left[(p+\psi_{i0})^2 e^{i\phi_{i0}}\right]\right) + \text{c.c.} + \text{N.S.T.}, \end{aligned} \tag{25b}$$

$$\begin{aligned} & (\bar{M}\lambda^2 + \bar{I})D_0^2 q_1 + \kappa^2 q_1 - \bar{M}\lambda\sin\gamma D_0^2 x_1 + \bar{M}\lambda\cos\gamma D_0^2 y_1 \\ & \quad = - i\omega_2 e^{i\omega_2 T_0}\left[\varsigma B_1 + \frac{2}{\Omega_2}\left(\frac{\partial B_1}{\partial T_1} + i\sigma B_1\right)\right]\kappa^2 - i\omega_3 e^{i\omega_3 T_0}\left[\varsigma C_1 + \frac{2}{\Omega_3}\left(\frac{\partial C_1}{\partial T_1} + i\sigma C_1\right)\right]\kappa^2 \\ & \qquad + i\omega_i e^{i\omega_i T_0}\left(-\frac{1}{2\omega_i}\bar{M}p^2\lambda\lambda_1 e^{-i\gamma} - \frac{1}{2\omega_i}\bar{M}p^2\lambda\lambda_2 e^{i(\beta-\gamma)} - \frac{1}{2\omega_i}\lambda\sum_{i=1}^{n}\left[(p+\psi_{i0})^2 e^{i(\phi_i-\gamma)}\right]\right) + \text{c.c.} + \text{N.S.T.}, \end{aligned} \tag{25c}$$

$$\begin{aligned} D_0^2\phi_{i1} = {} & -2\frac{\partial\psi_{i0}}{\partial T_1} - \mu_0\varsigma_1\psi_{i0} - \mu_0\varsigma_0(p+\psi_{i0})^2\,\text{sgn}(\psi_{i0}) - \frac{i}{2}\mu_0\omega_1^2\left(-A_1 e^{i[(\omega_i+\omega_1)T_0+\phi_{i0}-\gamma]} + A_1 e^{-i[(\omega_i-\omega_1)T_0+\phi_{i0}-\gamma]} - \bar{A}_1 e^{i[(\omega_i-\omega_1)T_0+\phi_{i0}-\gamma]}\right. \\ & \left. + \bar{A}_1 e^{-i[(\omega_i+\omega_1)T_0+\phi_{i0}-\gamma]}\right) + \frac{1}{2}\mu_0\omega_2^2\left(B_1 e^{i[(\omega_i+\omega_2)T_0+\phi_{i0}-\gamma]} + B_1 e^{-i[(\omega_i-\omega_2)T_0+\phi_{i0}-\gamma]} + \bar{B}_1 e^{i[(\omega_i-\omega_2)T_0+\phi_{i0}-\gamma]} + \bar{B}_1 e^{-i[(\omega_i+\omega_2)T_0+\phi_{i0}-\gamma]}\right) \\ & \times\left(\frac{\Omega_2}{1-\Omega_2}\bar{M} + 1\right)\lambda + \frac{1}{2}\mu_0\omega_3^2\left(C_1 e^{i[(\omega_i+\omega_3)T_0+\phi_{i0}-\gamma]} + C_1 e^{-i[(\omega_i-\omega_3)T_0+\phi_{i0}-\gamma]} + \bar{C}_1 e^{i[(\omega_i-\omega_3)T_0+\phi_{i0}-\gamma]} + \bar{C}_1 e^{-i[(\omega_i+\omega_3)T_0+\phi_{i0}-\gamma]}\right) \\ & \times\left(\frac{\Omega_3}{1-\Omega_3}\bar{M} + 1\right)\lambda + \mu_0(1-\mu_1)\left(B_1\omega_2^2 e^{i\omega_2 T_0} + \bar{B}_1\omega_2^2 e^{-i\omega_2 T_0} + C_1\omega_3^2 e^{i\omega_3 T_0} + \bar{C}_1\omega_3^2 e^{-i\omega_3 T_0}\right), \end{aligned} \tag{25d}$$

where N.S.T.'s denote the nonsecular terms that do not affect the ensuing steady-state solutions and stability analysis. It is noted at this point that the couplings in the linear parts of Eqs. (25*a*)–(25*c*) hinder the advances of the multiple-scale analysis. To solve this problem, the modal coordinates utilized in the level of $O(\varepsilon^0)$, as shown in Eqs. (22), are again applied herein to decouple the linear parts of Eqs. (25*a*)–(25*c*) into

$$\ddot{\eta}_1 + \omega_1^2\eta_1 = -i\omega_1\left[\varsigma A_1 + 2\left(\frac{\partial A_1}{\partial T_1} + i\sigma A_1\right)\right]e^{i\omega_1 T_0} - i\omega_i(iFe^{-i\gamma})e^{i\omega_i T_0} + \text{c.c.} + \text{N.S.T.}, \tag{26a}$$

$$c_2(\ddot{\eta}_2 + \omega_2^2\eta_2) = -i\omega_2\left[\varsigma B_1 + \frac{2}{\Omega_2}\left(\frac{\partial B_1}{\partial T_1} + i\sigma B_1\right)\right]\cdot\left[\left(\frac{\Omega_2}{1-\Omega_2}\bar{M}\lambda\right)^2 + \kappa^2\right]e^{i\omega_2 T_0} - i\omega_i F\lambda e^{-i\gamma}\left(\frac{\Omega_2}{1-\Omega_2}\bar{M} + 1\right)e^{i\omega_i T_0} + \text{c.c.} + \text{N.S.T.}, \tag{26b}$$

$$c_3(\ddot{\eta}_3+\omega_3^2\eta_3)=-i\omega_3\left[\varsigma C_1+\frac{2}{\Omega_3}\left(\frac{\partial C_1}{\partial T_1}+i\sigma C_1\right)\right]$$

$$\cdot\left[\left(\frac{\Omega_3}{1-\Omega_3}\bar{M}\lambda\right)^2+\kappa^2\right]e^{i\omega_3T_0}-i\omega_iF\lambda e^{-i\gamma}\left(\frac{\Omega_3}{1-\Omega_3}\bar{M}+1\right)e^{i\omega_iT_0}+\text{c.c.}+\text{N.S.T.},\qquad(26c)$$

where

$$c_2=\frac{[4\kappa^2M^2\lambda^2+(\bar{I}-\kappa^2+\bar{M}\lambda^2)^2+(\bar{I}-\kappa^2+M\lambda^2-2M^2\lambda^2)\sqrt{4\kappa^2M^2\lambda^2+(\bar{I}-\kappa^2+\bar{M}\lambda^2)^2}]}{2\bar{M}^2\lambda^2},$$

$$c_3=\frac{[4\kappa^2M^2\lambda^2+(\bar{I}-\kappa^2+\bar{M}\lambda^2)^2-(\bar{I}-\kappa^2+M\lambda^2-2M^2\lambda^2)\sqrt{4\kappa^2M^2\lambda^2+(\bar{I}-\kappa^2+\bar{M}\lambda^2)^2}]}{2\bar{M}^2\lambda^2},$$

$$F=\frac{1}{2\omega_i}\bar{M}p^2(\lambda_1+\lambda_2e^{i\beta})+\frac{1}{2\omega_i}\sum_{i=1}^{n}[(p+\psi_{i0})^2e^{i\phi_{i0}}],$$

and $[\eta_1\ \eta_2\ \eta_3]$ are the modal coordinates in the level of $O(\varepsilon^1)$. Expressing A_1, B_1, and C_1 in Eqs. (26) in complex forms, that is,

$$A_1=a(T_1)+ib(T_1),\quad B_1=c(T_1)+id(T_1),\quad\text{and } C_1=e(T_1)+if(T_1),\qquad(27)$$

and incorporating them into rhs's of Eqs. (26) and (25*d*) for removal of secular terms, the slow dynamic equations evolved in time scale T_1 can be obtained. Note herein that with different resonance ω_i applied in the assumption (24) there would result a different set of slow dynamic equations, which are only valid in the neighborhood of the respective ω_i. With ω_1 considered, the set of slow dynamic equations in the following can be derived, which are only valid when the rotor speed is operated near the first translational resonance ω_1:

$$\frac{\partial a}{\partial\tau}=\frac{\varepsilon}{2}\left[-\varsigma a+2\sigma b-\frac{1}{2\omega_1}\left(\bar{M}p^2[\lambda_1\sin\gamma+\lambda_2\sin(\gamma-\beta)]+\sum_{i=1}^{n}[(p+\psi_{i0})^2\sin(\gamma-\phi_{i0})]\right)\right],$$

$$\frac{\partial b}{\partial\tau}=\frac{\varepsilon}{2}\left[-2\sigma a-\varsigma b-\frac{1}{2\omega_1}\left(\bar{M}p^2[\lambda_1\cos\gamma+\lambda_2\cos(\gamma-\beta)]+\sum_{i=1}^{n}[(p+\psi_{i0})^2\cos(\gamma-\phi_{i0})]\right)\right],$$

$$\frac{\partial c}{\partial\tau}=\frac{\varepsilon}{2}(-\Omega_2\varsigma c+2\sigma d),$$

$$\frac{\partial d}{\partial\tau}=\frac{\varepsilon}{2}(-2\sigma c-\Omega_2\varsigma d),\qquad(28a)$$

$$\frac{\partial e}{\partial\tau}=\frac{\varepsilon}{2}(-\Omega_3\varsigma e+2\sigma f),$$

$$\frac{\partial f}{\partial\tau}=\frac{\varepsilon}{2}(-2\sigma e-\Omega_3\varsigma f),$$

$$\frac{\partial\psi_{i0}}{\partial\tau}=-\frac{\varepsilon\mu_0}{2}\{-\omega_1^2[a\sin(\gamma-\phi_{i0})+b\cos(\gamma-\phi_{i0})]+\varsigma_1\psi_{i0}+\varsigma_0(p+\psi_{i0})^2\operatorname{sgn}(\psi_{i0})\},$$

$$\frac{\partial\phi_{i0}}{\partial\tau}=\psi_{i0}.$$

With ω_2 considered, the set of slow dynamic equations in the following can be derived, which are only valid when the rotor speed is operated near the second, translational resonance ω_2:

$$\frac{\partial a}{\partial\tau}=\frac{\varepsilon}{2}(-\varsigma a+2\sigma b),$$

$$\frac{\partial b}{\partial\tau}=\frac{\varepsilon}{2}(-2\sigma a-\varsigma b),$$

$$\frac{\partial e}{\partial\tau}=\frac{\varepsilon}{2}(-\Omega_3\varsigma e+2\sigma f),$$

$$\frac{\partial f}{\partial\tau}=\frac{\varepsilon}{2}(-2\sigma e-\Omega_3\varsigma f),\qquad(28b)$$

$$\frac{\partial c}{\partial\tau}=\frac{\varepsilon}{2}\left[-\Omega_2\varsigma c+2\sigma d-\frac{\Omega_2}{2\omega_2}\left(\bar{M}p^2[\lambda_1\cos\gamma+\lambda_2\cos(\gamma-\beta)]+\sum_{i=1}^{n}[(p+\psi_{i0})^2\cos(\gamma-\phi_{i0})]\right)\frac{\lambda[1+(\bar{M}-1)\Omega_2]}{2\kappa^2-(\bar{M}\lambda^2+\bar{I}+\kappa^2)\Omega_2}\right],$$

$$\frac{\partial d}{\partial\tau}=\frac{\varepsilon}{2}\left[-2\sigma c-\Omega_2\varsigma d+\frac{\Omega_2}{2\omega_2}\left(\bar{M}p^2[\lambda_1\sin\gamma+\lambda_2\sin(\gamma-\beta)]+\sum_{i=1}^{n}[(p+\psi_{i0})^2\sin(\gamma-\phi_{i0})]\right)\frac{\lambda[1+(\bar{M}-1)\Omega_2]}{2\kappa^2-(\bar{M}\lambda^2+\bar{I}+\kappa^2)\Omega_2}\right],$$

$$\frac{\partial\psi_{i0}}{\partial\tau}=-\frac{\varepsilon\mu_0}{2}\left[-\omega_2^2[c\cos(\gamma-\phi_{i0})-d\sin(\gamma-\phi_{i0})]\times\left(\frac{\Omega_2}{1-\Omega_2}\bar{M}+1\right)\lambda+\varsigma_1\psi_{i0}+\varsigma_0(p+\psi_{i0})^2\operatorname{sgn}(\psi_{i0})\right],$$

$$\frac{\partial\phi_{i0}}{\partial\tau}=\psi_{i0}.$$

With ω_3 considered, the set of slow dynamic equations in the following can be derived, which are only valid when the rotor speed is operated near the third, torsional resonance ω_3.

$$\frac{\partial a}{\partial\tau}=\frac{\varepsilon}{2}(-\varsigma a+2\sigma b),$$

$$\frac{\partial b}{\partial \tau}=\frac{\varepsilon}{2}(-2\sigma a-\varsigma b),$$

$$\frac{\partial c}{\partial \tau}=\frac{\varepsilon}{2}(-\Omega_2\varsigma c+2\sigma d),$$

$$\frac{\partial d}{\partial \tau}=\frac{\varepsilon}{2}(-2\sigma c-\Omega_3\varsigma d),$$

$$\tag{28c}$$

$$\frac{\partial e}{\partial \tau}=\frac{\varepsilon}{2}\left[-\Omega_3\varsigma e+2\sigma f-\frac{\Omega_3}{2\omega_3}\left(\bar{M}p^2[\lambda_1\cos\gamma+\lambda_2\cos(\gamma-\beta)]+\sum_{i=1}^{n}[(p+\psi_{i0})^2\cos(\gamma-\phi_{i0})]\right)\frac{\lambda[1+(\bar{M}-1)\Omega_3]}{2\kappa^2-(\bar{M}\lambda^2+\bar{I}+\kappa^2)\Omega_3}\right],$$

$$\frac{\partial f}{\partial \tau}=\frac{\varepsilon}{2}\left[-2\sigma e-\Omega_3\varsigma f+\frac{\Omega_3}{2\omega_3}\left(\bar{M}p^2[\lambda_1\sin\gamma+\lambda_2\sin(\gamma-\beta)]+\sum_{i=1}^{n}[(p+\psi_{i0})^2\sin(\gamma-\phi_{i0})]\right)\frac{\lambda[1+(\bar{M}-1)\Omega_3]}{2\kappa^2-(\bar{M}\lambda^2+\bar{I}+\kappa^2)\Omega_3}\right],$$

$$\frac{\partial \psi_{i0}}{\partial \tau}=-\frac{\varepsilon\mu_0}{2}\left[-\omega_3^2[e\cos(\gamma-\phi_{i0})-f\sin(\gamma-\phi_{i0})]\times\left(\frac{\Omega_3}{1-\Omega_3}\bar{M}+1\right)\lambda+\varsigma_1\psi_{i0}+\varsigma_0(p+\psi_{i0})^2\,\mathrm{sgn}(\psi_{i0})\right],$$

$$\frac{\partial \phi_{i0}}{\partial \tau}=\psi_{i0}.$$

Note in Eqs. (28) that ψ_{i0} and ϕ_{i0} provide the dynamics of the balancing balls. With the slow dynamic equations (28) in hand, the steady-state solutions and corresponding stabilities of the original system in Eqs. (13) are sought next in Secs. 4 and 5, respectively, especially for the ABS equipped with a pair of balancing balls, which is a most-common and simple design that is able to counteract the inherent imbalance in a varied range [1].

4 Approximate Steady-State Responses

The steady-state solutions of the system slow dynamic equations (28) are sought in this section for the case of a pair of balancing balls considered. The solutions would be used to predict balancing ball positions and residual vibrations for evaluating the performance of the balancer system. The solving process is started by setting the rhs's of Eqs. (28) equal to zeros, and also incorporating the steady-state status that $\psi_{s10}=\psi_{s20}=0$, i.e., both balls are motionless at steady state. Four different mathematical types of solutions are found. Type I has the pair of balancing balls settled at the angular positions separated with a certain angle. Types II and III, inequivalent in mathematical sense, however, both have the balancing balls settled at identical angular positions at steady state. Type IV has the balls settled at the positions 180 degrees opposite to each other. The mathematical expressions of the steady-state solutions are given in the following.

Type I: Solutions with distinct ball angular positions. There exist trivial steady-state solutions from setting the rhs's of Eqs. (28) to be zeros; i.e., $a_s=b_s=c_s=d_s=e_s=f_s=0$, which leads to zero level of residual vibration, i.e., $A=\sqrt{X^2+Y^2}=0$ up to $O(\varepsilon)$. The corresponding steady-state ball positions can be easily found by numerically solving

$$\sum_{i=1}^{2}\cos\phi_{si0}=-\bar{M}\lambda_1-\bar{M}\lambda_2\cos\beta, \tag{29a}$$

$$\sum_{i=1}^{2}\sin\phi_{si0}=-\bar{M}\lambda_2\sin\beta. \tag{29b}$$

Based on the forms of Eqs. (29), the type I solutions have the pair of balancing balls settled at distinct positions with the resulted net counter-balance located at the position 180 degrees opposite to the inherent imbalance. For this type of solution, since $a_s=b_s=c_s=d_s=e_s=f_s=0$ the system exhibits almost no residual vibrations, that is, zero residual vibration up to first linear order of ε; this solution is the desired solution for ABS designers to minimize residual vibrations.

Type II: Solutions with identical ball angular positions. There exist two other different types of solutions in mathematical expressions, both of which have the pair of balls settled at identical positions. The first type of solution can be easily found by numerically solving the following sets of equations for three different cases with the rotor speed operated near three resonances, respectively.

Type II-1: For the case that the rotor speed is operated near ω_1, i.e., $\omega_i=\omega_1$, the set of equations used to numerically solve for steady-state solutions is

$$c_s=d_s=e_s=f_s=0,$$

$$(-\varsigma a_s+2\sigma b_s)-\frac{1}{2\omega_1}p^2\left(\bar{M}\lambda_1\sin\gamma+\bar{M}\lambda_2\sin(\gamma-\beta)+2\frac{b_s}{\sqrt{a_s^2+b_s^2}}\right)=0,$$

$$(-2\sigma a_s-\varsigma b_s)-\frac{1}{2\omega_1}p^2\left(\bar{M}\lambda_1\cos\gamma+\bar{M}\lambda_2\cos(\gamma-\beta)-2\frac{a_s}{\sqrt{a_s^2+b_s^2}}\right)=0,$$

$$\sin\upsilon=\frac{b_s}{\sqrt{a_s^2+b_s^2}},\quad \text{and}\quad \cos\upsilon=\frac{a_s}{\sqrt{a_s^2+b_s^2}}.$$

With numerically solved υ from the above equations, both steady-state ball positions can be determined by

$$\phi_{s10}=\phi_{s20}=\gamma+\upsilon-\pi.$$

Type II-2: For the case that the rotor speed is operated near ω_2, i.e., $\omega_i=\omega_2$, the set of equations used to numerically solve for steady-state solutions is

$$c_s=d_s=e_s=f_s=0,$$

$$\left(-\varsigma c_s+\frac{2}{\Omega_2}\sigma d_s\right)-\frac{\{[\Omega_2/(1-\Omega_2)]\bar{M}+1\}\lambda}{(\{[\Omega_2/(1-\Omega_2)]\bar{M}\lambda\}^2+\kappa^2)}\cdot\frac{p^2}{2\omega_2}\left(\bar{M}\lambda_1\cos\gamma+\bar{M}\lambda_2\cos(\gamma-\beta)-2\frac{d_s}{\sqrt{c_s^2+d_s^2}}\right)=0,$$

$$\left(-\frac{2}{\Omega_2}\sigma c_s-\varsigma d_s\right)-\frac{\{[\Omega_2/(1-\Omega_2)]\bar{M}+1\}\lambda}{(\{[\Omega_2/(1-\Omega_2)]\bar{M}\lambda\}^2+\kappa^2)}\cdot\frac{p^2}{2\omega_2}\left(-\bar{M}\lambda_1\sin\gamma-\bar{M}\lambda_2\sin(\gamma-\beta)+2\frac{c_s}{\sqrt{c_s^2+d_s^2}}\right)=0,$$

$$\sin\upsilon=\frac{b_s}{\sqrt{a_s^2+b_s^2}},\quad \text{and}\quad \cos\upsilon=\frac{a_s}{\sqrt{a_s^2+b_s^2}}.$$

With numerically solved υ from the above equations, both steady-state ball positions can be determined by

$$\phi_{s10}=\phi_{s20}=\gamma+\upsilon-\pi.$$

Type II-3: For the case that the rotor speed is operated near ω_3, i.e., $\omega_i=\omega_3$, the set of equations used to numerically solve for steady-state solutions is

$$c_s=d_s=e_s=f_s=0,$$

$$\left(-\varsigma e_s+\frac{2}{\Omega_3}\sigma f_s\right)-\frac{\{[\Omega_3/(1-\Omega_3)]\bar{M}+1\}\lambda}{(\{[\Omega_3/(1-\Omega_3)]\bar{M}\lambda\}^2+\kappa^2)}\cdot\frac{p^2}{2\omega_3}\left(\bar{M}\lambda_1\cos\gamma+\bar{M}\lambda_2\cos(\gamma-\beta)-2\frac{f_s}{\sqrt{e_s^2+f_s^2}}\right)=0,$$

$$\left(-\frac{2}{\Omega_3}\sigma e_s-\varsigma f_s\right)-\frac{\{[\Omega_3/(1-\Omega_3)]\bar{M}+1\}\lambda}{(\{[\Omega_3/(1-\Omega_3)]\bar{M}\lambda\}^2+\kappa^2)}\cdot\frac{p^2}{2\omega_3}\left(-\bar{M}\lambda_1\sin\gamma-\bar{M}\lambda_2\sin(\gamma-\beta)+2\frac{e_s}{\sqrt{e_s^2+f_s^2}}\right)=0,$$

$$\sin\upsilon=\frac{b_s}{\sqrt{a_s^2+b_s^2}},\quad\text{and}\quad\cos\upsilon=\frac{a_s}{\sqrt{a_s^2+b_s^2}}.$$

With numerically solved υ from the above equations, both steady-state ball positions can be determined by

$$\phi_{s10}=\phi_{s20}=\gamma+\upsilon-\pi.$$

Type III: Solutions also with identical ball angular positions. The second type of solution that has both balls settled at identical positions can be easily found by numerically solving the following sets of equations for three different cases with the rotor speed operated near three resonances, respectively.

Type III-1: For the case that the rotor speed is operated near ω_1, i.e., $\omega_i=\omega_1$, the set of equations used to numerically solve for steady-state solutions is

$$c_s=d_s=e_s=f_s=0,$$

$$(-\varsigma a_s+2\sigma b_s)-\frac{1}{2\omega_1}p^2\left(\bar{M}\lambda_1\sin\gamma+\bar{M}\lambda_2\sin(\gamma-\beta)-2\frac{b_s}{\sqrt{a_s^2+b_s^2}}\right)=0,$$

$$(-2\sigma a_s-\varsigma b_s)-\frac{1}{2\omega_1}p^2\left(\bar{M}\lambda_1\cos\gamma+\bar{M}\lambda_2\cos(\gamma-\beta)+2\frac{a_s}{\sqrt{a_s^2+b_s^2}}\right)=0,$$

$$\sin\upsilon=\frac{b_s}{\sqrt{a_s^2+b_s^2}},\quad\text{and}\quad\cos\upsilon=\frac{a_s}{\sqrt{a_s^2+b_s^2}}.$$

With numerically solved υ from the above equations, both steady-state ball positions can be determined by

$$\phi_{s10}=\phi_{s20}=\gamma+\upsilon.$$

Type III-2: For the case that the rotor speed is operated near ω_2, i.e., $\omega_i=\omega_2$, the set of equations used to numerically solve for steady-state solutions is

$$c_s=d_s=e_s=f_s=0,$$

$$\left(-\varsigma c_s+\frac{2}{\Omega_2}\sigma d_s\right)-\frac{\{[\Omega_2/(1-\Omega_2)]\bar{M}+1\}\lambda}{(\{[\Omega_2/(1-\Omega_2)]\bar{M}\lambda\}^2+\kappa^2)}\cdot\frac{p^2}{2\omega_2}\left(\bar{M}\lambda_1\cos\gamma+\bar{M}\lambda_2\cos(\gamma-\beta)+2\frac{d_s}{\sqrt{c_s^2+d_s^2}}\right)=0,$$

$$\left(-\frac{2}{\Omega_2}\sigma c_s-\varsigma d_s\right)-\frac{\{[\Omega_2/(1-\Omega_2)]\bar{M}+1\}\lambda}{(\{[\Omega_2/(1-\Omega_2)]\bar{M}\lambda\}^2+\kappa^2)}\cdot\frac{p^2}{2\omega_2}\left(-\bar{M}\lambda_1\sin\gamma-\bar{M}\lambda_2\sin(\gamma-\beta)-2\frac{c_s}{\sqrt{c_s^2+d_s^2}}\right)=0,$$

$$\sin\upsilon=\frac{b_s}{\sqrt{a_s^2+b_s^2}},\quad\text{and}\quad\cos\upsilon=\frac{a_s}{\sqrt{a_s^2+b_s^2}}.$$

With numerically solved υ from the above equations, both steady-state ball positions can be determined by

$$\phi_{s10}=\phi_{s20}=\gamma-\upsilon.$$

Type III-3: For the case that the rotor speed is operated near ω_3, i.e., $\omega_i=\omega_3$, the set of equations used to numerically solve for steady-state solutions is

$$c_s=d_s=e_s=f_s=0,$$

$$\left(-\varsigma e_s+\frac{2}{\Omega_3}\sigma f_s\right)-\frac{\{[\Omega_3/(1-\Omega_3)]\bar{M}+1\}\lambda}{(\{[\Omega_3/(1-\Omega_3)]\bar{M}\lambda\}^2+\kappa^2)}\cdot\frac{p^2}{2\omega_3}\left(\bar{M}\lambda_1\cos\gamma+\bar{M}\lambda_2\cos(\gamma-\beta)+2\frac{f_s}{\sqrt{e_s^2+f_s^2}}\right)=0,$$

$$\left(-\frac{2}{\Omega_3}\sigma e_s-\varsigma f_s\right)-\frac{\{[\Omega_3/(1-\Omega_3)]\bar{M}+1\}\lambda}{(\{[\Omega_3/(1-\Omega_3)]\bar{M}\lambda\}^2+\kappa^2)}\cdot\frac{p^2}{2\omega_3}\left(-\bar{M}\lambda_1\sin\gamma-\bar{M}\lambda_2\sin(\gamma-\beta)-2\frac{e_s}{\sqrt{e_s^2+f_s^2}}\right)=0,$$

$$\sin\upsilon=\frac{b_s}{\sqrt{a_s^2+b_s^2}},\quad\text{and}\quad\cos\upsilon=\frac{a_s}{\sqrt{a_s^2+b_s^2}}.$$

With numerically solved υ from the above equations, both steady-state ball positions can be determined by

$$\phi_{s10}=\phi_{s20}=\gamma-\upsilon.$$

Note in fact that the steady-state dynamics pertaining to solutions of types II and III are identical to that with a single ball balancer system, which achieves favorable balancing effect only if the total mass of balancing ball is sized perfectly. This is usually highly difficult to achieve due to manufacture tolerance.

Type IV: Solutions with balls separated by 180 *degrees*. The solutions of this type can easily be found by solving following sets of equations near three resonances.

Type IV-1: For the case that the rotor speed is operated near ω_1, i.e., $\omega_i=\omega_1$, the set of equations used to numerically solve for steady-state solutions are

$$c_s=d_s=e_s=f_s=0,$$

$$(-\varsigma a_s+2\sigma b_s)-\frac{1}{2\omega_1}p^2[\bar{M}\lambda_1\sin\gamma+\bar{M}\lambda_2\sin(\gamma-\beta)]=0,$$

$$(-2\sigma a_s-\varsigma b_s)-\frac{1}{2\omega_1}p^2[\bar{M}\lambda_1\cos\gamma+\bar{M}\lambda_2\cos(\gamma-\beta)]=0,$$

$$\sin\upsilon=\frac{b_s}{\sqrt{a_s^2+b_s^2}},\quad\text{and}\quad\cos\upsilon=\frac{a_s}{\sqrt{a_s^2+b_s^2}}.$$

With numerically solved υ from the above equations, both steady-state ball positions can be determined by

$$\phi_{s10}=\gamma-\upsilon\quad\text{and}\quad\phi_{s20}=\gamma-\upsilon+\pi.$$

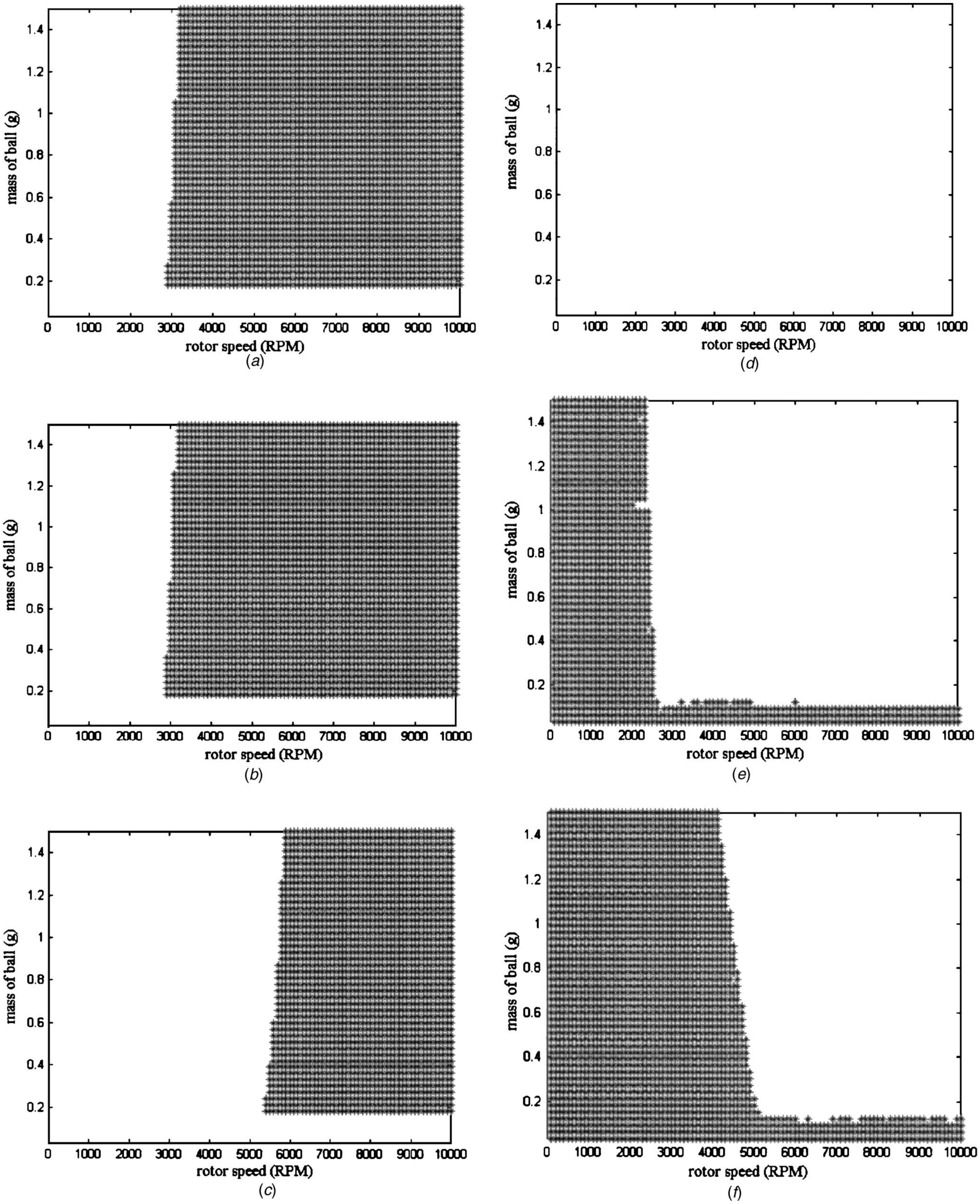

Fig. 4 System stability diagram of ball mass m versus rotor speed ω; shaded areas are stable regions while blanks are unstable ones. (*a*)–(*c*) Stability diagrams of type I solution near three resonances ω_1, ω_2, and ω_3, respectively. (*d*)–(*f*) Stability diagrams of type II solution near three resonances, respectively. (*g*)–(*i*) Stability diagrams of type III solution near three resonances, respectively. (*j*)–(*l*) Stability diagrams of type IV solution near three resonances, respectively.

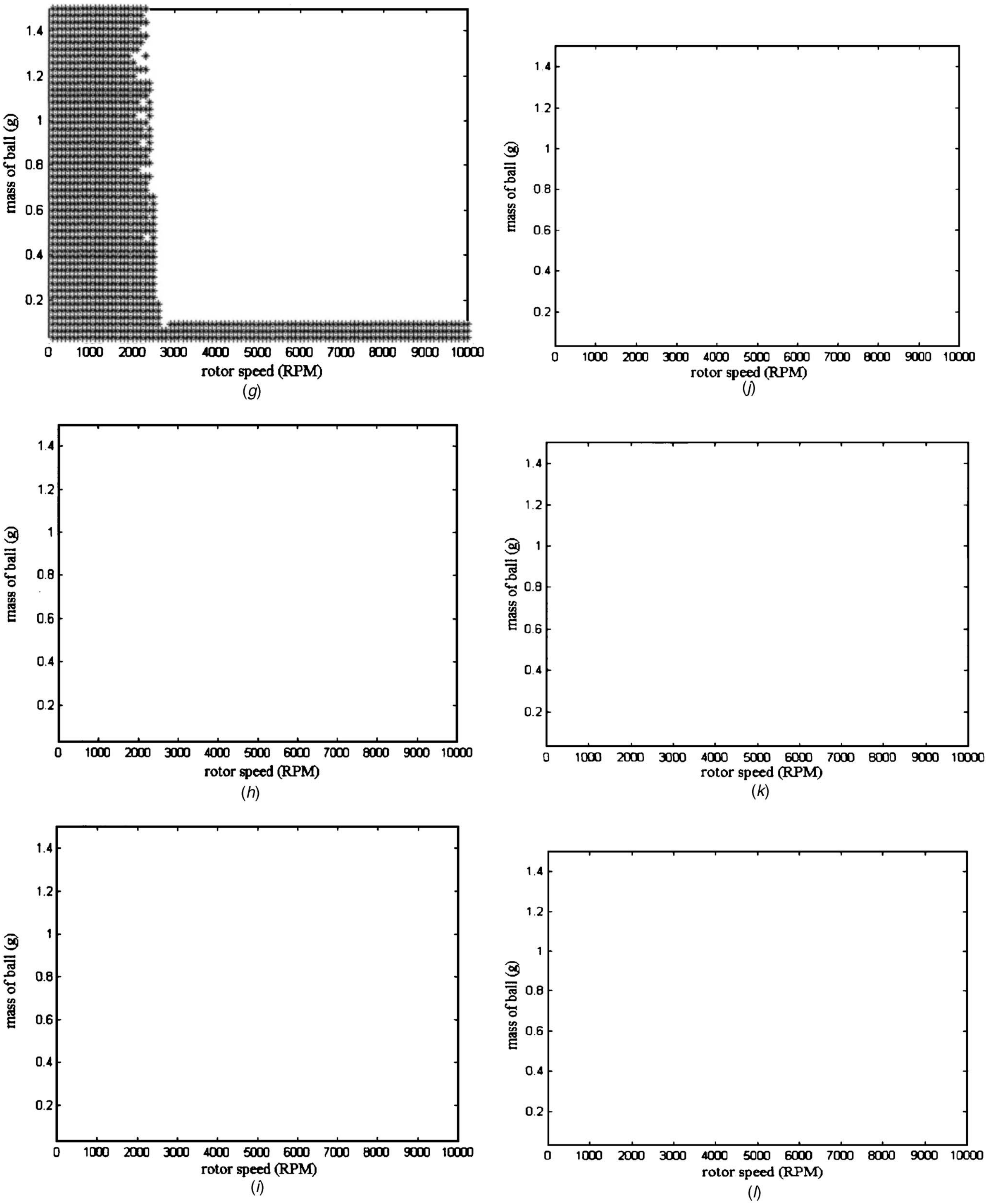

(*g*) (*j*) (*h*) (*k*) (*i*) (*l*)

Fig. 4 (***Continued***).

Type IV-2: For the case that the rotor speed is operated near ω_2, i.e., $\omega_i = \omega_2$, the set of equations used to numerically solve for steady-state solutions are

$$c_s = d_s = e_s = f_s = 0,$$

$$\left(-\varsigma c_s + \frac{2}{\Omega_2}\sigma d_s\right)\frac{\{[\Omega_2/(1-\Omega_2)]\bar{M}+1\}\lambda}{(\{[\Omega_2/(1-\Omega_2)]\bar{M}\lambda\}^2+\kappa^2)} \cdot \frac{p^2}{2\omega_2}[\bar{M}\lambda_1 \cos\gamma + \bar{M}\lambda_2\cos(\gamma-\beta)] = 0,$$

$$\left(-\frac{2}{\Omega_2}\sigma c_s - \varsigma d_s\right) - \frac{\{[\Omega_2/(1-\Omega_2)]\bar{M}+1\}\lambda}{(\{[\Omega_2/(1-\Omega_2)]\bar{M}\lambda\}^2+\kappa^2)} \cdot \frac{p^2}{2\omega_2}[-\bar{M}\lambda_1 \sin\gamma - \bar{M}\lambda_2\sin(\gamma-\beta)] = 0,$$

$$\sin\upsilon = \frac{b_s}{\sqrt{a_s^2+b_s^2}}, \quad \text{and} \quad \cos\upsilon = \frac{a_s}{\sqrt{a_s^2+b_s^2}}.$$

With numerically solved υ from the above equations, both steady-state ball positions can be determined by

$$\phi_{s10} = \gamma - \upsilon \quad \text{and} \quad \phi_{s20} = \gamma - \upsilon + \pi.$$

Type IV-3: For the case that the rotor speed is operated near ω_3, i.e., $\omega_i = \omega_3$, the set of equations used to numerically solve for steady-state solutions is

$$c_s = d_s = e_s = f_s = 0,$$

$$\left(-\varsigma e_s + \frac{2}{\Omega_3}\sigma f_s\right) - \frac{\{[\Omega_3/(1-\Omega_3)]\bar{M}+1\}\lambda}{(\{[\Omega_3/(1-\Omega_3)]\bar{M}\lambda\}^2+\kappa^2)} \cdot \frac{p^2}{2\omega_3}[\bar{M}\lambda_1 \cos\gamma + \bar{M}\lambda_2\cos(\gamma-\beta)] = 0,$$

$$\left(-\frac{2}{\Omega_3}\sigma e_s - \varsigma f_s\right) - \frac{\{[\Omega_3/(1-\Omega_3)]\bar{M}+1\}\lambda}{(\{[\Omega_3/(1-\Omega_3)]\bar{M}\lambda\}^2+\kappa^2)} \cdot \frac{p^2}{2\omega_3}[-\bar{M}\lambda_1 \sin\gamma - \bar{M}\lambda_2\sin(\gamma-\beta)] = 0,$$

$$\sin\upsilon = \frac{b_s}{\sqrt{a_s^2+b_s^2}}, \quad \text{and} \quad \cos\upsilon = \frac{a_s}{\sqrt{a_s^2+b_s^2}}.$$

With numerically solved υ from the above equations, both steady-state ball positions can be determined by

$$\phi_{s10} = \gamma - \upsilon \quad \text{and} \quad \phi_{s20} = \gamma - \upsilon + \pi.$$

Note that type IV renders no counter-balance due to an exact mutual cancellation of two counter-balancing centrifugal forces generated by two 180-degree-separated balls at steady state.

5 Stability Analysis and Design Guidelines

Analysis is performed herein to determine the stability of each steady-state solution found in the previous section. Design guidelines are then distilled in the next section for achieving desired performance by balanced solutions; i.e., substantial radial vibration reduction. The analysis is conducted via construction of stability diagrams with respect to variation of two main design parameters, operating speed ω and ball mass m. Other system parameters are fixed to representative and practical values as follows: $M_s = 90.5$ g, $M_r = 49.5$ g, $I_s = 1.45 \times 10^{-4}$ kg·m^2, $r = 1.5$ mm, $R = 16.5$ mm, $K = 2650$ N/m, $\zeta = 0.01$, $C = 0.193$ Kg/s, $e = 0.1$ mm, $\alpha_1 = 5 \times 10^{-3}$ N·s/m^2, $\alpha_0 = 10^{-5}$, $S = 30$ mm, $\gamma = 10°$, $l = 67.5$ mm, and $\tau = 33.7°$. Without loss of representativeness in stability, $\rho = 0$ is employed herein for stability analysis. The tool for stability analysis is the commonly known Routh-Hurwitz criterion, which is able to establish an characteristic equation based on the Jacobians of the scaled slow-dynamic equations (28*a*)–(28*c*). Subsequent stability results for all solutions are discussed accordingly in the followings.

Figures 4(*a*)–4(*l*) show various stability diagrams near three resonances ω_1, ω_2, and ω_3, respectively, where the shaded regions represent the ones full of stable solutions while the unshadeds are the ones filled with unstable solutions. Owing to the perturbation theorem, the stability results shown in each diagram are only guaranteed valid near the resonances considered. Among all solutions, type I solutions, based on the conclusion drawn in Sec. 3, are desired balanced ones which render the most substantial radial and torsional vibration reductions compared to other types of solutions. To completely ensure stability of this type I solution at steady state, the ABS can be conservatively designed and operated by designers such that (ω, m) simultaneously fall in three shaded areas in Figs. 4(*a*)–4(*c*), which results in a region that coincides with the shaded area in Fig. 4(*c*) [since it is entirely contained in those in Figs. 4(*a*) and 4(*b*)]. The aforementioned requirements lead to two design guidelines. First, the system needs to be operated above three resonances, i.e., $\omega > \omega_1$ ($\omega_1 = 2622$ rpm for the simulated case herein), $\omega > \omega_2$ ($\omega_2 = 2579$ rpm), and $\omega > \omega_3$ ($\omega_3 = 5115$ rpm). Second, the maximal counter-balance must be greater than inherent unbalance, i.e., $2mR > M_r e$, which corresponds to the area $m > 0.15$ g in Fig. 4(*c*). Acknowledging $\omega_3 = 5115$ rpm being well below the commonly operated rotor speeds for modern ODDs (usually above 8000 rpm), a suitable design of m such that $2mR > M_r e$ suffices to offer the ABS a fair chance to achieve substantial vibration reduction for modern ODDs.

Figures 4(*d*)–4(*i*) also show stability regions of type II and III solutions as well obtained in Sec. 3. These solutions have two balls settled at the same position such that only a slim chance of perfect-sizing makes possible effective vibration reductions, which, for ABS designers, are the solutions much less desirable as compared to type I solutions for balancing balls to settle. To avoid the dynamic convergence of the balancing balls to these solutions, based on Figs. 4(*d*)–4(*i*), one needs to assign ball mass and also operate rotor speed such that $\omega > \omega_1$, $\omega > \omega_2$, $\omega > \omega_3$, and $2mR > M_r e$. This is equivalent to force (ω, m) fallen in the stability region of type I solutions shown in Fig. 4(*c*). As to the type IV solutions, which have the two balancing balls settled at positions 180 degrees opposite to each other such that they generate no effect of vibration reduction, the analytical result shows that with the same ranges of ω and m considered in the previous cases, no

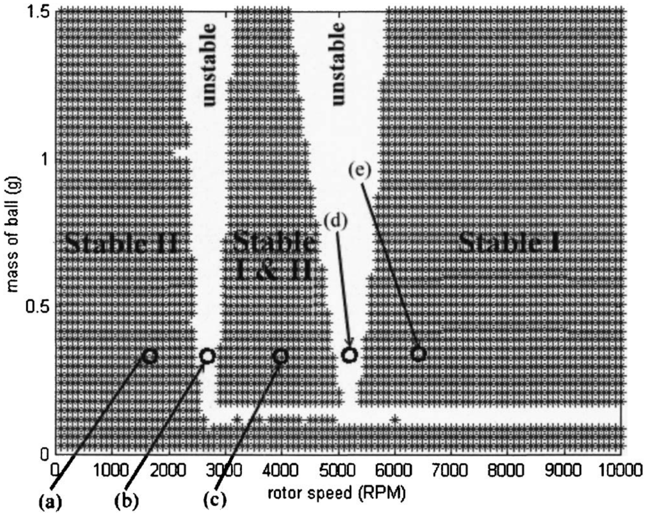

Fig. 5 Combined stability diagram

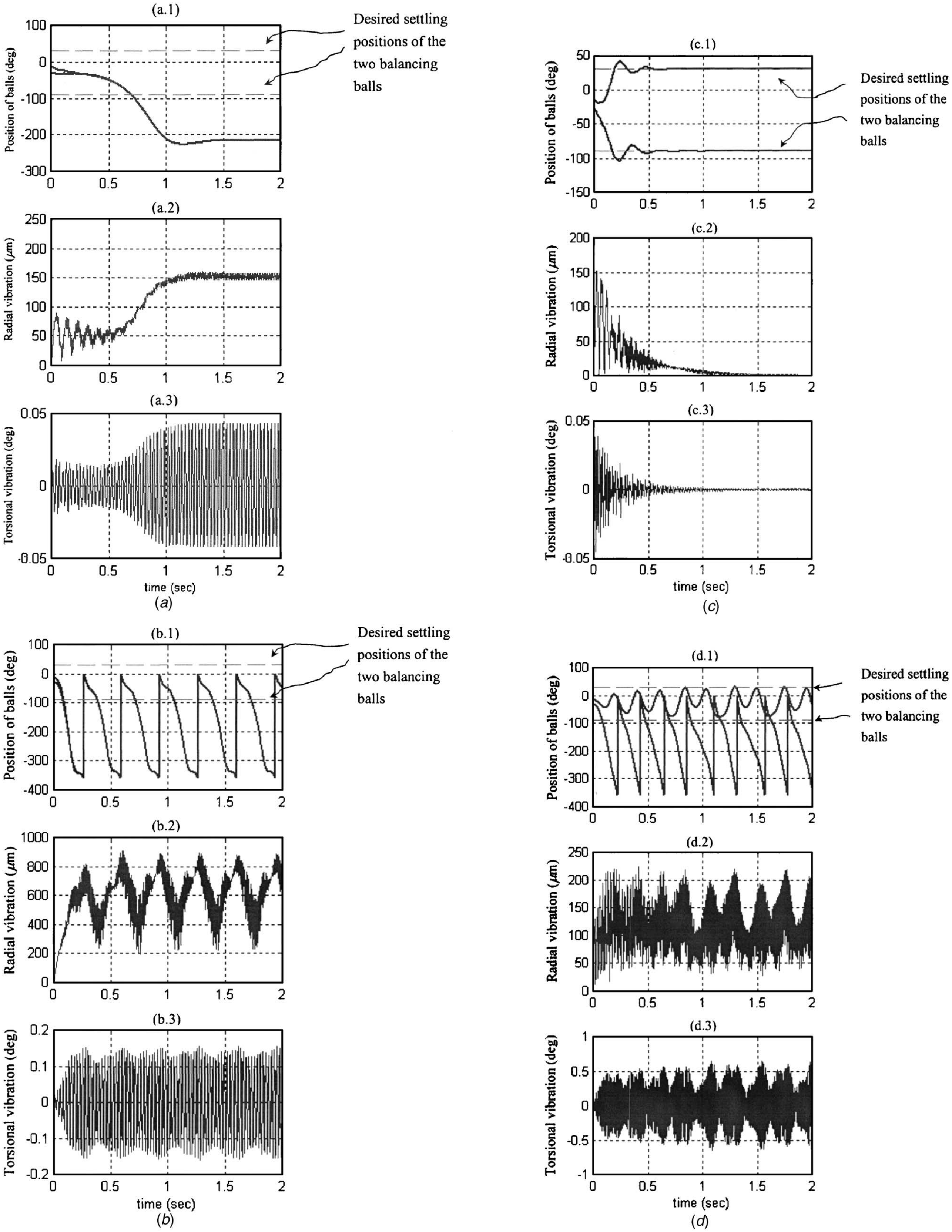

Fig. 6 Dynamic responses corresponding to the marked points in Fig. 5

stability region is affirmed. This denies any convergence chance of the ball dynamics to type IV solutions in practice.

Based on the stability diagrams given in Figs. 4, the total system stability can be integrally represented in Fig. 5, where stable I region refers to the region where only type I solution is stable, stable II region refers to where type II and III solutions are stable,

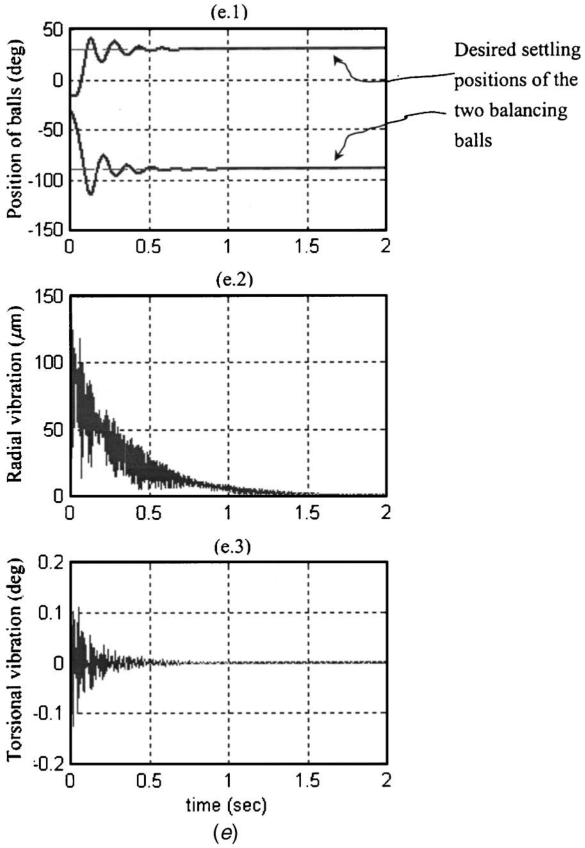

Fig. 6 (*Continued*).

while stable I&II region refers to where type I and II solutions are both stable. Note that the stability results in stable II and stable I&II indicate coexistence of multiple stable solutions for the nonlinear system considered in this study. The unstable regions near translational and torsional resonances correspond to the cases where no previously solved solutions are stable—the balancing balls may not be able to stop or stick together at steady state, which is demonstrated in simulations in the next section. Finally, it can be seen from this figure that stable I region, being exactly the desired stable region of type I solution shown in Fig. 4(*c*), shares no overlap with any other shades corresponding to other stable solutions. This indicates that with (ω,m) assigned in stable I region, the balancing balls are guaranteed to converge to the type I solutions, leading to the desired, substantial reduction in radial and torsional vibrations. On the other hand, with (ω,m) assigned in stable I&II region, the designer of the ABS stands a risk that the balancing balls might converge to type II solution, one of unbalanced solutions. Conclusively speaking from the above, with appropriate designation of total balancer mass one could operate the ODD spindle above the transnational/torsional resonances conservatively to converge system dynamics to the region with only one stable type I solution, the balanced one, such that substantial vibration reduction is achieved.

6 Simulation Validation

With stability results obtained and design guidelines distilled, numerical simulations are conducted in this section for validation. The numerical simulation method used is the conventional Runge-Kutta method. Figures 6 show the resulted dynamic responses corresponding to the five marked points with determined rotor speeds and ABS mass in Fig. 5. Each response is observed in terms of ball positions, $(\phi_1(t),\phi_2(t))$, level of radial vibration, $A(t)=\sqrt{X(t)^2+Y(t)^2}$, and level of torsional vibration, $\varphi(t)$, in three respective subfigures. Note in Figs. 6(*a*)(1), 6(*b*)(1), 6(*c*)(1), 6(*d*)(1), and 6(*e*)(1) that the dashed lines denote the desired steady-state settling ball positions of type I solutions, which render almost zero radial and torsional vibrations. Figures 6(*a*)(1)–6(*a*)(3) depict the responses corresponding to point *a* in Fig. 5, in which it is seen that the system dynamics converges to one of type II (or III) solution with both balls settled at identical positions and then resulting in large, unreduced radial and torsional vibrations. Figures 6(*b*)(1)–6(*b*)(3) depict the responses corresponding to point *b* in Fig. 5, in which it is seen that with (ω,m) in one of the unstable regions in Fig. 5, the response is oscillatory at steady state since no stable fixed-point-type solution exists, as found in previous stability analysis on the asymptotic solutions. Figures 6(*c*)(1)–6(*c*)(3) depict the responses corresponding to point *c* in Fig. 5, in which the system converges to one of type I solutions with the balls settled at distinct positions. Note in fact that with values of (ω,m) in the stable I&II region of Fig. 5, it is found from simulations herein that the dynamics might converge to either type I solution as shown in Fig. 6(*c*) or type II solution which is not shown herein. Figures 6(*d*)(1)–6(*d*)(3) depict the responses corresponding to point *d* in Fig. 5, which exhibit the same dynamic characteristics as those shown in Figs. 6(*b*)(1)–6(*b*)(3). Figures 6(*e*)(1)–6(*e*)(3) depict the responses corresponding to point *e* in Fig. 5, in which the system dynamics converges to one of desired type I solutions with the balls settled at the distinct positions as predicted by previous multiple scale analysis in the dashed lines. These solutions are the desired solutions for the balls to converge to, resulting in a substantial vibration reduction in both radial and torsional directions.

7 Conclusion

A complete dynamics and stability analysis on the automatic balancer system (ABS) installed in optical disk drives with consideration of torsional motion due to the turntable are accomplished in this study. A mathematical model was first established to precisely describe the dynamics of the whole system, which is followed by reasonable scalings and application of multiple scales analysis. Through the perturbed equations derived from the method of multiple scales, all possible steady-state solutions are found and the associated stabilities are analyzed. The results show coexistence of multiple stable balanced/unbalanced solutions between translational and torsional resonances with one single balanced solution above the torsional resonance. Therefore, it is recommended that along with appropriate designation of total balancer mass, the spindle speed of an ODD could be operated above the torsional resonances conservatively for the system dynamics to converge to the only one stable solution, the balanced one, such that substantial vibration reduction is achieved.

Acknowledgment

The authors would like to pay special thanks to National Science Council of Republic of China and LITE-ON IT Corp. for financially supporting this research project. The supporting Contract Nos. are NSC 91-2212-E-194-019 and NSC 91-2212-E-033-004.

References

[1] Kang, J. R., Chao, C. P., Huang, C. L., and Sung, C. K., 2001, "The Dynamics of a Ball-Type Balancer System Equipped With a Pair of Free-Moving Balancing Masses," ASME J. Vibr. Acoust., **123**(4), pp. 456–465.
[2] Thearle, E. L., 1950, "Automatic Dynamic Balancers (Part 1 Leblanc Balancer)," Mach. Des., **22**, pp. 119–124.
[3] Thearle, E. L., 1950, "Automatic Dynamic Balancers (Part 2-Ring, Pendulum, Ball Balancers)," Mach. Des., **22**, pp. 103–106.
[4] Inoue, J., Jinnouchi, Y., and Kubo, S., 1979, "Automatic Balancers," Trans. Jpn. Soc. Mech. Eng., Ser. C, **49**, pp. 2142–2148.
[5] Bövik, P., and Högfors, C., 1986, "Autobalancing of Rotors," J. Sound Vib., **111**, pp. 429–440.
[6] Jinnouchi, Y., Araki, Y., Inoue, J., Ohtsuka, Y., and Tan, C., 1993, "Automatic Balancer (Static Balancing and Transient Response of a Multi-Ball Balancer),"

Trans. Jpn. Soc. Mech. Eng., Ser. C, **59**, pp. 79–84.
[7] Majewski, T., 1988, "Position Errors Occurrence in Self Balancers Used on Rigid Rotors of Rotating Machinery," Mech. Mach. Theory, **23**, pp. 71–78.
[8] Rajalingham, C., and Rakheja, S., 1998, "Whirl Suppression in Hand-Held Power Tool Rotors Using Guided Rolling Balancers," J. Sound Vib., **217**, pp. 453–466.
[9] Hwang, C. H., and Chung, J., 1999, "Dynamic Analysis of an Automatic Ball Balancer With Double Races," JSME Int. J., Ser. C, **42**(2), pp. 265–272.
[10] Huang, W. Y., Chao, C. P., Kang, J. R., and Sung, C. K., 2002, "The Application of Ball-Type Balancers on Radial Vibration Reduction of High-Speed Optic Disk Drives," J. Sound Vib., **250**(3), pp. 415–430.
[11] Sung, C.-K., Chao, C. P., and Wu, S.-T., 2002, "Modeling and Experimental Validation of a Spindle0disk System Equipped With an Automatic Balancer System for Optical Disc Drives," International Symposium on Experimental Mechanics, Dec. 28–30, Taipei, Taiwan.
[12] Kim, W., and Chung, J., 2002, "Performance of Automatic Ball Balancers on Optical Disc Drives," Proc. Inst. Mech. Eng., Part C: J. Mech. Eng. Sci., **216**(11), pp. 1071–1080.

H. Kobayashi

R. Vanderby[1]
e-mail: vanderby@surgery.wisc.edu

Department of Engineering Physics,
Department of Biomedical Engineering,
Department of Orthopedics and Rehabilitation,
University of Wisconsin—Madison,
600 Highland Avenue,
Madison, WI 53792

New Strain Energy Function for Acoustoelastic Analysis of Dilatational Waves in Nearly Incompressible, Hyper-Elastic Materials

Acoustoelastic analysis has usually been applied to compressible engineering materials. Many materials (e.g., rubber and biologic materials) are "nearly" incompressible and often assumed incompressible in their constitutive equations. These material models do not admit dilatational waves for acoustoelastic analysis. Other constitutive models (for these materials) admit compressibility but still do not model dilatational waves with fidelity (shown herein). In this article a new strain energy function is formulated to model dilatational wave propagation in nearly incompressible, isotropic materials. This strain energy function requires four material constants and is a function of Cauchy–Green deformation tensor invariants. This function and existing (compressible) strain energy functions are compared based upon their ability to predict dilatational wave propagation in uniaxially prestressed rubber. Results demonstrate deficiencies in existing functions and the usefulness of our new function for acoustoelastic applications. Our results also indicate that acoustoelastic analysis has great potential for the accurate prediction of active or residual stresses in nearly incompressible materials. [DOI: 10.1115/1.2041661]

Introduction

When waves propagate through a prestressed medium, the speed of propagation is stress dependent. This phenomenon, called acoustoelasticity, is the basis for a nondestructive method to determine active or residual stresses in materials and structures. Hughes and Kelly [1] initiated the modern theory of acoustoelasticity, relating prestress in compressible elastic media to velocity changes in bulk waves. Toupin and Bernstein [2], Truesdell [3], and Tokuoka and Iwashimizu [4] developed the theory further. Stress was determined from the measurement of bulk waves by Blinka and Sachse [5]; Kino et al. [6]; King and Furtunko [7]; Thompson, Lee, and Smith [8]; and Dike and Johnson [9]. Iwashimizu and Kobori [10] and Mase and Johnson [11] formulated theory and numerically analyzed surface waves in prestressed conventional elastic media (e.g., steel and aluminum). Lee, Kim and Achenbach [12] performed surface wave experiments to corroborate their acoustoelastic predictions of prestress in conventional materials. Pao, Sache, and Fukuoka [13] reviewed and summarized many applications for acoustoelastic theory. Although intensively studied, most acoustoelastic analyses have been applied to conventional compressible engineering materials, e.g., steel or aluminum.

Acoustoelastic analyses have also been performed on rubber by Ogden [14], Erigen and Suhubi, [15], and Fu [16], but dilatational waves are not considered because they assumed rubber to be incompressible. If an elastic material is modeled as purely incompressible, then the theoretical propagation velocity of dilatational waves becomes infinite. That is, an incompressible material cannot hold a dilatational wave, and acoustoelastic analysis is limited to the two shear waves. Rubber is, however, slightly compressible with a Poisson's ratio around 0.499, [17], and it can sustain dilatational waves, [18]. Treating rubber and other hyper-elastic materials as nearly incompressible materials is inconsistent for any analysis of dilatational wave propagation.

To our knowledge, no previous acoustoelastic formulations exist for hyper-elastic materials in which the material is treated as "nearly" incompressible. The goals of this article then are first to formulate an appropriate, strain energy function for a nearly incompressible, hyper-elastic material and then to demonstrate its potential for acoustoelastic analyses by comparing it with existing strain energy functions. In this study, we propose a new strain energy function by modifying the well-known Mooney–Rivlin function to admit compressibility. We add terms related to volumetric change. These terms model dilatational waves with fidelity without disturbing other mechanical characteristics, e.g., stress-strain behavior and shear wave propagation.

Acoustoelastic Theory for a Compressible, Hyper-Elastic Material

The theory of acoustoelasticity superposes small dynamic deformations of an ultrasonic wave onto a static, finite deformation. For convenience, three configurations are introduced.

(1) The stress-free or *reference configuration* is defined with vector X_A to denote a material point in the body.
(2) The initial, finite, static deformation is defined as the *deformed configuration* with position vector x_i.
(3) The small dynamic wave deformation is defined as the *current configuration* with position vector x_i^*.

All Latin indices range from 1 to 3 and a repeated summation convention is assumed unless stated otherwise.

---

[1] To whom correspondence should be addressed.

Contributed by the Applied Mechanics Division of THE AMERICAN SOCIETY OF MECHANICAL ENGINEERS for publication in the ASME JOURNAL OF APPLIED MECHANICS. Manuscript received by the Applied Mechanics Division: October 6, 2003; final revision: February 11, 2005. Associate Editor: S. Mukherjee. Discussion on the paper should be addressed to the Editor, Prof. Robert M. McMeeking, Journal of Applied Mechanics, Department of Mechanical and Environmental Engineering, University of California—Santa Barbara, Santa Barbara, CA 93106-5070, and will be accepted until four months after final publication in the paper itself in the ASME JOURNAL OF APPLIED MECHANICS.

As defined in previous acoustoelastic studies, e.g., Refs. [2,13], the equation of motion referred to the *deformed configuration* is

$$\frac{\partial}{\partial x_j}\left[\bar{C}_{ijks}u_{k,s} + t_{js}\frac{\partial u_i}{\partial x_s}\right] = \rho \ddot{u}_i. \tag{1}$$

In the above equation, $\bar{C}_{ijks}$ and t_{js}, respectively, represent the fourth order stiffness tensor and Cauchy stress tensor caused by a finite static deformation. For a general compressible, hyper-elastic material, $\bar{C}_{ijks}$ and t_{js} are related to the strain energy function $W(E_{AB})$, deformation gradient tensor F_{jA} and finite Green strain tensor E_{AB} by

$$\bar{C}_{ijks} = \frac{1}{\det F_{jA}} F_{iA}F_{jB}F_{kC}F_{sD}\frac{\partial^2 W}{\partial E_{AB}\partial E_{CD}} \tag{2}$$

and

$$t_{js} = \frac{1}{\det F_{jA}} F_{jA}F_{sB}\frac{\partial W(E_{AB})}{\partial E_{AB}}, \tag{3}$$

where $F_{jA}=\partial x_j/\partial X_A$ and $E_{AB}=\frac{1}{2}(F_{iA}F_{iB}-\delta_{AB})$.

When prestress is zero, tensor $\bar{C}_{ijks}$ becomes stiffness tensor c_{ijks} for generalized Hooke's law, and Eq. (1) reduces to the wave equation. Due to symmetry of the strain and stress tensors, the tensor $\bar{C}_{ijks}$ is symmetric as the Hookean stiffness tensor c_{ijks}, ie.,

$$\bar{C}_{ijks} = \bar{C}_{ksij} = \bar{C}_{ijsk} = \bar{C}_{jiks}. \tag{4}$$

Finally, Cauchy stress in the current configuration can be written as

$$t^*_{ij} = \bar{C}_{ijks}u_{k,s} + (1 - u_{i,i})t_{ij} + u_{i,k}t_{kj} + u_{j,s}t_{is}. \tag{5}$$

Due to symmetry, tensor $\bar{C}_{ijks}$ is replaced hereafter with a 6 by 6 matrix $\tilde{C}_{pq}$ for convenience with the contracting subscript notations $1\rightarrow 11$, $2\rightarrow 22$, $3\rightarrow 33$, $4\rightarrow 23$, $5\rightarrow 13$, $6\rightarrow 12$ to relate $\bar{C}_{ijks}$ to $\tilde{C}_{pq}$ $(i,j,k,l=1,2,3$ and $p,q=1,2,\ldots,6)$. Toupin and Bernstein [2] or Pao, Sache, and Fukuoka [13] provide a detailed derivation of the above equations.

Strain Energy Function for a Nearly Incompressible Material

In this section we propose a new strain energy function for an isotropic, nearly incompressible material (rubber or biological materials) under finite deformation. Acoustoelastic behavior of this function is then compared with other compressible, strain energy functions from previous studies.

Due to its very small compressibility, a rubber-like material is often assumed to be incompressible within its strain energy function. Such functions can be categorized into the following two major groups.

(1) *Invariants-based functions*

Most constitutive equations in this group are derived as a function of the first two invariants of the Cauchy–Green deformation tensor C_{AB}. The most widely used invariants-based strain energy function, proposed by Rivlin [19], is

$$W = C_1(I_C - 3) + C_2(II_C - 3).$$

$$III_C = 1, \tag{6}$$

where I_C, II_C, and III_C represent first, second, and third invariants of Cauchy–Green tensor C_{AB}, respectively. In turn, Cauchy–Green tensor C_{AB} is related to the deformation gradient tensor F_{jA} by

$$C_{AB} = F_{iA}F_{iB}, \tag{7}$$

where $F_{jA}=\partial x_j/\partial X_A$.

(2) *Principal stretch based functions*

Equations in this group are derived as functions of principal stretches. The most widely used function in this group, proposed by Ogden [20], is

$$W = \sum_{p=1}^{N}\frac{\mu_p}{\alpha_p}(\lambda_1^{\alpha_p} + \lambda_2^{\alpha_p} + \lambda_3^{\alpha_p} - 3). \tag{8}$$

$$\lambda_1\lambda_2\lambda_3 = 1,$$

where λ_i $(i=1,2,3)$ are eigenvalues of the Cauchy–Green tensor C_{AB}.

The above incompressible functions are generally useful but do not model dilatational waves. Since rubber-like materials can sustain the propagation of dilatational waves, a strain energy function with compressibility is necessary to model this phenomenon.

Numerous strain energy functions for nearly incompressible materials have been formulated for nonlinear finite element analyses where material incompressibility causes computational problems (Cescotto and Fonder [21], Liu, Hofsteller, and Mang [22], Watanabe [23], Doll and Schweizerhof [24]). Recently, strain energy functions based on the principal stretches have gained popularity, especially to characterize a very high level of strain. Because these require an extra computational step to evaluate the principal stretches, invariants-based functions are still attractive. They are easier to implement into finite element formulations and save computational time. Doll and Schweizerhof [24] determined the mathematical requirements for the parts of strain energy functions that govern volumetric change. They separated isochoric (non-volume changing) and volumetric (volume-changing) parts of many published strain energy functions and then showed which of them satisfied the mathematical requirements. Any new function that admits compressibility must also satisfy these requirements.

Strain energy functions can either be formulated as a function of Cauchy–Green invariants or principal stretches. In acoustoelasticity, three different waves are potentially able to propagate in each direction. Except for the special case when the direction of wave propagation coincides with the direction of principal stress, the equations are coupled and difficult to evaluate. This study then is limited to invariants-based strain energy functions, which are easier to use in acoustoelastic analysis.

The following five invariants-based strain energy functions are considered [Eqs. (9)–(13)]. The first function [Eq. (9)], proposed by Smith and Rivlin [25], has been utilized both by Tokuoka [26] and Johnson [27] in studies of acoustoelasticity in anisotropic material. Since only isotropic material is considered herein, only the isotropic terms are retained [Eq. (9)]. The second function [Eq. (10)] was proposed by Watanabe et al. [23] to study the kinking of hyper-elastic materials like rubber. The third and fourth functions [Eqs. (11) and (12), respectively] were proposed by Doll [24] in his study on the volumetric behavior of strain energy functions. In addition to these four functions, we propose a new function [Eq. (13)], based on the Moony–Rivlin function [Eq. (6)], but developed with additional terms that are a function of the third invariant of the Cauchy–Green tensor. These five strain energy functions listed in order are

$$W_1 = b_1 I_E^2 + b_2 II_E + g_1 I_E^3 + g_2 I_E II_E + g_3 III_E, \tag{9}$$

where $I_E=E_{AA}$, $II_E=\frac{1}{2}(E_{AB}E_{BA}-E_{AA}E_{BB})$ and $III_E=\det E_{AB}$.

$$W_2 = C_1(I_C - 3) + C_2(II_C - 3) - (2C_1 + 4C_2)Ln[III_C] + \hat{K}[(J-1)^2 + Ln[J]^2], \tag{10}$$

where (as defined by Watanabe et al. [22]) $\hat{K}=3(C_1+C_2)(1-\nu)/(1+\nu)(1-2\nu)-(4C_1+8C_2)$ and ν is Poisson's ratio.

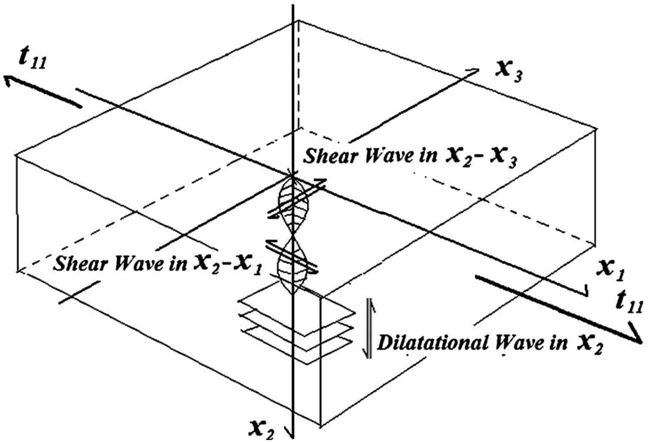

Fig. 1 Three potential waves propagate in x_2 direction in prestretched media

$$W_3 = \frac{K}{2}[\mathrm{Exp}(J-1) - \mathrm{Log}\,J - 1] + C_1(\Gamma_1 - 3) + C_2(\Gamma_2 - 3) \qquad (11)$$

$$W_4 = \frac{K}{2}(J-1)\mathrm{Log}\,J + C_1(\Gamma_1 - 3) + C_2(\Gamma_2 - 3), \qquad (12)$$

where $\Gamma_1 = I_C/III_C^{1/3}$, $\Gamma_2 = II_C/III_C^{2/3}$, and $J = \sqrt{III_C}$.

$$\begin{aligned} W_5 &= C_1(I_C - 3) + C_2(II_C - 3) + (C_1 + C_3)(III_C - 1) \\ &\quad + 2(-2C_1 - 2C_2 - C_3)(\sqrt{III_C} - 1) + C_4(\sqrt{III_C} - 1)^3. \end{aligned} \qquad (13)$$

In functions (10) through (13), I_C, II_C, and III_C represent the first, second, and third invariants of the Cauchy–Green tensor C_{AB}, respectively. When $\sqrt{III_C} = 1$, i.e., when the material is incompressible, Eq. (13) becomes a Moony–Rivlin formulation. The additional terms represent a power series in $\sqrt{III_C}$, the significance of which is described in subsequent sections.

Formation of the Acoustoelastic Problem

The dilatational wave problem addressed in this study (Fig. 1) is a hyper-elastic, nearly incompressible material stretched in the x_1 direction while wave propagation is measured and computed in the x_2 direction. Because the material has slight compressibility, it potentially can sustain three different waves in the y direction, i.e., a longitudinal wave and two shear waves with displacements in the $x_2 - x_1$ direction and $x_2 - x_3$ direction, respectively.

In this section, velocities of the three potential waves are derived. The acoustoelastic Eq. (1) for this problem is given in x_1 direction as

$$\begin{aligned} &(\tilde{C}_{11} + t_{11})\frac{\partial^2 u_1}{\partial x_1^2} + \tilde{C}_{66}\frac{\partial^2 u_1}{\partial x_2^2} + \tilde{C}_{55}\frac{\partial^2 u_1}{\partial x_3^2} \\ &\quad + (\tilde{C}_{12} + \tilde{C}_{66})\frac{\partial^2 u_2}{\partial x_1 \partial x_2} + (\tilde{C}_{13} + \tilde{C}_{55})\frac{\partial^2 u_3}{\partial x_1 \partial x_3} = \rho \frac{d^2 u_1}{dt^2}, \end{aligned} \qquad (14a)$$

in x_2-direction as

$$\begin{aligned} &(\tilde{C}_{12} + \tilde{C}_{66})\frac{\partial^2 u_1}{\partial x_1 \partial x_2} + (\tilde{C}_{66} + t_{11})\frac{\partial^2 u_2}{\partial x_1^2} + \tilde{C}_{22}\frac{\partial^2 u_2}{\partial x_2^2} + \tilde{C}_{44}\frac{\partial^2 u_2}{\partial x_3^2} \\ &\quad + (\tilde{C}_{23} + \tilde{C}_{44})\frac{\partial^2 u_3}{\partial x_2 \partial x_3} = \rho \frac{d^2 u_2}{dt^2}, \end{aligned} \qquad (14b)$$

and in x_3-direction as

$$\begin{aligned} &(\tilde{C}_{13} + \tilde{C}_{55})\frac{\partial^2 u_1}{\partial x_1 \partial x_3} + (\tilde{C}_{23} + \tilde{C}_{44})\frac{\partial^2 u_2}{\partial x_2 \partial x_3} + (\tilde{C}_{55} + t_{11})\frac{\partial^2 u_3}{\partial x_1^2} \\ &\quad + \tilde{C}_{44}\frac{\partial^2 u_3}{\partial x_2^2} + \tilde{C}_{33}\frac{\partial^2 u_3}{\partial x_3^2} = \rho \frac{d^2 u_3}{dt^2}, \end{aligned} \qquad (14c)$$

where u_1, u_2, u_3 are wave displacements in the x_1, x_2, x_3 directions. In the above equations, $\tilde{C}_{pq}$ and t_{11}, respectively, represent the pq entry of the matrix and Cauchy stress in x_1 direction as evaluated by Eqs. (2) and (3). Since wave propagation is only in the y direction, displacements in three directions can be assumed to be

$$\begin{Bmatrix} u_1 \\ u_2 \\ u_3 \end{Bmatrix} = \begin{Bmatrix} D_1 \\ D_2 \\ D_3 \end{Bmatrix} \mathrm{Exp}\{i(\xi_2 \cdot x_2 - \omega t)\}. \qquad (15)$$

By substituting these assumed displacements into Eqs. (14a) through (14c), the following eigenvalue equations are derived:

$$\begin{bmatrix} -\tilde{C}_{66}\xi_2^2 + \rho\omega^2 & 0 & 0 \\ 0 & -\tilde{C}_{22}\xi_2^2 + \rho\omega^2 & 0 \\ 0 & 0 & -\tilde{C}_{44}\xi_2^2 + \rho\omega^2 \end{bmatrix} \begin{Bmatrix} D_1 \\ D_2 \\ D_3 \end{Bmatrix} = 0. \qquad (16)$$

We introduce a relationship between wave velocity c, wave number ξ_2, and frequency ω into the above equations, that is

$$c = \frac{\omega}{\xi_2}. \qquad (17)$$

Wave velocities in three distinct directions are then given as dilatational waves with displacement in x_2 direction

$$c_D = \sqrt{\frac{\tilde{C}_{22}}{\rho}}, \qquad (18a)$$

shear wave with displacement in $x_2 - x_3$ direction

$$c_{S1} = \sqrt{\frac{\tilde{C}_{44}}{\rho}} \qquad (18b)$$

and shear wave with displacement in $x_2 - x_1$ direction

$$c_{S2} = \sqrt{\frac{\tilde{C}_{66}}{\rho}}. \qquad (18c)$$

Later we describe experiments in which only the dilatational wave in the y direction was measured. Hence, only $\tilde{C}_{22}$ is evaluated.

Expressions for $\tilde{C}_{22}$, $\tilde{C}_{44}$, $\tilde{C}_{66}$ and t_{11} are derived for the five strain energy functions [Eqs. (9)–(13)] in the Appendix. Since matrix $\tilde{C}_{pq}$ must reduce to a Hookean matrix c_{pq} when prestress is zero, $\tilde{C}_{22}$, $\tilde{C}_{44}$, and $\tilde{C}_{66}$ must become

$$\tilde{C}_{22}|_{e=0} = \lambda + 2\mu = c_{22} \qquad (19a)$$

and

$$\tilde{C}_{44}|_{e=0} = \tilde{C}_{66}|_{e=0} = \mu = c_{44} = c_{66} \qquad (19b)$$

when prestrain e is zero. Here λ and μ are Lame's constant and shear modulus, respectively. Using these expressions, we can determine relationships between each material constants and λ and μ for each function under consideration.

For function (9):

$$\tilde{C}_{22}|_{e=0} = 2b_1 = \lambda + 2\mu \qquad (20a)$$

and

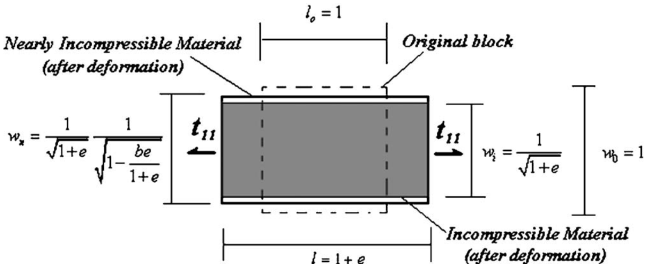

Fig. 2 Before and after the deformation of a unit block

$$\tilde{C}_{44}|_{e=0} = \tilde{C}_{66}|_{e=0} = b_2/2 = \mu. \tag{20b}$$

Hence the Lame's constant is given as $\lambda = 2b_1 - b_2$.

For function (10)

$$\tilde{C}_{22}|_{e=0} = 8C_1 + 16C_2 + 4\hat{K} = \lambda + 2\mu \tag{21a}$$

and

$$\tilde{C}_{44}|_{e=0} = \tilde{C}_{66}|_{e=0} = 4C_1 + 6C_2 = \mu. \tag{21b}$$

Hence the Lame's constant is given as $\lambda = 4C_2 + 4\hat{K}$.

For functions (11) and (12)

$$\tilde{C}_{22}|_{e=0} = \frac{8(C_1 + C_2)}{3} + K = \lambda + 2\mu \tag{22a}$$

and

$$\tilde{C}_{44}|_{e=0} = \tilde{C}_{66}|_{e=0} = 2(C_1 + C_2) = \mu. \tag{22b}$$

Hence the Lame's constant is given as $\lambda = -\frac{4}{3}(C_1 + C_2) + K$.

For function (13)

$$\tilde{C}_{22}|_{e=0} = 4C_1 + 4C_2 + 2C_3 = \lambda + 2\mu \tag{23a}$$

and

$$\tilde{C}_{44}|_{e=0} = \tilde{C}_{66}|_{e=0} = 2(C_1 + C_2) = \mu. \tag{23b}$$

Hence the Lame's constant is given as $\lambda = 2C_3$.

From the above relationships, the following observation can be made.

1. For functions (11)–(13), the shear modulus is given by $\mu = 2(C_1 + C_2)$. The same result can be derived from Moony–Rivlin function (6). Since all three functions can be considered as derivations of function (6), this result is expected.
2. However, the shear modulus for function (10) is $\mu = 4C_1 + 6C_2$ and slightly different from the shear modulus evaluated from function (6).
3. The Lame's constants from functions (11) and (12) are the same and comply with the definition of bulk modulus $K = \lambda + \frac{2}{3} \cdot 2(C_1 + C_2) = \lambda + \frac{2}{3}\mu$.
4. For our new function (13), the third constant C_3 is directly related to Lame's constant by $C_3 = \lambda/2$. The fourth constant C_4 only shows up in $\tilde{C}_{22}$ with prestrain and disappears when prestrain is removed. This implies that fourth constant C_4 governs the higher order volumetric term.

To evaluate width change after a longitudinal stretch in a nearly incompressible material, b is introduced as the magnitude of first order, transverse shrinkage. Magnitude of shrinkage b is assumed to be a small perturbation of the width change in an incompressible material. When an incompressible material is stretched (Fig. 2), the width change can be evaluated from Eq. (24). However, for a nearly incompressible material, the width change is slightly smaller and can be estimated from Eq. (25)

$$w_i = \frac{1}{\sqrt{1+e}}, \tag{24}$$

$$w_n = \frac{1}{\sqrt{1 + (1-b)e}} \approx \frac{1}{\sqrt{1+e}} \frac{1}{\sqrt{1 - \frac{be}{1+e}}}. \tag{25}$$

The magnitude of lateral shrinkage b (evaluated in the Appendix) for a stress-free condition of function (10) approaches infinity, and therefore strain energy function (10) is eliminated as a candidate for acoustoelastic analysis hereafter.

Doll [24] shows that the volumetric part of the strain energy function has to satisfy the following two conditions

$$U(J) \geq 0, \tag{26}$$

$$\left.\frac{\partial^2 U}{\partial J^2}\right|_{J=1} = K = \lambda + \frac{2}{3}\mu. \tag{27}$$

Here K, λ, and μ represent bulk modulus, Lame's constant, and shear modulus for infinitesimal theory. Both functions (11) and (12) satisfy these conditions. The newly proposed function (13) also must satisfy these conditions. If the isochoric portion of the strain energy function is assumed to be

$$W(I_C, II_C, J) - U(J) = C_1(\Gamma_1 - 3) + C_2(\Gamma_2 - 3), \tag{28}$$

then the volumetric part of function (13) for infinitesimal case ($J \sim 1$) is

$$U(J) = C_1(-4J + J^2 + 3J^{2/3}) + C_2(1 - 4J + 3J^{4/3}) + 6C_3(-1 + J)^2. \tag{29}$$

In deriving the above equation, infinitesimal strain is assumed and the following relationships are introduced:

$$I_C \approx 3J^{2/3} = 3III_C^{1/3} \tag{30}$$

$$II_C \approx 3J^{4/3} = 3III_C^{2/3}. \tag{31}$$

By differentiating the volumetric part $U(J)$ by J twice,

$$\frac{\partial^2 U}{\partial J^2} = 2C_3 + C_1 \cdot \left(2 - \frac{2J^{2/3}}{3J^2}\right) + C_2 \cdot \frac{4J^{4/3}}{3J^2}. \tag{32}$$

For the zero-strain condition ($J = 1$), the following required relationship is obtained:

$$\left.\frac{\partial^2 U}{\partial J^2}\right|_{J=1} = 2C_3 + \frac{4}{3}C_1 + \frac{4}{3}C_2 = K. \tag{33}$$

Equation (33) confirms that our new strain energy formulation [Eq. (13)] satisfies this mathematical requirement for volumetric behavior, i.e., Eq. (27).

Experimental Methods

The experiment setting is depicted in Fig. 3. A strip of rubber (L 12 cm × W 3 cm × T 0.3 cm) was placed in a servo-hydraulic testing system and stress versus stretch behavior was obtained and confirmed with repeated testing. Then, the ultrasound transmitter and receiver transducers were placed in contact with the rubber after increments of uniaxial stretch. A 2.25 MHz (nominal frequency) nonfocused ultrasonic transducer (0.635 cm diameter) was utilized. Travel time of the wave was measured directly from a digital oscilloscope (Tektronix 2232) and rubber thickness was measured with digital calipers. Dilatational wave velocity was computed from travel time divided by thickness starting with a stress-free (non-stretched) condition.

Rubber was stretched from 100% to 110% of its original length in 2% stretch increments. After 110% of stretch, it was stretched in 5% increments. At each increment, travel time of the dilatational wave, specimen thickness, and applied force was recorded.

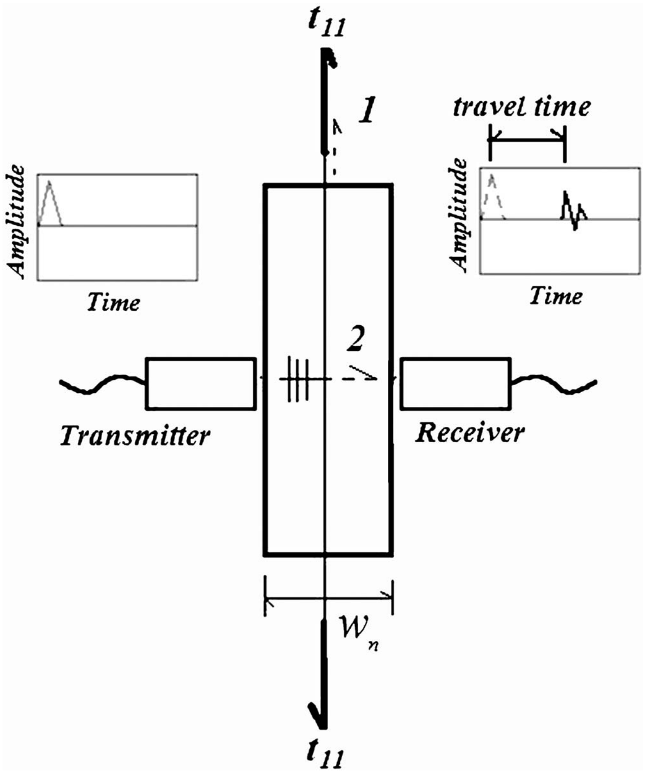

Fig. 3 Experiment setting to stretch a rubber specimen and to measure dilatational wave travel time as a function of stretch

Stress-Strain Relationship

To explore the utility of each strain energy function still under consideration for acoustoelastic analysis [i.e., Eqs. (9) and (11)–(13)], the stress-strain relations were analytically evaluated and compared with experimental data as follows:

1. Moony–Rivlin material function (6) was fit to four repetitions of stress versus stretch data, and material coefficients C_1 and C_2 were evaluated using a least squares technique. This yields the following mean values:

$$C_1 = 8.60 \times 10^5 \text{ Pa}, \quad C_2 = -1.55 \times 10^5 \text{ Pa}.$$

2. Bulk modulus K for functions (11) and (12) and C_4 for function (13) were evaluated from Eq. (18*a*) and Eqs. (C3) and (E3) from the Appendix. Also required were C_1 and C_2, obtained in the previous step, and the dilatational wave velocity c_L measured in the stress-free condition. From these we obtain

$$K = 2.19 \times 10^9 \text{ Pa and } C_3 = 2.18 \times 10^9 \text{ Pa}.$$

3. The five coefficients for function (9) were obtained via a nonlinear, least squares method by using function (6) with C_1 and C_2 (from step 1) to yield

$$b_1 = 1.09 \times 10^9 \text{ Pa}, \quad b_2 = 28.2 \times 10^5 \text{ Pa}$$

$$g_1 = 2.78 \times 10^9 \text{ Pa}, \quad g_2 = -4.45 \times 10^9 \text{ Pa},$$

$$g_3 = 1.03 \times 10^{10} \text{ Pa}.$$

4. The stress-strain relations for each function [Eqs. (9) and (11)–(13)] were evaluated and are compared with experimental data (Fig. 4).

The four strain energy functions under current consideration [Eqs. (9) and (11)–(13)] model material behavior with almost identical fits of the stress-strain data [Eq. (4)]. In the evaluation with Eq. (11), C_4 was set at 3.0×10^{11} Pa. Figure 4 shows that the higher order terms in $\sqrt{III_C}$ [that we added in Eq. (13)] govern volume change, but they do not affect the stress-strain behavior of a Moony–Rivlin function. The purpose of these additional terms is to model dilatational wave propagation, without affecting other mechanical behaviors.

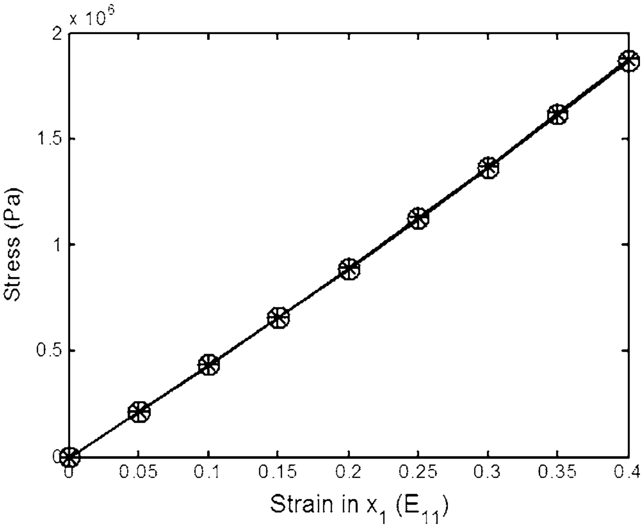

Fig. 4 Stress-strain relations for a simple tension test. Solid line (-) shows the least squared experimental results. The dot (.), circle (○), cross (×), and plus (+) effectively superimpose to show the similar analytical results evaluated from functions (9) and (11)–(13), respectively.

By using the above parameters in the volumetric part of the new strain energy function [Eq. (13)], the constraint in Eq. (26) can be considered. The volumetric part of Eq. (13) satisfies Eq. (26) $U(J) \geq 0$ near $J \approx 1.0$ (Fig. 5). Since only the behavior of a nearly incompressible material is under consideration (e.g., rubber has compressibility $\nu \approx 0.499$), Eq. (13) is an acceptable strain energy function.

Figure 6 shows the relationship between strain in the x_1 direction E_{11} and ξ_2^2 of one of the shear waves as computed from the Smith and Rivlin [25] function (9). ξ_2^2, as defined in Eqs. (15) and (16), must be positive for shear waves to propagate. Since only dilatational waves were experimentally measured, shear wave behavior is not considered. However, this figure indicates that by

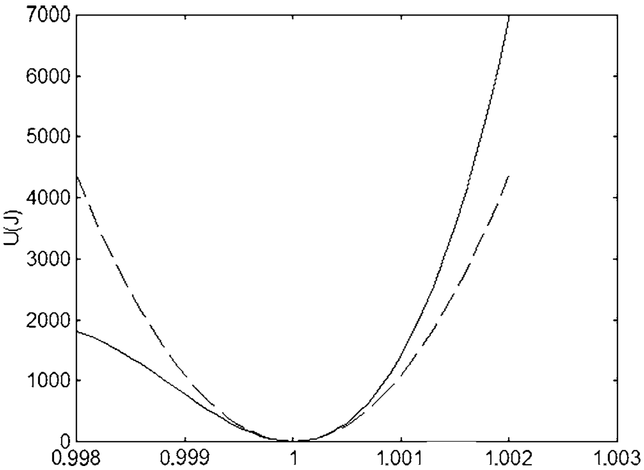

Fig. 5 Relationship between the strain energy function (13) and $J = (III_C)^{1/2}$. Solid line: Volumetric part of function (13) as a function of J. Dashed line: The entire strain energy function (13) as a function of J.

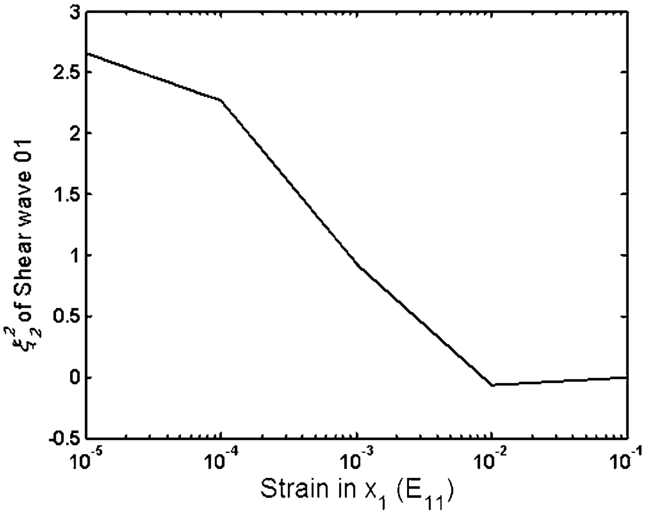

Fig. 6 Relation between E_{11} and ξ_2^2 for shear wave in function (9)

increasing the applied strain E_{11} to 0.01 (i.e., when $\xi_2^2=0$), one of the quasi-shear waves is converted from a bulk wave into a surface wave (an impossible event when the incidence wave is perpendicular). This result casts doubt on the ability of function (9) to simulate acoustoelastic phenomena. Hence, function (9) will not be further compared with the remaining strain energy functions.

Analytical and Experimental Results

In this section, dilatational wave velocities evaluated from the three strain energy functions still under consideration [Eqs. (11)–(13)] are compared with our experimental results. The experiment depicted in Fig. 3 was previously described.

In Fig. 7, normalized thickness changes of rubber (x_2 direction) were measured during axial stretch (x_1 direction). Also plotted and compared are the normalized travel time and analytically evaluated normalized travel times from functions (11)–(13). From the figure, we observe the following:

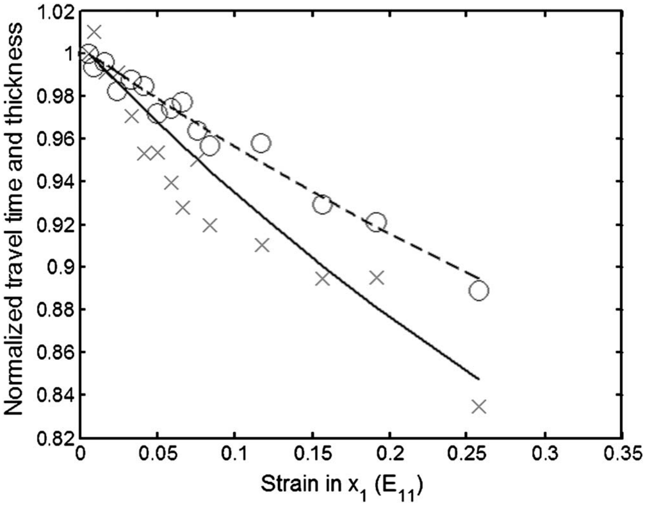

Fig. 7 Stress-strain relation of rubber from a simple tension test. Crosses (×): Normalized travel time from experiment. Circles (○): Normalized thickness from experiment. Dashed line (- -): Normalized travel times predicted by functions (11) and (12). Solid line: Normalized travel time predicted by function (13).

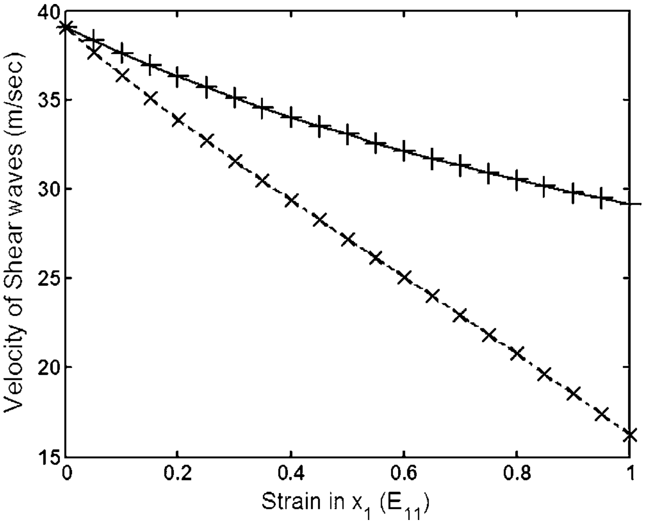

Fig. 8 Velocity of two shear waves evaluated by functions (6) and (13). Solid line: Shear wave 01 by function (6). Dashed line (- -): Shear wave 02 by function (6). Pluses (+): Shear wave 01 by function (13). Crosses (×): Shear wave 02 by function (13).

(1) A nearly incompressible material like rubber can sustain dilatational waves.
(2) Since the change of normalized travel time of the dilatational wave is larger than the normalized change of thickness, the velocity change in the dilatational wave must be an acoustoelastic effect due to prestretch.
(3) To model this acoustoelastic effect, the material description must contain a higher order compressibility term than is contained in Eqs. (11) and (12).

Acoustoelasticity affects shear waves in addition to dilatational waves. Therefore, it is important to check if the higher order terms (in $\sqrt{III_C}$) in function (13) affect the function's ability to model shear waves in the same prestressed media. The major difference between functions (6) and (13) lies in the terms that describe volumetric change, hence the behavior of shear waves derived from function (13) should be very close to the behavior of shear waves predicted by a Moony–Rivlin function (6). Erigen and Suhubi [15] have studied acoustoelastic effects on shear waves in a Moony–Rivlin material. They shear wave velocities in a prestrained hyper-elastic incompressible isotropic material modeled by function (6) where the velocities are eigenvalues of the following equation:

$$\begin{aligned}&[\rho\cdot c_S^2-2(\lambda_1^2\cdot n_1^2+\lambda_3^2\cdot n_3^2)\cdot(C_1+C_2\cdot\lambda_2^2)\\&\quad-2\lambda_2^2\cdot n_2^2(C_1+C_2\cdot\lambda_3^2)]\cdot[\rho\cdot c_S^2-2\lambda_1^2\cdot n_1^2(C_1+C_2\cdot\lambda_3^2)\\&\quad-2(\lambda_2^2\cdot n_2^2+\lambda_3^2\cdot n_3^2)\cdot(C_1+C_2\cdot\lambda_1^2)]\\&\quad-2\cdot\lambda_1^2\cdot\lambda_3^2\cdot(\lambda_1^2-\lambda_3^2)\cdot(\lambda_2^2-\lambda_3^2)n_1^2\cdot n_2^2=0. \qquad (34)\end{aligned}$$

Here c_S and ρ represent shear wave velocity and density of the media, respectively; λ_1, λ_2, and λ_3 represent principal stretches in 1, 2, and 3 directions; n_1, n_2, and n_3 represent wave normals ($n_1=n_3=0$ and $n_2=1$ for our problem).

Figure 8 shows that the velocities of the two shear waves using both functions (6) and (13) are almost identical. These results indicate that our new function (13), which appropriately simulates the acoustoelastic effect of dilatational waves in a nearly incompressible material, does not disturb the acoustoelastic predictions of shear waves (with a Moony–Rivlin formulation).

Discussion

The goal of this study was to formulate, for the first time, an acoustoelastic method that could determine prestresses in nearly incompressible, hyperelastic materials. Well-known strain energy functions [Eqs. (9)–(12)] and a newly proposed function [Eq. (13)] were compared. By comparing the analytical and experimental results, we conclude the following:

1. A dilatational acoustoelastic effect does exist in nearly incompressible, hyper-elastic materials (e.g., rubber or biological materials).
2. Although compressibility is quite small in these materials, it must be included in material formulations to simulate dilatational waves. Therefore, constitutive terms using the third invariant III_C of the Cauchy–Green tensor cannot be ignored, and higher order terms in $\sqrt{III_C}$ are necessary to simulate the acoustoelastic effect in dilatational waves.
3. The acoustoelastic effect is relatively large in these materials (compared to materials like steel and aluminum) and can be measured more easily. Hence this phenomenon may be a useful experimental tool to analyze these nearly incompressible, hyper-elastic materials.
4. Acoustoelastic experiments and analysis can therefore determine prestress (or prestretch) in hyper-elastic, nearly incompressible materials. Similarly, experiments and analysis can identify the mechanical properties of these materials (i.e., the inverse problem). However, a constitutive equation appropriate for the analysis is required.
5. For acoustoelastic analyses of nearly incompressible materials, we propose a new strain energy function [Eq. (13)] that is based on a Moony–Rivlin material and satisfies mathematical and physical conditions. The newly proposed function contains four material constants, yet the Cauchy stress and each entry of the matrix $\widetilde{C}_{pq}$ derived from this function has a very simple form [Eqs. (E1)–(E3)]. Therefore, this function is easier to use when solving the inverse problem (i.e., determining material properties) than many other functions.
6. In these materials, the velocity of a dilatational wave is much larger than velocities of the two shear waves (Figs. 7 and 8). Behavior of the dilatational wave is properly simulated by our newly proposed function, without disturbing any other mechanical characteristics, e.g., stress-strain behavior and shear wave propagation associated with a Moony–Rivlin material.
7. This study suggests that more detailed, three-dimensional strain energy functions for nearly incompressible materials can be developed with the help of both acoustoelastic measurements and stress-strain relationships.

Herein we have formulated a new strain energy function and demonstrated its potential value for acoustoelastic analysis of nearly incompressible materials. It is based on the well-known Moony–Rivlin strain energy function (6), hence it has a relatively simple, isotropic formulation defined by four parameters. The purpose of the new function (13) is to properly simulate dilatational waves. It is not intended to handle complicated mechanical behaviors that cannot be appropriately represented by a Moony–Rivlin strain energy function, and it is unnecessarily complex if dilatational waves are not of interest. However, the acoustoelastic method (using dilatational wave experiments) coupled with the proposed strain energy function appears to hold great promise. Many applications can be envisaged for analysis of rubber-like materials or biological tissues.

Appendix

In this appendix, detailed expressions for $\widetilde{C}_{22}$, $\widetilde{C}_{44}$, $\widetilde{C}_{66}$, t_{11} and $t_{22}=t_{33}$ derived from five different strain energy functions are given.

(A) From Eq. (9), $\widetilde{C}_{22}$, $\widetilde{C}_{44}$, and $\widetilde{C}_{66}$ are derived as follows:

$$\widetilde{C}_{22}=\frac{1}{J}\left[\frac{2b_1+(2b_1-g_2)e+(9g_1-3g_2)e^2+(3g_1-g_2)e^3}{(1+e)^3}+b\frac{e(4b_1+6g_1-g_2+(4b_1-2g_2)e+(18g_1-6g_2)e^2+(6g_1-2g_2)e^3)}{(1+e)^4}\right] \tag{A1}$$

$$\widetilde{C}_{44}=\frac{1}{J}\left[\frac{2b_2+(2b_2-2g_3)e-3(g_2-g_3)e^2+(g_2-g_3)e^3}{4(1+e)^3}\right.$$
$$\left.+b\frac{2b_2+g_2+(2b_2-g_3)e+3(g_2-g_3)e^2+(g_2-g_3)e^3}{2(1+e)^4}\right] \tag{A2}$$

$$\widetilde{C}_{66}=\frac{1}{J}\left[\frac{1}{4}(2b_2+(2b_2+g_3)e+3g_2e^2+g_2e^3)\right.$$
$$\left.+b\cdot e\cdot\frac{2b_2+2g_2-g_3+(2b_2+g_3)e+3g_2e^2+g_2e^3}{2(1+e)}\right] \tag{A3}$$

where $1/J=2\sqrt{2}(1+b\cdot e)/(1+e)\sqrt{e^3(2+e)/(1+e)^2}$.

The prestresses in all three directions are derived as

$$t_{11}=\frac{e(1+e)[4b_2+(12b_1+4b_2+3g_2+g_3)e+(16b_1+12g_2)e^2]}{\sqrt{2}\sqrt{e^3(2+e)}}$$
$$+\frac{e(1+e)[(4b_1+27g_1+4g_2)e^3+18g_1e^4+3g_1e^5]}{\sqrt{2}\sqrt{e^3(2+e)}}$$
$$+\frac{b\cdot e(1+e)[8b_1+(20b_1+5g_2-3g_3)e+(16b_1+36g_1)e^2]}{\sqrt{2}\sqrt{e^3(2+e)}}$$
$$+\frac{b\cdot e(1+e)[(4b_1+27g_1+4g_2)e^3+18g_1e^4+3g_1e^5]}{\sqrt{2}\sqrt{e^3(2+e)}} \tag{A4}$$

$$t_{22}=t_{33}=\frac{e[4b_2+(12b_1+4b_2+3g_2+g_3)e+(16b_1+12g_2)e^2]}{(1+e)^2\sqrt{2}\sqrt{e^3(2+e)}}$$
$$+\frac{b\cdot e[8b_1+(20b_1+5g_2-3g_3)e+(16b_1+36g_1)e^2]}{(1+e)^2\sqrt{2}\sqrt{e^3(2+e)}}$$
$$+\frac{b\cdot e[(4b_1+39g_1)e^3+18g_1e^4+3g_1e^5]}{(1+e)^2\sqrt{2}\sqrt{e^3(2+e)}} \tag{A5}$$

The magnitude of lateral shrinkage b for this function is evaluated as

$$b=\frac{nb}{db}$$

$$\begin{aligned}nb=&-(1+e)[4b_2+(-12b_1+8b_2-3g_2+2g_3)e+(16b_1+8b_2\\&+3g_2-3g_3)e^2]-(1+e)[(-4b_1+2b_2-27g_1+8g_2+g_3)e^3\\&+(-18g_1+12g_2)e^4+(-3g_1+g_2)e^5]\end{aligned}$$

$$\begin{aligned}db=&-8b_1+4b_2+(-20b_1+12b_2+g_2)e+(-28b_1+16b_2-36g_1\\&+9g_2+2g_3)e^2+(-20b_1+10b_2-39g_1+10g_2+3g_3)e^3\\&+(-4b_1+2b_2-45g_1+14g_2+g_3)e^4+(-21g_1+7g_2)e^5\\&+(-3g_1+g_2)e^6\end{aligned}\tag{A6}$$

At stress-free condition, the lateral shrinkage is

$$b|_{e=0}=\frac{2b_2}{-8b_1+4b_2}\tag{A7}$$

(B) From function (10), $\tilde{C}_{22}$, $\tilde{C}_{44}$, and $\tilde{C}_{66}$ are derived as follows:

$$\tilde{C}_{22}=\frac{1}{J}\left[4(2C_1+4C_2+\hat{K})-2b\cdot e\frac{\hat{K}+(4C_1+8C_2+2\hat{K})e}{(1+e)^2}\right]\tag{B1}$$

$$\tilde{C}_{44}=\frac{1}{J}\left[4C_1+2C_2\frac{3+8e+4e^2}{(1+e)^2}-4b\cdot e\frac{C_2+(1+e)^2\hat{K}}{(1+e)^3}\right]\tag{B2}$$

$$\tilde{C}_{66}=\frac{1}{J}\left[4C_1+6C_2-2C_2e-2b\cdot e\frac{C_2+C_2e+2\hat{K}}{1+e}\right]\tag{B3}$$

where $1/J=1+e/(1+e+b\cdot e)$.

The prestresses in all three directions are

$$\begin{aligned}t_{11}=&2[-C_1-2C_2+2(C_1+C_2)e+C_1e^2]\\&+2b\cdot e\frac{C_1+4C_2-2C_1e-C_1e^2+2\hat{K}}{1+e}\end{aligned}\tag{B4}$$

$$\begin{aligned}t_{22}=t_{33}=&2\frac{[-C_1-2C_2-(3C_1+5C_2)e-(2C_1+C_2)e^2+C_2e^3]}{(1+e)^2}\\&+b\cdot e\frac{4C_1+4\hat{K}}{1+e}+b\cdot e\frac{C_2(5+8e+4e^2)}{(1+e)^3}\end{aligned}\tag{B5}$$

The magnitude of lateral shrinkage b for this function is

$$b=\frac{(1+e)(C_1+2C_2+3C_1e+5C_2e+2C_1e^2+C_2e^2-C_2e^3)}{2C_1e+5C_2e+4C_1e^2+8C_2e^2+2C_1e^3+4Ce^3+2\hat{K}e(1+2e+e^2)}\tag{B6}$$

For the stress-free condition, lateral shrinkage is

$$b|_{e=0}=\infty\tag{B7}$$

(C) From function (11), $\tilde{C}_{22}$, $\tilde{C}_{44}$, and $\tilde{C}_{66}$ are derived as

$$\begin{aligned}\tilde{C}_{22}=&\frac{1}{J}\left\{\frac{[(24C_1+24C_2+9K)+(72C_1+96C_2+18K)e]}{9(1+e)^2}+\frac{[(96C_1+96C_2+9K)e^2+32(2C_1+C_2)e^3+16C_1e^4]}{9(1+e)^2}\right.\\&\left.-b\cdot e\frac{[(48C_1+96C_2+27K)+(240C_1+192C_2-54K)e]}{54(1+e)^3}-b\cdot e\frac{[(384C_1+192C_2+27K)e^2+(256C_1+64C_2)e^3+64C_1e^4]}{54(1+e)^3}\right\}\end{aligned}\tag{C1}$$

$$\begin{aligned}\tilde{C}_{44}=&\frac{1}{J}\left\{\frac{2[C_1(3+6e+6e^2+4e^3+e^4)+C_2(3+12e+12e^2+4e^3)]}{3(1+e)^2}\right.\\&\left.-b\cdot e\frac{4C_2(3+6e+6e^2+2e^3)+(1+e)[4C_1e(3+3e+e^2)+9(1+e)K]}{9(1+e)^3}\right\}\end{aligned}\tag{C2}$$

$$\tilde{C}_{66}=\frac{1}{J}\left\{\frac{2(C_1+C_2+C_1e)(3+3e+3e^2+e^3)}{3(1+e)^2}-b\cdot e\frac{2C_2(-3+3e+3e^2+e^3)+(1+e)[4C_1\cdot e(3+3e+e^2)+9(1+e)K]}{9(1+e)^3}\right\}\tag{C3}$$

where $1/J=1+e-b\cdot e/1+e$.

The prestresses in all three directions are derived as

$$\begin{aligned}t_{11}=&\frac{4e(C_1+C_2+C_1e)(3+3e+e^2)}{3(1+e)^2}-b\cdot e\frac{(12C_1+12C_2-9K)+(72C_1+48C_2-18K)e}{9(1+e)^3}\\&-b\cdot e\frac{(120C_1+48C_2-9K)e^2+(80C_1+16C_2)e^3+20C_1e^4}{9(1+e)^3}\end{aligned}\tag{C4}$$

$$t_{22}=t_{33}=\frac{4e(C_1+C_2+C_1e)(3+3e+e^2)}{3(1+e)^5}-b\cdot e\frac{4C_1(3+9e+12e^2+8e^3+2e^4)+4C_2(3+3e+3e^2+e^3)-9(1+e)^2K}{9(1+e)^6}\tag{C5}$$

The magnitude of lateral shrinkage b for this function is evaluated as

$$b=\frac{nb}{db}$$

$$nb=12(1+e)(C_1+C_2+C_1e)(3+3e+e^2)$$

$$db=4C_1(3+9e+12e^2+8e^3+2e^4)+4C_2(3+3e+3e^2+e^3) \\ -9(1+e)^2K \tag{C6}$$

In the stress-free condition, lateral shrinkage is

$$b\big|_{e=0}=\frac{9(C_1+C_2)}{4(C_1+C_2)-3K} \tag{C7}$$

(D) From function (12), $\widetilde{C}_{22}$, $\widetilde{C}_{44}$, $\widetilde{C}_{66}$, and t_{11} are the same as those evaluated from function (11). Only the prestresses $t_{22}=t_{33}$ are slightly different as follows:

$$t_{22}=t_{33}=\frac{-2e(C_1+C_2+C_1e)(3+3e+e^2)}{3(1+e)^5} \\ +b\cdot e\frac{6C_1+6C_2+9K+(36C_1+24C_2+18K)e}{9(1+e)^3} \\ +b\cdot e\frac{(60C_1+24C_2+9K)e^2+(40C_1+8C_2)e^3+10C_1e^4}{9(1+e)^3} \tag{D5}$$

The magnitude of lateral shrinkage b for this function is evaluated as

$$b=\frac{nb}{db}$$

$$nb=6(1+e)(C_1+C_2+C_1e)(3+3e+e^2)$$

$$db=6C_1+6C_2+9K+(36C_1+24C_2+18K)e+(60C_1+24C_2 \\ +9K)e^2+(40C_1+8C_2)e^3+10C_1e^4 \tag{D6}$$

in the stress free condition, lateral shrinkage is

$$b\big|_{e=0}=\frac{6(C_1+C_2)}{2(C_1+C_2)+9K} \tag{D7}$$

(E) From function (13), $\widetilde{C}_{22}$, $\widetilde{C}_{44}$, and $\widetilde{C}_{66}$ are derived as

$$\widetilde{C}_{22}=\frac{1}{J}\left[4C_1+4C_2+2C_3+b\frac{2e(2C_1+2C_2+C_3+3C_4)}{1+e}\right] \tag{E1}$$

$$\widetilde{C}_{44}=\frac{1}{J}\left\{\frac{2[C_1(1+e)^2+2C_2\cdot(1+4e+2e^2)]}{(1+e)^2} \right. \\ \left. -b\frac{2e[C_3(1+e)^2-2C_2\cdot e\cdot(2+e)]}{(1+e)^3}\right\} \tag{E2}$$

$$\widetilde{C}_{66}=\frac{1}{J}\left[2C_1+2C_2-2C_2\cdot e-b\frac{2e(C_2e-C_2+C_4)}{1+e}\right] \tag{E3}$$

where $1/J=1+e-b\cdot e/1+e$.

The prestresses in all three directions are derived as

$$t_{11}=2e\cdot(2C_2+2C_1+C_1\cdot e)+b\frac{2e(C_4-2C_1\cdot e+C_1\cdot e^2)}{1+e} \tag{E4}$$

$$t_{22}=t_{33}=\frac{2e[-C_1(1+e)+C_2(-1+e+e^2)]}{(1+e)^2} \\ +b\frac{2e[(C_1+C_4)(1+e)^2+C_2]}{(1+e)^3} \tag{E5}$$

The magnitude of lateral shrinkage b for this function is evaluated as

$$b=\frac{(1+e)[C_1(1+e)-C_2(-1+e+e^2)]}{C_2+C_1(1+e)^2+C_4(1+e)^2} \tag{E6}$$

In the stress-free condition, lateral shrinkage is

$$b\big|_{e=0}=\frac{C_1+C_2}{C_1+C_2+C_4} \tag{E7}$$

References

[1] Hughes, D. S., and Kelly, J. L., 1953, "Second-Order Elastic Deformation of Solids," Phys. Rev., **92**, pp. 1145–1149.

[2] Toupin, R. A., and Bernstein, B., 1961, "Sound Waves in Deformed Perfectly Elastic Materials; the Acoustoelastic Effect," J. Acoust. Soc. Am., **33**, pp. 216–225.

[3] Truesdell, D., 1961, "General and Exact Theory of Waves in Finite Elastic Strain," Arch. Ration. Mech. Anal., **8**, pp. 263–296.

[4] Tokuoka, T., and Iwashimizu, Y., 1968, "Acoustical Birefringence of Ultrasonic Waves in Deformed Isotropic Elastic Material," Int. J. Solids Struct., **4**, pp. 383–389.

[5] Blinka, J., and Sachse, W., 1976, "Application of Ultrasonic-Pulse-Spectroscopy Measurements of Experimental Stress Analysis," Exp. Mech., **16**, pp. 448–453.

[6] Kino, G. S., Hunter, J. B., Johnson, G. C., Selfridge, A. R., Barnett, D. M., Hermann G., and Steele, C. R., 1979, "Acoustoelastic Imaging of Stress Fields," J. Acoust. Soc. Am., **50**(4), pp. 2606–2613.

[7] King, R. B., and Furtunko, C. M., 1983, "Determination of In-Plane Residual Stress States in Plates Using Horizontally Polarized Shear Waves," J. Appl. Phys., **54**(6), pp. 3027–3035.

[8] Thompson, R. B., Lee, S. S., and Smith, J. F., 1986, "Angular Dependence of Ultrasonic Wave Propagation in a Stressed Orthorhombic Continuum: Theory and Application to the Measurement of Stress and Texture," J. Acoust. Soc. Am., **80**(3), pp. 921–931.

[9] Dike. J. J., and Johnson, G. C., 1990, "Residual Stress Determination Using Acoustoelasticity," ASME J. Appl. Mech., **57**, pp. 12–17.

[10] Iwashimizu, Y., and Kobori, O., 1978, "The Rayleigh Wave in a Finitely Deformed Isotropic Elastic Material," J. Acoust. Soc. Am., **64**(3), pp. 910–916.

[11] Mase, G. T., and Johnson, G. C., 1987 "An Acoustoelastic Theory for Surface Waves in Anisotropic Media," ASME J. Appl. Mech., **54**, pp. 127–135.

[12] Lee, Y. C., Kim, J. O., and Achenbach, J. D., 1994, "Measurement of Stresses by Line-Focused Acoustic Microscopy," Ultrasonics, **32**(5), pp. 359–365.

[13] Pao, Y. H., Sache, W., and Fukuoka, H., 1984, *Physical Acoustics*, Academic, Orlando, Vol. XVII, Chap. 2.

[14] Ogden, R. W., 1984, *Non-Linear Elastic Deformations*, Dover, Mineola, Chap. 6.4.

[15] Erigen, A. C., and Suhubi, E. S., 1974, *Elastodynamics*, Academic, New York, Vol. 1, Chap. 4.

[16] Fu, Y., 1993, "On the Propagation of Nonlinear Traveling Waves in an Incompressible Elastic Plate," Wave Motion, **19**, pp. 271–292.

[17] Gent, A. N., 2001, *Engineering with Rubber*, Hanser, Munich, Chap. 3.2.

[18] Folds, D. L., 1974, "Speed of Sound and Transmission Loss in Silicone Rubbers at Ultrasonic Frequencies," J. Acoust. Soc. Am., **56**(4), pp. 1295–1296.

[19] Rivlin, R. S., 1949, "Large Elastic Deformations of Isotropic Materials VI. Further Results in the Theory of Torsion, Shear and Flexuer," Philos. Trans. R. Soc. London, Ser. A, **242**(A845), pp. 173–195.

[20] Ogden, R. W., 1997, *Non-Linear Elastic Deformations*, Dover, Mineola, Chap. 4.3, p. 221.

[21] Cescotto, S., and Fonder, G., 1979, "A Finite Element Approach for Large Strain of Nearly Incompressible Rubber-Like Materials," Int. J. Solids Struct., **15**(8), pp. 589–605.

[22] Liu, C. H., Hofstetter, G., and Mang, H. A., 1994, "3D Finite Element Analysis of Rubber-Like Materials at Finite Strains," Eng. Comput., **11**, pp. 111–128.

[23] Watanabe, H., Hisada, T., and Noguchi, H., 1995, "Kinking Analysis by Hyper-Elastic Finite Element Method," JSME Int. J., Ser. A, **38**, pp. 30–37.

[24] Doll, S., and Schweizerhof, K., 2000, "On the Development of Volumetric Strain Energy Functions," ASME J. Appl. Mech., **67**, pp. 17–21.

[25] Smith, G. F., and Rivlin, R. S., 1958, "The Strain Energy Functions for Anisotropic Elastic Materials," Trans. Am. Math. Soc., **88**, pp. 175–193.

[26] Tokuoka T., 1979, "Nonlinear Acoustoelasticity of Isotropic Elastic Materials," J. Acoust. Soc. Am., **65**(5), pp. 1134–1139.

[27] Johnson, G. C., 1982, "Acoustoelastic Response of Polycrystalline Aggregates Exhibiting Transverse Isotropy," J. Nondestruct. Eval., **3**(1), pp. 1–8.

Crack Identification in Thin Plates With Anisotropic Damage Model and Vibration Measurements

D. Wu

S. S. Law

Department of Civil and Structural Engineering,
Hong Kong Polytechnic University,
Yuk Choi Road,
Hunghom Kowloon, Hong Kong

Many approaches on modeling of cracks in structural members have been reported in the literatures. However, most of them are explicitly developed for the purpose of studying the changes in static and dynamic responses of the structure due to the crack damage, which is a forward problem mathematically. Thereby the use of these models is inconvenient or even impossible for detecting damage in structures from vibration measurements, which is usually an inverse problem. An anisotropic damage model is proposed for a two-dimensional plate element with an edge-parallel crack. The cracked plate element is represented by a plate element with orthotropic anisotropic material expressed in terms of the virgin material stiffness and a tensor of damage variables. Instead of using the effective stress concept, strain equivalence, or strain energy equivalence principles, the vector of damage variables is identified based on the principle of equivalent static and dynamic behaviors. A nonmodel-based damage identification approach is developed incorporating the proposed anisotropic model and the estimated uniform load surface curvature (ULSC) from vibration measurements. The actual length of the crack is then predicted from the identified variables based on conservation law of potential energy for crack growth. The validity of the methodology is demonstrated by numerical examples and experiment results with comparison to results from existing strain energy equivalence theory. [DOI: 10.1115/1.1985432]

1 Introduction

The presence of a crack in a structural member introduces a local flexibility affecting its static behavior and vibration response. Many efforts have been devoted by structural engineers to the research in modeling the crack-induced flexibility and investigating its effect on dynamic characteristics of the damaged structure. Dimarogonas [1] has summarized these works into three categories, namely: Continuous model, discrete-continuous model, and discrete models, i.e., finite element models.

Historically the earliest method to model a fatigue crack in a beam is proposed by Hetenyi [2] for determining the static deflection of beams with nonconstant cross sections, in which a crack is represented by additional external equivalent loads. This method is further developed by Kirsmer [3], Thomson [4], and Petroski and Glazik [5] to study the vibration response of the beams or shells with fatigue cracks. However, the lack of explicit relation between the size of the crack and the magnitude of its external equivalent load makes it infeasible for the sensitivity analysis with the modal parameters of the structural members. Another approach related to the continuous model divides the cracked members into sub-domains by the crack lines. Special boundary conditions along the crack line are introduced [6–8] to connect the sub-domains. The principal limitation of these continuous models is the fact that their partial differential-based mathematical derivation can provide sufficiently accurate results only in the case when the structural members have a very simple geometry.

In the discrete-continuous models, a crack in a structural member is represented by additional spring-like elements. A system with two parts of the undamaged member jointed with specific spring elements is created to model the cracked member in this manner. Many special compliance matrices for the spring elements were studied by the laws of fracture mechanics [9]. These methods can successfully be used for modeling cracks in one-dimensional members. However, in the case of two or three-dimensional members, this approach is practically inapplicable due to the fact that the large number of equations required for the boundary conditions of the connecting spring elements is not available.

Real structures are more complicated than the geometrically simple ones described by the analytically continuous or discrete-continuous models. Researchers hence started to use discrete models to study the cracked structures, in which the finite element method (FEM) is the most popular and commonly utilized. From the published literature on FEM-based model of a cracked plate, one may find mainly three groups of methods. The simplest model represents the crack as a reduction in the elasticity modulus of the element at the crack position [10] or a reduction in the cross-sectional area of the element [11]. These models have been successfully used in damage localization of plate-like structures [12,13]. However, as these methods study the approximate crack size and location at the element level, a very fine finite element mesh is required to avoid large error.

Another method models a crack by separating the nodes of finite elements along the crack line [14]. To properly model the singular character of the stress and strain fields around the crack tip, a very dense mesh of finite elements or singular-shaped isoparametric elements [15] are used to cover the crack tip area. Obviously, this method can model the cracked structure very well, but is not suitable or feasible for damage identification. This is due to the low computation efficiency associated with the large number of finite element. Also a finite element mesh has to be constructed for one suspected location of damage in the plate at one time.

In the third group of methods, a rectangular plate element with

---

Contributed by the Applied Mechanics Division of THE AMERICAN SOCIETY OF MECHANICAL ENGINEERS for publication in the ASME JOURNAL OF APPLIED MECHANICS. Manuscript received by the Applied Mechanics Division, December 31, 2003; Final revision, February 7, 2005. Associate Editor: E. A. Arruda. Discussion on the paper should be addressed to the Editor, Prof. Robert M. McMeeking, Journal of Applied Mechanics, Department of Mechanical and Environmental Engineering, University of California - Santa Barbara, Santa Barbara, CA 93106-5070, and will be accepted until four months after final publication in the paper itself in the ASME JOURNAL OF APPLIED MECHANICS.

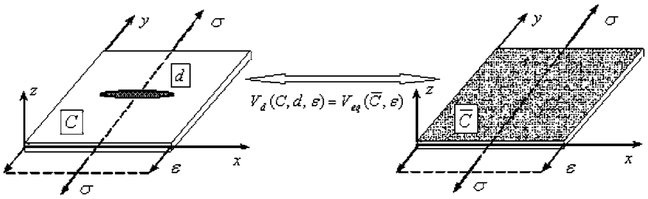

Fig. 1 The effective stiffness model from strain energy equivalence principle

an open and depth-through crack parallel to the plate boundary is modeled [16–18] The stiffness matrix of a cracked element is written as

$$K = TF^{-1}T^T$$

where F is the matrix representing the sum of the flexibility of noncracked plate and the additional flexibility due to the crack, and T is a transformation matrix. However, as the derived stiffness matrix cannot be explicitly parametrized in terms of damage variable(s) to indicate the location, orientation, and the extend of the crack, it is still difficult to incorporate this model into the inverse problem of structural damage identification.

All the above-mentioned crack models were explicitly proposed for the purpose of studying the static behavior or dynamic response of the cracked structure. The system parameters are usually not related directly to the damage variables. Generally, it is not suitable to use them for solving the inverse problem of damage identification. Therefore, a damage detection oriented crack model for plate-like structure is in demand.

2 Anisotropic Model of Elliptical Crack With Strain Energy Equivalence

The earliest crack model oriented to damage identification is probably presented by Lee et al. [21], although their work originally focuses on fracture mechanics and aims to derive a damage evolution equation that is consistent with the continuum damage mechanics. Prior to Lee and his colleagues' effort, there have been a number of theories developed on continuum damage mechanics to derive the equivalent constitutive equation of a damaged material and its crack growth law on the basis of the strain equivalence principle introduced by Lemaitre [19] or the stress equivalence principle by Simo and Ju [20]. By introducing the strain energy equivalence principle as an alternative to the above principles, an effective stiffness model of the damaged material can be obtained in terms of the undamaged material properties and damage variable(s) as illustrated in Fig. 1, where C denotes the elastic stiffness of the intact host element, $\bar{C}$ is the effective continuum stiffness of the damaged host element, d is the selected damage variable (or tensor), and ε denotes the equal strain on the boundaries of the intact and damaged host elements.

Restricting the strain energy principle to a two-dimensional elastic solid under biaxial stress (σ_1 and σ_2) and inplane shear (τ_{12}) at infinity, Lee et al. [21] introduced a damage in the form of an elliptical through crack with the major axis (length $2a$) and the minor axis (length $2b$), respectively, aligned with the Cartesian coordinates *1* and *2*. For the intact state of the isotropic solid and the effective stiffness model of the damaged solid, the strain energy contained in the circular host element of radius R can be expressed, respectively, as

$$V_0 = \frac{1}{2}\pi R^2 h \begin{Bmatrix} \varepsilon_1 \\ \varepsilon_2 \\ \gamma_{12} \end{Bmatrix}^T \begin{bmatrix} C_{11} & C_{12} & 0 \\ C_{12} & C_{22} & 0 \\ 0 & 0 & C_{66} \end{bmatrix} \begin{Bmatrix} \varepsilon_1 \\ \varepsilon_2 \\ \gamma_{12} \end{Bmatrix}, \tag{1}$$

$$V_{\text{eq}} = \frac{1}{2}\pi R^2 h \begin{Bmatrix} \varepsilon_1 \\ \varepsilon_2 \\ \gamma_{12} \end{Bmatrix}^T \begin{bmatrix} \bar{C}_{11} & \bar{C}_{12} & 0 \\ \bar{C}_{12} & \bar{C}_{22} & 0 \\ 0 & 0 & \bar{C}_{66} \end{bmatrix} \begin{Bmatrix} \varepsilon_1 \\ \varepsilon_2 \\ \gamma_{12} \end{Bmatrix}$$

where h denotes the thickness of the plate-like solid. For plane stress condition, the intact stiffness coefficients are defined in terms of the usual engineering constants as

$$C_{11} = C_{22} = \frac{E}{1 - v^2}, \quad C_{12} = \frac{vE}{1 - v^2}, \quad \text{and } C_{66} = G,$$

in which E, v, G denote the Young's modulus, Poisson's ratio and Shear modulus, respectively.

The strain energy released during the growth of the elliptical cavity has been derived by Sih and Liebowitz [22] as

$$V_1 = \frac{1}{2}\pi a^2 h \begin{Bmatrix} \varepsilon_1 \\ \varepsilon_2 \\ \gamma_{12} \end{Bmatrix}^T \begin{bmatrix} C_{11}e_{11} & C_{12}e_{12} & 0 \\ C_{12}e_{12} & C_{22}e_{22} & 0 \\ 0 & 0 & C_{66}e_{66} \end{bmatrix} \begin{Bmatrix} \varepsilon_1 \\ \varepsilon_2 \\ \gamma_{12} \end{Bmatrix} \tag{2}$$

where the coefficients e_{ij} generally depend on the Poisson's ratio and the cavity geometry. For plane stress condition, one can get $e_{11}=2v^2/(1-v^2)+(1-v)s/(1+v)+2s^2/(1-v^2)$, $e_{22}=2/(1-v^2)+(1-v)s/(1+v)+2v^2s^2/(1-v^2)$, $e_{12}=2/(1-v^2)-(1-v)s/v(1+v)+2s^2/(1-v^2)$ and $e_{66}=(1+s)^2/(1+v)$, with $s=b/a$ denotes the aspect ratio of the elliptical cavity.

According to the strain energy equivalence principle, the strain energy contained in the effective stiffness continuum model of the damaged circle region can be expressed as

$$V_{eq} = V_d = V_0 - V_1 \tag{3}$$

Substituting (1) and (2) into (3), one finds the effective stiffness coefficients of the damaged plate cell as

$$\bar{C}_{ij} = C_{ij}(1 - e_{ij}d) \tag{4}$$

where the damage variable $d=(a/R)^2$ represents the ratio of the effective damaged area to the total area of the considered solid host element, and the coefficients e_{ij} represents the anisotropic behavior of the host element due to the crack.

By further restricting the aspect ratio of the elliptical hole $s=0$, Lee et al. [23] studied the effective stiffness model of a thin plate with line micro-cracks, and then developed a model updating technique to identify the damage size and orientation by using the frequency response functions measured from the damaged plate. Numerical examples were simulated for demonstration; however, the validity of the theory requires the support from experimental evidences. According to the authors' knowledge, the following considerations have to be taken into account before Lee's theory can be used in practical applications:

(1) The crack released strain energy calculated from Eq. (2) is derived and only valid for an infinite plate containing a central crack subjected to uniform stress load. Although the result can be approximately used for a micro-crack away from the plate boundary, corrections must be made for the case of a macro-crack to take into account the finite dimensions of the plate and different load patterns.
(2) Equation (2) is derived based on the Griffith theory of ideal brittle fracture mechanics. For ductile materials, plastically deforming area induced by stress concentration around the crack tip will consume a part of the released energy, which is usually not negligible.
(3) The model updating based damage identification technique requires an initial FEM model to represent the undamaged structure. However, a good quality model for a complex structure is difficult to achieve. Model reduction or simplification could easily result in initial model errors smearing the damage induced localized changes in the updated model.

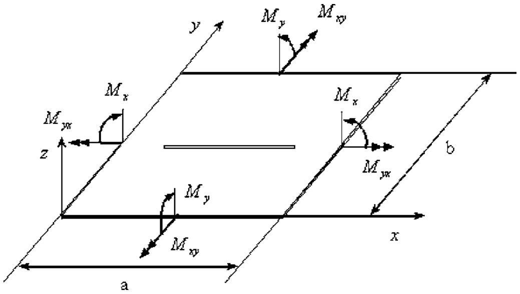

Fig. 2 Thin plate element hosting a through crack parallel to its edge

Thus, the objectives of this paper include: (1) To introduce a new effective stiffness model for thin plate elements with a central line-crack, in which the damage scalar in Lee et al. [23] model is expanded and replaced by a vector of damage variables; (2) as the crack released strain energy is difficult to estimate accurately due to the complexity of fracture mechanics, a principle of behavior equivalence is used to determine the damage variables; (3) to develop a nonmodel-based damage identification method requiring only the measured uniform load surface curvatures (ULSC) from the undamaged and damaged plates; (4) to carry out numerical simulation and experiment studies to verify the validity of the proposed methodology.

3 Anisotropic Crack Model From Dynamic Characteristic Equivalence

The problem considered in this section is a thin plate with a nonpropagating, open crack parallel to one side of the plate. It is assumed that the crack is depth-through but narrow so that it does not change the plate mass. With a small rectangular plate element containing the crack, as shown in Fig. 2, one can write the constitutive relations between the internal moments and rotational displacement derivatives as

$$M(x,y)=\begin{Bmatrix} M_x \\ M_y \\ M_{xy} \end{Bmatrix} = D\begin{bmatrix} \frac{\partial}{\partial x} & 0 \\ 0 & \frac{\partial}{\partial y} \\ \frac{\partial}{\partial y} & \frac{\partial}{\partial x} \end{bmatrix}\begin{Bmatrix} \theta_x \\ \theta_y \end{Bmatrix} = DL\theta \tag{5}$$

where $M(x,y)$ denotes the internal moments per unit length, and $\{\theta_x\ \theta_y\}^T$ denotes the rotation of the normal planes induced by the moments. The matrix D contains the flexural and twisting stiffness components of the plate. For an intact plate with isotropic elasticity, and plane stress behavior, the constitutive matrix D is defined as D_0 in the form of

$$D_0=\frac{h^3}{12}C \tag{6}$$

where the matrix C represents the stress-strain constitutive stiffness of isotropic material.

A crack will induce local flexibility in the plate. According to Lee et al. [23] continuum elastic stiffness theory, the cracked plate element would exhibit orthotropic stiffness properties compatible with the orientation of the crack line. Furthermore, based on the observation from fracture mechanics point of view that the highest stress intensity at the crack edge along the major axis direction would effectively reduce the stiffness in the minor axis direction, a rational supposition can be made that the crack will mainly affect the flexural stiffness normal to the crack line, while contributing relatively little effect on the plate stiffness parallel to the crack. (In Lee's model, the stiffness reduction along the major axis is v^2 times that along the minor axis). In order to verify this presumption, the cracked plate element is represented by an effective element of continuum anisotropic material with the major axis of the material parallel to the crack line and the minor axis normal to the crack. Thus, under the plane stress condition, the constitutive matrix D of the cracked element can be written as

$$D=\frac{h^3}{12}\bar{C} \tag{7}$$

where the stiffness components are $\bar{C}_{11}=E_1/(1-v_{12}v_{21}),\bar{C}_{22}=E_2/(1-v_{12}v_{21}),\bar{C}_{12}=v_{12}E_1/(1-v_{12}v_{21})=v_{21}E_2/(1-v_{12}v_{21})$ and $\bar{C}_{66}=G$.

A vector of damage variables, $\{\alpha\ \beta\ \chi\}$, is selected to relate the effective continuum stiffness model of the cracked plate element to the isotropic stiffness of the undamaged material as

$$E_1=E\alpha,\quad v_{21}=v,\quad E_2=E\beta,\quad G_{12}=G\chi \tag{8}$$

where α,β, and χ denotes stiffness reduction factors due to the crack. Considering the relation $v_{12}/E_2=v_{21}/E_1$, one gets

$$v_{12}=v_{21}\frac{E_2}{E_1}=v\frac{\beta}{\alpha} \tag{9}$$

Substituting (8) and (9) into (7), one obtains

$$D=\frac{h^3}{12}\begin{bmatrix} \frac{E\alpha^2}{\alpha-\beta v^2} & \frac{vE\alpha\beta}{\alpha-\beta v^2} & 0 \\ \frac{vE\alpha\beta}{\alpha-\beta v^2} & \frac{E\alpha\beta}{\alpha-\beta v^2} & 0 \\ 0 & 0 & \frac{E\chi}{2(1+v)} \end{bmatrix} \tag{10}$$

To determine the coupled damage variables, the above-mentioned principles of strain equivalence and strain energy equivalence do not work. They are extended to a more general principle that *the effective continuum model of a damaged structure should have identical macro-behaviors with those exhibited by the real damaged structure*. The macro-behaviors here include the static and dynamic characteristics of the structure such as deformations under loads, natural frequencies, mode shapes, frequency response functions, etc. Based on this principle, the following section presents a methodology to identify the damage variables using the estimated ULSC from vibration measurements.

4 Nonmodel-Based Damage Identification With ULSC

4.1 Deflection and Curvature Formulations. According to the Kirchhoff's theory, the shear deformations are neglected and we have

$$\nabla w-\theta=0 \tag{11}$$

Substituting (11) into (5), we get

$$M(x,y)=D\kappa(x,y) \tag{12}$$

where the vector $\kappa(x,y)=\{(\partial^2 w/\partial x^2)(\partial^2 w/\partial y^2)2(\partial^2 w/\partial x\partial y)\}=\{\kappa_x\kappa_y\kappa_{xy}\}$ contains the flexural curvatures and twisting curvature at the middle plane of the plate.

Now one can define the transverse deflection function $w(x,y)$ as a biquadratic polynomial

$$w(x,y)=p\alpha \tag{13}$$

where the vector $p=\{1\ x\ y\ x^2\ xy\ y^2\ x^3\ x^2y\ xy^2\ y^3\ x^3y\ xy^3\}$, and the vector $\alpha=\{\alpha_1\alpha_2\cdots\alpha_{12}\}$ denotes the unknown coefficients. It is then convenient to express the deflection in terms of displacements at the four nodes of the plate element as

$$w(x,y)=H(x,y)\bar{w} \tag{14}$$

where $H(x,y)$ is the vector of isoparametric shape functions of the element, and $\bar{w}=\{w_1w_2w_3w_4\theta_{x1}\theta_{x2}\theta_{x3}\theta_{x4}\theta_{y1}\theta_{y2}\theta_{y3}\theta_{y4}\}$ is the nodal displacement vector. Substituting (14) into the constitutive relation (12) yields

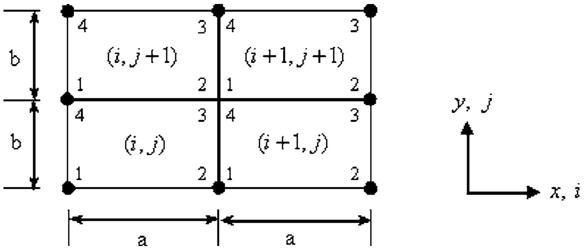

Fig. 3 Four adjacent rectangular plate elements

$$M(x,y) = DB(x,y)\bar{w} \tag{15}$$

where $B(x,y)=[\partial^2H/\partial x^2;\partial^2H/\partial y^2;2(\partial^2H/\partial x\partial y)]$. Equation (15) relates the internal moments at any point in the element with the nodal displacements. The internal moments at the four nodes are found by substituting the corresponding nodal coordinates, $(x_i,y_i)i=1\ldots4$, into Eq. (15). Writing in matrix form

$$\begin{Bmatrix} \bar{M}_B \\ \bar{M}_T \end{Bmatrix} = \begin{bmatrix} K_{BT} & K_{BR} \\ K_{TT} & K_{TR} \end{bmatrix} \begin{Bmatrix} \bar{w}_T \\ \bar{w}_R \end{Bmatrix} = K\bar{w} \tag{16}$$

where $\bar{M}_B=\{M_{x1}M_{y1}M_{x2}M_{y2}M_{x3}M_{y3}M_{x4}M_{y4}\}^T$ denotes the bending moments at the four nodes, and $\bar{M}_T=\{M_{xy1}M_{xy2}M_{xy3}M_{xy4}\}^T$ denotes the nodal twisting moments. $\bar{w}_T=\{w_1w_2w_3w_4\}$ denotes the translational DOFs at the four nodes, and $\bar{w}_R$ denotes the nodal rotational DOFs. The matrix K represents the general constitutive relation between the nodal loads and nodal displacements. Rewriting Eq. (16) in partitioned form, the rotational and translational displacements can be expressed separately as

$$\bar{w}_R = K_{BR}{}^{-1}\bar{M}_B - K_{BR}{}^{-1}K_{BT}\bar{w}_T \tag{17a}$$

$$\bar{w}_T = K_{TT}{}^{*}\bar{M}_T - K_{TT}{}^{*}K_{TR}\bar{w}_R \tag{17b}$$

where the superscript * denotes the pseudo inverse of the matrix. Detailed formulation of Eq. (17) is referred to Appendix A.

Consider a group of four adjacent rectangular plate elements as shown in Fig. 3, in which all the elements are suspected of crack damage. For the element (i,j), the rotation about y axis, θ_x, at its second node can be evaluated using Eq. (17a)

$$\theta_{x2}\big|_{(i,j)} = \left(\frac{2a}{\alpha Eh^3}M_{x1} - \frac{2a\upsilon}{\alpha Eh^3}M_{y1} + \frac{4a}{\alpha Eh^3}M_{x2} - \frac{4a\upsilon}{\alpha Eh^3}M_{y2} + \frac{w_2 - w_1}{a} \right)_{(i,j)} \tag{18}$$

Similarly, the rotation about y axis at the first node of the element $(i+1,j)$ can be estimated by

$$\theta_{x1}\big|_{(i+1,j)} = \left(-\frac{4a}{\alpha Eh^3}M_{x1} + \frac{4a\upsilon}{\alpha Eh^3}M_{y1} - \frac{2a}{\alpha Eh^3}M_{x2} + \frac{2a\upsilon}{\alpha Eh^3}M_{y2} + \frac{w_2 - w_1}{a} \right)_{(i+1,j)} \tag{19}$$

According to the continuity condition, the slope at node 2 of the element (i,j) equals to the slope at the node 1 of the element $(i+1,j)$. Thus, we have

$$\theta_{x2}{}^{(i,j)} = \theta_{x1}{}^{(i+1,j)} \tag{20}$$

It is important to note that Eqs. (18)–(20) are derived for the damaged plate.

The moment-curvature relationship for an intact plate can be obtained from Eqs. (5) and (6) as

$$\tilde{M}_x(x,y) = \frac{Eh^3}{12(1-\upsilon^2)}\left[\tilde{\kappa}_x(x,y) + \upsilon\tilde{\kappa}_y(x,y)\right],$$

$$\tilde{M}_y(x,y) = \frac{Eh^3}{12(1-\upsilon^2)}\left[\tilde{\kappa}_y(x,y) + \upsilon\tilde{\kappa}_x(x,y)\right] \tag{21}$$

$$\tilde{M}_{xy}(x,y) = \frac{Eh^3}{12(1+\upsilon)}\tilde{\kappa}_{xy}(x,y)$$

where the superscript ~ denotes the terms for the intact plate. It is assumed that the applied loads only produce small deflection in the plate structure, and that the additional deflection induced by the crack damage is also small such that the internal forces in the damaged structure can be approximately taken as those for the intact structure, which means $M_x \approx \tilde{M}_x$, $M_y \approx \tilde{M}_y$, and $M_{xy} \approx \tilde{M}_{xy}$. Therefore, one can directly substitute Eq. (21) into Eqs. (18)–(20) to have

$$\left(\frac{\tilde{\kappa}_{x1} + 2\tilde{\kappa}_{x2}}{\alpha}\right)_{(i,j)} + \left(\frac{2\tilde{\kappa}_{x1} + \tilde{\kappa}_{x2}}{\alpha}\right)_{(i+1,j)} = 6\kappa_{x2}{}^{(i,j)} \tag{22a}$$

Similarly considering the slope continuity condition at node 3 of element (i,j) and the node 1 of element $(i+1,j)$, we have $\theta_{x3}{}^{(i,j)} = \theta_{x4}{}^{(i+1,j)}$, yielding

$$\left(\frac{\tilde{\kappa}_{x4} + 2\tilde{\kappa}_{x3}}{\alpha}\right)_{(i,j)} + \left(\frac{2\tilde{\kappa}_{x4} + \tilde{\kappa}_{x3}}{\alpha}\right)_{(i+1,j)} = 6\kappa_{x3}{}^{(i,j)} \tag{22b}$$

Also, from the slope continuity condition of rotation θ_y along the y direction we have $\theta_{y4}{}^{(i,j)} = \theta_{y1}{}^{(i,j+1)}$ and $\theta_{y3}{}^{(i,j)} = \theta_{y2}{}^{(i,j+1)}$, leading to

$$\left(\frac{\tilde{\kappa}_{y1} + 2\tilde{\kappa}_{y4} + \upsilon(\tilde{\kappa}_{x1} + 2\tilde{\kappa}_{x4})}{\beta}\right)_{(i,j)} + \left(\frac{\tilde{\kappa}_{y4} + 2\tilde{\kappa}_{y1} + \upsilon(\tilde{\kappa}_{x4} + 2\tilde{\kappa}_{x1})}{\beta}\right)_{(i,j+1)} = 6(1-\upsilon^2)\kappa_{y4}{}^{(i,j)} + S_{14} \tag{23a}$$

and

$$\left(\frac{\tilde{\kappa}_{y2} + 2\tilde{\kappa}_{y3} + \upsilon(\tilde{\kappa}_{x2} + 2\tilde{\kappa}_{x3})}{\beta}\right)_{(i,j)} + \left(\frac{\tilde{\kappa}_{y3} + 2\tilde{\kappa}_{y2} + \upsilon(\tilde{\kappa}_{x3} + 2\tilde{\kappa}_{x2})}{\beta}\right)_{(i,j+1)} = 6(1-\upsilon^2)\kappa_{y3}{}^{(i,j)} + S_{23} \tag{23b}$$

respectively, where

$$S_{14} = \left(\frac{\upsilon(\tilde{\kappa}_{x1} + 2\tilde{\kappa}_{x4}) + \upsilon^2(\tilde{\kappa}_{y1} + 2\tilde{\kappa}_{y4})}{\alpha}\right)_{(i,j)} + \left(\frac{\upsilon(\tilde{\kappa}_{x4} + 2\tilde{\kappa}_{x1}) + \upsilon^2(\tilde{\kappa}_{y4} + 2\tilde{\kappa}_{y1})}{\alpha}\right)_{(i,j+1)}$$

and

$$S_{23} = \left(\frac{\upsilon(\tilde{\kappa}_{x2} + 2\tilde{\kappa}_{x3}) + \upsilon^2(\tilde{\kappa}_{y2} + 2\tilde{\kappa}_{y3})}{\alpha}\right)_{(i,j)} + \left(\frac{\upsilon(\tilde{\kappa}_{x3} + 2\tilde{\kappa}_{x2}) + \upsilon^2(\tilde{\kappa}_{y3} + 2\tilde{\kappa}_{y2})}{\alpha}\right)_{(i,j+1)}.$$

Next, the transverse deflection at the nodes are estimated from Eq. (17b), and taking into account the continuity condition of deflection w along the x and y directions separately, we have $w_2{}^{(i,j)} = w_1{}^{(i+1,j)}$ and $w_4{}^{(i,j)} = w_1{}^{(i,j+1)}$, leading to

$$\left(\frac{\tilde{\kappa}_{xy1}+\tilde{\kappa}_{xy2}+\tilde{\kappa}_{xy3}+\tilde{\kappa}_{xy4}}{\chi}\right)_{(i,j)}+\left(\frac{\tilde{\kappa}_{xy1}+\tilde{\kappa}_{xy2}+\tilde{\kappa}_{xy3}+\tilde{\kappa}_{xy4}}{\chi}\right)_{(i+1,j)}$$
$$=4(\kappa_{xy2}+\kappa_{xy3})_{(i,j)} \qquad (24a)$$

and

$$\left(\frac{\tilde{\kappa}_{xy1}+\tilde{\kappa}_{xy2}+\tilde{\kappa}_{xy3}+\tilde{\kappa}_{xy4}}{\chi}\right)_{(i,j)}+\left(\frac{\tilde{\kappa}_{xy1}+\tilde{\kappa}_{xy2}+\tilde{\kappa}_{xy3}+\tilde{\kappa}_{xy4}}{\chi}\right)_{(i,j+1)}$$
$$=4(\kappa_{xy3}+\kappa_{xy4})_{(i,j)} \qquad (24b)$$

The following observations can be made based on Eqs. (22)–(24):

(1) The coupled damage variables α,β, and χ in the crack model in Eq. (10) are decoupled by the curvature expressions on the nodal transverse deflection.
(2) The curvature-based formulations are valid for any load condition that satisfies the small deformation assumption.
(3) Provided that curvatures of the intact and cracked plates, $\tilde{\kappa}$ and κ, respectively, are measured on a regular mesh of the rectangular plate, three sets of equations containing the decoupled damage variables can be established separately in Eqs. (22)–(24). Taking the reciprocal of the damage variables as unknowns, the equations are linear and determinate.

4.2 ULS Curvatures. This section presents a method to estimate the plate curvatures under a full set of uniform unit load from the vibration measurements. For a linear structural system with n degrees-of-freedom, its flexibility matrix can be expressed by the superposition of mass normalized modes ϕ_g, where $\phi_g^T M \phi_g = 1$ $(g=1,\ldots,n)$, as [24]

$$F=\sum_{g=1}^{n}\frac{\phi_g\phi_g^T}{\omega_g^2} \qquad (25)$$

where ω_g is the gth natural frequency. Physically, each element of the flexibility matrix, $f_{k\ell}$, can be interpreted as the displacement at the kth DOF due to a unit load at ℓth DOF. Thus, the deflection vector of a plate under uniform unit load can be evaluated by

$$u=F\cdot L \qquad (26)$$

where $L=\{1,\ldots,1\}_{1\times n}^T$ is the unit vector representing the uniform load acting on the plate. The deflection component u_k can be expressed as

$$u_k=\sum_{l=1}^{n}f_{kl}=\sum_{g=1}^{n}\sum_{l=1}^{n}\frac{\phi_g(k)\phi_g(\ell)}{\omega_g^2} \qquad (27)$$

This modal based formulation of the structural deflection vector under uniform load was defined as Uniform Load Surface (ULS) by Zhang and Aktan [25]. An approach to estimate the ULS curvature of plate structures using the Chebyshev polynomial approximation has been proposed by Wu and Law [26]. This approach is adopted in this paper, and is outlined as follows.

The ULS function of a plate can be modeled by the Chebyshev polynomial in two variables:

$$u(x,y)=\sum_{r=1}^{N}\sum_{s=1}^{M}c_{rs}T_r(x)T_s(y) \qquad (28)$$

where $T_r(x), T_s(y)$ are the first kind Chebyshev polynomials, and N, M are their orders. It is assumed that there are Q measuring points on the rectangular mesh of the plate. The ULS value, $u(x_p,y_q)$, can be obtained at all the measuring points from Eq. (27). When substituting them into Eq. (28) separately, one has a system of Q equations written in matrix form

$$\lfloor T(x_p)T(y_q)\rfloor_{Q\times P}\{c_{rs}\}_{P\times 1}=\{u(x_p,y_q)\}_{P\times 1} \qquad (29)$$

where $P=N\times M$. The coefficient vector $\{c_{rs}\}$ can then be solved by the least-squares technique

$$\{c_{rs}\}_{P\times 1}=\left([T(x_p)T(y_q)]_{Q\times P}^T[T(x_p)T(y_q)]_{Q\times P}\right)^{-1}$$
$$\times[T(x_p)T(y_q)]_{Q\times P}^T\{u(x_p,y_q)\}_{Q\times 1} \qquad (30)$$

By making use of the orthogonal property of Chebyshev polynomial, the curvature of the ULS is obtained as the second derivatives of the Chebyshev polynomials in Eq. (28) as

$$uc_{xx}=\sum_{r=1}^{N}\sum_{s=1}^{M}c_{rs}\frac{\partial T_r^2(x)}{\partial x^2}T_s(y)$$

$$uc_{yy}=\sum_{r=1}^{N}\sum_{s=1}^{M}c_{rs}T_r(x)\frac{\partial T_s^2(y)}{\partial y^2} \qquad (31)$$

$$uc_{xy}=\sum_{r=1}^{N}\sum_{s=1}^{M}c_{rs}\frac{\partial T_r^2(x)}{\partial x^2}\frac{\partial T_s^2(y)}{\partial y^2}$$

Now considering that Eqs. (22)–(24) are valid for an arbitrary load satisfying the small deflection assumption and the behavior equivalence principle that the effective model has equal deflection curvatures as those obtained from the cracked plate when subject to identical loads, one can replace the curvature terms $\tilde{\kappa}$ and κ with the measured ULS curvatures in Eq. (31) from the undamaged and damaged states, respectively. The resulting Eqs. (22)–(24) form the curvature relationship between the intact and cracked plates subjected to a uniform unit load, from which the damage variables can then be solved.

4.3 Crack Length Prediction. Although no known exact solution exists for the released energy of finite plate with a crack under arbitrary bending and twisting moments, the following approximate formulas are derived such that the crack length can be predicted from the identified damage variables. The elastic strain energy contained by the undamaged plate element can be expressed as

$$\tilde{U}=\frac{1}{2}\int_0^b\int_0^a\tilde{M}(x,y)\tilde{\kappa}(x,y)dxdy=\frac{1}{2}\int_0^b\int_0^a\tilde{\kappa}^T(x,y)D_0\tilde{\kappa}(x,y)dxdy \qquad (32)$$

Separately writing the curvature fields of the plate element in the nodal terms as

$$\tilde{\kappa}_x=\sum_{i=1}^{nn}H_i(x,y)\tilde{\kappa}_{x,i},\quad \tilde{\kappa}_y=\sum_{i=1}^{nn}H_i(x,y)\tilde{\kappa}_{y,i},\quad \tilde{\kappa}_{xy}=\sum_{i=1}^{nn}H_i(x,y)\tilde{\kappa}_{xy,i} \qquad (33)$$

where $H_i(x,y)$ is the isoparametric shape function at the ith node and nn denotes the number of nodes per element, Eq. (32) can be rewritten as

$$\tilde{U}=\frac{h^3}{24}\tilde{\kappa}_{nd}{}^T\int_0^b\int_0^a H^TCHdxdy\tilde{\kappa}_{nd} \qquad (34)$$

where $\tilde{\kappa}_{nd}=\{\tilde{\kappa}_{x,1}\ \tilde{\kappa}_{y,1}\ \tilde{\kappa}_{xy,1}\cdots\tilde{\kappa}_{x,nn}\ \tilde{\kappa}_{y,nn}\ \tilde{\kappa}_{xy,nn}\}^T$ denotes the nodal curvatures and

$$H=\begin{bmatrix}H_1 & 0 & 0 & \cdots & H_{nn} & 0 & 0\\ 0 & H_1 & 0 & \cdots & 0 & H_{nn} & 0\\ 0 & 0 & H_1 & \cdots & 0 & 0 & H_{nn}\end{bmatrix}.$$

Now considering the cracked plate element exhibits identical deflection curvatures as the undamaged element, one can infer the equality of the moment load $M(x,y)\approx\tilde{M}(x,y)$ according to the

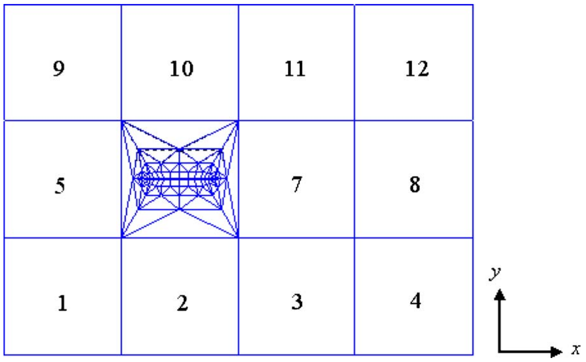

Fig. 4 Finite element model of the cracked thin plate

small deflection assumption. Hence, by replacing the isotropic material with the identified effective stiffness model, the strain energy of the cracked plate element is similarly written as

$$U=\frac{h^3}{24}\tilde{\kappa}_{nd}{}^T\int_0^b\int_0^a H^T\bar{C}Hdxdy\tilde{\kappa}_{nd} \tag{35}$$

The crack released strain energy is approximately estimated through the stress intensity around the crack as

$$U_k=\frac{1}{E}\int_{-c}^{c}\int_{-h/2}^{h/2}(K_I^2+K_{II}^2)dzd\xi \tag{36}$$

where c indicates half length of the crack. K_I and K_{II} are the stress intensity factors corresponding to the two modes of cracking [27]. Assuming the crack surfaces are subject to equal and opposite arbitrary bending and twisting moments in an infinite thin plate (assuming plane stress state), the stress intensity factors are written as

$$\begin{aligned} K_I^{\mathrm{inf}}&=\frac{12z}{h^3\sqrt{\pi c}}\int_{-c}^{c}M_y(\xi)\sqrt{\frac{c+\xi}{c-\xi}}d\xi\\ &=\frac{z}{\sqrt{\pi c}}\int_{-c}^{c}(C_{12}H_{r1}+C_{22}H_{r2})\sqrt{\frac{c+\xi}{c-\xi}}d\xi\tilde{\kappa}_{nd}\\ K_{II}^{\mathrm{inf}}&=\frac{-12z}{h^3\sqrt{\pi c}}\int_{-a}^{a}M_{xy}(\xi)\sqrt{\frac{c+\xi}{c-\xi}}d\xi\\ &=\frac{-z}{\sqrt{\pi c}}\int_{-c}^{c}C_{66}H_{r3}\sqrt{\frac{c+\xi}{c-\xi}}d\xi\tilde{\kappa}_{nd} \end{aligned} \tag{37}$$

As Eq. (37) is only suitable for infinite plate with a crack, it is necessary to correct it for the finite plate. According to the results from Yagawa and Nishioka [28], the difference of the correction factor is small for different plate width-to-crack length ratio $0<h/c<1$, and approximately equal correction factors can be used to correct both the stress intensity factors of opening-type cracks (type I) and sliding-type cracks (type II). Therefore, the corrected stress intensity factors are obtained as

$$K_I=K_I^{\mathrm{inf}}f(s),\quad K_{II}=K_{II}^{\mathrm{inf}}f(s) \tag{38}$$

where the correction factor $f(s)$ can be obtained through polynomial interpolation [28] and plotted in Fig. 4, where

$$f(s)=1.0+0.0187s+0.1825s^2+2.024s^3-2.431s^4 \tag{39}$$

and $s=2c/a$.

Assuming the crack propagates in quasi-static state and neglecting the energy loss by thermal terms, one will get the following equilibrium of strain energy:

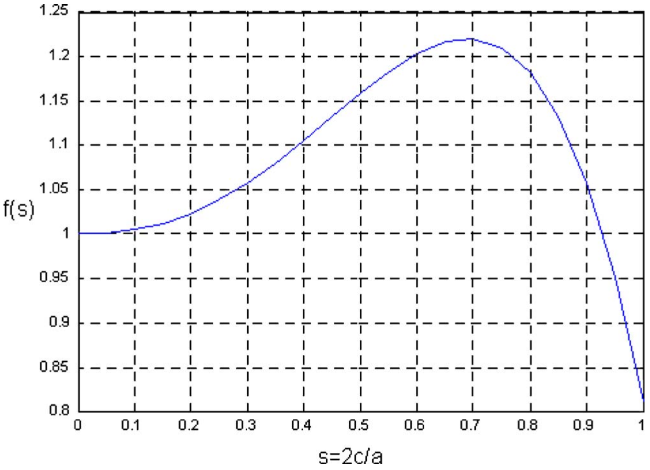

Fig. 5 Correction factor on stress intensity factor for finite plate

$$\tilde{U}=U+U_k \tag{40}$$

Substituting Eqs. (34)–(36) into (40), one obtains

$$\begin{aligned} &\frac{h^3}{24}\tilde{\kappa}_{nd}{}^T\int_0^b\int_0^a H^TCHdxdy\tilde{\kappa}_{nd}\\ &\quad=\frac{h^3}{24}\tilde{\kappa}_{nd}{}^T\int_0^b\int_0^a H^T\bar{C}Hdxdy\tilde{\kappa}_{nd}\\ &\qquad+\frac{1}{E}\tilde{\kappa}_{nd}{}^T\int_{-c}^{c}\int_{-h/2}^{h/2}\frac{z^2}{\pi c}f^2\left(\int_{-c}^{c}(C_{12}H_{r1}+C_{22}H_{r2}\right.\\ &\qquad\left.-C_{66}H_{r3})\sqrt{\frac{c+\xi}{c-\xi}}d\xi\right)dzd\xi\tilde{\kappa}_{nd} \end{aligned} \tag{41}$$

Since Eq. (41) are valid for arbitrary nodal deflection curvatures $\tilde{\kappa}_{nd}$ that statisfies the small deformation assumption, it can be simplified into a characteristic equation of the crack half-length c. Provided the damage variables in the effective constitutive matrix $\bar{C}$ are identified, the crack length can be numerically solved by the Newton-Raphson method.

5 Numerical Examples

An aluminium plate with free boundary condition is studied in this section to validate the proposed methodology. The plate has the dimensions of 400 mm × 300 mm × 3 mm. The whole intact plate is divided into 4 × 3 plate elements. An open and through crack, as shown in Fig. 5, is then assumed to occur in element 6 with a length of 80 mm with the crack line parallel to the x axis. The intact and cracked plates are separately modeled using an open-source finite element toolbox, called OPENFEM, integrated with MATLAB. The natural frequencies and corresponding mode shapes of the plate at the 20 finite element nodes are "measured" through eigenvalue analysis of the finite element model. The ULS curvatures are then estimated from the modal data via the procedure described in Eqs. (27)–(31), and they serve as input into the MATLAB program based on the nonmodel ULSC algorithm for the identification of crack location and damage variables.

According to the proposed effective stiffness model for the cracked plate element, there are three unknowns for each suspicious element. Therefore, we have totally 12 × 3 unknowns for the whole model of the cracked plate. Referring to Eq. (22), one can obtain 18 equations from the slope continuity condition of rotation θ_x to construct an over-determined system for the values of crack parameter α_i $(i=1,\ldots,12)$. Similarly, from the slope continuity

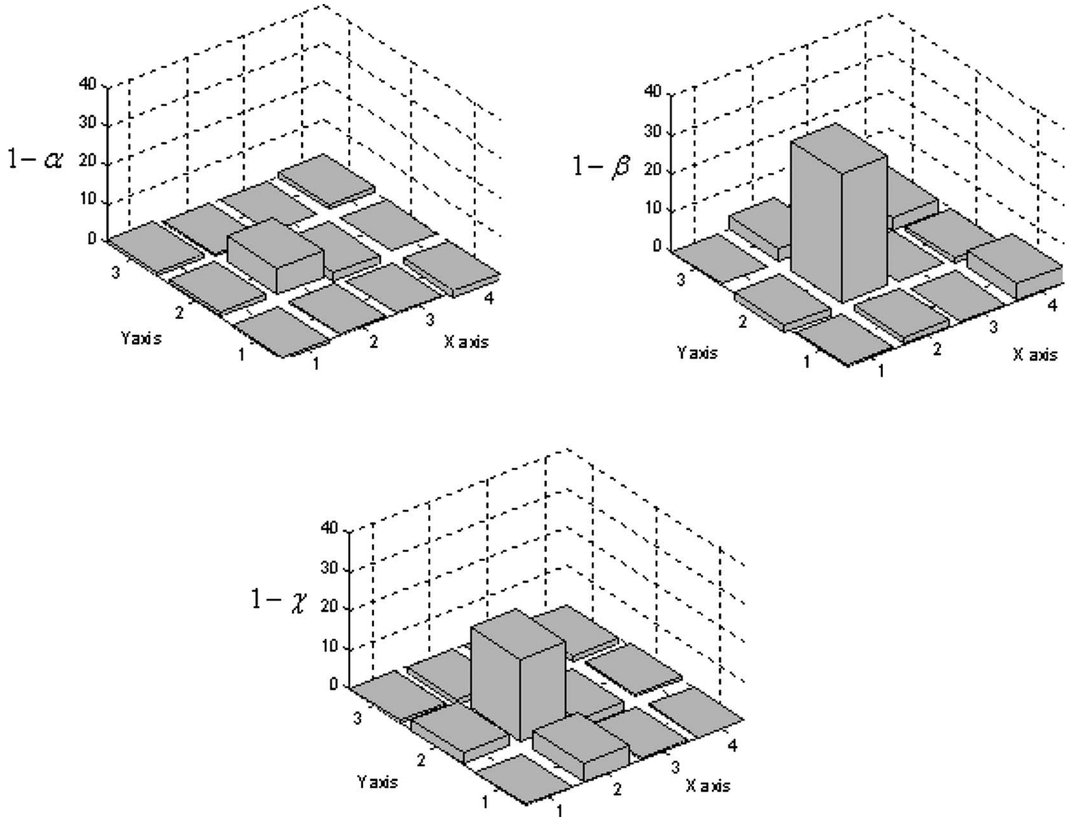

Fig. 6 Identified crack parameter for the numerical example of thin plate

condition of rotation θ_y and the transverse deflection w in Eqs. (23) and (24), we obtain a total of 16 equations to solve the unknowns β_i and 17 equations for the solution of χ_i. The resulting damage indices are shown in Fig. 6. It is clear that element 6 is damaged. Further, for this cracked element, the relative stiffness normal to the crack line, given as $\beta=0.6832$, and the inplane twisting stiffness, $\chi=0.7717$, show clearly larger reductions from the initial value than the relative stiffness along the crack line shown as $\alpha=0.9465$. This result verifies the supposition we proposed earlier that a crack in a plate element mainly affects its stiffness normal to the crack line. The crack length $2c$ predicted from the identified damaged variables equals to 86.15 mm, which is close to the true value with an error less than 8%.

6 Experimental Verification

Similar to many existing validated models, an experimental verification is performed to investigate the problems with a real working environment. The aluminum plate specimen has the dimension of 600 mm × 500 mm × 3 mm. Figure 7 shows the experimental setup for testing. A rectangular mesh of 7 × 6 measuring points is outlined on each plate. The intact plate is suspended from a rigid frame by two steel wires of 0.5 mm in diameter and 0.75 m in length to simulate the free boundary condition. An impulsion signal was generated by hitting the hammer at each measuring point, and the vibration response of the plate due to the impulse is collected by an accelerometer model B&K 4370 as shown in the figure. Both signals are amplified and inputted into a commercial modal testing and analysis system DASP2000. The natural frequencies and corresponding mode shapes of the plate at the rectangular mesh are then extracted through a MISO transfer function analysis.

An artificial crack is cut in the specimen, as shown in Fig. 8(a). To verify the proposed crack model and identification method with cases of different crack length, a scheme of crack cutting is devised and listed in Table 1. The crack in the first state is 0.5 mm wide, and it is 0.25 mm wide for the other two states. After each crack cutting exercise, the above hammer test is repeated to obtain the modal data of the plate for each damage state. The first five natural frequencies of the plate specimen in different damage states are also listed in Table 1. The ULS curvatures for the undamaged plate and the cracked plate in different session are estimated from the measured modal data of the first five modes. The identified damage parameters for each crack state are plotted in Fig. 9, where the x axis measures the relative crack length defined by $2c/a$, here a denotes the dimension of the crack containing element along the x axis.

Besides testing the plate specimen with a crack of different length, a refined finite element model is also constructed by

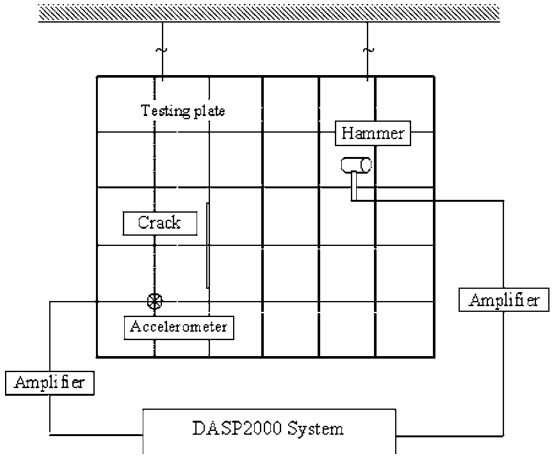

Fig. 7 Diagram of the experimental system

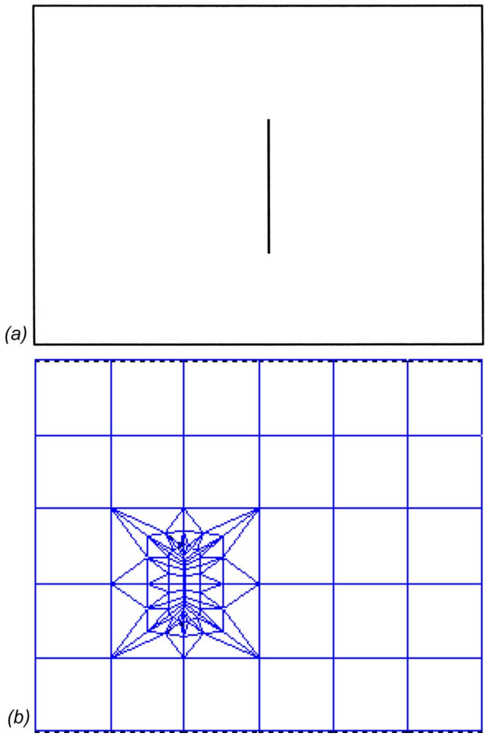

Fig. 8 (***a***) **Artificial cracks (session I) in the plate specimen. (*b*) Finite element meshes to model the cracked plate specimen.**

OPENFEM to model the cracked aluminium plate, as shown in Fig. 8(*b*), to study the relationship between values of the proposed damage variables and the crack length. The finite element model has initially a crack of 40 mm in length, and then the crack is lengthened in steps of 20 mm each and the finite element mesh is modified for each case. In each case with a definite crack length, the ULS curvatures are estimated from the "measured" modal data of the plate model, and then they are used as references for crack identification. The resulting damage variables are shown separately in Figs. 9(*a*)–9(*c*) with symbol "*," and they are curve-fitted as shown. The other curves shown in Figs. 9(*a*)–9(*c*) with symbol "o" are the results from Lee et al. [21].

It is seen that the test results are consistent with the numerical result using the present model and identification method, with the damage variables exhibiting the same trend of changing with the crack propagation. Parameter α decays very slowly and changes little, which means the stiffness reduction in the direction of crack extension is limited. Parameter β sharply drops with the extension of the crack indicating a remarkable reduction in the stiffness normal to the crack line. There are two phases for parameter χ, which represents the in-plane twisting stiffness of the cracked plate element. Firstly, the parameter drops uniformly when the relative crack length is less than 0.6 of the element dimension, and then the twisting stiffness degrades abruptly as the crack propagating towards the element edges. However, the results from Lee

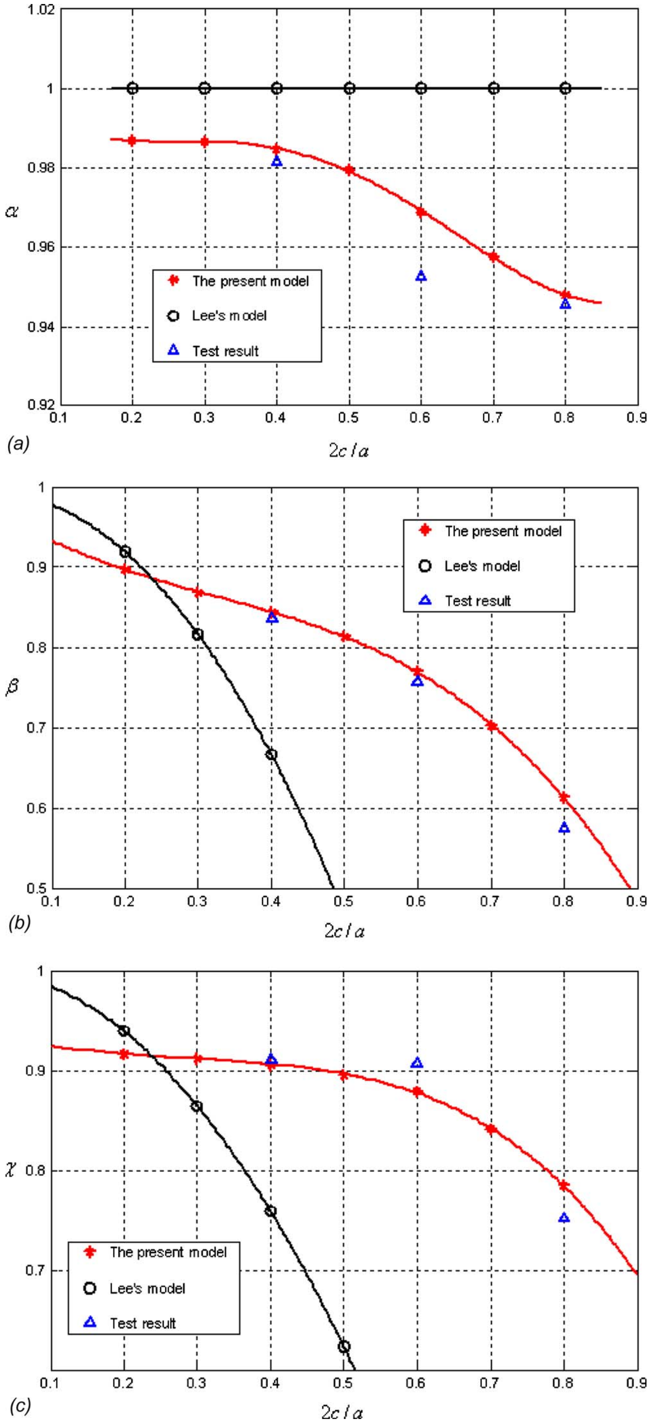

Fig. 9 Damage variables from experiment and finite element model

Table 1 Scheme of artificial crack and corresponding natural frequencies of the plate specimen

Crack information			Natural frequencies (Hz) in order of modes				
Center (x,y)		(200,200)	1	2	3	4	5
Length (mm)	Intact	N/A	31.379	41.578	65.859	78.105	88.263
	State I	80	31.372	41.228	65.571	78.040	88.245
	State II	120	31.372	40.812	65.238	77.991	88.194
	State III	160	31.361	40.133	64.843	77.870	88.028

et al. [21] are very different. Parameter α remains unchanged with different crack length, which means the line crack never affect the stiffness along its extension direction; while the stiffness normal to the crack line and the twisting stiffness, shown as β and χ, respectively, may take up negative values when the crack is close to the element edge. The presence of these contradictory results can be explained by the infinite plate assumption in the model of Lee et al. [21] and the model is only suitable for micro-cracks.

7 Conclusions

Aiming at the nondestructive fault detection with vibration measurements, an effective stiffness continuum model for a thin plate with an edge-parallel crack is proposed based on the behavior equivalence principle. The model is then incorporated into a nonmodel system identification approach. The estimated Uniform Load Surface curvatures for the intact and cracked plates are used without any baseline model of the plate. The model parameters are decoupled and solved from the resulting set of linear equation. After the crack in each suspicious element is localized directly from the identified damaged variables, the crack length is further predicted through the corrected stress intensity factors on the basis of total potential energy conservation. In contrast to the micro-crack model (Lee et al. [21]), the present methodology can be applied to the identification of a larger practical crack with larger relative length. Both numerical examples and experiment results demonstrate that the proposed model predicts the real cracked plate well and the identification method is effective for localizing and quantifying the crack in thin plates.

Acknowledgment

The work described in this paper was supported by a grant from the Hong Kong Polytechnic University Research Funding Project No. G-W092.

Appendix: Formulation of the Modal Rotational and Translational Displacements

Equations (17a) and (17b) can be simply rewritten as

$$\bar{w}_R = U_R \bar{M}_B - V_R \bar{w}_T, \quad \bar{w}_T = U_T \bar{M}_T - V_T \bar{w}_R \tag{A1}$$

where

$$U_R = K_{BR}^{-1} = \begin{bmatrix} \frac{-4a}{\alpha Eh^3} & \frac{4av}{\alpha Eh^3} & \frac{-2a}{\alpha Eh^3} & \frac{2av}{\alpha Eh^3} & 0 & 0 & 0 & 0 \\ \frac{2a}{\alpha Eh^3} & \frac{-2a}{\alpha Eh^3} & \frac{4a}{\alpha Eh^3} & \frac{-4av}{\alpha Eh^3} & 0 & 0 & 0 & 0 \\ 0 & 0 & 0 & 0 & \frac{4a}{\alpha Eh^3} & \frac{-4av}{\alpha Eh^3} & \frac{2a}{\alpha Eh^3} & \frac{-2av}{\alpha Eh^3} \\ 0 & 0 & 0 & 0 & \frac{-2a}{\alpha Eh^3} & \frac{2a}{\alpha Eh^3} & \frac{-4a}{\alpha Eh^3} & \frac{4av}{\alpha Eh^3} \\ \frac{4bv}{\alpha Eh^3} & \frac{-4b}{\beta Eh^3} & 0 & 0 & 0 & 0 & \frac{2bv}{\alpha Eh^3} & \frac{-2b}{\beta Eh^3} \\ 0 & 0 & \frac{4bv}{\alpha Eh^3} & \frac{-4b}{\beta Eh^3} & \frac{2bv}{\alpha Eh^3} & \frac{-2b}{\beta Eh^3} & 0 & 0 \\ 0 & 0 & \frac{-2bv}{\alpha Eh^3} & \frac{2b}{\beta Eh^3} & \frac{-4bv}{\alpha Eh^3} & \frac{4b}{\beta Eh^3} & 0 & 0 \\ \frac{-2bv}{\alpha Eh^3} & \frac{2b}{\beta Eh^3} & 0 & 0 & 0 & 0 & \frac{-4bv}{\alpha Eh^3} & \frac{4b}{\beta Eh^3} \end{bmatrix},$$

$$V_R = K_{BR}^{-1} K_{BT} = \begin{bmatrix} -1/a & -1/a & 0 & 0 & -1/b & 0 & 0 & -1/b \\ 1/a & 1/a & 0 & 0 & 0 & -1/b & -1/b & 0 \\ 0 & 0 & 1/a & 1/a & 0 & 1/b & 1/b & 0 \\ 0 & 0 & -1/a & -1/a & 1/b & 0 & 0 & 1/b \end{bmatrix}^T,$$

and

$$U_T = K_{TT}^{*} = \begin{bmatrix} \frac{-3ab(1+v)}{2\chi Eh^3} & \frac{-3ab(1+v)}{2\chi Eh^3} & \frac{-3ab(1+v)}{2\chi Eh^3} & \frac{-3ab(1+v)}{2\chi Eh^3} \\ \frac{3ab(1+v)}{2\chi Eh^3} & \frac{3ab(1+v)}{2\chi Eh^3} & \frac{3ab(1+v)}{2\chi Eh^3} & \frac{3ab(1+v)}{2\chi Eh^3} \\ \frac{-3ab(1+v)}{2\chi Eh^3} & \frac{-3ab(1+v)}{2\chi Eh^3} & \frac{-3ab(1+v)}{2\chi Eh^3} & \frac{-3ab(1+v)}{2\chi Eh^3} \\ \frac{3ab(1+v)}{2\chi Eh^3} & \frac{3ab(1+v)}{2\chi Eh^3} & \frac{3ab(1+v)}{2\chi Eh^3} & \frac{3ab(1+v)}{2\chi Eh^3} \end{bmatrix},$$

$$V_T = K_{TT}{}^{*}K_{TR} = \begin{bmatrix} a/8 & a/8 & -a/8 & -a/8 & b/8 & b/8 & -b/8 & -b/8 \\ -a/8 & -a/8 & a/8 & a/8 & -b/8 & -b/8 & b/8 & b/8 \\ a/8 & a/8 & -a/8 & -a/8 & b/8 & b/8 & -b/8 & -b/8 \\ -a/8 & -a/8 & a/8 & a/8 & -b/8 & -b/8 & b/8 & b/8 \end{bmatrix}$$

in which a and b are dimensions of the plate element along the x and y axes, respectively, as shown in Fig. 1.

References

[1] Dimarogonas, A. D., 1996, "Vibration of Cracked Structures: A State of the Art Review," Eng. Fract. Mech., **55**(5), pp. 831–857.

[2] Hetenyi, M., 1937, "Deflection of Beams of Varying Cross Section," ASME Trans. J. Appl. Mech., **4**, pp. A49–A52.

[3] Kirsmer, P. G., 1944, "The Effect of Discontinuities on the Natural Frequency of Beams," *Proceedings of ASTM*, **44**, pp. 897–900.

[4] Thomson, W. J., 1949, "Vibration of Slender Bars With Discontinuities in Stiffness," ASME J. Appl. Mech., **17**, pp. 361–367.

[5] Petroski, H. J., and Glazik, J. L., 1980, "The Response of Cracked Cylindrical Shells," ASME J. Appl. Mech., **44**, pp. 444–446.

[6] Stahl, B., and Keer, L. M., 1972, "Vibration and Stability of Cracked Rectangular Plates," Int. J. Solids Struct., **8**, pp. 69–91.

[7] Aggarwala, B. D., and Ariel, P. D., 1981, "Vibration and Bending of a Cracked Plate," Eng. Trans., **29**, pp. 295–310.

[8] Lee, H. P., 1992, "Fundamental Frequencies of Annular Plates With Internal Cracks," Comput. Struct., **43**, pp. 1085–1089.

[9] Ostachowicz, W., and Krawczak, M., 2001, "On Modeling of Structural Stiffness Loss Due to Damage," *Proceedings of the 4th International Conference on Damage Assessment of Structures*, Key Engineering Materials, **204–205**, pp. 185–200.

[10] Cawley, P., and Adams, R. D., 1979, "The Location of Defects in Structures From Measurement of Natural Frequencies," J. Strain Anal. Eng. Des., **14**, pp. 49–57.

[11] Baschmid, A., Dizua, G., and Pizzigoni, B., 1984, "The Influence of Unbalance on Cracked Rotors," *Vibration of Rotating Machinery*, Inst. Mech. Eng., London, pp. 193-198.

[12] Cornwell, P., Doebling, S. W., and Farrar, C. R., 1999, "Application of the Strain Energy Damage Detection Method to Plate-Like Structures," J. Sound Vib., **224**(2), pp. 359–374.

[13] Li, Y. Y., Cheng, L., Yam, L. H., and Wong, W. O., 2002, "Identification of Damage Locations for Plate-Like Structures Using Damage Sensitive Indices: Strain Modal Approach," Comput. Struct., **80**, pp. 1881–1894.

[14] Zastrau, B., 1985, "Vibration of Cracked Structures," Arch. Mech., **37**, pp. 781–743.

[15] Shen, M. H. H., and Pierre, C., 1990, "Natural Modes of Bernoulli-Euler Beams With Symmetric Cracks," J. Sound Vib., **138**, pp. 115–134.

[16] Qian, G. L, Gu, S. N., and Jiang, J. S., 1991, "A Finite Element Model of Cracked Plates and Application to Vibration Problems," Comput. Struct., **39**, pp. 483–487.

[17] Krawczuk, M., 1993, "A Rectangular Plate Finite Element With an Open Crack," Comput. Struct., **46**, pp. 487–493.

[18] Krawczak, M., and Ostachowicz, W., 1994, "A Finite Plate Element for Dynamic Analysis of a Crack Plate," Comput. Methods Appl. Mech. Eng., **115**, pp. 67–78.

[19] Lematire, J., 1985, "A Continuous Damage Mechanics Model for Ductile Fracture," J. Eng. Mater. Technol., **107**, pp. 83–89.

[20] Simo, J. C., and Ju, J. W., 1987, "Strain- and Stress-Based Continuum Damage Models," Int. J. Solids Struct., **23**(7), pp. 821–869.

[21] Lee, U., Lesieutre, G. A., and Fang, L., 1997, "Anisotropic Damage Mechanics Based on Strain Energy Equivalence and Equivalent Elliptical Microcracks," Int. J. Solids Struct., **34**, pp. 4377–4397.

[22] Sih, G. C., and Liebowitz, H., 1968, "Mathematical Theories of Brittle Fracture," *Fracture*, edited by Liebowitz, H., Vol. II, Chap. 2, Academic Press, New York.

[23] Lee, U., Cho, K. K., and Shin, J., 2003, "Identification of Orthotropic Damages Within a Thin Uniform Plate," Int. J. Solids Struct., **40**, pp. 2195–2213.

[24] Berman A., and Flannelly, W. G., 1971, "Theory of Incomplete Models of Dynamic Structures," AIAA J., **9**(8), pp. 1481–1487.

[25] Zhang, Z., and Aktan A. E., 1998, "Application of Modal Flexibility and Its Derivatives in Structural Identification," Res. Nondestruct. Eval., **10**(1), pp. 43–61.

[26] Wu, D., and Law, S. S., 2004, "Damage Localization in Plate Structures From Uniform Load Surface Curvature," J. Sound Vib., **276**(1-2), pp. 227–244.

[27] Sih, G. C., 1973, "*Handbook of Stress Intensity Factors*," Lehigh University, Bethlehem, PA.

[28] Yagawa, G., and Nishioka, T., 1979, "Finite Element Analysis of Stress Intensity Factors for Plane Extension and Plate Bending Problems," Int. J. Numer. Methods Eng., **14**, pp. 727–740.

Stochastic Dynamics of Impact Oscillators

N. Sri Namachchivaya[1]
e-mail: navam@uiuc.edu

Jun H. Park

Department of Aerospace Engineering,
University of Illinois at Urbana-Champaign,
104 South Wright Street,
Urbana, IL 61801

The purpose of this work is to develop an averaging approach to study the dynamics of a vibro-impact system excited by random perturbations. As a prototype, we consider a noisy single-degree-of-freedom equation with both positive and negative stiffness and achieve a model reduction, i.e., the development of rigorous methods to replace, in some asymptotic regime, a complicated system by a simpler one. To this end, we study the equations as a random perturbation of a two-dimensional weakly dissipative Hamiltonian system with either center type or saddle type fixed points. We achieve the model-reduction through stochastic averaging. Examination of the reduced Markov process on a graph yields mean exit times, probability density functions, and stochastic bifurcations.
[DOI: 10.1115/1.2041660]

1 Introduction

When interactions of mechanical and structural systems with the boundaries are of short duration, they are modeled as *impacts*. Mathematically, such interactions result in nonsmooth nonlinear effects which usually give rise to complex response characteristics. Proper accounting for such nonsmooth effects has been a roadblock, particularly in the presence of random excitation, that must be overcome while developing accurate analytical and numerical techniques. The analytical and numerical techniques presented here can be easily applied to vibrating systems with uni- and bilateral constraints and repeated impacts, such as aircraft flaps, gear rattle, heat-exchanger tube wear in nuclear power stations, and ships colliding against fenders.

For systems undergoing "small" amplitude vibrations, nonlinearities that are smooth functions of position and velocity can be properly neglected; the nonlinear effects become observable only when the system state moves sufficiently far from equilibrium. On the other hand, nonsmooth nonlinearities may have a significant effect on the dynamic response, even if the vibration amplitudes are small. Thus, nonsmooth nonlinear effects are important in situations in which nonlinear behavior has traditionally been ignored. This is an important difference between smooth and nonsmooth nonlinear systems. Hence, we are concerned essentially with small amplitude vibration in the presence of nonsmooth nonlinearity for which the nonsmoothness is exhibited at or near equilibrium. Impact discontinuities in dynamical systems, which are our primary concern in the study, are known to result in nonlinear behavior with possible dramatic changes in local and global stability characteristics.

Nonsmooth nonlinearities due to dead band or impact with piecewise linear restoring forces have been studied under harmonic excitations for more than three decades. Thompson and Ghaffari [1] studied numerically the impact oscillator which occurs in the offshore environment. Using a Poincaré map, Shaw and Holmes [2] investigated a similar system and showed comparable results analytically. Shaw [3,4], Shaw and Holmes [5], and Shaw and Rand [6] also looked into a similar system with some variations. Because of the piecewise linear nature of these problems, most of these results are obtained in exact analytic form, based on small parameter assumptions or topological arguments. The main interest in the references above has been to find, quantify, and model basic nonlinear phenomena such as nonlinear resonances and chaotic motion in rigid oscillator systems with nonsmooth nonlinearities. These works have inspired a great deal of recent research in impacting systems which is impossible to summarize to any degree of completeness.

Although we have several results for deterministic impact problems, only a limited number of analytical results have been reported for random excitations. Dimentberg and Menyailov [7] considered a simple linear oscillator with one or two constraints—here, the impacts are assumed instantaneous—and obtained stationary probability density under external or parametric white noise using stochastic averaging. A single-degree-of-freedom impact oscillator under external random excitations was also studied by Fogli et al. [8], where the impacts are modeled as springs and the stationary probability density and the power spectral density are obtained based on the averaging principle.

This paper deals with the nonlinear response of a general single-degree-of-freedom nonsmooth system under *stochastic* excitations. In the following sections, we achieve a model reduction through *stochastic averaging* and the reduced Markov process takes its values on *a line* for the system with a *center type fixed point*. A *saddle type fixed point* leads to *a graph* with certain gluing conditions at the vertex of the graph. To get this reduced space, we consider the flow $\mathfrak{z}_t$ on $\mathbb{R}^2$ generated by the fast motion, and define an averaging operator, limiting domain, and generator. Finally, we apply these results to a vertical pendulum problem to obtain mean exit times and probability density functions. Numerical simulations are also used to verify these results.

2 Problem Statement

The general form of the equations studied here is given by

$$\ddot{q}_t + \frac{\partial U}{\partial q}(q_t) + G(q_t,\dot{q}_t)\dot{q}_t = \mu_1 \xi(t) q_t + \mu_2 \eta(t),$$

$$\text{for } -\frac{\Delta}{2} < q_t < \frac{\Delta}{2}, \qquad (1)$$

where $q \in \mathbb{R}^{\Delta}$ represents a generalized coordinate defined for $\mathbb{R}^{\Delta} \overset{\text{def}}{=} (-\Delta/2, \Delta/2)$ and the potential $U:\mathbb{R}\to\mathbb{R}$ has an elliptic or saddle fixed point. The above equation is augmented with the impact law,

---

[1] To whom correspondence should be addressed.

Contributed by the Applied Mechanics Division of THE AMERICAN SOCIETY OF MECHANICAL ENGINEERS for publication in the ASME JOURNAL OF APPLIED MECHANICS. Manuscript received by the Applied Mechanics Division, February 4, 2004; final revision, September 29, 2004. Review conducted by R. M. McMeeking. Discussion on the paper should be addressed to the Editor, Prof. Robert M. McMeeking, Journal of Applied Mechanics, Department of Mechanical and Environmental Engineering, University of California—Santa Barbara, Santa Barbara, CA 93106-5070, and will be accepted until four months after final publication in the paper itself in the ASME JOURNAL OF APPLIED MECHANICS.

$$\dot{q}_{t_+} = -r\dot{q}_{t_-}, \quad \text{at } q_{t^*} = \pm\frac{\Delta}{2}, \tag{2}$$

where $t_{\mp}$ are the time prior and after the instant t^* of impact, which is determined by the condition $q_{t^*}=\pm\Delta/2$. There are several different models for an impact oscillator, but the simplest is the coefficient of restitution rule, $\dot{q}_t \to -r\dot{q}_t$, which is adopted in this paper. This rule provides an instantaneous reversal of velocity. Positive coefficients of restitution, $0 < r \leqslant 1$, indicate a loss of energy at impact. In (1), G represents dissipative terms and ξ and η represent mean zero, stationary, independent Gaussian white noise processes. More precisely, we require that $U \in C^\infty(\mathbb{R};\mathbb{R}_+)$ and that

$$\{q \in \mathbb{R}: U'(q) = 0\} = \{q \in \mathbb{R}: U(q) = 0\} = 0,$$

and that $\omega^2 \overset{\text{def}}{=} U''(0) > 0$ for an elliptic fixed point and $\omega^2 \overset{\text{def}}{=} -U''(0) > 0$ for a saddle fixed point. For convenience, we shall define

$$U_h^e(q) \overset{\text{def}}{=} U(q) - \tfrac{1}{2}\omega^2 q^2 \quad \text{and} \quad U_h^s(q) \overset{\text{def}}{=} U(q) + \tfrac{1}{2}\omega^2 q^2, \quad q \in \mathbb{R},$$

for the elliptic and saddle fixed points, respectively. Since an exact solution of (1) is not known, the purpose of this paper is to develop a reduction procedure to approximate the solutions of (1) by a graph-valued Markov process.

In order to make use of the periodic properties of the transformations introduced by Zhuravlev [9], let us define $y = q\pi/\Delta$. Then

$$\ddot{y}_t + \frac{\partial V}{\partial y}(y_t) + g(y_t,\dot{y}_t)\dot{y}_t = \mu_1 \xi(t) y_t + \mu_2 \eta(t), \quad \text{for } -\frac{\pi}{2} < y_t < \frac{\pi}{2} \tag{3}$$

and the impact law simplifies to

$$\dot{y}_{t_+} = -r\dot{y}_{t_-}, \quad \text{at } y_{t^*} = \pm\frac{\pi}{2}. \tag{4}$$

Following Zhuravlev [9], let us introduce the following 2π-periodic functions

$$\Pi(x) \overset{\text{def}}{=} \begin{cases} x & \text{if } -\frac{1}{2}\pi < x \leqslant \frac{1}{2}\pi, \\ -x+\pi & \text{if } \frac{1}{2}\pi < x \leqslant \frac{3}{2}\pi, \end{cases}$$

$$M(x) \overset{\text{def}}{=} \Pi'(x) = \begin{cases} 1 & \text{if } -\frac{1}{2}\pi < x \leqslant \frac{1}{2}\pi, \\ -1 & \text{if } \frac{1}{2}\pi < x \leqslant \frac{3}{2}\pi, \end{cases}$$

and consider a nonsmooth transformation

$$y_t = \Pi(x_t), \quad \dot{y}_t = M(x_t)\dot{x}_t, \quad \ddot{y}_t = M(x_t)\ddot{x}_t + M'(x_t)\dot{x}_t^2, \tag{5}$$

which transforms (3) with *elastic impacts* (that is, $r=1$) to

$$\begin{aligned} \ddot{x}_t + \frac{\partial V}{\partial x}(\Pi(x_t)) + g(\Pi(x_t),M(x_t)\dot{x}_t)\dot{x}_t \\ = \mu_1 \xi(t) M(x_t)\Pi(x_t) + \mu_2 \eta(t) M(x_t), \end{aligned} \tag{6}$$

where we have made use of (4). In the case of inelastic impact ($0 < r < 1$), one can get a similar result from the following transformation by Dimentberg and Menyailov [7], which is based on Zhuravlev [9],

$$\begin{aligned} & y_t = \Pi(x_t) + \lambda N(x_t), \quad \dot{y}_t = M(x)\dot{x}_t + \lambda\Pi(x_t)\dot{x}_t, \\ & \ddot{y}_t = M'(x_t)\dot{x}_t^2 + M(x_t)\ddot{x}_t + \lambda M(x_t)\dot{x}_t^2 + \lambda\Pi(x_t)\ddot{x}_t \end{aligned} \tag{7}$$

where

$$\lambda \overset{\text{def}}{=} \frac{2}{\pi}\frac{1-r}{1+r}, \quad N(x) \overset{\text{def}}{=} \begin{cases} \dfrac{x^2}{2} - \dfrac{\pi^2}{8} & \text{if } -\frac{1}{2}\pi < x \leqslant \frac{1}{2}\pi \\ \dfrac{-(x-\pi)^2}{2} + \dfrac{\pi^2}{8} & \text{if } \frac{1}{2}\pi < x \leqslant \frac{3}{2}\pi \end{cases}$$

After the transformation, (3) becomes

$$\begin{aligned} \ddot{x}_t + \frac{\partial V}{\partial x}(\Pi(x_t)) = {} & -g(\Pi(x_t) + \lambda N(x_t), M(x_t)\dot{x}_t + \lambda\Pi(x_t)\dot{x}_t)\dot{x}_t \\ & + \lambda F(x_t,\dot{x}_t) + M(x_t)[\mu_1(\Pi(x_t) + \lambda N(x_t))\xi(t) \\ & + \mu_2 \eta(t)], \end{aligned} \tag{8}$$

where

$$F(x,\dot{x}) = -\dot{x}^2 + \frac{\partial V}{\partial x}(\Pi(x),N(x)) + 2\frac{\partial V}{\partial x}(\Pi(x))M(x)\Pi(x).$$

The transformation and its derivatives for the elastic impact (5) and the inelastic impact (7) make $\dot{x}_t$ continuous. Hence, the nonsmooth transformation brings the equation of motion to a standard form where the order one Hamiltonian is smooth and the dissipation and noise are small. The transformation changes the problem of restricted domain to the problem of periodic boundaries and makes averaging on each period possible.

3 Averaged Equations

In this section, we will develop rigorous methods to replace in a limiting regime the transformed system (8) by a *simpler*, lower-dimensional model of the dynamical system.

3.1 Problem Formulation. Define next the *Hamiltonian* or the *total energy* (i.e., kinetic plus potential) as

$$H(x_1,x_2) = \frac{x_2^2}{2} + V(\Pi(x_1)), \quad (x_1,x_2) \in \mathbb{R}^2.$$

Thus H is in general a nonsymmetric potential on $\mathbb{R}^2$. The function H has a single critical point at $\mathfrak{o} \overset{\text{def}}{=} (0,0)$ and this critical point is a minimum or a saddle. The state space of our problem will be (a subset of) $\mathbb{R}^2$. Define the the vector field $\bar{\nabla} H$ on $\mathbb{R}^2$ as

$$\begin{aligned} [(\bar{\nabla} H)\varphi](x_1,x_2) & \overset{\text{def}}{=} \frac{\partial H}{\partial x_2}(x_1,x_2)\frac{\partial \varphi}{\partial x_1}(x_1,x_2) - \frac{\partial H}{\partial x_1}(x_1,x_2)\frac{\partial \varphi}{\partial x_2}(x_1,x_2) \\ & = x_2\frac{\partial \varphi}{\partial x_1}(x_1,x_2) - V'(\Pi(x_1))\frac{\partial \varphi}{\partial x_2}(x_1,x_2) \end{aligned}$$

for all $\varphi \in C^1(\mathbb{R}^2)$ and all $(x_1,x_2) \in \mathbb{R}^2$. We use H to define a deterministic flow on $\mathbb{R}^2$.

Definition 3.1. Hamiltonian flow: Set

$$\begin{aligned} & \dot{\mathfrak{z}}_t(x) = \bar{\nabla} H(\mathfrak{z}_t(x)) \\ & \mathfrak{z}_0(x) = x. \end{aligned} \qquad t \in \mathbb{R}, x \in \mathbb{R}^2 \tag{9}$$

We recast (8) as a perturbation of a two-dimensional Hamiltonian system (9) with an isolated elliptic or saddle fixed point. We assume that the system is subject to small damping and small excitation. We also consider the loss of energy from impacts is small and introduce a small parameter ε such that $-g(.,.) = \varepsilon^2\beta(.,.)$, $\lambda = \varepsilon^2\gamma$. This scaling of damping and noise terms is such that the leading order diffusion part balances the leading order drift term in the reduced system. Specifically, we want to consider the stochastic differential equation (SDE)

$$\begin{aligned} & d\hat{Z}_t^\varepsilon = \bar{\nabla} H(\hat{Z}_t^\varepsilon)dt + \varepsilon^2\tilde{b}(\hat{Z}_t^\varepsilon)dt + \varepsilon\tilde{\sigma}(\hat{Z}_t^\varepsilon)dW_t, \\ & \hat{Z}_0^\varepsilon = x \in \mathbb{R}^2 \end{aligned} \tag{10}$$

where the vector $\tilde{b}$ and the matrix $\tilde{\sigma}$ are given by

$$\tilde{b}(x_1,x_2) \overset{\text{def}}{=} \begin{pmatrix} 0 \\ \beta(\Pi(x_1),M(x_1)x_2)x_2 + \gamma F(x_1,x_2) \end{pmatrix}$$

$$\tilde{\sigma}(x_1,x_2) \overset{\text{def}}{=} M(x_1)\begin{pmatrix} 0 & 0 \\ \mu_1\Pi(x_1) & \mu_2 \end{pmatrix}.$$

In (10), W is a $\mathbb{R}^2$-valued Wiener process given on some probability space $(\Omega^\circ, \mathcal{F}^\circ, \mathbb{P}^\circ)$; as usual, we let $\mathbb{E}^\circ$ denote the expectation operator with respect to $\mathbb{P}^\circ$. We attach the superscript ° to denote that this is the *original* probability triple.

We can understand the effects of the dissipation and noise via a diffusive *generator*

$$(\mathcal{L}f)(x_1,x_2) \overset{\text{def}}{=} \frac{1}{2}[\mu_1^2\Pi^2(x_1) + \mu_2^2]\frac{\partial^2 f}{\partial x_2^2}(x_1,x_2) + \beta[\Pi(x_1,M(x_1)x_2)x_2 + \gamma F(x_1,x_2)]\frac{\partial f}{\partial x_2}(x_1,x_2)$$

for $f \in C^2(\mathbb{R}^2)$ and $(x_1,x_2) \in \mathbb{R}^2$. Thus the generator of (10) is $\bar{\nabla}H + \varepsilon^2\mathcal{L}$. Using Ito's rule and (10), we see that

$$H(\hat{Z}_t^\varepsilon) = H(x) + \varepsilon^2\int_0^t \mathcal{L}H(\hat{Z}_s^\varepsilon)ds + \varepsilon\int_0^t \tilde{\sigma}(\hat{Z}_s^\varepsilon)dW_s$$

for all $t \geqslant 0$. Thus, the dynamics of the slowly varying quantity $H(\hat{Z}_t^\varepsilon)$ only appear on intervals of length ε^{-2} or larger. To make the dynamics of $H(\hat{Z}_t^\varepsilon)$ more transparent, we rescale time and look at $\{Z_{t/\varepsilon^2}^\varepsilon; t \geqslant 0\}$; i.e., we look at the SDE

$$\boxed{\begin{aligned} &dZ_t^\varepsilon = \frac{1}{\varepsilon^2}\bar{\nabla}H(Z_t^\varepsilon)dt + \tilde{b}(Z_t^\varepsilon)dt + \tilde{\sigma}(Z_t^\varepsilon)dW_t \quad t \geqslant 0 \\ &Z_0^\varepsilon = x \end{aligned}} \tag{11}$$

(i.e., we look at the slow time scale $t \to \varepsilon^2 t$). Then we have that

$$H(Z_t^\varepsilon) = H(x) + \int_0^t \mathcal{L}H(Z_s^\varepsilon)ds + \int_0^t \tilde{\sigma}(Z_s^\varepsilon)dW_s \tag{12}$$

for all $t \geqslant 0$. We note that the generator of Z^ε is

$$\mathcal{L}^\varepsilon \overset{\text{def}}{=} \mathcal{L} + \frac{1}{\varepsilon^2}\bar{\nabla}H, \tag{13}$$

and a core for the domain of $\mathcal{L}^\varepsilon$ is $C_b^2(\mathbb{R}^2)$.

Loosely speaking, our goal is to study (12) and show that as ε tends to zero, the dynamics of the slowly varying quantity $H(Z_t^\varepsilon)$ converge to a Markov process and to identify the generator of the limiting law.

3.2 Main Results. The first extension of averaging to include multiple fixed points with homoclinic orbits was given by Freidlin and Wentzell [10] and was extended by Freidlin and Weber [11] and Sowers [12] for more realistic cases via the *martingale problem*. We shall make use of these results to identify a reduced stochastically averaged model for a near elastic noisy impacting system (8).

Fix $H^* > 0$ and define

$$\mathbf{S} \overset{\text{def}}{=} \{x \in \mathbb{R}^2 : H(x) < H^*\}.$$

Let $\mathfrak{e}$ be the first time that Z_t^ε leaves $\mathbf{S}$, i.e.,

$$\mathfrak{e} \overset{\text{def}}{=} \inf\{t \geqslant 0; Z_t^\varepsilon \notin \mathbf{S}\}.$$

Let $C([0,\infty);\bar{\mathbf{S}})$ be the space of continuous functions on $[0,\infty)$ with values in $\bar{\mathbf{S}}$. Since we are interested in the laws of Markov processes, we move from the original probability space with measure $\mathbb{P}^\circ$ to a canonical space of paths with induced measure $\mathbb{P}_x^\varepsilon$. For each $\varepsilon > 0$, let $\mathbb{P}_x^\varepsilon \in \mathcal{P}(C([0,\infty);\bar{\mathbf{S}}))$ be the law of $\{Z_t^\varepsilon; t \geqslant 0\}$, i.e.,

$$\mathbb{P}_x^\varepsilon(A) \overset{\text{def}}{=} \mathbb{P}^\circ\{Z^\varepsilon \in A\}, \quad A \in \mathcal{B}(C([0,\infty);\bar{\mathbf{S}})). \tag{14}$$

We are, roughly, interested in the behavior of $\mathbb{P}_x^\varepsilon$ as ε tends to zero. The averaged system will in general take values in a *reduced state space* which in this case is diffeomorphic to a closed interval.

3.2.1 Reduced State Space. We are interested in the behavior of $\mathbb{P}_x^\varepsilon$ as ε tends to zero. In essence, the underpinning of the classical stochastic averaging method is a separation of time scales; under $\mathbb{P}_x^\varepsilon$, the process Z_t^ε runs around the level sets of H very quickly, and thus a coarse-grained description of the process records only $H(Z_t^\varepsilon)$, and the $\mathbb{P}_x^\varepsilon$-dynamics of $H(Z_t^\varepsilon)$ depends only on $H(Z_t^\varepsilon)$ itself, i.e., $\{H(Z_t^\varepsilon); 0 \leqslant t \leqslant \mathfrak{e}\}$ is a slowly varying process, where $\mathfrak{e}$ is the stopping time. As ε tends to zero, one should be able to find closed dynamics for the projection of the process onto the space of such level sets. Consider the flow (9), we use $\mathfrak{z}$ to generate an equivalence relation on the original state space $\bar{\mathbf{S}}$. Mathematically, the level sets can be understood via an equivalence relation; we say that any two points x and y in $\mathbb{R}^2$ are equivalent, i.e., $x \sim y$, if $H(x) = H(y)$ and they are in the same connected component of $H^{-1}(H(x)) = H^{-1}(H(y))$; as usual, if $x \in \bar{\mathbf{S}}$, we let $[x] \overset{\text{def}}{=} \{y \in \bar{\mathbf{S}} : y \sim x\}$ be the equivalence class of x and we define $\pi(x) \overset{\text{def}}{=} [x]$. The above comments mean that the $\mathbb{P}_x^\varepsilon$ law of $\{[Z_t^\varepsilon]; t \geqslant 0\}$ should converge to that of a Markov process on the state space of equivalence classes, namely

$$\mathfrak{M} \overset{\text{def}}{=} \bar{\mathbf{S}}/\sim.$$

Note that

$$\mathfrak{M} = \bigcup_{i=1}^{N}\Gamma_i \cup \bigcup_{i=1}^{N_c}[\mathfrak{c}_i] \cup \bigcup_{i=1}^{N_b}\circledast_i,$$

where $\mathfrak{c}_i$'s are the fixed points, the $\circledast_i$'s are closed orbits whose union is $\partial\bar{\mathbf{S}}$, and each Γ_i is the π image of a maximal open subset of $\mathbb{R}^2$ which does not intersect any of the $[\mathfrak{c}_i]$'s or $\circledast_i$'s, as explained by Namachchivaya and Sowers [13] and Sowers [12].

To make our analysis easier, let us take advantage of the fact that $\mathfrak{M}$ looks like several intersecting lines. Let us map each Γ_i into an interval $\mathcal{I}_i$. For each $1 \leqslant i \leqslant N$, let $\mathcal{I}_i \overset{\text{def}}{=} H\pi^{-1}(\Gamma_i)$ which denotes all points belonging to the connected components of a level set $\{\mathbf{S} : H(x) = H\}$ of the state space. We can then treat $\mathfrak{M}$ as

$$\mathfrak{G} \overset{\text{def}}{=} \bigcup_{i=1}^{N}\bar{\mathcal{I}}_i,$$

this being interpreted as a disjoint union with the various ends of different $\bar{\mathcal{I}}_i$'s identified as in [13].

3.2.2 Reduced Process. The goal is to show that the $\mathbb{P}_x^\varepsilon$ law of

$$\yen_t \overset{\text{def}}{=} H(Z_{t\wedge e}^\varepsilon), \quad t \geqslant 0$$

converges to that of an $\mathfrak{G}$-valued Markov process as ε tends to zero and to identify the generator of the limiting law. To be even more precise, for each $x \in \mathbf{S}$ and $\varepsilon > 0$, define the probability measure

$$\mathbb{P}_x^{\varepsilon,\dagger}(A) \overset{\text{def}}{=} \mathbb{P}_x^\varepsilon\{\yen \in A\}; \quad A \in \mathcal{B}(C(([0,\infty)),\mathfrak{G})). \tag{15}$$

We want to understand what the asymptotics of the $\mathbb{P}_x^{\varepsilon,\dagger}$'s are as ε tends to zero, i.e., identify a limit

$$\mathbb{P}_{\pi(x)}^\dagger \overset{\text{def}}{=} \lim_{\varepsilon\to 0}\mathbb{P}_x^{\varepsilon,\dagger}, \tag{16}$$

this limit being in the Prohorov topology on $\mathcal{P}(C([0,\infty),\mathfrak{G}))$.

To study the dynamics of the slowly varying quantity $H(Z_t^\varepsilon)$, we need a limiting generator on $\mathfrak{G}$ which is obtained through averaging. To this end, we define for each $1 \leqslant i \leqslant N$ an elliptic operator $\mathcal{L}_i$ on $C(\mathcal{I}_i)$ as

$$(\mathcal{L}_i f)(h) \overset{\text{def}}{=} \tfrac{1}{2}\sigma_i^2(h)\ddot{f}(h) + b_i(h)\dot{f}(h)$$

for all $h \in \mathcal{I}_i$, where σ_i^2 and b_i are the drift and diffusion coefficients

$$b_i(h) \overset{\text{def}}{=} (\mathbf{A}_i \mathcal{L}H)(h) = \frac{\displaystyle\oint_{C_i(h)} \mathcal{L}H(x)|\nabla H(x)|^{-1}dl}{\displaystyle\oint_{C_i(h)} |\nabla H(x)|^{-1}dl}$$

$$\sigma_i^2(h) \overset{\text{def}}{=} (\mathbf{A}_i\langle dH, dH\rangle)(h) = \frac{\displaystyle\oint_{C_i(h)} \langle dH, dH\rangle(x)|\nabla H(x)|^{-1}dl}{\displaystyle\oint_{C_i(h)} |\nabla H(x)|^{-1}dl} \tag{17}$$

with x restricted to $\pi^{-1}(\Gamma_i)$ and dl the length element on the level set $H(x): C(h) = \{x \in \mathbf{S} : H(x) = h\}$. We want to put these $\mathcal{L}_i$'s together to get a Markov process on $\mathfrak{G}$ with generator $\mathcal{L}_{\mathfrak{G}}^{\dagger}$ with domain $\mathcal{D}_{\mathfrak{G}}^{\dagger}$. Finally, for notational convenience, when $N \geqslant 2$, we also define $f_i \overset{\text{def}}{=} f|_{I_i}$ for all $1 \leqslant i \leqslant N$.

We make use of the results in [11,12] to yield the limiting domain for the noisy impacting system (8) as

$$\mathcal{D}_{\mathfrak{G}}^{\dagger} = \left\{ f \in C(\mathfrak{G}) \cap C^2(\cup_{i=1}^N \mathcal{I}_i) : \lim_{h \searrow H(\mathfrak{c}_i)} (\mathcal{L}_i f_i)(h) \text{ exists } \forall\, i, \right. \\ \left. \lim_{h \nearrow H^*} (\mathcal{L}_N f_N)(h) = 0 \text{ and } \sum_{i=1}^{N} \{\pm\}\mathring{\sigma}_i^2(\mathcal{O}) f_i'(\mathcal{O}) = 0 \right\}, \tag{18}$$

where the "+" sign is taken if the coordinate h on the leg $\mathcal{I}_i$ is greater than h_o, the "−" sign is taken otherwise. Finally, the last expression in (18) represents the gluing condition at the vertex $\mathcal{O}$ and the gluing coefficients are

$$\mathring{\sigma}^2(h) \overset{\text{def}}{=} \oint_{C_i(h)} \langle dH, dH\rangle(x)|\nabla H(x)|^{-1}dl. \tag{19}$$

Then for $f \in \mathcal{D}_{\mathfrak{G}}^{\dagger}$, the generator is

$$\boxed{(\mathcal{L}_{\mathfrak{G}}^{\dagger} f)(h) = \lim_{\substack{h' \to h \\ h \in \mathcal{I}_i}} (\mathcal{L}_i f_i)(h') = b_i(h)\dot{f}_i(h) + \frac{1}{2}\sigma_i^2(h)\ddot{f}_i(h)} \tag{20}$$

for all $h \in \bar{\mathcal{I}}_i$.

4 Application: Impacting Vertical Pendulum

In this section, we will apply the main results to a vertical pendulum constrained between two walls with inelastic impact. We consider a pendulum that undergoes small amplitude vibrations where the stiffness and damping can be modeled as linear. Therefore, the nonlinearity comes primarily from the impacts at the constraints. This simplified application has practical relevance because many "real-world" models fit into this category. After getting a SDE for the model, analytical and numerical approaches are applied to get probability density functions and mean exit times.

The Lagrangian of a free pendulum under a prescribed horizontal motion $z(t)$ is given by

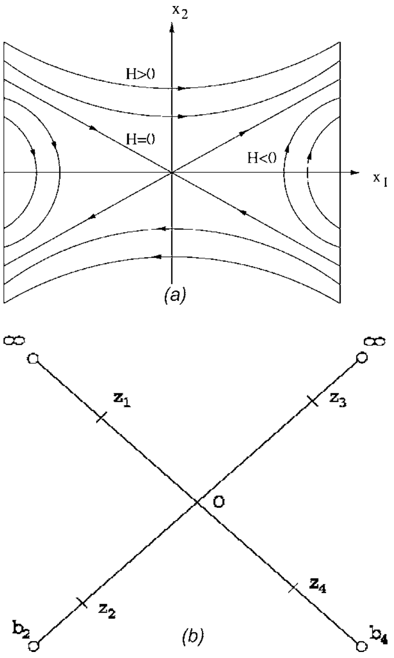

Fig. 1 Phase portrait and graph of system

$$L = \frac{m}{2}(l^2\dot{\theta}_t^2 + \dot{z}_t^2) + ml\dot{z}_t\dot{\theta}_t \cos\theta_t \pm mgl\cos\theta_t,$$

where θ is measured counter-clockwise from negative and positive vertical axes for the hanging and inverted pendulum, respectively, the + (or −) sign is used for the hanging (or inverted) pendulum, and g is the gravitational acceleration. The equations of motion for the impacting pendulum are

$$ml^2\ddot{\theta}_t + d\dot{\theta}_t \pm mgl\sin\theta_t = -ml\ddot{z}_t\cos\theta_t, \quad |\theta_t| < \theta^*$$

$$\dot{\theta}_{t_+} = -r\dot{\theta}_{t_-}, \quad |\theta_t| = \theta^*, \tag{21}$$

where the second equation is called the impact law, d is the effective angular viscous damping coefficient, and the constraints are placed symmetrically at $\theta = \pm\theta^*$. The coefficient of restitution, $0 < r < 1$, depends on colliding material and surface properties and $t_{\mp}$ represents the time prior and after the instant t^* of impact, which is determined by the condition $\theta_{t^*} = \pm\theta^*$. After appropriate scaling, one can get the linearized model under stochastic excitations

$$\ddot{y}_t + 2\alpha\dot{y}_t - \Omega^2 y_t = \mu_1\xi(t)y_t + \mu_2\eta(t) \tag{22}$$

with the same impact law (4).

4.1 Analytical Approach. After applying the inelastic transformation (7), one can get a time-rescaled SDE (11) with the Hamiltonian, dissipation, and noise coefficients given by

$$H(x_1, x_2) = \tfrac{1}{2}x_2^2 - \tfrac{1}{2}\Omega^2\Pi^2(x_1), \quad \beta(\Pi(x_1), M(x_1)x_2) = -2\alpha,$$

$$F(x_1, x_2) = -\tfrac{1}{2}\Omega^2\Pi^2(x_1) - \tfrac{1}{8}\Omega^2\pi^2 - x_2^2.$$

Here, we assumed small dissipation, damping, and excitation. The Hamiltonian system has multiple fixed points, one of which is connected to itself by a homoclinic orbit, and $H(Z_t^{\varepsilon})$ no longer converges to a diffusive Markov process. Here the reduced state space is a graph $\mathfrak{M}=\cup_{i=0}^{4}[\mathfrak{c}_i]\cup\cup_{i=1}^{4}\Gamma_i$ (Fig. 1), where

$$\Gamma_1\overset{\text{def}}{=}\bigcup_{\substack{x\in\mathfrak{M}\\ H(x)>0\\ x_2>0}}[x],\quad \Gamma_2\overset{\text{def}}{=}\bigcup_{\substack{x\in\mathfrak{M}\\ H(x)<0\\ x\neq\mathfrak{c}_2\\ x_1<0}}[x],$$

$$\Gamma_3\overset{\text{def}}{=}\bigcup_{\substack{x\in\mathfrak{M}\\ H(x)>0\\ x_2<0}}[x],\quad \Gamma_4\overset{\text{def}}{=}\bigcup_{\substack{x\in\mathfrak{M}\\ H(x)<0\\ x\neq\mathfrak{c}_4\\ x_1>0}}[x],$$

and $\mathfrak{c}_i$'s are the critical points (including points at infinity). Then the limiting process on the graph is defined by the generator (20) on the four segments of the graph, where h is only a local coordinate in each edge and it can take the same value for different trajectories. In evaluating the drift and diffusion coefficients for each segment we make use of (11). We change the time integral to the path integral with respect to the fast variable Z_t^{ε} while averaging over one period of the fast motion of Z_t^{ε}. This process effectively removes the fast variable Z_t^{ε} and yields on each segment I_i of the graph the following averaged drift and diffusion coefficients:

$$b_i(h)=\frac{1}{T_i(h)}\int_0^{T_i(h)}[-2\alpha Q(x_1,h)+\gamma F(x_1,\sqrt{Q(x_1,h)})\sqrt{Q(x_1,h)}$$

$$+R(x_1)]dt=\frac{1}{T_i(h)}[B_i(h)+C_i(h)]$$

$$B_i(h)=\alpha B_i^1(h)+\gamma B_i^2(h)$$

$$B_i^1(h)=\int_{x_{1i}^-}^{x_{1i}^+}-2\sqrt{Q(x_1,h)}dx_1,\quad B_i^2(h)=\int_{x_{1i}^-}^{x_{1i}^+}F(x_1,\sqrt{Q(x_1,h)})dx_1$$

$$C_i(h)=\int_{x_{1i}^-}^{x_{1i}^+}\frac{R(x_1)}{\sqrt{Q(x_1,h)}}dx_1,\quad T_i(h)=\int_0^T dt=\int_{x_{1i}^-}^{x_{1i}^+}\frac{dx_1}{\sqrt{Q(x_1,h)}}$$

$$\sigma_i^2(h)=\frac{1}{T_i(h)}\int_0^{T_i(h)}2R(x_1)Q(x_1,h)dt=\frac{\mathring{\sigma}_i^2(h)}{T_i(h)}$$

$$\mathring{\sigma}_i^2(h)=\int_{x_{1i}^-}^{x_{1i}^+}2R(x_1)\sqrt{Q(x_1,h)}dx_1,\quad R(x_1)=\frac{1}{2}[\mu_1^2\Pi^2(x_1)+\mu_2^2]$$

$$Q(x_1,h)=2[h-P(x_1)],\quad P(x_1)=-\tfrac{1}{2}\Omega^2\Pi^2(x_1)$$

$$F(x_1,\sqrt{Q(x_1,h)})=-\tfrac{1}{2}\Omega^2\Pi^2(x_1)-\tfrac{1}{8}\Omega^2\pi^2-Q(x_1,h),$$

where $x_{1i}^{(\pm)}\overset{\text{def}}{=}x_{Ii}^{(\pm)}(h)$ are the points where the periodic orbit meets the boundary. The domain of the averaged generator (20) is given by (18), where $f_i'(\mathcal{O})=\lim_{h\to H(\mathcal{O})}f_i'(h)$ for $(h,i)\in I_i$ and the ± sign denotes whether the coordinate h on the segment I_i is *greater than or less than* $H(\mathcal{O})$. In (18), the gluing condition

$$\sum_{i=1}^{4}(\pm)\mathring{\sigma}_i^2(\mathcal{O})f_i'(\mathcal{O})=0 \qquad (23)$$

for the vertex $\mathcal{O}$ roughly means the following. Define

$$\alpha\overset{\text{def}}{=}\sum_{i=1}^{n}\mathring{\sigma}_i^2(\mathcal{O}).$$

If the limiting process starts in leg $\mathcal{I}_1$ of the graph $\mathfrak{G}$, it evolves according to $(\mathcal{L}_{\mathfrak{G}}^{\dagger}f_1)(h)$ for $h\in\mathcal{I}_1$. Upon reaching the vertex $\mathcal{O}$, the limiting process flips an n-sided coin to decide where to go next. It will go back to leg 1 with likelihood $\mathring{\sigma}_1^2(\mathcal{O})/\alpha$, to leg 2 with likelihood $\mathring{\sigma}_2^2(\mathcal{O})/\alpha$, and to leg n with likelihood $\mathring{\sigma}_n^2(\mathcal{O})/\alpha$. Once it is in any of these legs, it will evolve according to $(\mathcal{L}_{\mathfrak{G}}^{\dagger}f_i)(h)$ with σ_1 and b_1 replaced by the appropriate σ_i and b_i. When it hits the vertex again, the coin-flipping procedure is repeated (with a new coin).

Making use of the relation $d\mathring{\sigma}_i^2(h)/dh=2C_i(h)$, the generator (20) reduces to

$$\mathcal{L}_i^{\dagger}f_i(h)=\frac{1}{T_i(h)}[B_i(h)f_i'(h)]+\frac{1}{2}\frac{1}{T_i(h)}[\mathring{\sigma}_i^2(h)f_i'(h)]'. \qquad (24)$$

For different values of h, we have different path integrals (one or two impacts) and thus different drift $b(h)$ and diffusion coefficients $\sigma(h)$. They are evaluated as follows:

(1) $H>0$: The integrals are calculated along the paths which correspond to the "two impacts." Due to the Z_2 symmetry of the Hamiltonian we have two such segments and these are denoted by $i=1,3$ and the coefficients are

$$T_i(h)=2\int_0^{\pi/2}\frac{dx_1}{\sqrt{2h+\Omega^2x_1^2}}=\frac{2}{\Omega}\sinh^{-1}\sqrt{\frac{\Omega^2\pi^2}{8h}}$$

$$B_i^1(h)=-4\int_0^{\pi/2}\sqrt{2h+\Omega^2x_1^2}dx_1=-\frac{\pi}{2}\sqrt{\pi^2\Omega^2+8h}$$

$$-\frac{4h}{\Omega}\sinh^{-1}\sqrt{\frac{\Omega^2\pi^2}{8h}}$$

$$B_i^2(h)=2\int_0^{\pi/2}\left(-2h-\frac{3}{2}\Omega^2x_1^2-\frac{1}{8}\Omega^2\pi^2\right)dx_1=-\frac{1}{4}\Omega^2\pi^3-2h\pi$$

$$C_i(h)=\int_0^{\pi/2}\frac{\mu_1^2x_1^2+\mu_2^2}{\sqrt{2h+\Omega^2x_1^2}}dx_1=\frac{1}{\Omega}\left[\mu_1^2\left(\frac{\pi}{4}\sqrt{\frac{\pi^2}{4}+\frac{2h}{\Omega^2}}\right.\right.$$

$$\left.\left.-\frac{h}{\Omega^2}\sinh^{-1}\sqrt{\frac{\Omega^2\pi^2}{8h}}\right)+\mu_2^2\sinh^{-1}\sqrt{\frac{\Omega^2\pi^2}{8h}}\right]$$

$$\sigma_i^2(h)=\frac{\mathring{\sigma}_i^2(h)}{T_i(h)}=\frac{2}{T_i(h)}\int_0^{\pi/2}(\mu_1^2x_1^2+\mu_2^2)\sqrt{2h+\Omega^2x_1^2}dx_1$$

$$\mathring{\sigma}_i^2(h)=2\Omega\left[\mu_1^2\left\{\frac{\pi}{8}\sqrt{\frac{\pi^2}{4}+\frac{2h}{\Omega^2}}\left(\frac{\pi^2}{4}+\frac{h}{\Omega^2}\right)\right.\right.$$

$$\left.-\frac{h^2}{2\Omega^4}\sinh^{-1}\sqrt{\frac{\Omega^2\pi^2}{8h}}\right\}+\mu_2^2\left\{\frac{\pi}{4}\sqrt{\frac{\pi^2}{4}+\frac{2h}{\Omega^2}}\right.$$

$$\left.\left.+\frac{h}{\Omega^2}\sinh^{-1}\sqrt{\frac{\Omega^2\pi^2}{8h}}\right\}\right].$$

Here $T_i(h)$ is the period of the oscillations.

(2) $H<0$: In this case, the integrals are calculated along the paths which correspond to the "one impact" and, as before, the system has two symmetric segments denoted by $i=2,4$ with

$$T_i(h)=2\int_{\sqrt{2|h|}/\Omega}^{\pi/2}\frac{dx_1}{\sqrt{-2|h|+\Omega^2x_1^2}}=\frac{2}{\Omega}\cosh^{-1}\sqrt{\frac{\Omega^2\pi^2}{8|h|}}$$

$$B_i^1(h) = -4\int_{\sqrt{2|h|}/\Omega}^{\pi/2} \sqrt{-2|h| + \Omega^2 x_1^2}\,dx_1 = -\frac{\pi}{2}\sqrt{\Omega^2\pi^2 - 8|h|} + \frac{4|h|}{\Omega}\cosh^{-1}\sqrt{\frac{\Omega^2\pi^2}{8|h|}}$$

$$B_i^2(h) = 2\int_{\sqrt{2|h|}/\Omega}^{\pi/2}\left(2|h| - \frac{3}{2}\Omega^2 x_1^2 - \frac{1}{8}\Omega^2\pi^2\right)dx_1 = -\frac{1}{4}\Omega^2\pi^3 + 2|h|\pi - \frac{2|h|\sqrt{2|h|}}{\Omega} + \frac{1}{4}\sqrt{2|h|}\Omega\pi^2$$

$$C_i(h) = \int_{\sqrt{2|h|}/\Omega}^{\pi/2} \frac{\mu_1^2 x_1^2 + \mu_2^2}{\sqrt{-2|h| + \Omega^2 x_1^2}}dx_1 = \frac{1}{\Omega}\left[\mu_1^2\left(\frac{\pi}{4}\sqrt{\frac{\pi^2}{4} - \frac{2|h|}{\Omega^2}} + \frac{|h|}{\Omega^2}\cosh^{-1}\sqrt{\frac{\Omega^2\pi^2}{8|h|}}\right) + \mu_2^2\cosh^{-1}\sqrt{\frac{\Omega^2\pi^2}{8|h|}}\right]$$

$$\sigma_i^2(h) = \frac{\mathring{\sigma}_i^2(h)}{T_i(h)} = \frac{2}{T_i(h)}\int_{\sqrt{2|h|}/\Omega}^{\pi/2}(\mu_1^2 x_1^2 + \mu_2^2)\sqrt{-2|h| + \Omega^2 x_1^2}\,dx_1$$

$$\mathring{\sigma}_i^2(h) = 2\Omega\left[\mu_1^2\left\{\frac{\pi}{8}\sqrt{\frac{\pi^2}{4} - \frac{2|h|}{\Omega^2}}\left(\frac{\pi^2}{4} - \frac{|h|}{\Omega^2}\right) - \frac{|h|^2}{2\Omega^4}\cosh^{-1}\sqrt{\frac{\Omega^2\pi^2}{8|h|}}\right\} + \mu_2^2\left\{\frac{\pi}{4}\sqrt{\frac{\pi^2}{4} - \frac{2|h|}{\Omega^2}} - \frac{|h|}{\Omega^2}\cosh^{-1}\sqrt{\frac{\Omega^2\pi^2}{8|h|}}\right\}\right].$$

Here, we considered the interval of $[-\pi/2, \pi/2]$, where $\Pi(x_1) = x_1$. Due to the periodicity of the transformed system, we can get the same result for the other intervals using a change of variable.

The h_t process can move from one region of closed trajectories to another. The aim of this paper is to consider the results pertaining to the ends of the segments where there is a homoclinic orbit connecting a saddle point and to examine the fate of the trajectories which leave the region where they originated. We are also interested in the qualitative changes in the probability densities p_α which are solutions of the *Fokker-Planck equation* (FPE) associated with the generator (20).

4.1.1 Mean First Passage Time. The scale and speed measures on the edges $(i=2,4)$ connecting the vertex are given by

$$S_i(h) \overset{\text{def}}{=} \int_{z_i}^{h} s_i(\eta)d\eta, \quad \text{and} \quad M_i(h) \overset{\text{def}}{=} \int_{z_i}^{h} m_i(\eta)d\eta,$$

where

$$s_i(\eta) = \frac{1}{\mathring{\sigma}_i^2(\eta)}\exp\left(-2\int_{z_i}^{\eta}\frac{B_i(\xi)}{\mathring{\sigma}_i^2(\xi)}d\xi\right),$$

$$m_i(\eta) = T_i(\eta)\exp\left(2\int_{z_i}^{\eta}\frac{B_i(\xi)}{\mathring{\sigma}_i^2(\xi)}d\xi\right),$$

and h is an interior point for each edge I_i. For $i=1,3$, the lower limits of integration are h and the upper ones are z_1, z_3, respectively. In order to examine the boundary behavior, we consider roughly the time to reach the left or right boundary starting from an interior point $h_i \in I_i$ and the time to reach an interior point h starting from the boundary z_i or $\mathcal{O}$. A thorough discussion on boundary classification is given in [14]. The ends of the edges I_i are fixed points of elliptic or saddle type. The Feller classification defines whether the end of an edge is accessible from the inside and whether the inside is accessible from the end of an edge. We find that the boundaries b_2 and b_4 are entrance boundaries while the boundaries b_1 and b_3 are natural boundaries. Since $\mathcal{D}'(h) = T(h)$, where $\mathcal{D}(h)$ is the area bounded by $E(h)$, it is clear that $S_i(h)$ and $M_i(h)$ are finite as $h \to H(\mathcal{O})$. Thus, according to the Feller classification, vertex $\mathcal{O}$ is accessible and the gluing condition is needed to solve the mean exit time problem.

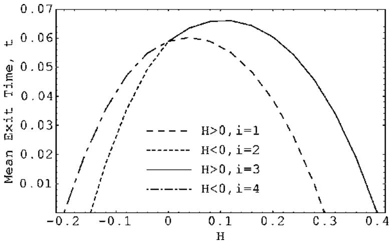

Fig. 2 Variation of the mean exit time, *t*, with *H*

Suppose that at time $t=0$, the state of the system corresponds to some point defined by $H(0)=h$ within $\mathcal{D}$ which is the domain of attraction with boundary $\partial\mathcal{D}$. Let z_i be the points on the edge of the graph corresponding to the boundary $\partial\mathcal{D}$. We are interested in the time $\tau_c \overset{\text{def}}{=} \min\{\tau_i\}$ where $\tau_i = \inf\{t \geqslant 0; H(t) = z_i\}$ is the hitting time of the averaged process to the level z_i. Define the mean time to reach either z_1, z_2, z_3, or z_4 by the function $u(h) \overset{\text{def}}{=} \mathrm{E}[\tau_c : H(0) = h]$. Since the averaged process is Markovian with the generator (20) it follows from the classical theory of Markov processes

$$\mathcal{L}_i^{\dagger} u_i(h) = -1, \quad (h,i) \in I_i \tag{25}$$

with the boundary and gluing conditions given by

$$u_i(z_i) = 0 \;\forall\, i, \quad \text{and} \quad \sum_{i=1}^{4}(\pm)\sigma_i^2(\mathcal{O})u_i'(\mathcal{O}) = 0.$$

The generator (20) is defined for continuous functions $u_i(h), h \in I_i$. Hence, at the vertex $\mathcal{O}$ we have $u_1(\mathcal{O}) = u_2(\mathcal{O}) = u_3(\mathcal{O}) = u_4(\mathcal{O})$. Thus, we have eight boundary conditions for determining uniquely the mean first passage time. Imposing the boundary conditions at $h = z_1$, z_2, z_3, and z_4 the solution of (25) is given by

$$u_i(h) = -2\int_{h}^{z_i}\left(\int_{\eta}^{z_i} m_i(\xi)d\xi\right)s_i(\eta)d\eta + \beta_i[S_i(z_i) - S_i(h)], \quad i = 1,3$$

$$u_i(h) = -2\int_{z_i}^{h}\left(\int_{z_i}^{\eta} m_i(\xi)d\xi\right)s_i(\eta)d\eta + \beta_i[S_i(h) - S_i(z_i)], \quad i = 2,4,$$

where h is an interior point for each edge I_i.

From the symmetry of the system, the gluing conditions simplify to

$$-u_1'(\mathcal{O}) + u_2'(\mathcal{O}) - u_3'(\mathcal{O}) + u_4'(\mathcal{O}) = 0. \tag{26}$$

Applying the continuity and gluing conditions at the vertex $\mathcal{O}$, the constants β_1, β_2, β_3, and β_4 can be determined for various values of the system parameters $\alpha, \gamma, \mu_1, \mu_2$. In this work, the numerical calculations were performed with the aid of *Mathematica 5.0*. Figure 2 shows the variation of the mean exit time with H for $z_1=0.3$, $z_2=-0.15$, $z_3=0.4$, $z_4=-0.2$, $\alpha=1$, $\gamma=1$, $\mu_1=1$, and $\mu_2=1$.

4.1.2 Fokker-Planck Equation (FPE). In this section, we shall examine the stationary behavior of the Fokker-Planck equation (FPE) associated with the generator (24). In order to obtain the FPE, let

$$E(h)\overset{\text{def}}{=}\{(x,y)\in\mathbb{R}^2 : H(x,y)=h\}.$$

The inner product with respect to the Lebesgue measure is given by the usual definition

$$\langle f(x_1,x_2),g(x_1,x_2)\rangle_{\mathbb{R}^2}\overset{\text{def}}{=}\int\int_{\mathcal{D}(h)} f(x_1,x_2)g(x_1,x_2)dx_1dx_2,$$

where $\mathcal{D}(h)$ is the area bounded by $E(h)$. Making use of the relation $\mathcal{D}'(h)=T(h)$ (where the prime denotes differentiation with respect to the energy level, h), the appropriate inner product in the local coordinate h is given by

$$\langle f(h),g(h)\rangle_H\overset{\text{def}}{=}\int_h f(h)g(h)T(h)dh. \tag{27}$$

Given the generator $\mathcal{L}^\dagger$ of the process $(\text{¥}(t),\mathbb{P}^\dagger_{\pi(x)})$ on the graph defined in (24), the associated adjoint operator is obtained using the inner product (27) as

$$\mathcal{L}_i^{\dagger *}g_i(h)=\frac{1}{T_i(h)}\left(-[B_i(h)g_i(h)]'+\frac{1}{2}[\mathring{\sigma}_i^2(h)g_i'(h)]'\right),$$

$$\text{for all } h\in\bar{\mathcal{I}}_i,$$

with the boundary conditions

$$\begin{aligned}&\sum_{i=1}^4(\pm)\ \frac{1}{2}\mathring{\sigma}_i^2(h)f_i'(h)g_i(h)\Big|_0^{b_i},\\ &\sum_{i=1}^4(\pm)\ \left\{B_i(h)g_i(h)-\frac{1}{2}\mathring{\sigma}_i^2(h)g_i'(h)\right\}f_i(h)\Big|_0^{b_i},\end{aligned} \tag{28}$$

and once again the "+" sign is taken if the coordinate h on the segment I_i is greater than $H(\mathcal{O})$ and the "−" sign is taken otherwise.

We shall consider the boundary conditions at the exterior vertices and the interior vertex $\mathcal{O}$ separately. Consider the first boundary condition in (28). At the exterior vertices b_1 and b_3, it is obvious that the probability densities $g_1(h)$ and $g_3(h)$ are equal to zero. At the exterior vertices b_2 and b_4, from an asymptotic analysis, it can be shown that $\lim_{h\searrow b_i}f_i'(h)$ is finite (see Lemma 5.3 of [15]), and $\lim_{h\searrow b_i}\mathring{\sigma}_i^2(h)=0$. Hence, the first boundary condition in the above expression vanishes at the exterior vertices b_1, b_2, b_3, and b_4. Further, at the interior vertex $\mathcal{O}$, the probability density is continuous, i.e., $g_1(\mathcal{O})=g_2(\mathcal{O})=g_3(\mathcal{O})=g_4(\mathcal{O})=g(\mathcal{O})$. Thus, the first boundary condition reduces to the expression

$$(\pm)\sum_{i=1}^4\mathring{\sigma}_i^2(\mathcal{O})f_i'(\mathcal{O})g(\mathcal{O}). \tag{29}$$

In view of the gluing conditions (23), the above expression is identically equal to zero. Now, we shall consider the second boundary condition in (28). Since the exterior vertices, b_i are the entrance boundaries, the probability flux at these vertices is zero, i.e.,

$$\left\{B_i(b_i)g_i(b_i)-\frac{1}{2}\mathring{\sigma}_i^2(b_i)g_i'(b_i)\right\}=0,\quad i=1,2,3,4. \tag{30}$$

Furthermore, from (18), the function $f_i(H)$ is continuous at the interior vertex $\mathcal{O}$, i.e., $f_1(\mathcal{O})=f_2(\mathcal{O})=f_3(\mathcal{O})=f_4(\mathcal{O})=f(\mathcal{O})$. Thus, the second boundary condition reduces to

$$\sum_{i=1}^4(\pm)\left\{B_i(\mathcal{O})g_i(\mathcal{O})-\frac{1}{2}\mathring{\sigma}_i^2(\mathcal{O})g_i'(\mathcal{O})\right\}\overset{\text{def}}{=}\sum_{i=1}^4(\pm)\mathcal{J}_i(\mathcal{O})=0, \tag{31}$$

where $\mathcal{J}_i(\mathcal{O})$ denotes the probability flux in each segment I_i of the vertex $\mathcal{O}$. Equation (31) reflects the fact that the *probability flux* is conserved. Finally, the probability density is normalized to unity

$$\int_0^\infty g_1(h)dh+\int_{b_2}^0 g_2(h)dh+\int_0^\infty g_3(h)dh+\int_{b_4}^0 g_4(h)dh=1. \tag{32}$$

The stationary probability density is the solution of the FPE:

$$\mathcal{L}_i^{\dagger *}g_i=0 \tag{33}$$

subjected to the conditions given in (31) and (32). The solution of (33) is obtained as

$$\begin{aligned}g_i(h)=&\exp\left(2\int_{H_{i0}}^h\frac{B_i(\eta)}{\mathring{\sigma}_i^2(\eta)}d\eta\right)\\ &\times\left(-2G_i^{st}\int_{H_{i0}}^h\frac{\exp\left\{-2\displaystyle\int_{H_{i0}}^{\eta}[B_i(\xi)/\mathring{\sigma}_i^2(\xi)]d\xi\right\}}{\mathring{\sigma}_i^2(\eta)}d\eta+D_i\right),\end{aligned}$$

where G_i^{st} and D_i are to be determined from the conditions mentioned above. Since the flux is zero at the exterior vertices indicated by b_i, it can be shown that the G_i^{st} are identically zero. Now, from the symmetry of the system, the flux condition (31) reduces to

$$-g_1'(\mathcal{O})+g_2'(\mathcal{O})-g_3'(\mathcal{O})+g_4'(\mathcal{O})=0, \tag{34}$$

which is automatically satisfied due to the fact

$$g_i'(h)=\frac{2B_i(h)}{\mathring{\sigma}_i^2(h)}g_i(h).$$

Upon applying the continuity and the flux conditions at the vertex $\mathcal{O}$, we obtain

$$D_1=D_3,\quad D_2=D_4,\quad D_1=D_2\exp\left(\int_{b_2}^{H(\mathcal{O})}\frac{2B_2(\eta)}{\mathring{\sigma}_2^2(\eta)}d\eta\right). \tag{35}$$

Now, we make use of the normalization condition to obtain the constants D_i from

$$\begin{aligned}D_2^{-1}=&\,2\int_{b_2}^{H(\mathcal{O})}\exp\left(\int_{b_2}^h\frac{2B_2(\eta)}{\mathring{\sigma}_2^2(\eta)}d\eta\right)dh\\ &+2\exp\left(\int_{b_2}^{H(\mathcal{O})}\frac{2B_2(\eta)}{\mathring{\sigma}_2^2(\eta)}d\eta\right)\\ &\times\int_{H(\mathcal{O})}^\infty\exp\left(\int_{H(\mathcal{O})}^h\frac{2B_1(\eta)}{\mathring{\sigma}_1^2(\eta)}d\eta\right)dh.\end{aligned} \tag{36}$$

The expressions in (36) were evaluated numerically for various values of the system parameters α, γ, μ_1, and μ_2 using *Mathematica 5.0*. Figure 3 shows the stationary density with respect to various intensities of additive noise, μ_2, and different values of the coefficient of restitution, r, for $\alpha=1$, $\mu_1=0$.

4.2 Numerical Approach. Here, we use a Monte Carlo approach to simulate the SDE. The starting point is the linearized model (22) with the impact law (4). In the first-order form, we can rewrite it as

$$\dot{x}_1(t)=x_2(t)$$

$$\dot{x}_2(t)=-2\alpha x_2(t)+\Omega^2x_1(t)+\mu_1\xi(t)x_1(t)+\mu_2\eta(t). \tag{37}$$

It is usual to write the above equations in differential forms with the appropriate scaling

$$dx_1(t)=x_2(t)dt$$

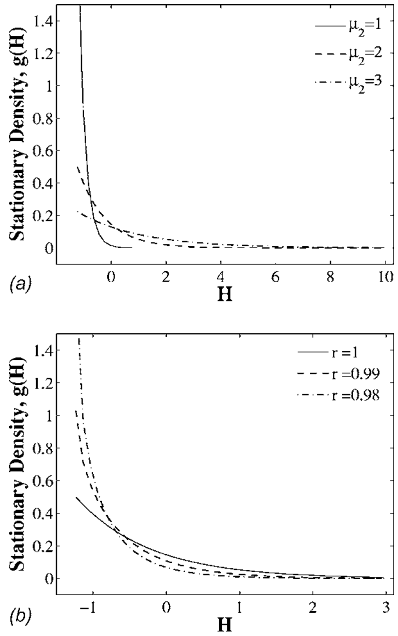

Fig. 3 Stationary density $g(h)$: (*a*) effect of additive noise ($r=1$), (*b*) effect of r ($\mu_2=2$)

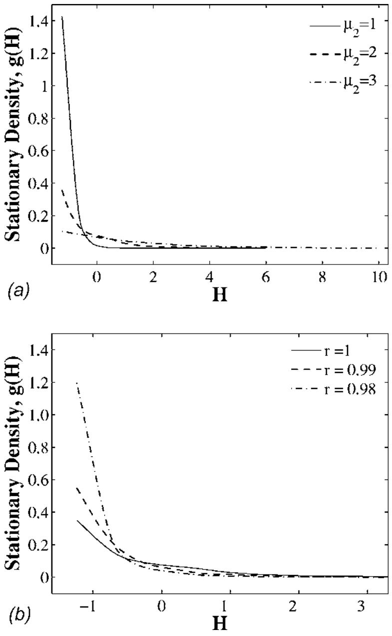

Fig. 5 Stationary density $g(h)$: (*a*) effect of additive noise ($r=1$), (*b*) effect of r ($\mu_2=2$)

$$dx_2(t) = \Omega^2 x_1(t)dt - 2\epsilon^2 \alpha x_2(t)dt + \epsilon[\mu_1 dW_t^1 x_1(t) + \mu_2 dW_t^2], \tag{38}$$

which are in the same form as (10). We apply the stochastic Euler scheme (Euler-Maruyama method [16]) using the same parameter values as in Sec. 4.1.2. The following graphs are obtained from the simulations using *Matlab 6.5* through 10^7 iterations of 0.01 time steps with the scale parameter $\epsilon=0.1$. Care must be taken when the value of coefficient of restitution r is chosen since the averaged system is only valid for small perturbations. In this simulation $(1-r)$ is taken to be either 0.01 or 0.02, which guarantees the smallness assumption of λ (see Eq. (7)). Figure 4 shows the probability density plot for x_1 and x_2 for two different values of the additive noise intensity μ_2. In order to compare the simulations with the analytical results of the previous section, we project the probability density plot for the Hamiltonian $H(u,v) = \frac{1}{2}x_2^2 - \frac{1}{2}\Omega x_1^2$ and it is shown in Fig. 5. From the numerical values presented in Figs. 3 and 5, it is clear that the approximate results are close to the numerical simulations.

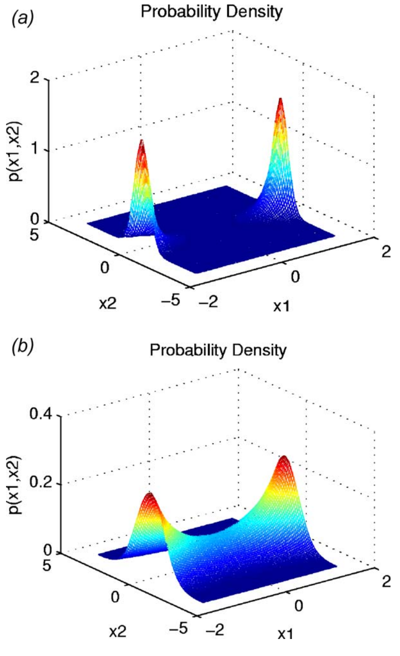

Fig. 4 Stationary density $p(u,v)$: (*a*) $\mu_2=1$, (*b*) $\mu_2=2$

5 Conclusion

In this paper we have shown the dynamics of a general single-degree-of-freedom system with nonsmooth nonlinearities under random excitations. Through stochastic averaging we developed rigorous methods to replace the original nonsmooth system by a simpler, lower-dimensional model and obtained the analytical solutions for the reduced system. First, we transformed the system to standard form where the order one Hamiltonian is smooth. Under the smallness assumption of perturbation, we were able to achieve a model reduction and the reduced Markov process takes its values on a graph with gluing conditions at the vertex of the graph. As an application, we studied the vertical pendulum constrained between two walls under additive and multiplicative noises and found the analytical solutions for the mean exit times and probability density functions. To our knowledge, such analytical results have not been found by others. Finally, these results are validated numerically using Monte Carlo simulations. The theoretical values are very close to those obtained numerically for the coefficient of restitution r very close to 1. The concept of P-bifurcation (*phenomenological*) is associated with qualitative changes of the probability density $g(h)$. The reader is referred to Arnold et al. [17] for details. We also found that bifurcation does not occur under additive noise in these systems, similar to a result that was also obtained by Namachchivaya et al. [18].

Acknowledgment

The authors would like to acknowledge the support of the National Science Foundation under Grant No. CMS 03-01412. Any opinions, findings, and conclusions or recommendations expressed in this paper are those of the authors and do not necessarily reflect the views of the National Science Foundation. We would like to thank Richard Sowers for helpful and stimulating discussions on the topic of martingale problem.

References

[1] Thompson, J. M. T., and Ghaffari, R., 1982, "Chaos After Period-Doubling Bifurcations in the Resonance of an Impact Oscillator," Phys. Lett. A, **91**(1), pp. 5–8.

[2] Shaw, S. W., and Holmes, P. J., 1983, "A Periodically Forced Piecewise Linear Oscillator," J. Sound Vib., **90**(1), pp. 129–155.

[3] Shaw, S. W., 1985, "Forced Vibrations of a Beam With One-Sided Amplitude Constraint; Theory and Experiment," J. Sound Vib., **99**, pp. 199–212.

[4] Shaw, S. W., 1985, "The Dynamics of a Harmonically Excited System Having Rigid Amplitude Constraints, Parts 1 and 2," ASME J. Appl. Mech., **52**, pp. 453–464.

[5] Shaw, S. W., and Holmes, P. J., 1983, "A Periodically Forced Oscillator With Large Dissipation," ASME J. Appl. Mech., **50**, pp. 849–857.

[6] Shaw, S. W., and Rand, R. H., 1989, "The Transition to Chaos in a Simple Mechanical System," Int. J. Non-Linear Mech., **24**(1), pp. 41–56.

[7] Dimentberg, M. F., and Menyailov, A. I., 1979, "Response of a Single-Mass Vibro-Impact System to White-Noise Random Excitation," Z. Angew. Math. Mech., **59**, pp. 709–716.

[8] Fogli, M., Bressolette, P., and Bernard, P., 1996, "The Dynamics of a Stochastic Oscillator With Impacts," Eur. J. Mech. A/Solids, **15**(2), pp. 213–241.

[9] Zhuravlev, V. F., 1976, "A Method for Analyzing Vibration-Impact Systems by Means of Special Functions," Mech. Solids, **11**, pp. 23–27.

[10] Freidlin, M. I., and Wentzell, A. D., 1994, *Random Perturbations of Hamiltonian Systems*, American Mathematical Society, Providence, RI.

[11] Freidlin, M. I., and Weber, M., 1998, (Random Perturbations of Nonlinear Systems,) Ann. Prob., **26**(3), 925–967.

[12] Sowers, R. B., 2003, "Stochastic Averaging Near a Homoclinic Orbit With Multiplicative Noise," Stochastics Dyn., **3**(3), pp. 299–391.

[13] Namachchivaya, N. Sri, and Sowers, R. B., 2001, "Unified Approach for Noisy Nonlinear Mathieu-Type Systems," Stochastics Dyn., **1**(3), pp. 405–450.

[14] Karlin, S., and Taylor, H. M., 1981, *A Second Course in Stochastic Processes*, Academic Press, New York.

[15] Namachchivaya, N. Sri, and Sowers, R., 2002, "Rigorous Stochastic Averaging at a Center With Additive Noise," Meccanica, **37**(2), pp. 85–114.

[16] Higham, D. J., 2001, "An Algorithmic Introduction to Numerical Simulation of Stochastic Differential Equations," SIAM Rev., **43**, pp. 525–546.

[17] Arnold, L., Namachchivaya, N. Sri, and Schenk, K. L., 1996, "Toward an Understanding of Stochastic Hopf Bifurcations: A Case Study," Int. J. Bifurcation Chaos Appl. Sci. Eng., **6**(11), pp. 1947–1975.

[18] Namachchivaya, N. Sri, Sowers, R. B., and Vedula, L., 2001, "Non-standard Reduction of Noisy Duffing-van der Pol Equation," Dyn. Syst., **16**(3), pp. 223–245.

Elastic Fields due to Eigenstrains in a Half-Space

Shuangbiao Liu[1]

Qian Wang

Department of Mechanical Engineering,
Northwestern University,
Evanston, IL 60208

Engineering components inevitably encounter various eigenstrains, such as thermal expansion strains, residual strains, and plastic strains. In this paper, a set of formulas for the analytical solutions to cases of uniform eigenstrains in a cuboidal region-influence coefficients, is presented in terms of derivatives of four key integrals. The linear elastic field caused by arbitrarily distributed eigenstrains in a half-space is thus evaluated by the discrete correlation and fast Fourier transform algorithm, along with the discrete convolution and fast Fourier transform algorithm. By taking advantage of both the convolution and correlation characteristics of the problem, the formulas of influence coefficients and the numerical algorithms are expected to enable efficient and accurate numerical analyses for problems having nonuniform distribution of eigenstrains and for contact problems. [DOI: 10.1115/1.2047598]

1 Introduction

Driven by modern design concepts such as compactness, reliability, and power density, components encounter severe conditions with significant thermal expansion, and residual and plastic strains. These strains are generically named as eigenstrains. The effects of eigenstrains on elastic field or inclusion problems with regard to a half-space have been investigated for decades [1–6] and summarized in the field of micromechanics [6]. Chiu [3,4] developed solutions for isotropic and elastic infinite spaces and half-spaces, respectively, due to eigenstrains in a cuboid (see also Chapter 2 in [6]). The half-space solution [4] is the summation of two infinite space solutions [3] with two mirror-image eigenstrains, respectively, and the Boussinesq solution for the half-space subject to pressure. Recent studies on inclusion problems can be found in [7–10], among many others. Yoffe [11] studied the indentation of brittle materials and used the Blister field for surface inclusions. Sainsot et al. [12] and Jacq et al. [13] utilized Chiu's theory and developed a semianalytical elastic-plastic contact model to study the rolling contact fatigue of dented surfaces.

However, Chiu's superposition method is an indirect way to find the elastic field in a half-space with eigenstrains. In this paper, a direct way is adopted and the Mindlin and Cheng's half-space results [2] or more general results reported by Yu and Sanday [14] for joint half-spaces are utilized. Cases of uniform eigenstrains in a cuboidal region are solved to derive influence coefficients. A set of formulas for influence coefficients in terms of derivatives of four key integrals is presented and is used to express the elastic field caused by arbitrary distribution of eigenstrains in a half-space. In numerical analyses for the elastic field due to plastic strains, Sainsot et al. [12] and Jacq et al. [13] used two-dimensional fast Fourier transform (FFT) to reduce computational burden. It is desirable to further improve numerical efficiency, particularly for thermo-elasto-plastic contact analyses where elastic field has to be repetitively evaluated during the iteration process to solve the contact problem [15]. Based on the nature of the expressions of the elastic field in general cases, two unique numerical schemes—the discrete correlation and fast Fourier transform (DCR-FFT) [16] and the discrete convolution and fast Fourier transform (DC-FFT) [16], are applied with three-dimensional FFT. These algorithms take advantage of the convolution and correlation characteristics. The straightforward formulae and the numerical algorithms are expected to reduce the difficulties of code development and enable fast and accurate analyses for inclusion problems and contact problems.

2 Theory

An isotropic and elastic half-space with a coordinate system $Ox_1x_2x_3$ (Fig. 1) is subject to eigenstrains (e_{ij}) distributed in an arbitrary way inside a volumetric region (Ω). This region may have irregular shape. In the following derivation, the sign of e_{ij} follows conventional rules and a comma in the subscript means derivative, e.g., $F_{i,j}=\partial F_i/\partial x_j$. Note that symbols in boldface are vectors. Vector $\mathbf{x}$ denotes any observation or response point, while $\mathbf{x}'$ denotes any source or excitation point. The elastic field due to the eigenstrains can be expressed in terms of Galerkin vectors, $\mathbf{F}$ [17]:

1) Displacements.

$$2\mu u_i(\mathbf{x}) = 2(1-\nu)F_{i,jj} - F_{k,ki} \tag{1}$$

2) Stresses outside Ω. According to the Hooke's law, one can obtain

$$\sigma_{ij}(\mathbf{x}) = \lambda\delta_{ij}u_{k,k} + \mu(u_{i,j}+u_{j,i}) \tag{2a}$$

$$\text{or } \sigma_{ij}(\mathbf{x}) = \nu F_{k,kmm}\delta_{ij} - F_{k,kij} + (1-\nu)(F_{i,kkj}+F_{j,kki}) \tag{2b}$$

3) Stresses inside Ω. Stresses inside Ω are evaluated by Eq. (2) minus stresses σ_{ij}^* determined from e_{ij} by using the Hooke's law, $\sigma_{ij}^*(\mathbf{x})=2\mu e_{ij}+\lambda e_{kk}\delta_{ij}$. Thus,

$$\sigma_{ij}(\mathbf{x}) = \nu F_{k,kmm}\delta_{ij} - F_{k,kij} + (1-\nu)(F_{i,kkj}+F_{j,kki}) - 2\mu e_{ij} - \lambda e_{kk}\delta_{ij} \tag{3}$$

If it is not specially indicated, the summation convention is always applied for repeating indices. Note that Eqs. (1)–(3) involves only high-order derivatives of the Galerkin vectors. The Galerkin vectors are written in a form of volumetric integral as [17]

---

[1] Currently at Caterpillar Inc., Technical Center E/854, P. O. Box 1875, Peoria, IL 61656. e-mail: Liu_Jordan@cat.com.

Contributed by the Applied Mechanics Division of THE AMERICAN SOCIETY OF MECHANICAL ENGINEERS for publication in the ASME JOURNAL OF APPLIED MECHANICS. Manuscript received by the Applied Mechanics Division, May 23, 2003; final revision; March 24, 2005. Associate Editor: A. A. Ferri. Discussion on the paper should be addressed to the Editor, Prof. Robert M. McMeeking, Journal of Applied Mechanics, Department of Mechanical and Environmental Engineering, University of California-Santa Barbara, Santa Barbara, CA 93106-5070, and will be accepted until four months after final publication in the paper itself in the ASME JOURNAL OF APPLIED MECHANICS.

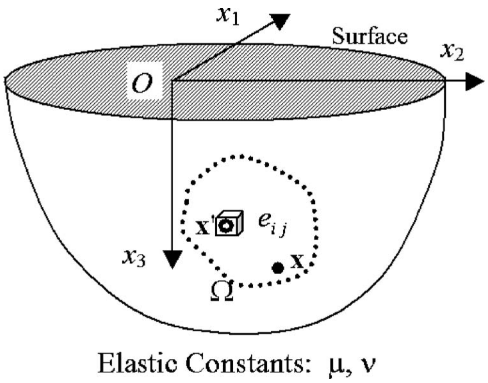

Fig. 1 A half-space subject to eigenstrains, e_{ij}, inside a domain Ω. x′ and x are source points and observation points, respectively

$$\mathbf{F}(\mathbf{x}) = -C\int_\Omega (2\nu e_{kk}\mathbf{g}_c - e_{jk}\mathbf{g}_{jk})d\mathbf{x}' \qquad (4)$$

where $C=-\mu/[4\pi(1-\nu)]$, $\mathbf{g}_c$ is a basic Galerkin vector for a center of dilatation in a half-space, and $\mathbf{g}_{jk}$ are basic Galerkin vectors for a double force in the k direction $(j=k)$ or a double force in the k direction with moment in the direction normal to the Ox_jx_k plane $(j\neq k)$ in a half-space. The expressions of the basic Galerkin vectors for a center of dilatation, double forces and double forces with moment can be found in Mindlin and Cheng [2] or Yu and Sanday [14], where expressions for other types of nuclei of strain are listed as well.

2.1 Infinite Space. Although problems of an infinite space subject to eigenstrains are the simplest, formulae are shown here to illustrate the method with the Galerkin vectors. Equations (1)–(4) are also valid for infinite spaces except that the Galerkin vectors in this case are listed as follows:

$$\mathbf{g}_{ij} = R^I_{,i}\hat{x}_j \qquad (5a)$$

$$\mathbf{g}_c = \ln[R^I + (x_3 - x_3')]\hat{x}_3 \qquad (5b)$$

$$F_i = C\int_\Omega [e_{ij}R^I_{,j} - 2\nu e_{kk}\delta_{i3}\ln\{R^I + (x_3 - x_3')\}]d\mathbf{x}' \qquad (5c)$$

$$F_{i,kk} = 2C\int_\Omega e_{im}\phi^I_{,m}d\mathbf{x}'$$

$$(\text{since } R^I_{,kk} = 2\phi^I \text{ and } \{\ln[R^I + (x_3 - x_3')]\}_{,kk} = 0) \qquad (5d)$$

$$F_{k,ki} = C\int_\Omega (e_{km}R^I_{,kmi} - 2\nu e_{kk}\phi^I_{,i})d\mathbf{x}' \qquad (5e)$$

where $\hat{x}_j$ is the unit vector in the x_j direction, $R^I = \sqrt{(x_1-x_1')^2+(x_2-x_2')^2+(x_3-x_3')^2}$, and $\phi^I=1/R^I$. Superscript "I" denotes the infinite space. When the eigenstrains are plastic strains, it is known that the trace of the plastic strains is zero, i.e., $e_{kk}=0$. In other words, the plastic strains are only one special type of the eigenstrains considered in this paper. In general, the terms related to the trace of the eigenstrains in Eqs. (5c) and (5e) should be kept. Thus, the elastic field in an infinite space is obtained by substituting Eqs. (5) into Eqs. (1)–(3),

$$2\mu u_i/C = 4(1-\nu)\int_\Omega e_{im}\phi^I_{,m}d\mathbf{x}' - \int_\Omega (e_{km}R^I_{,kmi} - 2\nu e_{kk}\phi^I_{,i})d\mathbf{x}' \qquad (6a)$$

$$\sigma_{ij}/C = 2\nu\int_\Omega e_{mk}\phi^I_{,km}d\mathbf{x}'\,\delta_{ij} - \int_\Omega (e_{km}R^I_{,kmij} - 2\nu e_{kk}\phi^I_{,ij})d\mathbf{x}'$$
$$+ 2(1-\nu)\int_\Omega (e_{im}\phi^I_{,mj} + e_{jm}\phi^I_{,mi})d\mathbf{x}' \quad \mathbf{x}\notin\Omega \qquad (6b)$$

$$\sigma_{ij}/C = 8\pi[(1-\nu)e_{ij} + \nu e_{kk}\delta_{ij}] + 2\nu\int_\Omega e_{mk}\phi^I_{,km}d\mathbf{x}'\,\delta_{ij}$$
$$- \int_\Omega (e_{km}R^I_{,kmij} - 2\nu e_{kk}\phi^I_{,ij})d\mathbf{x}' + 2(1-\nu)\int_\Omega (e_{im}\phi^I_{,mj}$$
$$+ e_{jm}\phi^I_{,mi})d\mathbf{x}' \quad \mathbf{x}\in\Omega \qquad (6c)$$

The first term in Eq. (6c) consists of two parts: (1) σ^*_{ij} expressed in Eq. (3) and (2) an extra part originated from $\lambda\delta_{ij}u_{k,k}$ of Eq. (2a),

$$\lambda\delta_{ij}C\int_\Omega 2\nu e_{kk}\phi^I_{,jj}d\mathbf{x}'/(2\mu) = -8\pi C\delta_{ij}e_{kk}\nu^2/(1-2\nu) \quad x\in\Omega$$

with the following identity, (see Eq. (12.6) in [6])

$$\left(\int_\Omega e_{ij}\phi^I d\mathbf{x}'\right)_{,kk} = \begin{cases} -4\pi e_{ij}(\mathbf{x}) & x\in\Omega \\ 0 & x\notin\Omega \end{cases}$$

Similarly, if the strain is a dilatation strain, i.e., $\delta_{ij}e_0$, the second term in Eq. (6c) will be $-8\pi\nu e_0\delta_{ij}$. A one-dimensional convolution has the form of $\int_{-\infty}^{\infty}e(x_i')G(x_i-x_i')dx_i'$. Eq. (6) consists of volumetric integrals, which are indeed three-dimensional convolutions.

2.2 Half-Space. Galerkin vectors due to unit single forces at $\mathbf{x}'$ in a half-space are written as [2,14],

$$\mathbf{g}_1 = \begin{pmatrix} R^I + R - 2x_3'^2\phi - 4(1-\nu)D\theta \\ 0 \\ 2x_3'R_{,1} + 2D(x_1 - x_1')\psi \end{pmatrix} \qquad (7a)$$

$$\mathbf{g}_2 = \begin{pmatrix} 0 \\ R^I + R - 2x_3'^2\phi - 4(1-\nu)D\theta \\ 2x_3'R_{,2} + 2D(x_2 - x_2')\psi \end{pmatrix} \qquad (7b)$$

$$\mathbf{g}_3 = [R^I + (3-4\nu)R - 2x_3'x_3\phi - 4Dx_3'\psi - 4(1-\nu)D\theta]\hat{x}_3 \quad (7c)$$

where $D=1-2\nu$, $R=\sqrt{(x_1-x_1')^2+(x_2-x_2')^2+(x_3+x_3')^2}$, $\psi=\ln[R+(x_3+x_3')]$, $\phi=1/R$, and $\theta=R-(x_3+x_3')\psi$. Note that $\psi_{,3}=\phi$ and $\theta_{,3}=-\psi$. Galerkin vectors due to unit double forces, double forces with moment, and a center of dilatation are,

$$\mathbf{g}_{ij} = -\frac{\partial\mathbf{g}_j}{\partial x_i'} \qquad (8a)$$

$$\mathbf{g}_c = [\ln\{R^I + (x_3 - x_3')\} + (1-4\nu)\psi + 2x_3\phi]\hat{x}_3 \qquad (8b)$$

Note that the derivative in Eq. (8a) is with respect to the excitation point. According to Eq. (4), the Galerkin vectors due to the eigenstrains in the region, Ω, could be written as an integral with respect to $\mathbf{x}'$,

$$F_i(\mathbf{x}) = \int_\Omega f_i(\mathbf{x},\mathbf{x}')d\mathbf{x}' \qquad (9)$$

with $\mathbf{f}=C[e_{i1}(g_{i1})_1, e_{i2}(g_{i2})_2, e_{ij}(g_{ij})_3 - 2\nu e_{ii}(g_c)_3]^T$. Equations (1) and (2) show that only the derivatives of Galerkin vectors will be used in the elastic field. The sequence of integration and differentiation can be interchanged, thus the derivatives of f_i are shown in the following equations,

$$f_{i,jj}/C = 2e_{1i}(\phi^I_{,1} + \phi_{,1}) + 2e_{2i}(\phi^I_{,2} + \phi_{,2}) + 2e_{3i}(\phi^I_{,3} - \phi_{,3}) \quad (i = 1 \text{ or } 2) \tag{10a}$$

$$\begin{aligned} f_{3,jj}/C = {} & 2e_{13}(\phi^I_{,1} + 4x_3\phi_{,13} - 4R_{,133} + 3\phi_{,1}) + 2e_{23}(\phi^I_{,2} + 4x_3\phi_{,23} \\ & - 4R_{,233} + 3\phi_{,2}) + 8e_{12}(-x_3\phi_{,12} + R_{,123} + D\psi_{,12}) \\ & + 4e_{11}(-x_3\phi_{,11} + R_{,113} + D\psi_{,11}) + 4e_{22}(-x_3\phi_{,22} + R_{,223} \\ & + D\psi_{,22}) + 2e_{33}[\phi^I_{,3} - 2x_3\phi_{,33} + 2R_{,333} - (5-4\nu)\phi_{,3}] \\ & - 8\nu e_{ii}\phi_{,3} \end{aligned} \tag{10b}$$

$$\begin{aligned} f_{m,jjm}/C = {} & 4e_{13}(\phi^I_{,13} - 2R_{,1333} + 2x_3\phi_{,133} + 3\phi_{,13}) \\ & + 4e_{23}(\phi^I_{,23} - 2R_{,2333} + 2x_3\phi_{,233} + 3\phi_{,23}) \\ & + 4e_{12}[\phi^I_{,12} + 2R_{,1233} - 2x_3\phi_{,123} + (1-4\nu)\phi_{,12}] \\ & + 2e_{11}[\phi^I_{,11} + 2R_{,1133} - 2x_3\phi_{,113} + (1-4\nu)\phi_{,11}] \\ & + 2e_{22}[\phi^I_{,22} + 2R_{,2233} - 2x_3\phi_{,223} + (1-4\nu)\phi_{,22}] \\ & + 2e_{33}[\phi^I_{,33} + 2R_{,3333} - 2x_3\phi_{,333} - (7-4\nu)\phi_{,33}] \\ & - 8\nu e_{ii}\phi_{,33} \end{aligned} \tag{10c}$$

$$\begin{aligned} f_{j,j}/C = {} & 2e_{13}[R^I_{,13} - (3-4\nu)R_{,13} + 4(1-\nu)x_3\phi_{,1} - 2x_3R_{,133} \\ & + 2x_3^2\phi_{,13}] + 2e_{23}[R^I_{,23} - (3-4\nu)R_{,23} + 4(1-\nu)x_3\phi_{,2} \\ & - 2x_3R_{,233} + 2x_3^2\phi_{,23}] + 2e_{12}[R^I_{,12} + (1-2D^2)R_{,12} \\ & + 4(1-\nu)D(x_3 + x_3')\psi_{,12} + 2x_3R_{,123} - 2x_3^2\phi_{,12}] \\ & + e_{11}[R^I_{,11} + (1-2D^2)R_{,11} + 4(1-\nu)D(x_3 + x_3')\psi_{,11} \\ & + 2x_3R_{,113} - 2x_3^2\phi_{,11}] + e_{22}[R^I_{,22} + (1-2D^2)R_{,22} \\ & + 4(1-\nu)D(x_3 + x_3')\psi_{,22} + 2x_3R_{,223} - 2x_3^2\phi_{,22}] \\ & + e_{33}[R^I_{,33} + (3-4\nu)R_{,33} + 8(\nu-1)x_3\phi_{,3} - 4(1-\nu)D\phi \\ & + 2x_3R_{,333} - 2x_3^2\phi_{,33}] - 2\nu e_{ii}[\phi^I + (3-4\nu)\phi + 2x_3\phi_{,3}] \end{aligned} \tag{10d}$$

The contribution of e_{33} in Eq. (10b) and Eq. (10d) could be equally written as $2e_{33}[\phi^I_{,3} - 2x_3\phi_{,33} + 2R_{,333} + 2D\psi_{,33} - (7-8\nu)\phi_{,3}]$ and $e_{33}[R^I_{,33} + (1-2D^2)R_{,22} + 4(1-\nu)D(x_3+x_3')\psi_{,22} + 8(\nu-1)x_3\phi_{,3} + 2x_3R_{,333} - 2x_3^2\phi_{,33}]$, respectively. The derivatives of F_i in Eq. (9) are complicated and consist of two types of volumetric integrals: (a) Terms with superscript I are identical to those for an infinite space and are 3D convolutions. This type of integral could be generically written as [16]

$$\int_\Omega e(\mathbf{x}')G(\mathbf{x} - \mathbf{x}')d\mathbf{x}' \tag{11}$$

where G is a generic function. (b) A one-dimensional correlation [16] has a form of $\int_{-\infty}^{\infty} e(x_i')G(x_i + x_i')dx_i'$. x_3 in Eq. (10) is an integral constant of the volumetric integrals. Terms without superscript I, which are modifying parts, are indeed convolutions in the x_1 and x_2 directions and correlation in the x_3 direction. This type of integral could be generically written as

$$\int\int\int_\Omega e(\mathbf{x}')G(x_1 - x_1', x_2 - x_2', x_3 + x_3')dx_1'dx_2'dx_3' \tag{12}$$

Given the convolution and correlation nature of individual terms in the derivatives of Eq. (9), the elastic field in a half-space is the summation of convolution and correlation terms. In contact mechanics research, the fast Fourier transform (FFT) is applied to improve the numerical evaluation process for convolution terms [18–23]. In this paper, FFT is applied to efficiently compute not only convolution terms but also correlation terms. FFT, once again, is a powerful numerical tool in contact mechanics studies.

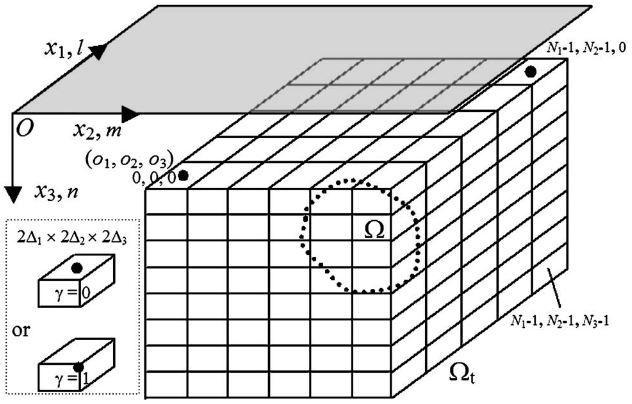

Fig. 2 Target domain, elements, grid points, and labels

The elastic field of a half-space could be obtained by Eqs. (1)–(3) with the similar procedure used for the infinite space problem described in the previous section.

2.3 Influence Coefficients and Integrals. In the formula for the elastic field, volumetric integrals consist of convolution and correlation. As pointed out by Chiu [3], one can subdivide the region Ω into a number of small cuboidal elements (see Fig. 2), each of which has a uniform distribution of eigenstrains. It should be pointed out that beside the region Ω (source), one should be aware of the other region where the elastic field is of interest. Generally the stress field inside and around Ω is necessary for a model. Since the plastic zone may reach the surface, the surface may be part of the region of interest. In order to do so, a rectangular domain called target domain (Ω_t) is defined, which encloses both Ω and the region, Ω_i, where the elastic field is of interest. When the region Ω_i is smaller than Ω, Sainsot et al. [12] pointed out a way to reduce the computation burden. The eigenstrains outside of Ω but inside of Ω_t are set as zero (zero padding for a series [16,23]). Ω_t has the size of $L_1 \times L_2 \times L_3$ and is divided into cuboidal elements (ΔE) of $2\Delta_1 \times 2\Delta_2 \times 2\Delta_3$. The total number of elements is $N_1 \times N_2 \times N_3$ with $N_j = L_j/(2\Delta_j)$. N_i is usually the power of 2. Each cuboidal element is labeled by three indices for three directions increasing along the axes. Discrete values of the elastic field can be evaluated theoretically at any location inside any element. These specific locations are called observation points. Here, element centers, or element upper-surface centers (with a normal of $-\hat{x}_3$), are recommended as observation points identified as element-centered ($\gamma = 1$) or face-centered ($\gamma = 0$), respectively. It is seen that the latter choice enables one to evaluate the surface elastic field. All discrete values are expressed by the name of the quantities with the element label as the subscript. The observation point with the smallest coordinates (o_1, o_2, o_3) is marked with subscript $\mathbf{x}_{0,0,0}$, where o_3 could be zero. All other observation points, $\mathbf{x}_{l,m,n}$, have coordinates of $(o_1 + 2l\Delta_1, o_2 + 2m\Delta_2, o_3 + 2n\Delta_3)$. Elements $\Delta E_{l,m,n}$ have intervals:

$$x_1 \in [o_1 + 2l\Delta_1 - \Delta_1, o_1 + 2l\Delta_1 + \Delta_1] \tag{13a}$$

$$x_2 \in [o_2 + 2m\Delta_2 - \Delta_2, o_2 + 2m\Delta_2 + \Delta_2] \tag{13b}$$

$$x_3 \in [o_3 + 2n\Delta_3 - \gamma\Delta_3, o_3 + 2n\Delta_3 + 2\Delta_3 - \gamma\Delta_3] \tag{13c}$$

where γ is determined by the type of observation points: Element-centered ($\gamma = 1$) and face-centered ($\gamma = 0$). Integrals labeled by (11) and (12) could be approximated by

$$\sum_{l=1}^{N_1}\sum_{m=1}^{N_2}\sum_{n=1}^{N_3} e_{l,m,n}\int_{\Delta E_{l,m,n}} G(x_i - x_1', x_j - x_2', x_k \mp x_3')d\mathbf{x}'$$

$$= \sum_{l=1}^{N_1}\sum_{m=1}^{N_2}\sum_{n=1}^{N_3} e_{l,m,n}\int_{o_3+(2n-\gamma)\Delta_3}^{o_3+(2n-\gamma+2)\Delta_3}\int_{o_2+(2m-1)\Delta_2}^{o_2+(2m+1)\Delta_2}$$

$$\times\int_{o_1+(2l-1)\Delta_1}^{o_1+(2l+1)\Delta_1} G(o_1 + 2i\Delta_1 - x_1', o_2 + 2j\Delta_2 - x_2', o_3$$

$$+ 2k\Delta_3 \mp x_3')d\mathbf{x}' \qquad (14)$$

One may use variable substitution of

$$\xi_1 = x_1 - x_1'$$

$$\xi_2 = x_2 - x_2' \qquad (15)$$

$$\text{and } \xi_3 = x_3 - x_3' \text{ for Eq. (11) (convolution)}$$

$$\text{or } \xi_3 = x_3 + x_3' \text{ for Eq. (12) (correlation),}$$

and change the integral limits so that the small value is the lower limit and the large value is the upper limit. Eq. (14) is rewritten as,

$$\sum_{l=1}^{N_1}\sum_{m=1}^{N_2}\sum_{n=1}^{N_3} e_{l,m,n}\int_{(2k-2n+\gamma-2)\Delta_3}^{(2k-2n+\gamma)\Delta_3}\int_{(2j-2m-1)\Delta_2}^{(2j-2m+1)\Delta_2}$$

$$\times\int_{(2i-2l-1)\Delta_1}^{(2i-2l+1)\Delta_1} G(\xi_1,\xi_2,\xi_3)d\xi \quad \text{(convolution)} \qquad (16a)$$

and

$$\sum_{l=1}^{N_1}\sum_{m=1}^{N_2}\sum_{n=1}^{N_3} e_{l,m,n}\int_{2o_3+(2k+2n-\gamma)\Delta_3}^{2o_3+(2k+2n+2-\gamma)\Delta_3}\int_{(2j-2m-1)\Delta_2}^{(2j-2m+1)\Delta_2}$$

$$\times\int_{(2i-2l-1)\Delta_1}^{(2i-2l+1)\Delta_1} G(\xi_1,\xi_2,\xi_3)d\xi \quad \text{(correlation and convolution)}$$

$$(16b)$$

Although Eq. (16*a*) and (16*b*) have different integral limits for $d\xi_3$, their 3D indefinite integrals are identical, which will be carried out in this section. Note that proper integral constants will be added or omitted in the indefinite integrals (not unique) in order to reach concise formulas, and these constants do not affect the definite integrals. Also the summation convention is not used in this section. Four key integrals can be pulled out from Eq. (9),

$$A_i = \int a_i d\xi \quad \text{with } a_1 = 1/r,\ a_2 = r,\ a_3 = \ln(r+\xi_3),$$

$$\text{and } a_4 = \xi_3\ln(r+\xi_3) \qquad (17)$$

where $r^2=\xi_1^2+\xi_2^2+\xi_3^2$. The explicit expressions of A_i are listed in the Appendix for reference. However, the derivatives of A_i are necessary for evaluating the elastic field. According to Eq. (15), a derivative with respect to x_3 is equivalent to one with respect to ξ_3. It is obvious that $A_{i,123}=a_i$ and $A_3=\int\int[\xi_3\ln(r+\xi_3)-r]d\xi_1 d\xi_2$. Since $A_4=\int\int\int(\partial/\partial\xi_3)[\xi_3\ln(r+\xi_3)-r]\xi_3 d\xi_1 d\xi_2 d\xi_3$, one can find that $2A_4=A_2+\xi_3 A_3$. Ahmadi's thesis [24] listed many useful double indefinite integrals and is helpful to obtain analytical expressions for the derivatives of A_i. Define four functions to simplify integral expressions,

$$U_k = \tan^{-1}\frac{\xi_j\xi_l}{\xi_k r} \qquad (18a)$$

$$V_k = \frac{1}{r(r+\xi_k)} \qquad (18b)$$

$$W_k = \frac{2r+\xi_k}{r^3(r+\xi_k)^2} \qquad (18c)$$

$$X_k = \tan^{-1}\frac{\xi_k}{r+\xi_l+\xi_j} \qquad (18d)$$

Note that $V_{k,l}=-\xi_l W_k$ and $V_{k,k}=-1/r^3$. Also, for a triple integration, $U_{k,l}=\xi_k\xi_j/[r(\xi_k^2+\xi_l^2)]$ is equivalent to $-\xi_k V_j$, and $U_{k,k}$ is equivalent to $\xi_l V_j+\xi_j V_l$. One can verify that the derivatives of X_k and $-\tan^{-1}[(r+\xi_l+\xi_j)/\xi_k]$ with respect to ξ_1, ξ_2, and ξ_3 are identical. Similarly, the derivatives of $\xi_k^n X_k$ and $(\xi_k^n/2)\tan^{-1}(\xi_j\xi_l/\xi_k r)$ (power n is a natural number) with respect to ξ_1, ξ_2, and ξ_3 are equal to each other. It seems that these terms are equivalent in terms of a triple integration. However, this is not the case due to the special characteristics of inverse tangent, and one should avoid interchanging them. Since ξ_1, ξ_2, and ξ_3 are interchangeable in a_1 and a_2, results for A_1 and A_2 could be concisely written with indices. In the following equations, indices j, k, and l are different ($j \neq k \neq l$) and each has a value of 1, 2, or 3.

$$A_{1,k} = \xi_j\ln(r+\xi_l) + \xi_l\ln(r+\xi_j) - \xi_k U_k,$$

$$A_{1,kl} = \ln(r+\xi_j), \quad A_{1,kk} = -U_k, \quad A_{1,kkl} = \xi_k V_j,$$

$$A_{1,kkk} = -\xi_j V_l - \xi_l V_j, \quad A_{1,123k} = -\xi_k/r^3, \quad A_{1,kkll} = -\xi_k\xi_l W_j,$$

$$A_{1,kkkk} = \xi_k\xi_l W_j + \xi_k\xi_j W_l, \quad A_{1,kkkl} = V_j - \xi_k^2 W_j,$$

$$A_{2,kkl} = \xi_k\ln(r+\xi_j), \quad A_{2,kkk} = \xi_j\ln(r+\xi_l) + \xi_l\ln(r+\xi_j) - 2\xi_k U_k,$$

$$A_{2,123k} = \xi_k/r, \quad A_{2,kkkl} = \ln(r+\xi_j) + \xi_k^2 V_j, \quad A_{2,kkll} = \xi_k\xi_l V_j, \qquad (19)$$

$$A_{2,kkkk} = -\xi_j\xi_k V_l - \xi_l\xi_k V_j - 2U_k,$$

$$A_{2,123kl} = -\xi_k\xi_l/r^3, \quad A_{2,123kk} = (\xi_l^2+\xi_j^2)/r^3,$$

$$A_{2,kkkll} = \xi_l V_j - \xi_k^2\xi_l W_j,$$

$$A_{2,kkkkl} = 3\xi_k V_j - \xi_k^3 W_j,$$

$$A_{2,kkkkk} = \xi_k^2\xi_l W_j - 3\xi_l V_j + \xi_k^2\xi_j W_l - 3\xi_j V_l$$

One can verify that the derivatives of the special integral function D in Chiu [3] are equivalent to those of A_2 times a factor of $-\pi^2$.

For A_3 and A_4, the derivative with respect to ξ_3 will change them into A_1 and $(A_3+A_{2,3})$, respectively. In the following equations, k and l are different and can only take a value of 1 or 2.

$$A_{3,kk} = -\xi_k\ln(r+\xi_l) - 2\xi_3 X_k, \quad A_{3,12} = \xi_3\ln(r+\xi_3) - r,$$

$$2A_{3,kkk} = -2\ln(r+\xi_l) - (\xi_k^2+\xi_3^2)V_l - (\xi_3 - r)\xi_l V_3,$$

$$A_{3,kkk} = -\frac{\xi_k}{r+\xi_3},$$

$$4A_{4,kkk} = 2\xi_l\ln(r+\xi_3) - \xi_3(\xi_k^2+\xi_3^2)V_l - \xi_3\xi_l(\xi_3 - r)V_3 - 4\xi_k U_k, \qquad (20)$$

$$2A_{4,kkl} = \xi_k\ln(r+\xi_3) - \frac{\xi_k\xi_3}{r+\xi_3}, \quad 2A_{4,kkll} = \xi_k\xi_l V_3 + \frac{\xi_k\xi_l\xi_3}{(r+\xi_3)^2 r},$$

$$4A_{4,kkkk} = V_3\xi_l\xi_k\left(\frac{\xi_3}{r} - 2\right) + \xi_3\xi_k[\xi_l(\xi_3 - r)W_3 - 6V_l + (\xi_k^2+\xi_3^2)W_l]$$

$$- 4U_k$$

$$4A_{4,kkkl} = 2\ln(r+\xi_3) + (3\xi_k^2 - 2\xi_3^2)V_3 + \xi_3\xi_l^2(\xi_3 - r)W_3 + \frac{\xi_l^2 r + (\xi_k^2 + \xi_3^2)\xi_3}{r^3}$$

One can verify these indefinite integrals by checking their derivatives with respect to ξ (since $\partial\xi = \partial\mathbf{x}$) with the help of software, such as MAPLE® or MATHEMATICA®. For instance, $\partial^3 A_{i,jk}/\partial\xi_1\partial\xi_2\partial\xi_3$ should equal $\partial^2 a_i/\partial\xi_j\partial\xi_k$.

The integrals over element $\Delta E_{l,m,n}$ evaluated at (x_i, x_j, x_k) in Eq. (14) are the influence coefficients (ICs). The ICs for convolution are considered first. In Eq. (16*a*), one can see that this type of ICs is related to the relative coordinates or relative labels. In order to remove redundancy, one can take the integral out from Eq. (16*a*) and set $l=m=n=0$,

$$D^{i,j,k} = \int_{(2k+\gamma-2)\Delta_3}^{(2k+\gamma)\Delta_3} \int_{(2j-1)\Delta_2}^{(2j+1)\Delta_2} \int_{(2i-1)\Delta_1}^{(2i+1)\Delta_1} G(\xi_1,\xi_2,\xi_3)d\xi \tag{21}$$

where i,j,k could be negative, $i \in [-N_1, N_1-1]$, $j \in [-N_2, N_2-1]$, and $k \in [-N_3, N_3-1]$. ICs for correlation are dependent on o_3 but can be handled in a similar way as those for convolution

$$D^{i,j,k} = \int_{2o_3+(2k-\gamma)\Delta_3}^{2o_3+(2k-\gamma+2)\Delta_3} \int_{(2j-1)\Delta_2}^{(2j+1)\Delta_2} \int_{(2i-1)\Delta_1}^{(2i+1)\Delta_1} G(\xi_1,\xi_2,\xi_3)d\xi \tag{22}$$

2.4 Surface Normal Displacement Due to Eigenstrains. Jacq et al. [13] utilized reciprocal theorem and the zero trace of plastic strains, then derived the integral and ICs formulae for surface normal displacement due to the plastic strains [see Eq. (1.13), (1.14) and Eq. (2.2)–(2.7) in [13]]. Note that (a) Eq. (2.2) in [13] is a convolution only after one properly adjusts (M,A) into (A,M); (b) The indefinite integrals are expressed in Eq. (2.7) where F_{ij} should be defined, in their notation, as follows instead of the definition given on p. 658 [13]

$$\frac{\partial^3 F_{ij}}{\partial x_1\partial x_2\partial x_3} = \begin{cases} \mu(u^*_{3i,j} + u^*_{3j,i}) & i=j \\ 2\mu(u^*_{3i,j} + u^*_{3j,i}) & i \neq j \end{cases}$$

These formulas are critical in contact analyses since efficient evaluation of the surface normal displacement directly shortens the computation time. In the following, the assumption of zero trace is removed, and an equation for surface normal displacement at $(x_1, x_2, 0)$ of a half-space subject to eigenstrains is simplified from Eqs. (1), (9), and (10) due to $x_3=0$,

$$\begin{aligned} u_3 = -\frac{1}{2\pi}\int_\Omega \{&-2e_{13}(R_{,133} - \phi_{,1}) - 2e_{23}(R_{,233} - \phi_{,2}) \\ &+ 2e_{12}(D\psi_{,12} + R_{,123}) + e_{11}(D\psi_{,11} + R_{,113}) + e_{22}(D\psi_{,22} + R_{,223}) \\ &+ e_{33}[(2\nu - 3)\phi_{,3} + R_{,333}] - 2\nu e_{ii}\phi_{,3}\}d\mathbf{x}' \end{aligned} \tag{23}$$

which is equivalent to the results by Jacq et al. [13]. One can see that in Eq. (23), except the integral with respect to x_3', the other two integrals are convolutions. The corresponding ICs can be found by using Eqs. (19) and (20) and the following:

$$D^{i,j,k} = \int_{o_3+(2k-\gamma)\Delta_3}^{o_3+(2k-\gamma+2)\Delta_3} \int_{(2j-1)\Delta_2}^{(2j+1)\Delta_2} \int_{(2i-1)\Delta_1}^{(2i+1)\Delta_1} G(\xi_1,\xi_2,\xi_3)d\xi \tag{24}$$

3 Numerical Scheme

3.1 Discrete Convolution-FFT Algorithm. Many researchers [20–23] have reported applications of FFT technique to linear elastic contact problems. The known FFT-based algorithms might fall into two categories [23]: (1) Continuous convolution and FFT (CC-FFT) algorithm, and (2) discrete convolution and FFT (DC-FFT) algorithm. The CC-FFT algorithm uses the frequency response function directly and encounters periodic error. The latter algorithm is more straightforward because a discrete series with a finite length requires the discrete convolution theorem and FFT. Zero padding and wrap around order are involved in the DC-FFT algorithm. Two-dimensional algorithms could be extended to three dimensional ones easily. The detailed algorithm can be found in [19,23].

3.2 Discrete Correlation-FFT Algorithm. A discrete correlation-FFT (DCR-FFT) algorithm, which is similar to the DC-FFT algorithm, is introduced here to handle correlation computation. The DCR-FFT algorithm is applicable for multidimension problems and can be combined with the DC-FFT algorithm to evaluate hybrid convolution and correlation expressions. However, in order to illustrate the principle of this algorithm clearly, a one-dimensional correlation is considered in this section.

$$\sigma_j = \sum_{i=1}^{N_3} e_i D_{i+j} \tag{25}$$

After zero padding and using a wrap-around order, the vector of the ICs, $\mathbf{D}$, becomes $\underline{\mathbf{D}}$, while the vector of the eigenstrains, $\mathbf{e}$, becomes $\underline{\mathbf{e}}$ after zero padding alone. Their FFT transformation, $\underline{\mathbf{D}}^F$ and $\underline{\mathbf{e}}^F$, have values corresponding to both positive and negative frequency. After the values in $\underline{\mathbf{D}}^F$ are interchanged between positive and negative frequency, the new vector is denoted by $\underline{\underline{\mathbf{D}}}^F$, and the application of the discrete correlation theorem to Eq. (25), vector σ could be recovered from the inverse FFT of the element-by-element multiplication between $\underline{\mathbf{e}}^F$ and $\underline{\underline{\mathbf{D}}}^F$,

$$\boldsymbol{\sigma} \Leftarrow IFFT(\underline{e}^F \underline{\underline{D}}^F) \tag{26}$$

For the hybrid expression of the convolution and the correlation, the DC-FFT algorithm and the DCR-FFT algorithm should be combined to handle the convolution and the correlation.

4 Results and Discussion

In this section, numerical results from the formulas and methods mentioned in the previous sections are compared to numerical results reported in [3,4] and to analytical results in order to verify all formulas and the numerical scheme. Simple strains are used, such as a strain with a single nonzero component or a thermoelastic strain, following the corresponding literature. Chiu's papers provide an excellent benchmark for Eqs. (18)–(20), since numerical results were obtained for problems with a cuboidal region specified with different uniform strains. Infinite space problems are always a good start for a numerical study, and numerical results of normal stresses using Eqs. (6*b*), (6*c*), and (18)–(20) are shown in Fig. 3 for $e_{11} \neq 0$ inside three different cuboids (2a × 2b × 2c). σ_{11} is shown by solid lines with filled symbols, and σ_{22} (or σ_{33}) is shown by dashed lines with unfilled symbols. Figure 3 is identical to Chiu's result (Fig. 2 in [3]). According to Eq. (23) and the corresponding indefinite integrals, the surface normal displacement at the origin is obtained for three types of strains inside a cube. The variation of u_3 with the depth of the cubic center in Fig. 4 clearly shows that the effect of the specified strain decays quickly as the cube goes deeper. Except the sign difference, Fig. 4 agrees with Chiu's result (Fig. 5 in [4]). The label of Fig. 5 in [4] may be missing a negative sign. The stress fields inside the half-space due to two different types of strains inside the same cube are shown in Figs. 5 and 6, respectively. The two figures overall agree with Figs. 2 and 3 in [4], although there are a few minor discrepancies, such as σ_{33} at point C with small Z_0/a. In general, all stresses decrease algebraically (less tensile stress or larger compressive stress) as the cube goes deeper, except for σ_{11} at the origin in Fig. 6 with small Z_0/a. These comparisons verify almost all formulae presented in previous sections.

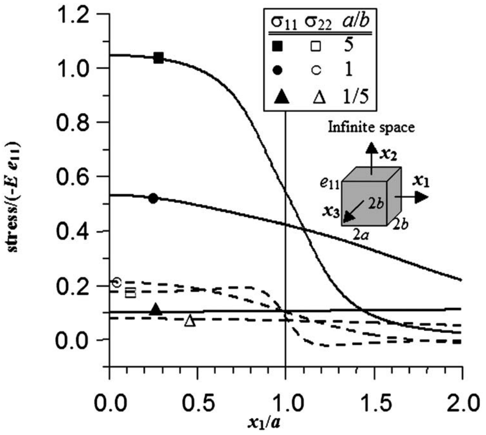

Fig. 3 Variation of stresses ($\sigma_{11}, \sigma_{22}=\sigma_{33}$) in an infinite space along the x_1 axis due to a specified strain, e_{11}, uniformly distributed over an origin-centered cuboid for three different a/b values

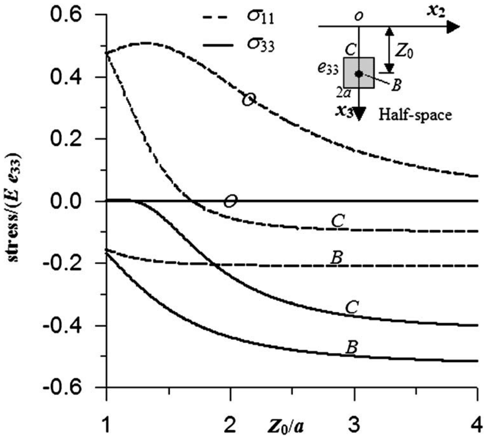

Fig. 6 Stress ($\sigma_{11}=\sigma_{22}$ and σ_{33}) of a half-space at three different locations (*o*, *C*, and *B*) due to a specified strain, e_{33}, inside a cuboid vs the depth of the cubic center

When Ω is a spherical region of radius a with the center at $(0,0,Z_0)$, Mindlin and Cheng [25] found the thermoelastic field by using the well-known results [26] for the potential for a homogeneous sphere

$$\int_\Omega \phi^I d\mathbf{x}' = \frac{4\pi a^3}{3R_-} \quad \mathbf{x} \in \Omega$$

$$\int_\Omega \phi^I d\mathbf{x}' = \frac{2\pi(3a^3 - R_-^2)}{3R_-} \quad \mathbf{x} \notin \Omega$$

$$\int_\Omega \phi d\mathbf{x}' = \frac{4\pi a^3}{3R_+} \quad \forall \mathbf{x} \tag{27}$$

where $R_\pm = \sqrt{x_1^2+x_2^2+(x_3 \pm Z_0)^2}$. The thermoelastic strain is expressed as $e_{ij}=\alpha T\delta_{ij}$, where αT is constant. Mindlin and Cheng's solutions [25] are used to benchmark both the formulas and the new numerical scheme. The target domain is $(-2a:2a, -2a:2a, 0:3a)$ in the three directions and is divided into $128 \times 128 \times 256$ elements. A personal computer with the Pentium 4 CPU (1.8 GHz) is used to carry out numerical simulation. Variations of stress σ_{33} along the x_3 axis due to a uniform thermoelastic strain inside the sphere for two different depths of the center (a or $1.5a$) are shown in Fig. 7, where the stress is normalized by $\sigma_0 = 2(1+\nu)\mu\alpha T/3(1-\nu)$. The corresponding analytical results are shown as well for comparison. The minor difference between the

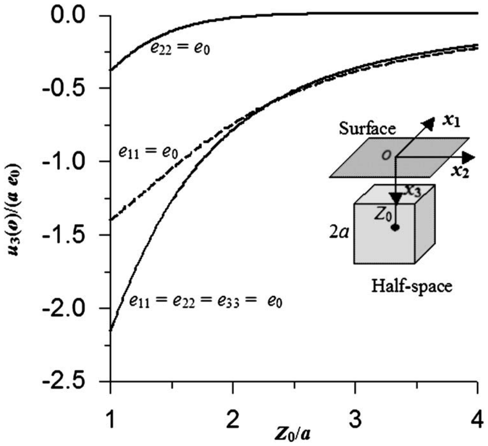

Fig. 4 Variation of u_3 at the origin of a half-space with the depth of the cubic center for three different strains

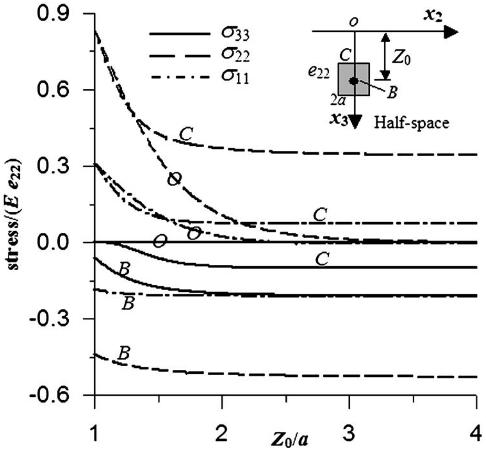

Fig. 5 Stresses (σ_{11}, σ_{22}, and σ_{33}) at three different locations (*o*, *A*, and *B*) in a half-space due to a specified strain, e_{22}, inside a cuboid vs the depth of the cubic center

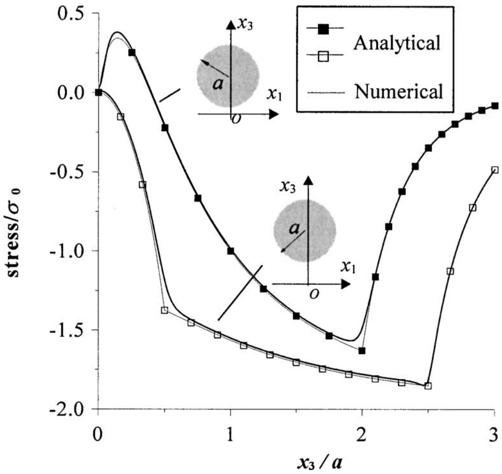

Fig. 7 Stress σ_{33} of a half-space along the x_3 axis due to a uniform thermoelastic strain inside a sphere (radius a) for two different depths of the center (a or $1.5a$)

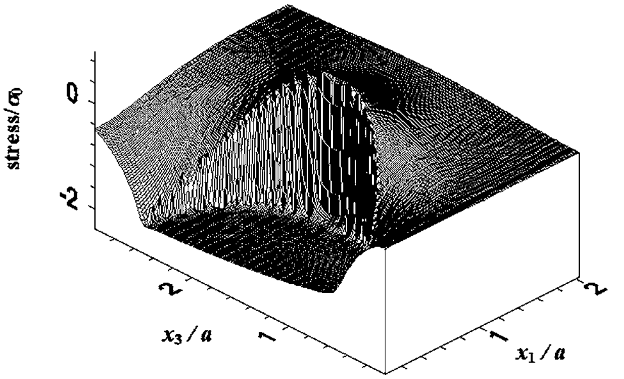

Fig. 8 Distribution of stress σ_{33} over the center section with $x_2=0$ due to a thermoelastic strain

numerical and analytical results could be attributed to discretization error. Similar to the case with the cube, the deeper the sphere, the smaller the stress σ_{33}. It is also noted that the existence of the surface causes tensile stress σ_{33} when the sphere is very close to the surface. No tensile stress σ_{33} is found for $Z_0=1.5a$. Figure 8 depicts the three-dimensional (3D) distribution of stress σ_{33} over the center section ($x_2=0$) for $Z_0=1.5a$. Although stress σ_{33} is continuous along the x_3 axis (Fig. 7), it is not continuous elsewhere due to the discontinuity of the applied strain. The compressive stress is dominant, while the tensile stress appears only in the neighborhood of the circle at the intersection of the sphere and the plane of $x_3=1.5a$. In order to demonstrate the capability of our method for solving problems with nonuniformly distributed strains, the region inside the sphere (radius$=a$) is specified with a thermoelastic strain proportional to the distance between a location and the spherical center, $e_{ij}=cR\_\delta_{ij}$, where c is a constant. Variations of stress σ_{33} along the x_3 axis due to this specified thermoelastic strain with two different depths of the center (a or $1.5a$) are depicted in Fig. 9. The corresponding 3D distribution is shown in Fig. 10. The stress is normalized by $\sigma_0=2(1+\nu)\mu c/3(1-\nu)$. It is interesting to see that stress σ_{33} is almost linear inside the sphere.

5 Conclusions

The existing superposition method used to find the elastic field in a half-space with eigenstrains is indirect and complicated. This paper presents a direct method by means of the Mindlin and Cheng's results. A set of analytical formulae for influence coefficients in terms of derivatives of four key integrals is presented and is used to express the elastic field caused by the eigenstrains with arbitrary distribution in a half-space. These formulae are benchmarked by analytical or existing numerical results. Based on the nature of the integral expressions of the elastic field, the discrete correlation and fast Fourier transform (DCR-FFT) is applied. Both discrete convolution and fast Fourier transform (DC-FFT) and DCR-FFT algorithms are used to accelerate the numerical calculation. The straightforward formulae and the numerical algorithms reduce the difficulties of code development and enable fast and accurate analyses of inclusion problems and contact problems.

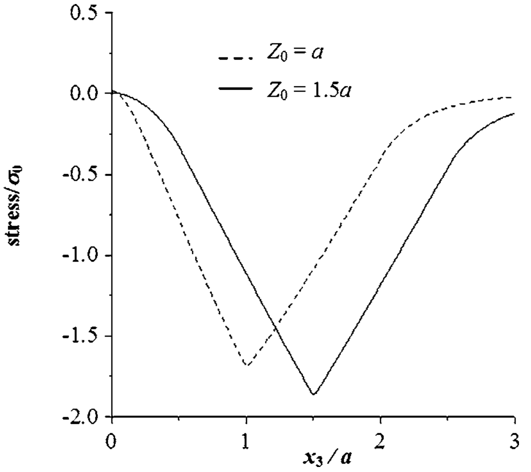

Fig. 9 Variation of stress σ_{33} of a half-space along the x_3 axis due to a thermoelastic strain

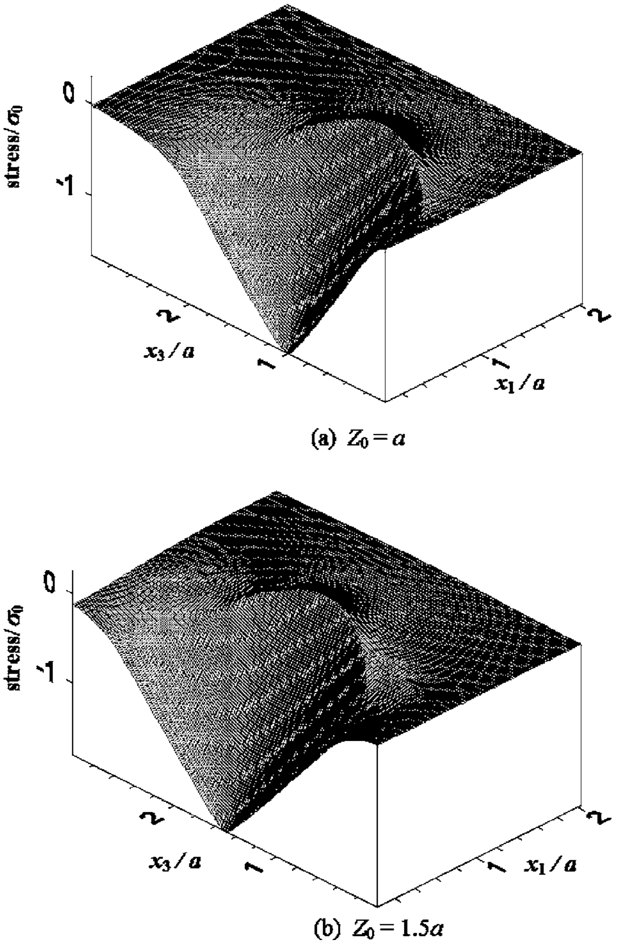

(a) $Z_0=a$

(b) $Z_0=1.5a$

Fig. 10 Distribution of stress σ_{33} over the center section with $x_2=0$ due to a thermoelastic strain. (a) $Z_0=a$; (b) $Z_0=1.5a$

Acknowledgment

S.L. would like to thank Dr. Keer, Dr. Nélias, Mr. Fan Wang, and Mr. Vincent Boucly for their helpful discussions. The authors would like to express their sincere gratitude to the support from US Office of Naval Research and National Science Foundation.

Nomenclature

$C = -\mu/4\pi(1-\nu)$
$D = 1-2\nu$
$r = \sqrt{\xi_1^2+\xi_2^2+\xi_3^2}$
$R^I = \sqrt{(x_1-x_1')^2+(x_2-x_2')^2+(x_3-x_3')^2}$
$R = \sqrt{(x_1-x_1')^2+(x_2-x_2')^2+(x_3+x_3')^2}$
$V_k = 1/r(r+\xi_k)$
$W_k = (2r+\xi_k)/r^3(r+\xi_k)^2$

X_k = $\tan^{-1}[\xi_k/(r+\xi_l+\xi_j)]$
U_k = $\tan^{-1}(\xi_l\xi_j/r\xi_k)$
u_i = displacements
δ_{ij} = Kronecker's delta
e_{ij} = eigenstrains (inelastic strains)
μ, λ = shear modulus and Lame's constant, $2\mu\nu/(1-2\nu)$
ν = Poisson's ratio
σ_{ij} = stress
θ = $R-(x_3+x'_3)\psi$
ϕ = $\phi^I=1/R^I$, $\phi=1/R$, harmonic potentials
ψ = $\ln[R+(x_3+x'_3)]$, logarithmic potential
Ω = domain with eigenstrains
Ω_{t} = target domain (domain of interest)

Appendix A: Equalities and Integrals

A.1 Useful Equalities

$$\psi_{,3}=\phi, \quad \theta_{,3}=-\psi$$

$$\nabla^2 R^I = 2\phi^I, \quad \nabla^2 R = 2\phi$$

$$\nabla^2\phi = 0$$

$$\nabla^2\psi = 0 \quad \nabla^2 \ln[R^I-(x_3-x'_3)] = 0$$

$$\nabla^2\theta = 0$$

$$\nabla^2[(x_i-x'_i)\psi] = 2\psi_{,i} \quad (i=1,2)$$

$$\nabla^2[x_3\psi] = 2\psi_{,3} = 2\phi$$

$$\nabla^2[x_3\phi] = 2\phi_{,3}, \quad \nabla^2[x_3\phi_{,3}] = 2\phi_{,33}$$

$$R_{,3} = (x_3+x'_3)\phi \quad \text{or} \quad x'_3\phi = R_{,3} - x_3\phi$$

$$\text{in general,} \quad R_{,\underbrace{3\ldots3}_{n}} = (x_3+x'_3)\phi_{,\underbrace{3\ldots3}_{n-1}} + (n-1)\phi_{,\underbrace{3\ldots3}_{n-2}}$$

$$\text{in general,} \quad R_{,3\underset{n}{\ldots}3} = (x_3+x'_3)\phi_{,3\underset{n-1}{\ldots}3} + (n-1)\phi_{,3\underset{n-2}{\ldots}3}$$

A.2 Volumetric Integrals

$$A_1 = \xi_1\xi_2\ln(r+\xi_3) + \xi_2\xi_3\ln(r+\xi_1) + \xi_3\xi_1\ln(r+\xi_2) - \frac{1}{2}(\xi_1^2U_1+\xi_2^2U_2+\xi_3^2U_3)$$

$\times$([26], p . 78 and 79)

$$A_2 = \frac{\xi_1\xi_2\xi_3 r}{4} - \frac{1}{12}(\xi_1^4U_1+\xi_2^4U_2+\xi_3^4U_3) + \frac{1}{6}[(r^2-\xi_1^2)\xi_2\xi_3\ln(r+\xi_1) + (r^2-\xi_2^2)\xi_3\xi_1\ln(r+\xi_2) + (r^2-\xi_3^2)\xi_1\xi_2\ln(r+\xi_3)]$$

The above expressions can be found in [6] (p. 108) or [27]

$$A_3 = \int\int[\xi_3\ln(r+\xi_3)-r]d\xi_1 d\xi_2$$

$$A_3 = \xi_1\xi_2\xi_3\ln(r+\xi_3) - \frac{1}{6}(\xi_1^2-3\xi_3^2)\xi_1\ln(r+\xi_2) - \frac{1}{6}(\xi_2^2-3\xi_3^2)\xi_2\ln(r+\xi_1) - \xi_1^2\xi_3X_1 - \xi_2^2\xi_3X_2 - \frac{\xi_3^3}{6}U_3 - \frac{3}{2}\xi_1\xi_2\xi_3 - \frac{1}{3}r\xi_1\xi_2$$

$$2A_4 = A_2 + \xi_3 A_3$$

$$2A_4 = -\frac{\xi_1\xi_2\xi_3 r}{12} - \frac{3\xi_1\xi_2\xi_3^2}{2} - \frac{1}{12}(\xi_1^4U_1+\xi_2^4U_2+3\xi_3^4U_3) + \frac{2}{3}[\xi_2\xi_3^2\ln(r+\xi_1) + \xi_1\xi_3^2\ln(r+\xi_2)] + \xi_1\xi_2\left(\xi_3^2 + \frac{\xi_1^2+\xi_2^2}{6}\right)\ln(r+\xi_3) - \xi_3^2\xi_1^2X_1 - \xi_3^2\xi_2^2X_2$$

References

[1] Seo, K., and Mura, T., 1979, "The Elastic Field in a Half Space Due to Ellipsoidal Inclusions With Uniform Dilatational Eigenstrains," ASME J. Appl. Mech., **46**, pp. 568–572.
[2] Mindlin, R. D., and Cheng, D. H., 1950, "Nuclei of Strain in the Semi-Infinite Solid," J. Appl. Phys., **21**, pp. 926–930.
[3] Chiu, Y. P., 1977, "On the Stress Field Due to initial Strains in a Cuboid Surrounded by an Infinite Elastic Space," ASME J. Appl. Mech., **44**, pp. 587–590.
[4] Chiu, Y. P., 1978, "On the Stress Field and Surface Deformation in a Half Space With a Cuboidal Zone in Which initial Strains are Uniform," ASME J. Appl. Mech., **45**, pp. 302–306.
[5] Lee, S., and Hsu, C. C., 1985, "Thermoelastic Stress Due to Surface Parallelepiped Inclusions," ASME J. Appl. Mech., **52**(1), pp. 225–228.
[6] Mura, T., 1987, *Micromechanics of Defects in Solids*, 2nd ed., Martinus-Nijhoff, Dordrecht.
[7] Wu, L. Z., and Du, S. Y., 1996, "The Elastic Field in a Half-space With a Circular Cylindrical Inclusion," ASME J. Appl. Mech., **63**(4), pp. 925–932.
[8] Mura, T., 1997, "The Determination of the Elastic Field of a Polygonal Star Shaped Inclusion," Mech. Res. Commun., **24**(5), pp. 473–482.
[9] Korsunsky, A. M., 1997, "An Axisymmetric Inclusion in One of Two Perfectly Bonded Dissimilar Elastic Half-Spaces," ASME J. Appl. Mech., **64**, pp. 697–700.
[10] Müller, W. H., and Neumann, S., 1998, "An Approximate Analytical 3-D Solution for the Stresses and Strains in Eigenstrained Cubic Materials," Int. J. Solids Struct., **35**(22), pp. 2931–2958.
[11] Yoffe, E. H., 1982, "Elastic Stress Fields Caused by Indenting Brittle Materials," Philos. Mag. A, **46**, pp. 617–628.
[12] Sainsot, P., Jacq, C., and Nélias, D., 2002, "A Numerical Model for Elastoplastic Rough Contact," Comput. Model. Eng. Sci., **3**(4), pp. 497–506.
[13] Jacq, C., Nélias, D., Lormand, G., and Girodin, D., 2002, "Development of a Three-Dimensional Semi-Analytical Elastic-Plastic Contact Code," ASME J. Tribol., **124**(4), pp. 653–667.
[14] Yu, H. Y., and Sanday, S. C., 1991, "Elastic Fields in Joined Half-Spaces Due to Nuclei of Strain," Proc. R. Soc. London, Ser. A, **434** (1892), pp. 503–519.
[15] Johnson, K. L., 1996, *Contact Mechanics*, Cambridge University Press, Cambridge, UK.
[16] Press, W. H., Teukolsky, S. A., Vetterling, W. T., and Flannery, B. P., 1992, *Numerical Recipes in Fortran 77—The Art of Scientific Computing*, 2nd ed., Cambridge University Press, Cambridge.
[17] Yu, H. Y., and Sanday, S. C., 1991, "Elastic Field In Joined Semi-Infinite Solids With An Inclusion," Proc. R. Soc. London, Ser. A, **434** (1892), pp. 521–530.
[18] Liu, S., and Wang, Q., 2003, "Transient Thermoelastic Stress Fields in a Half-Space," ASME J. Tribol., **125**, pp. 33–43.
[19] Liu, S., and Wang, Q., 2002, "Studying Contact Stress Fields Caused by Surface Tractions With a Discrete Convolution and Fast Fourier Transform Algorithm," ASME J. Tribol., **124**, pp. 36–45.
[20] Ju, Y., and Farris, T. N., 1996, "Spectral Analysis of Two-Dimensional Contact Problems," ASME J. Tribol., **118**, pp. 320–328.
[21] Nogi, T., and Kato, T., 1997, "Influence of a Hard Surface Layer on the Limit of Elastic Contact—Part I: Analysis Using a Real Surface Model," ASME J. Tribol., **119**, pp. 493–500.
[22] Polonsky, I. A., and Keer, L. M., 2000, "A Fast and Accurate Method for Numerical Analysis of Elastic Layered Contacts," ASME J. Tribol., **122**, pp. 30–35.
[23] Liu, S., Wang, Q., and Liu, G., 2000, "A Versatile Method of Discrete Convolution and FFT (DC-FFT) for Contact Analyses," Wear, **243**(1-2), pp. 101–110.
[24] Ahmadi, N., 1982, *Non-Hertzian Normal and Tangential Loading of Elastic Bodies in Contact*, Ph.D. dissertation, Northwestern University, Evanston, IL.
[25] Mindlin, R. D., and Cheng, D. H., 1950, "Thermoelastic Stress in the Semi-Infinite Solid," J. Appl. Phys., **21**, pp. 931–933.
[26] MacMillan, W. D., 1930, *Theory of the Potential*, McGraw-Hill, New York.
[27] Lee, J. K., and Johnson, W. C., 1977, "Elastic Strain Energy and Interactions of Thin Square Plates Which Have Undergone a Simple Shear," Scripta Metall., **11**, pp. 477–484.

Axisymmetrical Snapping of a Spinning Nonflat Disk

Jen-San Chen
Professor
e-mail: jschen@ccms.ntu.edu.tw

Chi-Chung Lin
Graduate Student

Department of Mechanical Engineering,
National Taiwan University,
Taipei, Taiwan 10617 R.O.C.

In this paper we study the steady-state deflection of a spinning nonflat disk, both theoretically and experimentally. Both the initial and the deformed shapes of the disk are assumed to be axisymmetrical. Von Karman's plate model is adopted to formulate the equations of motion, and Galerkin's method is employed to discretize the partial differential equations. In the case when the initial height of the nonflat disk is sufficiently large, multiple equilibrium positions can exist, among them the two stable one-mode solutions P_0^1 *and* P_0^3 *are of particular interest. Theoretical investigation shows that if the disk is initially in the stressed position* P_0^3, *it will be snapped to position* P_0^1 *when the rotation speed reaches a critical value. Experiments on a series of copper disks with different initial heights are conducted to verify the theoretical predictions. Generally speaking, the experimental measurements agree well with theoretical predictions when the initial height is small. For the disks with large initial heights, on the other hand, the measured snapping speeds are significantly below the theoretical predictions. The circumferential waviness of the copper disks induced in the manufacturing process and the aerodynamic force at high rotation speed are two possible factors causing this discrepancy.*

[DOI: 10.1115/1.2043188]

Introduction

Most of the research in flexible disk dynamics assume that the disk is perfectly flat before deformation. However, it is inevitable that runout be produced in the manufacturing process of the disk. In investigating the head-disk interface of a flexible disk, Ono and Maeno [1] concluded that it is necessary to take into account the nonflatness of the disk in order to model the interface force correctly. Capino [2] studied the interaction between the gas flow and a disk of initial transverse runout rotating close to a rigid flat plate. To study the effect of spinning speed on the disk runout, Benson and Cole [3] used the finite difference method to analyze four example warped disks and conducted experiments on one of them. Jia [4] worked on the same problem with the Galerkin method. In these previous studies, the runout and the deformation of the disks are assumed to be small, and a linearized plate equation is used to predict the steady-state deflection.

In this paper we extend Benson and Cole's [3] work to consider a "larger" initial warpage and deflection (but small strain and curvature still) of the spinning disk. To achieve this we formulate the nonlinear equations of a spinning disk based on von Karman's plate model, which is capable of taking into account the membrane stretching due to bending deflection. The nonlinear equations of motion of a spinning flat disk were first formulated by Nowinski [5]. Here we extend Nowinski's formulation to a spinning disk with initial runout. The equations are nondimensionalized with careful examination on the order of magnitude of the out-of-plane and in-plane deflections. The nonlinear equations can be reduced to the conventional equation as the thickness parameter of the plate approaches zero. We then use the Galerkin method twice to discretize the partial differential equations into a system of ordinary differential equations. By analyzing these nonlinear equations we can calculate the steady-state deflections and study the stability of these equilibrium configurations. Experiments on a series of copper disks are conducted to verify the theoretical predictions.

Equations of Motion

We consider an elastic circular thin nonflat disk spinning with constant speed Ω, as shown in Fig. 1(*a*). The nonflat disk is called "thin" if the ratio of its thickness to the radius of curvature of its middle surface is much less than unity. The disk is assumed to be fully clamped at the inner radius $r=a$ and free at the outer radius b. We assume that the initial (unstressed) shape w_0 and the transverse deflection w, both measured from the same base plane, are of the order of magnitude of the thickness h.

In order to derive the equation of motion, we consider a small element of the middle surface of the spinning disk, with transverse shear resultants Q_r, Q_θ, $Q_{r\theta}$, bending and twisting moments M_r, M_θ, $M_{r\theta}$, and membrane stress resultants N_r, N_θ, and $N_{r\theta}$ acting on the boundary, as shown in Fig. 1(*b*). The element is also subjected to a force $\rho h r^2\Omega^2 dr d\theta$ at the center of the element in the radial direction due to centrifugal body force, where ρ is the mass density of the disk. By considering the force balance in the z direction, we can write the equation of motion of the spinning disk with respect to the body-fixed coordinate system (r,θ) as

$$\rho h r w_{,tt} - (N_r r w_{,r})_{,r} - r^{-1}(N_\theta w_{,\theta})_{,\theta} - (N_{r\theta} w_{,\theta})_{,r} - (N_{r\theta} w_{,r})_{,\theta} = (rQ_r)_{,r} + Q_{\theta,\theta} \tag{1}$$

From the moment balance conditions with respect to the θ and r axes, we obtain the relations of the form

$$Q_\theta = r^{-1}[(rM_{r\theta})_{,r} + M_{\theta,\theta} + M_{r\theta}] \tag{2}$$

$$Q_r = r^{-1}[-M_\theta + (rM_r)_{,r} + M_{r\theta,\theta}] \tag{3}$$

The equilibrium equations in the radial and tangential directions are

$$(rN_r)_{,r} + N_{r\theta,\theta} - N_\theta + \rho h r^2\Omega^2 = 0 \tag{4}$$

$$(rN_{r\theta})_{,r} + N_{\theta,\theta} + N_{r\theta} = 0 \tag{5}$$

The two equilibrium equations (4) and (5) can be satisfied automatically by assuming a stress function ϕ, which is defined as follows:

Contributed by the Applied Mechanics Division of THE AMERICAN SOCIETY OF MECHANICAL ENGINEERS for publication in the ASME JOURNAL OF APPLIED MECHANICS. Manuscript received by the Applied Mechanics Division, June 3, 2004; final revision, March 5, 2005. Review conducted by O. O'Reilly. Discussion on the paper should be addressed to the Editor, Prof. Robert M. McMeeking, Journal of Applied Mechanics, Department of Mechanical and Environmental Engineering, University of California-Santa Barbara, Santa Barbara, CA 93106-5070, and will be accepted until four months after final publication of the paper itself in the ASME JOURNAL OF APPLIED MECHANICS.

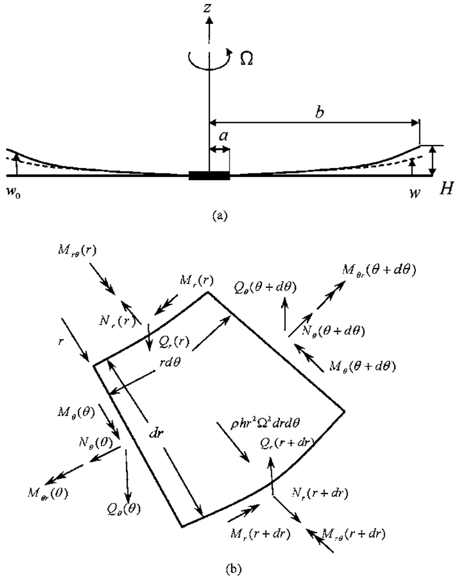

Fig. 1 (*a*) **A spinning nonflat disk and** (*b*) **a disk element**

$$N_r = r^{-1}\phi_{,r} + r^{-2}\phi_{,\theta\theta} - \tfrac{1}{2}\rho h\Omega^2 r^2 \tag{6}$$

$$N_\theta = \phi_{,rr} - \tfrac{1}{2}\rho h\Omega^2 r^2 \tag{7}$$

$$N_{r\theta} = -(r^{-1}\phi_{,\theta})_{,r} \tag{8}$$

We assume that Hooke's law is valid throughout, in particular, in its isotropic form. The relations between the bending moments and disk deflection are

$$M_r = -D[(w-w_0)_{,rr} + \nu(r^{-1}(w-w_0)_{,r} + r^{-2}(w-w_0)_{,\theta\theta})] \tag{9}$$

$$M_\theta = -D[r^{-1}(w-w_0)_{,r} + r^{-2}(w-w_0)_{,\theta\theta} + \nu(w-w_0)_{,rr}] \tag{10}$$

$$M_{r\theta} = -(1-\nu)D[r^{-1}(w-w_0)_{,r\theta} - r^{-2}(w-w_0)_{,\theta}] \tag{11}$$

where

$$D = \frac{Eh^3}{12(1-\nu^2)}$$

E and ν are Young's modulus and Poisson's ratio of the disk. Equations (9)–(11) assume that the curvatures of the initial and stressed shapes of the disk are small compared to unity. The relations between the stress resultants and the in-plane strains are

$$\varepsilon_r = \frac{1}{hE}(N_r - \nu N_\theta) \tag{12}$$

$$\varepsilon_\theta = \frac{1}{hE}(N_\theta - \nu N_r) \tag{13}$$

$$\gamma_{r\theta} = \frac{2(1+\nu)}{hE}N_{r\theta} \tag{14}$$

The relations between the strains and the displacement are nonlinear

$$\varepsilon_r = u_{r,r} + \tfrac{1}{2}(w_{,r})^2 - \tfrac{1}{2}(w_{0,r})^2 \tag{15}$$

$$\varepsilon_\theta = r^{-1}u_r + r^{-1}u_{\theta,\theta} + \tfrac{1}{2}r^{-2}(w_{,\theta})^2 - \tfrac{1}{2}r^{-2}(w_{0,\theta})^2 \tag{16}$$

$$\gamma_{r\theta} = [r^{-1}u_{r,\theta} + u_{\theta,r} - r^{-1}u_\theta + r^{-1}w_{,r}w_{,\theta} - r^{-1}w_{0,r}w_{0,\theta}] \tag{17}$$

where u_r and u_θ are the radial and tangential displacements of a material point relative to the body-fixed coordinate system.

After substituting Eqs. (2), (3), (6), and (11) into Eq. (1), we obtain the equation of motion of the spinning disk in the z direction

$$\begin{aligned}\rho h w_{,tt} + D\nabla^4(w-w_0) &= w_{,rr}(r^{-1}\phi_{,r} + r^{-2}\phi_{,\theta\theta}) + (r^{-1}w_{,r}\\ &\quad + r^{-2}w_{,\theta\theta})\phi_{,rr} - 2(r^{-1}w_{,\theta})_{,r}(r^{-1}\phi_{,\theta})_{,r}\\ &\quad - \rho h\Omega^2 r\left(\frac{r}{2}\nabla^2 w + w_{,r}\right)\end{aligned} \tag{18}$$

By using Eqs. (12)–(14) and (6)–(8), one can derive the following compatibility equation:

$$\begin{aligned}r^{-1}(r\varepsilon_\theta)_{,rr} - r^{-1}\varepsilon_{r,r} - r^{-2}(r\gamma_{r\theta,\theta})_{,r} + r^{-2}\varepsilon_{r,\theta\theta}\\ = \frac{1}{hE}\nabla^2(N_r + N_\theta) + 2(1+\nu)\rho h\Omega^2\end{aligned} \tag{19}$$

Substituting Eqs. (15)–(17) and (6)–(8) into Eq. (19), we obtain the equation governing the stress function ϕ as

$$\begin{aligned}\nabla^4\phi = Eh[&-w_{,rr}(r^{-1}w_{,r} + r^{-2}w_{,\theta\theta}) + (r^{-1}w_{,r\theta} - r^{-2}w_{,\theta})^2\\ &+ w_{0,rr}(r^{-1}w_{0,r} + r^{-2}w_{0,\theta\theta}) - (r^{-1}w_{0,r\theta} - r^{-2}w_{0,\theta})^2]\\ &+ 2(1-\nu)\rho h\Omega^2\end{aligned} \tag{20}$$

In the special case when $w_0=0$, Eqs. (18) and (20) reduce to the equations of motion formulated by Nowinski [5].

Nondimensionalization

Equations (18) and (20) can be nondimensionalized by introducing the following dimensionless quantities (with superposed asterisk):

$$t^* = \frac{t}{b^2}\sqrt{\frac{D}{\rho h}}, \quad \Omega^* = \Omega b^2\sqrt{\frac{\rho h}{D}}, \quad r^* = \frac{r}{b}, \quad (w^*, w_0^*) = \frac{1}{h}(w, w_0)$$

$$\phi^* = \frac{\phi}{D}, \quad \eta = \frac{a}{b}, \quad (N_r^*, N_\theta^*, N_{r\theta}^*) = \frac{b^2}{D}(N_r, N_\theta, N_{r\theta})$$

$$U^* = \frac{D}{b^2h^2}U, \quad (\sigma_{rb}^*, \sigma_{\theta b}^*) = \frac{b^2}{Dh}(\sigma_{rb}, \sigma_{\theta b})$$

The parameters U and $(\sigma_{rb}, \sigma_{\theta b})$ are the strain energy and bending stresses of the disk, which will be discussed later. After substituting the above relations into Eqs. (18) and (20), and dropping all the superposed asterisks thereafter for simplicity, we obtain the following dimensionless equations:

$$\begin{aligned}w_{,tt} + \nabla^4(w-w_0) &= w_{,rr}(r^{-1}\phi_{,r} + r^{-2}\phi_{,\theta\theta}) + (r^{-1}w_{,r} + r^{-2}w_{,\theta\theta})\phi_{,rr}\\ &\quad - 2(r^{-1}w_{,\theta})_{,r}(r^{-1}\phi_{,\theta})_{,r} - \Omega^2 r\left(\frac{r}{2}\nabla^2 w + w_{,r}\right)\end{aligned} \tag{21}$$

$$\begin{aligned}\nabla^4\phi = 12(1-\nu^2)[&-w_{,rr}(r^{-1}w_{,r} + r^{-2}w_{,\theta\theta}) + (r^{-1}w_{,r\theta} - r^{-2}w_{,\theta})^2\\ &+ w_{0,rr}(r^{-1}w_{0,r} + r^{-2}w_{0,\theta\theta}) - (r^{-1}w_{0,r\theta} - r^{-2}w_{0,\theta})^2]\\ &+ 2(1-\nu)\Omega^2\end{aligned} \tag{22}$$

Axisymmetrical Deformations

In this paper we assume that the initial shape w_0 is axisymmetric. It is well known that a shallow shell with an axisymmetric initial shape admits both axisymmetrical and asymmetrical deformations. However, the asymmetrical configurations are important only when the shallow shell is under dynamic load and the initial height of the shell is large [6,7]. Since in this paper we are interested in the steady-state deformation and static snap-through phenomenon of a nonflat disk with a relatively low initial height, we assume that the axisymmetrical deformation dominates the behavior of the disk to avoid unnecessary complication in algebraic manipulation. The justification of this simplification will be examined later by experimental observation. Following these simplifications, the governing equations (21) and (22) can be reduced to

$$u_{,tt}+\nabla^4 u = r^{-1}(u+w_0)_{,rr}\phi_{,r}+r^{-1}(u+w_0)_{,r}\phi_{,rr} - \Omega^2 r\left[\frac{r}{2}\nabla^2(u+w_0)+(u+w_0)_{,r}\right] \tag{23}$$

$$\nabla^4\phi = -12(1-\nu^2)r^{-1}[u_{,r}u_{,rr}+u_{,r}w_{0,rr}+w_{0,r}u_{,rr}]+2(1-\nu)\Omega^2 \tag{24}$$

where

$$u = w - w_0 \tag{25}$$

The boundary conditions for u at inner radius $r=\eta$ are

$$u = 0 \tag{26}$$

$$u_{,r} = 0 \tag{27}$$

At outer radius $r=1$ the boundary conditions are

$$(\nabla^2 u)_{,r} = 0 \tag{28}$$

$$u_{,rr}+\nu r^{-1}u_{,r} = 0 \tag{29}$$

The zero in-plane displacement boundary conditions for ϕ at $r=\eta$ can be written as [7]

$$\phi_{,rr}-\nu r^{-1}\phi_{,r} = 0 \tag{30}$$

$$r\phi_{,rrr}+(\nu-1)r^{-1}\phi_{,r} = 0 \tag{31}$$

The traction-free boundary condition $N_r=0$ at $r=1$ can be written as

$$r^{-1}\phi_{,r} = \tfrac{1}{2}\Omega^2 r^2 \tag{32}$$

The other condition $N_{r\theta}=0$ at $r=1$ is satisfied automatically. To fix the problem that we have only three boundary conditions for ϕ, we use a trivial condition $\phi=0$ at $r=1$. It is noted that the stress resultants will not be changed by adding an arbitrary constant to the stress function.

It is noted that although Eqs. (23) and (24) are nonlinear in terms of u, they are linear in ϕ. Therefore, we can divide the stress function ϕ in Eq. (24) into two parts

$$\phi = \phi_1 + \phi_2 \tag{33}$$

The first part ϕ_1 accounts for the centrifugal effect and satisfies the inhomogeneous equation

$$\nabla^4\phi_1 = 2(1-\nu)\Omega^2 \tag{34}$$

ϕ_1 satisfies the same inhomogeneous boundary conditions as ϕ does. The second part ϕ_2 satisfies the equation

$$\nabla^4\phi_2 = -12(1-\nu^2)r^{-1}[u_{,r}u_{,rr}+u_{,r}w_{0,rr}+w_{0,r}u_{,rr}] \tag{35}$$

and the homogeneous version of boundary conditions (30)–(32). After solving ϕ_1 and substituting it into the dimensionless forms of Eqs. (6) and (7) (replacing ϕ by ϕ_1), we can derive the axisymmetrical stress resultant fields N_{1r} and $N_{1\theta}$ due to centrifugal effect as

$$N_{1r} = \Omega^2(C_1+C_2r^{-2}+C_3r^2) = \Omega^2\bar{N}_{1r} \tag{36}$$

$$N_{1\theta} = \Omega^2(C_1-C_2r^{-2}+C_4r^2) = \Omega^2\bar{N}_{1\theta} \tag{37}$$

where

$$C_1 = \frac{(1+\nu)}{8}\frac{(\nu-1)\eta^4-(3+\nu)}{(\nu-1)\eta^2-(1+\nu)}$$

$$C_2 = \frac{(1-\nu)\eta^2}{8}\frac{(\nu+1)\eta^2-(3+\nu)}{(\nu-1)\eta^2-(1+\nu)}$$

$$C_3 = -\frac{(3+\nu)}{8},\quad C_4 = -\frac{(1+3\nu)}{8}$$

Here we extract Ω^2 from the stress resultants purposely by introducing $\bar{N}_{1r}$ and $\bar{N}_{1\theta}$. Both components are tensile throughout the disk.

After substituting Eq. (33) into Eq. (23), we can rewrite the equation of motion as

$$u_{,tt}+\nabla^4 u-\Omega^2 r^{-1}[\bar{N}_{1r}r(u+w_0)_{,r}]_{,r} = r^{-1}\phi_{2,r}(u+w_0)_{,rr}+r^{-1}(u+w_0)_{,r}\phi_{2,rr} \tag{38}$$

In the case when the membrane stretching effect is neglected [3], the solution ϕ_2 in Eq. (35) is identically zero, and as a consequence, Eq. (38) can be reduced to

$$u_{,tt}+\nabla^4 u-\Omega^2 r^{-1}[\bar{N}_{1r}r(u+w_0)_{,r}]_{,r} = 0 \tag{39}$$

In the following, we assume that the initial shape w_0 has a maximum H at the outer radius $r=1$. Therefore, we can write

$$w_0(r) = H\bar{w}_0(r) \tag{40}$$

where $\bar{w}_0(1)=1$.

Discretization

In order to solve the coupled nonlinear equations (35) and (38), we expand u and ϕ_2 in terms of $M+1$ assumed functions u_n and ψ_n as follows:

$$u(r,t) = \sum_{n=0}^{M} c_n(t)u_n(r) \tag{41}$$

$$\phi_2(r,t) = \sum_{n=0}^{M} d_n(t)\psi_n(r) \tag{42}$$

u_n and ψ_n satisfy the equations

$$\nabla^4 u_n - \alpha_n^4 u_n = 0 \tag{43}$$

$$\nabla^4 \psi_n - \beta_n^4 \psi_n = 0 \tag{44}$$

and the same homogeneous boundary conditions as u and ϕ_2 do. The subscript n represents the number of nodal circles of the characteristic functions, excluding the circle at the inner radius. It can be proved mathematically and verified numerically that both u_n and ψ_n are orthonormal.

After substituting Eqs. (41) and (42) into Eq. (35), multiplying both sides by ψ_p and integrating, we obtain

$$d_p = \sum_{i=0}^{M}\left(c_iH\Psi_{pi}+\sum_{j=0}^{M}c_ic_j\Psi_{pij}\right) \tag{45}$$

where

$$\Psi_{pi} = \frac{-24\pi(1-\nu^2)}{\beta_p^4}\int_{r=\eta}^{1}\psi_p(u_{i,r}\bar{w}_{0,rr}+u_{i,rr}\bar{w}_{0,r})dr$$

$$\Psi_{pij} = \frac{-24\pi(1-\nu^2)}{\beta_p^4}\int_{r=\eta}^{1}\psi_p u_{i,r}u_{j,rr}dr$$

After substituting Eqs. (41), (42), and (45) into Eq. (38), multiplying by u_m, and integrating over the annular region, we can discretize Eq. (38) into a system of coupled equations for $c_m(t)$

$$\ddot{c}_m + \alpha_m^4 c_m - \Omega^2 H\Lambda_m - \Omega^2 \sum_{n=0}^{M} c_n \Lambda_{mn}^{(1)}$$
$$= \sum_{i=0}^{M}\sum_{n=0}^{M}\sum_{p=0}^{M}\left(c_i c_n H\Psi_{pi} + \sum_{j=0}^{M} c_i c_n c_j \Psi_{pij}\right)\Lambda_{pnm}$$
$$+ \sum_{i=0}^{M}\sum_{p=0}^{M}\left(c_i H\Psi_{pi} + \sum_{j=0}^{\infty} c_i c_j \Psi_{pij}\right) H\Lambda_{pm}^{(2)} \qquad (46)$$

where

$$\Lambda_m = 2\pi \int_{\eta}^{1} (r\bar{N}_{1r}\bar{w}_{0,r})_{,r} u_m dr$$

$$\Lambda_{mn}^{(1)} = 2\pi \int_{\eta}^{1} (r\bar{N}_{1r}u_{n,r})_{,r} u_m dr$$

$$\Lambda_{pm}^{(2)} = 2\pi \int_{\eta}^{1} (\psi_{p.r}\bar{w}_{0,r})_{,r} u_m dr$$

$$\Lambda_{pnm} = 2\pi \int_{\eta}^{1} (\psi_{p,r}u_{n,r})_{,r} u_m dr$$

In the case when the membrane stretching due to bending is neglected, the right-hand side of Eq. (45) is excluded and the equations of motion become

$$\ddot{c}_m + \alpha_m^4 c_m - \Omega^2 H\Lambda_m - \Omega^2 \sum_{n=0}^{M} c_n \Lambda_{mn}^{(1)} = 0 \qquad (47)$$

It is interesting to note that removing all the quadratic and cubic terms from Eq. (46) does not exactly result in Eq. (47).

Equilibrium Positions and Convergence Test

With the hope that the first few modes in the expansions (41) and (42) will dominate the solutions, we assume that the initial shape of the disk is in the form of the fundamental mode shape $u_0(r)$

$$\bar{w}_0 = \frac{u_0(r)}{u_0(1)} \qquad (48)$$

The maximum physical radial slope of the initial shape is $Hh/b\bar{w}_{0,r}(1)$ at the outer rim. In order for the plate equations (18) and (20) to be acceptable, the maximum slope has to be small. To study the steady-state deflection of the disk at various rotation speeds, the acceleration terms in Eq. (46) are neglected. The thick lines in Fig. 2 show the one-mode approximation for the deformed position at outer rim $w(1)$, as a function of rotation speed Ω for initial heights $H=3$ and 5. The radius ratio η is assumed to be 0.25. For small initial height $H=3$, there exists only one equilibrium position at $\Omega=0$. As the rotation speed increases the disk is flattened as can be easily expected. At large value of Ω, the deformed height $w(1)$ approaches an asymptotic positive value. It appears that this slightly concave shape of the disk is persistent no matter how large the rotation speed is.

For the initial height $H=5$, there are three equilibrium positions at $\Omega=0$, denoted by P_0^1, P_0^2, and P_0^3, respectively. The subscript 0 signifies that the equilibrium positions contain mostly the u_0 mode. The superscripts denote the sequence number of these one-mode solutions from top to bottom. The stability of these positions is determined by the usual perturbation technique, for example, see [8]. It can be shown that both P_0^1 and P_0^3 are stable, while P_0^2 is unstable. In this paper we use solid and dashed lines to signify stable and unstable equilibrium positions, respectively. If the disk is in position P_0^1 when $\Omega=0$, it will be flattened smoothly as the rotation speed increases. On the other hand, if the disk is in position P_0^3 (under the base plane and stressed) when $\Omega=0$, it will be snapped to position P_0^1 when the rotation speed reaches a critical value $\Omega=8.26$.

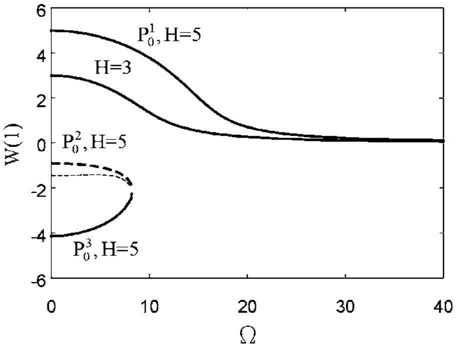

Fig. 2 Equilibrium positions as functions of rotation speed for *H*=3 and 5. The thick and thin lines represent the results from one- and two-term approximations, respectively. Solid and dashed lines represent stable and unstable positions, respectively

The results from the one-mode approximation in Fig. 2 for $H=3$ and 5 are compared to a two-mode approximation, represented by thin lines, for the convergence test. We found that the only noticeable difference between the results from one- and two-mode approximations is the middle branch P_0^2 for $H=5$. With this convergence test we can be sure that all the possible axisymmetrical positions have been obtained.

Figure 3 shows the equilibrium positions for $H=7$ via a two-mode approximation. These results are compared to a three-mode approximation for the convergence test. It is found that at this initial height, the difference between the results from two- and three-mode approximations is negligible. It is observed that there are five equilibrium positions when $\Omega=0$, among them three (denoted by P_0^1, P_0^2, and P_0^3) can be obtained via a simple one-mode approximation, and two (denoted by P_{01}^1 and P_{01}^2, both unstable) can be predicted only via a two-mode approximation. The two-digit subscript 01 signifies that these modes contain mostly modes u_0 and u_1. Stability analysis shows that among these five positions only P_0^1 and P_0^3 are stable. As the rotation speed increases, the position P_0^1 will be flattened, while position P_0^3 merges with P_{01}^2 at point B when $\Omega=15.65$, at which the disk snaps from P_0^3 to P_0^1. The two unstable positions P_0^2 and P_{01}^1 merge at point A to form a cusp when $\Omega=12.56$. In the case when only one mode is used in

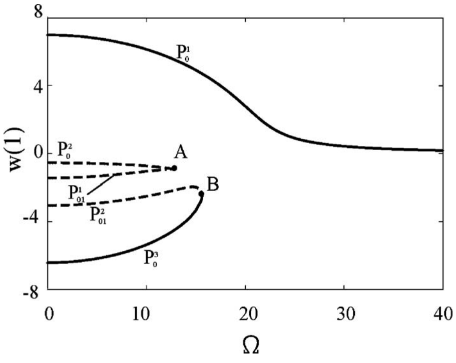

Fig. 3 Equilibrium positions as functions of rotation speed for *H*=7 from a one-term approximation

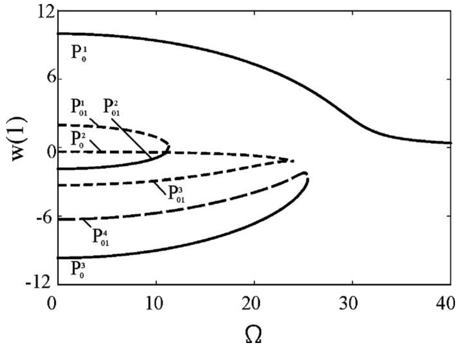

Fig. 4 Equilibrium positions as functions of rotation speed for *H*=10 from a two-term approximation

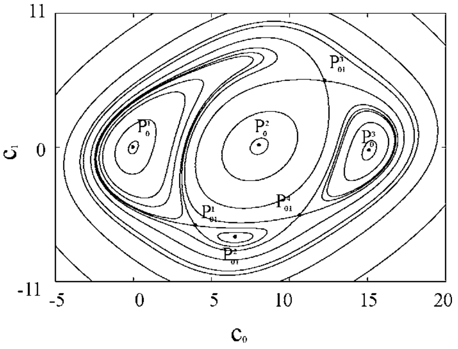

Fig. 5 Strain energy contour for *H*=10 at Ω=0

the expansion, the equilibrium loci will follow closely the P_0^1, P_0^2, and P_0^3 loci as in Fig. 3, except that the loci for P_0^2 and P_0^3 will be connected smoothly between points A and B.

Figure 4 shows the equilibrium positions for a larger initial height $H=10$. At this initial height, the two-mode approximation predicts four extra solutions P_{01}^1, P_{01}^2, P_{01}^3, and P_{01}^4, other than the three one-mode solutions P_0^1, P_0^2, and P_0^3 when $\Omega=0$. Among the four two-mode positions, P_{01}^2 is stable, whereas the other three are unstable. It is observed that snapping will occur at $\Omega=11.32$ and 25.44 for positions P_{01}^2 and P_0^3, respectively.

By observing the steady-state deflections in Figs. 2–4, we note that for small initial height ($H \leqslant 10$) the spinning disk can snap only from position P_0^3 to P_0^1. It is not clear whether the disk can snap quasi-statically from position P_0^1 to P_0^3 when the initial height H is large enough. Although we are unable to prove mathematically, our additional numerical results indicate that it will not happen for a wide range of radius ratio ($0.1 < \eta < 0.9$) and initial height H up to 50. This gives us the confidence that axisymmetrical snapping can occur only from P_0^3 to P_0^1 for a disk with initial shape Eq. (48).

For a disk with initial shape different from Eq. (48), for instance, the spherically curled disk proposed by Benson and Cole [3]

$$\bar{w}_0 = \frac{(r-\eta)^2}{(1-\eta)^2} \tag{49}$$

the convergence of the approximation procedure may not be as fast as the case with initial shape Eq. (48). In particular, the one-mode approximation may give erroneous prediction on the snapping behavior. For instance, for a disk with initial shape (49) with $H=30$, the one-mode approximation predicts that the disk will snap from position P_0^1 to P_0^3 at $\Omega=77.77$. However, two- and three-mode approximations show that the snapping actually occurs from P_0^3 to P_0^1 at $\Omega=81.20$.

Strain Energy Contour

It is interesting to note that at initial height $H=10$ there exists one extra stable position P_{01}^2 apart from the top and bottom positions P_0^1 and P_0^3. Other calculations show that there may exist more stable positions in the middle when H becomes even larger. For instance, there are two extra stable positions in the middle when $H=20$. In Fig. 5, we show the strain energy contour of the disk with $H=10$ in a c_0-c_1 plane at $\Omega=0$ via a two-mode approximation. The dimensionless strain energy U is calculated according to

$$U = \frac{\pi}{12(1-\nu^2)} \int_\eta^1 [(N_r + N_\theta)^2 - 2(1+\nu)N_r N_\theta] r dr + \pi \int_\eta^1 [(u_{,rr} + r^{-1}u_{,r})^2 - 2(1-\nu)r^{-1}u_{,r}u_{,rr}] r dr \tag{50}$$

As expected, the positions P_0^1 and P_0^3 correspond to two valleys, whereas P_0^2 corresponds to the hilltop on the energy surface. These three one-mode positions lie very close to the line $c_1=0$. It is also confirmed that the two-mode position P_{01}^2 corresponds to another valley on the energy surface with a much smaller domain of attraction. The other two-mode solutions are all saddle points. It is noted that the concept of equilibrium positions corresponding to stationary points on the energy surface is good only for a conservative system. A disk rotating at a constant speed is not a conservative system. Therefore, it is meaningless trying to plot the energy surface for the case with $\Omega \neq 0$.

Stress Distributions

It is noted that, in general, the membrane stress resultants are composed of two components, one (ϕ_1) from centrifugal force and the other (ϕ_2) due to membrane stretching via bending deflection. It is of particular interest to observe the membrane stress evolution of the bottom position P_0^3 as the rotation speed increases. Figure 6 shows the $N_r(r)$ and $N_\theta(r)$ of position P_0^3 at Ω

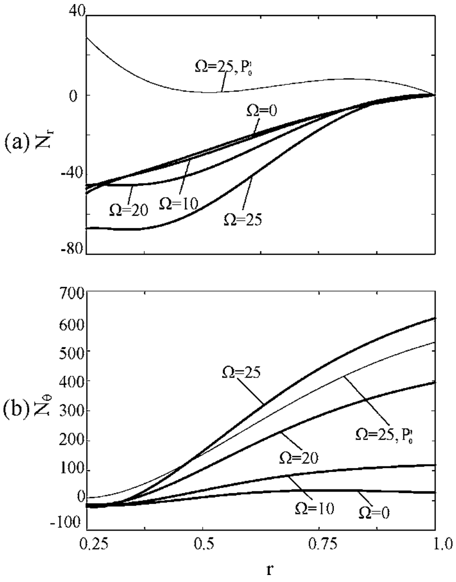

Fig. 6 Membrane stress resultant fields of position P_0^3 at various speeds: (*a*) N_r and (*b*) N_θ

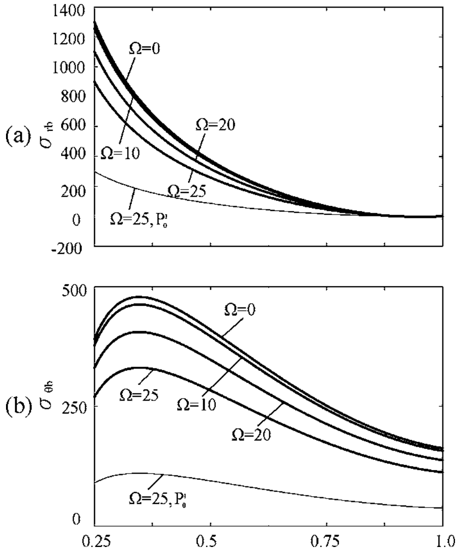

Fig. 7 Maximum bending stress fields of position P_0^3 at various speeds: (*a*) σ_{rb} and (*b*) $\sigma_{\theta b}$

$=0$, 10, 20, and 25. It is noted that the magnitude of the compressive $N_r(r)$ component increases as Ω increases. The increase is more profound as Ω approaches the snapping speed 25.44. On the other hand, the component $N_\theta(r)$ is mostly tensile with the magnitude increasing with rotation speed. The stress resultants $N_r(r)$ and $N_\theta(r)$ of the neighboring stable position P_0^1 at $\Omega=25$ are also shown (with thinner lines) for comparison. Apparently, both $N_r(r)$ and $N_\theta(r)$ of the position P_0^1 are tensile throughout the whole disk. It is noted that the maximum of $N_\theta(r)$ is about 10 times as large as the maximum of $N_r(r)$ in Fig. 6 as the rotation speed approaches 25. However, in the nonrotating case, the order of magnitude of $N_r(r)$ and $N_\theta(r)$ are about the same.

In addition to the membrane stress resultants discussed above, the deformed disk is also subject to bending stresses. The maximum dimensionless bending stresses σ_{rb} and $\sigma_{\theta b}$ on the top surface of the disk can be calculated as

$$\sigma_{rb} = -6[u_{,rr} + \nu r^{-1} u_{,r}] \tag{51}$$

$$\sigma_{\theta b} = -6[r^{-1} u_{,r} + \nu u_{,rr}] \tag{52}$$

Figures 7(*a*) and 7(*b*) show the σ_{rb} and $\sigma_{\theta b}$ distributions of position P_0^3 at $\Omega=0$, 10, 20, and 25. It is noted that the magnitudes of the bending stresses decrease as the rotation speed Ω increases because of the flattening of the disk. The bending stresses of the neighboring stable position P_0^1 at $\Omega=25$ are also shown (with thinner lines) for comparison.

It is noted that to calculate the physical stresses, both the dimensionless stress resultants (N_r and N_θ in Fig. 6) and bending stresses (σ_{rb} and $\sigma_{\theta b}$ in Fig. 7) should be multiplied by the same factor D/b^2h. Therefore, Figs. 6 and 7 can be compared directly to check the order of magnitude of the membrane and bending stresses. By comparing Figs. 6(*a*) and 7(*a*) for the radial stresses of position P_0^3, we see that the membrane stress is negligible compared to the maximum bending component both in the low- and high-speed ranges. The maximum dimensionless total radial stress 1300 occurs at inner radius when $\Omega=0$. On the other hand, the membrane stress in the hoop direction is about the same order of magnitude in all speed ranges compared to its bending counterpart. Further calculation shows that in the speed range from $\Omega=0-25$, the maximum dimensionless total hoop stress 723 occurs on the top surface at the outer radius when $\Omega=25$. Since the shear stress is zero in this axisymmetrical case, the radial stress and the hoop stress are the two principal stresses at any point in the disk. According to Tresca yield criteria, we conclude that the total radial stress on the top surface at the inner radius (mostly due to bending) at $\Omega=0$ is the critical stress for failure analysis of a spinning nonflat disk with $\eta=0.25$.

One-Mode Approximation

The above observations show that for a disk with small initial height ($H<5$, for example), the one-mode approximation predicts the equilibrium configurations of the spinning disk very accurately. For larger initial height it requires more modes to present a more complete picture of the disk deformation. However, even in the cases of large initial height, the simple one-mode approximation still predicts the equilibrium positions P_0^1, P_0^2, P_0^3, and the snapping speed of position P_0^3 very accurately. Therefore, for the ease of analytical study, we use a single mode in the expansions (41) and (42) as a first approximation. For one-mode approximation the equilibrium equation becomes

$$f_0 c_0^3 + f_1 H c_0^2 + (f_2 \Omega^2 + f_3 H^2 + f_4) c_0 + f_5 \Omega^2 H = 0 \tag{53}$$

where

$$f_0 = \Psi_{000}\Lambda_{000}, \quad f_1 = \Psi_{00}\Lambda_{000} + \Psi_{000}\Lambda_{00}^{(2)}. \quad f_2 = \Lambda_{00}^{(1)}$$

$$f_3 = \Psi_{00}\Lambda_{00}^{(2)}, \quad f_4 = -\alpha_0^4, \quad f_5 = \Lambda_0$$

First of all, when H is small enough, there will be only one equilibrium position when $\Omega=0$, as the case of $H=3$ in Fig. 2. As H increases to a certain value, there will exist three equilibrium positions. This special H can be determined from Eq. (53) as

$$H^2 = \frac{4 f_0 f_4}{f_1^2 - 4 f_0 f_3} \tag{54}$$

For $\eta=0.25$ as in Fig. 2, this H is equal to 3.87.

Our second observation is that as the rotation speed increases to a very large value, the disk will be flattened to a slightly concave shape above the base plane. The asymptotic generalized coordinate c_0^∞ corresponding to $\Omega \to \infty$ can be obtained from Eq. (53) as

$$c_0^\infty = -\frac{f_5 H}{f_2} \tag{55}$$

It can be shown that the corresponding outer-rim displacement $w^\infty(1)$ is always positive.

By using one-mode approximation, we can also conveniently calculate the relation between the snapping speed and the initial height. To do so, we differentiate Eq. (53) with respect to Ω^2. The condition $\partial c_0/\partial(\Omega^2) \to \infty$ gives us the equation

$$3 f_0 c_0^2 + 2 f_1 H c_0 + f_2 \Omega^2 + f_3 H^2 + f_4 = 0 \tag{56}$$

By eliminating c_0 from Eqs. (53) and (56), we can calculate the snapping speed as a function of initial height H. This theoretical prediction of snapping speed of position P_0^3 will be revisited later in Fig. 10 in the comparison with experimental observations.

Measurement of Steady-State Deflections

In order to verify the theoretical predictions, we conducted an experiment on the deflection measurement of a rotating disk with axisymmetrical initial shape. The disk is made from a rolled copper sheet with thickness 0.4 mm. The Young's modulus and mass density of the material are 103 GPa and 8864 $\mathrm{kg/m^3}$, respectively. The inner and outer radii of the disk are designed to be 3.75 and 15 cm, respectively. In other words, the clamping ratio η is 0.25. The initial shape of the disk is designed to approximate the first axisymmetrical mode u_0. We first machined a mold of the desired initial shape with two circular steel slabs on the lathe. The flat copper sheet is bent and locked in the mold. The mold together with the bent copper sheet is then put in an oven to heat to 250°C

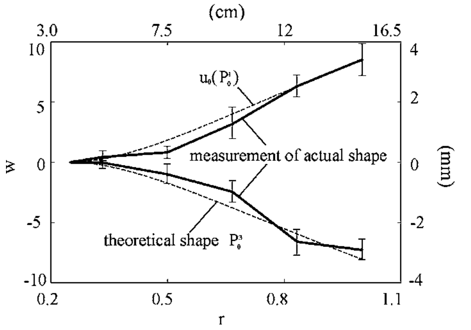

Fig. 8 Measurements of the radial variation of the nonflat disk prepared for experiment

for 1 h to relieve the internal stresses. The concave disks are then polished and mounted on a clamping device with clamping radius 3.75 cm.

To obtain a global picture of the actual initial shape P_0^1 of the disk, we measure the heights at five radial positions. At each radius we take the measurement at 12 evenly divided points on a circle. The disk is then pushed by hand gently to the stressed position P_0^3, whose shape is measured by the same method. The solid lines in Fig. 8 are the measured mean height and the mean deviation at these five radial positions of the disk with clamping collar on. In this measurement the plate surface is placed in the vertical plane, the same configuration when it is mounted on the motor. In this way we can minimize the effect of gravity on the disk deflection. Also shown for comparison with dashed lines are the ideal initial shape u_0 and the theoretical prediction of its P_0^3 configuration. The mean height of this disk at the outer radius is 3.40 mm($H=8.51$). The maximum radial slope of the initial shape is calculated to be 0.015, which is small enough to warrant the use of von Karman's plate model. The wavy deviation of this specimen shown in Fig. 8 is about 15% of the axisymmetrical mean height. Although the wavy deviation is not as small as desired, the mean height indeed approximates the theoretical shapes, both in the P_0^1 and P_0^3 positions. For convenient reference, we present the measured results with both dimensionless parameters (left and bottom sides) and the physical ones (right and top sides). The same labeling style is adopted in Fig. 9 as well.

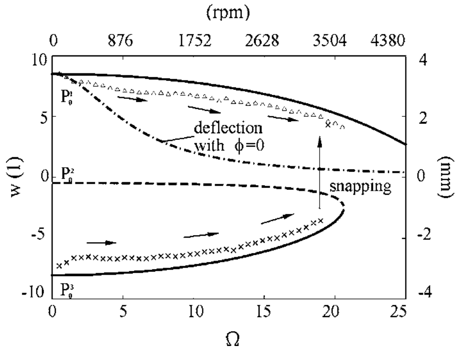

Fig. 9 Measurement of disk deflection as a function of rotation speed

The disk is first bent to position P_0^3 and is rotated by a motor. The maximum total radial stress is calculated to be 7.1 MPa at the inner radius, which is well under the yield stress 55 MPa of copper. The disk deflection at outer radius is measured with a photonic sensor (MTI 2000). The rotation speed of the motor is varied at an increment of 90 rpm. The measured mean deflections are recorded in Fig. 9 as cross marks (×). The disk snaps as the rotation speed reaches 3420 rpm ($\Omega=19.52$). Although the curvature of the initial shape is actually quite small, the snapping phenomenon can still be sighted clearly by the naked eye. After snapping occurs, the test is terminated because the deflection is so large that the disk surface is out of the measurement range of the sensor. To continue the measurement on the upper branch, the photonic sensor needs to be recalibrated. In another test, we start the disk at position P_0^1 and inc rease the speed incrementally up to 3600 rpm. The measured deflections of this test are recorded with triangular symbols (△). The arrows in the figure indicate the direction of rotation speed variation in both tests.

The solid and dashed lines in Fig. 9 are the theoretical predictions from the one-mode approximation. We found that the measured deflections agree with the theoretical predictions reasonably well in both the upper and lower branches. The actual snapping speed is about 5% lower than the theoretical value. To have a sense of the order of magnitude of the snapping speed, we also calculate the critical speed for divergence instability of this disk [9]. It is found that the first rotation speed of a flat disk at which the natural frequency of a backward-traveling mode becomes zero is ~1000 rpm.

In order to demonstrate the need to include the effect of transverse deflection on the membrane stretching in predicting the steady-state deflections, we also present the result from the simplified model (Eq. (47)), neglecting this effect as a chain line in Fig. 9 for comparison. It is noted that the simplified model overestimates the deformation significantly. Benson and Cole [3] reported that their experimentally measured deflections (similar to w in Fig. 9) on a skewed disk (with initial height in the order of $H=11$) are at least 50% greater than the mathematical prediction using the simplified model. Although the experiment described in [3] is not for an axisymmetrical disk, the trend that the simplified model overestimates the disk deformation away from the initially deformed state is the same as the behavior we predicted with the chain line in Fig. 9. These observations lead us to suspect that the neglect of the membrane stretching induced by transverse deflection may be another culprit causing the discrepancy described in [3].

Snapping Speed Measurements

In order to have a clearer picture on the relation between the snapping speed and the initial height, we run a series of tests on several disks with various initial heights. The disks are prepared with the same method as described in the last section, except that the heating time for each disk is purposely different. By controlling the heating time we allow the copper plates to partially spring back. The disks are divided into two groups, one with thickness 0.4 mm and the other 0.2 mm. Table 1 lists the measured mean

Table 1 Mean heights, circumferential deviations, and the measured snapping speeds of the nonflat disks tested in experiment

Disk number	1	2	3	4	5	6	7	8
Thickness (mm)	0.4	0.4	0.4	0.4	0.2	0.2	0.2	0.2
Height (mm)	3.40	3.42	1.93	1.68	4.09	3.99	2.80	2.68
Deviation (%)	15	20	25	24	37	27	23	37
Snapping speed (rpm)	3420	3510	1170	600	3600	3300	2160	1710

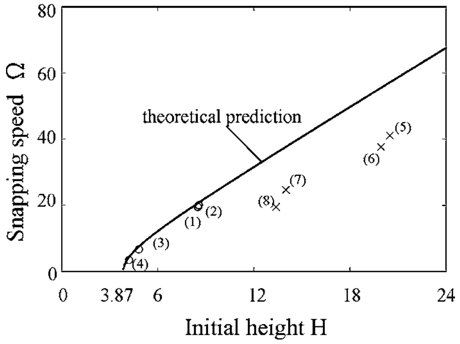

Fig. 10 Relation between snapping speed and initial height for eight disks

heights at the outer rim, wavy deviation percentages, and the measured snapping speeds of eight nonflat disks. It is noted that the deviations of the 0.2 mm disks are, in general, higher than the 0.4 mm disks.

The measured snapping speeds are also recorded in Fig. 10 to compare with the theoretical prediction via one-mode approximation. The test results from the 0.4 mm disks and 0.2 mm disks are marked with symbols (○) and (×), respectively. The disk numbers are labeled beside these marks. It is noted that the theoretical predictions on snapping speeds agree very well with the measurements for the 0.4 mm disks, which have smaller initial heights ($H < 10$). On the other hand, the measured snapping speeds are significantly below the theoretical values for the 0.2 mm disks, with error in the order of 25%. Two factors are speculated to cause this discrepancy when H is large. The first is the large circumferential waviness induced in the 0.2 mm disks. To reduce this waviness some more sophisticated methods have to be adopted in preparing the specimens. In addition, it is possible that the snapping process is no longer axisymmetrical when the initial height is large [7]. The second factor is the aerodynamic force at high rotation speed, which has been shown to have a destabilizing effect on a flexible spinning disk [10–12]. In the tests on the thin disks, we do observe flutter phenomenon at high speed before snapping occurs. More detailed investigations are needed in the future in order to clarify these complicated phenomena observed in the laboratory.

Conclusions

In this paper we study the steady-state deflection of a spinning nonflat disk, both theoretically and experimentally. The initial and the deformed shapes of the disk are assumed to be axisymmetrical. Von Karman's plate model, taking into account the membrane stretching due to bending deflection, is adopted to formulate the equations of motion. The Galerkin method is used to discretize the differential equations of motion into a set of ordinary differential equations. The convergence of the approximation scheme is very fast in the case when the initial shape is assumed to be in the form of the first vibration mode shape. Several conclusions regarding the steady-state deflection and snapping speed of the spinning nonflat disk can be summarized in the following:

1. In the case when the initial height of the nonflat disk is very small, there exists only one equilibrium configuration.
2. When the initial height is large enough, there can exist more than one steady-state configuration when the disk is at rest. Among these multiple solutions, the two stable one-mode solutions P_0^1 and P_0^3 are of particular interest because both have large domains of attraction and can be easily established in the laboratory.
3. If the disk is initially in the form of the unstressed shape P_0^1, it will be flattened smoothly when the rotation speed increases. On the other hand, if the disk is initially in the stressed position P_0^3, it will be snapped to position P_0^1 when the rotation speed reaches a critical value.
4. Experiments on a series of copper disks with different initial heights are conducted to verify the theoretical predictions. Generally speaking, the experimental measurements agree well with theoretical predictions when the initial height is small ($H < 10$). For the disks with large initial heights the measured snapping speeds are significantly below the theoretical predictions. The circumferential waviness of the copper disks induced in the manufacturing process and the aerodynamic force at high rotation speed are two possible factors causing this discrepancy.

Acknowledgment

The results presented here were obtained in the course of research supported by a grant from the National Science Council of the Republic of China.

References

[1] Ono, K., and Maeno, T., 1987, "Theoretical and Experimental Investigation on Dynamic Characteristics of a 3.5-Inch Flexible Disk Due to a Point Contact Head," *Tribology and Mechanics of Magnetic Storage Systems*, Vol. 3, SP.21 (STLE), pp. 144–151.
[2] Capino, M., 1991, "The Effect of Initial Curvature in a Flexible Disk Rotating Near a Flat Plate," ASME J. Tribol., **113**, pp. 355–360.
[3] Benson, R. C., and Cole, K. A., 1991, "Transverse "Runout" of a Nonflat Spinning Disk," Tribol. Trans., **34**, pp. 545–552.
[4] Jia, H. S., 2000, "Analysis of Transverse Runout in Rotating Flexible Disks by Using Galerkin's Method," Int. J. Mech. Sci., **42**, pp. 237–248.
[5] Nowinski, J. L., 1964, "Nonlinear Transverse Vibrations of a Spinning Disk," ASME J. Appl. Mech., **31**, pp. 72–78.
[6] Huang, N.-C., 1969, "Axisymmetric Dynamic Snap-Through of Elastic Clamped Shallow Spherical Shells," AIAA J., **7**, pp. 215–220.
[7] Huang, N.-C., 1964, "Unsymmetrical Buckling of Thin Shallow Spherical Shells," ASME J. Appl. Mech., **30**, pp. 447–457.
[8] Chen, J.-S., 1999, "Steady State Deflection of a Circular Plate Rotating Near Its Critical Speed," ASME J. Appl. Mech., **66**, pp. 1015–1017.
[9] Ono, K., Chen, J.-S., and Bogy, D. B., 1991, "Stability Analysis for the Head-Disk Interface in a Flexible Disk Drive," ASME J. Appl. Mech., **58**, pp. 1005–1014.
[10] D'Angelo, C., III, 1992, "Vibration and Aeroelastic Stability of a Disk Rotating in a Fluid," Ph.D. dissertation, Department of Mechanical Engineering, University of California, Berkeley.
[11] Renshaw, A. A., D'Angelo, C., and Mote, Jr., 1994, "Aeroelastically Excited Vibration of a Rotating Disk," J. Sound Vib., **177**, pp. 577–590.
[12] Kang, N., and Raman, A., 2004, "Aeroelastic Flutter Mechanisms of a Flexible Disk Rotating in an Enclosed Compressible Fluid," ASME J. Appl. Mech., **71**, pp. 120–130.

Dynamic Spherical Cavity Expansion in an Elastoplastic Compressible Mises Solid

Rami Masri[1]
e-mail: masri@aerodyne.technion.ac.il

David Durban

Faculty of Aerospace Engineering,
Technion,
Haifa 32000, Israel

The elastoplastic field induced by a self-similar dynamic expansion of a pressurized spherical cavity is investigated for the compressible Mises solid. The governing system consists of two ordinary differential equations for two stress components where radial velocity and density are known functions of these stresses. Numerical illustrations of radial profiles of field variables are presented for several metals. We introduce a new solution based on expansion in powers of the nondimensionalized cavity expansion velocity, for both elastic/perfectly plastic response and strain-hardening behavior. A Bernoulli-type solution for the dynamic cavitation pressure is obtained from the second-order expansion along with a more accurate third-order solution. These solutions are mathematically closed and do not need any best fit procedure to numerical data, like previous solutions widely used in the literature. The simple solution for elastic/perfectly plastic materials reveals the effects of elastic-compressibility and yield stress on dynamic response. Also, an elegant procedure is suggested to include strain-hardening in the simple elastic/perfectly plastic solution. Numerical examples are presented to demonstrate the validity of the approximate solutions. Applying the present cavitation model to penetration problems reveals good agreement between analytical predictions and penetration depth tests. [DOI: 10.1115/1.1985428]

1 Introduction

Since the pioneering work of Bishop et al. [1] the elastoplastic field induced by a pressurized spherical cavity expanding in an infinite medium is widely used in simulating penetration phenomena. The study of deep penetration depth projectiles is of much interest nowadays (Nelson [2]; Levi [3]), along with investigations of protection against different kinds of penetrators (gun bullets, projectiles, kinetic penetrators, etc.). An extensive review of earlier work on dynamic cavity expansion has been given by Hopkins [4] with emphasis on the incompressible Mises elastic/perfectly plastic solid. Later, Goodier [5] developed a model to predict the penetration depth of rigid spheres launched into metal targets. In that model the target response is approximated by the dynamic spherical cavity expansion in an incompressible Mises elastic/perfectly plastic material, derived by Hill [6] and discussed by Hopkins [4]. Elastic-compressibility in dynamic spherical cavity expansion has been considered by Hunter and Crozier [7], Forrestal and Luk [8], and Forrestal et al. [9] for an elastic/perfectly plastic solid while a pure power law for strain-hardening is examined by Luk et al. [10], for both compressible and incompressible response. In the present paper, we attempt to derive a power expansion solution for the problem of dynamic spherical cavity expansion in a compressible Mises solid. The solution is based on expanding field variables in powers of the nondimensionalized cavity expansion velocity, and accounts for both elastic/perfectly plastic and arbitrary strain-hardening (or softening) response.

We begin in the next section with a brief exposition of the field equations for self-similar dynamic expansion in an elastoplastic compressible Mises solid. We show that the governing system consists of two ordinary differential equations for two stress components where radial velocity and density are known functions of these stresses. Next, in Section 3, we examine the case of dynamic spherical cavity expansion in an arbitrary strain-hardening compressible solid. Numerical illustrations of radial profiles of field variables, for several metals, are presented and discussed. Motivated by the fact that in many practical situations the nondimensionalized cavity expansion velocity is small as compared to one, we seek a solution by expanding in powers of this nondimensionalized velocity. For the second-order approximation the solution for the dynamic cavitation pressure has the Bernoulli (parabolic) form. A Bernoulli form solution was first introduced for an incompressible elastic/perfectly plastic solid, in the extensive review by Hopkins [4], who quoted an unpublished paper by Hill [6]. In recent years, the Bernoulli form is well known as the best fit approximation for the dynamic cavitation pressure (Forrestal et al. [11]; Forrestal et al. [12]; Forrestal et al. [9]; Jones and Rule [13]). Recently, Durban and Masri [14] derived an exact Bernoulli form solution for an incompressible Mises solid with arbitrary strain-hardening (or softening) response.

In Section 4, we study the important case of dynamic spherical cavity expansion in an elastic/perfectly plastic compressible solid, again by seeking a second (and here also a third) order expansion solution in powers of the nondimensionalized velocity. We derive simple approximate solutions for the cavitation pressure which show the effect of elastic-compressibility and yield stress on dynamic behavior. In the absence of elastic-compressibility, we recover the solution for an incompressible Mises material, derived by Hill [6] and discussed by Hopkins [4], while for the quasi-static expansion we recover the solution obtained by Hill [15]. Finally, by defining the equivalent cavitation yield stress we introduce an elegant procedure to include strain-hardening in the simple elastic/perfectly plastic solution.

We conclude with the application of our dynamic cavitation pressure results to the problem of penetration into metal targets. The second- and third-order solutions for the dynamic cavitation pressure are used to obtain expressions for penetration depth.

---

[1] Author to whom correspondence should be addressed. This work is based on part of a Ph.D. thesis to be submitted to Technion.

Contributed by the Applied Mechanics Division of THE AMERICAN SOCIETY OF MECHANICAL ENGINEERS for publication in the ASME JOURNAL OF APPLIED MECHANICS. Manuscript received by the Applied Mechanics Division, July 20, 2004; final revision, December 13, 2004. Associate Editor: A Maniatty. Discussion on the paper should be addressed to the Editor, Prof. Robert M. McMeeking, Journal of Applied Mechanics, Department of Mechanical and Environmental Engineering, University of California-Santa Barbara, Santa Barbara, CA 93106-5070, and will be accepted until four months after final publication in the paper itself in the ASME JOURNAL OF APPLIED MECHANICS.

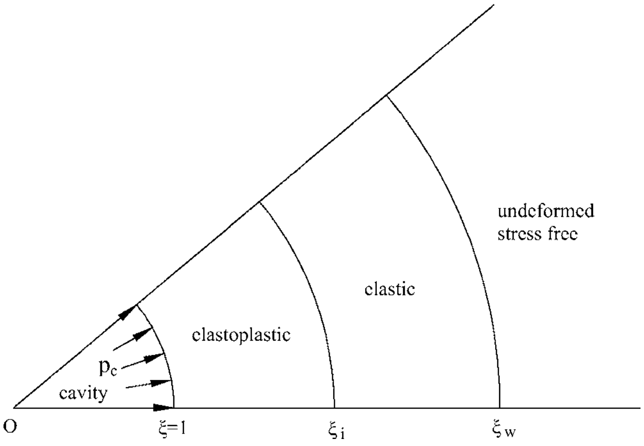

Fig. 1 Scheme of self-similar field in dynamic expansion of a spherical cavity. Cavitation pressure is p_c. The radial coordinate ξ is nondimensionalized with respect to the current radius of the cavity. The rigid-elastic wave front is at $\xi=\xi_w$. Plastic yielding occurs at the elastic-plastic interface $\xi=\xi_i$. The remote boundary at infinity is stress free.

These penetration depth predictions were compared to conical, ogival and spherical-nose penetration tests into aluminium 6061-T651 targets, conducted by Forrestal et al. [11,12]. We give also a brief comparison between the present cavitation model and the Rankine ovoid approach, suggested by Yarin et al. [16].

2 Steady Self-Similar Dynamic Expansion of a Spherical Cavity

Consider an internally pressurized spherical cavity (Fig. 1) of instantaneous radius A, expanding under self-similar conditions in an infinite medium. The surrounding spherical-symmetric stress field has the active Cauchy components σ_r, $\sigma_\theta=\sigma_\phi$ with the radial equation of motion

$$\frac{d\sigma_r}{dR} + \frac{2}{R}(\sigma_r - \sigma_\theta) = \rho\ddot{R}, \tag{1}$$

where R is the Eulerian radial coordinate of a spherical system (R,θ,ϕ), with the origin located at the center of the cavity (denotes by O in Fig. 1), ρ is the density and a superposed dot denotes differentiation with respect to time. Now, in steady-state expansion, where $\dot{A}$ is constant, we assume that the only independent variable is the nondimensional radial coordinate $\xi=R/A$. Accordingly, we transform the time derivative by the similarity relation (Durban and Fleck [17]; Durban and Masri [14])

$$\dot{(\,)} = \dot{\xi}\frac{d(\,)}{d\xi} = \left(\frac{\dot{R}}{A} - \xi\frac{\dot{A}}{A}\right)\frac{d(\,)}{d\xi} = \frac{\dot{A}}{A}(V-\xi)\frac{d(\,)}{d\xi}, \tag{2}$$

with $V=\dot{R}/\dot{A}$ denoting the nondimensional radial velocity. Also, since $\dot{R}=\dot{A}V$ we have for constant $\dot{A}$ that $\ddot{R}=\dot{A}\dot{V}$, and it follows from (2) that (1) can be rewritten as

$$\Sigma_r' + \frac{2}{\xi}(\Sigma_r - \Sigma_\theta) = m^2\left(\frac{\rho}{\rho_0}\right)(V-\xi)V', \tag{3}$$

where $(\Sigma_r,\Sigma_\theta)=(\sigma_r,\sigma_\theta)/E$ are the nondimensionalized stresses (with respect to the elastic modulus E), differentiation with respect to ξ is denoted by a superposed prime, ρ_0 is the reference density of the undeformed stress free state and the nondimensionalized cavity expansion velocity

$$m = \frac{\dot{A}}{\sqrt{E/\rho_0}} \tag{4}$$

is the ratio between the cavity expansion velocity $(\dot{A})$ and the axial wave speed in a long elastic rod $(\sqrt{E/\rho_0})$.

Material response is modeled by the elastoplastic J_2 Mises solid which centers on the effective stress σ_e, given here by

$$\sigma_e = \sigma_\theta - \sigma_r. \tag{5}$$

Notice that definition (5) remains valid for the Tresca effective stress. The elastoplastic J_2 flow theory formulation can be written in the standard hypoelastic form

$$\mathbf{D} = \left(\frac{1+\nu}{E}\right)\check{\boldsymbol{\sigma}} - \left(\frac{\nu}{E}\right)(\mathbf{I}\cdot\cdot\check{\boldsymbol{\sigma}})\mathbf{I} + \frac{3\dot{\epsilon}_p}{2\sigma_e}\mathbf{S}, \tag{6}$$

where $\mathbf{D}$ is the Eulerian strain rate, $\boldsymbol{\sigma}$–the Cauchy stress tensor, $\check{\boldsymbol{\sigma}}$–the Jaumann stress rate, $\mathbf{S}$–the stress deviator, $\mathbf{I}$–the second-order unit tensor, ν–Poisson's ratio and ϵ_p–the effective plastic strain and a known function of σ_e. The latter is suitably nondimensionalized, with respect to E, to obtain from (5),

$$\Sigma = \Sigma_\theta - \Sigma_r. \tag{7}$$

The active components of the Eulerian strain rate become, for the spherical symmetric field,

$$\dot{\epsilon}_r = \frac{d\dot{R}}{dR} = \left(\frac{\dot{A}}{A}\right)\frac{dV}{d\xi} \qquad \dot{\epsilon}_\theta = \dot{\epsilon}_\phi = \frac{\dot{R}}{R} = \left(\frac{\dot{A}}{A}\right)\frac{V}{\xi}. \tag{8}$$

Consequently, in the absence of material spin, the tensorial constitutive relation (6) separates into just two scalar equations, namely, with the aid of (2),

$$V' = (V-\xi)[(\Sigma_r - 2\nu\Sigma_\theta)' - \epsilon_p'], \tag{9}$$

$$\frac{V}{\xi} = (V-\xi)\left\{[-\nu\Sigma_r + (1-\nu)\Sigma_\theta]' + \frac{1}{2}\epsilon_p'\right\}. \tag{10}$$

Finally, conservation of matter requires that

$$\frac{\dot{\rho}}{\rho} + \dot{\epsilon}_r + 2\dot{\epsilon}_\theta = 0, \tag{11}$$

or, on account of (8) and (2),

$$(V-\xi)\ln'\left(\frac{\rho}{\rho_0}\right) + V' + 2\frac{V}{\xi} = 0. \tag{12}$$

To sum it up, we have the four governing equations (3), (9), (10), and (12), with four unknowns $(\Sigma_r,\Sigma_\theta,V,\rho)$ whose dependence on ξ should be determined. Integration of that system is carried from the cavity's wall where

$$\xi = 1: \quad V = 1 \tag{13}$$

to the rigid-elastic interface (wave front) $\xi=\xi_w$ where we have $\rho=\rho_0$, as a stress free condition, and both velocity and stresses should vanish (Fig. 1). Also, $P_c=-\Sigma_r(\xi=1)$ denotes the nondimensionalized $(P_c=p_c/E)$ cavitation pressure (Fig. 1), determined by the solution. Notice that the small strain elastic field solution dictates the location of the rigid-elastic interface (wave front) at $\xi_w=C_E/\dot{A}=1/M$, where C_E denotes the linear elastic dilatation wave speed, and M can be regarded as the subsonic cavity expansion Mach number (Durban and Masri [14]), defined by

$$M^2 = \frac{(1+\nu)(1-2\nu)}{1-\nu}m^2 = \left(\frac{\dot{A}}{C_E}\right)^2$$

with

$$C_{\mathrm{E}} = \sqrt{\frac{(1-\nu)E}{(1+\nu)(1-2\nu)\rho_0}}. \tag{14}$$

A subsonic expansion field is, therefore, possible under the constraint

$$m < \sqrt{\frac{1-\nu}{(1+\nu)(1-2\nu)}}, \tag{15}$$

where the upper bound on m is always greater than one.

In this formulation, the effective plastic strain ϵ_p is a given function of Σ, which describes plastic strain-hardening (or softening). For solids with a definite yield point, plastic response is activated at the elastic-plastic interface $\xi=\xi_i$, where ϵ_p vanishes, with $1<\xi_i<\xi_w$ (Fig. 1). However, for strain-hardening response, like the Ramberg-Osgood power-hardening law ($\epsilon_p=K\Sigma^{\alpha}$), the plastic branch is active within the entire deformation zone. For elastic/perfectly plastic response ϵ_p is not known a priori and an extra algebraic equation is obtained from (7), in the post-yield range,

$$\Sigma_\theta - \Sigma_r = \Sigma_y, \tag{16}$$

where Σ_y is the nondimensional yield stress ($\Sigma_y=Y/E$ with Y denoting the yield stress). For that particular model, the elastic-plastic interface $\xi=\xi_i$ appears at the location where Σ reaches the value of Σ_y.

Inserting (9) and (10) into (12) and integrating over ξ we get

$$\rho = \rho_0 \mathrm{e}^{-\Theta} \text{ with } \quad \Theta = (1-2\nu)(\Sigma_r + 2\Sigma_\theta), \tag{17}$$

using $\rho=\rho_0$ and $\Sigma_r=\Sigma_\theta=0$ as stress free conditions at the wave front.

The effective plastic strain goes to infinity at the cavity's wall (Durban and Masri [14]) so when strain-hardening is present both the effective stress and Σ_θ are not bounded there, hence the density reduces to zero at the cavity's wall. However, for elastic/perfectly plastic solids, ρ reaches a finite value at the wall because Σ_θ is bounded by relation (16),

$$\rho(\xi=1) = \rho_0 \mathrm{e}^{(1-2\nu)(3P_{\mathrm{c}}-2\Sigma_{\mathrm{y}})}. \tag{18}$$

Next, we subtract (10) from (9) and integrate the equation thus obtained. This gives

$$V = \xi(1-\mathrm{e}^{-\Phi}) \text{ with } \quad \Phi = (1+\nu)(\Sigma_\theta - \Sigma_r) + \tfrac{3}{2}\epsilon_p, \tag{19}$$

accounting for the conditions that V, Σ_r, and Σ_θ should vanish at the wave front. Substituting the velocity (19) back in (10) gives

$$\left[-\nu\Sigma_r + (1-\nu)\Sigma_\theta + \frac{1}{2}\epsilon_p\right]' = \frac{1}{\xi}(1-\mathrm{e}^{\Phi}). \tag{20}$$

Similarly, with the aid of (9), (17), and (19), the equation of motion (3) becomes

$$\Sigma_r' + \frac{2}{\xi}(\Sigma_r - \Sigma_\theta) = m^2\xi^2(\Sigma_r - 2\nu\Sigma_\theta - \epsilon_p)'\mathrm{e}^{-\Theta-2\Phi}. \tag{21}$$

Equations (20) and (21) should be solved for the radial profiles of the stresses Σ_r and Σ_θ that develop in the material, with Θ and Φ defined in (17) and (19). A further simplification of (20) and (21) is possible upon elimination of Σ_θ with the aid of the effective stress relation (7) resulting in two equations for Σ_r and Σ.

Durban and Masri [14] have given an exact closed-form solution to the problem of dynamic spherical expansion in an incompressible Mises solid, for arbitrary strain hardening or softening, along with numerical solutions of dynamic expansion in compressible Mises solid, that include high cavity expansion velocities. That analysis is a special case of a more comprehensive treatment of dynamic spherical cavitation in a Drucker-Prager material.

3 The Compressible Strain-Hardening Solid

A simpler version of the two governing equations (20) and (21) can be derived by introducing the total strain $\epsilon=\Sigma+\epsilon_p$, which is a known function of Σ, using (7) and putting $\beta=1-2\nu$ for the elastic-compressibility parameter. It follows that (20) and (21) can be written as

$$\beta\Sigma_r' + \frac{\beta}{2}\Sigma' + \frac{1}{2}\epsilon' = \frac{1}{\xi}\left(1-\mathrm{e}^{-\frac{\beta}{2}\Sigma+\frac{3}{2}\epsilon}\right), \tag{22}$$

$$\Sigma_r' - \frac{2}{\xi}\Sigma = m^2\xi^2(\beta\Sigma_r' + \beta\Sigma' - \epsilon')\mathrm{e}^{-3\beta\Sigma_{\mathrm{r}}-\beta\Sigma-3\epsilon}. \tag{23}$$

These equations admit exact closed form solutions, in terms of quadratures, for the cavitation pressure with any hardening characteristic, when the material is incompressible ($\beta=0$) (Durban and Masri [14])

$$P_{\mathrm{c}} = \int_0^\infty \frac{\Sigma\,\mathrm{d}\epsilon}{\mathrm{e}^{\frac{3}{2}\epsilon}-1} + \frac{3}{2}m^2, \tag{24}$$

and in quasi-static expansion ($m=0$) (Durban and Baruch [18])

$$P_{\mathrm{c}} = \int_0^\infty \frac{\left(\frac{\mathrm{d}\epsilon}{\mathrm{d}\Sigma}+\beta\right)\Sigma\mathrm{d}\Sigma}{\mathrm{e}^{\frac{3}{2}\epsilon-\frac{\beta}{2}\Sigma}-1+2\beta\Sigma}. \tag{25}$$

These exact relations simplify to the approximate, yet practical ($\Sigma_y \ll 1$), solutions for elastic/perfectly plastic response, derived by Hill [6,15].

Radial profiles of density, velocity, and stresses (Σ_r and Σ) for cavitation in four metals, in quasi-static ($m=0$) and dynamic ($m=0.35$) expansions, are illustrated in Figs. 2–5. The curves have been obtained numerically from Eqs. (22) and (23) for the following metals:

Aluminum7075-T6: $\epsilon_p=3.94\cdot 10^{21}\Sigma^{10.9}$, $\nu=0.32$, $\rho_0=2700$[kg/m^3], $E=72.4$[GPa].

Steel D6AC: $\epsilon_p=2.52\cdot 10^{55}\Sigma^{28}$, $\nu=0.27$, $\rho_0=7800$[kg/m^3], $E=213$[GPa].

Stainless steel: $\epsilon_p=5.78\cdot 10^{4}\Sigma^{3}$, $\nu=0.30$, $\rho_0=7800$[kg/m^3], $E=206$[GPa].

TitaniumB120VCA: $\epsilon_p=2.4\cdot 10^{29}\Sigma^{16.5}$, $\nu=\frac{1}{3}$, $\rho_0=4400$[kg/m^3], $E=106$[GPa].

The expected tendency of Σ towards infinity, and of ρ towards zero, upon approaching the cavity's wall, are not seen in Figs. 2–5 because the boundary layer near the wall (Durban and Masri [14]) is extremely small for these metals. It can be seen that from a macroscopic point of view, the radial profiles of density, velocity, and stresses, for given cavity expansion velocity m, remain similar for different metals, and that the effective stress Σ is hardly sensitive to the cavity expansion velocity. While for the quasi-static expansion ($m=0$) the wave front is at infinity, for dynamic expansion ($m=0.35$) the wave front location is obtained from $\xi_w=1/M$, using (14). The wave front locations, along with the cavity expansion velocities (4) and the cavitation pressures $P_c=-\Sigma_r(\xi=1)$, in dynamic expansion with $m=0.35$ for the four metals are:

$\xi_w=3.42$, $\dot{A}=1812$[m/s], $P_c=0.155$ (aluminum),

$\xi_w=3.20$, $\dot{A}=1830$[m/s], $P_c=0.152$ (steel),

$\xi_w=3.31$, $\dot{A}=1800$[m/s], $P_c=0.164$ (stainless steel),

$\xi_w=3.50$, $\dot{A}=1718$[m/s], $P_c=0.167$ (titanium).

For quasi-static expansion ($m=0$) the velocity profile (V) describes a mathematical limit and the respective cavitation pres-

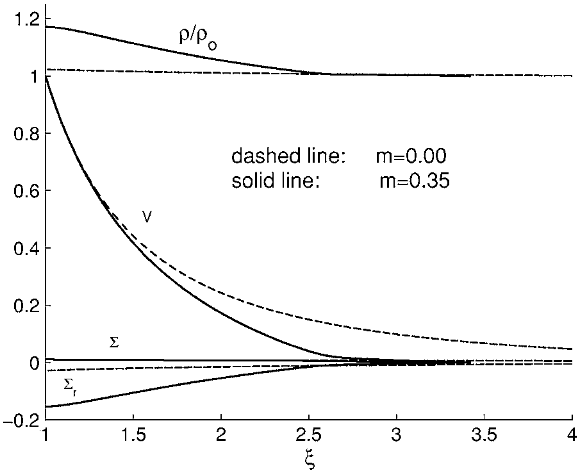

Fig. 2 Radial profiles of essential field variables for a compressible strain-hardening Mises solid. Results are for AL 7075-T6.

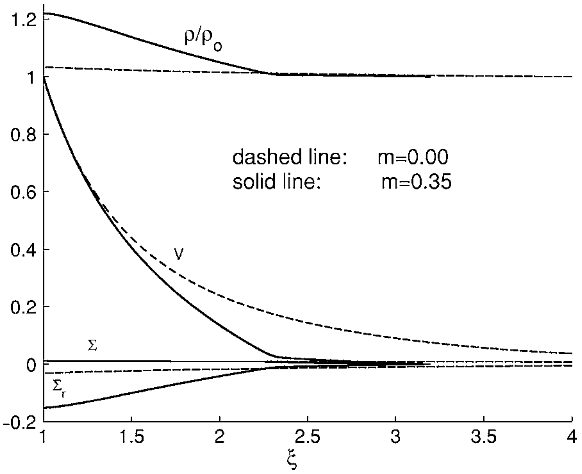

Fig. 3 Radial profiles of essential field variables for a compressible strain-hardening Mises solid. Results are for ST D6AC.

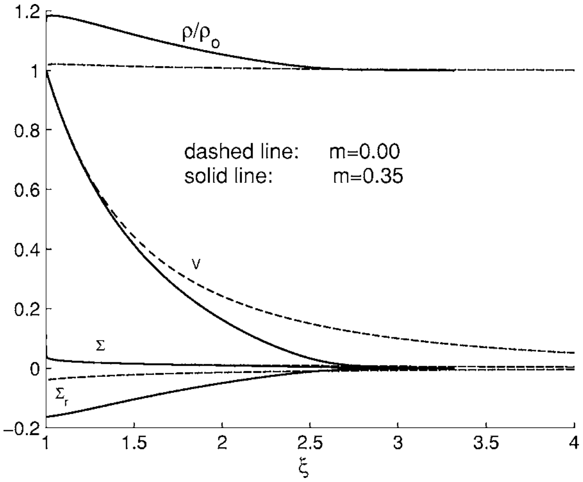

Fig. 4 Radial profiles of essential field variables for a compressible strain-hardening Mises solid. Results are for Stainless steel.

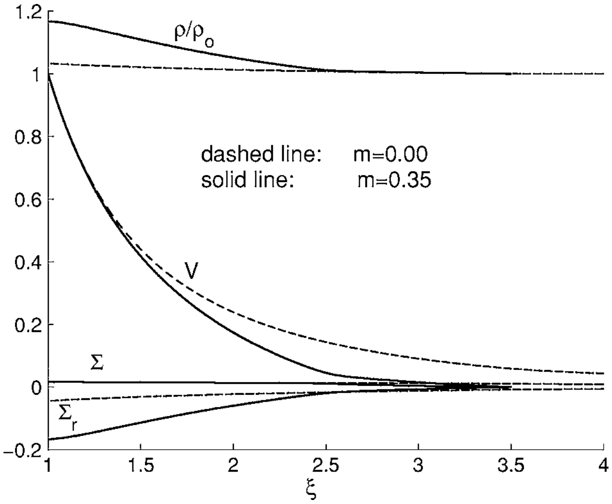

Fig. 5 Radial profiles of essential field variables for a compressible strain-hardening Mises solid. Results are for TI B120VCA.

sures for the metals are: $P_c=0.0281$ (aluminum), $P_c=0.0314$ (steel), $P_c=0.0394$ (stainless steel), and $P_c=0.0440$ (titanium). The latter results can also be calculated from the exact relation (25).

Motivated by the exact solutions (24) and (25) and by recently available studies (Forrestal et al. [11]; Forrestal et al. [12]; Forrestal et al. [9]; Jones and Rule [13]) that suggest a parabolic dependence of the dynamic cavitation pressure on cavity expansion velocity, and recalling that in many practical situations $m^2 \ll 1$, we seek a solution of (22) and (23) by expanding Σ and Σ_r in powers of m, namely

$$\Sigma = \Sigma_0 + m^2\Sigma_1 + \cdots , \tag{26}$$

$$\Sigma_r = \Sigma_{r0} + m^2\Sigma_{r1} + \cdots , \tag{27}$$

where $\Sigma_0, \Sigma_1, \ldots, \Sigma_{r0}, \Sigma_{r1}, \ldots$ are functions of ξ. It should be mentioned that the linear terms do not appear in expansions (26) and (27) because the equations for the first-order $O(m)$ do not depend on the solution of the zeroth order. A support to this argument can be deduced from the exact solution for cavitation pressure, for the

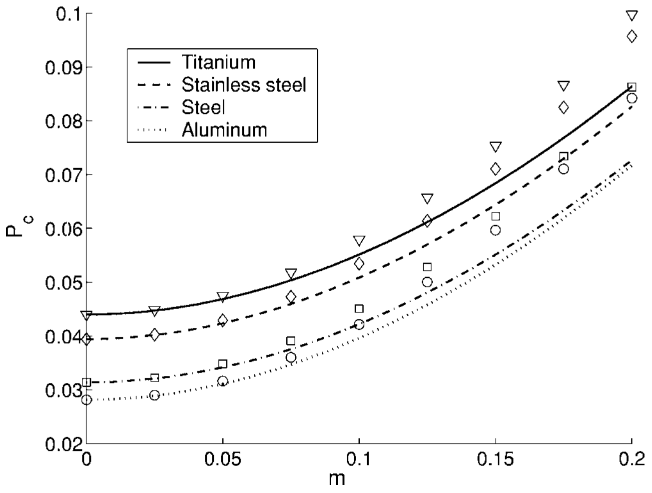

Fig. 6 Variation of cavitation pressure P_c with expansion velocity m for four metals. The different markers represent the second order approximation (46).

four metals mentioned previously, obtained numerically from Eqs. (22) and (23) and illustrated by curves in Fig. 6.

Inserting (26) and (27) into (22) and (23) and expanding in powers of m^2 results in the zeroth-order system

$$\beta\Sigma_{r0}' + \frac{\beta}{2}\Sigma_0' + \frac{1}{2}\epsilon_0' = \frac{1}{\xi}\left(1 - \mathrm{e}^{-\frac{\beta}{2}\Sigma_0 + \frac{3}{2}\epsilon_0}\right), \tag{28}$$

$$\Sigma_{r0}' - \frac{2}{\xi}\Sigma_0 = 0, \tag{29}$$

where ϵ_0 is the value of the total strain at $\Sigma = \Sigma_0$ ($\epsilon_0 = \Sigma_0 + \epsilon_p(\Sigma_0)$). Thus, from (26) we deduce the power expansion for the total strain

$$\epsilon = \epsilon_0 + m^2\epsilon_1 + \cdots, \tag{30}$$

where

$$\epsilon_1 = \Psi_0\Sigma_1 \text{ with } \quad \Psi_0 = \frac{\mathrm{d}\epsilon_0}{\mathrm{d}\Sigma_0} = 1 + \frac{\mathrm{d}\epsilon_p(\Sigma_0)}{\mathrm{d}\Sigma_0}. \tag{31}$$

Similarly, the second-order (m^2) system obtained from the power expansion of (22) and (23) is

$$\beta\Sigma_{r1}' + \frac{\beta}{2}\Sigma_1' + \frac{1}{2}(\Psi_0\Sigma_1)' = -\frac{1}{\xi}H_0\Sigma_1, \tag{32}$$

$$\Sigma_{r1}' - \frac{2}{\xi}\Sigma_1 = \xi^2 I_0, \tag{33}$$

where

$$H_0 = \frac{1}{2}(3\Psi_0 - \beta)\mathrm{e}^{\frac{3}{2}\epsilon_0 - \frac{\beta}{2}\Sigma_0}, \tag{34}$$

$$I_0 = (\beta\Sigma_{r0}' + \beta\Sigma_0' - \epsilon_0')\mathrm{e}^{-3\beta\Sigma_{r0} - \beta\Sigma_0 - 3\epsilon_0}. \tag{35}$$

Higher order pairs of equations can be constructed along similar lines, here however, we shall limit the analysis to a second order approximation under the assumption that $m^2 \ll 1$. This assumption is of practical significance because, for example, under cavity expansion velocity of $\dot{A} = 1[\mathrm{km/s}]$, which represents the barrel velocity of an M-16 rifle or striking velocity of deep penetration depth projectile (Nelson [2]; Levi [3]), we get $m^2 \simeq 0.04$ for all four metals mentioned before. Recall that in applying the dynamic spherical cavitation model to penetration analysis the expansion velocity is not greater than the penetration velocity because of the dependence on the local penetrator slope (Jones and Rule [13]), and that during the penetration process the projectile velocity decreases.

To solve the zeroth-order equations (28) and (29) we substitute Σ_{r0} from (29) in (28) to obtain the useful differential relation

$$2\frac{\mathrm{d}\xi}{\xi} = -J_0\mathrm{d}\Sigma_0, \tag{36}$$

where

$$J_0 = \frac{\Psi_0 + \beta}{\mathrm{e}^{\frac{3}{2}\epsilon_0 - \frac{\beta}{2}\Sigma_0} - 1 + 2\beta\Sigma_0} \tag{37}$$

is a function of Σ_0 only. Relation (36) is now combined with (29) to give

$$\mathrm{d}\Sigma_{r0} = -J_0\Sigma_0\mathrm{d}\Sigma_0. \tag{38}$$

Recalling that at the cavity ($\xi = 1$) $\Sigma_0 \to \infty$ and $\Sigma_{r0} = -P_{c0}$ (the zeroth-order cavitation pressure, which is the quasi-static cavitation pressure), we integrate (36) and (38) to arrive at the quadrature-type solution for the quasi-static expansion

$$\xi = \mathrm{e}^{K_0} \qquad \Sigma_{r0} = -P_{c0} + \int_{\Sigma_0}^{\infty} J_0(s)s\mathrm{d}s, \tag{39}$$

where

$$K_0 = \tfrac{1}{2}\int_{\Sigma_0}^{\infty} J_0(s)\mathrm{d}s. \tag{40}$$

At infinity Σ_0 and Σ_{r0} vanish, so from the second of (39) we find the zeroth-order cavitation pressure

$$P_{c0} = \int_0^{\infty} J_0(\Sigma_0)\Sigma_0\mathrm{d}\Sigma_0. \tag{41}$$

Solutions (39) and (40) transform ξ to Σ_0 as the independent variable and give the exact cavitation pressure (41) for quasi-static expansion in a compressible Mises solid with any hardening or softening characteristics. The same value of P_{c0}, as indicated earlier (25), has been obtained by Durban and Baruch [18] as the limit of the cavity expansion process under monotonously increasing internal pressure.

Turning to the second-order system (32) and (33), we can eliminate Σ_{r1} between the two equations to construct a single equation for Σ_1, viz

$$\frac{1}{2}(\Psi_0 + \beta)\Sigma_1' + \left(\frac{1}{2}\Psi_0' + \frac{H_0 + 2\beta}{\xi}\right)\Sigma_1 = -\beta\xi^2 I_0, \tag{42}$$

which can be integrated in terms of quadratures. However, the solution for Σ_1 turns out to be complicated, offering no new insight, and is less effective by comparison with a numerical solution. Now, Figs. 2–5 suggest the observation that the effective stress Σ is hardly sensitive to the cavity expansion velocity m. For the incompressible material ($\beta = 0$) that observation is accurate over the entire field (Durban and Masri [14]). This observation is also accurate for elastic/perfectly plastic response within the plastic field where $\Sigma \equiv \Sigma_y$. In this spirit we proceed with the assumption that in (33) $\frac{2}{\xi}|\Sigma_1| \ll \xi^2|I_0|$ leading to the approximate solution for Σ_{r1}

$$\Sigma_{r1} = -P_{c1} + \int_{\Sigma_0}^{\infty}[\exp(-3\epsilon_0 - \beta s - 3\beta\Sigma_{r0} + 2K_0)]$$
$$(\beta J_0 s - \beta + \Psi_0)\mathrm{d}s, \tag{43}$$

where P_{c1} is the second-order coefficient in the power expansion of the cavitation pressure

$$P_c = P_{c0} + m^2 P_{c1} + \cdots, \tag{44}$$

and the integrand in (43) is understood to depend on the integration variable s. Thus, the second-order coefficient in the power expansion of the cavitation pressure is simply

$$P_{\mathrm{c}1} = \int_0^{\infty}(\beta J_0\Sigma_0 - \beta + \Psi_0)[\exp(-3\epsilon_0 - \beta\Sigma_0 - 3\beta\Sigma_{\mathrm{r}0} + 2K_0)]\mathrm{d}\Sigma_0, \tag{45}$$

and upon inserting this result, along with (41), in (44) we obtain the second-order approximation

$$P_{\mathrm{c}} = m^2\int_0^{\infty}(\beta J_0\Sigma_0 - \beta + \Psi_0)$$
$$[\exp(-3\epsilon_0 - \beta\Sigma_0 - 3\beta\Sigma_{\mathrm{r}0} + 2K_0)]\mathrm{d}\Sigma_0$$
$$+ \int_0^{\infty} J_0\Sigma_0\mathrm{d}\Sigma_0. \tag{46}$$

As a quick check we substitute in (41) and (45) the value of $\beta=0$ to see whether we recover the incompressible Mises result (24), obtained by Durban and Masri [14]. Now, it is a matter of ease to show, by (37) and (41), that for $\beta=0$

$$J_0 = \frac{\Psi_0}{e^{\frac{3}{2}\epsilon_0} - 1} \qquad P_{c0} = \int_0^\infty \frac{\Sigma_0 \mathrm{d}\epsilon_0}{e^{\frac{3}{2}\epsilon_0} - 1}. \tag{47}$$

Similarly, from (40)

$$K_0 = -\tfrac{1}{3}\ln\left(1 - e^{-\frac{3}{2}\epsilon_0}\right), \tag{48}$$

which is now substituted in (45) to obtain the exact (24) second-order coefficient P_{c1} as a Beta function integral

$$P_{c1} = \int_0^\infty \frac{e^{-3\epsilon_0}\mathrm{d}\epsilon_0}{\left(1 - e^{-\frac{3}{2}\epsilon_0}\right)^{\frac{2}{3}}} = \frac{2}{3}\int_0^1 \frac{s\mathrm{d}s}{(1-s)^{\frac{2}{3}}} = \frac{2}{3}\frac{\Gamma(2)\Gamma\left(\frac{1}{3}\right)}{\Gamma\left(2+\frac{1}{3}\right)} = \frac{3}{2}, \tag{49}$$

where Γ denotes the Gamma function and s is here defined by $s = \exp\left(-\frac{3}{2}\epsilon_0\right)$.

Just to give an example, the values of P_{c1} from (45) for the four metals of Figs. 2–5, are: $P_{c1}=1.402$ ($P_{c0}=0.0281$) for the aluminum, $P_{c1}=1.373$ ($P_{c0}=0.0314$) for the steel, $P_{c1}=1.408$ ($P_{c0}=0.0394$) for the stainless steel and $P_{c1}=1.395$ ($P_{c0}=0.0440$) for the titanium. That data suggests that P_{c1} is much larger than P_{c0} and that P_{c1} is bounded by $3/2$.

Variation of the cavitation pressure P_c with expansion velocity m for the four strain-hardening metals is displayed in Fig. 6. The different types of markers show the second-order approximation (46) while the curves show the exact solution obtained numerically from Eqs. (22) and (23). It may be concluded that for the practical range of $m<0.15$ the deviation of the approximation from the exact solution is less than 10%. Also notice that it appears that the approximate solution is an upper bound on the exact solution. From the exact solutions it can be seen that the cavitation pressure has no linear term in m, which supports the power expansions (26) and (27).

4 The Compressible Elastic/Perfectly Plastic Solid

An instructive and important example is provided by the elastic/perfectly plastic characteristic where

$$\epsilon = \Sigma \text{ for } \Sigma \leqslant \Sigma_y \text{ and } \Sigma \equiv \Sigma_y \text{ for } \epsilon \geqslant \Sigma_y. \tag{50}$$

Expansion (26) is now not applicable within the plastic zone, neither is relation (31) since after initial yield $\Sigma_1 \equiv 0$ and Ψ_0 from (31) becomes unbounded.

The quasi-static elastic field is governed by the zeroth-order system (28) and (29) with $\epsilon_0=\Sigma_0$. The appropriate solution is again given by the integrals of (36) and (38) with

$$J_0 = \frac{1+\beta}{e^{\frac{3-\beta}{2}\Sigma_0} - 1 + 2\beta\Sigma_0}. \tag{51}$$

Thus, for $\Sigma_0 \leqslant \Sigma_y$ and J_0 given by (51), the exact zeroth-order solution in the elastic zone is

$$\xi = \xi_{i0}\exp\left(\frac{1}{2}\int_{\Sigma_0}^{\Sigma_y} J_0(s)\mathrm{d}s\right), \tag{52}$$

$$\Sigma_{r0} = -\int_0^{\Sigma_0} J_0(s)s\mathrm{d}s, \tag{53}$$

where ξ_{i0} is the location of the elastic-plastic interface for quasi-static expansion, to be determined shortly. Notice that ξ_{i0} is the leading term in the interface location power expansion

$$\xi_i = \xi_{i0} + m^2\xi_{i1} + \cdots. \tag{54}$$

For sufficiently small elastic strains ($\Sigma_y \ll 1$) it is permissible to approximate (52) and (53) by the leading terms

$$\xi^3 = \frac{\Sigma_y \xi_{i0}^3}{\Sigma_0} = \frac{C_0}{\Sigma_0} \qquad \Sigma_{r0} = -\frac{2}{3}\Sigma_0, \tag{55}$$

which are identical with the well-known linear elastic approximation (Durban and Masri [14]) where C_0 is the integration constant in that solution.

The exact zeroth-order equations for the perfectly plastic field are, by (28) and (29),

$$\beta\Sigma_{r0}' + \frac{1}{2}\epsilon_0' = \frac{1}{\xi}\left(1 - e^{-\frac{\beta}{2}\Sigma_y} e^{\frac{3}{2}\epsilon_0}\right), \tag{56}$$

$$\Sigma_{r0}' = \frac{2}{\xi}\Sigma_y, \tag{57}$$

with the immediate exact solution (recalling that at the cavity's wall $\Sigma_{r0}=-P_{c0}$ and $\epsilon_0 \to \infty$)

$$\Sigma_{r0} = 2\Sigma_y\ln(\xi) - P_{c0}, \tag{58}$$

$$\xi = \left[1 - (1 - 2\beta\Sigma_y)e^{\frac{\beta}{2}\Sigma_y} e^{-\frac{3}{2}\epsilon_0}\right]^{-\frac{1}{3(1-2\beta\Sigma_y)}}. \tag{59}$$

The exact elastic-plastic interface location ξ_{i0} (where $\epsilon_0=\Sigma_y$) can be found from (59), but for all practical purposes $\Sigma_y \ll 1$ so we recover the well-known approximate location of the elastic-plastic interface (Hill [15])

$$\xi_{i0} = [3(1-\nu)\Sigma_y]^{-1/3}. \tag{60}$$

Thus, from (55), the integration constant C_0 is now given by $[3(1-\nu)]^{-1}$, in agreement with the value $C=2/3$ obtained by Durban and Masri [14] for the incompressible Drucker-Prager solid. Equating the approximate elastic result (55) with the plastic result (58), for the radial stress at the interface location (60), gives the zeroth-order cavitation pressure, which coincides with the approximate quasi-static cavitation pressure (Hill [15])

$$P_{c0} = \frac{2}{3}\Sigma_y\ln\left[\frac{1}{3(1-\nu)\Sigma_y}\right] + \frac{2}{3}\Sigma_y. \tag{61}$$

By equating the exact elastic (53) and plastic (58) solutions, for the radial stress at the exact elastic-plastic interface, from (59),

$$\xi_{i0} = \left[1 - (1 - 2\beta\Sigma_y)e^{\frac{\beta-3}{2}\Sigma_y}\right]^{-\frac{1}{3(1-2\beta\Sigma_y)}}, \tag{62}$$

we find the exact cavitation pressure for spherical quasi-static expansion in an elastic/perfectly plastic compressible Mises solid

$$P_{c0} = \frac{2\Sigma_y}{3(1-2\beta\Sigma_y)}\ln\left[1 - (1-2\beta\Sigma_y)e^{\frac{\beta-3}{2}\Sigma_y}\right]^{-1} + \int_0^{\Sigma_y} \frac{(1+\beta)\Sigma_0\mathrm{d}\Sigma_0}{\exp\left(\frac{3-\beta}{2}\Sigma_0\right) - 1 + 2\beta\Sigma_0}. \tag{63}$$

This exact solution can be also obtained as a particular result from (41) for the elastic/perfectly plastic case, and can be reduced to the approximate solution (61) under the practical assumption $\Sigma_y \ll 1$. A second-order expansion of (63) in powers of Σ_y gives the relation

$$P_{c0} = \frac{2\Sigma_y}{3}\left\{1 + (1+2\beta\Sigma_y)\ln\left[\frac{2}{3(\beta+1)\Sigma_y}\right] + \frac{(3-\beta)(5\beta+1)}{8(\beta+1)}\Sigma_y\right\}, \tag{64}$$

which explains the validity of Hill's solution (61) for $\Sigma_y \ll 1$. Notice that (59), and hence also (62), can be obtained as particular results from solutions (39) and (40). In fact, the location ξ_{i0} for solids with definite yield point can also be calculated using $\Sigma_0 = \Sigma_y$ as the lower limit in (40).

Now, we turn to a derivation of the second-order coefficient P_{c1} in the cavitation pressure power expansion (44). To this end, we note that for the perfectly plastic field the second-order equation (33) takes the form

$$\Sigma'_{r1} = \xi^2(\beta\Sigma'_{r0} - \epsilon'_0)e^{-3\beta\Sigma_{r0}}e^{-\beta\Sigma_y}e^{-3\epsilon_0}, \tag{65}$$

where the dependence of Σ_{r0} and ϵ_0 on ξ is given by (58) and (59). By using the assumption $\Sigma_y \ll 1$ we get from (59) the approximate relation

$$\epsilon_0 = -\beta\Sigma_y + \frac{2}{3}\ln\left(\frac{\xi^3}{\xi^3-1}\right), \tag{66}$$

from which we recover (60) with $\epsilon_0 = \Sigma_y$. Substituting (58), with the aid of (61) and (66) into (65) we get

$$\Sigma'_{r1} = 2e^{4\beta\Sigma_y}\left[\frac{2}{3(\beta+1)\Sigma_y}\right]^{2\beta\Sigma_y}\xi^{-5-6\beta\Sigma_y}(\xi^3-1)[1+\beta\Sigma_y(\xi^3-1)]. \tag{67}$$

Integrating this equation from $\xi=1$ (where $\Sigma_{r1} = -P_{c1}$) to $\xi = \xi_i$, leads to an expression for P_{c1} that depends on the value of Σ_{r1} at the elastic-plastic interface. For $\epsilon = \Sigma$ equations (22) and (23) reduce to the elastodynamic equations and by using the small strains assumption these equations can be linearized and solved, as discussed by Durban and Masri [14]. Hence, for the compressible elastic/perfectly plastic Mises solid, under the assumption $m^2 \ll 1$, the expression for Σ_r at the elastic-plastic interface is

$$\Sigma_r(\xi_i) = -\frac{2}{3}\Sigma_y - \frac{\Sigma_y\xi_i^2(3-\beta)^2}{3(\beta+1)}m^2 + \frac{1}{3}\Sigma_y\xi_i^3\sqrt{\frac{\beta(3-\beta)^5}{(\beta+1)^3}}m^3 + \cdots. \tag{68}$$

Substituting the power expansion for the interface location (54) into (68) gives

$$\Sigma_r(\xi_i) = -\frac{2}{3}\Sigma_y - \frac{\Sigma_y\xi_{i0}^2(3-\beta)^2}{3(\beta+1)}m^2 + \frac{1}{3}\Sigma_y\xi_{i0}^3\sqrt{\frac{\beta(3-\beta)^5}{(\beta+1)^3}}m^3 + \cdots. \tag{69}$$

Notice that the first term coincides with the perfectly plastic quasi-static solution (58) together with (61), at the elastic-plastic interface (60), so the expression for Σ_{r1} at the elastic-plastic interface is simply

$$\Sigma_{r1}(\xi_{i0}) = -\frac{\Sigma_y\xi_{i0}^2(3-\beta)^2}{3(\beta+1)} = -[12(\beta+1)\Sigma_y]^{1/3}\left[\frac{(3-\beta)}{3(\beta+1)}\right]^2. \tag{70}$$

Substituting this expression, and using again the assumption $\Sigma_y \ll 1$ in the integration of (67), we obtain an elegant approximation for P_{c1}

$$P_{c1} = \frac{3}{2} - \frac{1}{3}\left(\frac{2}{3}\right)^{2/3}\frac{\beta(5\beta+21)}{(\beta+1)^{5/3}}\Sigma_y^{1/3}, \tag{71}$$

which reduces to the well-known result, $P_{c1} = 3/2$, for elastic-incompressibility ($\beta=0$). It is evident from (71) that P_{c1} is less than $3/2$ for compressible solids regardless of the value of the yield stress, and decreases with increasing β or Σ_y. Combining (61) with (71) gives a useful approximate cavitation pressure (44) for dynamic spherical cavity expansion in an elastic/perfectly plastic compressible Mises solid, valid for $\Sigma_y, m^2 \ll 1$,

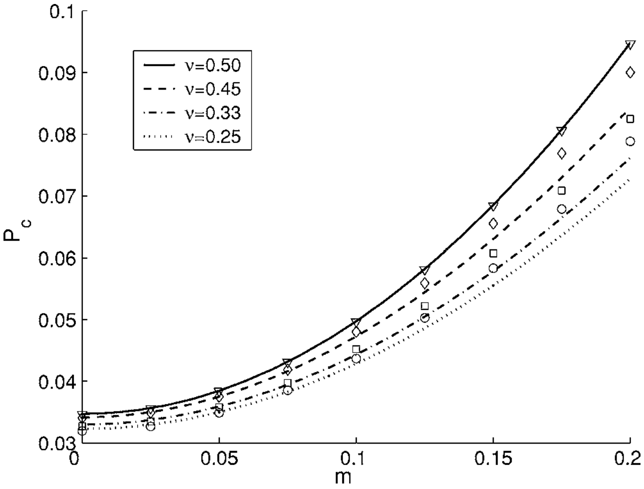

Fig. 7 Variation of cavitation pressure P_c with expansion velocity *m* for elastic/perfectly plastic compressible Mises solids (Σ_y=0.01) with several values of Poisson's ratio. The different markers represent the second-order approximation (72).

$$P_c = \frac{2}{3}\Sigma_y\ln\left[\frac{2}{3(\beta+1)\Sigma_y}\right] + \frac{2}{3}\Sigma_y + \left[\frac{3}{2} - \frac{1}{3}\left(\frac{2}{3}\right)^{2/3}\frac{\beta(5\beta+21)}{(\beta+1)^{5/3}}\Sigma_y^{1/3}\right]m^2. \tag{72}$$

It is worth mentioning that (72) reduces to (61) for quasi-static expansion ($m=0$), while for the incompressible Mises solid ($\beta=0$) we recover the solution derived by Hill [6]

$$P_c = \frac{2}{3}\Sigma_y\ln\left(\frac{2}{3\Sigma_y}\right) + \frac{2}{3}\Sigma_y + \frac{3}{2}m^2. \tag{73}$$

Variations of the cavitation pressure P_c with expansion velocity m for an elastic/perfectly plastic compressible Mises solid ($\Sigma_y = 0.01$) are displayed in Fig. 7. The different markers show the second-order approximation (72) while the curves show the exact solution obtained numerically from Eqs. (22) and (23), using the special relations for elastic/perfectly plastic solids (50). It may be concluded that for $m < 0.2$ the deviation of the approximation from the exact solution is less than 10% and appears to decrease

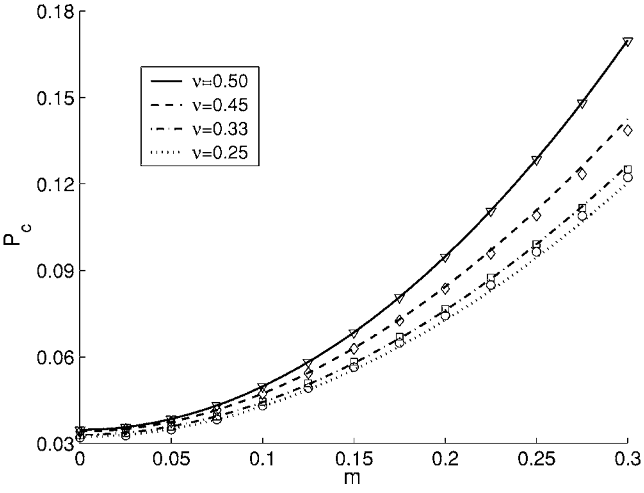

Fig. 8 Variation of cavitation pressure P_c with expansion velocity *m* for elastic/perfectly plastic compressible Mises solids (Σ_y=0.01). The different markers represent the third-order approximation (79).

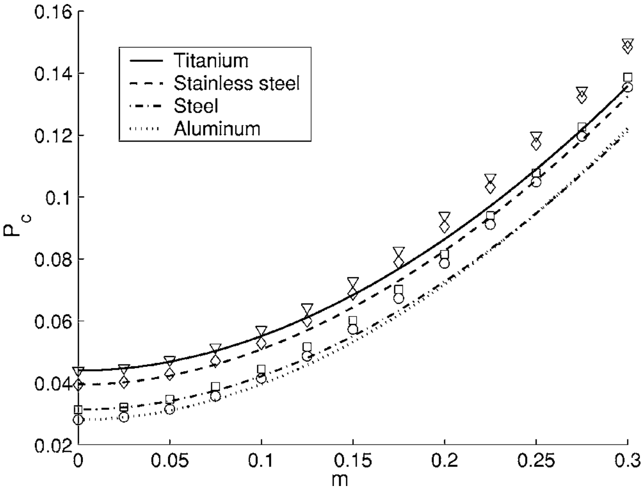

Fig. 9 Variation of cavitation pressure P_c with expansion velocity m for four metals. The different markers represent the modified solution (80).

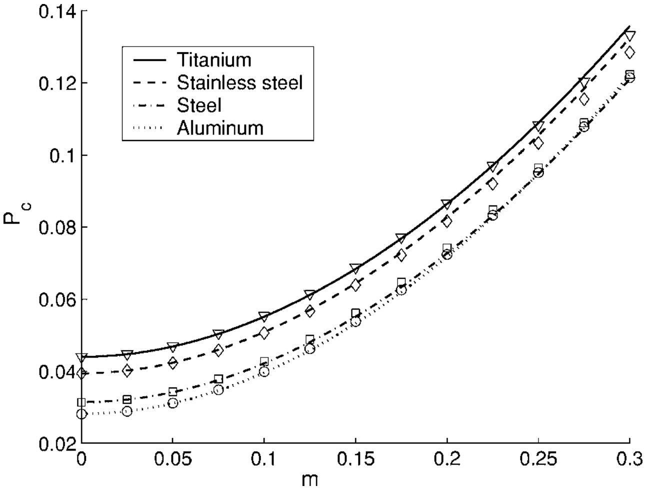

Fig. 10 Variation of cavitation pressure P_c with expansion velocity m for four metals. The different markers represent the equivalent solution (82).

with increasing ν. A similar behavior can be shown for other values of Σ_y. Notice also that the approximate solution appears to be an upper bound on the exact solution.

In Eq. (69) the third term is of order m^3. It appears, therefore, that the approximation of the cavitation pressure can be improved with the third-order term

$$\Sigma_r = \Sigma_{r0} + m^2\Sigma_{r1} + m^3\Sigma_{r2} + \cdots \tag{74}$$

hence, we turn to a derivation of the third-order coefficient P_{c2} in the cavitation pressure power expansion

$$P_c = P_{c0} + m^2 P_{c1} + m^3 P_{c2} + \cdots . \tag{75}$$

Using Eq. (23) for the perfectly plastic field we note that the third-order (m^3) system leads to the simple solution

$$\Sigma_{r2} = \text{Const.} \tag{76}$$

Equating (76) with the third term in (69), at the elastic-plastic interface, leads to the expression

$$\Sigma_{r2} = \frac{1}{3}\Sigma_y \xi_{i0}^3 \sqrt{\frac{\beta(3-\beta)^5}{(\beta+1)^3}}. \tag{77}$$

Now, with the aid of (60), we get

$$P_{c2} = -\frac{2}{9}\sqrt{\beta\left[\frac{(3-\beta)}{(\beta+1)}\right]^5}, \tag{78}$$

which does not depend on the yield stress and is always negative. Combining (61) with (71) and (78) we obtain a useful approximation, valid for $\Sigma_y, m^2 \ll 1$,

$$\begin{aligned} P_c = {} & \frac{2}{3}\Sigma_y \ln\left[\frac{2}{3(\beta+1)\Sigma_y}\right] + \frac{2}{3}\Sigma_y \\ & + \left[\frac{3}{2} - \frac{1}{3}\left(\frac{2}{3}\right)^{2/3}\frac{\beta(5\beta+21)}{(\beta+1)^{5/3}}\Sigma_y^{1/3}\right]m^2 \\ & - \frac{2}{9}\sqrt{\beta\left[\frac{(3-\beta)}{(\beta+1)}\right]^5}\, m^3. \end{aligned} \tag{79}$$

Expression (79) reduces to (61) for quasi-static expansion ($m=0$), while for the incompressible Mises solid ($\beta=0$) we recover (73). Notice that since the term of order m^3 is always negative the second-order approximation provides an upper bound as we have already mentioned. By subtracting (73) from (79) we can isolate the influence of the elastic-compressibility, which is always negative and coupled with the yield stress and dynamic expansion velocity.

For example, with $\beta=1/3$ ($\nu=1/3$) and $\Sigma_y=0.01$ we have $P_{c0}=0.0327$, $P_{c1}=1.244$ and $P_{c2}=-0.726$; while with $\beta=1/2$ ($\nu=1/4$) and $\Sigma_y=0.01$ we find $P_{c0}=0.0320$, $P_{c1}=1.172$ and $P_{c2}=-0.563$. If $\beta=1/3$ ($\nu=1/3$) and $\Sigma_y=0.0025$ then $P_{c0}=0.0105$, $P_{c1}=1.338$ and $P_{c2}=-0.726$. That data suggests that P_{c1} is much larger than P_{c0} but of the same order as P_{c2}.

Variations of the cavitation pressure P_c with expansion velocity m are illustrated in Fig. 8. The different markers show the third-order approximation (79) while the curves show the exact solution obtained numerically from Eqs. (22) and (23) using the special relations for elastic/perfectly plastic solid (50). By comparison with Fig. 7 it can be seen that the third-order approximation (79) is in much better agreement with the exact solution than the second-order approximation (72).

Returning to the expression for P_{c2} in (78), recalling that it is always negative and does not depend on the yield stress, we suggest to add it, as it stands, to the strain-hardening approximate solution (46), to improve the accuracy of the cavitation pressure prediction. Thus, we arrive at the modified expression

$$\begin{aligned} P_c = {} & m^2\int_0^\infty (\beta J_0\Sigma_0 - \beta + \Psi_0) \\ & [\exp(-3\epsilon_0 - \beta\Sigma_0 - 3\beta\Sigma_{r0} + 2K_0)]\mathrm{d}\Sigma_0 \\ & + \int_0^\infty J_0\Sigma_0\mathrm{d}\Sigma_0 - \frac{2}{9}\sqrt{\beta\left[\frac{(3-\beta)}{(\beta+1)}\right]^5}\, m^3. \end{aligned} \tag{80}$$

Application of (80) to the four strain-hardening metals is illustrated in Fig. 9. The different types of markers show the modified solution (80) while the curves show the exact solution obtained numerically from Eqs. (22) and (23). By comparison with Fig. 6 it can be seen that the modified relation (80) improves the approximation, especially for high values of m.

Recalling that the expression for the cavitation pressure, with any strain-hardening relation (80), is much more cumbersome than the expression for elastic/pefectly plastic response (79), we suggest to use the latter to include the strain-hardening effect by the following procedure. From expression (79) it can be concluded that the effect of the yield stress is more dominant in P_{c0} than in P_{c1}, while it does not have any effect on P_{c2}. Also, it appears that P_{c1} is less than 3/2 for compressible solids regardless of the value of the yield stress. Therefore, we define the equivalent cavitation yield stress (Σ_y^c) by equating the quasi-static cavitation pressure solutions (25) and (61), obtained by Durban and Baruch [18] and Hill [15], respectively,

$$\int_0^\infty \frac{\left(\frac{\mathrm{d}\epsilon}{\mathrm{d}\Sigma}+\beta\right)\Sigma \mathrm{d}\Sigma}{\mathrm{e}^{\frac{3}{2}\epsilon-\frac{\beta}{2}\Sigma}-1+2\beta\Sigma} = \frac{2}{3}\Sigma_y^{\mathrm{c}}\left\{1+\ln\left[\frac{1}{3(1-\nu)\Sigma_y^{\mathrm{c}}}\right]\right\}. \quad (81)$$

Thus, using (79) along with $\frac{1}{3}\left(\frac{2}{3}\right)^{2/3} \simeq \frac{159}{625}$, a simple solution for the cavitation pressure, which accounts for strain-hardening, is proposed as the equivalent solution

$$P_c = \frac{2\Sigma_y^c}{3}\left\{1+\ln\left[\frac{1}{3(1-\nu)\Sigma_y^c}\right]\right\} + \left[\frac{3}{2}-\frac{159}{625}\frac{\beta(5\beta+21)\Sigma_y^{c1/3}}{(\beta+1)^{5/3}}\right]m^2 - \frac{2}{9}\sqrt{\beta\left[\frac{(3-\beta)}{(\beta+1)}\right]^5}m^3, \quad (82)$$

which differs from (80) only in the second order coefficient P_{c1}. This simple solution reduces to the exact relations (24) and (25) for dynamic expansion in an incompressible strain-hardening Mises solid ($\beta=0$) and for quasi-static expansion ($m=0$) in a compressible strain-hardening Mises solid, respectively. Relation (25) is accurate, so for consistency we need to equate it, in (81), with the accurate relation (63), but in practice ($\Sigma_y^c \ll 1$) the simple approximate solution (61) is sufficient.

We have already calculated, in Sec. 3, the values of P_{c0} (LHS of (81)) for the four metals considered there. Hence, from Eq. (81), the equivalent cavitation yield stresses for these metals are: $\Sigma_y^c=0.00830$ (aluminum), $\Sigma_y^c=0.00971$ (steel), $\Sigma_y^c=0.01280$ (stainless steel), and $\Sigma_y^c=0.01455$ (titanium). For these equivalent cavitation yield stresses the values of P_{c1} for the four metals are: $P_{c1}=1.247$ ($P_{c2}=-0.700$) for the aluminum, $P_{c1}=1.190$ ($P_{c2}=-0.602$) for the steel, $P_{c1}=1.188$ ($P_{c2}=-0.661$) for the stainless steel and $P_{c1}=1.210$ ($P_{c2}=-0.726$) for the titanium. It is interesting to note that for these four metals and other few examples (including aluminum 6061-T651, which will be discussed in the next section) the ratio P_{c0}/Σ_y^c is in the range of 3 to 4.

Application of (82) to the four strain-hardening metals is shown in Fig. 10. The different types of markers show the equivalent solution (82), while the curves show the exact solution obtained numerically from Eqs. (22) and (23). By comparison with Fig. 9 it can be seen that the simple relation (82) is much more accurate than the complex relation (80).

5 Application to the Problem of Penetration Into Metal Targets

Applying the well-known technique (Forrestal et al. [11]; Jones and Rule [13]), of using the dynamic spherical cavitation pressure along with the Coulomb friction law, to analyze penetration of axisymmetric rigid projectile into a uniform target, at normal incidence, we use our relation for the cavitation pressure $P_c=P_{c0}+m^2P_{c1}+m^3P_{c2}$ with the definition of m in (4) to derive an expression for the penetration depth

$$H=\frac{M_p}{2\pi\rho_0}\int_0^{\Lambda_s}\frac{\Lambda\,\mathrm{d}\Lambda}{A_0+A_1\Lambda^2+A_2\Lambda^3} \quad \text{with} \quad \Lambda=\frac{V_p}{\sqrt{E/\rho_0}}. \quad (83)$$

Here M_p denotes the penetrator mass, V_p denotes the instantaneous penetrator velocity and Λ_s is the nondimensionalized impact velocity, defined by the striking velocity V_s,

$$\Lambda_s=\frac{V_s}{\sqrt{E/\rho_0}}. \quad (84)$$

The coefficients A_i, that have the dimension of area, are defined by

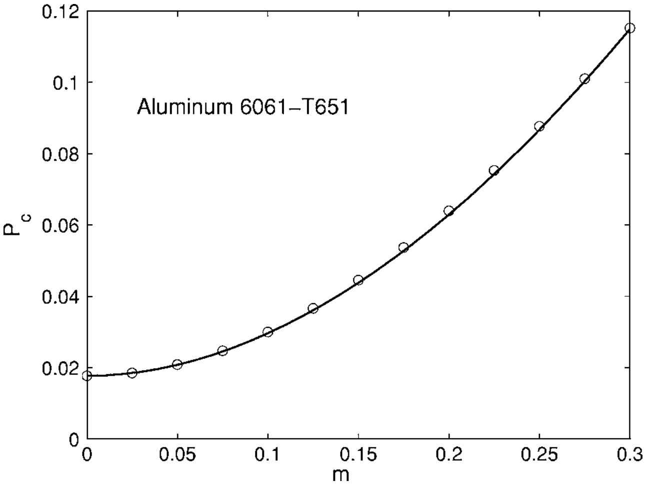

Fig. 11 Variation of cavitation pressure P_c with expansion velocity m for aluminum 6061-T651. The circle markers represent the equivalent solution (82) with $\Sigma_y^c=0.00466$.

$$A_i=P_{ci}\int_0^L(y'+\mu)y\left[\frac{y'}{\sqrt{1+(y')^2}}\right]^{i(5-i)/2}\mathrm{d}x \quad i=0,1,2 \quad (85)$$

where L is the projectile nose length, μ is the sliding-friction coefficient and $y=y(x)$ is the shape function of an axisymmetric penetrator with $0\leqslant x\leqslant L$, which need to be nose-pointed [$y(0)=0$], must satisfy the condition $y'\geqslant 0$ and has a base diameter of $d=2y(L)$. Notice that in Eq. (85) superposed prime denotes differentiation with respect to x. The expressions for the coefficients P_{ci} ($i=0,1,2$) are given in (61), (71), and (78) for the elastic/perfectly plastic model, and in (41), (45), and (78) for strain-hardening response. To include the strain-hardening effect by using the elastic/perfectly plastic model we need to replace Σ_y with the equivalent cavitation yield stress (Σ_y^c) determined from Eq. (81). Notice that while A_0 and A_1 are positive, A_2 is negative and recall also that for the conical-nose projectile all three coefficients A_i have simple analytical expressions.

From (85) it can be seen that for any projectile shape and any metal targets $A_1\geqslant\Lambda|A_2|$ (under the assumption $\Lambda_s^2\ll 1$) so it appears that $A_2\Lambda^3$ is negligible in comparison with $A_1\Lambda^2$. Hence, for all practical purposes, a simple approximation to the penetration depth (83) is the well-known logarithmic type solution (Poncelet formula)

$$H=\frac{M_p}{2\pi\rho_0}\int_0^{\Lambda_s}\frac{\Lambda\,\mathrm{d}\Lambda}{A_0+A_1\Lambda^2}=\frac{M_p}{4\pi\rho_0A_1}\ln\left(1+\frac{A_1}{A_0}\Lambda_s^2\right), \quad (86)$$

but here we have the analytical expressions for the coefficients A_i ($i=0,1$), that include the influence of elastic-compressibility and strain-hardening of the target material. It is interesting to note that while the third-order correction is vital in improving the accuracy of the approximated cavitation pressure it is negligible for the calculation of penetration process. Also, because A_2 is negative, relation (83) provides an upper bound on the Poncelet formula (86), but for the incompressible response ($\beta=0$) relations (83) and (86) are exactly the same because $A_2=0$.

Employing expressions (83) and (86) to penetration into aluminum 6061-T651 targets, by conical, ogival and spherical-nose projectiles with a nominal mass of $M_p=24[gr]$ (Forrestal et al. [11]), and by different spherical-nose projectiles (Forrestal et al. [12]), we compare our results to the penetration depth tests (Figs. 12–17). The geometry of the penetrators and the aluminum characteristics were taken as suggested in those papers. The aluminum 6061-T651 characteristics are: $\nu=1/3$, $E=68.9$[GPa], ρ_0

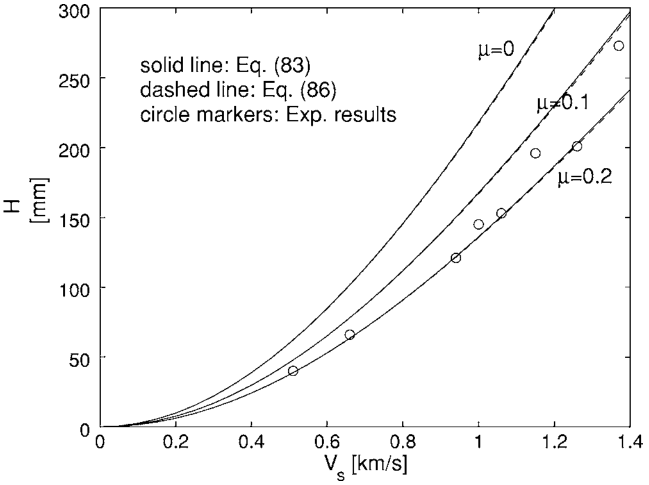

Fig. 12 Comparison between cavitation model and penetration depth tests for conical-nose projectiles (Forrestal et al. [11]). Differences between relation (83) and the logarithmic expression (86) are hardly noticeable.

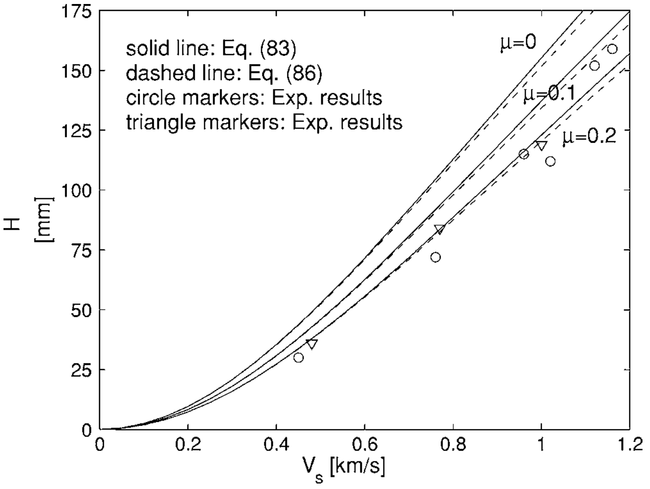

Fig. 14 Comparison between cavitation model and penetration depth tests for spherical-nose projectiles (Forrestal et al. [11])

$=2710[\mathrm{kg/m^3}]$ along with the modified Ludwik equation as the power-hardening law. We use this power-law relation in our notation, namely with the total strain $\epsilon=\epsilon(\Sigma)$ as a known function of the effective stress Σ

$$\epsilon=\Sigma \qquad 0\leqslant\Sigma\leqslant\Sigma_y,$$

$$\epsilon=\left(\frac{\Sigma}{\Sigma_y{}^{1-n}}\right)^{1/n} \qquad \Sigma\geqslant\Sigma_y, \tag{87}$$

where $n=0.051$ is the strain-hardening exponent. Here $Y=276[\mathrm{MPa}]$ denotes the yield stress so $\Sigma_y=0.00401$. For this power-hardening law the quasi-static cavitation pressure, from (25), is $P_{c0}=0.0176$. To include strain-hardening in the elastic/perfectly plastic model we calculate the equivalent cavitation yield stress (Σ_y^c) from Eq. (81) to obtain $\Sigma_y^c=0.00466$ ($\bar{Y}=321[\mathrm{MPa}]$). For this equivalent value $P_{c1}=1.301$ ($P_{c2}=-0.726$) and by applying (82) we show in Fig. 11 the cavitation pressure for aluminum 6061-T651. The circle markers show the equivalent solution (82) while the curve shows the exact solution obtained numerically from Eqs. (22) and (23).

Forrestal et al. [11] used the value of $\bar{Y}=400[\mathrm{MPa}]$ while Yarin et al. [16] used the value of $\bar{Y}=396[\mathrm{MPa}]$ for their perfectly plastic models. In a later paper (Forrestal et al. [9]) another value is suggested ($\bar{Y}=340[\mathrm{MPa}]$) which is closer to our calculation ($\bar{Y}=321[\mathrm{MPa}]$). It is obvious that the value of $\bar{Y}$ influences the choice of μ for best fit with test results. As mentioned by Forrestal et al. [11,12], several authors have presented high-speed sliding-friction data for metals in the range $\mu=0.02$ to $\mu=0.2$. In this spirit we have used several sliding-friction coefficients, as illustrated in Figs. 12–17. Clearly, other approximations, like the Coulomb friction law assumption and the relation between penetration and cavity expansion velocities, can be made in using the cavitation model as an engineering model for the penetration problem, so the selection of μ may compensate for the approximations involved in these assumptions.

From Figs. 12–17 it can be seen that the effect of the friction coefficient μ is more dominant as the striking velocity is higher, and that its value varies between 0.05 and 0.15. Another conclu-

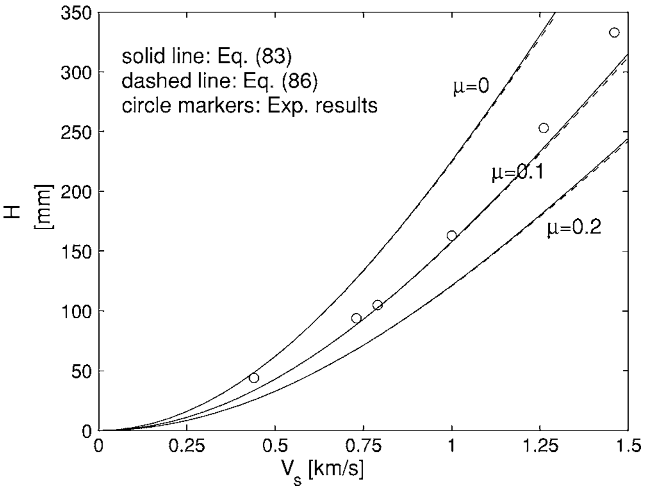

Fig. 13 Comparison between cavitation model and penetration depth tests for ogival-nose projectiles (Forrestal et al. [11]). Differences between relation (83) and the logarithmic expression (86) are hardly noticeable.

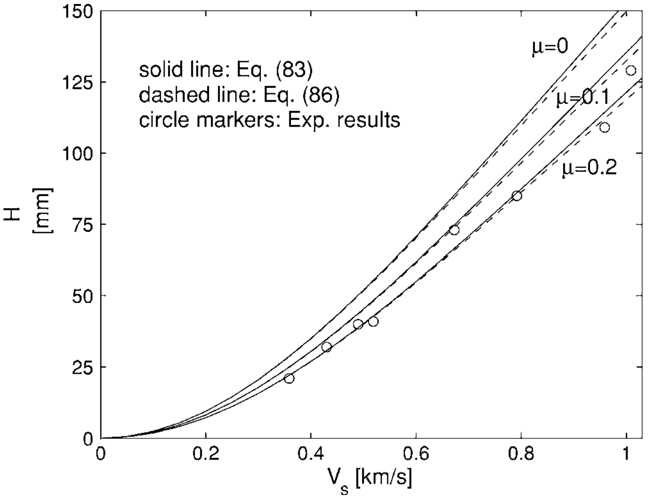

Fig. 15 Comparison between cavitation model and penetration depth tests for spherical-nose projectiles (Forrestal et al. [[12]-Table 1])

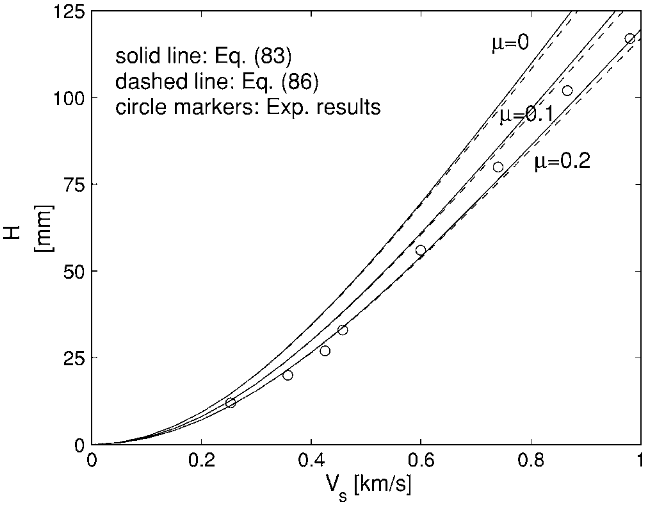

Fig. 16 Comparison between cavitation model and penetration depth tests for spherical-nose projectiles (Forrestal et al. [[12]-Table 2])

sion is that the influence of μ on the conical and ogival-nose projectiles is more dominant than on the spherical-nose projectiles. Also, it can be seen that the Poncelet formula (86) is a good approximation and we do not need to use the more complex relation (83), which is an upper bound for the Poncelet formula.

Finally, we present a brief comparison between our cavitation model and the Rankine ovoid model, developed by Yarin et al. [16]. The target response for the ovoid model assumed to be incompressible, rigid/perfectly plastic with a remote linear elastic zone. As mentioned before, Yarin et al. [16] used a higher value of $\bar{Y}$ for the aluminum 6061-T651 ($\bar{Y}=396[\text{MPa}]$) as compared to our suggestion of $\bar{Y}=321[\text{MPa}]$. Also, Yarin et al. [16] ignored the friction component acting on the ovoid. In Fig. 18 we show the penetration test results obtained by Forrestal et al. [11] for conical, ogival and spherical-nose projectiles as compared with our cavitation model predictions, and with Yarin et al. [16] ovoid engineering approximation. For our cavitation model (86) we used $\bar{Y}=321[\text{MPa}]$ and $\nu=1/3$ ($\beta=1/3$) along with $\mu=0.15$ for the conical and spherical-nose projectiles and $\mu=0.075$ for the ogival-nose projectile. For the ovoid model we used Yarin et al. [16] suggestions for the shear modulus $G=28[\text{GPa}]$ and the equivalent cavitation yield stress $\bar{Y}=396[\text{MPa}]$ along with our suggestions $G=68.9/[2(1+1/3)]\simeq 25.8[\text{GPa}]$ and $\bar{Y}=321[\text{MPa}]$. According to the ovoid penetration depth formula, the difference between the values of the shear modulus has a negligible influence comparing to the significant influence of the difference in $\bar{Y}$. From Fig. 18 it can be seen that for low striking velocities the differences are hardly noticeable while for high striking velocities the differences are significant. Also, it can be seen that the ovoid model needs to include a friction component for best fit with penetration depth tests, especially if the value of the equivalent cavitation yield stress is found from the procedure suggested in this article. Another conclusion is that consideration of the shape of the projectile nose is vital for improving the accuracy. Here it is worth mentioning that Yarin et al. [16] generalized the ovoid theory to describe penetration of arbitrary axisymmetric projectile nose shapes using the singularities distribution method.

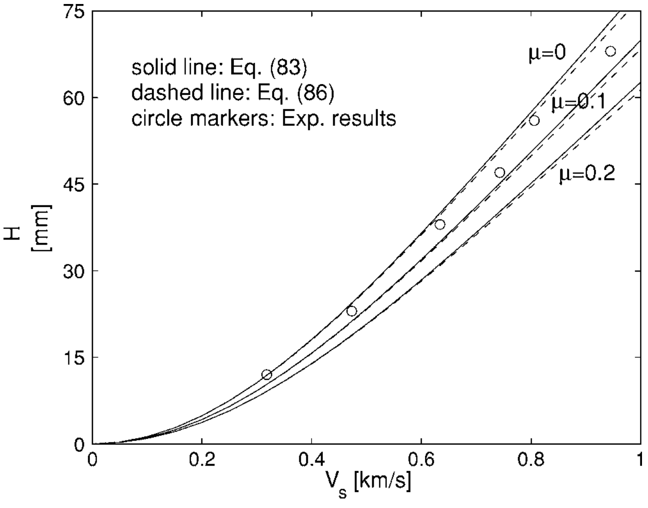

Fig. 17 Comparison between cavitation model and penetration depth tests for spherical-nose projectiles (Forrestal et al. [[12]-Table 3])

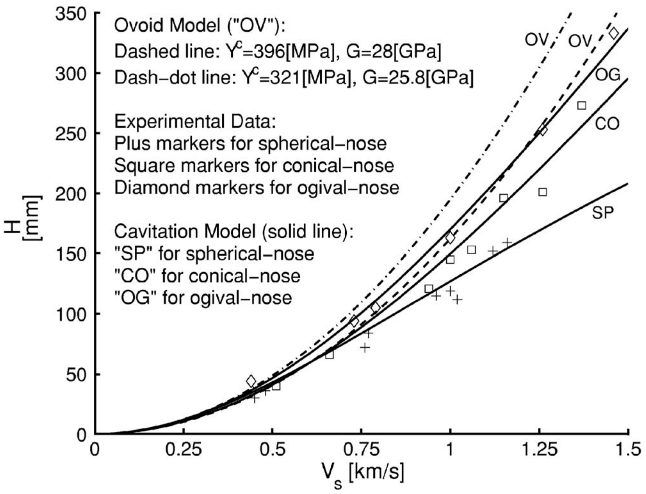

Fig. 18 Comparison between cavitation and Rankine ovoid models. The different markers represent penetration test results obtained by Forrestal et al. [11] and here Y^c represents $\bar{Y}$.

6 Concluding Remarks

We have presented a detailed analysis of the steady-state self-similar expansion of a pressurized spherical cavity in an infinite compressible Mises solid. The analytical study covers only the case where the expansion velocity is much smaller than the speed of sound in the solid, or mathematically when $m^2 \ll 1$, while numerical solutions can be obtained with much higher expansion velocities. We have analyzed the strain hardening solid along with the special case of an elastic/perfectly plastic solid, and demonstrated an application to metal penetration mechanics. We observe that the dynamic cavitation pressure has the Bernoulli form only for small expansion velocities and that the dynamic part of the cavitation pressure is influenced by elastic-compressibility and strain-hardening (or yield stress). It appears that the effect of elastic-compressibility is more dominant in the dynamic term than in the quasi-static term while the influence of strain-hardening (equivalent cavitation yield stress) is more dominant in the quasi-static term than in the dynamic term.

For the case of strain-hardening solids we obtained an approximate parabolic type solution along with a modified solution for the dynamic cavitation pressure. Both solutions reduce to the exact closed form relations for quasi-static expansion and the incompressible Mises solid. The common observation that can be deduced from Figs. 6 and 9 is that the second-order approximation (46) and the modified solution (80) are upper bounds for the exact solution. By introducing the equivalent cavitation yield stress, defined by Eq. (81), we suggest an elegant way to include strain-hardening in the simple elastic/perfectly plastic solution (82). A comparison between Figs. 9 and 10 reveals the accuracy of this approach.

For the case of elastic/perfectly plastic solids we obtained simple approximate parabolic solution (72), with a third-order power expansion approximation (79) for the dynamic cavitation pressure. From these solutions we can see the influence, of both elastic-compressibility and yield stress, on every term in the power expansion. The common observation that can be deduced analytically, and seen in Figs. 7 and 8, is that elastic-compressibility lowers the cavitation pressure. Another important observation is that the Bernoulli type solution (72) is an upper bound for the exact solution.

We have applied our dynamic spherical cavitation pressure results to the problem of metal penetration mechanics. The simple elastic/perfectly plastic model can be used to incorporate strain-hardening effects by using the equivalent cavitation yield stress (81) and (82). Comparison between penetration depth predictions to penetration tests of conical, ogival and spherical-nose projectiles into aluminum 6061-T651 targets show good agreement. Another important result is that while the third order correction is vital in improving the accuracy of the approximated cavitation pressure it is negligible for calculations of penetration depth. For all practical purposes a simple approximation to the penetration depth is the well-known logarithmic type formula (86), but here we have derived analytical expressions for the coefficients A_i ($i=0,1$), that include the influence of elastic-compressibility and strain-hardening of the target material.

Acknowledgment

One of us (D.D.) wishes to acknowledge the support of the Sydney Goldstein Chair in Aerospace Engineering. Part of this study was supported by the fund for the promotion of research at the Technion.

References

[1] Bishop, R. F., Hill, R., and Mott, N. F., 1945, "The Theory of Indentation and Hardness," Proc. Phys. Soc. London **57**, pp. 147–159.
[2] Nelson, R. W., 2003, "Nuclear Bunker Busters, Mini-Nukes, and the US Nuclear Stockpile," Phys. Today **56**, pp. 32–37.
[3] Levi, M., 2004, "Nuclear Bunker Buster Bombs," Sci. Am. **291**, pp. 50–57.
[4] Hopkins, H. G., 1960, "Dynamic Expansion of Spherical Cavities in Metal," in *Progress in Solid Mechanics*, Vol. 1, edited by I. N. Sneddon, R. Hill North-Holland, Amsterdam.
[5] Goodier, J. N., 1965, "On the Mechanics of Indentation and Cratering in the Solid Targets of Strain-Hardening Metal by Impact of Hard and Soft Spheres," *Proceedings of the 7th Symposium on Hypervelocity Impact. III*, 215–259.
[6] Hill, R., 1948, "A Theory of Earth Movement Near a Deep Underground Explosion," Memo No. 21-48, Armament Research Establishment, Fort Halstead, Kent, England.
[7] Hunter, S. C., and Crozier, R. J. M, 1968, "Similarity Solution for the Rapid Uniform Expansion of a Spherical Cavity in a Compressible Elastic-Plastic Solid," Q. J. Mech. Appl. Math. **21**, pp. 467–486.
[8] Forrestal, M. J., and Luk, V. K., 1988, "Dynamic Spherical Cavity-Expansion in a Compressible Elastic-Plastic Solid," J. Appl. Mech. **55**, pp. 275–279.
[9] Forrestal, M. J., Tzou, D. Y., Askari E., and Longcope, D. B., 1995, "Penetration Into Ductile Metal Targets With Rigid Spherical-Nose Rods," Int. J. Impact Eng. **16**, pp. 699–710.
[10] Luk, V. K., Forrestal, M. J., and Amos, D. E., 1991, "Dynamic Spherical Cavity Expansion of Strain-Hardening Materials," J. Appl. Mech. **58**, pp. 1–6.
[11] Forrestal, M. J., Okajima K., and Luk, V. K., 1988, "Penetration of 6061-T651 Aluminum Targets With Rigid Long Rods," J. Appl. Mech. **55**, pp. 755–760.
[12] Forrestal, M. J., Brar, N. S., and Luk V. K., 1991, "Penetration of Strain-Hardening Targets With Rigid Spherical-Nose Rods," J. Appl. Mech. **58**, pp. 7–10.
[13] Jones, S. E, and Rule, W. K., 2000, "On the Optimal Nose Geometry for a Rigid Penetrator, Including the Effects of Pressure-Dependent Friction," Int. J. Impact Eng. **24**, pp. 403–415.
[14] Durban, D., and Masri, R., 2004, "Dynamic Spherical Cavity Expansion in a Pressure Sensitive Elastoplastic Medium," Int. J. Solids Struct. **41**, pp. 5697–5716.
[15] Hill, R., 1950, *The Mathematical Theory of Plasticity*, Oxford University Press, London.
[16] Yarin, A. L., Rubin, M. B., and Roisman I. V., 1995, "Penetration of a Rigid Projectile Into an Elastic-Plastic Target of Finite Thickness," Int. J. Impact Eng. **16**, pp. 801–831.
[17] Durban, D., and Fleck, N. A., 1997, "Spherical Cavity Expansion in a Drucker-Prager Solid," J. Appl. Mech. **64**, pp. 743–750.
[18] Durban, D., and Baruch, M., 1976, "On the Problem of a Spherical Cavity in an Infinite Elasto-Plastic Medium," J. Appl. Mech. **43**, pp. 633–638.

A Nonlinear Model for Dielectric Elastomer Membranes

Nakhiah Goulbourne

Eric Mockensturm
e-mail: emm10@psu.edu

Mary Frecker

Department of Mechanical Engineering,
Pennsylvania State University,
University Park, PA 16802

The material and geometrical nonlinearities of novel dielectric elastomer actuators make them more difficult to model than linear materials used in traditional actuators. To accurately model dielectric elastomers, a comprehensive mathematical formulation that incorporates large deformations, material nonlinearity, and electrical effects is derived using Maxwell-Faraday electrostatics and nonlinear elasticity. The analytical model is used to numerically solve for the resultant behavior of an inflatable dielectric elastomer membrane, subject to changes in various system parameters such as prestrain, external pressure, applied voltage, and the percentage electroded membrane area. The model can be used to predict acceptable ranges of motion for prescribed system specifications. The predicted trends are qualitatively supported by experimental work on fluid pumps [A. Tews, K. Pope, and A. Snyder, Proceedings SPIE, 2003)]. For a potential cardiac pump application, it is envisioned that the active dielectric elastomer membrane will function as the motive element of the device. [DOI: 10.1115/1.2047597]

Keywords: dielectric elastomer, membrane, electroactive polymer, electroelastic model, blood pump

1 Introduction

Artificial blood pump systems have gone through various design changes and upgrades in response to progress made in our understanding of mammalian physiology, engineering techniques, and materials science. Unfortunately, currently available devices have various limitations; the most common issues are associated with weight, size, complexity and durability [1,2]. The energy efficient natural heart functions both as a fluid receptacle and its own actuation source; the very walls of the heart chambers (ventricles) contract and relax to effect fluid displacement [3]. In contrast, mechanical positive displacement pumps use separate actuation sources (such as an electromechanical driver coupled to a pusher-plate) to drive a fluid-filled passive polyurethane sac via a diaphragm intermediary. To minimize the problems associated with these pumps, and move towards a design that captures the essence of the natural heart, we seek to incorporate electroactive materials in the device.

Materials that exhibit mechanical displacement in the presence of an electric field are commonly referred to as being electroactive. This group of materials includes polymer gels, piezoelectrics, electrostrictives, dielectric elastomers, and others. Here, we study the dielectric elastomer primarily because of its high strain capability. The dielectric elastomer *actuator* is a three-component system consisting of a soft dielectric elastomer sandwiched between two deformable electrodes. In essence, it functions as a very compliant deformable capacitor.

For an artificial pump, we imagine replacing the pneumatically actuated passive diaphragm with an electroactive membrane. The membrane in the presence of an external electric field will be deformed in such a way as to effectively pump blood out of the receptacle. The electroactive diaphragm will function as the motive element of the pump, eliminating the need for a separate actuation source, reducing some of the bulk associated with the current device, and thus creating simpler, lighter, more compact designs.

Simple elastic models for uniform uniaxial deformations of dielectric elastomer actuators have been formulated by Pelrine et al. [4] and by Kofod [5]. Here, we develop a method for modeling a dielectric elastomer membrane that accounts for material nonlinearities and large deformations. Although the method is specifically tailored to inflatable axisymmetric elastomer membranes, the form is general enough to be extended for other mechanical configurations with minor modifications. For the case of a dielectric elastomer pump, we assume that electrostatic Coulomb forces between the compliant electrodes causes thinning of the dielectric elastomer and that the electrostrictive effects, the relative displacements of the charges of the individual dipoles of the dielectric, are negligibly small [6]. Piezoelectric effects are not present since the dielectric is isotropic. We employ the theory of elasticity to characterize the mechanical portion of our model; electrostatic theory describes the electrical portion. The complete equations of state for an elastic dielectric can be derived by applying a variational principle of virtual work or by the more general Cauchy method analogous to elasticity theory [7].

2 Electroelastic Stress and Electrical Traction

Incorporating the electrical properties of the system into the preexisting framework of nonlinear elasticity renders an augmentation of the elastic Cauchy stress. If the augmentation to the in-plane Cauchy stresses is small compared to the pre-stress, the electrical force per unit area of the deformable conductors on the soft dielectric elastomer appears as tractions on the major surfaces. These expressions are developed in the following segments. A comprehensive coverage of electrostatic theory in the presence of dielectrics can be found in many physics texts, for example, Landau and Lifshitz [8], Jackson [9], and Schwinger [10]. We consider a dielectric material placed in an electrostatic field created by the presence of externally charged conductors. Of marked interest is the presence and nature of the electric field and not of the particular configuration of the conductors themselves. In a dielectric, the relationship between the electric field **E** and the electric displacement **D** is described by

---

Contributed by the Applied Mechanics Division of THE AMERICAN SOCIETY OF MECHANICAL ENGINEERS for publication in the ASME JOURNAL OF APPLIED MECHANICS. Manuscript received by the Applied Mechanics Division, July 21, 2004; final revision, April 21, 2005. Review conducted by N. Triantafyllides. Discussion on the paper should be addressed to the Editor, Prof. Robert M. McMeeking, Journal of Applied Mechanics, Department of Mechanical and Environmental Engineering, University of California—Santa Barbara, Santa Barbara, CA 93106-5070, and will be accepted until four months after final publication in the paper itself in the ASME JOURNAL OF APPLIED MECHANICS.

$$\mathbf{D} = \varepsilon_0 \mathbf{E} + \mathbf{P}, \tag{1}$$

where ε_0 is the permittivity of free space and $\mathbf{P}$ is the polarization vector which is a function of the electric field. In vacuum, the polarization vector vanishes. Our presentation on dielectric elastomers is specific to the case of uniform homogeneous isotropic hyperelastic materials. In this case, it is customary to assume a linear electrical constitutive relation between $\mathbf{D}$ and $\mathbf{E}$ such that Eq. (1) is given by

$$\mathbf{D} = \varepsilon \mathbf{E}. \tag{2}$$

where ε is the dielectric constant of the material.

2.1 Stress Definition. In elasticity theory, the stress tensor is expressed as a function of the displacement gradients. If the system is conservative, there is a constitutive relation between the stress and the displacement gradients that can be derived from a single strain energy potential. Since both mechanical and electrical fields are present in hyperelastic dielectrics, we assume that the state of stress at a point in the deformed medium is determined by (1) the local elastic state of the medium and (2) the electrostatic field. In a zero electric field situation, the equations of elasticity are fully recovered.

We defer to Maxwell-Faraday electrostatics to account for electrical effects in the system. Maxwell postulated that a state of stress exists in the intervening medium between two charged bodies (conductive surfaces) which renders the observable force of attraction or repulsion between the charged bodies [11]. The well-known electrostatic Maxwell stress tensor $\boldsymbol{\sigma}_{\mathbf{M}}$ is given for a homogenous isotropic dielectric [11] by

$$\boldsymbol{\sigma}_M = \varepsilon \mathbf{E} \otimes \mathbf{E} - \frac{\varepsilon \bar{E} \,.\, \bar{E} \bar{I}}{2}, \tag{3}$$

where $\mathbf{I}$ is the identity tensor and electrostrictive effects have been neglected.

We adopt the postulate that for an elastic dielectric the Cauchy stress tensor σ can be written as the sum of the local elastic stress tensor and the Maxwell stress tensor [7]

$$\boldsymbol{\sigma} = \boldsymbol{\sigma}_E + \boldsymbol{\sigma}_M, \tag{4}$$

where $\boldsymbol{\sigma}_{\mathbf{E}}$ is the local elastic stress tensor given as a function of the displacement gradients. For a truly coupled response, such as that occurring in piezoelectric and electrostrictive materials, the stress $\boldsymbol{\sigma}_{\mathbf{E}}$ is derivable from a single internal energy function Σ that depends on electrical variables such as the polarization $\mathbf{P}$ (or the electric displacement $\mathbf{D}$) in addition to the deformation gradients $\mathbf{F}$ [7,12]. For an isotropic hyperelastic dielectric, this internal energy is ultimately reduced to a function of six independent scalar invariants (I_Γ), where I_Γ is not a unique combination of strain invariants and electrical invariants [12]. Consequently, the total stress is

$$\boldsymbol{\sigma} = \frac{\rho_m}{\rho_0} \frac{\partial \Sigma(I_\Gamma)}{\partial \mathbf{F}} \mathbf{F} + \boldsymbol{\sigma}_M, \tag{5}$$

where ρ_0 is the initial mass density, and ρ_m is the current mass density. If there is no direct coupling between the polarization and the mechanical stress, where direct coupling implies that a change in the polarization effects change in the deformation and vice versa, then the internal energy is a state function of only three scalar strain invariants; two independent scalar invariants for an incompressible material. For the uniform dielectric elastomer under consideration—homogenous, isotropic, incompressible, and hyperelastic—the elastic stress tensor is derived from a purely mechanical strain energy function $\Sigma(I_1, I_2)$. In this case the total stress is

$$\boldsymbol{\sigma} = \frac{\rho_m}{\rho_0} \frac{\partial \Sigma(I_1, I_2)}{\partial \mathbf{F}} \mathbf{F} + \boldsymbol{\sigma}_M. \tag{6}$$

2.2 The Electrical Traction. The boundary of the dielectric merits special consideration particularly when conductors are present. Under the assumption of electrostatics, the electric field is zero within a conductor, both the interior and exterior of the conductor are at constant potential, and all the excess charge resides on the conductor surface. At the boundary between a dielectric and a conductor, the tangential component of the electric field is zero and the normal component of the electric displacement vector is equal to the surface charge density ω_c of the conductor [8]

$$\begin{aligned} \mathbf{n} \otimes \mathbf{E} &= \mathbf{0}, \\ \mathbf{n} \,.\, \mathbf{D} &= \omega_c, \end{aligned} \tag{7}$$

where $\mathbf{n}$ is the outward normal vector to the conductor surface. The electrical force acting on a unit area of the conductor surface is determined from the Maxwell stress tensor as

$$\mathbf{n} \,.\, \boldsymbol{\sigma}_M = -\frac{\varepsilon E^2}{2} \mathbf{n} + \mathbf{n} \,.\, \mathbf{D} \otimes \mathbf{E}. \tag{8}$$

Expressing the electric field in terms of tangential and normal components [10]

$$\varepsilon E^2 = \varepsilon (\mathbf{n} \otimes \mathbf{E})^2 + \frac{1}{\varepsilon} (\mathbf{n} \,.\, \mathbf{D})^2, \tag{9}$$

and using the boundary conditions [Eq. (7)] we can rewrite Eq. (8) as

$$\mathbf{n} \,.\, \boldsymbol{\sigma}_M = -\frac{\omega_c^2}{2\varepsilon} \mathbf{n} + \omega_c \mathbf{E}. \tag{10}$$

Clearly, the tangential components of the force per unit area are zero, only the normal component of the force per unit area (traction) remains

$$\mathbf{n} \,.\, \boldsymbol{\sigma}_M \,.\, \mathbf{n} = -\frac{\omega_c^2}{2\varepsilon} + \frac{\omega_c}{\varepsilon} \mathbf{n} \,.\, \mathbf{D} = \frac{\omega_c^2}{2\varepsilon}. \tag{11}$$

The dielectric elastomer is flanked by two compliant electrodes across its thickness that we assume to be perfectly attached. For identical parallel conducting surfaces the equal and opposite traction on each of the conductors (Eq. (11)) pulls the conductors toward each other into the electric field and squeezes the intervening dielectric elastomer; the soft elastomer thins and increases in area. The compliance of the soft electrodes means that during the deformation, the area of the conductors change in unit proportionality to the elastomer area without restraining the elastomers in-plane motion. At any point in the deformation, we assume a uniform surface charge density over the area of the parallel conductors such that the magnitude is

$$\omega_c = Q/A, \tag{12}$$

where Q and A are not constants. When the conductor area increases or decreases the surface charge density changes accordingly. Consequently, to maintain constant potential more charge will be deposited or removed from the respective conductors. It is reasonable to assume that the charging response is instantaneous, that is to say, on the time scale of the mechanical response.

The geometry of parallel conducting surfaces, where the thickness separation is much smaller than the area, and the intervening dielectric is characterized by a uniform dielectric constant ε, leads to the following reduced expression for the charge [10]

$$Q = \int \mathrm{d}A\, \omega_c = (\phi_1 - \phi_2) \frac{\varepsilon}{\mathrm{d}} \int \mathrm{d}A = (\phi_1 - \phi_2) \frac{\varepsilon}{\mathrm{d}} A, \tag{13}$$

where dA is the deformed area element, $\phi_{1,2}$ is the constant potential on each conductor, d is the present conductor separation and A is the current area. Then the traction on each of the conducting surfaces is simply

$$\mathbf{n} \cdot \boldsymbol{\sigma}_M \cdot \mathbf{n} = \frac{\omega_c^2}{2\varepsilon} = \frac{\varepsilon(\phi_1 - \phi_2)^2}{2\mathrm{d}^2} = \frac{\varepsilon E^2}{2}. \tag{14}$$

This is similar to the expression generally obtained for rigid parallel plate capacitors where the total force on each conductor is calculated by multiplying Eq. (14) by the current area. Using Eq. (4) for the total stress in the dielectric elastomer and Eq. (14) for the traction on its major surfaces, we can develop an analytical model of our system from equilibrium equations, geometrical relations, and constitutive equations. It should be noted that here we focus on the surface tractions since they are the major contributors in a membrane theory although in-plane Maxwell stresses do exist.

3 Electroelastic Model

3.1 General Approach. In this section we develop an analytical model for the inflation of an axisymmetric dielectric elastomer actuator. We seek to solve the problem of a thin film dielectric elastomer subject to both mechanical forces in the form of an external pressure, and an external electric field created by the presence of two parallel conductors that exert an equal and opposite traction on the elastomer's major surfaces. Electrostatic theory and the theory of elasticity are combined to produce a comprehensive model to solve for the response.

Since dielectric elastomers are often prestrained to generate larger forces, we consider a membrane of initial radius R_i that is prestretched by an amount λ_o, and then clamped at radius R_o. The circular diaphragm is initially flat and no field is present. We then apply an external electric field and a pressure differential across the diaphragm. The following formulation presumes an electric field created by a constant potential difference between the electrodes, typically a thin layer of conductive grease that is assumed to adhere perfectly to the dielectric in such a way that it does not impede the motion of the dielectric elastomer. For less compliant electrodes, mechanical effects may become prominent as the membrane deforms.

The nonlinear large deformation model of elastic membranes by Adkins and Rivlin [13] interrelates geometric, constitutive, and equilibrium equations to produce a system of second order nonlinear differential equations that can be solved given the necessary system parameters. Using their approach, we can solve for the case of inflatable dielectric elastomer membranes. The geometric equations and the form of the equilibrium equations are unaltered.

3.2 Equations of Equilibrium. Given that the membrane thickness is much less than the radii of curvature and the extension ratios are greater than unity, we presume that the dielectric elastomer can be modeled as a membrane. The form of the three-dimensional equilibrium equations of elasticity theory is applicable for a homogenous isotropic dielectric elastomer where the purely mechanical stress tensor is replaced with an augmented Cauchy stress tensor that now has both mechanical and electrical components (Eq. (4)). In membrane theory, the three-dimensional equilibrium equations can be expressed with respect to a set of orthogonal curvilinear coordinates (θ_1, θ_2) on the middle surface of a deformed sheet in terms of the principal stress resultants [14]. After deformation, the major surfaces of the membrane are given by $\theta_3 = \pm\lambda_3 h$, where λ_3 is the thickness extension ratio and h is the initial membrane thickness. The generalized theory of elastic membranes by Green and Adkins [15] gives the resultant equilibrium equations

$$n^{\alpha\beta}_{;\alpha} = 0, \tag{15}$$

$$n^{\alpha\beta} b_{\alpha\beta} + p = 0, \tag{16}$$

given the relations

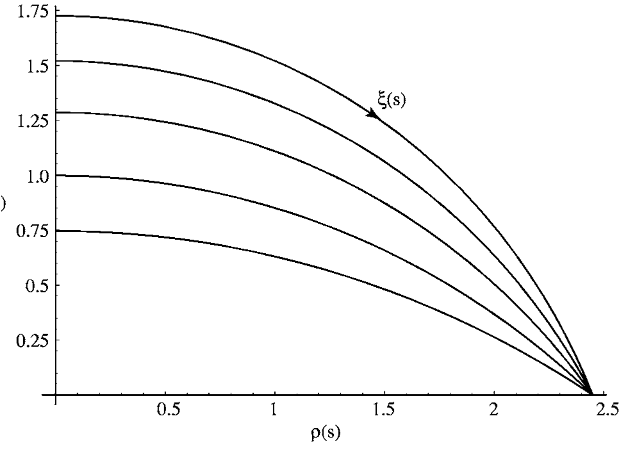

Fig. 1 Actual deformed profiles (1/2 symmetry) of an inflated membrane

$$n^{\alpha\beta} = \int_{-\lambda_3 h}^{\lambda_3 h} \sigma^{\alpha\beta} \mathrm{d}\theta_3, \quad b_{\alpha\beta} = \mathbf{a}_3 \cdot \mathbf{a}_{\alpha,\beta}, \tag{17}$$

where Greek indices take on the values (1, 2), $n^{\alpha\beta}$ are the stress resultants, $\lambda_3 h$ is the deformed membrane thickness, $b_{\alpha\beta}$ is the second fundamental form of the deformed surface, $\mathbf{a}_i$ are base vectors $(i=1,2,3), \sigma^{\alpha\beta}$ are the physical components of the stress, and p is the pressure differential across the membrane. Note that the electrical traction is equal and opposite on both sides of the elastomer and hence does not appear in p.

We employ a cylindrical coordinate system such that $(\rho, \theta) = (\theta_1, \theta_2)$. For an axisymmetric elastic membrane subject to an external (inflating) pressure differential p, Eqs. (15) and (16) are reduced to

$$\frac{\mathrm{d}(T_1 \rho)}{\mathrm{d}\rho} = T_2, \tag{18a}$$

$$\kappa_1 T_1 + \kappa_2 T_2 = p, \tag{18b}$$

where T_1, T_2 are the stress resultants in the longitudinal and latitudinal directions, respectively, defined by

$$\begin{gathered} \kappa_1 = b_{11}, \quad \kappa_2 = b_{22}, \quad b_{12} = b_{21} = 0, \\ n^{11} = T_1, \quad \rho^2 n^{22} = T_2, \quad n^{12} = n^{21} = 0, \end{gathered} \tag{19}$$

and $\kappa_{1,2}$ are the corresponding curvatures. Electrostatic effects appear explicitly in Eqs. (18) once the stress is defined in terms of the principal extension ratios, the elastic strain energy function, the electric field, and the material's dielectric constant.

3.3 Geometric Principles. We can describe the undeformed and deformed configurations of the diaphragm as surfaces of rotation. The independent variable of our analysis is the arc length, s, of the undeformed membrane. The clamped radius R_o is used to nondimensionalize variables containing a length scale. Inflation and activation of the membrane leads to a deformed profile as illustrated in Fig. 1. The profiles depicted in the figure are for different inflation pressures applied to the membrane. The prestretch λ_0 is 2.5.

Assuming an incompressible material, the longitudinal, latitudinal, and transverse stretch ratios are given by

$$\lambda_1 = \frac{\mathrm{d}\xi}{\mathrm{d}s}, \quad \lambda_2 = \frac{\rho}{R}, \quad \lambda_3 = \frac{1}{(\lambda_1 \lambda_2)}, \tag{20}$$

and the curvatures by

$$\kappa_1 = \frac{1}{R_1}, \quad \kappa_2 = \frac{1}{R_2}, \tag{21}$$

where ξ is the meridian curve length in the deformed state, R is the radius of the undeformed membrane, ρ is the radial position of particles of the deformed membrane, and R_1 and R_2 are the meridional and latitudinal radii of curvature, respectively. The perpendicular distance of material points, y, from the symmetry axis of the inflated actuated membrane is given by

$$y = \int \sqrt{\lambda_1^2 - \rho'^2}. \tag{22}$$

3.4 Material Modeling. The most comprehensive work on the large elastic deformation of membranes is attributed to Rivlin [16]. The experimental and theoretical studies of Treloar [17] and Ogden [18], respectively, serve to complement Rivlin's formulation, providing a complete schema for the mechanical modeling of our system. More specifically our approach is based on Rivlin and Adkins' [13] analysis of inflated elastic membranes. We modify their formulation to account for material stiffening at high strains (using an Ogden model), prestretch, and electrical effects. Experimental uniaxial force-extension data was obtained to determine the necessary material constants for the model. The Mooney-Rivlin strain energy function gives a first approximation to the data. However, due to inconsistencies pointed out by Rivlin and Saunders [19], and confirmed by Treloar and others, it is not appropriate to assign constants based solely on uniaxial tension tests, as this will render misleading analytical results. The Ogden strain energy function provides a more general form that can be comfortably applied to uniaxial tension data.

The material assumptions of homogeneity, isotropy, and electrical linearity in our system mean that there is no direct coupling between the mechanical and the electrical response normally occurring in piezoelectric and electrostrictive materials. Therefore, it is sufficient that we determine the mechanical portion of the stress from a purely elastic strain energy function; the electrical portion is given by the Maxwell stress tensor. Given that the electric field E_3 is uniform in the thickness direction and recalling Eq. (4), the contribution to the total stress from the Maxwell stress tensor is equal to

$$\mp \frac{\varepsilon_r \varepsilon_0 \nabla^2}{2(\lambda_3 h)^2}, \tag{23}$$

where $\bar{V}$ is the applied voltage, h is the dimensional initial membrane thickness, ε_0 is the vacuum permittivity, and ε_r is the relative dielectric constant.

The Mooney-Rivlin material model is given, along with the corresponding expression for the total stresses in an incompressible solid by

$$\Sigma(I_1, I_2) = (I_1 - 3) + \gamma(I_2 - 3), \tag{24}$$

$$I_1 = \lambda_1^2 + \lambda_2^2 + \lambda_3^2, \tag{25}$$

$$I_2 = \frac{1}{\lambda_1^2} + \frac{1}{\lambda_2^2} + \frac{1}{\lambda_3^2}, \tag{26}$$

$$t_i = \lambda_i^2 \frac{\partial \Sigma}{\partial I_1} - \left(\frac{1}{\lambda_i^2}\frac{\partial \Sigma}{\partial I_2}\right) + p_m \mp \frac{1}{C_1}\left(\frac{1}{2}\varepsilon_r \varepsilon_0 \left(\frac{\bar{V}}{\lambda_3 h}\right)^2\right), \tag{27}$$

where $i=(1,2,3)$, p_m is the hydrostatic pressure enforcing the incompressibility constraint, I_1 and I_2 are strain invariants, C_1 is a dimensional material constant, γ is the dimensionless material constant. The electrical term is subtracted for $i=(1,2)$ and is added for $i=3$. The corresponding set of equations for the Ogden material model is:

$$\Sigma(\lambda_1, \lambda_2) = \left(\frac{((\lambda_1^{q_1} + \lambda_2^{q_1} + (\lambda_1\lambda_2)^{-q_1}) - 3)}{q_1}\right) + \alpha\left(\frac{((\lambda_1^{q_2} + \lambda_2^{q_2} + (\lambda_1\lambda_2)^{-q_2}) - 3)}{q_2}\right), \tag{28}$$

$$t_i = \lambda_i \frac{\partial \Sigma}{\partial \lambda_i} - p_m - \frac{1}{\mu_1}\left(\frac{1}{2}\varepsilon_r \varepsilon_0 \left(\frac{\bar{V}}{\lambda_3 h}\right)^2\right) \quad (i = 1,2), \tag{29}$$

$$t_3 = \lambda_3 \frac{\partial \Sigma}{\partial \lambda_3} - p_m + \frac{1}{\mu_1}\left(\frac{1}{2}\varepsilon_r \varepsilon_0 \left(\frac{\bar{V}}{\lambda_3 h}\right)^2\right) = 0, \tag{30}$$

where q_1 and q_2 are dimensionless constants, μ_1 is the dimensional Ogden material constant, and α is the nondimensional ratio μ_2/μ_1. Equations (27), (29), and (30) explicitly give the total stress for the dielectric elastomer in a uniform electric field E_3.

According to the Rivlin and Adkins general theory, the surface tractions on the major surfaces are equal to zero, even though there is a nonzero external inflating pressure. Since the conductors on either side of the elastomer produce equal and opposite tractions on the elastomer surfaces, their contribution to the pressure differential across the membrane is zero. The approximation is, therefore, sufficiently accurate for the membrane because the actual surface traction produced from the external mechanical pressure is negligible compared to the meridional and latitudinal stresses t_1 and t_2. Thus, we neglect the external mechanical pressure contribution to the surface traction in accordance with the Rivlin-Adkins assumption and set $t_3=0$.

Mechanical material constants were experimentally determined for 3M VHB 4910 using both models. We henceforth acknowledge the superiority of the Ogden material model which has been utilized in both the comprehensive formulation and the analytical results. In the results, the electrical component of the stresses, t_1 and t_2, are assumed to be small in comparison to the mechanical portion of the stresses and neglected. Using Eq. (30), we can eliminate the arbitrary hydrostatic pressure p_m from t_1 and t_2. After deformation, the thickness, initially h, becomes $\lambda_3 h$. Thus the principal resultant stress components T_1 and T_2 are

$$T_1 = -\frac{\bar{V}^2 \varepsilon_r \varepsilon_0 \lambda_1^2 \lambda_2^2 - 2h^2 \mu_1 \left(\lambda_1^{q_1} + \alpha \lambda_1^{q_2} - \left(\frac{1}{\lambda_1\lambda_2}\right)^{q_1} - \alpha\left(\frac{1}{\lambda_1\lambda_2}\right)^{q_2}\right)}{2h^2 \lambda_1 \lambda_2 \mu_1}, \tag{31}$$

$$T_2 = -\frac{\bar{V}^2 \varepsilon_r \varepsilon_0 \lambda_1^2 \lambda_2^2 + 2h^2 \mu_1 \left(\left(\frac{1}{\lambda_1\lambda_2}\right)^{q_1} + \alpha\left(\frac{1}{\lambda_1\lambda_2}\right)^{q_2} - \lambda_2^{q_1} - \alpha \lambda_2^{q_2}\right)}{2h^2 \lambda_1 \lambda_2 \mu_1}. \tag{32}$$

The form of the equilibrium equations (Eqs. (18)) is the same for the passive and active membranes. In the active model, however, the equations for the stresses T_1 and T_2 (Eqs. (31) and (32)) are no longer purely mechanical and, therefore, depend on the electric field.

3.5 Electroelastic System. Combining Eqs. (20)–(22) and Eqs. (28)–(32) provides a system of first-order equations that we solve to yield the stretch ratio $\lambda_1(s)$, the deformed radius $\rho(s)$, and the vertical deflection, $y(s)$ (see Appendix). The relationship between the dimensional (denoted by an overbar) and the nondimensional variables are

$$\bar{p} = \frac{\mu_1 h_0}{R_0} p, \quad \bar{T}_{1,2} = \mu_1 h_0 T_{1,2}, \quad \bar{\forall} = R_0^3 \forall ,$$

$$\bar{V} = \left(\frac{\varepsilon_r \varepsilon_0 R_0^3}{\mu_1 h_0}\right)^{-1/2} V, \quad \bar{E} = \left(\frac{\varepsilon_r \varepsilon_0 R_0}{\mu_1 h_0}\right)^{-1/2} E, \tag{33}$$

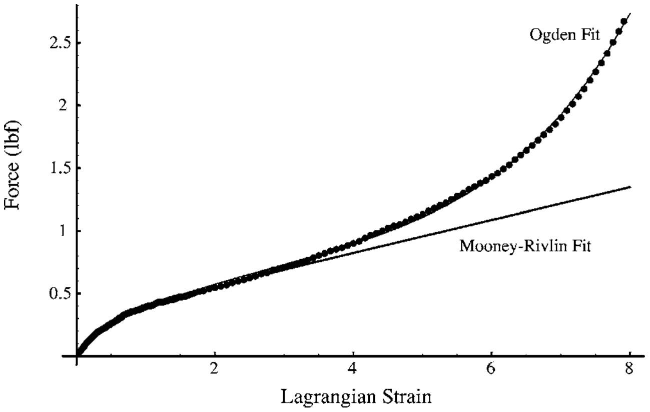

Fig. 2 The nonlinear curve-fit of the experimental data for a sample of VHB 4910. The Mooney-Rivlin fit is a good approximation only to approximately 300% strain

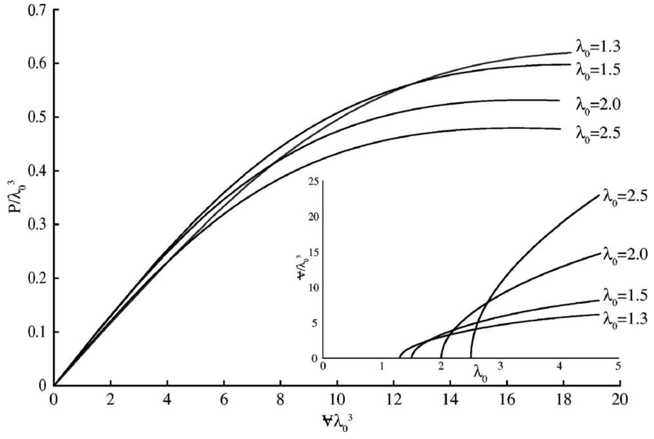

Fig. 3 Pressure-volume curves (main graph) and volume-stretch curves (inset) for different prestretch values

where $h_0=h/(\lambda_0)^2$ is the prestretched thickness.

The system of equations is iteratively solved by numerically integrating from 0 to 1 for a specified stretch at the pole and applied electrical pressure. The inflating pressure is then updated until the mechanical boundary conditions are satisfied.

4 Results

4.1 Material Characterization. Data from tensile tests on various samples of 3M VHB 4910 elastomer were used to determine the corresponding material constants of the two strain energy functions considered. Nonlinear curvefits of the experimental data using both the Mooney-Rivlin and the Ogden strain energy functions were obtained. As shown in Fig. 2, the Mooney-Rivlin model does not accurately capture the material's behavior for the entire range of strain. A superior fit of the experimental data is obtained by the Ogden model. The curve-fit of the experimental data using both functions is given in Fig. 2, where the points are the experimental data and the curves are the nonlinear fits.

4.2 Numerical Results. Numerical results are obtained by simulating the conditions of the active membrane in the prosthetic pump. We analyze a circular axisymmetric membrane that is prestretched and clamped at its edges, subject to an inflating pressure and a voltage induced squeeze pressure across the thickness of the diaphragm. The results have been compiled into pressure-volume (P-$\forall$) curves, which are often used to gauge and evaluate the biomechanical behavior of blood pumps. For pump applications, volumetric efficiency is of utmost importance within physiologically reasonable pressure bounds. The membrane is radially prestretched to improve its dielectric performance and endure higher electric fields as has been reported [1]. We assume a dielectric constant of 4.7 for 3M VHB [5].

Figure 3 depicts the P-$\forall$ curves for membranes with various prestretch values. The results were calculated for a constant dimensional applied voltage of 2040 V, resulting in a nondimensional voltage of $(1/\lambda_o)$ 8.31e-6, with $\mu_1=54.88$ kPa, $h_0=0.5$ mm, and $R_0=2.22$ cm. Within a prestretch range of 1.7 and 2.5, we observe that the pressure required to obtain a certain volume decreases with increasing prestretch of the material. This implies that, for the range considered, material softening occurs with increasing prestretch. This can be explained by studying the volume as a function of pole stretch (see Fig. 3 inset). At higher prestretch values, material stiffening with increasing prestretch is observed. A prestretch of 1.3 presents an anomaly to the trend at lower volumes that can be understood by careful consideration of Fig. 2. There, the force-strain curve becomes increasingly steep up until approximately a stretch of 1.7. The slope is approximately constant in the stretch range from 1.7 to 2.65 and rises again until material failure. It is clear that a higher pressure will be needed to inflate the membrane while operating in the "steep" regions of the force-strain curve; conversely, less pressure is required when operating in the "flat" regions of the curve. The observed trend is in accordance with experimental data obtained by Tews et al. [1] for inflated dielectric elastomers subject to electric pressure.

The P-$\forall$ relation with $\lambda_0=2.65$ for various applied voltages is shown in Fig. 4. Activating the membrane causes tangential material relaxation and, hence, larger transverse deformation for a prescribed inflating pressure. The result is an increase in volume for increasing voltage.

The external electrical source applied to the dielectric membrane can be modeled as either a constant electric field or a constant voltage. In the present situation, it is physically more representative to consider a constant applied voltage. Since the material changes thickness during deformation, it would be difficult to maintain a constant electric field in practice. This is particularly so for the membrane configuration under consideration since the thickness of the material is not constant along radial lines in the deformed state. As the membrane is clamped around the edges, once pressurized it tends to be thinnest at the center with increasing thickness towards the edge. The P-$\forall$ curve at a constant electric field is equivalent in trend to the voltage analysis; that is, an

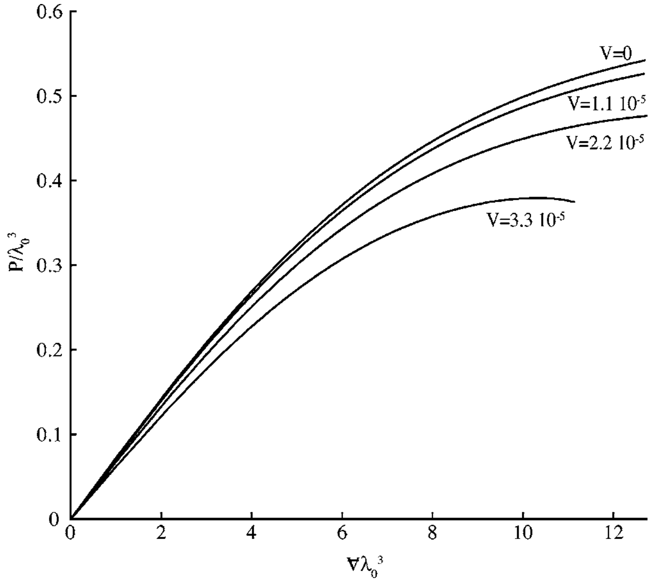

Fig. 4 Pressure-volume curves for various applied voltages

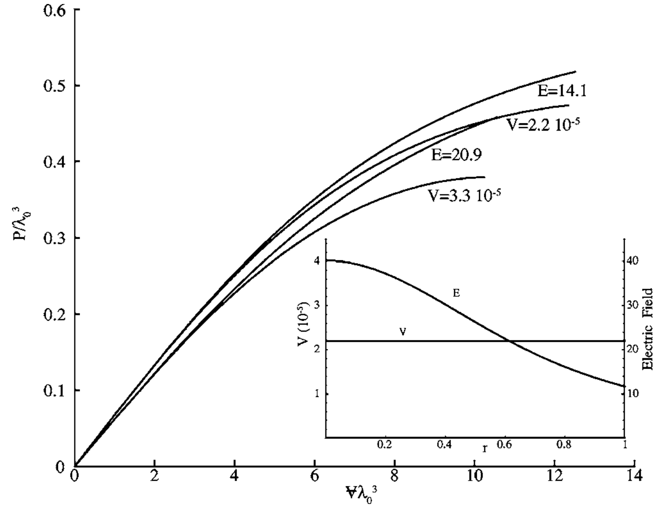

Fig. 5 Comparative pressure-volume curves (main graph) for various electric fields voltages. Voltage and electric field versus the arc length from the pole to the edge of the membrane (inset)

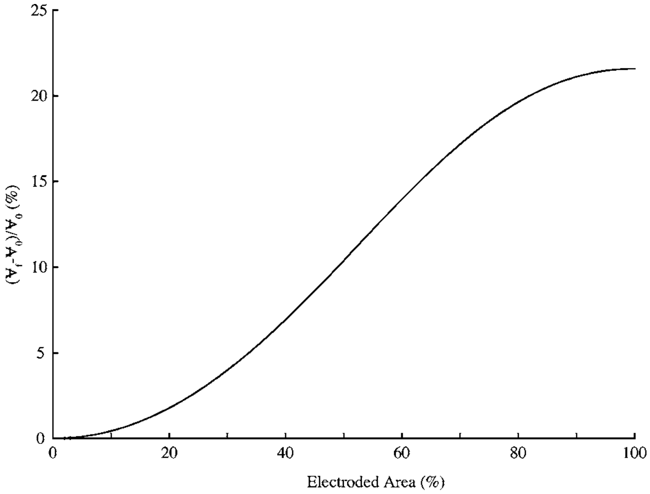

Fig. 7 The % variance in volume versus the % electroded area of the membrane

increase in field (voltage) results in an increase in volume for a given pressure. In assuming a constant electric field, there is a noticeable quantitative change in the results as depicted in Fig. 5. A constant electric field predicts higher external pressure values for a given volume. The electric field values in Fig. 5 are for an initial dimensionless thickness (before prestretch) of 0.02. In the figure, the electric fields are calculated using the initial values of the voltages applied over the entire membrane in its initially flat configuration. Thus, $E=14.1$ and $E=20.9$ correspond to the initial voltages of $V=2.2\text{e-}5$ and $V=3.3\text{e-}5$, respectively, for a radial prestretch of 2.65. As the membrane is inflated, the voltages are varied proportionally with the membrane thickness such that the electric field is kept constant. Conversely, for a constant voltage, the field is varied proportionally with the inverse of the membrane thickness. For $\forall=2.23$ and a constant $V=2.2\text{e-}5$, the inset in Fig. 5 illustrates the change in the electric field from the pole to the edge of the prestretched membrane. With a constant applied voltage, the field is largest at the center and smallest at the clamped edge.

Biological requirements dictate that a stroke volume of 70 cm^3($\forall=6.4$) in systole (active contraction of heart ventricles to eject blood from its chambers) be obtained [3]. Using a radius within physiological constraints of 4.44 cm, we observe for an applied voltage of 2.34e-5 and a prestretch of 2.3 (Fig. 6) that a volume of 6.4 is indeed attainable for reasonable stretch of the material, i.e., prior to mechanical material failure, experimentally determined to be in the region of $\lambda=3.5$).

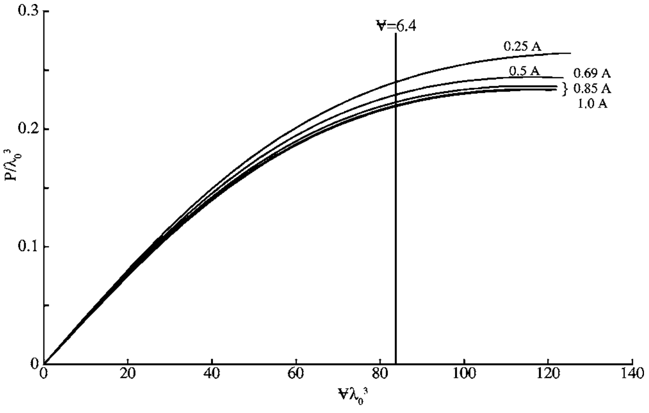

Fig. 6 Pressure-volume curves for different electroded areas of the total membrane area (A)

As it may not be practical or possible to electrode the entire surface area in an actual device, we consider the performance of partially electroded configurations. The P-$\forall$ curves for different electroded areas of the total membrane area (A) are shown in Fig. 6. There is very little difference for electroded areas greater than 80% of the total area A. Figure 7 depicts the effect of varying the central circular area of the electroded surface on the elastomer membrane for a prescribed external pressure of 5.11 ($\lambda_0=2.3$) and a voltage of 2.34e-5, where % A means percent of the entire prestretched membrane area that is electroded. The quantitative measure $\Delta\forall/\forall_0$ is the difference ($\Delta\forall$) between the volume calculated at a given % A and 0% A (unelectroded) divided by the 0% volume ($\forall_0$). The variance is particularly significant between electroded areas of 25% A and 70% A. Quantitatively, this pattern is specific to values of the applied voltage and the prestretch. Figure 7 is simply representative of the observation that there is a threshold percentage electroded area beyond which very little difference in $\forall$ is calculated. The cut-off threshold is consistently observed for different prestretch values. It should be noted that electroding near the pole as opposed to electroding from the outer circumference is better for obtaining higher stroke volumes.

The numerical results can be used to predict regions of instability as indicated by the descending and ascending portions of the P-$\forall$ curve ($\lambda_0=2.3$) in Fig. 8, which extend to much larger volumes than Figs. 3–6. For the presently discussed application these results are useful in determining a reasonable operating range. An interesting observation can be made in comparing the extended P-$\forall$ curve for different voltages. For a sufficiently elastic material, we can consider the case of an applied voltage of 0.468e-5, at a pressure of 6.42, to obtain $\forall=1.05$ (Fig. 8(a)). For the same pressure we can increase the voltage to 1.97e-5 and "jump" to $\forall=36.56$ (Fig. 8(b)). Conceptually, for a purely high volume-oriented application, the above method could be used to achieve very significant increases in swept volume if the pressure can be held constant during this transition.

Although dielectric elastomers typically have very low force

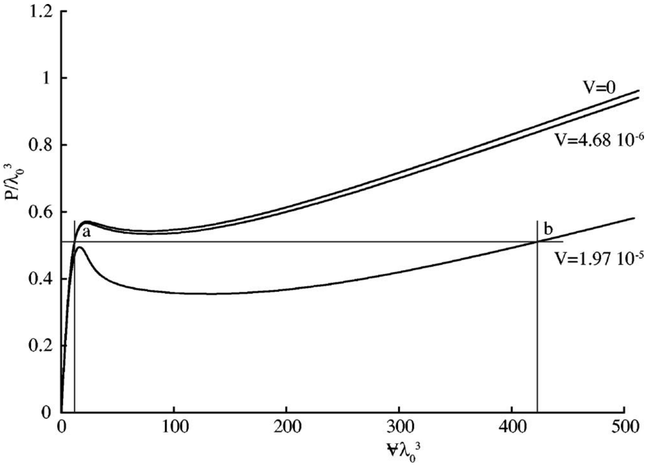

Fig. 8 Stable and unstable regions of pressure-volume curves for different applied voltages

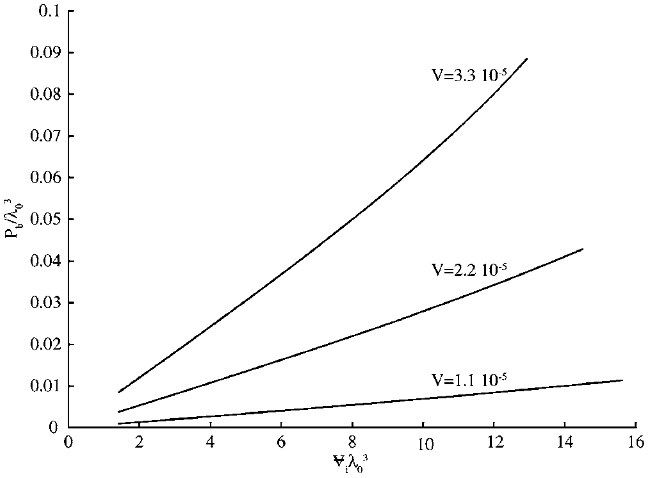

Fig. 10 The blocked pressure for various initial volumes and applied voltages

output, it is instructive to calculate the output pressure of the active membrane due solely to the applied voltage. Here, we define the blocked pressure ($P_{\text{blocked}} = P_A - P_C$ in Fig. 9) as the reduction in pressure differential across the membrane to return to the zero voltage volume. Figure 9 illustrates a hypothetical work loop used to obtain the blocked pressure (P_{blocked}). For $V=0$ we can choose a point, A, having the coordinates $(\forall_A, P_A)$. While holding the external pressure constant, an increase in voltage ($V = 3.3\text{e}-5$) leads to an increase in the volume from $\forall_A$ to $\forall_B$. To return to the starting volume $\forall_A$, the pressure decreases to P_C. The difference $P_A - P_C$ is the blocked pressure; the area of ABC is the work. In Fig. 10, we observe that the blocked pressure for the inflatable dielectric membrane is dependent on two parameters: The initial pressure (or initial volume) and the applied voltage. The blocked pressure increases with increasing initial volume (pressure) and increasing applied voltage. Accordingly, to extract the most mechanical work during activation of the dielectric elastomer, both the initial volume and the applied voltage should be large.

5 Summary

A nonlinear mathematical formulation for dielectric elastomer actuators for a potential blood pump application was presented. This formulation combined Maxwell-Faraday electrostatics and nonlinear elasticity for axisymmetric membranes, where an augmented Cauchy stress was used to define the electroelastic state of the dielectric elastomer. The elastic behavior of the membrane was determined by using a purely elastic strain energy function. The presented model can be extended to include fully coupled effects by employing an electroelastic function for the energy stored in the material and obtaining the corresponding stress-strain-polarization experimental data. For cardiac pump applicability, a stroke volume of 70 cm^3 is attainable for reasonable stretch of the material during activation. Numerical results indicate that increasing the applied voltage increases volume. For a particular operating range, approximately between a stretch of 1.7 and 3.3, increasing the prestretch leads to material softening which further increases the calculated volume. There is agreement between the observed trends determined numerically by this model and experimental work reported by Tews et al. [1]. A comparison of P-$\forall$ results, calculated using a constant voltage versus a constant electric field, revealed quantitative differences between the two although the trends were similar. Further, calculations indicated that there is very little change in the P-$\forall$ behavior of the membrane for a certain threshold percentage electroded area. This threshold electroded area can be calculated for a prescribed prestretch and applied voltage. Additionally, we confirmed that although dielectric elastomer actuators are capable of very large deformations, their purely electrical pressure output is quite low, ranging from 34 Pa ($V=1020\ V$, $\forall_i = 11.6$ cm^3) to 268 Pa ($V = 3060\ V$, $\forall_i = 9.6$ cm^3).

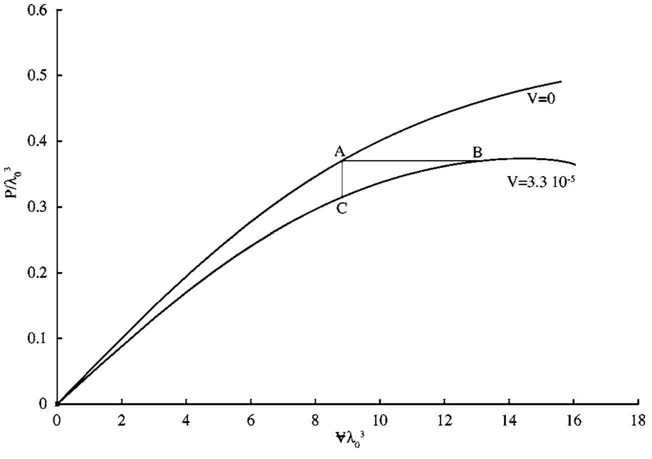

Fig. 9 Hypothetical work-loop from pressure-volume curves for different voltages

The model is useful for studying the behavior and effect of various design variables by conducting parameter studies. The numerical results are used to predict regions of instability that delimit a reasonable operating range for the pump. Applying optimization techniques yields superior designs within the necessary biomedical constraints.

Acknowledgment

The authors gratefully acknowledge the support of the National Institutes of Health Bioengineering Research Partnership Grant No. R01-HL65959.

Appendix: Final Equations of the Analysis

$$\begin{aligned}\lambda_1'(s) = \Bigg(&\lambda_1(s)\Bigg(-2h^2s^2\mu_1\Bigg(\lambda_1(s)^{q_1}+\alpha\lambda_1(s)^{q_2}-\left(\frac{s}{\lambda_1(s)\rho(s)}\right)^{q_1}-q1\left(\frac{s}{\lambda_1(s)\rho(s)}\right)^{q_1}-\alpha\left(\frac{s}{\lambda_1(s)\rho(s)}\right)^{q_2}-q_2\alpha\left(\frac{s}{\lambda_1(s)\rho(s)}\right)^{q_2}\Bigg)\rho(s)\\
&-\bar{V}^2\varepsilon_r\varepsilon_0\lambda_1(s)^2\rho(s)^3+s\bar{V}^2\varepsilon_r\varepsilon_0\lambda_1(s)^2\rho(s)^2\omega(s)-2h^2s^3\mu_1\Bigg(\left(\frac{s}{\lambda_1(s)\rho(s)}\right)^{q_1}+q_1\left(\frac{s}{\lambda_1(s)\rho(s)}\right)^{q_1}-\left(\frac{\rho(s)}{s}\right)^{q_1}+\alpha\Bigg(\left(\frac{s}{\lambda_1(s)\rho(s)}\right)^{q_2}\\
&+q_2\left(\frac{s}{\lambda_1(s)\rho(s)}\right)^{q_2}-\left(\frac{\rho(s)}{s}\right)^{q_2}\Bigg)\Bigg)\omega(s)\Bigg)\Bigg)\Bigg/\Bigg(s\rho(s)\Bigg(2h^2s^2\mu_1\Bigg((-1+q_1)\lambda_1(s)^{q_1}+(-1+q_2)\alpha\lambda_1(s)^{q_2}+\left(\frac{s}{\lambda_1(s)\rho(s)}\right)^{q_1}\\
&+q_1\left(\frac{s}{\lambda_1(s)\rho(s)}\right)^{q_1}+\alpha\left(\frac{s}{\lambda_1(s)\rho(s)}\right)^{q_2}+q_2\alpha\left(\frac{s}{\lambda_1(s)\rho(s)}\right)^{q_2}\Bigg)-\bar{V}^2\varepsilon_r\varepsilon_0\lambda_1(s)^2\rho(s)^2\Bigg)\Bigg)\end{aligned}\tag{A1}$$

$$\rho'(s)=\omega(s)\tag{A2}$$

$$\begin{aligned}\omega'(s)=\Bigg(&\lambda_1(s)^3\rho(s)\sqrt{1-\frac{\omega(s)^2}{\lambda_1(s)^2}}\Bigg(-p-\frac{1}{2h^2\mu_1\lambda_1(s)\rho(s)^2}\Bigg(s\Bigg(\frac{\bar{V}^2\varepsilon_r\varepsilon_0\lambda_1(s)^2\rho(s)^2}{s^2}+2h^2\mu_1(s^{q_1}\lambda_1(s)^{-q_1}\rho(s)^{-q_1}-s^{-q_1}\rho s^{q_1}\\
&+\alpha(s^{q_2}\lambda_1(s)^{-q_2}\rho(s)^{-q_2}-s^{-q2}\rho(s)^{q2}))\Bigg)\sqrt{1-\frac{\omega(s)^2}{\lambda_1(s)^2}}\Bigg)+\Bigg(s\Bigg(\lambda_1(s)^{q_1}+\alpha\lambda_1(s)^{q_2}-\frac{\bar{V}^2\varepsilon_r\varepsilon_0\lambda_1(s)^2\rho(s)^2}{2h^2s^2\mu_1}-s^{q_1}\lambda_1(s)^{-q_1}\rho(s)^{-q_1}\\
&-s^{q_2}\alpha\lambda_1(s)^{-q_2}\rho(s)^{-q_2}\Bigg)\omega(s)\lambda_1'(s)\Bigg)\Bigg/\Bigg(\lambda_1(s)^4\rho(s)\sqrt{1-\frac{\omega(s)^2}{\lambda_1(s)^2}}\Bigg)\Bigg)\Bigg)\Bigg/\Bigg(s\Bigg(\lambda_1(s)^{q_1}+\alpha\lambda_1(s)^{q_2}-\frac{\bar{V}^2\varepsilon_r\varepsilon_0\lambda_1(s)^2\rho(s)^2}{2h^2s^2\mu_1}\\
&-s^{q_1}\lambda_1(s)^{-q_1}\rho(s)^{-q_1}-s^{q_2}\alpha\lambda_1(s)^{-q_2}\rho(s)^{-q_2}\Bigg)\Bigg)\end{aligned}\tag{A3}$$

$$y'(s)=\sqrt{\lambda_1(s)^2R'(s)^2-\omega(s)^2}\tag{A4}$$

References

[1] Tews, A., Pope, K., and Snyder, A., 2003, "Pressure-Volume Characteristics of Dielectric Elastomer Diaphragms," presented at Proceedings SPIE Smart Structures and Materials: Electroactive Polymers and Devices, San Diego.

[2] Lubeck, D. P., and Bunker, J. P., 1982, Case Study #9: "The Artificial Heart: Costs, Risks, and Benefits," *The Implications of Cost-Effectiveness Analysis of Medical Technologies*, Background Paper No. 2 "Case Studies of Medical Technologies," U.S. Government Printing Office, National Heart, Lung and Blood Institute, Morbidity and Mortality Chartbook, Washington, DC.

[3] Ungluab, S. D., 1998, *Human Physiology an Integrated Approach*, Prentice Hall, New Jersey.

[4] Pelrine, R., Kornbluh, R., and Joseph, J., 1998, "Electrostriction of Polymer Dielectrics with Compliant Electrodes as a Means of Actuation," Sens. Actuators, A, **64**, pp. 77–85.

[5] Kofod, G., 2001, "Dielectric Elastomer Actuators," in *Chemistry*, The Technical University of Denmark, Denmark.

[6] Wolfson, R., and Pasachoff, J. M., 1999, *Physics with Modern Physics for Scientists and Engineers*, Addison-Wesley, Reading.

[7] Toupin, R. A., 1956, "The Elastic Dielectric," Journal of Rational Mechanics and Analysis, **5**, pp. 850–915.

[8] Landau, L. D., and Lifshitz, E. M., 1984, *Electrodynamics of Continuous Media*, Butterworth-Heinemann, Oxford.

[9] Jackson, J. D., 1962, *Classical Electro-Dynamics*, Wiley, New York.

[10] Schwinger, J., DeRaad, L., Milton, K., and Tsai, W., 1998, *Classical Electrodynamics*, Perseus Books, Reading.

[11] Maxwell, J. C., 1954, *A Treatise on Electricity and Magnetism*, Dover, Oxford.

[12] Eringen, A. C., 1962, *Nonlinear Theory of Contiuous Media*, McGraw-Hill, New York.

[13] Adkins, J. E., and Rivlin, R. S., 1952, "Large Elastic Deformations of Isotropic Materials IX The Deformation of Thin Shells," Philos. Trans. R. Soc. London, Ser. A, **244**, pp. 505–531.

[14] Green, A. E., and Zerna, W., 1968, *Theoretical Elasticity*, Clarendon Press, Oxford.

[15] Green, A. E., and Adkins, J. E., 1970, *Large Elastic Deformations*, Oxford University Press, London.

[16] Rivlin, R. S., 1947–52, "Large Elastic Deformations of Isotropic Materials I-IX," Philos. Trans. R. Soc. London, Ser. A, **240–244**.

[17] Treloar, R. G., 1974, "The Mechanics of Rubber Elasticity," J. Polym. Sci., Polym. Symp., **48**, pp. 107–123.

[18] Ogden, R. W., 1972, "Large Deformation Isotropic Elasticity—On the Correlation of Theory and Experiment for Incompressible Rubberlike Solids," Philos. Trans. R. Soc. London, Ser. A, **326**, pp. 565–584.

[19] Rivlin, R. S., and Saunders, D. W., 1951, "Large Elastic Deformations of Isotropic Materials. VII. Experiments on the Defromation of Rubber," Philos. Trans. R. Soc. London, Ser. A, **243**, pp. 251–288.

Barna A. Szabo
The Albert P. and Blanche Y. Greensfelder
Professor of Mechanics
e-mail: szabo@wustl.edu

Daniel E. Muntges
e-mail: dem2@wustl.edu

Washington University,
St. Louis, MO 63130

Procedures for the Verification and Validation of Working Models for Structural Shells

Shell-like structures are viewed as fully three-dimensional solid bodies that allow the imposition of restrictions on the transverse variation of displacement vector components in certain regions. An important practical problem is to select a simplified mathematical model for a particular application so that the simplifications do not affect the data of interest significantly. This involves application of expert knowledge aided by virtual and/or physical experimentation. An example is presented. [DOI: 10.1115/1.2043189]

1 Introduction

The mathematical formulation of a physical problem for purposes of engineering decision making involves application of expert knowledge. A formulation, comprised of a mathematical problem characterized by the solution domain, physical properties, essential and weak boundary conditions, a statement of the objectives of analysis, and the acceptable error tolerances, is called a working model. The statement of objectives identifies the data of interest, such as deformations, stresses, reactions, natural frequencies, etc. Incorporated in any working model are certain simplifying assumptions that, on the basis of expert knowledge, are expected to have negligibly small effect on the data of interest.

In general, it is not possible to guarantee that a working model, based on *a priori* information and expert knowledge alone, will meet the objectives of an analysis. Working models must be evaluated with the objective to determine whether the simplifying assumptions incorporated in the model are justified in relation to the data of interest and the established set of tolerances. Should the evaluation indicate that a working model is inadequate, a more comprehensive working model must be chosen and the process repeated. In practice, this is feasible only when a hierarchic framework is available that makes systematic construction of sequences of working models possible.

Conceptually, the exact solutions corresponding to a sequence of working models converge to the exact solution of the state of the art model (also called supermodel), i.e., a model that accounts for all known physical laws that pertain to the system or process being modeled. An important requirement is that the boundary conditions and other data must have consistent meaning in the model hierarchy. The process by which it is ascertained that a working model satisfies a set of necessary conditions is called validation. The conditions depend on the objectives of analysis.

With the exception of very highly idealized formulations, the exact solutions of working models are approximated by numerical methods, thereby incurring errors of approximation. It is necessary to ensure that the errors of approximation, in terms of the data of interest, are within acceptable tolerances. The process by which the computed data are shown to satisfy necessary conditions to be within acceptable tolerances is called verification.

The plan of this paper is as follows: In Sec. 2 physical experiments performed at Oak Ridge National Laboratory (ORNL) in the 1970s [1,2] are summarized. The principles that govern the use of mathematical models for purposes of interpretation of experimental results are described in Sec. 3. In Sec. 4, the formulation of hierarchic models for shells and thin solids is outlined and the differences between classical shell models and hierarchic models are noted. In Sec. 5, the finite element spaces used in the ORNL and the present investigations are described. In Sec. 6, questions pertaining to the reliability and usefulness of computed information from the point of view of the accuracy of prediction of the responses of structural shells to various loading conditions are addressed with reference to the first of four models investigated at ORNL. Numerical results are presented in Sec. 7. The main conclusion, presented in Sec. 8, is that virtual experimentation, aided by a hierarchic framework of working models, is indispensable in the development of expert knowledge.

2 Experiments

Physical experiments were performed at the Oak Ridge National Laboratory in the 1970s [1,2]. The goal of the experiments was to determine whether the classical model for shells, known as the Novozhilov-Koiter model, discretized by an assembly of flat plate elements, is capable of predicting strains in the vicinity of the intersection of two cylindrical shells. Four carbon steel test articles were manufactured and instrumented with great care. A detailed analysis of the first test article, based on hierarchic modeling techniques, is available in [3].

The first test article was made by welding two carbon steel pipes then carefully machining the weldment to the test dimensions. The test article was annealed at several points in the machining process. The experimental arrangement is shown in Fig. 1. The horizontal part is called the cylinder; the vertical part is called the nozzle. The length of the cylinder was 39.0 in. (991 mm). The length of the nozzle, measured from the point of intersection of the centerline of the nozzle with the centerline of the cylinder was 19.5 in. (495 mm). The outside diameter of the cylinder (resp. nozzle) was 10 in. (254 mm) (resp. 5.0 in. (127 mm)). The intended wall thickness of the cylinder (resp. nozzle) was 0.1 in. (2.54 mm) (resp. 0.05 in. (1.27 mm)).

2.1 Constraint Conditions. As shown in Fig. 1, the right end of the cylinder was rigidly clamped to a heavy flat plate bolted to a frame. Small flanges were machined into the ends of the cylinder and nozzle to support the seal and the clamping forces. Heavy loading fixtures were attached on the left end of the cylinder and the end of the nozzle to provide seal and seating for the application of forces.

2.2 Loading Conditions. A total of 13 load cases that included pressure loading and axial forces, shear forces, and mo-

---

Contributed by the Applied Mechanics Division of The American Society of Mechanical Engineers for publication in the ASME Journal of Applied Mechanics. Manuscript received by the Applied Mechanics Division, July 22, 2004; final revision, March 25, 2005. Review conducted by S. Govindjee. Discussion on the paper should be addressed to the Editor, Prof. Robert M. McMeeking, Journal of Applied Mechanics, Department of Mechanical and Environmental Engineering, University of California-Santa Barbara, Santa Barbara, CA 93106-5070, and will be accepted until four months after final publication in the paper itself in the ASME Journal of Applied Mechanics.

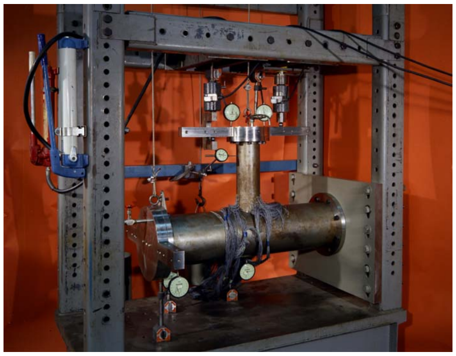

Fig. 1 Experimental arrangement (reproduced with permission from Oak Ridge National Laboratory)

ments were investigated. The forces and moments were applied to the cylinder and the nozzle through hydraulic rams acting through load cells. The pressure loading was applied by means of a hydraulic fluid. In order to compensate for the weight of the hydraulic fluid, a counterbalancing force was applied to the fixture at the free end of the cylinder through a cable that is visible in Fig. 1.

For all 13 load cases, the load was applied in increments of 20% of the full load, then decreased to zero again in 20% decrements. In this paper, only one of the loading cases—the pressure load—is discussed. Additional load cases are discussed in [3]. The maximum value of the pressure was 50.0 psi (344.8 kPa).

2.3 Measurements. A total of 322 three-gage (Micro-Measurements type EA-06-030YB-120, option SE) foil rosettes were bonded on the inside and outside surfaces by epoxy adhesive and cured. The gages in the rosettes were arranged in a Y pattern (i.e., the directions of measurement were 120 deg apart) [1]. Details of the instrumented intersection region is shown in Fig. 2.

The ratio of the resistance change in a strain gage to the Lagrangian strain causing the change is called the gage factor. The gage factor of each production lot is determined by sample measurements and is given on each package with its tolerance. Typical tolerances are 0.5–1.0 %. No tolerance data are provided in Ref. [1,2].

3 Comparison Between the Results of Experiments and Finite Element Analyses

In order to interpret experimental data and to allow eventual generalization of the experimental results, it is necessary to construct a working model. We are concerned only with working models that have unique exact solutions. We denote the exact solution of working model m by $\mathbf{u}_m$. We are interested in some set of measurable data, such as displacements and strains, in specific points. We will denote these data corresponding to $\mathbf{u}_m$ by $\Phi_i(\mathbf{u}_m), i=1,2,\ldots$. Of course, the exact solution is generally unknown, only an approximation to the exact solution, computed by the finite element method or some other numerical method, is known. We denote the approximate solution by $\mathbf{u}_a$ and the data computed from $\mathbf{u}_a$ by $\Phi_i(\mathbf{u}_a)(i=1,2,\ldots)$. The error of numerical approximation is denoted by e_i^{num}:

$$e_i^{\mathrm{num}} := \Phi_i(\mathbf{u}_m) - \Phi_i(\mathbf{u}_a) \tag{1}$$

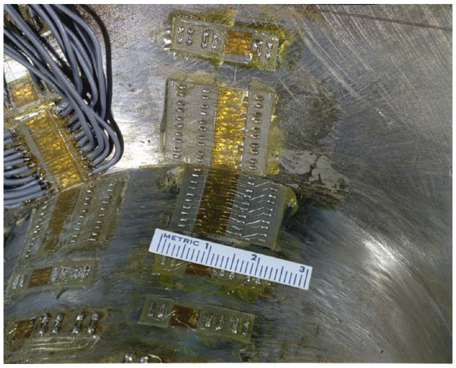

Fig. 2 Detail of test article instrumented with strain gages (reproduced with permission from Oak Ridge National Laboratory)

We denote the experimental measurement corresponding to $\Phi_i(\mathbf{u}_m)$ by $\Phi_i^\star$. Associated with $\Phi_i^\star$ is a random and (possibly) systematic error in the experimental observation, which is denoted by e_i^{exp}. We denote the ideal (error-free) measurement by $\bar{\Phi}_i$. Therefore,

$$e_i^{\mathrm{exp}} := \bar{\Phi}_i - \Phi_i^\star \tag{2}$$

Let us assume that all necessary information concerning the object of an experiment is available. Then, in any comparison of experimental data with predictions based on a working model, three sources of error are present: (i) errors in the working model itself, including the formulation, variations in dimensions, material properties and boundary conditions; (ii) systematic and random errors in the experimental observations e_i^{exp}, and (iii) errors in the numerical approximation of the solution of the mathematical model e_i^{num}, called the errors of discretization.

We will consider mathematical model m a reasonable representation of the physical reality of an experiment if

$$|\Phi_i(\mathbf{u}_m) - \bar{\Phi}_i| \le \tau_i |\Phi_i(\mathbf{u}_m)|, \quad i = 1,2,\cdots \tag{3}$$

where τ_i are prescribed tolerances. Using Eqs. (1) and (2) and the triangle inequality, we have

$$|\Phi_i(\mathbf{u}_m) - \bar{\Phi}_i| = |\Phi_i(\mathbf{u}_a) + e_i^{\mathrm{num}} - \Phi_i^\star - e_i^{\mathrm{exp}}| \le |\Phi_i(\mathbf{u}_a) - \Phi_i^\star| + |e_i^{\mathrm{num}}| + |e_i^{\mathrm{exp}}| \tag{4}$$

It is seen that replacement of $\Phi_i(\mathbf{u}_m)$ with $\Phi_i(\mathbf{u}_a)$ and $\bar{\Phi}_i$ with $\Phi_i^\star$ is permissible only if it can be shown that the relative errors $|e_i^{\mathrm{exp}}/\Phi_i(\mathbf{u}_m)|$ and $|e_i^{\mathrm{num}}/\Phi_i(\mathbf{u}_m)|$ are much smaller than τ_i. If this condition is not satisfied, then it is possible that large errors in the mathematical model are obscured by similarly large errors in the numerical approximation and/or the experimental observations. Therefore, estimation and control of e_i^{num} and e_i^{exp} are essential.

Remark 3.1. We have assumed that all information necessary for the formulation of a working model is available. This requirement can be difficult to meet. Requirements for validation experiments are discussed in [4].

Remark 3.2. Successful prediction of the outcomes of one or more physical experiments does not prove that a working model will provide correct predictions for other experiments. On the other hand, failure to correctly predict the outcome of any one experiment is sufficient evidence for rejection. Therefore, the grounds for rejection of working models are well established (in principle), but it is not possible to prove through experimentation that a particular working model is correct. With each successful prediction of the outcome of a physical experiment, the probability that the working model will give correct results increases but guarantees cannot be given. In other words, acceptance of a working model is tentative, whereas rejection is conclusive.

4 Formulation

The formulation of working models for structural shells is a large and complicated subject that cannot be discussed in sufficient detail here. Only a brief overview of the main points relevant to the present investigation is presented.

4.1 Kinematic Assumptions. A structural shell is characterized by a surface, called midsurface x_i, and the thickness t. Both are given in terms of two parameters α_1, α_2

$$x_i = x_i(\alpha_1, \alpha_2), \quad t = t(\alpha_1, \alpha_2)$$

The indices for α_i take on the values $i=1,2$, whereas the indices of x range from 1 to 3. Associated with each point of the midsurface are three basis vectors. Two of the basis vectors lie in the tangent plane

$$b_i^{(1)} := \frac{\partial x_i}{\partial \alpha_1}, \quad b_i^{(2)} := \frac{\partial x_i}{\partial \alpha_2}$$

Note that $b_i^{(1)}$ and $b_i^{(2)}$ are not necessarily orthogonal. The third basis vector $b_i^{(3)}$ is the cross product of $b_i^{(1)}$ and $b_i^{(2)}$; therefore, it is normal to the tangent plane. These are called curvilinear basis vectors. The normalized curvilinear basis vectors will be denoted by $\mathbf{e}_\alpha, \mathbf{e}_\beta, \mathbf{e}_n$. The Cartesian unit basis vectors corresponding to the coordinates x_i will be denoted by $\mathbf{e}_x, \mathbf{e}_y, \mathbf{e}_z$. A vector $\mathbf{u}$, given in terms of the curvilinear basis vectors, denoted by $\mathbf{u}_{(\alpha)}$, can be transformed to Cartesian coordinates, denoted by $\mathbf{u}_{(x)}$. The transformation is

$$\mathbf{u}_{(x)} = [R]\mathbf{u}_{(\alpha)} \tag{5}$$

where the columns of the transformation matrix $[R]$ are the unit vectors $\mathbf{e}_\alpha, \mathbf{e}_\beta, \mathbf{e}_n$. The displacement vector components are given in the following form:

$$\begin{aligned} u_\alpha &:= \sum_{i=0}^{m_\alpha} u_{\alpha|i}(\alpha,\beta)\phi_i(\nu) \\ u_\beta &:= \sum_{i=0}^{m_\beta} u_{\beta|i}(\alpha,\beta)\phi_i(\nu) \\ u_n &:= \sum_{i=0}^{m_n} u_{n|i}(\alpha,\beta)\phi_i(\nu) \end{aligned} \tag{6}$$

where ν is the independent variable in the direction of the normal. The functions $u_{\alpha|i}, u_{\beta|i}, u_{n|i}$ are called field functions, the functions $\phi_i(\nu)$ are called director functions. When the material is isotropic then $\phi_i(\nu)$ are polynomials; when the shell is laminated then $\phi_i(\nu)$ are piecewise polynomials (see, for example, [5,6]). Equation (6) represents a semi-discretization in the sense that $\phi_i(\nu)$ are fixed; hence, the number of dimensions is reduced from three to two. The kinematic assumptions incorporated in a particular shell model are characterized by the indices (m_α, m_β, m_n). The lowest member of the hierarchy is the model (1, 1, 0), which, from the point of view of kinematic assumptions, is the same as the Naghdi shell model [7]. The kinematic assumptions of the Novozhilov-Koiter model [8] are more restrictive than those of the model (1, 1, 0) in that the field functions $u_{\alpha|1}$ and $u_{\beta|1}$ are constrained to be linear combinations of the first derivatives of $u_{n|0}$, i.e., there are only three independent field functions.

The classical development of shell models was strongly influenced by the limitations of the methods available for solving the resulting systems of equations. The use of curvilinear coordinates allowed the treatment of shells with simple geometric description, such as cylindrical, spherical, and conical shells by classical methods, subject to the assumption that the thickness of the shell is small in relation to its other dimensions. Such limitations no longer exist. It is possible to formulate the problem in terms of either the curvilinear or the Cartesian components of the displacement vector. When the formulation is based on the curvilinear (resp. Cartesian) components of the displacement vector then we refer to the formulation as a shell (resp. thin solid) formulation.

In the following we will be concerned with the thin solid formulation only, that is, the formulation in terms of the Cartesian components of the displacement field

$$\begin{aligned} u_x &:= \sum_{i=0}^{m} u_{x|i}(\alpha,\beta)\phi_i(\nu) \\ u_y &:= \sum_{i=0}^{m} u_{y|i}(\alpha,\beta)\phi_i(\nu) \\ u_z &:= \sum_{i=0}^{m} u_{z|i}(\alpha,\beta)\phi_i(\nu) \end{aligned} \tag{7}$$

Note that, in the case of thin solid models, the kinematic assumptions are characterized by the single index m. In other words, the transverse variation of the three displacement vector components is approximated by the same functions $\phi_i(\nu)$, $i=0,1,2,\ldots,m$.

Certain advantages and disadvantages are associated with formulating shell models in terms of the Cartesian rather than the curvilinear components of the displacement vector. The advantages are that continuity with other bodies, such as stiffeners, are easier to enforce, and implementation is simpler. The disadvantages are that thin solid formulations cannot be applied to laminated shells unless each lamina is explicitly modeled or homogenized material properties are used; the number of field functions must be the same for each displacement component. For example, the (1, 1, 0) shell model has five field functions, and the thin solid model characterized by $m=1$ has six field functions.

4.2 Linear Working Models for Shells. In the hierarchical view of working models, the highest (i.e., most comprehensive) model accounts for all possible nonlinear effects, such as geometric nonlinearities, material nonlinearities, and mechanical contact. In the case of beams, plates, and shells, there is an important subset of model hierarchy where the highest model is the fully three-dimensional problem of linear elasticity. For this subset, the accuracy of the exact solution of a working model is understood to be in relation to the exact solution of the corresponding fully three-dimensional problem of linear elasticity, not the underlying problem of solid mechanics. This subset is discussed in this section.

The vector of strain tensor components corresponding to $\mathbf{u}$ is denoted by $\{\epsilon\}$. The relationship between $\mathbf{u}$ and $\{\epsilon\}$ is given by $\{\epsilon\}=[D]\mathbf{u}$, where $[D]$ is the differential operator associated with small strain elasticity. The vector of stress tensor components is denoted by $\{\sigma\}$. The relationship between $\{\sigma\}$ and $\{\epsilon\}$ is given by Hooke's law: $\{\sigma\}=[E]\{\epsilon\}$, where $[E]$ is the elastic material stiffness matrix. Traction vectors acting on $\partial\Omega$ are denoted by $\mathbf{T}$. The virtual work of internal stresses is defined as follows:

$$B(\mathbf{u},\mathbf{v}) := \int_\Omega ([D]\mathbf{v})^T[E][D]\mathbf{u}\,d\Omega \tag{8}$$

and the virtual work of external forces is defined by

$$F(\mathbf{v}) := \int_\Omega \mathbf{F}\cdot\mathbf{v}\,d\Omega + \int_{\partial\Omega} \mathbf{T}\cdot\mathbf{v}\,dS + \int_\Omega ([D]\mathbf{v})^T[E]\{c\}\tau\,d\Omega \tag{9}$$

where $\{c_t\}:=\{c_t\ c_t\ c_t\ 0\ 0\ 0\}^T$, c_t is the coefficient of thermal expansion and $\tau=\tau(x,y,z)$ is the change in temperature from a reference temperature.

The energy space is defined by $E(\Omega):=\{\mathbf{u}\,|\,B(\mathbf{u},\mathbf{u})\leqslant C<\infty\}$, where C is some positive constant. The energy norm is defined by

$$\|\mathbf{u}\|_{E(\Omega)} := \left(\tfrac{1}{2}B(\mathbf{u},\mathbf{u})\right)^{1/2} \tag{10}$$

The generic form of the principle of virtual work is stated as follows: Find $\mathbf{u} \in E(\Omega)$ such that

$$B(\mathbf{u},\mathbf{u}) = F(\mathbf{v}) \quad \text{for all } \mathbf{v} \in E(\Omega) \tag{11}$$

Specific statements of the principle of virtual work depend on the boundary conditions. For details we refer to [9]. In the generic case, and whenever the prescribed displacement constraints are insufficient to prevent all possible rigid-body displacements, the solution of Eq. (11) is unique up to rigid-body displacements.

There is an important difference between the classical shell models, such as the Novozhilov-Koiter and the Naghdi model, and the hierarchic shell and thin solid models. In using hierarchic models, the goal is to approximate the fully three-dimensional solution; hence, the stress-strain law is that of the three-dimensional theory of elasticity. In index notation,

$$\sigma_{ij} = \lambda\delta_{ij}\varepsilon_{kk} + 2\mu\varepsilon_{ij} \tag{12}$$

where $\sigma_{ij}, \varepsilon_{ij}$ are the Cartesian stress and strain tensors, respectively, λ and μ are the Lamé parameters, and δ_{ij} is the Kronecker delta. Incorporated in the stress-strain relationship of the Naghdi and the Novozhilov-Koiter models is the assumption that the stress component normal to the midsurface is zero, a condition which is the limiting case of the fully three-dimensional solution with respect the thickness approaching zero. The Naghdi shell model yields the correct solution in the limit $t \to 0$; however, neither the hierarchic shell model (1, 1, 0) nor the thin solid model $m=1$ does, unless Poisson's ratio is zero. The Naghdi model is not a member of the hierarchic sequence of models but rather an extension of the sequence for small t values. Hierarchic shell (resp. thin solid) models characterized by $m_n \geqslant 3$ (resp. $m \geqslant 3$) give the correct limit solution with respect to $t \to 0$ and are said to be asymptotically consistent.

Remark 4.1. In the case of shells, the distinction between the notions of mathematical model and its discretization is blurred by conventions in terminology. It is customary to refer to the various shell formulations as theories or models. In fact, the hierarchic models are semi-discretizations of the fully three-dimensional model. Therefore, modeling errors that can be attributed to the choice of indices (m_α, m_β, m_n) in the case of hierarchic shell models, and the index m in the case of thin solid models, are related to discretization rather than model definition.

4.3 Nonlinear Working Models for Shells.

The model hierarchy must account for nonlinear effects. This large and important topic is not within the scope of this paper. For discussion and examples, we refer to [10–12].

5 Finite Element Spaces

The accuracy of the finite element solution is determined by the finite element space. Finite element spaces are constructed by partitioning the solution domain Ω into finite elements. A partition will be denoted by Δ, the number of elements of the partition by $M(\Delta)$, and the kth element by Ω_k. Typically, Ω_k is mapped from a corresponding standard element Ω_{st} by smooth mapping functions $\mathbf{Q}^{(k)}$.

Ideally, finite element spaces are constructed by adaptive methods such that the tolerance criteria for the data of interest are satisfied. The initial finite element mesh should be laid out utilizing *a priori* information concerning the regularity of the exact solution. For example, in the neighborhood of singular points and lines the mesh should be graded in geometric progression with a fixed common factor when p-extension is used [9]. If h-extension is used then radical grading is optimal [13]. In the case of plate and shell models the presence of boundary layers has to be taken into account.

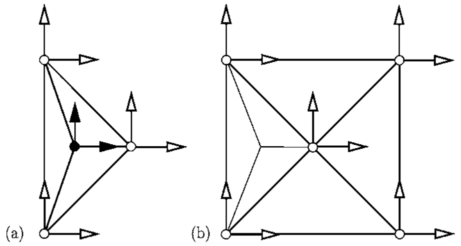

Fig. 3 (*a*) The 12 degrees of freedom HCT triangle and (*b*) composite nonplanar quadrilateral element assembled from four HCT triangles

5.1 Finite Element Space Used in the ORNL Investigation.

At the time of the ORNL investigation, the treatment of shell models by the finite element method was in its very early stages of development. Although the investigators were aware of some contemporary work on curved shell elements, shells were commonly approximated by flat plate elements and most of the available experience was with those elements. For this reason the investigators decided to use flat plate elements for the purpose of analyzing the shell intersection problem [1]. The Hsieh-Clough-Tocher (HCT) triangular element [14] was chosen for the approximation of the displacement component normal to the midsurface of the shell. The constrained linear strain triangle (CLST) was used for approximating the membrane components. A brief description follows.

The HCT triangle is a composite element, comprised of three subtriangles. On each subtriangle, an incomplete cubic polynomial approximation, comprised of nine terms, is used. The polynomials are chosen so that along the external edges the normal derivative varies linearly. Therefore, there are nine coefficients per subtriangle. C^0 continuity is enforced for the subelements by constructing basis functions corresponding to the three nodal displacements and six rotations for each subtriangle, as indicated in Fig. 3(*a*) where the circles represent transverse displacements and the arrows represent first derivatives (rotations in the sense of the arrows). The subtriangles are assembled, which is equivalent to satisfying C^0 continuity over the triangle.

At this point there are three internal degrees of freedom, indicated in Fig. 3(*a*) by the closed circles and arrows, and nine external degrees of freedom, indicated by the open circles and arrows. In order to satisfy exact and minimal C^1 continuity, the continuity of the normal derivatives along the internal edges is enforced leading to three constraint equations, which establish a relationship between the sets of internal and external degrees of freedom. Using these constraint equations, the internal degrees of freedom are eliminated. Thus, the HCT triangle has nine degrees of freedom: three displacements and three rotations in each coordinate direction.

Nonplanar quadrilateral plate elements assembled from four HCT elements were used for approximating the displacement vector components normal to the shell surface. A typical element is shown in Fig. 3(*b*). Since the center node generally does not lie in the same plane as the vertex nodes, there is a third rotation component, not present in the constituent triangles. A third rotation component is also present in the assembly of the quadrilateral elements into the stiffness matrix, since adjacent elements are generally not coplanar. The usual treatment is that the rotation components are transformed into a Cartesian system, the origin of which lies on the shell surface at the node and one axis is coincident with the normal to the surface. The rotation component in the direction of the normal is usually neglected. This causes various problems, for details we refer to [1,2,15]. For a discussion on low-order shell elements we refer to [16].

The in-plane (membrane) components of the displacement vector were approximated by a similar assembly of triangles. These vector components were approximated over each component tri-

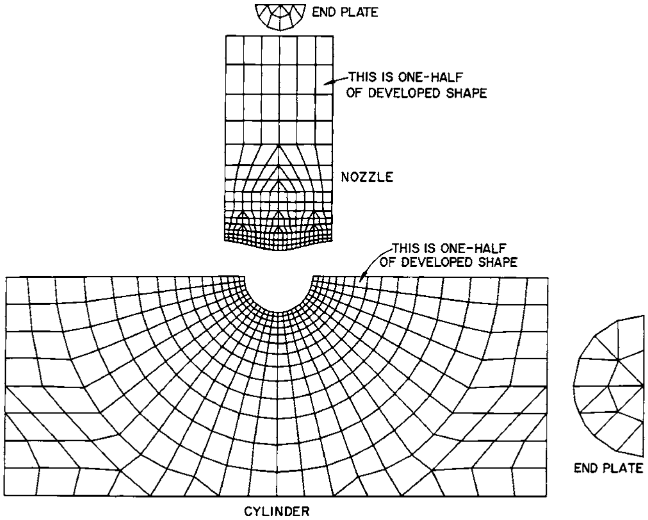

Fig. 4 Finite element mesh used in the ORNL investigation. There are 649 nodal points, of which 25 nodal points are at the intersection: Source: ORNL-DWG 69-10664R (reprinted with permission from Oak Ridge National Laboratory)

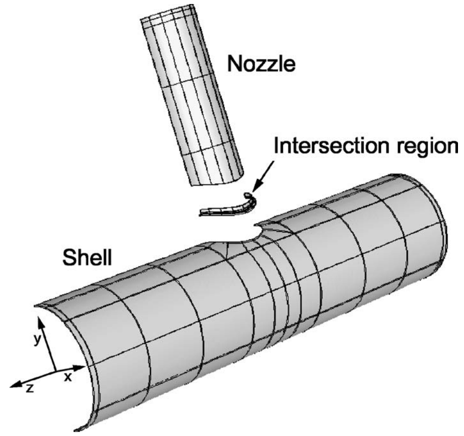

Fig. 5 The 188-element mesh used in the present investigation

angle by quadratic polynomials constrained so that the variation is linear over the external edges. This is known as the constrained linear strain triangle (CLST). A quadrilateral membrane element has two degrees of freedom at each of its five nodes [1]. The finite element space is the span of the assembled of HCT and CLST triangles shown in Fig. 4.

The investigators recognized two sources of error: The errors caused by using plate elements rather than curved shell elements and by using a limited number of elements. Implied is the tacit assumption that, as the number of elements is increased, the approximate solution will converge to the exact solution of the Novozhilov-Koiter shell model. This has not been proven. There is no guarantee that the sequence of finite element solutions obtained by *h*-extension will converge to the exact solution of the Novozhilov-Koiter model of this problem.

Remark 5.1. The definition of the HCT triangle given in [17] is different from the one described here in that all subtriangles are complete polynomials of degree 3 in which case there are 12 degrees of freedom, the nine degrees of freedom shown in Fig. 3(*a*) plus the first derivative in the direction of the normal at the midpoint of each side.

5.2 Finite Element Spaces Used in the Present Investigation. In the present investigation the thin solid formulation implemented in the finite element analysis software product StressCheck[1] was used. The finite element mesh, consisting of 188 elements, is shown in Fig. 5. The nozzle and the shell were partitioned into hexahedral elements, the intersection region was partitioned into hexahedral and pentahedral elements. The hexahedral elements were mapped from the standard hexahedron

$$\Omega_{\mathrm{st}}^{(h)} := \{(\xi,\eta,\zeta) \| \xi| < 1, |\eta| < 1, |\zeta| < 1\} \tag{13}$$

by smooth mapping functions. For details on mapping procedures, we refer to [18].

The standard polynomial spaces used in the present investigation are known as anisotropic trunk spaces. For $p > 1$, $1 \leqslant q \leqslant p$, these spaces are defined by

$$S_{\mathrm{tr}}^{ppq}(\Omega_{\mathrm{st}}^{(h)}) := \mathrm{span}(\xi^k \eta^\ell \zeta^m, \xi^p \eta \zeta^m, \xi \eta^p \zeta^m, (\xi,\eta,\zeta) \in \Omega_{\mathrm{st}}^{(h)}$$

$$k,\ell = 0,1,2,\cdots,k+\ell \leqslant p, m = 0,1,2\cdots,q \tag{14}$$

For definitions of the isotropic trunk space on the standard hexahedron $S_{\mathrm{tr}}^{p}(\Omega_{\mathrm{st}}^{(h)})$ and the standard pentahedron $S_{\mathrm{tr}}^{p}(\Omega_{\mathrm{st}}^{(p)})$, we refer to [9]. The finite element space $S(\Omega)$ is the span of the mapped basis functions defined on the standard elements, subject to the exact and minimal continuity requirement of the formulation. Referring to Eq. (7), $q = m$, corresponds to the thin solid formulation characterized by the index m. For additional details, we refer to [10,12,19].

6 Working Models

The quality of a working model is determined by the proximity of its exact solution to the exact solution of the state-of-the-art model, more precisely, the proximity of functionals that would be computed from the exact solution of the state of the art model and the working model. Here we examine a sequence of working models from the point of view of their ability to approximate physical observations and data computed from physical observations through simple transformation.

The objective of the ORNL experiments was to investigate how well thin shell theory is capable of predicting the stress distribution in intersecting cylindrical shells in the neighborhood of the intersection. The investigators had in mind the Novozhilov-Koiter shell model only. This model is a reasonable choice for representing the smooth parts of the intersecting shells. However, given that the data of interest are the strain values in the vicinity of the intersection, neither the kinematic assumptions nor the material properties (plane stress) incorporated in this model are valid in that region. Although the mathematical problem of the intersecting cylinders for the Novozhilov-Koiter shell model is well defined [20], it is not a good representation of the physical problem.

The working models employed in the present investigation were also based on the theory of elasticity, but differ from the Novozhilov-Koiter shell model in kinematic assumptions and material properties, as described in Sec. 4. The intersection region was treated as a three-dimensional elastic region for each model. The size of the intersection region (characterized by the dimensions d_s and d_n shown in Fig. 6) is fixed for each working model. Elsewhere, the kinematic assumptions of the thin solid formulation were used with $m = q = 1, 2, \ldots$.

The problem of selecting a working model with respect to the goals of computation of the ORNL experiments is understood as follows: A particular working model based on the thin solid formulation is judged to meet the necessary conditions for acceptance if the equivalent (von Mises) stresses computed in the gage locations do not differ by more than τ percent from the corresponding equivalent stresses computed from the fully three-dimensional model. The choice of tolerance is, of course, arbi-

---

[1] StressCheck is a trademark of Engineering Software Research and Development, Inc., St. Louis, MO.

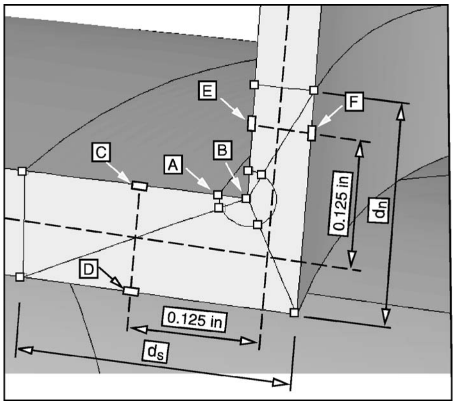

Fig. 6 Mesh detail at the intersection region and location of the strain gages in the plane of symmetry nearest to the intersection; 188-element mesh

trary; however, the accuracy required of the numerical solution depends on this choice. The relative error in the numerical solution has to be less than $\sim 0.5\tau$ percent.

Using the 188-element mesh shown in Fig. 5 and the anisotropic spaces $S_{\mathrm{tr}}^{ppq}(\Omega_{\mathrm{st}}^{(h)})$ with $q=1,2,\ldots,8$, all working models yielded consistent results within the prescribed tolerance of $\tau = 2.5\%$. Therefore the simplest model $(q=1)$ is preferred.

In comparing data computed from working models with physical measurements, it is necessary to recognize the differences between the mathematical problem being solved and the physical system being modeled. These differences are enumerated in relation to the ORNL test article in the following:

1. Geometric variations. The ORNL investigators were careful to minimize errors in manufacturing the test article; however, owing to unavoidable machining tolerances, some variations in wall thickness and the other dimensions had to be present. Quoting from Ref. [1]:

> "*A careful dimensional inspection of the machined model indicated that, despite the care taken in machining, there were wall thickness variations in both nozzle and cylinder with the nozzle thickness being as much as* 15% *greater* (0.007 *to* 0.008 in. *compared with the nominal* 0.050 in.) *in the fourth quadrant than in the second*."

   In the working models it is assumed that the shells are defined by perfect cylindrical surfaces and constant wall thickness.

   The intent of the ORNL investigators was to manufacture the intersection with zero fillet radius. In reality, the milling tool leaves some fillet, see Fig. 2. In the working models the fillet radius is zero. The test article had small flanges at the ends. The working models do not account for those flanges.
2. Variations in material properties. The material properties assumed by the ORNL investigators are the nominal elastic constants of carbon steel. Modulus of elasticity: $E=30 \times 10^6$ psi (207 GPa); Poisson's ratio: $\nu=0.3$. The actual elastic constants of the test article can differ from the nominal values by a few percent. There are no data on the statistical variations of the modulus of elasticity and Poisson's ratio; however, it is reasonable to expect that the mean value of E (resp. ν) is within about 2% (resp. 5%) of the nominal value. Therefore, systematic as well as random errors are present in making comparisons between measured strains and strains computed from the working models.

   The relationship between stress and strain in the test article will become nonlinear when the strain corresponding to the proportional limit is exceeded. In the working models examined herein, the material is assumed to be perfectly elastic, independently of the magnitude of strain.
3. Differences in constraint conditions. Rigid end fixtures were attached to the free end of the cylinder and the nozzle, as described in Sec. 2.1. Details on the end fixtures are not given in the ORNL reports; however, the investigators assumed that the end fixtures were sufficiently rigid to constrain the ends of the cylinder and nozzle so as to maintain the ends as plane circles [1]. In the working model constructed by the ORNL investigators the end fixtures were represented by end plates. In the present investigation, the fixture attached to the nozzle was represented by an end plate. At the free end of the cylinder, the radial and tangential displacement components were set to zero.
4. Differences in loading conditions. The test article was loaded through hydraulic rams acting on the end fixtures. The accuracy of the applied load, and hence the accuracy of the stress resultants, was determined by the accuracy of the load cells. The transfer of the load through the end fixtures was through mechanical contact. The precise distribution of the tractions acting on the ends is not known. In the working models used in the present investigation, uniform tractions were applied on the free end of the cylinder.
5. Symmetry. The working model was assumed to be perfectly symmetric. The test article was not perfectly symmetric and, very likely, the strain gages were not installed to be perfectly symmetric.

It is seen that even under very carefully controlled experimental conditions some degree of uncertainty concerning the physical system is present. Some of these uncertainties can be reduced, other uncertainties either cannot be reduced or may not be feasible to reduce. For example, the mean value of the elastic constants can be determined by simple coupon tests. The dimensions of the test article can be measured with high accuracy. On the other hand, it would be very difficult to determine the distribution of the tractions or constraint conditions imposed by the end fixtures. In addition, some degree of uncertainty is associated with the instruments employed in making the observations and the effects of the environment on the instruments.

In view of these uncertainties one cannot expect very close correlation between computed and experimental data. In the ORNL experiments the largest uncertainties are caused by the difficulties associated with manufacturing thin-walled objects to tight tolerances and mathematical representation of the constraint conditions.

7 Numerical Results

It is necessary to ascertain that the errors in the computed data are well below the threshold set for rejection of a working model. In this investigation, the following steps were taken: (i) The relative error in energy norm was estimated. This provides an overall view of the quality of the approximation. The error in energy norm is roughly equivalent to the rms error in stresses [9]. For the 188-element mesh the estimated relative error in energy norm ranged between 1.15 and 3.20 %. (ii) The dependence of the data of interest on the mesh and the polynomial degree of elements was examined. It was found that the data of interest are substantially independent of the mesh and the polynomial degree of elements. (iii) The data of interest were examined for jump discontinuities at interelement boundaries. Substantial jump discontinuities in locations where the data should be continuous is an indication that the discretization is inadequate. No significant discontinuities were found. These are necessary conditions that an approximate solution will satisfy when the errors of approximation are not large.

Because of space limitations, only some of these procedures are illustrated in the following. Details of the finite element mesh in the shell intersection region are shown in Fig. 6. The size of the

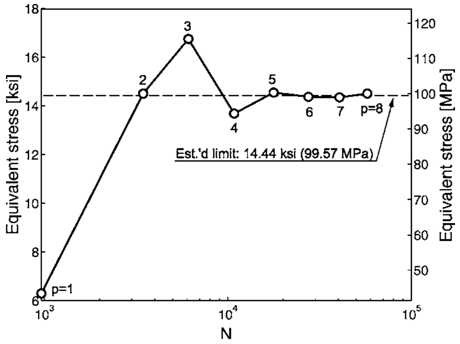

Fig. 7 Convergence of the equivalent stress at node A shown in Fig. 6, 188-element mesh

Table 1 Equivalent stresses (psi) in the gage locations C, D, E, F identified in Fig. 6. Fully three-dimensional model, the points are located on the fixed-end side of the cylinder (1 psi =6.895 kPa).

p	N	Pt. C	Pt. D	Pt. E	Pt. F
3	6095	11225	11959	13729	16589
4	10828	12461	11680	16729	19687
5	17774	12455	12158	17644	19441
6	27497	12535	12089	17237	19005
7	40561	12542	12021	17108	19104
8	57530	12544	11982	17094	18903
EXPT		15569	14554	16981	13100
DIFF. (%)		28.6	24.1	−0.3	−28.9

shell intersection region is characterized by the dimensions d_s and d_n. Unless otherwise stated, in the numerical investigation described herein these dimensions were fixed: $d_s = 0.25$ in. (6.35 mm); $d_n = 0.20$ in. (5.08 mm).

The layout of the mesh in the intersection region is typical of meshes used in p-extensions when corner singularities are present [9]. Nodal point B lies on the line of intersection between the outer surface of the nozzle and the outer surface of the shell in the plane of symmetry. Nodal point A lies on the line of intersection between the outer surface of the shell and the plane of symmetry.

The convergence of the equivalent stress at Point A, with respect to the number of degrees of freedom N, is shown in Fig. 7 on a semi-log scale for the fully three-dimensional model. It is seen that the stress is substantially independent of the polynomial degree p for $p \geqslant 5$. The equivalent stress computed from the finite element solution cannot be close to its exact value if this criterion is not satisfied.

A similar plot shown in Fig. 8 for the equivalent stress computed for point B clearly indicates divergence. This is caused by the presence of an edge singularity. The equivalent stress computed for the exact solution of the elasticity problem is infinity in this point; hence, the equivalent stress computed from the finite element solution cannot converge to a finite value. Consequently, extrapolation of strain data from the gage locations to the intersection is not permissible.

Equivalent stresses in strain gage locations nearest to the intersection region in the plane of symmetry (toward the fixed-end of the cylinder) are shown in Table 1. These data were computed from the solutions obtained for the fully three-dimensional model with p ranging from 1 to 8. The number of degrees of freedom (N) are shown in the second column. Points C, D, E, and F are shown in Fig. 6. Each stress value converges strongly to a limit value, similar to the convergence shown in Fig. 7. The corresponding experimental data and the relative differences (DIFF), using the computed values as the base, are shown in the last two rows. It is seen that the differences are very substantial in three of the four points.

These differences are attributed primarily to variations in wall thickness. All other uncertainties would have a much smaller effect. Inspection of the test article revealed variations in wall thickness as large as 15% [1]. Variations in wall thickness affect both the distribution and magnitude of stresses. The magnitude of these effects depends on whether the solution is bending- or membrane-dominated. Assuming that the bending moments and membrane forces are independent of the wall thickness, in a bending (resp. membrane) dominated region, 10% change in wall thickness causes ~24% (resp. 11%) change in stress.

In experiments designed for purposes of validation it is necessary to eliminate uncertainties with respect to the object of the experiment as much as possible [4]. In the ORNL test article described in this paper the dominant source of uncertainty is the unknown variation in wall thickness. Ideally, the external and internal surfaces would be carefully measured and the actual surfaces would be used in the working model. With today's technology it would be possible to produce a CAD model of the test article as manufactured, to within 0.001 in. (0.025 mm) tolerance. The complexity of the resulting geometrical description of the test article would however, make construction of the working model significantly more complicated.

In the immediate vicinity of the junction there are large bending moments that decay with respect to distance from the junction. The computed and experimentally obtained values of the equivalent stress in gage locations along the line of intersection of the plane of symmetry with the outer surface of the cylinder on the fixed-end side are tabulated in Table 2. It is seen that the errors are larger near the junction than away from it, and the errors are roughly consistent with ~10% variation in wall thickness. The magnitude of the actual variation is unknown.

The other sources of error are inelastic deformation in the vicinity of the junction, variations in material properties, errors in

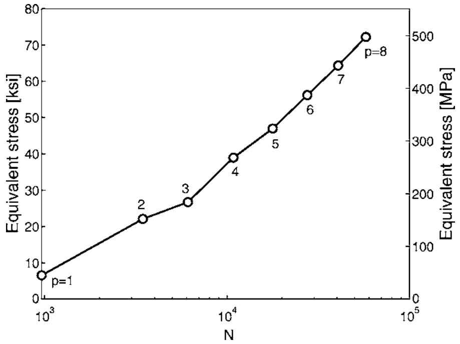

Fig. 8 Convergence of the equivalent stress at node B shown in Fig. 6; 188-element mesh

Table 2 Computed (EFA) and experimentally (EXP) obtained values of the equivalent stress (psi) in gage locations on the intersection of the plane of symmetry with the outside surface of the cylinder as a function of the distance (s) from the mid-surface of the nozzle (inches).

s	FEA	EXP	err (%)
0.125	12541	15569	24.14
0.250	10129	12381	22.23
0.375	8190	8870	8.31
0.500	6531	7453	14.13
0.625	5086	5783	13.70
1.000	2105	2242	6.49
1.500	1836	1844	0.42
2.000	2343	2230	−4.84
3.000	2431	2292	−5.71

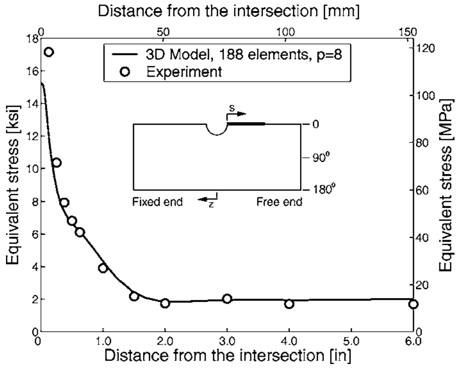

Fig. 9 Equivalent stress on the inside surface of the cylinder versus distance from the midsurface of the nozzle

the location of the strain rosettes, errors in measurement, errors caused by idealization of the actual constraint condition, and errors in loading. None of these errors are large enough to explain the observed differences. For example, to test the effect of inelastic deformation, elastic perfectly plastic material behavior was assumed, the yield stress being 36.0 ksi (248 MPa). Using the deformation theory of plasticity it was found that the plastic zone was confined to a very small neighborhood of the line of intersection of the outer surfaces, and hence, its effect on the stresses in the gage locations was negligible. For a discussion on the other effects, we refer to [3].

A comparison between data computed from experimental measurements and data computed from the fully three-dimensional working model along the inner surface of the cylinder, measured from the midsurface of the nozzle, is shown in Fig. 9.

Equivalent stresses computed in the strain gage locations labeled C, D, E, F in Fig. 6 (see also Table 1) from solutions obtained by means of the hierarchic thin solid models based on the spaces $S_{\mathrm{tr}}^{ppq}(\Omega_{\mathrm{st}}^{(h)})$ are shown in Table 3. The estimated relative errors in energy norm, denoted by $(e_r)_E$, are also given in Table 3. These estimates are based on p-extension. Details are available in [9]. It is seen that the stress data are insensitive to the choice of thin solid model characterized by q.

One of the modeling assumptions is the selection of the size of the intersection region indicated in Fig. 6 by labels d_s and d_n. The data presented thus far was computed with $d_s=0.25$ in. (6.35 mm) $d_n=0.20$ in. (5.08 mm). Therefore, points C, D, E, F were located within the intersection region. Letting $d_s=0.13$ in. (3.30 mm) $d_n=0.15$ in. (3.81 mm), the points are located in the thin solid region. Repeating the computations the results shown in Table 4 are obtained. On comparing Table 3 with Table 4 it is seen that the differences are negligibly small. This indicates that the working models are insensitive to the size of the intersection region.

8 Summary and Conclusions

The intent of the ORNL investigation was to determine whether the finite element space characterized by the mesh shown in Fig. 4, and the HCT plate elements, combined with the CLST plane stress elements, are capable of approximating strains in the given gage locations. We understand this problem to consist of three parts: (i) whether the Novozhilov-Koiter model is capable of representing the deformation of the test article in the intersection region; (ii) whether the three-dimensional assembly of planar plate and membrane elements converge to the exact solution of the Novozhilov-Koiter model as the size of the elements is reduced, and (iii) whether the mesh shown in Fig. 4 is suitable for controlling the errors of discretization in the sense of Eq. (4). The ORNL investigation did not address these questions separately.

In the present investigation the need to address these questions was avoided by (i) demonstrating that hierarchic thin solid formulations provide consistent results in the gage locations even for the lowest member of the hierarchy, characterized by $q=1$; (ii) curved elements mapped by smooth functions rather than planar elements were used, and (iii) the data of interest were shown to be substantially independent of the discretization. Another important difference between the present investigation and the ORNL investigation is that in the present investigation the intersection region was exempt from the kinematic assumptions of the thin solid formulation.

The ORNL investigation highlights some of the difficulties and limitations of experimental validation of working models for shell problems. The experimental data are dominated by uncertainties caused by difficulties associated with the fabrication of thin-walled objects to exacting tolerances. Increasing the wall thickness would reduce errors caused by manufacturing tolerances, but then the thin shell model may not be applicable.

The primary objective in defining a working model is to account for all physical laws and relationships that have a significant influence on the data of interest. Therefore, the choice of a working model depends on the data of interest and has to be validated with respect to the data of interest. The secondary objective is to identify the simplest working model that will satisfy the tolerances set for the data of interest.

Table 3 Equivalent stresses (psi) in the gage locations C, D, E, F identified in Fig. 6. Thin solid models, the points are located on the fixed-end side of the cylinder (1 psi=6.895 kPa).

		$d_s=0.25$ in. (6.35 mm), $d_n=0.2$ in. (5.08 mm)					
p	q	$(e_r)_E$	N	Pt. C	Pt. D	Pt. E	Pt. F
8	1	3.20	41032	12110	11730	16926	18432
8	2	1.15	44766	12570	11978	17094	18904
8	3	1.35	47832	12552	11979	17094	18904
8	8	1.35	57530	12544	11982	17094	18903

Table 4 Equivalent stresses (psi) in the gage locations C, D, E, F identified in Fig. 6. Thin solid models, the points are located on the fixed-end side of the cylinder (1 psi=6.895 kPa).

		$d_s=0.13$ in. (3.30 mm), $d_n=0.15$ in. (3.81 mm)					
p	q	$(e_r)_E$	N	Pt. C	Pt. D	Pt. E	Pt. F
8	1	2.44	41032	12111	12470	17076	18169
8	2	1.11	44766	12621	12026	17104	19141
8	3	1.32	47832	12564	11941	17104	19143
8	8	1.31	57530	12546	11964	17106	19143

In correlation with experimental observations, a working model is tested against data that are either observable or can be computed from observable data. In the model problem discussed herein, the strain components in surface points located in the vicinity of the shell intersection were measured and the von Mises stresses were computed in the gage locations.

The data of interest are, generally, not observable and cannot be computed from observable data. For example, one may be interested in the maximum value of the integral of the normal stress over some small area. Therefore, even if a working model were shown to be successful in predicting certain measured data, it may not be suitable for computing other data of interest. It is necessary to have means for systematic evaluation of the effects of various assumptions, incorporated in a working model, on the data of interest. Virtual experimentation based on a hierarchic framework of models and hierarchic discretizations is indispensable in the development of expert knowledge.

The validity of a working model cannot be established by experimental correlation, in general. The purpose of validation experiments is to determine whether certain necessary conditions are met by a working model. Validation experiments cannot establish sufficient conditions for acceptance of a working model.

Acknowledgment

The authors acknowledge with thanks partial support received from the Air Force Office of Scientific Research under Grant No. F49620-01-1-0074. The authors thank Oak Ridge National Laboratory for the copies of reports and photographs that document the physical experiments and numerical investigation of the shell intersection problem discussed herein. Dr. Ricardo Actis of Engineering Software Research and Development, Inc. provided valuable advice on the uses of StressCheck in connection with this investigation.

References

[1] Corum, J. M., Bolt, S. E., Greenstreet, W. L., and Gwaltney, R. C., 1972, "Theoretical and Experimental Stress Analysis of ORNL Thin-Shell Cylinder-to-Cylinder Model No. 1," Tech. Report ORNL 4553, Oak Ridge National Laboratory, Oct.

[2] Gwaltney, R. C., Corum, J. M., Bolt, S. E., and Bryson, J. W., 1976, "Experimental Stress Analysis of Cylinder-to-Cylinder Shell Models and Comparisons With Theoretical Predictions," ASME J. Pressure Vessel Technol., **98**, pp. 283–289.

[3] Muntges, D., 2004, "Validation of Working Models for Thin Cylindrical Shells," M.S. thesis, Washington University, The Henry Edwin Sever Graduate School, St. Louis.

[4] Oberkampf, W., 2001, "What are Validation Experiments?" Exp. Tech., pp. 35–40.

[5] Actis, R., Szabó, B., and Schwab, C., 1999, "Hierarchic Models for Laminated Plates and Shells," Comput. Methods Appl. Mech. Eng., **172**, pp. 79–107.

[6] Babuška, I., Szabó, B. A., and Actis, R. L., 1992, "Hierarchic Models for Laminated Composites," Int. J. Numer. Methods Eng., **33**, pp. 503–535.

[7] Naghdi, P. M., 1972, "The Theory of Shells and Plates," *Encyclopedia of Physics*, S. Flügge, ed. Springer-Verlag, Berlin, pp. 425–640.

[8] Novozhilov, V. V., 1964, *Thin Shell Theory*, 2nd Edition, Noordhoff, Groningen.

[9] Szabó, B., and Babuška, I., 1991, *Finite Element Analysis*, Wiley, New York.

[10] Rank, E., Düster, A., Nübel, V., Preusch, K., and Bruhns, O. T., 2005, "High Order Finite Elements for Shells," Comput. Methods Appl. Mech. Eng. **194**, pp. 2494–2512.

[11] Szabó, B., and Actis, R., 2005, "On the Importance and Uses of Feedback Information in FEA," Appl. Numer. Math., **52**, pp. 219–234.

[12] Szabó, B., Düster, A., and Rank, E., 2004, "The *p*-Version of the Finite Element Method," *Encyclopedia of Computational Mechanics*, E. Stein, R. de Borst, and T. J. R. Hughes, eds., Wiley, Chichester, Vol. 1, Chap. 5.

[13] Babuška, I., and Strouboulis, T., 2001, *The Finite Element Method and its Reliability*, Oxford University Press, Oxford.

[14] Clough, R. W., and Tocher, J. L., 1966, "Finite Element Stiffness Matrices for Analysis of Plate Bending," *Proc. of Conference on Matrix Methods in Structural Mechanics*, Report AFFDL-TR-66-80, Wright-Patterson Air Force Base, OH, pp. 515–545.

[15] Greste, O., 1970, "Finite Element Analysis of Tubular K Joints," Tech. Report UCSESM 70-11, University of California at Berkeley.

[16] Pitkäranta, J., 2003, "Mathematical and Historical Reflections on the Lowest Order Finite Element Models for Thin Structures," Comput. Struct., **81**, pp. 895–121.

[17] Ciarlet, P. G., 1978, *The Finite Element Method for Elliptic Problems*, North-Holland, Amsterdam.

[18] Királyfalvi, G., and Szabó, B. A., 1997, "Quasi-Regional Mapping for the *p*-Version of the Finite Element Method," Finite Elem. Anal. Design, **27**, pp. 85–97.

[19] Düster, A., Bröker, H., and Rank, E., 2001, "The *p*-Version of the Finite Element Method for Three-Dimensional Curved Thin Walled Structures," Int. J. Numer. Methods Eng., **52**, pp. 673–703.

[20] Geymonat, G., and Sanchez-Palencia, E., 1995, "On the Rigidity of Certain Surfaces With Folds and Applications to Shell Theory," Arch. Ration. Mech. Anal., **129**, pp. 11–45.

Plane-Strain Propagation of a Fluid-Driven Fracture: Small Toughness Solution

Dmitry I. Garagash[1]
Department of Civil and Environmental Engineering,
Clarkson University,
Potsdam, NY 13699-5710
e-mail: garagash@clarkson.edu

Emmanuel Detournay
Department of Civil Engineering,
University of Minnesota,
Minneapolis, MN 55455

The paper considers the problem of a plane-strain fluid-driven fracture propagating in an impermeable elastic solid, under condition of small (relative) solid toughness or high (relative) fracturing fluid viscosity. This condition typically applies in hydraulic fracturing treatments used to stimulate hydrocarbons-bearing rock layers, and in the transport of magma in the lithosphere. We show that for small values of a dimensionless toughness $\mathcal{K}$, the solution outside of the immediate vicinity of the fracture tips is given to $O(1)$ by the zero-toughness solution, which, if extended to the tips, is characterized by an opening varying as the $(2/3)$ power of the distance from the tip. This near tip behavior of the zero-toughness solution is incompatible with the Linear Elastic Fracture Mechanics (LEFM) tip asymptote characterized by an opening varying as the $(1/2)$ power of the distance from the tip, for any nonzero toughness. This gives rise to a LEFM boundary layer at the fracture tips where the influence of material toughness is localized. We establish the boundary layer solution and the condition of matching of the latter with the outer zero-toughness solution over a lengthscale intermediate to the boundary layer thickness and the fracture length. This matching condition, expressed as a smallness condition on $\mathcal{K}$, and the corresponding structure of the overall solution ensures that the fracture propagates in the viscosity-dominated regime, i.e., that the solution away from the tip is approximately independent of toughness. The solution involving the next order correction in $\mathcal{K}$ to the outer zero-toughness solution yields the range of problem parameters corresponding to the viscosity-dominated regime. [DOI: 10.1115/1.2047596]

Introduction

The problem of a fluid-driven fracture propagating in rock arises in hydraulic fracturing, a technique widely used in the petroleum industry to enhance the recovery of hydrocarbons from underground reservoirs [1]. Other applications include magma-driven fracture [2], preconditioning of rock masses in mining operation to promote caving [3], formation of barriers to stop contaminant transport in environmental remediation projects [4]. Despite numerous publications on this problem since the seminal paper of Khristianovic and Zheltov [5], the dependence of the solution on the problem parameters has not yet been fully addressed. The main difficulty arises from the complicated mathematical structure of the problem, which involves nonlocal relationship between fracture opening and fluid pressure in the crack, and a nonlinear equation governing the flow of fluid in the fracture. Furthermore, the coupling between nonlinear flow and nonlocal fracture deformation results in a complex solution structure near the tip [6–10], which, nevertheless, controls the global solution.

This paper is concerned with the problem of the quasi-static propagation of a plane-strain hydraulic fracture in an impermeable linear elastic solid. The fracture is driven by an incompressible Newtonian fluid injected at a constant rate at the fracture inlet (Fig. 1). It is assumed that the fracture is filled by the injected fluid, which flowing in the fracture according to lubrication theory [11]. This model has been initially formulated by Geertsma and de Klerk [12] and by Spence and Sharp [6], while similar models of the plane-strain propagation of fluid-driven fractures have been considered by various authors including Nilson [13,14] (for compressible fluid and pressure boundary condition at the inlet), Huang et al. [15] (for inviscid Eulerian fluid), and Adachi and Detournay [16] and Garagash [17] (for non-Newtonian fluids).

In the considered model, two limiting propagation regimes can be identified with the dominance of one of the two energy dissipation mechanisms, either in fracturing of the rock or in flow of the viscous fluid [18,19]. In the *viscosity-dominated regime*, dissipation in extending the fracture in the rock is negligible compared to the losses in the viscous fluid flow, while in the *toughness-dominated regime*, the opposite is true. The solution in and near the viscosity-dominated regime and the corresponding parametric range is the focus of this paper. In contrast, the solution obtained by Spence and Sharp [6] applies in the intermediate regime when the effects of both toughness and viscosity are of the same order. (Their numerical scheme for the finite toughness has been further improved by Adachi [20].) The solution in and near the toughness-dominated regime has been considered by Garagash [21,22].

In the *viscosity-dominated regime*, one expects that the solution can be approximated to a reasonable degree of accuracy by the zero-toughness solution [16,23]. The zero-toughness solution, however, cannot be readily applied over the complete extent of the fracture for any nonzero value of toughness, as the near tip weakly singular behavior of the zero-toughness solution [6–8] is incompatible with the Linear Elastic Fracture Mechanics (LEFM) singularity [24]. This paper establishes the conditions under which the influence of material toughness is localized to the near tip LEFM boundary layer. It also describes the construction of the solution, which matches with the outer (zero-toughness) solution over a lengthscale intermediate to the boundary layer thickness and the fracture length. The matching condition and the corre-

---

[1] To whom correspondence should be addressed.

Contributed by the Applied Mechanics Division of THE AMERICAN SOCIETY OF MECHANICAL ENGINEERS for publication in the ASME JOURNAL OF APPLIED MECHANICS. Manuscript received by the Applied Mechanics Division, September 30, 2004; final revision, April 10, 2005. Review conducted by K. Ravi-Chandar. Discussion on the paper should be addressed to the Editor, Prof. Robert M. McMeeking, Journal of Applied Mechanics, Department of Mechanical and Environmental Engineering, University of California—Santa Barbara, Santa Barbara, CA 93106-5070, and will be accepted until four months after final publication in the paper itself in the ASME JOURNAL OF APPLIED MECHANICS.

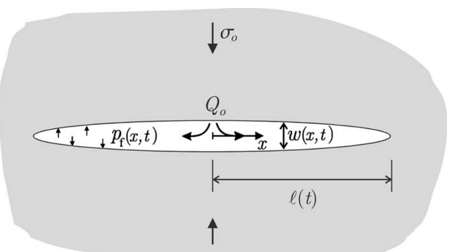

Fig. 1 Sketch of a plane-strain fluid-driven fracture

sponding structure of the overall solution ensure the existence of the viscosity-dominated regime, when the solution away from the tip is independent of the material toughness and is given by the zero-toughness solution. To establish the range of problem parameters corresponding to the viscosity-dominated regime, the next-order toughness correction to the outer zero-toughness solution is considered. The paper is concluded by a discussion of the limiting propagation regimes and corresponding parametric ranges.

Problem Formulation

We consider a finite two-dimensional hydraulic fracture of half length $\ell(t)$ propagating in an impermeable linear elastic medium characterized by Young's modulus E, Poisson's ratio ν, and toughness K_{Ic} (Fig. 1). An incompressible fluid of viscosity μ is injected at the center of the fracture at a constant injection rate Q_o. The crack is loaded by an internal fluid pressure $p_{\mathrm{f}}(x,t)$ and by a far-field confining stress σ_o. We look for the solution of this problem in terms of the net pressure $p(x,t)=p_{\mathrm{f}}(x,t)-\sigma_o$, the fracture opening $w(x,t)$, and the fracture half-length $\ell(t)$, where x is the position along the crack with the origin at the inlet and t is the time counted from the moment injection has started. The analysis is performed under the following assumptions.

(i) The fracture is always completely filled by fluid; i.e., there is no lag between the fracture and the fluid fronts, and the fracture volume is given by the volume of injected fluid $V(t)=Q_o t$. This assumption can be justified under conditions of "slow" fracture propagation or high confining stress [9,25]. As a consequence of this assumption, the far-field stress σ_o enters the solution only as a reference value for the fluid pressure in the expression for the net pressure p.

(ii) The fracture is always in mobile equilibrium and its quasi-static propagation can be described within the framework of LEFM [24].

(iii) Fluid flow in the crack is described by lubrication theory [11]. No exchange of fluid taking place between the fracture and the surrounding impermeable solid.

The governing equations of the model can be formulated over half of the crack, $0 \leqslant x \leqslant \ell$, by accounting for the problem symmetry. The set of effective material parameters

$$E' = \frac{E}{1-\nu^2}, \quad \mu' = 12\mu, \quad K' = 4\left(\frac{2}{\pi}\right)^{1/2} K_{\mathrm{Ic}}. \tag{1}$$

corresponding to the elastic modulus, the fluid viscosity, and the material toughness, respectively, is used in the formulation.

The fluid flow inside the crack is described by the continuity equation and Poiseuille law

$$\frac{\partial w}{\partial t} + \frac{\partial q}{\partial x} = 0, \quad q = -\frac{w^3}{\mu'}\frac{\partial p}{\partial x}, \tag{2}$$

where q denotes the fluid flow rate per unit (out-of-plane) width. An alternative form of the continuity equation can be obtained by integrating Eq. $(2)_a$ and taking into account the continuity condition at the fracture tip, $q/w = d\ell/dt$,

$$\frac{\partial}{\partial t}\int_x^{\ell} w\,\mathrm{d}x = q. \tag{3}$$

Global fluid continuity requires the injected fluid volume $V(t)$ to be equal to the fracture volume; hence

$$2\int_0^{\ell} w\,\mathrm{d}x = V(t). \tag{4}$$

Deformation of the solid and the fracture propagation criterion are prescribed by the LEFM equations. The net pressure $p=p_{\mathrm{f}}-\sigma_o$ is related to the crack opening w by an integral equation of linear elasticity theory [24], which can be written in view of the problem symmetry as

$$p(x,t) = -\frac{E'}{2\pi}\int_0^{\ell} \frac{\partial w(x',t)}{\partial x'}\frac{x'\,\mathrm{d}x'}{x'^2 - x^2}. \tag{5}$$

The assumption that the fracture is in mobile equilibrium requires that the stress intensity factor K_I is always equal to the toughness K_{Ic}. The propagation condition $K_I = K_{\mathrm{Ic}}$ can be prescribed as a tip asymptote for the crack opening [24]

$$w = \frac{K'}{E'}(\ell - x)^{1/2} \quad \ell - x \ll \ell. \tag{6}$$

Equations (2) to (6) fully define the fracture length $\ell(t)$, the opening $w(x,t)$, and the net pressure $p(x,t)$ as functions of the injection law $V(t)$ and the set of parameters (1).

Viscosity Scaling

A scaling appropriate for constructing the "small" toughness solution should not contain K' in the scaling factors used to define dimensionless crack opening Ω, net pressure Π, and crack half-length γ. Such a viscosity scaling, together with the corresponding normalized governing equations, is presented in Appendix A for a general injection law, $V=V(t)$. For a constant injection rate, $V = Q_o t$, these scaling laws reduce to [19]

$$\begin{aligned} w(x,t) &= \varepsilon(t)L(t)\Omega(\xi;\mathcal{K}), \\ p(x,t) &= \varepsilon(t)E'\Pi(\xi;\mathcal{K}), \\ \ell(t) &= L(t)\gamma(\mathcal{K}), \end{aligned} \tag{7}$$

where $\xi = x/\ell(t)$ is the scaled coordinate ($\xi=0$ and $\xi=1$ correspond to the crack inlet and the crack tip, respectively), and where the parameter $\varepsilon(t)$, the length scale $L(t)$, and the dimensionless toughness $\mathcal{K}$ are defined as

$$\varepsilon = \frac{Q_o t}{L^2}, \quad L = \frac{Q_o^{1/2}E'^{1/6}}{\mu'^{1/6}}t^{2/3}, \quad \mathcal{K} = \frac{K'}{E'}\left(\frac{E'}{\mu' Q_o}\right)^{1/4}. \tag{8}$$

It is also useful to define the alternative scaling for the fracture opening in the form

$$\bar{\Omega}(\xi;\mathcal{K}) = \Omega(\xi;\mathcal{K})/\gamma(\mathcal{K}). \tag{9}$$

The governing Eqs. (2)–(6) in terms of the new quantities and the variable $\xi \in [0,1]$ become (see Appendix A)

$$\int_\xi^1 \bar{\Omega}\,\mathrm{d}\xi + \frac{2}{3}\xi\bar{\Omega} = -\bar{\Omega}^3\frac{\mathrm{d}\Pi}{\mathrm{d}\xi}, \quad \gamma^{-2} = 2\int_0^1 \bar{\Omega}\,\mathrm{d}\xi, \tag{10}$$

$$\Pi(\xi) = \mathcal{L}\{\bar{\Omega}\}(\xi), \quad \xi \to 1: \bar{\Omega} = \mathcal{K}\gamma^{-1/2}(1-\xi)^{1/2} \tag{11}$$

with the elasticity operator $\mathcal{L}$ defined as

$$\mathcal{L}\{\bar{\Omega}\}(\xi) = -\frac{1}{2\pi}\int_0^1 \frac{\mathrm{d}\bar{\Omega}(\xi')}{\mathrm{d}\xi'}\frac{\xi'\,\mathrm{d}\xi'}{\xi'^2 - \xi^2}. \tag{12}$$

The solution $\mathcal{F}(\xi;\mathcal{K})=\{\bar{\Omega},\Pi,\gamma\}$ of the system of Eqs. (10) and (11) is thus self-similar [6]. The time-dependence of the dimensional solution is a power-law solely defined by the scaling (7)–(9).

The dimensionless toughness $\mathcal{K}$, the only parameter controlling the solution $\mathcal{F}$, characterizes the relative importance of the solid toughness K' and the fluid viscosity μ' on the propagation of a hydraulic fracture. The focus of this paper is on the solution when the former effect is small compared to the later, i.e., when the toughness $\mathcal{K}$ is small. This solution can be sought in the form of an asymptotic series expansion in a small toughness-dependent parameter $\mathcal{E}(\mathcal{K})\ll 1$ near $\mathcal{E}(0)=0$,

$$\mathcal{F}(\xi;\mathcal{K}) = \mathcal{F}_0(\xi) + \mathcal{E}(\mathcal{K})\mathcal{F}_1(\xi) + \cdots \qquad (13)$$

(A particular form of the expansion parameter $\mathcal{E}(\mathcal{K})$ is to be further determined from the asymptotic analysis of the governing equations.)

In the expansion (13), $\mathcal{F}_0(\xi)=\mathcal{F}(\xi;0)$ is the zero-toughness solution [16,23] and the small parameter $\mathcal{E}(\mathcal{K})$ is at this point an unknown function of $\mathcal{K}$. The fracture is said to propagate in the *viscosity-dominated regime* if its solution can be approximated by the zero-toughness solution, $\mathcal{F}_0(\xi)$, i.e., when the next-order term, $\mathcal{E}(\mathcal{K})\mathcal{F}_1(\xi)$, in the expansion (13) is negligible, $\mathcal{E}(\mathcal{K})\ll 1$. Once $\mathcal{E}(\mathcal{K})$ has been determined, the later condition provides the range $[0,\mathcal{K}_o]$ corresponding to the viscosity-dominated regime.

The zero-toughness solution is known to have a weakly singular near tip asymptote characterized by the fracture opening varying as a 2/3 power-law of the distance from the tip [8]. This zero toughness solution is thus incompatible with the LEFM tip singularity that takes place whenever the toughness is nonzero, and which is characterized by a 1/2 power-law for the fracture opening, Eq. $(11)_b$. Thus, the zero-toughness solution is not uniformly valid along the fracture for small toughness $\mathcal{K}\ll 1$, and a localized boundary layer possessing the LEFM behavior has to exist near the tip of the moving hydraulic fracture for arbitrary small $\mathcal{K}$. Therefore, the series expansion (13) has to actually correspond to the outer small toughness solution.

In the following, we first discuss the solutions for the terms in the outer expansion (13) and their asymptotes near the fracture tip; namely, the zero-toughness solution, which provides the solution on the length scale of the fracture in the viscosity-dominated regime, and the next order, $O(\mathcal{E}(\mathcal{K}))$, toughness correction to it. Then we analyze the solution in the LEFM boundary layer and its asymptotic behavior away from the tip. Finally, we establish the condition when there exists an intermediate length scale with respect to the LEFM boundary layer thickness and the fracture length scale, over which both inner and outer solutions possess the same intermediate asymptote. Under this condition, the inner and outer solutions can be matched to form the composite small-toughness solution uniformly valid along the length of the crack. In particular, this matching condition enables the determination of $\mathcal{E}(\mathcal{K})$, which characterizes the dependence of the outer solution (13) on the toughness.

Outer Problem

Zero-Toughness Solution. The zero-toughness solution, $\mathcal{F}_0=\{\bar{\Omega}_0(\xi),\Pi_0(\xi),\gamma_0\}$, is governed by the set of Eqs. (10) and (11) with $\mathcal{K}=0$

$$\int_\xi^1 \bar{\Omega}_0 \mathrm{d}\xi + \frac{2}{3}\xi\bar{\Omega}_0 + \bar{\Omega}_0^3\frac{\mathrm{d}\Pi_0}{\mathrm{d}\xi} = 0, \quad \gamma_0^{-2} = 2\int_0^1 \bar{\Omega}_0 \mathrm{d}\xi, \qquad (14)$$

$$\Pi_0 = \mathcal{L}\{\bar{\Omega}_0\}, \quad \lim_{\xi\to 0}(1-\xi)^{-1/2}\bar{\Omega}_0(\xi) = 0 \qquad (15)$$

The system of Eqs. (14) and (15) can be solved by means of a series expansion over a class of special functions [16]. The normalized fracture length is $\gamma_0\simeq 0.61524$, and the fracture opening $\bar{\Omega}_0(\xi)$ and pressure $\Pi_0(\xi)$ are plotted in Fig. 2. Importantly, the near tip asymptote of the zero-toughness solution is given by the HF eigensolution [8], which corresponds to the solution of a semi-infinite hydraulic crack with zero lag propagating steadily in a zero-toughness elastic solid. In the scaling for a finite fracture, this tip asymptote is given by

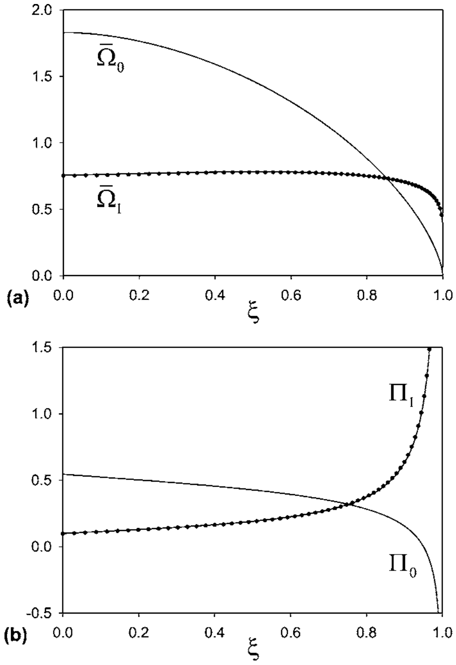

Fig. 2 Zero- (after Adachi and Detournay [16]) and first-order terms in the outer solution expansion (13) for the normalized opening $\bar{\Omega}$, (a), and net-pressure Π, (b). Solution for $\bar{\Omega}_1$ and Π_1 is shown for $n=1$ (dotted lines) and $n=10$ (solid lines) terms in series (21).

$$\xi\to 1: \bar{\Omega}_0 = \left(\frac{2}{3}\right)^{1/3}\beta(1-\xi)^{2/3}, \quad \Pi_0 = \left(\frac{2}{3}\right)^{1/3}\delta(1-\xi)^{-1/3} \qquad (16)$$

with $\beta=2^{1/3}3^{5/6}$ and $\delta=-6^{-2/3}$.

The near tip asymptotic behavior of the opening, Eq. (16), satisfies the fracture propagation condition for zero toughness, Eq. $(15)_b$. However, if the toughness is arbitrarily small, the propagation condition $(11)_b$ together with the lubrication equation (10) yields a logarithmic pressure singularity at the fracture tip. Thus, the zero toughness solution with the asymptotic behavior (16) does not satisfy the tip boundary condition for nonzero toughness and, consequently, points to the existence of a LEFM boundary layer near the fracture tip for small $\mathcal{K}$.

Next-Order Toughness Correction.

Governing Equations and Asymptotic Behavior. The governing equations for the term $\mathcal{F}_1(\xi)$ in Eq. (13) are obtained by substituting the outer expansion (13) into Eqs. (10) and (11) and retaining terms of order $\mathcal{E}(\mathcal{K})$

$$\int_\xi^1 \bar{\Omega}_1 \mathrm{d}\xi + \frac{2}{3}\xi\bar{\Omega}_1 = -\left[\bar{\Omega}_0^3\frac{\mathrm{d}\Pi_1}{\mathrm{d}\xi} + 3\bar{\Omega}_1\bar{\Omega}_0^2\frac{\mathrm{d}\Pi_0}{\mathrm{d}\xi}\right],$$

$$\gamma_1 = -\gamma_0^3 \int_0^1 \bar{\Omega}_1 \mathrm{d}\xi, \quad \Pi_1 = \mathcal{L}\{\bar{\Omega}_1\}. \tag{17}$$

The LEFM tip boundary condition $(11)_b$ is inconsequential for the outer solution, as it should be accounted for in the boundary layer solution.

Let us assume that the opening term $\bar{\Omega}_1$ behaves asymptotically as $A(1-\xi)^h$ near the fracture tip, where $h \in (0,1)$ and A is a constant. Then, according to the asymptotic properties of the elasticity Eq. $(17)_c$, the near tip asymptote of the pressure term Π_1 is given by $A4^{-1}h\cot(\pi h)(1-\xi)^{h-1}$ (see also Appendix C of [6]). However, since the coefficient $\mathcal{E}(\mathcal{K})$ in front of the next-order term $\mathcal{F}_1(\xi)$ in the outer expansion (13) is yet to be determined, we can arbitrarily set $A=1$. Thus, the term $\{\bar{\Omega}_1, \Pi_1\}$ has the following tip asymptote

$$\xi \to 1: \bar{\Omega}_1 = (1-\xi)^h, \quad \Pi_1 = 4^{-1}h\cot(\pi h)(1-\xi)^{h-1}. \tag{18}$$

Substitution of the asymptotes, Eqs. (16) and (18), into the lubrication Eq. $(17)_a$ yields

$$\xi \to 1: \left[-\frac{4}{3} + \frac{\beta^3}{6}h(1-h)\cot(\pi h)\right](1-\xi)^h + O((1-\xi)^{h+1}) = 0. \tag{19}$$

The value of the power law index h is then obtained by equating the coefficient in front of the leading term in Eq. (19) to zero. Numerical solution of the resulting transcendental equation in $h \in (0,1)$ gives

$$h \simeq 0.138673. \tag{20}$$

It can further be established from the governing Eqs. (17) that the next order terms in the tip asymptotic expansion of $\bar{\Omega}_1$ and Π_1 are $O((1-\xi)^{h+1})$ and $O(1)$, respectively.

Numerical Solution. We proceed with the solution $\mathcal{F}_1(\xi)$ of Eqs. (17) with Eq. (18) via a series expansion approach [6,16]. The solution is sought in terms of a truncated series which satisfies the elasticity equation exactly

$$\bar{\Omega}_1 \simeq \sum_{j=0}^{n} A_j \bar{\Omega}_j^* + B\bar{\Omega}^{**}, \quad \Pi_1 \simeq \sum_{j=1}^{n} A_j \Pi_j^* + B\Pi^{**}, \tag{21}$$

where $\bar{\Omega}_j^*$ and $\Pi_j^* = \mathcal{L}\{\bar{\Omega}_j^*\}$ $(j=1,\ldots,n)$ are 'base functions,' $\bar{\Omega}^{**}$ and $\Pi^{**} = \mathcal{L}\{\bar{\Omega}^{**}\}$ are "particular functions," and $n+1$ is the finite number of terms in the solution approximation. The leading base function $\bar{\Omega}_0^*$ and the corresponding coefficient A_0 are chosen to be compatible with the near tip asymptote (18)

$$\bar{\Omega}_0^* = (1-\xi^2)^h, \quad A_0 = 2^{-h}. \tag{22}$$

The rest of the base functions for the opening are chosen in the form of the product of $(1-\xi^2)^{h+1}$ times a polynomial (assuming that $(1-\xi^2)^{-h}\bar{\Omega}_1$ is a regular function),

$$\bar{\Omega}_j^* = (1-\xi^2)^{h+1} C_{2j}^{(h+1/2)}(\xi), \quad j = 1, \ldots, n, \tag{23}$$

where $C_{2j}^{(\lambda)}(\cdot)$ is the Gegenbauer polynomial of degree $2j$ and index λ [26]. The base functions for the opening, Eqs. (22) and (23), are even over the interval $[-1,1]$; furthermore they are zero at the tips $(\xi = \pm 1)$ and finite at the inlet $(\xi=0)$. The index $\lambda = h+1/2$ is selected to enable close form integration of the elasticity equation [16]. The corresponding pressure base functions Π_j^*, gradients $\mathrm{d}\Pi_j^*/\mathrm{d}\xi$, and $\int_\xi^1 \bar{\Omega}_j^* \mathrm{d}\xi$ [needed for further evaluation of different terms in the lubrication Eq. $(17)_a$] are listed in Appendix B.

Since the gradient of the pressure base functions (B10) and (B11) is identically zero at the fracture inlet, $\xi=0$, the particular functions $\{\bar{\Omega}^{**}, \Pi^{**}\}$ are chosen to account for a nonzero pressure gradient at the inlet, i.e., $\mathrm{d}\Pi^{**}/\mathrm{d}\xi$ is nonzero at $\xi=0$. The form of the particular functions $\{\bar{\Omega}^{**}, \Pi^{**}\}$, which satisfies the elasticity Eq. $(17)_c$ and the latter condition, is chosen as in [16,23],

Table 1 Numerical values of coefficients and other overall parameters in the solution $\bar{\Omega}_1(\xi), \Pi_1(\xi), \gamma_1$ for the next order term in the outer solution

	$n=1$	$n=5$	$n=10$
A_1	$-4.0042\cdot 10^{-2}$	$-5.8281\cdot 10^{-2}$	$-6.3997\cdot 10^{-2}$
A_2	-	$-1.4754\cdot 10^{-2}$	$-2.3096\cdot 10^{-2}$
A_3	-	$-7.3942\cdot 10^{-3}$	$-1.5558\cdot 10^{-2}$
A_4	-	$-2.0583\cdot 10^{-3}$	$-8.4194\cdot 10^{-3}$
A_5	-	$-6.5172\cdot 10^{-4}$	$-4.7703\cdot 10^{-3}$
A_6	-	-	$-2.2503\cdot 10^{-3}$
A_7	-	-	$-1.0271\cdot 10^{-3}$
A_8	-	-	$-3.5380\cdot 10^{-4}$
A_9	-	-	$-1.0931\cdot 10^{-4}$
A_{10}	-	-	$-4.4877\cdot 10^{-6}$
B	$-4.5476\cdot 10^{-2}$	$-4.5930\cdot 10^{-2}$	$-4.6015\cdot 10^{-2}$
$\bar{\Omega}_1(0)$	0.75202	0.75693	0.75802
$\Pi_1(0)$	0.09683	0.09920	0.09951
γ_1	−0.17475	−0.17520	−0.17536
$e^{(n)}$	$4.89\cdot 10^{-4}$	$1.80\cdot 10^{-5}$	$1.49\cdot 10^{-6}$

$$\bar{\Omega}^{**} = 4\sqrt{1-\xi^2} + 2\xi^2 \ln\left|\frac{1-\sqrt{1-\xi^2}}{1+\sqrt{1-\xi^2}}\right|, \quad \Pi^{**} = 2 - \pi|\xi|. \tag{24}$$

Expression for the next order term in the crack length, γ_1, is obtained from substitution of Eq. $(21)_a$ into Eq. $(17)_b$

$$\gamma_1 = -\frac{1}{2}\gamma_0^3 \left[B\left(\frac{1}{2}, 1+h\right)A_0 - \frac{\frac{1}{2}+h}{\frac{5}{2}+h}\mathrm{B}\left(\frac{1}{2}, 2+h\right)A_1 + \frac{4\pi}{3}B \right], \tag{25}$$

where $\mathrm{B}(\cdot,\cdot)$ is Euler's beta function [26]. (Note that the contribution of the terms $\bar{\Omega}_j^*$ with $j=2,\ldots,n$ is zero.)

The series expansion of $\{\bar{\Omega}_1, \Pi_1\}$ in the form Eqs. (21) with (22), (23), (B7), and (B8) satisfies the elasticity Eq. $(17)_c$ and the tip asymptote (18). Let us denote the difference between the left-hand-side and the right-hand-side of the lubrication Eq. $(17)_a$, evaluated at a pair $\{\bar{\Omega}_j^*(\xi), \Pi_j^*(\xi)\}$ $(j=0,\ldots,n)$ or the pair $\{\bar{\Omega}^{**}(\xi), \Pi^{**}(\xi)\}$ by $Q_j^*(\xi)$ $(j=0,\ldots,n)$ or $Q^{**}(\xi)$, respectively. Readily derived expressions for $Q_j^*(\xi)$ and $Q^{**}(\xi)$ are omitted here. Substitution of Eq. (21) into Eq. $(17)_a$ and evaluation at $n+1$ collocation points $\{\xi_0, \xi_1, \ldots, \xi_n\}$ then yields a linear system of algebraic equations in $\{A_1, \ldots, A_n, B\}$

$$\sum_{j=1}^{n} Q_{ij}^* A_j + Q_i^{**} B = -2^{-h} Q_{i0}^*, \quad i = 0, \ldots, n, \tag{26}$$

where $Q_{ij}^* = Q_j^*(\xi_i)$, $Q_i^{**} = Q^{**}(\xi_i)$, $i,j = 0,\ldots,n$.

The solution of the linear system of Eqs. (26) in $\{A_1,\ldots,A_n,B\}$ is carried out for $n=1$, 5, 10, and using collocation points regularly distributed on the interval $\xi \in [0,1]$. The results are summarized in Table 1. The convergence error of the solution for a given number of coefficients $n+1$ is computed in the form $e^{(n)} = \int_0^1 Q^2(\xi)\mathrm{d}\xi$, where $Q(\xi)$ is the difference between the left and the right hand sides of the lubrication Eq. $(17)_a$.

The next-order opening $\bar{\Omega}_1$ and pressure Π_1 terms, computed for $n=1$ and $n=10$, are plotted in Fig. 2 with solid and dotted lines, respectively. This figure suggests that the numerical scheme is robust since the solution for $n=1$, which consists of three terms: The leading term (correct tip asymptote), the first regular term, and the particular solution (correct inlet behavior), e.g., for the opening $\bar{\Omega}_1 \simeq A_0\bar{\Omega}_0^* + A_1\bar{\Omega}_1^* + B\bar{\Omega}^{**}$, is already an excellent approximation.

LEFM Boundary Layer

Scaling and Governing Equations. We look for a scaling of the solution in the LEFM boundary layer in the form: $1-\xi = \mathcal{K}^{\beta_\xi}\hat{\xi}$, $\bar{\Omega}=\mathcal{K}^{\beta_\Omega}\hat{\Omega}$, $\Pi=\mathcal{K}^{\beta_\Pi}\hat{\Pi}$ where $\hat{\xi}$ is a scaled distance from the tip. The scaling exponents β_ξ, β_Ω, and β_Π are obtained by substituting the above expressions into the governing Eqs. (10) and (11) and requiring that the solution $\{\hat{\Omega}(\hat{\xi}),\hat{\Pi}(\hat{\xi})\}$ of the resulting boundary layer equations is non-trivial in the limit $\mathcal{K}\to 0$, and possesses the LEFM square root behavior at the fracture tip ($\hat{\xi}\to 0$). This procedure yields the unique set $\beta_\xi=6$, $\beta_\Omega=4$, $\beta_\Pi=-2$.

Consequently, the thickness of the tip boundary layer is of order $\mathcal{K}^6\ell$, and the $\mathcal{K}$-scaling of the tip coordinate $1-\xi$, opening $\bar{\Omega}$, and pressure Π is as follows

$$1-\xi=\hat{\mathcal{K}}^6\hat{\xi},\quad \bar{\Omega}(\xi)=\left(\frac{2}{3}\right)^{1/3}\hat{\mathcal{K}}^4\hat{\Omega}(\hat{\xi}),\quad \Pi(\xi)=\left(\frac{2}{3}\right)^{1/3}\hat{\mathcal{K}}^{-2}\hat{\Pi}(\hat{\xi}), \tag{27}$$

where $\hat{\mathcal{K}}$ bears the meaning of toughness parameter given by dimensionless toughness $\mathcal{K}$ multiplied by an $O(1)$ factor,

$$\hat{\mathcal{K}}=\left(\frac{2}{3}\right)^{1/3}\gamma^{-1/2}\mathcal{K}, \tag{28}$$

and the numerical factor $(2/3)^{1/3}$ have been introduced to the boundary layer scaling above in order to simplify the numerical coefficients in the equations resulting from Eqs. (10), (11), and (27)

$$\hat{\Omega}\left(1-\hat{\Omega}^2\frac{d\hat{\Pi}}{d\hat{\xi}}\right)+\hat{\mathcal{K}}^6\left(\frac{3}{2}\int_0^{\hat{\xi}}\hat{\Omega}\,d\hat{\xi}-\hat{\xi}\hat{\Omega}\right)=0,\quad 0\leqslant\hat{\xi}\leqslant\hat{\mathcal{K}}^{-6}, \tag{29}$$

$$\hat{\Pi}(\hat{\xi})=\frac{1}{4\pi}\int_0^{\hat{\mathcal{K}}^{-6}}\frac{d\hat{\Omega}(s)}{ds}\,\frac{1-\hat{\mathcal{K}}^6 s}{1-\frac{1}{2}\hat{\mathcal{K}}^6(\hat{\xi}+s)}\,\frac{ds}{\hat{\xi}-s},\quad \hat{\xi}\to 0:\hat{\Omega}=\hat{\xi}^{1/2}. \tag{30}$$

In the limit $\hat{\mathcal{K}}\to 0$, Eqs. (29) and (30) reduce to the following system of integro-differential equations in $\hat{\xi}\in[0,\infty)$,

$$\hat{\Omega}_0^2\frac{d\hat{\Pi}_0}{d\hat{\xi}}=1,\quad \hat{\Pi}_0(\hat{\xi})=\hat{\mathcal{L}}\{\hat{\Omega}_0\}(\hat{\xi}),\quad \hat{\xi}\to 0:\hat{\Omega}_0=\hat{\xi}^{1/2}, \tag{31}$$

where $\hat{\mathcal{L}}$ is the elasticity operator for a semi-infinite crack [24]

$$\hat{\mathcal{L}}\{\hat{\Omega}\}(\hat{\xi})=\frac{1}{4\pi}\int_0^{\infty}\frac{d\hat{\Omega}(s)}{ds}\,\frac{ds}{\hat{\xi}-s}. \tag{32}$$

Equations (31) and (32) govern the $O(1)$ boundary layer solution $\{\hat{\Omega}_0(\hat{\xi}),\hat{\Pi}_0(\hat{\xi})\}$.

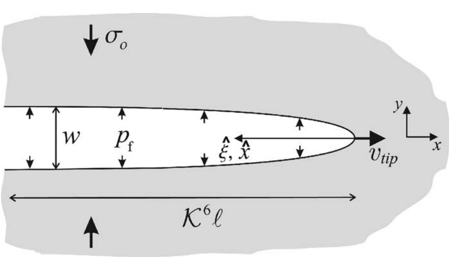

Fig. 3 Semi-infinite fluid driven fracture

Semi-Infinite Fracture. Intuitively, if the tip boundary layer were to exist in the small toughness case, its $O(1)$ solution has to be given by the solution of a semi-infinite crack propagating at the velocity prescribed by the outer solution. Indeed, using relation (27) between inner and outer scalings and definitions (7) and (8) of the outer scaling, we can rewrite Eqs. (31) in terms of the physical field variables, namely the net pressure p and the opening w

$$\frac{w^2(\hat{x})}{\mu'}\frac{dp}{d\hat{x}}=v_{\mathrm{tip}},\quad p(\hat{x})=E'\hat{\mathcal{L}}\{w\}(\hat{x}),\quad \hat{x}\to 0:w=\frac{K'}{E'}\hat{x}^{1/2}, \tag{33}$$

where $\hat{x}=x_{\mathrm{tip}}-x$ is a coordinate moving with the crack tip (Fig. 3), and the propagation velocity v_{tip} is given by the instantaneous propagation velocity of the finite fracture in the zero-toughness solution, $v_{\mathrm{tip}}=\gamma_0\dot{L}(t)$. Equations (33) are in fact identical to the governing equations of the problem of a semi-infinite fluid-driven fracture steadily propagating at constant velocity and characterized by zero lag [9]. In other words, the boundary layer solution is given at any time by the solution of the semi-infinite crack problem with a constant tip velocity corresponding to the current propagation speed of the finite fracture.

The tip boundary layer scaling defined by Eqs. (27) (i.e., normalized distance from the tip $\hat{\xi}$, opening $\hat{\Omega}$, and net-pressure $\hat{\Pi}$) in relation to the scaling of the finite fracture, Eqs. (7), can be equivalently redefined in terms of the "tip" parameters only (i.e., the tip velocity and the material parameters) as follows,

$$\hat{x}=\hat{\ell}\hat{\xi},\quad w(\hat{x})=\hat{\varepsilon}\hat{\ell}\hat{\Omega}(\hat{\xi}),\quad p(\hat{x})=\hat{\varepsilon}E'\hat{\Pi}(\hat{\xi}) \tag{34}$$

where the tip lengthscale $\hat{\ell}$ and the small tip parameter $\hat{\varepsilon}$ are given by

$$\hat{\ell}=\left(\frac{K'}{E'^{2/3}\mu'^{1/3}v_{\mathrm{tip}}^{1/3}}\right)^6,\quad \hat{\varepsilon}=\frac{K'^2}{E'\mu' v_{\mathrm{tip}}}. \tag{35}$$

We can verify that the tip lengthscale $\hat{\ell}$ does, indeed, define the tip boundary layer thickness which relates to the global fracture lengthscale ℓ via the toughness parameter $\hat{\mathcal{K}}$, Eq. (28), as in

$$\hat{\mathcal{K}}=(\hat{\ell}/\ell)^{1/6}. \tag{36}$$

We further observe that the boundary layer solution of Eqs. (31) is actually a particular case of a more general solution, which allows for a lag between the fluid and fracture fronts [9]. This particular solution emerges under the condition of vanishing lag, $(K'/E')(\sigma_o/(\mu' v_{\mathrm{tip}}))^{1/2}\gtrsim 4$. The latter provides the sufficient condition when the zero-lag assumption adopted in this study holds.

Asymptotic Behavior. The near tip asymptotic expansion of $\{\hat{\Omega}_0,\hat{\Pi}_0\}$ can be obtained from an asymptotic analysis of the boundary layer Eqs. (31) as follows. The leading term (square root) in the $\hat{\Omega}_0$ asymptotic expansion at the tip is given by Eq. $(31)_c$; the corresponding leading term (logarithmic) in the $\hat{\Pi}_0$ asymptotic expansion then follows from the lubrication Eq. $(31)_a$.

The second term (linear) in the $\hat{\Omega}_0$ expansion is obtained from the leading term in the $\hat{\Pi}_0$ expansion and the use of the elasticity Eq. $(31)_b$. The second term in the $\hat{\Pi}_0$ expansion then follows from the second term in the $\hat{\Omega}_0$ expansion via the lubrication equation. This alternating use of the lubrication and the elasticity equations enables us to establish the following asymptotic expansion of the boundary layer solution near the fracture tip

$$\hat{\xi} \to 0: \hat{\Omega}_0 = \hat{\xi}^{1/2} + 4\pi\hat{\xi} + \frac{128}{3}\hat{\xi}^{3/2} \ln \hat{\xi} + O(\hat{\xi}^{3/2}), \tag{37}$$

$$\hat{\xi} \to 0: \hat{\Pi}_0 = \ln \hat{\xi} + \delta_{k0} - 16\pi\hat{\xi}^{1/2} - \frac{256}{3}\hat{\xi} \ln \hat{\xi} + O(\hat{\xi}). \tag{38}$$

The constant δ_{k0} in the $\hat{\Pi}_0$ asymptotic expansion and the coefficients for the terms of $O(\hat{\xi}^{3/2})$ in Eq. (37) and of $O(\hat{\xi})$ in Eq. (38), cannot be obtained from asymptotic considerations only and are part of the complete boundary layer solution.

The far-field asymptote ($\hat{\xi} \gg 1$) of the boundary layer solution can be proven [9], to be given by the HF eigensolution discussed earlier: $\hat{\Omega}_0 \sim \beta\hat{\xi}^{2/3}$, $\hat{\Pi}_0 \sim \delta\hat{\xi}^{-1/3}$ for $\hat{\xi} \to \infty$, with the constants β and δ defined in Eqs. (16). Since the above asymptote is actually the exact solution of the elasticity Eq. $(31)_b$, the remainder $\{\hat{\Omega}_0 - \beta\hat{\xi}^{2/3}, \hat{\Pi}_0 - \delta\hat{\xi}^{-1/3}\}$ has also to be the exact solution of the elasticity equation, in view of its linearity. Assuming that $\hat{\Omega}_0 - \beta\hat{\xi}^{2/3}$ behaves asymptotically as $\beta_1\hat{\xi}^{\hat{h}}$ for $\hat{\xi} \gg 1$ with $\hat{h} \in (0, 2/3)$, the corresponding asymptotic form of $\hat{\Pi}_0 - \delta\hat{\xi}^{-1/3}$ follows from the general properties of the Cauchy integral in the elasticity equation. Hence, the far-field asymptotic expansion of the boundary layer solution can be written as

$$\hat{\xi} \to \infty: \hat{\Omega}_0 = \beta\hat{\xi}^{2/3} + \beta_1\hat{\xi}^{\hat{h}} + o(\hat{\xi}^{\hat{h}}), \tag{39}$$

$$\hat{\xi} \to \infty: \hat{\Pi}_0 = \delta\hat{\xi}^{-1/3} + \beta_1\frac{\hat{h}\cot(\pi\hat{h})}{4}\hat{\xi}^{\hat{h}-1} + o(\hat{\xi}^{\hat{h}-1}). \tag{40}$$

Substituting Eqs. (39) and (40) into the lubrication Eq. $(31)_a$, and equating the coefficient in front of the leading term $\hat{\xi}^{\hat{h}-2/3}$ (when $\hat{\xi} \gg 1$) to zero yields a transcendental equation for $\hat{h}$, identical to the one for the exponent h in the near tip asymptote (18) of the term $\mathcal{F}_1(\xi)$ of the outer solution (13). Hence, $\hat{h} = h \simeq 0.138673$, according to Eq. (20). However, the coefficient β_1 like the coefficient δ_{k0} of the near tip expansion can only be computed when constructing the complete boundary layer solution.

According to relationship (27) between the outer and inner scalings, the leading term in the far field ($\hat{\xi} \gg 1$) asymptotic expansions (39) and (40) of the inner solution is identical to the near tip ($1 - \xi \ll 1$) asymptote (16) of the zero-toughness (outer) solution. This correspondence of these inner and outer solution asymptotes is actually anticipated as the inner solution is expected to provide the tip boundary layer solution. In other words, the inner solution has to be a "smooth continuation" of the outer solution into the near tip region.

Solution. The solution of Eqs. (31) has been originally obtained by Garagash and Detournay [9]. Their solution relies on constructing numerically the transition between the leading terms in the asymptotic expansions (37)–(40). Appendix C describes an improved numerical scheme that takes into account the complete asymptotic expansions, rather than their leading terms only. Incorporation of additional asymptotic terms reduces, by several orders of magnitude of $\hat{\xi}$, the extent of the intermediate region where the solution has to be computed numerically.

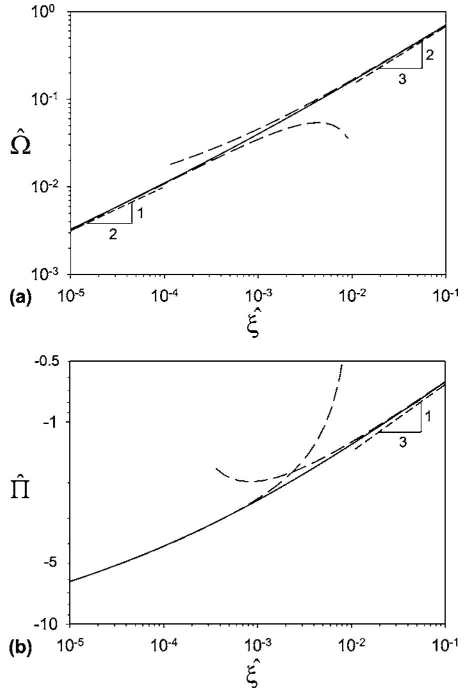

Fig. 4 LEFM tip boundary layer solution: Variation of dimensionless (a) opening $\hat{\Omega}$ and (b) net-pressure $\hat{\Pi}$ with the distance from the tip $\hat{\xi}$. Asymptotic expansions of the solution in the near-field (near-tip) and the far-field are shown by long dash lines.

The numerical solution yields the numerical values of the two a priori unknown coefficients in the asymptotic expansions (37)–(40)

$$\delta_{k0} \simeq 5.504, \quad \beta_1 \simeq 3.719 \cdot 10^{-2}. \tag{41}$$

The opening $\hat{\Omega}_0$ and pressure $\hat{\Pi}_0$ in the boundary layer solution are shown in Fig. 4. The boundaries of the near tip region, $\hat{\xi}_0$, and of the far-field region, $\hat{\xi}_\infty$, where the solution for the opening is approximated by the leading asymptotic terms in Eqs. (37) and (39) within 1% accuracy (i.e., $4\pi\hat{\xi}_0/\hat{\xi}_0^{1/2} = 1\%$, $\beta_1\hat{\xi}_\infty^{\hat{h}}/\beta\hat{\xi}_\infty^{2/3} = 1\%$) are given by

$$\hat{\xi}_0 \simeq 6.33 \cdot 10^{-7}, \quad \hat{\xi}_\infty \simeq 1.34. \tag{42}$$

These boundaries are outside of the $\hat{\xi}$-range of Fig. 4, where the leading terms in the near tip and far field expansions for the opening are shown by the short dash lines with the appropriate slope tags. However, the boundaries corresponding to the regions where the solution for the opening is given by the complete asymptotic expansions near the tip, Eq. (37), and away from the tip, Eq. (39), were computed from the numerical solution as

$$\hat{\xi}_0^* \simeq 5.69 \cdot 10^{-5}, \quad \hat{\xi}_\infty^* \simeq 3.39 \cdot 10^{-2}. \tag{43}$$

We are now able to estimate the thickness of the LEFM boundary layer, which is defined as the extent of the region where the boundary layer solution is sufficiently different from the leading term in the far field asymptote. According to Eq. $(42)_b$, the extent of the LEFM layer is of order unity in the boundary layer scaling and is consequently of order $\mathcal{K}^6$ in the outer scaling (27).

Matching of Outer and Inner Solutions. The asymptotic behavior of the small toughness expansion (13) of the outer solution follows from the asymptotes (16) and (18) of the $O(1)$ and $O(\mathcal{E}(\mathcal{K}))$ terms of the expansion (13), respectively,

$$\text{outer solution}, 1-\xi \ll 1: \begin{cases} \bar{\Omega}(\xi) \simeq \left(\dfrac{2}{3}\right)^{1/3} \beta(1-\xi)^{2/3} + \mathcal{E}(\mathcal{K})(1-\xi)^h, \\ \Pi(\xi) \simeq \left(\dfrac{2}{3}\right)^{1/3} \delta(1-\xi)^{-1/3} + \mathcal{E}(\mathcal{K}) \dfrac{h\cot(\pi h)}{4}(1-\xi)^{h-1}. \end{cases} \tag{44}$$

As discussed previously, the above tip behavior of the outer solution fails to comply with the LEFM boundary condition $(11)_b$ for $\mathcal{K} > 0$. On the other hand, the LEFM boundary layer solution satisfies the LEFM condition at the tip and possesses the following asymptotic behavior away from the fracture tip, obtained by expressing Eqs. (39) and (40) in the outer scaling (27)

$$\text{inner solution}, \hat{\xi} = \hat{\mathcal{K}}^{-6}(1-\xi) \gg 1:$$

$$\begin{cases} \bar{\Omega}(\xi) \simeq \left(\dfrac{2}{3}\right)^{1/3} \hat{\mathcal{K}}^4 [\beta \hat{\mathcal{K}}^{-4}(1-\xi)^{2/3} + \beta_1 \hat{\mathcal{K}}^{-6h}(1-\xi)^h], \\ \Pi(\xi) \simeq \left(\dfrac{2}{3}\right)^{1/3} \hat{\mathcal{K}}^{-2} \left[\delta \hat{\mathcal{K}}^2 (1-\xi)^{-1/3} + \beta_1 \dfrac{h\cot(\pi h)}{4} \hat{\mathcal{K}}^{-6h+6}(1-\xi)^{h-1} \right]. \end{cases} \tag{45}$$

Matching to $O(1)$. The leading terms in the asymptotic expansions of the outer solution near the fracture tip, Eqs. (44), and of the inner solution away from the fracture tip, Eqs. (45), are thus identical. This term, which is given by the HF eigensolution, actually corresponds to an intermediate asymptote. Under the *matching condition*

$$\mathcal{K}^6 \ll 1 \tag{46}$$

there exists an *overlap domain* $\xi^{\text{out}} \leqslant \xi \leqslant \xi^{\text{in}}$ with $\hat{\mathcal{K}}^6 \ll 1 - \xi^{\text{in}} \leqslant 1 - \xi^{\text{out}} \ll 1$, over which the outer and inner solutions share an intermediate asymptote (Fig. 5).

Thus, the matching condition (46) ensures the existence of the viscosity-dominated regime, when the $O(1)$ solution on the lengthscale of the fracture can be approximated by the zero-toughness solution, whereas the effect of material toughness is localized to the tip boundary layer.

Matching to $O(\mathcal{E}(\mathcal{K}))$. The range of applicability of the zero-toughness solution and the $\mathcal{K}$-dependent error with which the $\mathcal{K}=0$ solution approximates the solution when $\mathcal{K}$ is small can only be deduced from an analysis of the next term of order $O(\mathcal{E}(\mathcal{K}))$ in the solution.

Matching of the outer and the inner solutions to order $O(\mathcal{E}(\mathcal{K}))$ requires the equivalence of the next-order terms in the asymptotic expansions (44) and (45). The latter condition provides an expression for the unknown small parameter $\mathcal{E}(\mathcal{K})$ in the outer expansion (13) in the form

$$\mathcal{E}(\mathcal{K}) = B_1 \mathcal{K}^b = \beta_1 \hat{\mathcal{K}}^b, \tag{47}$$

where b and B_1 can be computed from the constants $\gamma_0 \simeq 0.61524$, $h \simeq 0.138673$, and $\beta_1 \simeq 0.03719$ according to

$$b = 4 - 6h \simeq 3.16796, \tag{48}$$

$$B_1 = (2/3)^{2h-1} \gamma_0^{3h-2} \beta_1 \simeq 0.1076. \tag{49}$$

The expression (47) for $\mathcal{E}(\mathcal{K})$ completely defines the outer next order, $O(\mathcal{E}(\mathcal{K}))$, solution (13).

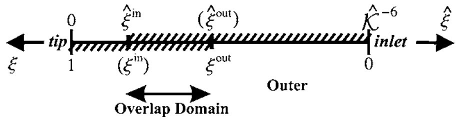

Fig. 5 Matching of the inner and outer solutions; structure of the composite solution

Composite Solution. A composite solution, [27], valid uniformly along the fracture to $O(\mathcal{E}(\mathcal{K}))$, is obtained by summation of the $O(\mathcal{E}(\mathcal{K}))$ outer solution, Eq. (13), and the $O(1)$ boundary layer solution (written in the outer scaling) and subtracting the common terms given by intermediate asymptotic expansion, Eqs. (44), or, equivalently, Eqs. (45),

$$\bar{\Omega}(\xi;\mathcal{K}) = \bar{\Omega}_0(\xi) + \frac{3}{2\gamma_0^2}\mathcal{K}^4 \hat{\Omega}_0\left(\frac{4\gamma_0^3}{9}\frac{1-\xi}{\mathcal{K}^6}\right) - \left(\frac{2}{3}\right)^{1/3} \beta(1-\xi)^{2/3} + B_1 \mathcal{K}^b (\bar{\Omega}_1(\xi) - (1-\xi)^h), \tag{50}$$

$$\Pi(\xi;\mathcal{K}) = \Pi_0(\xi) + \frac{2\gamma_0}{3}\frac{1}{\mathcal{K}^2}\hat{\Pi}_0\left(\frac{4\gamma_0^3}{9}\frac{1-\xi}{\mathcal{K}^6}\right) - \left(\frac{2}{3}\right)^{1/3} \delta(1-\xi)^{-1/3} + B_1 \mathcal{K}^b \left(\Pi_1(\xi) - \frac{h\cot(\pi h)}{4}(1-\xi)^{h-1}\right). \tag{51}$$

(Note that the first line in the expressions for the opening (50) and for the net pressure (51) corresponds to the $O(1)$ composite solution.) The solution for the dimensionless fracture length is given by

$$\gamma(\mathcal{K}) = \gamma_0 + B_1 \gamma_1 \mathcal{K}^b, \tag{52}$$

with $\gamma_0 \simeq 0.6152$, $B_1 \gamma_1 \simeq -1.887 \cdot 10^{-2}$, see Eq. (49) and Table 1. This solution corresponds to a fracture length decreasing with toughness as $\mathcal{K}^b$. The solution for $\Omega(\xi;\mathcal{K})$ is simply obtained from Eqs. (50) and (52) as the product $\gamma(\mathcal{K})\bar{\Omega}(\xi;\mathcal{K})$.

Discussion

We have established that under condition $\mathcal{K}^6 \ll 1$, which ensures existence of the LEFM tip boundary layer, the solution away from the tip (layer) can be approximated by the *outer* solution for fracture opening $w(x,t)$, net-pressure $p(x,t) = p_f - \sigma_o$, and fracture half-length $\ell(t)$, whose dependence on time and material parameters is given by scaling and that of the toughness parameter $\mathcal{K} = K'/E'(E'/\mu' Q_o)^{1/4}$,

$$w(x,t) = \frac{\mu'^{1/6} Q_o^{1/2} t^{1/3}}{E'^{1/6}} [\gamma_0 + \mathcal{E}(\mathcal{K})\gamma_1][\bar{\Omega}_0(\xi) + \mathcal{E}(\mathcal{K})\bar{\Omega}_1(\xi)],$$

$$p(x,t) = \frac{\mu'^{1/3} E'^{2/3}}{t^{1/3}} [\Pi_0(\xi) + \mathcal{E}(\mathcal{K})\Pi_1(\xi)], \tag{53}$$

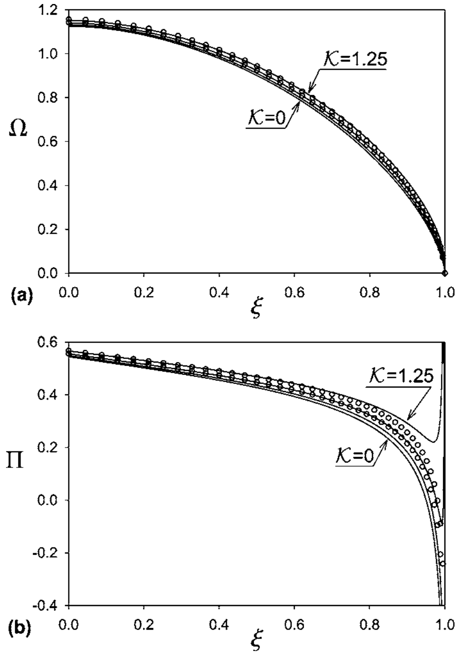

Fig. 6 Small toughness *outer* solution for (a) opening Ω and (b) net-pressure Π for various values of $\mathcal{K}$={0,0.75,1,1.25}. The finite-toughness solution for $\mathcal{K}$=1 and $\mathcal{K}$=1.25 is shown by open circles (after Adachi [20]). The ascending parts of the pressure curves correspond to the continuation of the outer solution into the near tip region where the outer solution is no longer valid and the solution has to be given by the LEFM boundary layer solution.

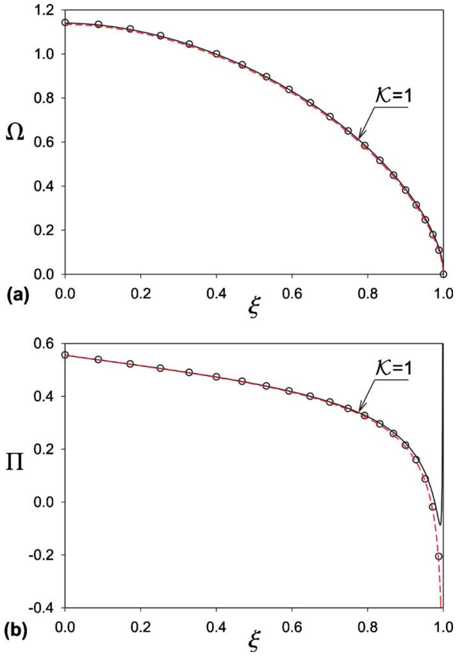

Fig. 7 Comparison between the small toughness *outer* solution and uniformly valid *composite* solution for (a) opening Ω and (b) net-pressure Π for $\mathcal{K}$=1. The composite solution is shown by dashed line, the rest of the curves as in Fig. 6.

$$\ell(t) = \frac{Q_o^{1/2}E'^{1/6}t^{2/3}}{\mu'^{1/6}}[\gamma_0 + \mathcal{E}(\mathcal{K})\gamma_1],$$

where $\gamma_0 \simeq 0.6152, \gamma_1 \simeq -0.01887, \mathcal{E}(\mathcal{K}) \simeq 0.1076\mathcal{K}^{3.16796}$. A practically useful (yet very accurate) implementation of the small-toughness solution (53) results from the approximation of the opening $\bar{\Omega}_{0,1}$ and pressure $\Pi_{0,1}$ terms using the series, e.g., (21), truncated to contain only three terms: the leading term (correct tip asymptote), the first regular term, and the particular solution (correct inlet behavior). The explicit formulae are given in Appendix D.

From a practical point of view, the fracture propagates in the viscosity-dominated regime, i.e., its solution on the outer length scale is given by the zero-toughness solution $\{\Omega_0(\xi), \Pi_0(\xi), \gamma_0\}$, if the next order term (measuring the departure of the solution from the zero-toughness limit) is small

$$\mathcal{E}(\mathcal{K}) = B_1\mathcal{K}^b \ll 1. \tag{54}$$

In this case the effects of toughness are localized to a boundary layer near the fracture front of thickness $\mathcal{K}^6\ell$, where ℓ is the fracture half-length. (Note that the condition of existence of a LEFM tip boundary layer in the overall fracture solution, $\mathcal{K}^6 \ll 1$, is automatically met if Eq. (54) is satisfied, since $b<6$). If $\mathcal{E}(\mathcal{K})$ is not negligibly small but the matching condition $\mathcal{K}^6 \ll 1$ still holds, then the $O(\mathcal{E}(\mathcal{K}))$ small toughness outer solution (13) [or in its dimensional form (53)] with Eq. (47) has to be used. The latter solution for the normalized opening $\Omega = \gamma\bar{\Omega}$ and pressure Π is shown in Fig. 6 for various values of toughness $\mathcal{K}$ ={0,0.75,1,1.25}. The open circles indicate the numerical finite toughness solution [6,20], for $\mathcal{K}$={1,1.25}. We note from the comparison with the finite toughness solution that the small-toughness outer solution remains valid (away from the fracture tip) for values of toughness $\mathcal{K}$ exceeding 1 (when the outer solution expansion (13) is expected to diverge).

Figure 6(*b*) (the ascending parts of the outer solution pressure plots for $\mathcal{K} \geqslant 1$) clearly shows the breakdown of the outer solution approximation when extended to the fracture tip dominated by the LEFM boundary layer. The composite solution, Eqs. (50) and (51), plotted on Fig. 7 for $\mathcal{K}=1$ by dashed lines, provides a uniform approximation of the opening and net-pressure along the whole fracture extent (including the tip), which matches perfectly with the finite toughness solution (open circles). (The relatively "high" values of toughness $\mathcal{K}$ have purposefully been chosen for this Figure, as the solution for $\mathcal{K}$ less than 0.5 is practically indistinguishable from the zero toughness-solution.)

For moderate values of the dimensionless toughness, $\mathcal{E}(\mathcal{K}) \sim 1$, the solution departs from the zero-toughness solution and its dependence on $\mathcal{K}$ cannot be neglected. The semianalytical method originally proposed by Spence and Sharp [6] and later refined by Adachi [20] is appropriate to find the solution in this intermediate regime, where the effects of fluid viscosity and rock toughness are of the same order. However, as $\mathcal{K}$ increases, the fracturing fluid viscosity becomes eventually irrelevant, $\mathcal{M}(\mathcal{K}) \ll 1$, where $\mathcal{M}(\mathcal{K}) = \mathcal{K}^{-4}$ is a dimensionless viscosity parameter with $\mathcal{M}(\infty) = 0$, [21,22], and the limiting solution corresponding to the inviscid fluid limit has to hold. Then the fracture is said to propagate in the toughness-dominated regime.

A threshold value $\mathcal{K}_o$ for the viscosity-dominated regime ($\mathcal{K} < \mathcal{K}_o$) can be determined by imposing an arbitrarily small relative difference between the $O(1)$ (zero-toughness) and $O(\mathcal{E}(\mathcal{K}))$ (small toughness) outer solutions for the crack opening (52). For example, a 1% relative difference gives $\mathcal{K}_o = (0.01|\gamma_0/B_1\gamma_1|)^{1/b} \simeq 0.70$. In terms of dimensional problem parameters, the corresponding condition when toughness is irrelevant for fracture propagation can simply be stated as

$$\text{viscosity-dominated regime: } \frac{\mathcal{K}_{\text{Ic}}}{E'^{3/4}\mu^{1/4}Q_o^{1/4}} \lesssim 0.41. \tag{55}$$

Similarly, the threshold $\mathcal{K}_\infty \simeq 4.13$ for the toughness-dominated regime ($\mathcal{K} > \mathcal{K}_\infty$) can be established requiring the viscosity correction $\mathcal{M}(\mathcal{K}) = \mathcal{K}^{-4}$ to the zero-viscosity solution be bounded by

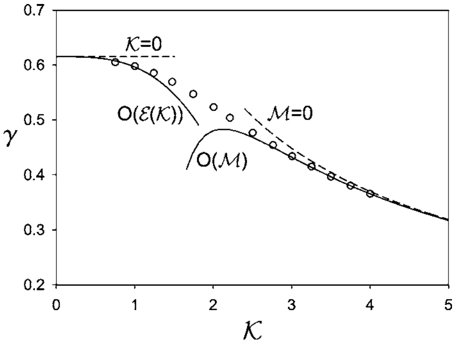

Fig. 8 Variation of dimensionless fracture half-length γ with toughness $\mathcal{K}$. Zero-toughness, [23,16], and zero-viscosity, [21,22], solutions are shown by dashed lines. Small toughness and large toughness asymptotic solutions are shown by solid lines. The finite toughness solution (after Adachi [20]) is shown by open circles.

1% [22]. In terms of the physical parameters the latter condition when viscosity is irrelevant for fracture propagation can be stated as

$$\text{toughness-dominated regime: } \frac{\mathcal{K}_{\text{Ic}}}{E'^{3/4}\mu^{1/4}Q_o^{1/4}} \gtrsim 2.41. \quad (56)$$

The thresholds for viscosity $\mathcal{K}_o \simeq 0.70$ and toughness $\mathcal{K}_\infty \simeq 4.13$ dominated regimes provide the parametric range $\mathcal{K} \in (\mathcal{K}_o, \mathcal{K}_\infty)$ where both the toughness and the viscosity influence the propagation of a hydraulic fracture. Figure 8 shows the variation of dimensionless fracture length in viscosity scaling with dimensionless toughness $\mathcal{K}$, in (i) the small-toughness asymptotic solution, $\gamma = \gamma_0 + \mathcal{E}(\mathcal{K})\gamma_1$ with $\gamma_0 \simeq 0.6152$ and $\gamma_1 \simeq -0.1754$, Eq. (52), and (ii) large-toughness asymptotic solution, $\gamma = \mathcal{K}^{-2/3}(\gamma_0 + \mathcal{M}(\mathcal{K})\gamma_1)$ with $\gamma_0 \simeq 0.9324$ and $\gamma_1 \simeq -2.7220$ [21,22]. The finite toughness solution [6,20] is also shown in this plot by open circles. The range of toughness in which the solution departs from the small-toughness and large-toughness asymptotic expansions is thus relatively narrow, $1 \lesssim \mathcal{K} \lesssim 2.5$. Figure 8 also illustrates the profound influence of the propagation regime on the solution; for example, it can be observed from Fig. 8 that the fracture length for $\mathcal{K} \sim 5$ is about half the length of a fracture propagating in the viscosity dominated regime for the same volume of fluid (injected at constant rate).

Conclusions

In this paper, we have obtained the similarity solution for a fluid-driven fracture of plane-strain geometry propagating in the viscosity-dominated regime and its next-order correction in the dimensionless toughness $\mathcal{K} \ll 1$. The structure of the small toughness solution consists of the outer solution away from the fracture tip, given to the $O(1)$ by the zero-toughness solution, [16,23], and of the LEFM boundary layer solution near the fracture tip, given to the $O(1)$ by the solution of the semi-infinite fluid-driven fracture in a solid with nonzero toughness, [9]. The existence of the small toughness solution is guaranteed by the matching condition, $\mathcal{K}^6 \ll 1$, under which the outer and the boundary layer solutions match on an intermediate lengthscale, where they posses the same intermediate asymptote given to the $O(1)$ by the HF eigensolution [8]. The condition under which the fracture propagates in the viscosity-dominated regime (i.e., the outer solution is given by the zero-toughness solution) is established as the smallness condition of the next-order term in the outer small toughness solution, $\mathcal{E}(\mathcal{K}) = B_1\mathcal{K}^b \ll 1$ with $b \simeq 3.168$ and $B_1 \simeq 0.1076$. If the latter condition is not satisfied but the matching condition is met, the small toughness solution involving the next-order toughness term has to be used to capture the fracture propagation.

Even though, the small toughness asymptotic analysis has been developed in this paper for the plane-strain hydraulic fractures with a constant volume expansion rate (constant injection rate Q_o) under various assumption (e.g., zero fluid leak-off, zero fluid lag, etc.). The main result regarding the dependence of the global hydraulic fracture solution on the material toughness is *universal* (i.e., independent of fracture geometry, injection rate, spatial variation in solid parameters, etc.) [28] when expressed in terms of the tip toughness parameter $\hat{\mathcal{K}}$, see Eqs. (36) and (47),

$$\left|\frac{(\text{small-toughness solution}) - (\text{zero-toughness solution})}{(\text{zero-toughness solution})}\right| \sim \mathcal{E} = \beta_1\hat{\mathcal{K}}^b \quad (b \simeq 3.168) \qquad (57)$$

This universality is a direct consequence of the fact that the dependence of the global fracture solution on small toughness is solely determined by the LEFM boundary layer solution (from matching of the boundary layer solution to the outer solution on the intermediate lengthscale) and that the latter, when expressed in terms of the local fracture tip velocity and material parameters, is invariant of a particular fracture geometry, injection rate, etc. The tip toughness parameter $\hat{\mathcal{K}}$ in Eq. (57) is expressed in terms of the local fracture tip velocity v_{tip}, material parameters and the lengthscale ℓ of the global fracture solution (e.g., half-length for a plane-strain fracture, fracture radius for a penny-shaped fracture) as, Eqs. (36) and (35),

$$\hat{\mathcal{K}} = \frac{K'}{E'^{2/3}\mu'^{1/3}v_{\text{tip}}^{1/3}\ell^{1/6}} \qquad (58)$$

In the case of the plane-strain fracture, using $v_{\text{tip}} = d\ell/dt$ and the zero-toughness solution for the length $\ell = \gamma_0(Q_o^{1/2}E'^{1/6}/\mu'^{1/6})t^{2/3}$ we recover from Eq. (58) the correspondence to the plane-strain fracture toughness parameter $\mathcal{K}$ up to a $O(1)$ numerical coefficient, $\hat{\mathcal{K}} = \gamma_0^{-1/2}\left(\frac{2}{3}\right)^{-1/3}\mathcal{K}$. Similarly, one can show the correspondence between $\hat{\mathcal{K}}$ and the penny-shape fracture toughness parameter arising from the analysis of Savitski and Detournay [29].

Acknowledgments

Acknowledgment is made to the Donors of The Petroleum Research Fund, administered by the American Chemical Society, for partial support of this research under Grant Nos. ACS-PRF 36729-G2 and ACS-PRF 37588-AC2.

Selected Nomenclature

Problem parameters		
E'		Plane-strain elastic modulus of the solid
$\mu' = 12\mu$		Fluid effective viscosity
$K' = 4\sqrt{2/\pi}K_{\text{Ic}}$		Solid effective toughness
σ_o		Remote confining stress
Q_o		Fluid injection rate
Field variables (dimensional and normalized)		
t		Time
x	ξ	Spatial coordinate with the origin at the crack inlet
w	Ω	Crack opening
p	Π	Net pressure in the crack
ℓ	γ	Crack half-length
Scaling parameters and Normalized solution		
L		Fracture lengthscale
ε		Parameter scaling the net-pressure as a fraction of the modulus E'
$\mathcal{K}$		Dimensionless toughness parameter

$\mathcal{F}(\xi,\mathcal{K})$		Normalized solution $\{\bar{\Omega}(\xi,\mathcal{K}),\Pi(\xi,\mathcal{K}),\gamma(\mathcal{K})\}$
$\mathcal{E}(\mathcal{K})$		Dimensionless small toughness parameter in the solution asymptotic expansion: $\mathcal{F}(\xi,\mathcal{K})=\mathcal{F}_0(\xi)+\mathcal{E}(\mathcal{K})\mathcal{F}_1(\xi)$
$\mathcal{F}_0(\xi)$ and $\mathcal{F}_1(\xi)$		Zero-toughness and next-order small toughness terms

Tip boundary layer solution (dimensional and normalized)

$\hat{x}$	$\hat{\xi}$	Moving spatial coordinate with the origin at the crack tip
$\hat{w}$	$\hat{\Omega}$	Crack opening in the tip boundary layer
$\hat{p}$	$\hat{\Pi}$	Net pressure in the tip boundary layer
v_{tip}		Crack tip velocity
$\hat{\ell}$		Tip lengthscale (boundary layer thickness)
	$\hat{\mathcal{K}}=(\hat{\ell}/\ell)^{1/6}$	Tip dimensionless toughness parameter

Appendix A: Scaling

Let us introduce the scaled coordinate $\xi = x/\ell(t) \in [0,1]$ and the dimensionless opening Ω, net pressure Π, and crack half-length γ as [19],

$$w(x,t) = \varepsilon(t)L(t)\Omega(\xi,\mathcal{K}),$$

$$p(x,t) = \varepsilon(t)E'\Pi(\xi,\mathcal{K}), \tag{A1}$$

$$\ell(t) = L(t)\gamma(\mathcal{K}).$$

In the above scaling, $L(t)$ is the crack length scale, $\varepsilon(t)$ is a small dimensionless parameter with the meaning of a characteristic crack aspect ratio, and $\mathcal{K}(t)$ is a dimensionless toughness defined in terms of the volume of injected fluid $V(t)$ and the material parameters (1)

$$\varepsilon = \frac{V}{L^2}, \quad L = V^{1/2}\left(\frac{E't}{\mu'}\right)^{1/6}, \quad \mathcal{K} = \frac{K'}{E'}\left(\frac{E't}{\mu'V}\right)^{1/4}. \tag{A2}$$

In terms of the alternative scaled opening $\bar{\Omega}=\Omega/\gamma$ and Eqs. (A1) and (A2), the "fluid" Eqs. (3) and (4) and "solid" Eqs. (5) and (6) governing equations over the half of the crack, $\xi \in [0,1]$, reduce to their respective forms

$$\frac{1}{6}\xi\bar{\Omega} + \frac{t\dot{V}}{V}\Psi_V + \frac{t\dot{\mathcal{K}}}{\mathcal{K}}\mathcal{K}\Psi_{\mathcal{K}} = -\bar{\Omega}^3\frac{\partial\Pi}{\partial\xi}, \quad \gamma^{-2} = 2\int_0^1 \bar{\Omega}\,\mathrm{d}\xi, \tag{A3}$$

$$\Pi(\xi,\mathcal{K}) = -\frac{1}{2\pi}\int_0^1 \frac{\partial\bar{\Omega}(\xi,\mathcal{K})}{\partial\xi'}\frac{\xi'\mathrm{d}\xi'}{\xi'^2 - \xi^2},$$

$$\xi \to 1{:}\bar{\Omega} = \mathcal{K}\gamma^{-1/2}(1-\xi)^{1/2}. \tag{A4}$$

The terms Ψ_V and $\Psi_{\mathcal{M}}$ in the lubrication Eq. $(\text{A-3})_a$ are defined, respectively, by

$$\Psi_V = \int_\xi^1 \bar{\Omega}\,\mathrm{d}\xi + \frac{1}{2}\xi\bar{\Omega},$$

$$\Psi_{\mathcal{K}} = \mathcal{K}\int_\xi^1 \left[\frac{\partial\bar{\Omega}}{\partial\mathcal{K}} + \frac{1}{\gamma}\frac{\mathrm{d}\gamma}{\mathrm{d}\mathcal{K}}\left(\bar{\Omega} - \xi\frac{\partial\bar{\Omega}}{\partial\xi}\right)\right]\mathrm{d}\xi. \tag{A5}$$

Consequently, Eqs. (A3)–(A5) define the solution in the "viscosity" scaling (A1) and (A2),

$$\mathcal{F}(\xi,\mathcal{K}) = \{\bar{\Omega}(\xi,\mathcal{K}),\Pi(\xi,\mathcal{K}),\gamma(\mathcal{K})\}, \tag{A6}$$

where the dimensionless toughness $\mathcal{K}$ plays the role of an evolution parameter.

For a *constant injection rate*, $V(t)=Q_o t$, the specific expressions of the scaling parameters (8) and of the lubrication Eq. $(10)_a$ follow directly from Eqs. (A2) and (A3). Note that, according to Eq. (A2), $t\dot{V}/V$ in the lubrication Eq. $(\text{A-3})_a$ can be replaced by $1-4t\dot{\mathcal{K}}/\mathcal{K}$, while $t\dot{\mathcal{K}}/\mathcal{K}$ can be generally defined as function of $\mathcal{K}$ given a particular form of injection law $V=V(t)$ in the definition of $\mathcal{K}$, Eq. $(\text{A-2})_c$. For constant $\mathcal{K}$, the term $t\dot{\mathcal{K}}/\mathcal{K}$ vanishes, and the lubrication Eq. $(\text{A-3})_a$ then assumes the self-similar form, Eq. $(10)_a$.

Appendix B: Base Functions for the Numerical Method

The pressure base functions Π_j^* can be obtained from the corresponding opening base functions via close-form integration of elasticity equation $(17)_c$

$$\Pi_0^* = \frac{\Gamma(1+h)}{2\pi^{1/2}\Gamma\left(\frac{1}{2}+h\right)}\ {}_2F_1\left(\frac{1}{2}-h,1;\frac{1}{2};\xi^2\right) \tag{B7}$$

for the leading term, and

$$\Pi_j^* = \frac{(-1)^j}{B\left(\frac{1}{2}+h,\frac{1}{2}+j\right)}\left[\frac{1}{2}{}_2F_1\left(-\frac{1}{2}-j-h,j;\frac{1}{2};\xi^2\right) - (1 + h)\xi^2{}_2F_1\left(\frac{1}{2}-j-h,j+1;\frac{3}{2};\xi^2\right)\right], \quad j=1,\ldots,n, \tag{B8}$$

for the rest of the terms. (The same polynomials in slightly different notation have been used by Adachi and Detournay [16] for the zero-toughness solution of a fracture driven by a non-Newtonian fluid.) In the formulas above $\Gamma(\cdot)$ and $\mathrm{B}(\cdot,\cdot)$ are Euler's gamma and beta functions, respectively, and ${}_2\mathrm{F}_1(\cdot,\cdot;\cdot;\cdot)$ is Gauss' hypergeometric function [26].

In view of Eq. (B7), the asymptotic behavior of the pressure leading term in Eq. (21) is given by

$$A_0\Pi_0^* = \frac{h\cot(\pi h)}{4}(1-\xi)^{h-1} + \frac{\Gamma(1+h)}{2^{2+h}\pi^{1/2}(1-h)\Gamma\left(\frac{1}{2}+h\right)} + O(1-\xi)^h \quad (1-\xi^2 \ll 1), \tag{B9}$$

which is consistent with the pressure asymptote prescribed by Eq. $(18)_b$ with (20).

The base functions for the pressure gradient and the indefinite integrals of the opening base functions necessary for the representation of the terms in the lubrication Eq. $(17)_a$, are obtained directly from Eqs. (B7), (B8), (22), and (23)

$$\frac{\mathrm{d}\Pi_0^*}{\mathrm{d}\xi} = -\frac{2\Gamma(h+1)}{\pi^{1/2}\Gamma\left(h-\frac{1}{2}\right)}\xi\ {}_2F_1\left(\frac{3}{2}-h,2;\frac{3}{2};\xi^2\right), \tag{B10}$$

$$\frac{\mathrm{d}\Pi_j^*}{\mathrm{d}\xi} = \frac{(-1)^j(j+1)(2j+2h-1)}{B\left(\frac{1}{2}+h,\frac{1}{2}+j\right)}\left[\frac{2(1+h)}{3}\xi^3{}_2F_1\left(\frac{3}{2}-j-h,j + 2;\frac{5}{2};\xi^2\right) + -\left(1+\frac{3}{(j+1)(2j+2h-1)}\right)\xi\ {}_2F_1\left(\frac{1}{2}-j-h,j + 1;\frac{3}{2};\xi^2\right)\right], \quad j=1,\ldots,n, \tag{B11}$$

and the indefinite integrals of the opening base functions are given by

$$\int_{\xi}^{1}\bar{\Omega}_j^{*}\mathrm{d}\xi=\begin{cases}\left[\frac{1}{2}B\left(\frac{1}{2},1+h\right)-\xi\;{}_2F_1\left(\frac{1}{2},-h;\frac{3}{2};\xi^2\right)\right], & j=0,\\ \dfrac{\frac{1}{2}+h}{\frac{5}{2}+h}\left[-\frac{1}{2}\mathrm{B}\left(\frac{1}{2},2+h\right)+\xi\;{}_2F_1\left(\frac{1}{2},-1-h;\frac{3}{2};\xi^2\right)+\left(\frac{3}{2}+h\right)\xi(1-\xi^2)^{2+h}\right], & j=1,\\ \dfrac{\left(\frac{1}{2}+h\right)\left(\frac{3}{2}+h\right)(1-\xi^2)^{2+h}}{2j+h+\frac{1}{2}}\left[\dfrac{C_{2j-1}^{(h+5/2)}(\xi)}{j(2j+2h+3)}-\dfrac{C_{2j-3}^{(h+5/2)}(\xi)}{(j-1)(2j+2h+1)}\right], & j=2,\ldots,n.\end{cases}\tag{B12}$$

Appendix C: Numerical Scheme for the Boundary Layer Solution

This Appendix outlines the numerical scheme, based on the earlier work of Garagash and Detournay [9], used to solve system of Eqs. (31) on the semi-infinite interval $\hat{\xi}\in[0,\infty)$. By assuming that the asymptotic expansions of the solution near the fracture tip, Eqs. (37) and (38), and in the far field, Eqs. (39) and (40), are appropriate representations of the solution in the intervals $\hat{\xi}\in[0,L_0]$ and $\hat{\xi}\in[L_\infty,\infty)$ $(L_\infty > L_o)$, respectively, we compute the intermediate solution in the interval $\hat{\xi}\in[L_0,L_\infty]$ as well as the unknown asymptotic coefficients δ_{k0} and β_1 numerically via the following scheme.

We start by dividing the interval $\hat{\xi}\in[L_0,L_\infty]$ into $n-1$ subintervals $[\hat{\xi}_i,\hat{\xi}_{i+1}]$, $i=1,\ldots,n-1$, where $\hat{\xi}_1=L_0$ and $\hat{\xi}_n=L_\infty$ and by approximating the variation of the pressure $\hat{\Pi}_0$ over each interval as a linear combination of the leading terms in the near tip, Eq. (38), and far-field asymptote, Eq. (40),

$$\hat{\Pi}_0(\hat{\xi})=a_i\ln\hat{\xi}+b_i\delta\hat{\xi}^{-1/3},\quad \hat{\xi}\in[\hat{\xi}_i,\hat{\xi}_{i+1}],\quad i=1,\ldots,n-1.\tag{C13}$$

Outside of the transition interval, the solution for the pressure is approximated by the respective asymptotic expansion

$$\hat{\Pi}_0(\hat{\xi})=\begin{cases}\hat{\Pi}_{00}(\hat{\xi})=\ln\hat{\xi}+\delta_{k0}-16\pi\hat{\xi}^{1/2}-\dfrac{256}{3}\hat{\xi}\ln\hat{\xi}, & \hat{\xi}\in[0,\hat{\xi}_1],\\ \hat{\Pi}_{0\infty}(\hat{\xi})=\delta\hat{\xi}^{-1/3}+\beta_1 4^{-1}h\cot(\pi h)\hat{\xi}^{h-1}, & \hat{\xi}\in[\hat{\xi}_n,\infty).\end{cases}\tag{C14}$$

Inversion of the elasticity Eq. $(31)_b$ in a form that accommodates the tip asymptote $(31)_c$ yields [9],

$$\hat{\Omega}_0(\hat{\xi})=\hat{\xi}^{1/2}+\frac{4}{\pi}\int_0^{\infty}K(\hat{\xi},\hat{\eta})\hat{\Pi}_0(\hat{\eta})\mathrm{d}\hat{\eta},\quad K(\hat{\xi},\hat{\eta})=\ln\left|\frac{\hat{\xi}^{1/2}+\hat{\eta}^{1/2}}{\hat{\xi}^{1/2}-\hat{\eta}^{1/2}}\right|-2\frac{\hat{\xi}^{1/2}}{\hat{\eta}^{1/2}}.\tag{C15}$$

With the pressure in Eq. (C15) approximated by Eqs. (C13) and (C14), we deduce that

$$\hat{\Omega}_0(\hat{\xi})=\hat{\xi}^{1/2}+F_{00}(\hat{\xi})+\sum_{j=1}^{n-1}\left[a_iF_{\ln}(\hat{\xi},\hat{\eta})+b_i\delta F\left(\frac{2}{3},\hat{\xi},\hat{\eta}\right)\right]_{\hat{\eta}=\hat{\xi}_j}^{\hat{\eta}=\hat{\xi}_{j+1}}+F_{0\infty}(\hat{\xi}).\tag{C16}$$

The various functions entering the above expression for $\hat{\Omega}_0(\hat{\xi})$ are defined as follows

$$F_{00}(\hat{\xi})=\frac{4}{\pi}\left(F_{\ln}(\hat{\xi},\hat{\xi}_1)+\delta_{k0}F_1(\hat{\xi},\hat{\xi}_1)-16\pi F_{3/2}(\hat{\xi},\hat{\xi}_1)-\frac{256}{3}F_{2\,\ln}(\hat{\xi},\hat{\xi}_1)\right),$$

$$F_{0\infty}(\hat{\xi})=\frac{4}{\pi}(\delta F(2/3;\hat{\xi},\hat{\xi}_n)+\beta_1 4^{-1}h\cot(\pi h)F(h;\hat{\xi},\hat{\xi}_n)),$$

and

$$F_{\ln}(\hat{\xi},\hat{\eta})=\int_0^{\hat{\eta}}K(\hat{\xi},\hat{\eta})\ln\hat{\eta}\,\mathrm{d}\hat{\eta}=2\hat{\eta}^{1/2}\hat{\xi}^{1/2}(1-\ln\hat{\eta})+(\hat{\xi}-\hat{\eta})(1-\ln\hat{\eta})\ln\left|\frac{\hat{\xi}^{1/2}+\hat{\eta}^{1/2}}{\hat{\xi}^{1/2}-\hat{\eta}^{1/2}}\right|+2\hat{\xi}f_{\ln}\left(\frac{\hat{\eta}}{\hat{\xi}}\right),\tag{C17}$$

$$F_1(\hat{\xi},\hat{\eta})=\int_0^{\hat{\eta}}K(\hat{\xi},\hat{\eta})\mathrm{d}\hat{\eta}=-2\hat{\eta}^{1/2}\hat{\xi}^{1/2}-(\hat{\xi}-\hat{\eta})\ln\left|\frac{\hat{\xi}^{1/2}+\hat{\eta}^{1/2}}{\hat{\xi}^{1/2}-\hat{\eta}^{1/2}}\right|,\tag{C18}$$

$$F_{3/2}(\hat{\xi},\hat{\eta})=\int_0^{\hat{\eta}}K(\hat{\xi},\hat{\eta})\hat{\eta}^{1/2}\mathrm{d}\hat{\eta}=\frac{2}{3}\left(-2\hat{\eta}\hat{\xi}^{1/2}+\hat{\eta}^{3/2}\ln\left|\frac{\hat{\xi}^{1/2}+\hat{\eta}^{1/2}}{\hat{\xi}^{1/2}-\hat{\eta}^{1/2}}\right|+\hat{\xi}^{3/2}\ln\left|1-\frac{\hat{\eta}}{\hat{\xi}}\right|\right),\tag{C19}$$

$$F_{2\,\ln}(\hat{\xi},\hat{\eta})=\int_0^{\hat{\eta}}K(\hat{\xi},\hat{\eta})\hat{\eta}\ln\hat{\eta}\,\mathrm{d}\hat{\eta}=\frac{1}{2}\hat{\eta}^{1/2}\hat{\xi}^{1/2}(\hat{\eta}-5\hat{\xi}+2(\hat{\xi}-\hat{\eta})\ln\hat{\eta})+\frac{1}{2}(\hat{\xi}^2-\hat{\eta}^2)\left(\frac{1}{2}-\ln\hat{\eta}\right)\ln\left|\frac{\hat{\xi}^{1/2}+\hat{\eta}^{1/2}}{\hat{\xi}^{1/2}-\hat{\eta}^{1/2}}\right|+\hat{\xi}^2f_{\ln}\left(\frac{\hat{\eta}}{\hat{\xi}}\right),\tag{C20}$$

$$F(h,\hat{\xi},\hat{\eta})=\int_{\hat{\eta}}^{\infty}K(\hat{\xi},\hat{\eta})\hat{\eta}^{h-1}\mathrm{d}\hat{\eta}=\frac{\hat{\xi}^h}{h}f\left(h,\frac{\hat{\eta}}{\hat{\xi}}\right),\quad 0<h<1,\tag{C21}$$

The functions $f(h,\zeta)$ and $f_{\ln}(\zeta)$ in the expression for $F(h,\hat{\xi},\hat{\eta})$, $F_{\ln}(\hat{\xi},\hat{\eta})$, and $F_{2\,\ln}(\hat{\xi},\hat{\eta})$ are given by

$$f(h,\zeta)=\begin{cases} 0<h\leqslant \dfrac{1}{2}:-\infty, \quad \dfrac{1}{2}<h<1:\pi\tan(\pi h), & \zeta=0,\\ \dfrac{2h}{h-1/2}\zeta^{h-1/2}-\zeta^{h}\ln\left|\dfrac{1+\zeta^{1/2}}{1-\zeta^{1/2}}\right|+\mathrm{B}_{\zeta}\left(\dfrac{1}{2}+h,0\right)+\pi\tan(\pi h), & \zeta<1,\\ \dfrac{2h}{h-1/2}-\ln 4-\psi\left(\dfrac{1}{2}-h\right)+\psi(1), & \zeta=1,\\ \dfrac{2h}{h-1/2}\zeta^{h-1/2}-\zeta^{h}\ln\left|\dfrac{1+\zeta^{1/2}}{1-\zeta^{1/2}}\right|+\mathrm{B}_{1/\zeta}\left(\dfrac{1}{2}-h,0\right), & \zeta>1, \end{cases}$$

$$f_{\ln}(\zeta)=\begin{cases} \mathrm{Li}_2(\zeta^{1/2})-\mathrm{Li}_2(-\zeta^{1/2}), & \zeta<1,\\ \pi^2/4, & \zeta=1,\\ \mathrm{Li}_2(-\zeta^{-1/2})-\mathrm{Li}_2(\zeta^{-1/2})+\pi^2/2, & \zeta>1, \end{cases}$$

where $\psi(\cdot)$ is the digamma function, $-\psi(1)\simeq 0.577216$ is Euler's constant, $\mathrm{B}_{\zeta}(a,b)=\int_0^{\zeta}t^{a-1}(1-t)^{b-1}\mathrm{d}t$ is the incomplete beta function, and $\mathrm{Li}_2(\zeta)=\int_{\zeta}^{0}\ln(1-t)t^{-1}\mathrm{d}t$ is the dilogarithm function [26]. When $\hat{\eta}=\hat{\xi}$, the functions (C17)–(C20) simplify to

$$F_{\ln}(\hat{\xi},\hat{\xi})=\left(\frac{\pi^2}{2}+2-2\ln\hat{\xi}\right)\hat{\xi}, \quad F_1(\hat{\xi},\hat{\eta})=-2\hat{\xi},$$

$$F_{3/2}(\hat{\xi},\hat{\xi})=\frac{4}{3}(\ln 2-1)\hat{\xi}^{3/2}, \quad F_{2\ln}(\hat{\xi},\hat{\xi})=\left(\frac{\pi^2}{4}-2\right)\hat{\xi}^2.$$

Continuity of $\hat{\Pi}_0(\hat{\xi})$ at the grid points yields expression for the coefficients a_i and b_i in Eq. (C13) in terms of the values of pressure at the grid points $\hat{\Pi}_0^{(i)}=\hat{\Pi}_0(\hat{\xi}_i)$

$$a_i=\frac{\hat{\xi}_i^{-1/3}\hat{\Pi}_0^{(i+1)}-\hat{\xi}_{i+1}^{-1/3}\hat{\Pi}_0^{(i)}}{\hat{\xi}_i^{-1/3}\ln\hat{\xi}_{i+1}-\hat{\xi}_{i+1}^{-1/3}\ln\hat{\xi}_i}, \quad b_i=-\frac{1}{\delta}\frac{\ln\hat{\xi}_i\hat{\Pi}_0^{(i+1)}-\ln\hat{\xi}_{i+1}\hat{\Pi}_0^{(i)}}{\hat{\xi}_i^{-1/3}\ln\hat{\xi}_{i+1}-\hat{\xi}_{i+1}^{-1/3}\ln\hat{\xi}_i}. \tag{C22}$$

The values of the net pressure at the end points $\hat{\xi}_1$ and $\hat{\xi}_n$ are prescribed from Eq. (C14)

$$\hat{\Pi}_0^{(1)}=\hat{\Pi}_{00}(\hat{\xi}_1), \quad \hat{\Pi}_0^{(n)}=\hat{\Pi}_{0\infty}(\hat{\xi}_n), \tag{C23}$$

and are functions of the unknowns coefficients δ_{k0} and β_1, respectively.

Finally, using Eq. (C16) for $\hat{\Omega}_0(\hat{\xi})$ and gradient of $\hat{\Pi}_0(\hat{\xi})$ given by Eq. (C13), the lubrication Eq. $(31)_a$, is evaluated at the midpoints of the intervals, $\hat{\xi}_{i+1/2}=(\hat{\xi}_{i+1}+\hat{\xi}_i)/2$, $i=1,\dots,n-1$, and are expressed as linear combinations of $\hat{\Pi}_0^{(i)}$ by means of Eqs. (C22). Taking into account Eq. (C23), this leads to $n-1$ equations in n unknowns, which can be taken as $\hat{\Pi}_0^{(2)},\dots,\hat{\Pi}_0^{(n-1)}$, δ_{k0}, and β_1. An additional equation is needed in the form of the lubrication equation evaluated at a point outside of the interval $[\hat{\xi}_1,\hat{\xi}_n]$, where the pressure is given by one of the asymptotic expansions, Eqs. (C14). In the numerical implementation, we select this point as $\hat{\xi}_{n+1/2}=\hat{\xi}_n+(\hat{\xi}_n-\hat{\xi}_{n-1})/2$ from the interval where the pressure is given by the far field expansion, Eq. $(\text{C-14})_b$. Summarizing, we obtained the following system of n nonlinear equations

$$\hat{\Omega}_0^2(\hat{\xi}_{i+1/2})\frac{\mathrm{d}\hat{\Pi}_0}{\mathrm{d}\hat{\xi}}\Bigg|_{\hat{\xi}_{i+1/2}}=1, \quad i=1,\dots,n, \tag{C24}$$

in n unknowns $\hat{\Pi}_0^{(2)},\dots,\hat{\Pi}_0^{(n-1)}$, δ_{k0}, and β_1 which is solved using the built-in Newton iteration procedure of the commercial software MATHEMATICA, version 4.1 (© 1988–2000 Wolfram Research, Inc.)

Appendix D: An Implementation of the Small-Toughness Solution (53)

A practically useful numerical implementation of (53) results from the approximation of the opening $\bar{\Omega}_{0,1}$ and pressure $\Pi_{0,1}$ terms using the series expansions, such as (21) for $\{\bar{\Omega}_1,\Pi_1\}$, truncated to three terms: the leading term (correct tip asymptote), the first regular term, and the particular solution (correct inlet behavior). Indeed, for the next-order toughness term $\{\bar{\Omega}_1,\Pi_1\}$, Fig. 2 shows that the three-term-implementation [$n=1$ in (21)] is in excellent agreement with the implementation using 12 terms ($n=10$). The values of the numerical error $e^{(n)}$ in these two implementations are of order 10^{-4} and 10^{-6}, respectively (Table 1). Similar conclusions can be drawn regarding the implementation of the zero-order toughness term $\{\bar{\Omega}_0,\Pi_0\}$ from [16,20].

The three-term-implementation of the zero-toughness solution extracted from [20] is as follows

$$\bar{\Omega}_0=a_{01}(1-\xi^2)^{2/3}+a_{02}(1-\xi^2)^{5/3}+a_{03}\left(2(1-\xi^2)^{1/2}+\xi^2\ln\left|\frac{1-(1-\xi^2)^{1/2}}{1+(1-\xi^2)^{1/2}}\right|\right);$$

$$\Pi_0=b_{01}\,{}_2F_1\left(-\frac{1}{6},1;\frac{1}{2};\xi^2\right)+b_{02}\,{}_2F_1\left(-\frac{7}{6},1;\frac{1}{2};\xi^2\right)+b_{03}(2-\pi|\xi|)$$

where $a_{01}\simeq 1.73205$, $a_{02}\simeq -0.15601$, $a_{03}\simeq 0.13264$, $b_{01}\simeq 0.475449$, $b_{02}\simeq -0.061178$, $b_{03}\simeq 0.066322$. Similarly, the three-term-implementation of the next-order term in the small-toughness solution is obtained from (21)–(23), (B7), and (B8), and Table 1 in the following form:

$$\bar{\Omega}_1=a_{11}(1-\xi^2)^h+(a_{12}+a_{13}\xi^2)(1-\xi^2)^{1+h}+a_{14}\left(2(1-\xi^2)^{1/2}+\xi^2\ln\left|\frac{1-(1-\xi^2)^{1/2}}{1+(1-\xi^2)^{1/2}}\right|\right);$$

$$\Pi_1=b_{11}\,{}_2F_1\left(c_{11},1;\frac{1}{2};\xi^2\right)+b_{12}\,{}_2F_1\left(c_{12},1;\frac{1}{2};\xi^2\right)\xi^2+b_{13}\,{}_2F_1\left(c_{13},2;\frac{3}{2};\xi^2\right)+b_{14}(2-\pi|\xi|)$$

where $h\simeq 0.13867$, $a_{11}\simeq 0.908354$, $a_{12}\simeq 0.025574$, $a_{13}\simeq -0.083814$, $a_{14}\simeq -0.09095$, $b_{11}\simeq 0.170654$, $b_{12}\simeq 0.017132$,

$b_{13} \simeq -0.039015$, $b_{14} \simeq -0.045476$, $c_{11} \simeq 0.36133$, $c_{12} \simeq -1.63867$, $c_{13} \simeq -0.638673$.

References

[1] Economides, M. J., and Nolte, K. G., eds., 2000, *Reservoir Stimulation*, 3rd ed., Wiley, Chichester, UK.
[2] Spence, D., and Turcotte, D., 1985, "Magma-Driven Propagation Crack," J. Geophys. Res., **90**, pp. 575–580.
[3] Jeffrey, R. G., and Mills, K. W., 2000, "Hydraulic Fracturing Applied to Inducing Longwall Coal Mine Goaf Falls," *Pacific Rocks 2000: Proceedings of the 4th American Rock Mechanics Symposium*, J. Girard, M. Liebman, C. Breeds, and T. Doe, eds., Balkema, Rotterdam, pp. 423–430.
[4] Murdoch, L. C., 2002, "Mechanical Analysis of Idealized Shallow Hydraulic Fracture," J. Geotech. Geoenviron. Eng., **128**(6), pp. 488–495.
[5] Khristianovic, S., and Zheltov, Y., 1955, "Formation of Vertical Fractures by Means of Highly Viscous Fluids," *Proc. 4th World Petroleum Congress, Rome*, **II**, pp. 579–586.
[6] Spence, D. A., and Sharp, P. W., 1985, "Self-Similar Solution for Elastohydrodynamic Cavity Flow," Proc. R. Soc. London, Ser. A, **400**, pp. 289–313.
[7] Lister, J. R., 1990, "Buoyancy-Driven Fluid Fracture: The Effects of Material Toughness and of Low-Viscosity Precursors," J. Fluid Mech., **210**, pp. 263–280.
[8] Desroches, J., Detournay, E., Lenoach, B., Papanastasiou, P., Pearson, J. R. A., Thiercelin, M., and Cheng, A. H.-D., 1994, "The Crack Tip Region in Hydraulic Fracturing," Proc. R. Soc. London, Ser. A, **447**, pp. 39–48.
[9] Garagash, D. I., and Detournay, E., 2000, "The Tip Region of a Fluid-Driven Fracture in an Elastic Medium," ASME J. Appl. Mech., **67**, pp. 183–192.
[10] Detournay, E., and Garagash, D., 2003, "The Tip Region of a Fluid-Driven Fracture in a Permeable Elastic Solid," J. Fluid Mech., **494**, pp. 1–32.
[11] Batchelor, G. K., 1967, *An Introduction to Fluid Dynamics*, Cambridge University Press, Cambridge UK.
[12] Geertsma, J., and de Klerk, F., 1969, "A Rapid Method of Predicting Width and Extent of Hydraulic Induced Fractures," JPT, **246**, pp. 1571–1581.
[13] Nilson, R., 1981, "Gas Driven Fracture Propagation," ASME J. Appl. Mech., **48**, pp. 757–762.
[14] Nilson, R., 1988, "Similarity Solutions for Wedge-Shaped Hydraulic Fracture Driven into a Permeable Medium by a Constant Inlet Pressure," Int. J. Numer. Analyt. Meth. Geomech., **12**, pp. 477–495.
[15] Huang, N., Szewczyk, A., and Li, Y., 1990, "Self-Similar Solution in Problems of Hydraulic Fracturing," ASME J. Appl. Mech., **57**, pp. 877–881.
[16] Adachi, J. I., and Detournay, E., 2002, "Self-Similar Solution of a Plane-Strain Fracture Driven by a Power-Law Fluid," Int. J. Numer. Analyt. Meth. Geomech., **26**, pp. 579–604.
[17] Garagash, D. I., 2005, "Transient Solution for a Plane-Strain Fracture Driven by a Power-Law Fluid," Int. J. Numer. Analyt. Meth. Geomech., (to be published).
[18] Detournay, E., 1999, "Fluid and Solid Singularities at the Tip of a Fluid-Driven Fracture," *Proc. IUTAM Symp. on Non-Linear Singularities in Deformation and Flow*, D. Durban and J. Pearson, eds., Haifa, Kluwer, Dordrecht, pp. 27–42.
[19] Detournay, E., 2004, "Propagation Regimes of Fluid-Driven Fractures in Impermeable Rocks," Int. J. Geomech., **4**(1), pp. 1–11.
[20] Adachi, J. I., 2001, "Fluid-Driven Fracture in Permeable Rock," PhD thesis, University of Minnesota.
[21] Garagash, D. I., 2000, "Hydraulic Fracture Propagation in Elastic Rock With Large Toughness," *Pacific Rocks 2000—Proc. 4th North American Rock Mechanics Symp.*, J. Girard, M. Liebman, C. Breeds, and T. Doe, eds.,, Balkema, Rotterdam, pp. 221–228.
[22] Garagash, D. I., 2004, "Plane Strain Propagation of a Hydraulic Fracture During Injection and Shut-In: Asymptotics of Large Toughness," Eng. Fract. Mech., (to be published).
[23] Carbonell, R., Desroches, J., and Detournay, E., 1999, "A Comparison Between a Semi-Analytical and a Numerical Solution of a Two-Dimensional Hydraulic Fracture," Int. J. Solids Struct., **36**(31–32), pp. 4869–4888.
[24] Rice, J. R., 1968, "Mathematical Analysis in the Mechanics of Fracture," *Fracture, an Advanced Treatise*, H. Liebowitz, ed., Academic, New York, Chap. 3, pp. 191–311.
[25] Garagash, D. I., 2005, "Propagation of a Plane-Strain Fluid-Driven Fracture With a Fluid Lag: Early-Time Solution," Int. J. Solids Struct., (to be published).
[26] Abramowitz, M., and Stegun, I. A., eds., 1965, *Handbook of Mathematical Functions*, Dover, New York.
[27] Kevorkian, J., and Cole, J., 1996, *Multiple Scale and Singular Perturbation Methods*, Springer, New York, NY.
[28] Garagash, D. I., 2004, "Relevance of Fluid Lag, Toughness, and Leak-Off for Hydraulic Fracture Propagation," unpublished.
[29] Savitski, A., and Detournay, E., 2002, "Propagation of a Fluid-Driven Penny-Shaped Fracture in an Impermeable Rock: Asymptotic Solutions," Int. J. Solids Struct., **39**(26), pp. 6311–6337.

Negative Poisson's Ratios in Anisotropic Linear Elastic Media

T. C. T. Ting
Division of Mechanics and Computation,
Stanford University,
Durand 262, Stanford, CA 94305-4040

D. M. Barnett
Department of Materials Science and
Engineering,
Stanford University,
416 Escondido Mall, Building 550,
Stanford, CA 94305-2205

Poisson's ratio for an anisotropic linear elastic material depends on two orthogonal directions $\mathbf{n}$ *and* $\mathbf{m}$. *Materials with negative Poisson's ratios for all* $(\mathbf{n},\mathbf{m})$ *pairs are called completely auxetic while those with positive Poisson's ratios for all* $(\mathbf{n},\mathbf{m})$ *pairs are called nonauxetic. Simple necessary and sufficient conditions on elastic compliances are derived to identify if any given material of cubic or hexagonal symmetry is completely auxetic or nonauxetic. When these conditions are not satisfied, the medium is auxetic for some* $(\mathbf{n},\mathbf{m})$ *pairs. Several simple necessary conditions for completely auxetic or nonauxetic media are derived for a general anisotropic elastic material.*

[DOI: 10.1115/1.2042483]

1 Introduction

Poisson's ratio $\nu(\mathbf{n},\mathbf{m})$ in a linear elastic solid for any two specified orthogonal unit vectors $\mathbf{n}$ and $\mathbf{m}$ is the ratio of the lateral contraction in the direction $\mathbf{m}$ to the axial extension in the direction $\mathbf{n}$ due to a uniaxial tension applied along the direction $\mathbf{n}$. For an anisotropic elastic material $\nu(\mathbf{n},\mathbf{m})$ depends on the choice of $\mathbf{n}$ and $\mathbf{m}$. Materials which exhibit a negative Poisson's ratio for at least one direction pair $(\mathbf{n},\mathbf{m})$ are referred to as *auxetic* media (see, for example, Refs. [1,2]). Obviously, an auxetic medium responds to an imposed uniaxial tension with a lateral extension rather than a lateral contraction, and such media may find interesting applications in future technologies as molecular strain amplifiers or as sensors [3]. Ting and Chen [4] and Ting [5] have shown that any anisotropic elastic material can have an arbitrarily large positive or negative Poisson's ratio. Thus an auxetic material with a very large negative Poisson's ratio can be very useful. For present purposes we shall refer to materials for which $\nu(\mathbf{n},\mathbf{m}) < 0$ for *all* pairs $(\mathbf{n},\mathbf{m})$ as *completely auxetic media*, and we shall denote media for which $\nu(\mathbf{n},\mathbf{m}) \geqslant 0$ for *all* pairs $(\mathbf{n},\mathbf{m})$ as *nonauxetic media*. In this paper we present rather simple necessary and sufficient conditions on the elastic compliances for media of cubic and hexagonal symmetry which determine whether a given medium in these symmetry classes is either completely auxetic or nonauxetic. Any material whose compliances do not satisfy these conditions is merely auxetic, and the auxetic directions may be found by a straightforward search. For a general anisotropic elastic material, some simple necessary conditions are derived for the material to be completely auxetic or nonauxetic. We remark that the compliances, rather than the stiffnesses (as suggested by Baughman et al. [1]), provide the more natural and, in fact, the simplest framework for developing the set of necessary and sufficient conditions presented here.

2 Isotropic and Cubic Materials

In a fixed rectangular coordinate system x_i $(i=1,2,3)$ the linear elastic strain-stress relations may be written as

$$\varepsilon_{ij} = S_{ijkl}\sigma_{kl}, \quad S_{ijkl} = S_{jikl} = S_{klij}, \tag{2.1}$$

where ε_{ij} and σ_{kl} are components of the (symmetric) strain and stress tensors, respectively, and the S_{ijkl} are components of the elastic compliance tensor. For a thermodynamically stable medium, the compliance tensor is positive definite. If the material in question is subjected to uniaxial tension along the x_1 direction, all σ_{ij} vanish except for σ_{11} so that

$$\varepsilon_{11} = S_{1111}\sigma_{11}, \quad \varepsilon_{12} = S_{2211}\sigma_{11} = S_{1122}\sigma_{11}. \tag{2.2}$$

Poisson's ratio ν_{12}, which is the ratio of the contraction in the x_2 direction to the extension in the x_1 direction, is

$$\nu_{12} = -\frac{\varepsilon_{22}}{\varepsilon_{11}} = -\frac{S_{2211}}{S_{1111}} = -\frac{s_{21}}{s_{11}} = -\frac{s_{12}}{s_{11}}. \tag{2.3}$$

$s_{\alpha\beta}$ $(\alpha,\beta=1,2,\ldots,6)$ is the contracted notation for the compliance [6–8]. Since s_{11} is necessarily positive (thermodynamic stability), $\nu_{12}<0$ if and only if $s_{12}>0$, and $\nu_{12}\geqslant 0$ if and only if $s_{12}\leqslant 0$. As the $s_{\alpha\beta}$ are symmetric in α and β, it is apparent that the sign of $\nu(\mathbf{n},\mathbf{m})$ is the same as the sign of $\nu(\mathbf{m},\mathbf{n})$. The above remarks are valid in any crystal symmetry class and for any choice of rectangular frame $x_i (i=1,2,3)$ for which $\mathbf{n}$ is along x_1 and $\mathbf{m}$ is along x_2. In an isotropic medium $\nu(\mathbf{n},\mathbf{m})$ is independent of the pair $(\mathbf{n},\mathbf{m})$, so that such a material is completely auxetic when $s_{12}>0$ and is nonauxetic when $s_{12}\leqslant 0$. Tungsten is of cubic symmetry, but is elastically isotropic and turns out to be nonauxetic [9].

In the discussion to follow it is convenient to reserve the x_1,x_2,x_3 frame for the so-called natural axes of the crystal, i.e., the frame or basis relative to which the S_{ijkl} and the $s_{\alpha\beta}$ are usually tabulated or displayed as, for example, in Ref. [10] (pp. 140–141). Let $\mathbf{n}$, $\mathbf{m}$, and $\mathbf{t}$ be a right-hand triad of mutually orthogonal unit vectors, and let the x_i' $(i=1,2,3)$ be a new coordinate system in which the x_1',x_2',x_3' axes are along $\mathbf{n}$, $\mathbf{m}$, and $\mathbf{t}$, respectively. The elastic compliance $S_{2211}'=S_{1122}'$ referred to the x_i' coordinate system is (see Ref. [11])

$$s_{12}' = S_{1122}' = n_i n_j m_k m_l S_{ijkl}. \tag{2.4}$$

We denote the contracted compliances in the "primed" coordinates by $s_{\alpha\beta}'$. For a medium of cubic symmetry in natural coordinates the only nonvanishing $s_{\alpha\beta}$ are

$$s_{11} = s_{22} = s_{33}, \quad s_{12} = s_{23} = s_{13}, \quad s_{44} = s_{55} = s_{66}. \tag{2.5}$$

Equation (2.4) takes the form

$$s_{12}' = s_{12} + \left(s_{11} - s_{12} - \tfrac{1}{2}s_{44}\right)P = (1-2P)s_{12} + \tfrac{1}{2}QP \tag{2.6}$$

where

Contributed by the Applied Mechanics Division of The American Society of Mechanical Engineers for publication in the ASME Journal of Applied Mechanics. Manuscript received by the Applied Mechanics Division, September 30, 2004; final revision, February 28, 2005. Review conducted by Z. Suo. Discussion on the paper should be addressed to the Editor, Prof. Robert M. McMeeking, Journal of Applied Mechanics, Department of Mechanical and Environmental Engineering, University of California—Santa Barbara, Santa Barbara, CA 93106-5070, and will be accepted until four months after final publication in the paper itself in the ASME Journal of Applied Mechanics.

$$Q = 2(s_{11} + s_{12}) - s_{44}, \quad P = n_1^2 m_1^2 + n_2^2 m_2^2 + n_3^2 m_3^2. \tag{2.7}$$

Hayes and Shuvalov [12] have shown that the value of P is between 0 and $1/2$ for all $(\mathbf{n},\mathbf{m})$ pairs, so that the value of s'_{12} is between s_{12} and $Q/4$. Thus we obtain the results that a crystal of cubic symmetry is *completely auxetic* ($s'_{12} > 0$) when

$$s_{12} > 0 \quad \text{and} \quad Q > 0, \tag{2.8}$$

and is *nonauxetic* ($s'_{12} \leqslant 0$) when

$$s_{12} \leqslant 0 \quad \text{and} \quad Q \leqslant 0. \tag{2.9}$$

When neither set of inequalities (2.8) and (2.9) is satisfied, the cubic crystal is auxetic with auxetic direction pairs $(\mathbf{n},\mathbf{m})$ to be found by a search requiring that the right-hand side of (2.6) be positive.

If one examines the literature for published elastic constant data ([9], p. 102, and [13]), only some measurements of the iron pyrites reveal a positive s_{12} (relative to the natural axes for media of cubic symmetry); all other cubic media have $s_{12} < 0$. Since Q is negative for all the pyrite measurements, *there are no known single crystals of cubic symmetry which are completely auxetic*.

The list of *auxetic* media of cubic symmetry ($s_{12} < 0$ and $Q > 0$) as determined by the data in Ref. [9] includes Au, AgCd, AgIn, AgMg, AgSn, AgPd, AgZn, brass, Cu, CuZn, CuAl, Cu_3Au (some measurements), CuGa, CuGe, CuSi, diamond (some), Au, InSb, Fe, Pb, Li, LiF, MgO, Ni, Pd, K, pyrites (some), Ag, Na, spinel, Th, and Zincblende (some). The remainder of the cubic media whose elastic compliances are given in Ref. [9] are nonauxetic.

3 Hexagonal Symmetry

The only nonvanishing elastic compliances for a crystal of hexagonal symmetry (relative to natural axes with the x_3 axis being the axis of sixfold symmetry) are

$$s_{11} = s_{22}, \quad s_{13} = s_{23}, \quad s_{12}, \quad s_{33}, \quad s_{44} = s_{55}, \quad s_{66} = 2(s_{11} - s_{12}). \tag{3.1}$$

Because the elastic compliance tensor is invariant under rotation about the x_3 axis (i.e., the hexagonal media are elastically isotropic in the basal plane, so that the choice of the x_1, x_2 axis pair is arbitrary), without loss of generality we may take $n_2 = 0$, with

$$n_1 = \sin\psi, \quad n_3 = \cos\psi, \tag{3.2}$$

where ψ is the angle between $\mathbf{n}$ and x_3. Any unit vector $\mathbf{m}$ normal to such a choice for $\mathbf{n}$ has components

$$m_1 = \cos\psi\cos\theta, \quad m_2 = -\sin\theta, \quad m_3 = -\sin\psi\cos\theta, \tag{3.3}$$

where $0 \leqslant \theta < 2\pi$. Equation (2.4) now takes the form

$$s'_{12} = (s_{11} + s_{33} - 2s_{13} - s_{44}) n_3^2 m_3^2 + s_{12} n_1^2 m_2^2 + s_{13}(n_3^2 + m_3^2). \tag{3.4}$$

Using (3.2), (3.3),(3.4) can be written as

$$s'_{12} = \left(s_{13}\cos^2 2\psi + \tfrac{1}{4} Q \sin^2 2\psi\right)\cos^2\theta + (s_{12}\sin^2\psi + s_{13}\cos^2\psi)\sin^2\theta, \tag{3.5}$$

where

$$Q = (s_{11} + s_{33} + 2s_{13} - s_{44}). \tag{3.6}$$

From (3.5) it is easily shown that a hexagonal medium is *completely auxetic* [$s'_{12} > 0$ for all $(\mathbf{n},\mathbf{m})$ pairs] provided that

$$s_{12} > 0, \quad s_{13} > 0, \quad \text{and} \quad Q > 0, \tag{3.7}$$

while the medium is nonauxetic when

$$s_{12} \leqslant 0, \quad s_{13} \leqslant 0 \quad \text{and} \quad Q \leqslant 0. \tag{3.8}$$

When neither (3.7) nor (3.8) is satisfied, the medium is auxetic and the auxetic directions may be found numerically using Eq. (3.5).

Of the single crystals of hexagonal symmetry whose elastic compliance data are listed in Ref. [9], only apatite and Zn have $s_{12} > 0$; no hexagonal media for which $s_{13} > 0$ have been reported in the literature. $Q < 0$ for all hexagonal media with the exception of Hg (some measurements). As a result the tabulated elastic constant data shows that *all* single crystals of hexagonal symmetry *are nonauxetic* with the exception of apatite, Zn, and Hg (some), which are simply auxetic.

4 General Anisotropic Materials

For anisotropic elastic materials other than cubic and hexagonal symmetries, let

$$\mathbf{n} = \begin{bmatrix} \cos\phi\sin\psi \\ \sin\phi\sin\psi \\ \cos\psi \end{bmatrix}, \tag{4.1}$$

and

$$\mathbf{m} = \cos\theta \begin{bmatrix} \cos\phi\cos\psi \\ \sin\phi\cos\psi \\ -\sin\psi \end{bmatrix} + \sin\theta \begin{bmatrix} \sin\phi \\ -\cos\phi \\ 0 \end{bmatrix}. \tag{4.2}$$

They reduce to (3.2) and (3.3) when $\phi = 0$. The s'_{12} in (2.4) is a homogeneous function of m_i $(i = 1, 2, 3)$ of degree two. With the $\mathbf{n}$ and $\mathbf{m}$ defined above it has the expression

$$s'_{12} = A\cos^2\theta + B\sin^2\theta + D\sin\theta\cos\theta, \tag{4.3}$$

where A, B, D depend on $s_{\alpha\beta}$, ϕ, and ψ, but are independent of θ.

When $\theta = 0$ (or $\pi/2$), (4.3) gives $s'_{12} = A$ (or B). Hence we have the result that

$$A > 0, \quad B > 0, \tag{4.4}$$

if the material is completely auxetic and

$$A \leqslant 0, \quad B \leqslant 0, \tag{4.5}$$

if the material is nonauxetic. These are necessary (not sufficient) conditions. However, they are necessary and sufficient conditions when $D = 0$, which is the case for hexagonal materials shown in (3.5). When $D \neq 0$, (4.3) can be written as

$$s'_{12} = \tfrac{1}{2}[(A + B) + (A - B)\cos 2\theta + D\sin 2\theta] = \frac{1}{2}[(A + B) + R\cos 2(\theta - \gamma)], \tag{4.6}$$

where

$$R = \sqrt{(A - B)^2 + D^2}, \quad \cos 2\gamma = (A - B)/R, \quad \sin 2\gamma = D/R. \tag{4.7}$$

In conjunction with (4.4) and (4.5), the material is completely auxetic if

$$A + B - R > 0 \quad \text{or} \quad 4AB > D^2, \tag{4.8}$$

and nonauxetic if

$$A + B + R \leqslant 0 \quad \text{or} \quad 4AB \geqslant D^2. \tag{4.9}$$

Equations (4.4) and (4.8) are necessary and sufficient conditions for the material to be completely auxetic while (4.5) and (4.9) are necessary and sufficient conditions for the material to be nonauxetic.

With the exception of hexagonal materials, A, B, and D have complicated expressions in terms of $s_{\alpha\beta}$, ϕ, and ψ, even for the cubic materials. Nevertheless, it can be shown that, for the cubic materials, (4.4), (4.8) and (4.5), (4.9) reduce to (2.8) and (2.9), respectively.

By considering a special **n**, simple necessary conditions for a general anisotropic elastic material to be completely auxetic or nonauxetic can be derived. For instance, let

$$n_3 = 1, \quad n_1 = n_2 = 0. \tag{4.10}$$

We can assume

$$m_1 = \cos\theta, \quad m_2 = \sin\theta, \quad m_3 = 0. \tag{4.11}$$

Equation (2.4) gives

$$s'_{12} = s_{31}\cos^2\theta + s_{32}\sin\theta + s_{36}\sin\theta\cos\theta. \tag{4.12}$$

This is in the form of (4.3) so that (4.4), (4.8) or (4.5), (4.9) apply. By considering the case $n_1=1$ and $n_2=1$ we obtain two more equations similar to (4.12). We then have the result that

$$\begin{gathered} s_{12} > 0, \quad s_{23} > 0, \quad s_{31} > 0, \\ 4s_{12}s_{13} > s_{14}^2, \quad 4s_{21}s_{23} > s_{25}^2, \quad 4s_{31}s_{32} > s_{36}^2, \end{gathered} \tag{4.13}$$

if the material is completely auxetic, and

$$\begin{gathered} s_{12} \leqslant 0, \quad s_{23} \leqslant 0, \quad s_{31} \leqslant 0, \\ 4s_{12}s_{13} \geqslant s_{14}^2, \quad 4s_{21}s_{23} \geqslant s_{25}^2, \quad 4s_{31}s_{32} \geqslant s_{36}^2, \end{gathered} \tag{4.14}$$

if the material is nonauxetic. These are necessary (not sufficient) conditions. Although they cannot positively identify if a material is completely auxetic or nonauxetic, they can be used to identify if a material is *not* completely auxetic or *not* nonauxetic if any one of the six conditions in (4.13) or (4.14) is violated. In particular, any one of the following conditions,

$$4s_{12}s_{13} < s_{14}^2, \quad 4s_{21}s_{23} < s_{25}^2, \quad 4s_{31}s_{32} < s_{36}^2, \tag{4.15}$$

is a necessary and sufficient condition for the material to be neither completely auxetic nor nonauxetic.

Another special **n** is

$$n_1 = n_2 = 1/\sqrt{2}, \quad n_3 = 0. \tag{4.16}$$

If we let

$$m_1 = -m_2 = 1/\sqrt{2}, \quad m_3 = 0, \tag{4.17}$$

(2.4) gives

$$s'_{12} = \tfrac{1}{4}(s_{11} + s_{22} + 2s_{12} - s_{66}). \tag{4.18}$$

By a permutation of the coordinate system x_1, x_2, x_3, two more equations similar to (4.18) can be obtained. If we define

$$\begin{gathered} Q_1 = s_{22} + s_{33} + 2s_{23} - s_{44}, \\ Q_2 = s_{33} + s_{11} + 2s_{31} - s_{55}, \\ Q_3 = s_{11} + s_{22} + 2s_{12} - s_{66}, \end{gathered} \tag{4.19}$$

we have

$$Q_i > 0 \quad (i = 1,2,3), \tag{4.20}$$

if the material is completely auxetic, and

$$Q_i \leqslant 0 \quad (i = 1,2,3), \tag{4.21}$$

if the material is nonauxetic.

In the special case of cubic materials, $Q_1=Q_2=Q_3$ and we recover (2.7). For hexagonal materials, $Q_1=Q_2=Q$ as in (3.6) while $Q_3=4s_{12}$ in view of (3.1).

Of course, other special **n** can be used to derive more necessary conditions.

It is interesting to note that, even though (4.13), (4.20) and (4.14), (4.21) are necessary, not sufficient, conditions for a general anisotropic material, they are necessary and sufficient conditions for cubic and hexagonal materials. Some of the conditions in these equations are either redundant or identical for cubic and hexagonal materials.

References

[1] Baughman, R. H., Shacklette, J., Zakhidov, A. A., and Stafström, S., 1998, “Negative Poisson’s Ratios as a Common Feature of Cubic Metals,” Nature (London), **392**, pp. 362–365.

[2] Baughman, R. H., 2003, “Avoiding the Shrink,” Nature (London), **425**, p. 667.

[3] Lakes, R. S., 1993, “Advances in Negative Poisson’s Ratio Materials,” Adv. Mater. (Weinheim, Ger.), **5**, pp. 293–296.

[4] Ting, T. C. T., and Chen, T., 2005, “Poisson’s Ratio for Anisotropic Elastic Materials can have no Bounds,” Q. J. Mech. Appl. Math., **58**(1), pp. 73–82.

[5] Ting, T. C. T., 2004, “Very Large Poisson’s Ratio With a Bounded Transverse Strain in Anisotropic Elastic Materials,” J. Elast., **77**(2), pp. 163–176.

[6] Voigt, W., 1910, *Lehrbuch der Kristallphysik*, Teubner, Leipzig.

[7] Lekhnitskii, S. G., 1963, *Theory of Elasticity of an Anisotropic Body*, Holden-Day, San Francisco.

[8] Ting, T. C. T., 1996, *Anisotropic Elasticity: Theory and Applications*, Oxford University Press, New York.

[9] Simmons, G., 1961, “Single Crystal Elastic Constants and Calculated Aggregate Properties,” *Journal of the Graduate Research Center*, Vol. XXXIV, March 1961, Vols. 1 and 2, Southern Methodist University Press, Dallas.

[10] Nye, J. F., *Physical Properties of Crystals: Their Representation by Tensors and Matrices*, Clarendon Press, Oxford.

[11] Sirotin, Yu. I., and Shakol’skaya, M. P., 1982, *Fundamentals of Crystal Physics*, MIR Publisher, Moscow.

[12] Hayes, M., and Shuvalov, A., 1998, “On the Extreme Values of Young’s Modulus, the Shear Modulus, and Poisson’s Ratio for Cubic Materials,” ASME J. Appl. Mech., **65**, pp. 786–787.

[13] Landolt, H. H., and Börnstein, R., 1979, *Numerical Data and Functional Relationships in Science and Technology*, New Series, editor-in-chief K. H. Hellwege, Group III: *Crystal and Solid State Physics*, Vol. 11, Revised and Extended Version of Vols. III/1 and III/2, *Elastic, Piezoelectric, Pyroelectric, Piezooptic, Electrooptic Constants and Non-Linear Dielectric Susceptibilities of Crystals*, Springer-Verlag, Berlin: Heidelberg, New York.

Ting Zhu
Department of Mechanical Engineering,
Massachusetts Institute of Technology,
Cambridge, MA 02139

Ju Li
Department of Materials Science and
Engineering,
Ohio State University,
Columbus, OH 43210

Sidney Yip
Departments of Nuclear Engineering and
Materials Science and Engineering,
Massachusetts Institute of Technology,
Cambridge, MA 02139
e-mail: syip@mit.edu

Nanomechanics of Crack Front Mobility

Minimum energy paths for unit advancement of a crack front are determined by reaction pathway sampling, thus providing the reaction coordinates for the analysis of crack tip mechanics in ductile and brittle materials. We compare results on activation energy barrier and atomic displacement distributions for an atomically sharp crack in Cu, where one observes the emission of a partial dislocation loop, and in Si, where crack front extension evolves in a kink-like fashion. [DOI: 10.1115/1.2047607]

1 Introduction

Is it possible to study how a sharp crack evolves in a crystal lattice without actually driving the system to the point of instability? By this we mean determining the pathway of crack front motion while the lattice resistance against such displacement is still finite. Despite a large number of molecular dynamics (MD) simulations on crack tip propagation (e.g., see [1]), this particular issue has not been examined. Most studies to date have been carried out in an essentially 2D setting, with a periodic boundary condition imposed along the direction of the crack front. In such simulations the crack tip is sufficiently constrained that the natural response of the crack front cannot be investigated. Besides the size constraint on the crack front, there is also the problem that in direct MD simulation one frequently drives the system to instability, resulting in abrupt crack-tip displacements which make it difficult to characterize the slow crack growth by thermal activation.

We have developed an approach capable of probing crack front evolution without subjecting the system to critical loading. This involves using reaction pathway sampling to probe the minimum energy path (MEP) [2] for the crack front to advance by one atomic lattice spacing, while the imposed load on the system is below the critical threshold. We have applied this method to characterize the atomistic configurations and energetics of crack extension in a metal (Cu) [3] and a semiconductor (Si) [4]. In this report we will compare the results of these two studies to show how ductility or brittleness of the crystal lattice can manifest in the mechanics of crack front deformation at the nanoscale.

Consider a 3D atomically sharp crack front which is initially straight, as shown in Fig. 1(*a*). Suppose we begin to apply a mode-I load in incremental steps. Initially the crack would not move spontaneously because the driving force is not sufficient to overcome the intrinsic lattice resistance. What does this mean? Imagine a final configuration, a replica of the initial configuration with the crack front translated by an atomic lattice spacing in the direction of crack advancement. At low loads, e.g., K_I' as shown in Fig. 1(*b*), the initial configuration (open circle) has a lower energy than the final configuration (closed circle). They are separated by an energy barrier which represents the intrinsic resistance of the lattice. As the loading increases, the crack will be driven toward the final configuration; one can regard the overall energy landscape as being tilted toward the final configuration with a corresponding reduction in the activation barrier [see the saddle-point states (shaded circle) in Fig. 1(*b*)]. As the load increases further the biasing becomes stronger. So long as the barrier remains finite the crack will not move out of its initial configuration without additional activation, such as from thermal fluctuations. When the loading reaches the point where the lattice-resistance barrier disappears altogether, the crack is then unstable at the initial configuration; it will move without any thermal activation. This is the athermal load threshold, denoted by K_{Iath} in Fig. 1(*b*). In our simulation, we study the situation where the applied load is below this threshold, thereby avoiding the problem of a fast moving crack that is usually over-driven.

The cracks in Cu and Si that we will compare are both semi-infinite cracks in a single crystal, with the crack front lying on a (111) plane and running along the $[\bar{1}10]$ direction. The simulation cells consist of a cracked cylinder cut from the crack tip, with a radius of 80 Å. The atoms located within 5 Å of the outer surface are fixed according to a prescribed boundary condition, while all the remaining atoms are free to move. To probe the detailed deformation of the crack front, the simulation cell along the cylinder is taken to be as long as computationally feasible, 24 (Cu) and 20 (Si) unit cells. A periodic boundary condition is imposed along this direction. With this setup, the numbers of atoms in the system are 103,920 (Cu) and 77,200 (Si). For interatomic potentials we use a many-body potential of the embedded atom method type for Cu [5], for which the unstable stacking energy has been fitted to the value of 158 $\mathrm{mJ/m^2}$, given by an ab initio calculation, and a well-known three-body potential model proposed by Stillinger and Weber (SW) for Si [6].

2 MEP for Crack Blunting in Cu

Prior to applying reaction pathway sampling, we first determine the athermal energy release rate, denoted by G_{emit} [corresponding to K_{Iath} in Fig. 1(*b*)]. This is the critical value at which the activation energy barrier for dislocation nucleation vanishes, or equivalently a straight dislocation is emitted without thermal fluctuations [7,8]. As detailed in [3], the athermal load is determined to be $K_{\mathrm{Iemit}}=0.508\ \mathrm{MPa}\sqrt{\mathrm{m}}$ (or $G_{\mathrm{emit}}=1.629\ \mathrm{J/m^2}$ based on the Stroh solution [9]) for the nucleation of a Shockley partial dislocation across the inclined $(\bar{1}\bar{1}0)$ slip plane. So long as the applied load is below K_{Iemit} the crack front will remain stable. It is in such

---

Contributed by the Applied Mechanics Division of THE AMERICAN SOCIETY OF MECHANICAL ENGINEERS for publication in the ASME JOURNAL OF APPLIED MECHANICS. Manuscript received by the Applied Mechanics Division, October 5, 2004; final revision, October 5, 2005. Review conducted by H. D. Espinosa. Discussion on the paper should be addressed to the Editor, Prof. Robert M. McMeeking, Journal of Applied Mechanics, Department of Mechanical and Environmental Engineering, University of California—Santa Barbara, Santa Barbara, CA 93106-5070, and will be accepted until four months after final publication in the paper itself in the ASME JOURNAL OF APPLIED MECHANICS.

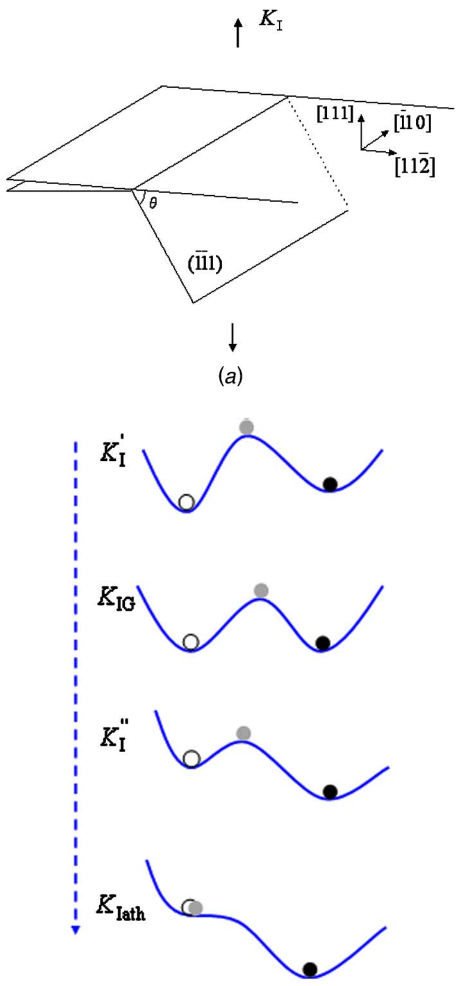

(*a*)

(*b*)

Fig. 1 (a) Schematics of a 3D atomically sharp crack front under a mode-I load K_I; (b) energy landscape of the crack system at different loads ($K_I'<K_{IG}<K_I''<K_{Iath}$). Open circle represents the initial state of a straight crack front under an applied load K_I, closed circle is the final state after the crack front uniformly advances by one atomic spacing (under the same load K_I as the initial state), and shaded circle corresponds to the saddle-point state in between.

a state that we will probe the reaction pathway for dislocation nucleation using the method of nudged elastic band (NEB) [2]. The quantity we wish to determine is the MEP for the emission of a partial dislocation loop from an initially straight crack front. MEP is a series of atomic configurations connecting the initial and final states. For this study the initial configuration is a crack front as prescribed by the Stroh solution which is then relaxed by energy minimization. The final configuration contains a fully formed straight Shockley partial dislocation at the same level of loading as the initial state. This is obtained by first loading the simulation cell at a level above the threshold G_{emit} so that a partial dislocation could instantaneously nucleate. Then the loading is reduced to the level of the initial state (below G_{emit}) thus generating a configuration with an embedded partial dislocation. To find the MEP 15 intermediate replicas of the system which connect the initial and final states are constructed. We choose intermediate replicas containing embryonic loops that result from the relaxation of a straight crack front, allowing for the nucleation of a curved dislocation. The relaxation of each replica is considered converged when the potential force vertical to the path is less than a prescribed value, 0.005 eV/Å in our case.

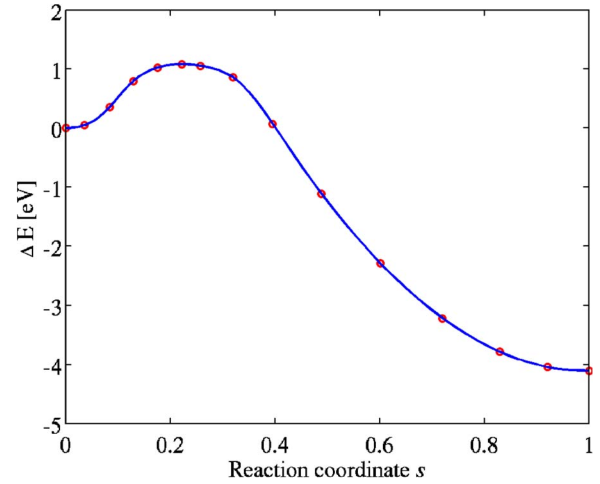

Fig. 2 MEP of dislocation loop emission in Cu at a load of $G=0.75G_{\mathrm{emit}}$ [3]

The sequence of replicas defines a reaction coordinate in the following sense. Each replica in the sequence is a specific configuration in $3N$ configurational hyperspace, where N is the number of movable atoms in the simulation. For each replica we calculate the hyperspace arc length l between the initial state $\mathbf{x}_i^{3N}$ and the state of the replica $\mathbf{x}^{3N}$. The normalized reaction coordinate s is defined to be $s\equiv l/l_f$, where l_f denotes the hyperspace arc length between the initial and final states.

The relaxed energy of any replica is a local minimum within a $3N$-1 hyperplane vertical to the path. By definition the MEP is a path that begins at $\Delta E=0(s=0)$, where ΔE is the relaxed energy measured relative to the energy of the initial state. Along the path (reaction coordinate s) ΔE will vary. The state with the highest energy on this path is the saddle point, and the activation energy barrier is the energy difference between the saddle point and the initial state. Figure 2 shows the MEP for the nucleation of a dislocation loop from the crack front in Cu, loaded at $G=0.75G_{\mathrm{emit}}$. Notice that at this loading the final state is strongly favored over the initial state. Figure 2 shows clearly the presence of a lattice-resistance barrier at this particular loading.

To visualize the variation of atomic configurations along the MEP, we turn to displacement distributions between atom pairs across the slip plane. Figure 3(*a*) is a contour plot of the *shear* displacement distribution along the crack front at the saddle-point state. One can see clearly the shape of a dislocation loop bowing out; the profile of $b/2$ shear displacement is a reasonable representation of the locus of dislocation core. Also this is an indication that the enclosed portion of the crack front has been swept by the Shockley partial dislocation loop. Besides shear displacement, normal, or *opening* displacement, in the direction along $x_3,[\bar{1}\bar{1}1]$, is also of interest. The corresponding distribution is shown in Fig. 3(*b*). One sees that large displacements are not at the center of the crack front. In Figs. 3(*a*) and 3(*b*) we have a detailed visualization of the crack front evolution in three dimensions. The largest displacements are indeed along the crack front but they are not of the same character; the atoms move in a shear mode in the central region and in an opening mode on the two sides.

3 MEP for Crack Advancement in Si

Turning to Si, we first repeat the determination of athermal load for crack extension in the (111) plane; $K_{\mathrm{Iath}}=0.88\ \mathrm{MPa}\sqrt{\mathrm{m}}$. Since Si is a brittle solid, a useful reference load is K_{IG}, the Griffith value at which the initial and final states are at the same energy [see Fig. 1(*b*)], the latter being identical to the initial state except the crack front advances one atomic spacing in the propagation

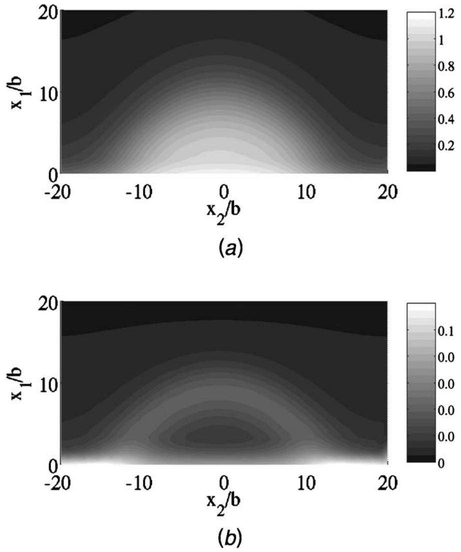

(*a*)

(*b*)

Fig. 3 Contour of (*a*) shear displacement (normalized by the Burgers vector of a partial dislocation $b=1.476$ Å) and (*b*) opening displacement (normalized by the interplanar spacing $h=2.087$ Å) across the slip plane at the saddle-point state [3]

direction. Direct simulation gives $K_{IG}=0.646\ \mathrm{MPa}\sqrt{\mathrm{m}}$. This value is lower than the athermal load K_{Iath}, a manifestation of the lattice-trapping effect [10]. Being a brittle solid, the relevant deformation in crack front advancement in Si is bond rupture rather than bond shearing as in the case of a ductile material such as Cu. Our simulation cell contains 20 bonds along the initially straight crack front. We find that the most energetically favored pathway for the front to advance by one atomic spacing is the breaking of the 20 bonds *sequentially*. At a load equal to the Griffith value, the MEP we obtain is shown in Fig. 4. A slightly different reaction coordinate is used in this case, with integer *s* labeling a locally equilibrated state with *s* broken bonds on the crack front. One sees the energy variation is a series of barriers, each one corresponding to the rupture of a bond along the crack front.

Figure 5 shows the opening displacement distribution in Si across the (111) cleavage plane. We see a new feature in the outline of displacements of intermediate magnitude (dark-gray line); in the region ahead of the crack front the distribution of these displacements has the shape of a rectangular wedge protruding in the direction of crack front advancement. The presence of a wedge shape suggests a kink mechanism of crack advancement, namely, nucleation of a local kink distortion followed by spreading across the entire crack front. It is significant that this behavior is not seen in Fig. 3(*b*). Taking Cu to be a prototypical ductile material, we see that while the crack opening still occurs at the front, the large normal displacements lie outside the central region enclosed by the emerging dislocation loop. We attribute this feature to a mode-switching, or shear-tension coupling, process. The initially large opening displacements in the region swept by the emerging loop are relaxed by giving way to large shear displacements, which are then carried away by the emitted dislocation loop.

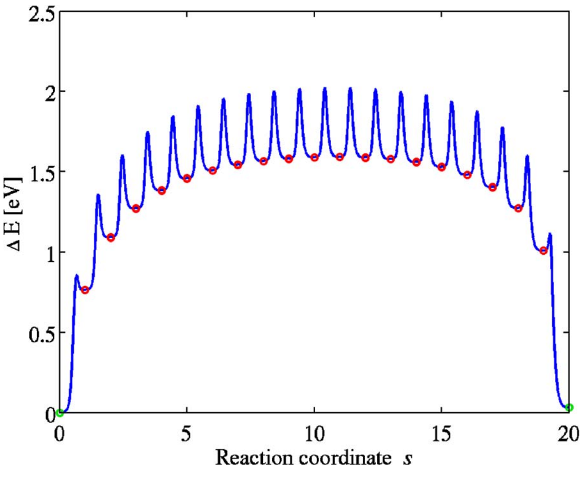

Fig. 4 MEP of crack extension in Si at the Griffith load K_{IG} [4]

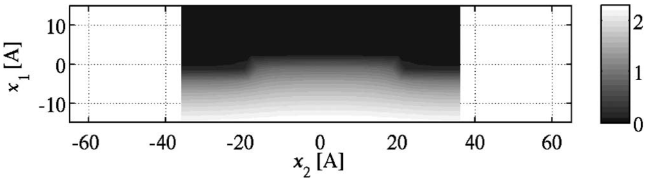

Fig. 5 Contour of opening displacement (normalized by interplanar spacing $h=2.35$ Å) at the Griffith load K_{IG} [4]

It is relevant to interpret the behavior of atomic displacements at the transition state in Cu and Si on the basis of the nature of interatomic bonding in these two materials. One expects that the crack front response in Cu should reflect delocalized metallic bonding while that in Si should correspond to directional, localized covalent bonding. In terms of characteristic features of the energy landscape along the reaction path, we see for Cu (in Fig. 2) a rather smooth MEP with a single major nucleation barrier, indicating that crack advancement involves a concerted motion of atoms to overcome this barrier by thermal activation. In contrast MEP in Si reveals the existence of significant secondary barrier (cusps in Fig. 4) which should be a general feature of covalently bonded crystals. In this case crack extension proceeds via individual bond breakings, a series of thermally activated events of kink-pair formation, and lateral kink migration along the front. It is of interest to point out the crack front mobility is not only controlled by kinks at the atomic scale as demonstrated in this work; acoustic emission and fractographic measurements have indicated the crack advancement at the mesoscopic scale is also governed by the kink mechanism which involves a process of unzipping along the crack front (W. W. Gerberich, private communication; [11]).

The fact that kink mechanism appears to play a central role in crack front mobility raises an interesting question of the implications of structural similarity between the crack front, acting as the core of a sharp crack, and the core of a dislocation, both being "*line defects*" in a crystal lattice. It is rather well known that dislocation mobility in a directionally bonded crystal like Si is governed by thermal activation of nucleation and migration of kink pairs [12]. The present results showing that a similar mechanism also operates in crack front advancement reinforces the notion that mobility fundamentally depends on crystal structure and chemical bonding. From this perspective the appearance of kink-like structure in Fig. 5 is perhaps to be expected. Since dislocation mobility and crack-tip extension are both active topics for modeling and simulation, recognition of their underlying connections could lead to a broader appreciation of the role of structure and bonding [13] in controlling both phenomena.

Acknowledgments

We thank A. S. Argon for stimulating discussions and W. W. Gerberich for a useful reference. TZ and SY acknowledge support by NSF, Honda R&D, DARPA-ONR, and the Lawrence Livermore National Laboratory. JL acknowledges support by Honda Research Institute of America, NSF, AFOSR, ONR, and Ohio Supercomputer Center.

References

[1] Buehler, M. J., Abraham, F. F., and Gao, H., 2003, "Hyperelasticity Governs Dynamic Fracture at a Critical Length Scale," Nature (London), **426**, pp. 141–146.

[2] Jonsson, H., Mills, G., and Jacobsen, K. W., 1998, "Nudged Elastic Band Method for Finding Minimum Energy Paths of Transitions," *Classical and Quantum Dynamics in Condensed Phase Simulations*, B. J. Berne, G. Ciccotti, and D. F. Coker, eds., World Scientific, Sinapore, pp. 385–404.

[3] Zhu, T., Li, J., and Yip, S., 2004, "Atomistic Study of Dislocation Loop Emission From a Crack Tip," Phys. Rev. Lett., **93**, 025503.

[4] Zhu, T., Li, J., and Yip, S., 2004, "Atomic Configurations and Energetics of Crack Extension in Silicon," Phys. Rev. Lett., **93**, 205504.

[5] Mishin, Y., Mehl, M. J., Papaconstantaopoulos, D. A., Voter, A. F., and Kress, J. D., 2001, "Structural Stability and Lattice Defects in Copper: *Ab initio*, Tight-Binding, and Embedded-Atom Calculations," Phys. Rev. B, **63**, 224106.

[6] Stillinger, F. H., and Weber, T. A., 1985, "Computer Simulation of Local Order in Condensed Phases of Silicon," Phys. Rev. B, **31**, pp. 5262–5271.

[7] Rice, J. R., 1992, "Dislocation Nucleation From a Crack Tip: An Analysis Based on the Peierls Concept," J. Mech. Phys. Solids, **40**, pp. 239–271.

[8] Xu, G., Argon, A. S., and Ortiz, M., 1997, "Critical Configurations for Dislocation Nucleation From Crack Tips," Philos. Mag. A, **75**, pp. 341–367.

[9] Stroh, A. N., 1958, "Dislocations and Cracks in Anisotropic Elasticity," Philos. Mag., **7**, pp. 625–646.

[10] Thomson, R., Hsieh, C., and Rana, V., 1971, "Lattice Trapping of Fracture Cracks," J. Appl. Phys., **42**, pp. 3145–3160.

[11] Lii, M. J., Chen, X. F., Katz, Y., and Gerberich, W. W., 1990, "Dislocation Modeling and Acoustic-Mission Observation of Alternating Ductile/Brittle Events in Fe-3 wt% Si Crystals," Acta Metall. Mater., **38**, pp. 2435–2453.

[12] Cai, W., Bulatov, V. V., Chang, J., Li, J., and Yip, S., 2004, "Dislocation Core Effects on Mobility," in *Dislocations in Solids*, F. R. N. Nabarro and J. P. Hirth, eds., Elsevier, Amsterdam, Vol. 12, Chap. 64, pp. 1–80.

[13] Ogata, S., Li, J., Hirosaki, N., Shibutani, Y., and Yip, S., 2004, "Ideal Shear Strain of Metals and Ceramics," Phys. Rev. B, **70**, pp. 104104.

Frequency Analysis of the Tuned Mass Damper

Steen Krenk
Department of Mechanical Engineering,
Technical University of Denmark,
DK-2800 Lyngby, Denmark

The damping properties of the viscous tuned mass damper are characterized by dynamic amplification analysis as well as identification of the locus of the complex natural frequencies. Optimal damping is identified by a combined analysis of the dynamic amplification of the motion of the structural mass as well as the relative motion of the damper mass. The resulting optimal damper parameter is about 15% higher than the classic value, and results in improved properties for the motion of the damper mass. The free vibration properties are characterized by analyzing the locus of the natural frequencies in the complex plane. It is demonstrated that for optimal frequency tuning the damping ratio of both vibration modes are equal and approximately half the damping ratio of the applied damper, when the damping is below a critical value corresponding to a bifurcation point. This limiting value corresponds to maximum modal damping and serves as an upper limit for damping to be applied in practice. [DOI: 10.1115/1.2062867]

1 Introduction

An efficient means to introduce additional damping into structures and machinery is via a combined mass-damper system that is tuned to act in resonance. The resonance generates a relative motion of the damped mass that is sufficient to enable the damper to extract the necessary energy. In practice this means that the motion of the structural mass should be reduced, while keeping the relative motion of the damper mass within acceptable bounds. The idea of reducing dynamic motion via a resonating mass is due to Frahm [1], who proposed the use of a spring-mass system. In this proposal there was no damper, and thus the function of the system was to balance the external load without absorbing energy. It was demonstrated by Ormondroyd and Den Hartog [2] that the introduction of a damper not only dissipated energy, but also increased the frequency interval over which the device is active. This led to development of a design procedure that is still in use. This procedure is based on analysis of the dynamic amplification of the motion of the structural mass and consists of two separate steps: tuning of the frequency of the damper, and selection of the optimal level of damping. The frequency tuning is based on the observation that there are two frequencies, where the dynamic amplification is independent of the applied damping, and optimal tuning is determined by setting the dynamic amplification at these two frequencies equal, Den Hartog [3]. The selection of the damping level is based on a more pragmatic argument that implies an average of the level that would give a local maximum of the dynamic amplification at each of the two neutral frequencies, Brock [4]. The use of an average implies that the resulting damping level does in fact not have the maximum properties used in its derivation, and as demonstrated in the following simultaneous consideration of the motion of the structural mass and the relative motion of the damped mass leads to the identification of a higher level of damping as optimal.

The original formulation of the tuned vibration damper dealt with excitation by a force with harmonic time variation. This problem has later been extended to excitation via motion of the base and to random load with wide band characteristics. The main results of these developments are summarized in [5–7]. In the case of random load the excitation has been assumed in the form of a white noise process, and optimal tuning and damping level have been determined in explicit form by minimizing the variance of, e.g., the displacement of the structural mass. In all cases the result has indicated a considerably lower level of damping to be optimal for random white noise load. This may be due to the influence of the high frequency excitation implied by the assumption of white noise, which has a spectral density extending at constant value to infinitely high frequencies. A more realistic representation would bring more emphasis on the frequencies around resonance, but preclude explicit determination of optimum values. However, an impression of the random response properties can be gained from the complex natural frequencies of the system, and the present paper gives a detailed analysis of these. Introduction of the additional mass leads to the introduction of two frequencies instead of the original one, and with the introduction of damping these frequencies move into the positive imaginary half-plane. It is demonstrated that for optimal frequency tuning the two branches of the complex locus of the natural frequencies meet at a bifurcation point. For damping levels lower than the bifurcation value the modes of the system have identical damping ratio, and the bifurcation point corresponds to maximum modal damping. Thus, this level of damping serves as an upper limit of the damping to be introduced into the system.

2 Basic Equations

The basic model of a viscous tuned mass damper is illustrated in Fig. 1. The figure shows the primary structure with mass m_0 and stiffness k_0. The primary structure is assumed to have negligible damping. The secondary structure consists of a mass m connected to the primary mass by a spring k and a viscous damper c. It is convenient to formulate the equations of motion from the energy balance equation, because this procedure can be extended in a fairly straightforward manner to multiple dampers on flexible structures. The energy balance equation is

$$\frac{d}{dt}(E_{\text{kin}} + E_{\text{pot}}) = -D \tag{1}$$

where E_{kin} and E_{pot} are the kinetic and potential energy, respectively, and D is the rate of energy dissipation. It is convenient to describe the motion of the system in terms of the absolute motion x_0 of the structural mass m_0 and the relative motion x_d of the damper mass m with respect to the structural mass. The terms in the energy equation then are

---

Contributed by the Applied Mechanics Division of THE AMERICAN SOCIETY OF MECHANICAL ENGINEERS for publication in the ASME JOURNAL OF APPLIED MECHANICS. Manuscript received by the Applied Mechanics Division, November 5, 2004; final revision, May 15, 2005. Review conducted by I. Mezic. Discussion on the paper should be addressed to the Editor, Prof. Robert M. McMeeking, Journal of Applied Mechanics, Department of Mechanical and Environmental Engineering, University of California—Santa Barbara, Santa Barbara, CA 93106-5070, and will be accepted until four months after final publication of the paper itself in the ASME JOURNAL OF APPLIED MECHANICS.

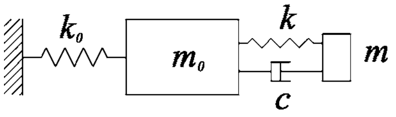

Fig. 1 Tuned mass damper

$$E_{\text{kin}} = \tfrac{1}{2}m_0\dot{x}_0^2 + \tfrac{1}{2}m(\dot{x}_0 + \dot{x}_d)^2$$

$$E_{\text{pot}} = \tfrac{1}{2}k_0x_0^2 + \tfrac{1}{2}kx_d^2 \tag{2}$$

$$D = c\dot{x}_d^2$$

The equations of motion of the two masses follow from isolation of the factors to $\dot{x}_0$ and $\dot{x}_d$ in the energy balance equation.

$$m_0\ddot{x}_0 + m(\ddot{x}_0 + \ddot{x}_d) + k_0x_0 = F(t)$$
$$m(\ddot{x}_0 + \ddot{x}_d) + c\dot{x}_d + kx_d = 0 \tag{3}$$

The equations of a harmonic response analysis are obtained by representing the response and the load in terms of harmonic components with angular frequency ω

$$x(t) = xe^{i\omega t}, \quad F(t) = Fe^{i\omega t} \tag{4}$$

where $x(t)$ is either $x_0(t)$ or $x_d(t)$. The harmonic response is then determined from

$$\begin{bmatrix} k_0 - (m_0+m)\omega^2 & -\omega^2 m \\ -\omega^2 m & k - \omega^2 m + i\omega c \end{bmatrix}\begin{bmatrix} x_0 \\ x_d \end{bmatrix} = \begin{bmatrix} F \\ 0 \end{bmatrix} \tag{5}$$

From this system of equations the complex amplitude of forced response of the structural mass is found as

$$\frac{x_0}{F} = \frac{k - \omega^2 m + i\omega c}{[k_0 - \omega^2(m_0+m)][k - \omega^2 m + i\omega c] - \omega^4 m^2} \tag{6}$$

and the frequency equation for free vibrations follows from the determinant as

$$[k_0 - \omega^2(m_0+m)][k - \omega^2 m + i\omega c] - \omega^4 m^2 = 0 \tag{7}$$

The response equation (6) forms the basis of the classical tuned mass damper analysis by Den Hartog [3], while Eq. (7) is the main instrument of the analysis of the natural frequencies presented later.

The tuned mass damper is characterized by the normalized parameters

$$\omega_0^2 = \frac{k_0}{m_0}, \quad \mu = \frac{m}{m_0}$$
$$\omega_d^2 = \frac{k}{m}, \quad \zeta_d = \frac{c}{2\sqrt{km}} \tag{8}$$

Typically the mass ratio μ is selected, and the secondary system is then described by the frequency ratio ω_d/ω_0 and the damping ratio ζ_d of a rigidly mounted damper. In terms of these parameters the complex amplitude equation (6) takes the form

$$\frac{x_0}{F/k_0} = \frac{\omega_0^2[\omega_d^2 - \omega^2 + 2i\zeta_d\omega_d\omega]}{\omega^4 - [\omega_0^2 + (1+\mu)\omega_d^2]\omega^2 + \omega_0^2\omega_d^2 + 2i\zeta_d\omega_d\omega[\omega_0^2 - (1+\mu)\omega^2]} \tag{9}$$

It follows from the last of the equations in (5) that the relative motion of the damper is

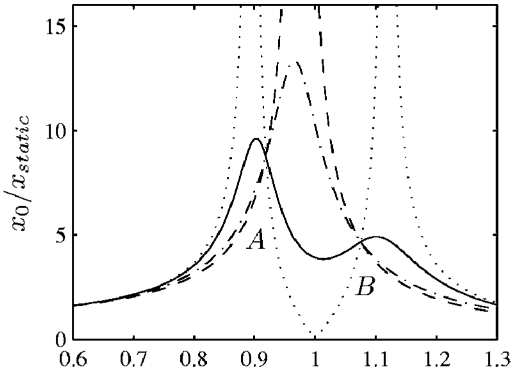

Fig. 2 Dynamic amplification for μ=0.05, ω_d=ω_0 and ζ: (···) 0, (—) 0.1, (---) 0.3, (---) ∞

$$\frac{x_d}{F/k_0} = \frac{\omega_0^2\omega^2}{\omega^4 - [\omega_0^2 + (1+\mu)\omega_d^2]\omega^2 + \omega_0^2\omega_d^2 + 2i\zeta_d\omega_d\omega[\omega_0^2 - (1+\mu)\omega^2]} \tag{10}$$

The corresponding normalized form of the frequency equation (7) is

$$\omega^4 - 2i\zeta_d(1+\mu)\omega_d\omega^3 - [\omega_0^2 + (1+\mu)\omega_d^2]\omega^2 + 2i\zeta_d\omega_0^2\omega_d\omega + \omega_0^2\omega_d^2 = 0 \tag{11}$$

While the forced response at a single frequency is given by Eqs. (9) and (10), the free vibration response including the modal damping follows from the frequency equation (11).

In the limit of infinite damping ratio ζ_d the the damper constrains the relative motion x_d of the damper mass, and thereby creates the effect of a single mass m_0+m. The frequency of the limiting situation of a locked damper will be denoted ω_∞. It is given by

$$\omega_\infty = \sqrt{\frac{k_0}{m_0+m}} = \frac{\omega_0}{\sqrt{1+\mu}} \tag{12}$$

This frequency plays a central role in the properties of a tuned mass damper as demonstrated in the following.

3 Dynamic Amplification Analysis

Traditionally the tuning of frequency and damping has been based on the dynamic amplification of the structural mass, given by the absolute value of Eq. (9). In this section the classical analysis is supplemented by consideration of the dynamic amplitude of the relative motion of the damper. In the mechanical design of tuned mass dampers the relative motion of the damper mass plays an important role as the magnitude may be restricted due to practical considerations.

3.1 Frequency Tuning. The dynamic amplification factor (9) is shown as a function of frequency in Fig. 2. It is a remarkable fact that there are two excitation frequencies ω_A and ω_B around the natural frequency ω_0 for which the magnitude of the response is independent of the damping parameter c. The neutral frequencies ω_A and ω_B are found by studying the structure of the dynamic amplification formula (9)

$$\frac{x_0}{F/k_0} = \frac{A + 2i\zeta_d B}{C + 2i\zeta_d D} \Rightarrow \left|\frac{x_0}{F/k_0}\right|^2 = \frac{A^2 + (2\zeta_d)^2B^2}{C^2 + (2\zeta_d)^2D^2} \tag{13}$$

For the magnitude to be independent of ζ_d the following ratios must be equal

$$\frac{A^2}{C^2} = \frac{B^2}{D^2} \Rightarrow \frac{A}{C} = \pm\frac{B}{D} \tag{14}$$

corresponding to

$$AD = \pm BC \tag{15}$$

Substitution of A B, C, and D gives, after canceling the common factor ω/ω_d,

$$\omega^4 - [\omega_0^2 + (1+\mu)\omega_d^2]\omega^2 + \omega_0^2\omega_d^2 = \pm(\omega_d^2 - \omega^2)[\omega_0^2 - (1+\mu)\omega^2] \tag{16}$$

Use of the plus sign leads to the root $\omega=0$. This is the static solution where there is no motion, and therefore no damping force. Use of the minus sign leads to the following quadratic equation in ω_A^2 and ω_B^2

$$(2+\mu)\omega^4 - 2[\omega_0^2 + (1+\mu)\omega_d^2]\omega^2 + 2\omega_0^2\omega_d^2 = 0 \tag{17}$$

The roots of this quadratic are denoted ω_A^2 and ω_B^2 corresponding to the points in Fig. 2. The roots are not needed explicitly at this point, but only in the form of their sum following from the coefficients of the equation

$$\omega_A^2 + \omega_B^2 = \frac{2}{2+\mu}[\omega_0^2 + (1+\mu)\omega_d^2] \tag{18}$$

The optimal damping parameters are determined by specifying equal magnitude of the dynamic amplification factor at the frequencies ω_A and ω_B. At these frequencies the response magnitude is independent of ζ_d, and the relevant response can therefore be determined for the limit $\zeta_d \rightarrow \infty$, corresponding to the combined mass m_0+m moving as a unit

$$\left|\frac{x_0}{F/k_0}\right|_{A,B} = \frac{\pm 1}{1-(1+\mu)(\omega/\omega_0)^2} \tag{19}$$

where plus applies to ω_A below the resonance frequency ω_0, while the minus applies to ω_B above. Thus equal dynamic amplification at ω_A and ω_B requires

$$\frac{1}{1-(1+\mu)(\omega_A/\omega_0)^2} = \frac{-1}{1-(1+\mu)(\omega_B/\omega_0)^2} \tag{20}$$

Multiplication with the denominators gives

$$\omega_A^2 + \omega_B^2 = \frac{2\omega_0^2}{1+\mu} \tag{21}$$

This is the condition that the points A and B have the same dynamic amplification. The tuning frequency ω_d now follows from setting the right-hand sides of Eqs. (18) and (21) equal.

$$\omega_d = \frac{\omega_0}{1+\mu} \tag{22}$$

This is the classic tuning frequency [3], and as demonstrated in Sec. 4.2 this tuning also leads to desirable modal damping properties.

3.2 Optimal Damping Ratio. The dynamic amplification at the frequencies ω_A and ω_B is determined by considering the quadratic equation (17) for the special tuning (22). In terms of the frequency $\omega_\infty=(\omega_0\omega_d)^{1/2}$ corresponding to a locked damper the equation is

$$\omega^4 - 2\omega_\infty^2\omega^2 + \frac{2\omega_\infty^4}{2+\mu} = 0 \tag{23}$$

with the solution

$$\left(\frac{\omega_{A,B}}{\omega_\infty}\right)^2 = 1 \pm \sqrt{\frac{\mu}{2+\mu}} \tag{24}$$

Substitution of these frequencies back into the dynamic amplification expression (19) for infinite damping then gives

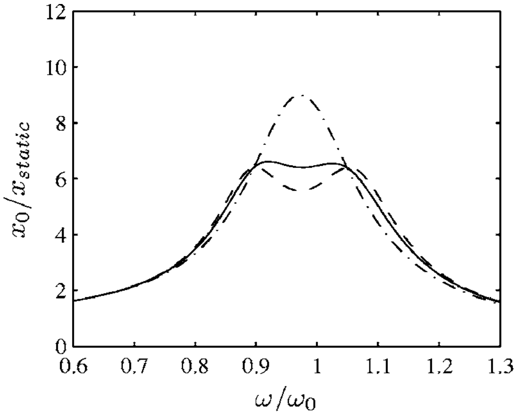

Fig. 3 Dynamic amplification of structural mass for $\mu=0.05$ and damping parameter: (---) ζ_{classic}, (—) ζ_{opt}, (-·-) ζ_*

$$\left|\frac{x_0}{F/k_0}\right|_{A,B} = \sqrt{\frac{2+\mu}{\mu}} \tag{25}$$

In practice the mass of the secondary structure is most often considerably less than that of the primary structure, and thus the dynamic amplification at the neutral frequencies is approximately $(2/\mu)^{1/2}$, i.e., inversely proportional to the square root of the mass ratio.

A simple and direct way to determine a suitable value of the damping ratio ζ_d consists in selecting a frequency located centrally in the interval between ω_A and ω_B, and selecting ζ_d such that the dynamic amplification is equal at these three frequencies. It is convenient to use the frequency ω_∞ of the system with locked damper introduced in Eq. (12). In fact it follows from Eq. (21) that ω_∞^2 is also the arithmetic mean of the neutral frequencies ω_A^2 and ω_B^2. The complex response amplitude and the dynamic amplification factor at ω_∞ follow from Eq. (9) as

$$\frac{x_0}{F/k_0} = \frac{\mu - 2i\zeta_d\sqrt{1+\mu}}{\mu} \Rightarrow \left|\frac{x_0}{F/k_0}\right|^2_{\omega_\infty} = \frac{\mu^2 + (2\zeta_d)^2(1+\mu)}{\mu^2} \tag{26}$$

By equating the dynamic amplification at ω_∞ to that at ω_A and ω_B given by Eq. (25) the optimal damping ratio is determined as

$$\zeta_{\text{opt}}^2 = \frac{1}{2}\frac{\mu}{1+\mu} \tag{27}$$

This value is larger than that of the classic presentation of Den Hartog [3], originally derived by Brock [4]. In the formula proposed by Brock the optimal parameter ζ_d^2 is found as the arithmetic mean of the values that give maximum dynamic amplification at the frequencies ω_A and ω_B, respectively. This leads to

$$\zeta_{\text{classic}}^2 = \frac{3}{8}\frac{\mu}{1+\mu} \tag{28}$$

The value ζ_{opt} is seen to be 15% larger than ζ_{classic}, and it will be demonstrated later that this implies 15% larger damping of the modes. It is interesting to note that in practical design of tuned mass dampers values of the damping parameter larger than ζ_{classic} are often used [8].

The dynamic amplification for mass ratio $\mu=0.05$ is illustrated in Fig. 3 for three different values of the damping parameter. The full line corresponds to ζ_{opt}, while the dashed line corresponds to the classic value ζ_{classic}. It is seen that the classic value of the damping parameter leads to a trough between the neutral values at ω_A and ω_B. It is demonstrated later that with the frequency tuning determined by Eq. (22) the modal damping attains a maximum value for $\zeta_* = \sqrt{2}\zeta_{\text{opt}}$. This value of the damping parameter may be

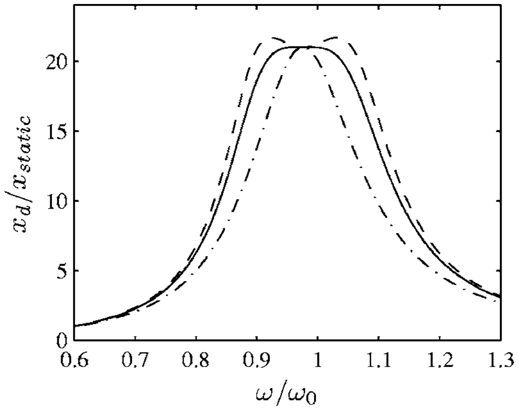

Fig. 4 Amplitude of relative damper motion $\mu=0.05$ and damping parameter: (---) ζ_{classic}, (—) ζ_{opt}, (-·-) ζ_*

considered as an upper value for applications, and the corresponding dynamic amplification is also shown in the figure. It is seen that this value leads to a peak between the neutral frequencies ω_A and ω_B. The value ζ_{opt} leads to a fairly level behavior of the curve between the neutral frequencies.

The choice of the value (27) of the damping parameter as optimal is further supported by considering the relative motion of the damped mass. It is seen from Eq. (10) that the relative motion of the damped mass x_d is independent of the damping at the frequency ω_∞. When the damper frequency is tuned according to Eq. (22) the motion of the damped mass at the neutral frequency ω_∞ is

$$\left|\frac{x_d}{F/k_0}\right|_{\omega_\infty} = \frac{1+\mu}{\mu} \tag{29}$$

For small damping ratio this gives a relative motion of the damper mass of order μ^{-1}. As it is desirable to limit the relative motion of the damper the neutral value at ω_∞ should be a maximum. The effect of the damping parameter ζ_d on the relative motion is illustrated in Fig. 4 using the same parameters as in the previous figure. It is seen that the parameter value ζ_{classic} leads to larger values of the relative motion at frequencies above and below ω_∞. The value ζ_* leads to a curve with a narrow peak at the frequency ω_∞. It is easily demonstrated that the value ζ_{opt} corresponds exactly to the transition between negative and positive curvature at ω_∞, and therefore gives the flattest maximum at the neutral point. Thus, the value ζ_{opt} constitutes the best combination of flat behavior of the dynamic amplification curve and limited relative motion of the damper mass.

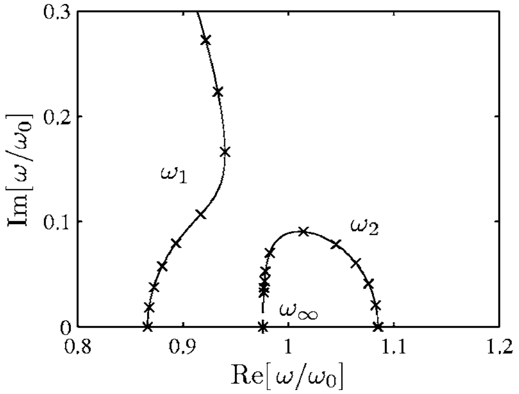

Fig. 5 Locus of modal frequencies, $\mu=0.05$ and $\omega_d/\omega_0=0.94$

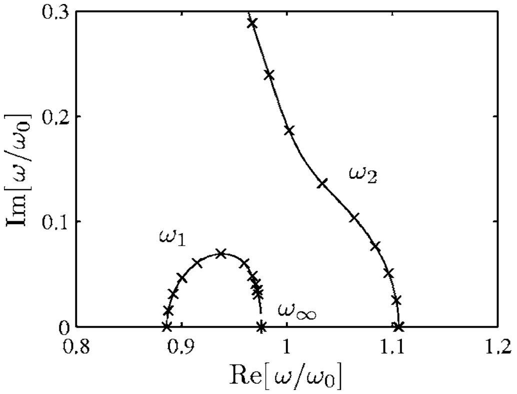

Fig. 6 Locus of modal frequencies, $\mu=0.05$ and $\omega_d/\omega_0=0.98$

4 Complex Frequencies

The vibration properties of the tuned mass damper are characterized by the natural frequencies of the free vibration modes, determined as the complex roots of the normalized frequency equation (11). For a given mass ratio μ the vibration properties are determined by the frequency tuning in terms of the ratio ω_d/ω_0 and the damping ratio ζ_d. The effect of frequency tuning is illustrated in Figs. 5–7 showing the locus of the complex natural frequencies ω_1 and ω_2 in terms of the damping parameter ζ_d for the fixed mass ratio $\mu=0.05$. At zero damping the natural frequencies ω_1 and ω_2 are located on the real axis, and as a matter of notation the branches are determined by $\omega_1 < \omega_2$ for zero damping. When damping is introduced the roots move into the positive imaginary half-plane. This is illustrated in the figures by marking the points corresponding to $\zeta_d=0, 0.04, 0.08, \ldots$ with crosses. Figure 5 shows the case of frequency tuning by $\omega_d/\omega_0=0.94$. In this case it is seen that the branch corresponding to ω_2 forms a local curve ending at the frequency ω_∞ corresponding to locking of the damper. In contrast the branch corresponding to ω_1 has non-local character with an increasing imaginary part. Figure 6 shows the case of frequency tuning by the slightly larger value $\omega_d/\omega_0=0.98$. In this case the characteristics of the branches corresponding to ω_1 and ω_2 are interchanged. Now the branch corresponding to ω_1 is local, while the branch corresponding to ω_2 has non-local character with increasing imaginary part.

4.1 The Frequency Bifurcation Point. For topological reasons the transition between the two situations shown in Figs. 5 and 6 must involve intersection of the two branches at a bifurcation point ω_*. This case is shown in Fig. 7 where the branches corresponding to ω_1 and ω_2 meet at a bifurcation point ω_*. For

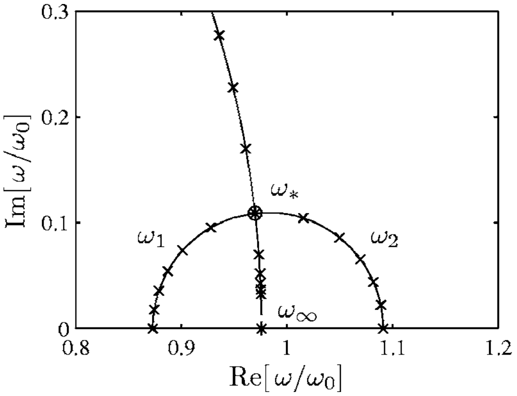

Fig. 7 Locus of modal frequencies, $\mu=0.05$ and $\omega_d/\omega_0=(1+\mu)^{-1}$

higher values of the damping parameter ζ_d the branches split into a decreasing branch ending at ω_∞ and an increasing branch of non-local character. For frequency tuning corresponding to existence of a bifurcation point the maximum modal damping is obtained at the bifurcation point ω_*, and it is of interest to determine the appropriate frequency tuning and the damping parameter ζ_* corresponding to the bifurcation point.

At moderate damping the full solution of the quartic frequency equation (11) contains four roots, ω_1 and ω_2 located in the first quadrant, and the symmetrically located roots $-\bar{\omega}_1$ and $-\bar{\omega}_2$ in the second quadrant with the bar symbol denoting the complex conjugate. For sufficiently large damping the non-local pair of roots may meet at a bifurcation point on the imaginary axis and continue as a pair of imaginary roots, however the main interest with respect to damping properties is in the local branches. The case of a local bifurcation frequency ω_* implies that the quartic frequency can be expressed as

$$(\omega - \omega_*)^2(\omega + \bar{\omega}_*)^2 = 0 \tag{30}$$

This equation may be written in a form similar to Eq. (11),

$$\omega^4 - 4i\,\mathrm{Im}[\omega_*]\omega^3 - (2|\omega_*|^2 + 4\,\mathrm{Im}[\omega_*]^2)\omega^2 + 4i\,\mathrm{Im}[\omega_*]|\omega_*|^2\omega + |\omega_*|^4 = 0 \tag{31}$$

The tuning condition, the bifurcation frequency ω_*, and the corresponding damping ratio ζ_* now follow from comparison of coefficients of this equation and the original frequency equation (11). The magnitude of the bifurcation frequency $|\omega_*|$ follows directly from the ratio of the coefficients to the linear and cubic terms, whereby

$$|\omega_*| = \frac{\omega_0}{\sqrt{1+\mu}} = \omega_\infty \tag{32}$$

Thus, the bifurcation frequency ω_* is located on a circle around the center of the complex plane with radius ω_∞. The frequency tuning corresponding to the existence of a bifurcation point then follows by comparison of the constant term in the two equations. The result is $\omega_d = \omega_\infty^2/\omega_0$, giving the value (22) already determined by the condition of equal dynamic amplification at the neutral frequencies.

The damping parameter ζ_* at the bifurcation point is obtained by comparison of the coefficient to the quadratic term in the two equations

$$\omega_0^2 + (1+\mu)\omega_d^2 = 2|\omega_*|^2 + 4\,\mathrm{Im}[\omega_*]^2 = 2\omega_0\omega_d + (\zeta_*\omega_0)^2 \tag{33}$$

where the term $\mathrm{Im}[\omega_*]^2$ has been eliminated by use of the coefficients to the linear and cubic terms. Substitution of the tuning frequency ω_d from Eq. (22) then gives the damping parameter at the bifurcation point

$$\zeta_*^2 = \frac{\mu}{1+\mu} \tag{34}$$

This value was used to illustrate the effect of the damping parameter on dynamic amplification and relative motion of the damper mass in Figs. 3 and 4.

The modal damping is defined as the relative magnitude of the imaginary part of the modal frequency

$$\zeta_j = \frac{\mathrm{Im}[\omega_j]}{|\omega_j|}, \quad j = 1,2 \tag{35}$$

The common modal damping coefficient ζ at the bifurcation point is then determined by the coefficient to the linear term in the frequency equation (11),

$$\zeta = \frac{\zeta_*}{2}\frac{\omega_0}{\omega_\infty} = \frac{\sqrt{\mu}}{2}, \quad \zeta_d = \zeta_* \tag{36}$$

As the mass ratio of a tuned mass damper is usually small, the frequency of the system is not changed substantially by addition of the extra mass m and therefore $\omega_\infty \simeq \omega_0$. At the bifurcation point the modal damping is proportional to the square root of the mass ratio, and it is seen that it corresponds to about half the damping ratio ζ_* in the tuned mass damper. This result will be generalized in the following to damping ratios below the bifurcation value.

4.2 Equal Modal Damping. At the particular damper frequency tuning (22) the frequency equation can be written in the symmetric normalized form

$$\omega^4 - 2i\zeta_d\sqrt{1+\mu}\,\omega_\infty\omega^3 - (2+\mu)\omega_\infty^2\omega^2 + 2i\zeta_d\sqrt{1+\mu}\,\omega_\infty^3\omega + \omega_\infty^4 = 0 \tag{37}$$

where ω_∞ defined in Eq. (12) serves as a convenient reference frequency. It follows from this equation that the product of the four roots is equal to ω_∞^4. This in connection with the location of corresponding roots shown in Fig. 7 leads to the hypothesis that for damping below the bifurcation value, $\zeta_d \leqslant \zeta_*$, the roots in the first quadrant are inverse points with respect to a circle centered at origo with radius ω_∞. This hypothesis is verified by the following analysis.

If ω_1 and ω_2 are inverse points with respect to the circle with radius ω_∞ they satisfy the relation

$$\omega_1\bar{\omega}_2 = \bar{\omega}_1\omega_2 = \omega_\infty^2 \tag{38}$$

Based on the hypothesis of the roots as inverse points the roots in the first and second quadrant of the complex plane are ω_j, $\omega_\infty^2/\bar{\omega}_j$, $-\bar{\omega}_j$ and $-\omega_\infty^2/\omega_j$ with $j=1$ or 2. This implies that the frequency equation can be written as

$$(\omega - \omega_j)(\omega - \omega_\infty^2/\bar{\omega}_j)(\omega + \bar{\omega}_j)(\omega + \omega_\infty^2/\omega_j) = 0 \tag{39}$$

This equation can be reorganized into a symmetric format similar to that of Eq. (37)

$$\omega^4 - 2i\frac{\mathrm{Im}[\omega_j]}{|\omega_j|}\left(\frac{|\omega_j|}{\omega_\infty} + \frac{\omega_\infty}{|\omega_j|}\right)\omega_\infty\omega^3 - \left(\frac{|\omega_j|^2}{\omega_\infty^2} + \frac{\omega_\infty^2}{|\omega_j|^2} + 4\frac{\mathrm{Im}[\omega_j]^2}{|\omega_j|^2}\right)\omega_\infty^2\omega^2 + 2i\frac{\mathrm{Im}[\omega_j]}{|\omega_j|}\left(\frac{|\omega_j|}{\omega_\infty} + \frac{\omega_\infty}{|\omega_j|}\right)\omega_\infty^3\omega + \omega_\infty^4 = 0 \tag{40}$$

In this form it is clearly seen that the coefficients depend on the roots through two properties: the relative magnitude of the imaginary part,

$$\zeta = \frac{\mathrm{Im}[\omega_j]}{|\omega_j|}, \quad j = 1,2 \tag{41}$$

and the combination of the magnitudes of the frequencies

$$r = \frac{1}{2}\left(\frac{|\omega_j|}{\omega_\infty} + \frac{\omega_\infty}{|\omega_j|}\right) = \frac{|\omega_1| + |\omega_2|}{2\omega_\infty} \tag{42}$$

The parameter ζ is the modal damping ratio, which by the assumed inverse point property is identical for the two modes. The parameter r is equal to the normalized arithmetic mean of the normalized magnitude of the two modal frequencies. It follows from its original definition in terms of $|\omega_j|$ that $r \geqslant 1$. The parameter r assumes its largest value for the undamped modes at zero damping, and decreases to the value $r=1$ at the bifurcation point.

In terms of the parameters ζ and r the frequency equation (40) becomes

$$\omega^4 - 4i\zeta r\omega_\infty\omega^3 - (4r^2 - 2 + 4\zeta^2)\omega_\infty^2\omega^2 + 4i\zeta r\omega_\infty^3\omega + \omega_\infty^4 = 0 \tag{43}$$

This equation permits unique determination of the parameters ζ and r by comparison of the coefficients with the frequency equation (37) and thereby confirms the inverse point hypothesis for damping parameter values below the bifurcation value ζ_*. The coefficients to the first and second degree terms give

$$2\zeta r = \zeta_d \sqrt{1+\mu} \tag{44a}$$

$$r^2 + \zeta^2 = 1 + \tfrac{1}{4}\mu \tag{44b}$$

The first equation immediately gives a useful result for the modal damping, when written in the form

$$\zeta = \frac{\sqrt{1+\mu}}{r}\frac{\zeta_d}{2}\,, \quad \zeta_d \leqslant \zeta_* \tag{45}$$

In practice the mass ratio μ is small and r is close to unity. Thus, the modal damping ratio ζ is approximately half of the value of the damping parameter ζ_d, with an upper limit of $\sqrt{\mu}/2$ reached at the bifurcation point.

Equation (44) is symmetric in the unknown variables r and ζ. The distinction is made by observing that $r \geqslant 1$ and $0 \leqslant \zeta < 1$. The formulation takes a particularly simple form, when the damping parameter ζ_d is normalized with respect to its value ζ_* at the bifurcation point, given by Eq. (34). When the first equation is used to eliminate ζ^2 from the second, the following quadratic equation in r^2 is obtained

$$r^4 - \left(1 + \tfrac{1}{4}\mu\right) r^2 + \tfrac{1}{4}\mu(\zeta_d/\zeta_*)^2 = 0 \tag{46}$$

The modal damping ratio ζ satisfies the same equation. With reference to the remark made about the magnitude of r and ζ the solution is

$$\left.\begin{matrix} r^2 \\ \zeta^2 \end{matrix}\right\} = \tfrac{1}{2}\left(1 + \tfrac{1}{4}\mu\right) \pm \tfrac{1}{2}\sqrt{\left(1 + \tfrac{1}{4}\mu\right)^2 - \mu(\zeta_d/\zeta_*)^2} \tag{47}$$

This solution is non-linear in the damping ratio μ. However, in practice the damping ratio will be much smaller than unity, and thus a satisfactory approximation can be obtained by linearizing the square root, whereby

$$r^2 \simeq 1 + \frac{\mu}{4}\left[1 - \left(\frac{\zeta_d}{\zeta_*}\right)^2\right], \quad \zeta \simeq \frac{\sqrt{\mu}}{2}\frac{\zeta_d}{\zeta_*} \tag{48}$$

These approximate relations contain the correct limits with r^2 decreasing from $1 + \frac{1}{4}\mu$ to 1, and ζ increasing from 0 to $\frac{1}{2}\sqrt{\mu}$, when the damping parameter ζ_d increases from zero to the bifurcation value $\zeta_* = \sqrt{\mu/(1+\mu)}$. In fact, the relations (48) satisfy Eq. (44*b*) identically, and the parameter in this approximation may therefore be considered as a preliminary estimate of ζ_d for which the correct value is found by substitution of the representation (48) into (44*a*). The difference between the preliminary estimate and the actual value of ζ_d is negligible for the range of mass ratios used in practice.

4.3 The Full Frequency Locus. For optimal frequency tuning the full solution for the complex free vibration frequencies can be found in explicit form by the following procedure. The quartic frequency equation (37) is divided by $\omega^2\omega_\infty^2$ and written in the symmetric form

$$\left(\frac{\omega}{\omega_\infty} - \frac{\omega_\infty}{\omega}\right)^2 - 2i\zeta_d\sqrt{1+\mu}\left(\frac{\omega}{\omega_\infty} - \frac{\omega_\infty}{\omega}\right) - \mu = 0 \tag{49}$$

It is seen that if ω is replaced by $\omega_\infty^2/\bar{\omega}$ the equation is merely replaced by its conjugate. Thus, if ω is a root, so is $\omega_\infty^2/\bar{\omega}$. This property has already been exploited for ζ_d below the bifurcation value ζ_*, where the roots in the first and second quadrant form pairs on a line from origo. For damping parameter values larger than the bifurcation value ζ_* this relation implies that the roots are located on a circle with radius ω_∞ or as an inverse pair on the imaginary axis. This behavior is illustrated in Fig. 8 and analyzed in the following.

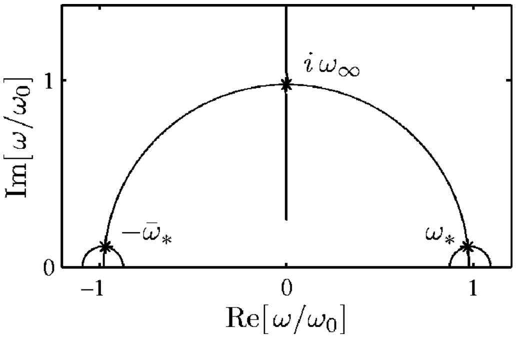

Fig. 8 Locus of modal frequencies, μ=0.05 and ω_d/ω_0=(1+μ)$^{-1}$

Equation (49) is a quadratic equation in the variable

$$2iw = \frac{\omega}{\omega_\infty} - \frac{\omega_\infty}{\omega} \tag{50}$$

with the solution

$$w = \frac{\sqrt{\mu}}{2}\left[\frac{\zeta_d}{\zeta_*} \pm \sqrt{\left(\frac{\zeta_d}{\zeta_*}\right)^2 - 1}\right] \tag{51}$$

where the damping parameter ζ_d has been normalized by the bifurcation value ζ_* from Eq. (34). The definition (50) of w in turn leads to the following quadratic equation for the frequencies

$$\left(\frac{\omega}{\omega_\infty}\right)^2 - 2iw\left(\frac{\omega}{\omega_\infty}\right) - 1 = 0 \tag{52}$$

The solution of this equation is

$$\frac{\omega}{\omega_\infty} = iw \pm \sqrt{1 - w^2} \tag{53}$$

Expressions (51) and (53) with four independent choices of the signs form a parametric representation of the locus of the four complex free vibration frequencies in terms of the mass ratio μ and the damping parameter ζ_d.

The locus of the complex frequencies is illustrated in Fig. 8 for μ=0.05. The roots depend on the magnitude of the damping parameter ζ_d. For zero damping the roots lie on the real axis with the positive values

$$\frac{\omega_{1,2}}{\omega_\infty} = \sqrt{1 + \frac{1}{4}\mu} \mp \sqrt{\frac{1}{4}\mu}\,, \quad \zeta_d = 0 \tag{54}$$

As the damping ratio increases to ζ_* the roots form curves meeting at the bifurcation point

$$\frac{\omega_*}{\omega_\infty} = \sqrt{1 - \frac{1}{4}\mu} + i\sqrt{\frac{1}{4}\mu}\,, \quad \zeta_d = \zeta_* \tag{55}$$

in the first quadrant and the symmetrically located bifurcation point in the second quadrant. As ζ_d increases beyond the bifurcation value ζ_* both values of the variable w become real and positive. For $|w| \leqslant 1$ expression (53) describes part of a circle with radius ω_∞. When the larger of the roots w reaches the value 1 the corresponding frequency becomes imaginary, with value $\omega = i\omega_\infty$, representing a non-local bifurcation point. This point is reached for

$$2\frac{\zeta_d}{\zeta_*} = \frac{\sqrt{\mu}}{2} + \frac{2}{\sqrt{\mu}} \tag{56}$$

The minimum value of $\zeta_d = \zeta_*$ at the non-local bifurcation point is reached for μ=4. It is seen from Eq. (55) that this is also the limit for positive imaginary part of the local bifurcation point. Thus, the topology shown in Fig. 8 is limited to mass ratio less than four. However, this greatly exceeds the values of practical interest, typically in the interval $0 < \mu < 0.1$, and the figure is therefore representative for typical application situations.

5 Conclusions

The design of tuned mass dampers involves the selection of mass ratio, frequency tuning, and damping parameter. It is desirable to use a small mass ratio in order to introduce a minimum of extra weight in the structure, and the problem then is to optimize tuning frequency and damping parameter. For harmonic load it is natural to consider the motion of the structural mass and the relative motion of the damper as function of frequency. The dynamic amplification of the motion of the structural mass has two neutral frequencies, at which the amplification does not depend on the introduced damping. Similarly the relative motion of the damped mass has a neutral frequency, where the motion is independent of damping. Optimal frequency tuning can be identified by the classic procedure of requiring equal amplification of the motion of the structural mass at the two neutral frequencies. A new criterion for the optimal damping level has been proposed based on simultaneous conditions on the dynamic amplification of the motion of the structural mass and the relative motion of the damper mass at the frequency corresponding to free vibrations of the combined mass with the damper locked. This criterion leads to an applied optimal damping ratio that is 15% larger than the classic value, and the analysis presented demonstrates that this results in a similar increase in the resulting modal damping of the system. Damping values smaller than this will lead to undesirable additional relative motion of the damper mass at frequencies around that corresponding to common motion of the total mass.

In many design situations the load may be transient or involve a frequency spectrum. In those cases it is of particular interest to know the damping ratio of the modes. It has been demonstrated that for the classic tuning of the damper frequency the complex locus of the natural frequencies has a bifurcation point corresponding to maximum damping of the modes. The corresponding damping represents an upper limit for damping that can be usefully introduced into the system. When the imposed damping is less than the limiting value it has been demonstrated that both modes have identical damping ratio, and that this damping ratio is approximately half of that used in the damper.

Acknowledgment

This work has been supported by the Danish Technical Research Council through the project “Damping Mechanisms in the Dynamics of Structures and Materials.”

References

[1] Frahm, H., 1909, “Device for Damped Vibrations of Bodies,” U.S. Patent No. 989958, October 30.

[2] Ormondroyd, J., and Den Hartog, J. P., 1928, “The Theory of the Dynamic Vibration Absorber,” Trans. ASME, **50**, pp. 9–22.

[3] Den Hartog, J. P., 1956, *Mechanical Vibrations*, 4th ed., McGraw-Hill, New York. (Reprinted by Dover, New York. 1985).

[4] Brock, J. E., 1946, “A Note on the Damped Vibration Absorber,” J. Appl. Mech., **13** p. A284.

[5] Warburton, G. B., 1982, “Optimum Absorber Parameters for Various Combinations of Response and Excitation Parameters,” Earthquake Eng. Struct. Dyn., **10**, pp. 381–401.

[6] Soong, T. T., and Dargush, G. F., 1997, *Passive Energy Dissipation Systems in Structural Engineering*, Wiley, Chichester, UK.

[7] Asami, T., Nishihara, O., and Baz, A. M., 2002, “Analytical Solution to H_∞ and H_2 Optimization of Dynamic Vibration Absorbers Attached to Damped Linear Systems,” J. Vibr. Acoust., **124**, pp. 284–295.

[8] Dalmer, F., private communication, GERB Schwingungsisolierungen, Essen.

On Scattering in a Piezoelectric Medium by a Conducting Crack

Shaofan Li[1]
e-mail: li@ce.Berkeley.edu

Albert C. To

Steven D. Glaser

Department of Civil and Environmental
Engineering,
University of California,
Berkeley, CA 94720

The work is concerned with the characterization of a Kirchhoff diffraction field in a piezoelectric material. An exact solution is obtained for the full scattering fields around the tip of a semi-infinite crack, which is electrically conducting and is loaded with both SH acoustic incident waves and in-plane electrical incident waves. First, it is found that a conducting crack in a piezoelectric solid is not completely opaque to the electro-acoustic wave, i.e., the electro-acoustic wave can penetrate and transmit to the other side of the crack surface. Second, the analysis has confirmed that the interaction between electrical wave and acoustic wave will provide multiple electrical and electro-acoustic head waves. Third, by solving the problem, we have established a rigorous electro-acoustic scattering theory in piezoelectric/ferroelectric media, which is different from the scattering theory in purely elastic media. The characterization of the scattering fields in piezoelectric media provides a unique signature database for electro-acoustic waves in piezoelectric materials. [DOI: 10.1115/1.2047627]

1 Introduction

Wave scattering theory in piezoelectric/ferroelectric materials has been an important research area for many years (e.g., [1]), and it is the very foundation of sensor technology because piezoelectric/ferroelectric ceramics and thin films are extensively used in the design of various sensors, transducers, and actuators (e.g., [2–6] and many others).

These devices are widely used in various micro-electro-mechanical systems, which include acoustic devices, optical wave devices and surface wave devices (SAW), integrated circuits, and random access memories. Nevertheless, traditional scattering theory has been mainly focused on electric wave scattering without considering electro-acoustic coupling effects. Recently, there are interests in studies on scattering of electro-acoustic waves by defects in piezoelectric/ferroelectric media, e.g., [7,8].

In fact, electro-acoustic wave scattering phenomena in sensors and thin films may be more important than purely electric wave scattering, because it is not only pertinent to the performance of the devices but also nondestructive evaluation of such devices (e.g., [9]). Surprisingly, the scattering theory of electro-acoustic waves in piezoelectric materials has rarely been studied, and it remains an open research subject. A lesser-known reason attributed to the fact is that the initial boundary value problem of the fully coupled Maxwell-Christoffel equations in piezoelectric materials are too complicated to solve, and the simplified wave equations under quasi-static approximation are not mathematically well-posed (see [10,11]). This theoretical inadequacy has, at least partly, attributed to the lack of understanding in electro-acoustic wave scattering theory.

To regularize wave equations in piezoelectric media while still retaining the simplicity of the quasi-static approximation, a few regularization procedures have been proposed recently. We would like to mention the contribution made by Li [12,13] and Daros [14]. Recent developments intend to provide a theoretical ground to establish a rigorous electro-acoustic wave scattering theory for piezoelectric materials. The first systematic effort of establishing an electro-acoustic scattering wave theory in piezoelectric materials has been performed in [15]. However, the solution obtained in [15] is limited by a special assumption that the electric potential in front of the crack tip is zero, which may not be valid in general cases. Moreover, the scattering fields due to an electric source have not been discussed [15].

The objective of this work is to establish a rigorous theory for electro-acoustic wave scattering in piezoelectric materials. In this work, we revisit the electro-acoustic wave scattering theory of piezoelectric materials. In specific, we shall seek to characterize the scattering fields generated by a conducting anti-plane crack (mode III) in a piezoelectric material, which is subjected to both plane SH incident acoustic waves and plane electrical incident waves. Using the standard terminology in wave mechanics, we are seeking the solution for a benchmark problem of wave mechanics in a piezoelectric medium, i.e., Kirchhoff diffraction in a piezoelectric medium. *It should be noted that although the analysis of electro-acoustic scatterings by a mode III crack may be simpler than that of in-plane crack, it does provide the essential characters for the in-plane crack scattering phenomena as well.*

The motivation for doing so is twofold: (1) the Kirchhoff diffraction is often used to describe a (scalar) wave scattering field due to a monochromatic line or point source in the presence of an “opaque” (e.g., electrically conducting) screen. Despite skepticism that the model lacks “physical ground,” the solution of a Kirchhoff field in a piezoelectric medium is an exact solution to the coupled wave equations, which *exactly obeys definite, though unusual, boundary conditions [16,17]*, and hence it will become an essential part of the theoretical foundation for other scattering problems from screens that have general impedance properties; (2) For many sensors and transducers, electric loading is applied by using thin electrode layers attached on a surface or embedded in an interface of a piezoelectric block or between ferroelectric thin films. Thus, discontinuous electrode layers are widely used in various layered devices in order to fulfill the designed purposes. *Recently, interfacial fracture between embedded electrode layers and ceramic layers has been identified as a major failure mode in sensors (e.g., by Suo [18,19] and Ru [20])*. For more background information, readers may consult works by Ru et al. [21,20], Winzer et al. [22], Furuta and Uchino [23] Aburatani et al. [24], Freiman and White [25], Hao et al. [26], and Uchino [6].

It may be more practical to find a scattering field by a permeable or an impermeable crack (e.g., [27–29]). Nonetheless, it is the opinion of the authors that a sensible and an appropriate de-

---

[1] To whom correspondence should be addressed.

Contributed by the Applied Mechanics Division of THE AMERICAN SOCIETY OF MECHANICAL ENGINEERS for publication in the ASME JOURNAL OF APPLIED MECHANICS. Manuscript received by the Applied Mechanics Division December 25, 2004; final revision April 9, 2005. Review conducted by Z. Suo. Discussion on the paper should be addressed to the Editor, Prof. Robert M. McMeeking, Journal of Applied Mechanics, Department of Mechanical and Environmental Engineering, University of California—Santa Barbara, Santa Barbara, CA 93106-5070, and will be accepted until four months after final publication in the paper itself in the ASME JOURNAL OF APPLIED MECHANICS.

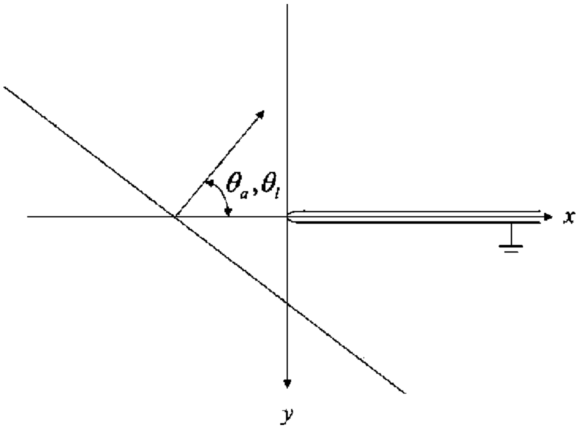

Fig. 1 Schematic illustration of a system of plane waves due to an incident acoustic wave approaching a semi-infinite crack

parture point for establishing a rigorous electro-acoustic wave scattering theory in piezoelectric media is to first study the Kirchhoff diffraction of electro-acoustic waves.

The presentation of the paper is organized in six sections: The initial boundary value problem of the scattering problem is set in Sec. 2. In Sec. 3, the main procedure solution is discussed; Sec. 4 provides a full characterization of the scattering fields in front of the crack tip, and in Sec. 5, the features of the scattering fields are discussed in details. At last, a few concluding remarks are made in Sec. 6.

2 The Scattering Problem

2.1 Formulation. Consider a transversely isotropic piezoelectric space that contains a semi-infinite slit, which lies at $y=0$ and $x\geqslant 0$ with respect to a Cartesian coordinate system (x,y,z) shown in Fig. 1. It is assumed that the interface slit is mechanically stress free and short circuited and has a vanishingly small thickness.

For the diffraction problem considered in this paper, the relevant electromechanical coupling on the transverse plane is between anti-plane displacement and in-plane electric field,

$$\mathbf{u} = (0,0,w(x,y,t)) \tag{1}$$

$$\mathbf{E} = \left(-\frac{\partial\phi}{\partial x}, -\frac{\partial\phi}{\partial y}, 0\right). \tag{2}$$

Following [12], we introduce a pseudo-electric wave potential function

$$\psi = \phi - \frac{e_{15}}{\epsilon_{11}} C_f w \tag{3}$$

where $C_f := c_\ell^2/(c_\ell^2 - c_a^2)$, e_{15} is the piezoelectric stress constant, and ϵ_{11} is the specific dielectric constant. $c_\ell := (\epsilon_{11}\mu_0)^{-1/2}$ is the speed of light and $c_a := \sqrt{\bar{c}_{44}/\rho}$ is the acoustic speed, where $\bar{c}_{44} := c_{44}^E + e_{15}^2/\epsilon_{11}$, μ_0 is the magnetic permeability constant in vacuum, and c_{44}^E is the purely elastic shear modulus in the transverse direction.

Based on the "quasi-hyperbolic approximation" introduced by Li [15], we can then derive a set of decoupled wave equations,

$$\left(\frac{\partial^2}{\partial x^2} + \frac{\partial^2}{\partial y^2} - \frac{1}{c_a^2}\frac{\partial^2}{\partial t^2}\right) w = 0 \tag{4}$$

$$\left(\frac{\partial^2}{\partial x^2} + \frac{\partial^2}{\partial y^2} - \frac{1}{c_\ell^2}\frac{\partial^2}{\partial t^2}\right) \psi = 0. \tag{5}$$

Under the quasi-hyperbolic approximation, the relevant constitutive equations are

$$\sigma_{xz} = \tilde{c}_{44}\frac{\partial w}{\partial x} + e_{15}\frac{\partial \psi}{\partial x} \tag{6}$$

$$\sigma_{yz} = \tilde{c}_{44}\frac{\partial w}{\partial y} + e_{15}\frac{\partial \psi}{\partial y} \tag{7}$$

$$D_x = e_{15}(1 - C_f)\frac{\partial w}{\partial x} - \epsilon_{11}\frac{\partial \psi}{\partial x}. \tag{8}$$

$$D_y = e_{15}(1 - C_f)\frac{\partial w}{\partial y} - \epsilon_{11}\frac{\partial \psi}{\partial y} \tag{9}$$

where $\tilde{c}_{44} := \bar{c}_{44}[1 - (1 - C_f)(e_{15}^2/\bar{c}_{44}\epsilon_{11})]$.

2.2 The Scattering Problem. For time $t<0$, an incident SH acoustic plane wave or an incident pseudo-electric wave propagates from afar toward the semi-infinite slit. The incident plane waves are assumed to have the following form:

$$w^{(i)}(x,y,t) = w_0^{(i)} G(t - s_a[\cos(\theta_a)x - \sin(\theta_a)y]) \tag{10}$$

$$\psi^{(i)}(x,y,t) = \psi_0^{(i)} G(t - s_\ell[\cos(\theta_\ell)x - \sin(\theta_\ell)y]) \tag{11}$$

where the subscripts "a" and "ℓ" correspond to the acoustic and pseudo-electric waves. $w_0^{(i)}$ and $\psi_0^{(i)}$ are the respective plane wave amplitudes and $s_a := 1/c_a$ and $s_\ell := 1/c_\ell$ are the respective slownesses. $0 \leqslant \theta_a, \theta_\ell \leqslant \pi/2$ are angles of incident waves. The shape function $G(\cdot)$ is a real-valued function defined to be

$$G(t) := H(t)\int_0^t g(\tau)d\tau \tag{12}$$

where $g(\cdot)$ is a given real value function, and $H(t)$ is the Heaviside function. For simplicity, it is assumed that both the incident acoustic and pseudo-electric waves have the same shape functions. In the case that they are different, superposition can be used to obtain the solution due to linearity of the problem.

Although the material properties in the upper and lower half spaces are identical, it may be more convenient to treat them separately for the time being. The field variables in the upper half space $(y\leqslant 0)$ and in the lower half space $(y>0)$ are labeled by the superscripts u and l, respectively. At time $t=0$, the incident plane wave arrives at the crack tip and is being scattered. The total solutions of the scattering problem are

$$w(x,y,t) = w^{(i)}(x,y,t) + w^{(s)}(x,y,t), \tag{13}$$

$$\psi(x,y,t) = \psi^{(i)}(x,y,t) + \psi^{(s)}(x,y,t). \tag{14}$$

The superscript "(i)" indicates the incident field and "(s)" indicates the scattering field.

For a conducting crack, the crack surface is traction-free and electrically grounded,

$$\sigma_{yz}^u(x,0,t) = \sigma_{yz}^l(x,0,t) = 0, \quad x \geqslant 0 \tag{15}$$

$$\phi^u(x,0,t) = \phi^l(x,0,t) = 0, \quad x \geqslant 0 \tag{16}$$

and ahead of the crack tip both mechanical and electrical displacements are continuous,

$$w^u(x,0,t) = w^l(x,0,t), \quad x < 0 \tag{17}$$

$$D_y^u(x,0,t) = D_y^l(x,0,t), \quad x < 0. \tag{18}$$

Consideration of Eqs. (13)–(18) leads to the following set of boundary conditions for the scattered waves:

$$\sigma_{yz}^{u(s)}(x,0,t) = \sigma_{yz}^{l(s)}(x,0,t) = -\sigma_{yz}^{(i)}(x,0,t), \quad x \geqslant 0 \tag{19}$$

$$\phi^{u(s)}(x,0,t) = \phi^{l(s)}(x,0,t) = -\phi^{(i)}(x,0,t), \quad -x > 0 \tag{20}$$

$$w^{u(s)}(x,0,t) = w^{l(s)}(x,0,t), \quad x < 0 \tag{21}$$

$$D_y^u(x,0,t) = D_y^l(x,0,t), \quad x < 0. \tag{22}$$

For scattering fields, the following initial conditions and radiation conditions are imposed as

$$w^{(s)}(x,y,t) = \dot{w}^{(s)}(x,y,t) = 0, \quad t < 0 \tag{23}$$

$$\psi^{(s)}(x,y,t) = \dot{\psi}^{(s)}(x,y,t) = 0, \quad t < 0 \tag{24}$$

and

$$\lim_{r\to\infty}(w^{(s)}, \psi^{(s)}, \dot{w}^{(s)}, \dot{\psi}^{(s)}) = 0, \quad t > 0 \tag{25}$$

Since the incident and total displacement fields and pseudo-electric potential obey the wave equations (4) and (5), by virtue of (13) and (14), the scattered displacement field $w^{(s)}$ and the scattered pseudo-electric potential $\psi^{(s)}$ must also obey the same equations. For simplicity, the superscript "(s)" denoting the scattering fields is dropped in the rest of the paper if no confusion may occur.

3 Solution Procedures

3.1 Transform Methods. In this section, the standard procedure of multiple Laplace transforms is employed to seek the solution of the above mixed initial boundary value problem. The multiple transforms are introduced for the variable pair (x,t). To suppress the time variable t, the usual, one-sided Laplace transform is applied:

$$f^*(x,y,p) = \int_0^\infty f(x,y,t)\exp(-pt)dt, \tag{26}$$

$$f(x,y,t) = \frac{1}{2\pi i}\int_{Br_1} f^*(x,y,p)\exp(pt)dp, \tag{27}$$

where the inversion integration is taken over the usual Bromwich path.

To suppress the spatial variable x, the two-sided Laplace transform is used:

$$\hat{f}^*(\zeta,y,p) = \int_{-\infty}^\infty f^*(x,y,p)\exp(-p\zeta x)dx \tag{28}$$

$$f^*(x,y,p) = \frac{p}{2\pi i}\int_{Br_2} \hat{f}^*(\zeta,y,p)\exp(p\zeta x)d\zeta \tag{29}$$

After transformation, the governing equations (4) and (5) for the scattered waves become

$$\left(\frac{d^2}{dy^2} - p^2\alpha^2(\zeta)\right)\hat{w}^*(\zeta,y,p) = 0 \tag{30}$$

$$\left(\frac{d^2}{dy^2} - p^2\beta^2(\zeta^2)\right)\hat{\psi}^*(\zeta,y,p) = 0 \tag{31}$$

where $\alpha(\zeta) := \sqrt{s_a^2 - \zeta^2}$ and $\beta(\zeta) := \sqrt{s_\ell^2 - \zeta^2}$.

To satisfy the boundary conditions at infinity, we choose the solution of the following form:

$$\left.\begin{aligned} \hat{w}^{l*}(\zeta,y,p) &= \frac{1}{p^2}A^l(\zeta)\exp(-p\alpha y) \\ \hat{\psi}^{l*}(\zeta,y,p) &= \frac{1}{p^2}B^l(\zeta)\exp(-p\beta y) \end{aligned}\right\} y > 0, \tag{32}$$

$$\left.\begin{aligned} \hat{w}^{u*}(\zeta,y,p) &= -\frac{1}{p^2}A^u(\zeta)\exp(p\alpha y) \\ \hat{\psi}^{u*}(\zeta,y,p) &= -\frac{1}{p^2}B^u(\zeta)\exp(p\beta y) \end{aligned}\right\} y < 0. \tag{33}$$

In Eqs. (32) and (33), $\mathrm{Re}(\alpha(\zeta), \beta(\zeta)) \geqslant 0$ in the plane with branch cuts:

$$\alpha: \quad \mathrm{Im}(\zeta) = 0, \quad \mathrm{Re}(\zeta) < -s_a, \quad \text{and} \quad \mathrm{Re}(\zeta) > s_a, \tag{34}$$

$$\beta: \quad \mathrm{Im}(\zeta) = 0, \quad \mathrm{Re}(\zeta) < -s_\ell, \quad \text{and} \quad \mathrm{Re}(\zeta) > s_\ell. \tag{35}$$

3.2 The Wiener-Hopf Decomposition. A powerful technique to find the solution in transformed space is the Wiener-Hopf decomposition. To apply the Wiener-Hopf technique, it is expedient to expand the mechanical and electrical boundary conditions over the full range of the x axis. This can be done by introducing two unknown functions:

$$\sigma_-(x,t) := \begin{cases} \sigma_{yz}^l(x,0,t) = \sigma_{yz}^u(x,0,t) & x < 0, \\ 0 & x \geqslant 0, \end{cases} \tag{36}$$

$$\phi_-(x,t) := \begin{cases} \phi^l(x,0,t) = \phi^u(x,0,t) & x < 0, \\ 0 & x \geqslant 0, \end{cases} \tag{37}$$

$$\Delta w_+(x,t) := \begin{cases} 0 & x < 0, \\ w^l(x,0,t) - w^u(x,0,t) & x \geqslant 0, \end{cases} \tag{38}$$

$$\Delta D_+(x,t) := \begin{cases} 0 & x < 0, \\ D_y^l(x,0,t) - D_y^u(x,0,t) & x \geqslant 0. \end{cases} \tag{39}$$

so that

$$\sigma_{yz}^l(x,0,t) = \sigma_{yz}^u(x,0,t) = \sigma_-(x,t) - \sigma_{yz}^{(i)}(x,0,t), \quad -\infty < x < \infty \tag{40}$$

$$\phi^l(x,0,t) = \phi^u(x,0,t) = \phi_-(x,t) - \phi^{(i)}(x,0,t), \quad -\infty < x < \infty \tag{41}$$

$$w^l(x,0,t) - w^u(x,0,t) = 0 + \Delta w_+(x,t), \quad -\infty < x < \infty \tag{42}$$

$$D_y^l(x,0,t) - D_y^u(x,0,t) = 0 + \Delta D_+(x,t), \quad -\infty < x < \infty. \tag{43}$$

After suppressing both x and t,

$$\hat{\sigma}_{yz}^{l*}(\zeta,0,p) = \hat{\sigma}_{yz}^{u*}(\zeta,0,p) = \frac{\Sigma_-(\zeta)}{p} - \hat{\sigma}_{yz}^{*(i)}(\zeta,0,p) \tag{44}$$

$$\hat{\phi}^{l*}(\zeta,0,p) = \hat{\phi}^{u*}(\zeta,0,p) = \frac{\Phi_-(\zeta)}{p^2} - \hat{\phi}^{*(i)}(\zeta,0,p) \tag{45}$$

$$\frac{\hat{w}^{l*}(\zeta,0,p) - \hat{w}^{u*}(\zeta,0,p)}{2} = \frac{\Delta U_+(\zeta)}{p^2} \tag{46}$$

$$\frac{\hat{D}_y^{l*}(\zeta,0,p) - \hat{D}_y^{u*}(\zeta,0,p)}{2} = \frac{\Delta D_+(\zeta)}{p} \tag{47}$$

where

$$\Sigma_-(\zeta) := p\int_{-\infty}^0 \sigma_-^*(x,p)\exp(-p\zeta x)dx \tag{48}$$

$$\Phi_-(\zeta) := p^2\int_{-\infty}^0 \phi_-^*(x,p)\exp(-p\zeta x)dx \tag{49}$$

$$\Delta U_+(\zeta) := p^2\int_0^\infty \frac{\Delta w_+^*(x,p)}{2}\exp(-p\zeta x)dx \tag{50}$$

$$\Delta D_+(\zeta) := p\int_0^\infty \frac{\Delta D_+^*(x,p)}{2}\exp(-p\zeta x)dx \tag{51}$$

On the other hand, employing the constitutive equations (6)–(9) and substituting the general solutions and (32) and (33) into Eqs. (48)–(51), one may obtain the following sets of equations:

$$\hat{\sigma}_{yz}^{l*} + \hat{\sigma}_{yz}^{u*} \Rightarrow -\hat{c}_{44}\alpha(\zeta)A_{sy}(\zeta) - e_{15}\beta(\zeta)B_{sy}(\zeta) = \Sigma_-(\zeta) - p\hat{\sigma}_{yz}^{*(i)} \tag{52}$$

$$\hat{\phi}^{l*} - \hat{\phi}^{u*} \Rightarrow \frac{e_{15}}{\epsilon_{11}}C_f A_{sy}(\zeta) + B_{sy}(\zeta) = 0 \tag{53}$$

$$\hat{w}^{l*} - \hat{w}^{u*} \Rightarrow A_{sy} = \Delta U_+(\zeta) \tag{54}$$

$$\hat{\phi}^{l*} + \hat{\phi}^{u*} \Rightarrow \frac{e_{15}}{\epsilon_{11}}C_f A_{an}(\zeta) + B_{an}(\zeta) = \Phi_-(\zeta) - p^2\hat{\phi}^{*(i)} \tag{55}$$

$$\hat{\sigma}_{yz}^{l*} - \hat{\sigma}_{yz}^{u*} \Rightarrow -\tilde{c}_{44}\alpha(\zeta)A_{an}(\zeta) - e_{15}\beta(\zeta)B_{an}(\zeta) = 0 \tag{56}$$

$$\hat{D}_y^{l*} - \hat{D}_y^{u*} \Rightarrow -e_{15}(1-C_f)\alpha(\zeta)A_{an}(\zeta) + \epsilon_{11}\beta B_{an}(\zeta) = \Delta D_+(\zeta) \tag{57}$$

where $A_{sy}(\zeta)=[A^l(\zeta)+A^u(\zeta)]/2$, $A_{an}(\zeta)=[A^l(\zeta)-A^u(\zeta)]/2$, $B_{sy}(\zeta)=[B^l(\zeta)+B^u(\zeta)]/2$, and $B_{an}(\zeta)=[B^l(\zeta)-B^u(\zeta)]/2$. Now, from these equations, it becomes obvious that two decoupled Wiener-Hopf equations can be obtained:

$$-BG(\zeta)\Delta U_+(\zeta) = \Sigma_-(\zeta) - p\hat{\sigma}_{yz}^{*(i)}(\zeta,0,p) \tag{58}$$

$$\frac{BG(\zeta)\Delta D_+(\zeta)}{\alpha(\zeta)\beta(\zeta)[e_{15}^2(1-C_f)+\epsilon_{11}\tilde{c}_{44}]} = \Phi_-(\zeta) - p^2\hat{\phi}^{*(i)}(\zeta,0,p) \tag{59}$$

where

$$BG(\zeta) = \tilde{c}_{44}(\alpha(\zeta) - \tilde{k}_e^2\beta(\zeta)) \tag{60}$$

is recognized as the Bleustein-Gulyaev wave function [30,31], and $\tilde{k}_e^2$ is the electro-mechanical coupling coefficient:

$$\tilde{k}_e^2 := \frac{e_{15}^2}{\epsilon_{11}\tilde{c}_{44}}C_f. \tag{61}$$

The terms $\hat{\sigma}_{yz}^{*(i)}(\zeta,0,p)$ and $\hat{\phi}^{*(i)}(\zeta,0,p)$ in Eqs. (58) and (59) are dependent on the type of incident waves. Employing the incident acoustic wave field and pseudo-electric wave field in Eqs. (10) and (11) and the constitutive equations for stress and electric potential in (7) and (9), one may obtain the stress and electric potential for an incident wave:

$$\hat{\sigma}_{yz}^{*(i)}(\zeta,0,p) = -\frac{\sigma_0 g^*(p)}{p(\zeta+s_h)} \tag{62}$$

$$\hat{\phi}^{*(i)}(\zeta,0,p) = -\frac{\phi_0 g^*(p)}{p^2(\zeta+s_h)} \tag{63}$$

where

$$\sigma_0 = -\bar{c}_{44}s_a\sin(\theta_a)w_0^{(i)} \tag{64}$$

$$\phi_0 = -\frac{e_{15}}{\epsilon_{11}}C_f w_0^{(i)} \tag{65}$$

$$s_h = s_a\cos(\theta_a) \tag{66}$$

for an incident acoustic wave $w^{(i)}$, whereas for an incident pseudo-electric wave $\psi^{(i)}$,

$$\sigma_0 = -e_{15}s_\ell\sin(\theta_\ell)\psi_0^{(i)} \tag{67}$$

$$\phi_0 = -\psi_0^{(i)} \tag{68}$$

$$s_h = s_\ell\cos(\theta_\ell). \tag{69}$$

For convenience, define the Bleustein-Gulyaev wave velocity and slowness:

$$c_{bg} := c_a\sqrt{\tilde{C}_f(1-k_e^4)} \quad \text{and } s_{bg} := 1/c_{bg}, \tag{70}$$

where

$$\tilde{C}_f := \frac{c_\ell^2}{c_\ell^2 - \tilde{k}_e^4 c_a^2}. \tag{71}$$

The detailed solutions to the two Wiener-Hopf equations (58) and (59) are presented in the Appendix, and the main results are

$$A_{sy}(\zeta) = -\frac{\sigma_0 g^*(p)\sqrt{s_a+\zeta}R_-(-s_h)}{(\zeta+s_h)(s_{bg}+\zeta)D_s\mathcal{T}_+(\zeta)}, \tag{72}$$

$$B_{sy}(\zeta) = \frac{e_{15}C_f\sigma_0 g^*(p)\sqrt{s_a+\zeta}R_-(-s_h)}{\epsilon_{11}(\zeta+s_h)(s_{bg}+\zeta)D_s\mathcal{T}_+(\zeta)}, \tag{73}$$

$$A_{an}(\zeta) = -\frac{\phi_0 g^*(p)\sqrt{s_a+\zeta}\sqrt{s_\ell+\zeta}S_-(-s_h)e_{15}}{\sqrt{s_a-\zeta}(s_{bg}+\zeta)\mathcal{T}_+(\zeta)D_s}, \tag{74}$$

$$B_{an}(\zeta) = \frac{\phi_0 g^*(p)(s_a+\zeta)S_-(-s_h)\tilde{c}_{44}}{\sqrt{s_\ell-\zeta}(s_{bg}+\zeta)\mathcal{T}_+(\zeta)D_s}, \tag{75}$$

where $R_-(\zeta)$ and $\mathcal{T}_+(\zeta)$ are sectionally analytic functions given in the Appendix.

To this end, from Eqs. (72)–(75), the coefficients of $A^l(\zeta)$, $B^l(\zeta)$, $A^u(\zeta)$, and $B^u(\zeta)$ can be found:

$$A^l(\zeta) = A_{sy}(\zeta) + A_{an}(\zeta) = -\left(\sigma_0 + \frac{e_{15}\sqrt{s_\ell+\zeta}\sqrt{s_a+s_h}\sqrt{s_\ell+s_h}}{\sqrt{s_a-\zeta}}\phi_0\right)K(\zeta), \tag{76}$$

$$B^l(\zeta) = B_{sy}(\zeta) + B_{an}(\zeta) = \left(\frac{e_{15}}{\epsilon_{11}}C_f\sigma_0 + \frac{\tilde{c}_{44}\sqrt{s_a+\zeta}\sqrt{s_a+s_h}\sqrt{s_\ell+s_h}}{\sqrt{s_\ell-\zeta}}\phi_0\right)K(\zeta), \tag{77}$$

$$A^u(\zeta) = A_{sy}(\zeta) - A_{an}(\zeta) = -\left(\sigma_0 - \frac{e_{15}\sqrt{s_\ell+\zeta}\sqrt{s_a+s_h}\sqrt{s_\ell+s_h}}{\sqrt{s_a-\zeta}}\phi_0\right)K(\zeta), \tag{78}$$

$$B^u(\zeta) = B_{sy}(\zeta) - B_{an}(\zeta) = \left(\frac{e_{15}}{\epsilon_{11}}C_f\sigma_0 - \frac{\tilde{c}_{44}\sqrt{s_a+\zeta}\sqrt{s_a+s_h}\sqrt{s_\ell-s_h}}{\sqrt{s_\ell-\zeta}}\phi_0\right)K(\zeta), \tag{79}$$

where

$$K(\zeta) := \left(\frac{g^*(p)(s_{bg}-\zeta)\sqrt{s_a+s_h}\mathcal{T}_-(\zeta)}{(\zeta+s_h)\sqrt{s_a-\zeta}(s_{bg}+s_h)\mathcal{T}_-(-s_h)BG(\zeta)}\right). \tag{80}$$

Substituting Eqs. (76)–(79) into Eqs. (32) and (33) and performing an inverse transform, one obtains the scattered displacement and pseudo-electric wave fields:

$$w^*(x,y,p) = -\frac{1}{2\pi ip}\int_{\zeta_\alpha-i\infty}^{\zeta_\alpha+i\infty}\left\{\left(\sigma_0 + \text{sgn}(y)\frac{e_{15}\sqrt{s_\ell+\zeta}\sqrt{s_a+s_h}\sqrt{s_\ell+s_h}}{\sqrt{s_a-\zeta}}\phi_0\right)\cdot K(\zeta)\right\} \times\exp[-p(\alpha(\zeta)\text{sgn}(y)y-\zeta x)]d\zeta, \tag{81}$$

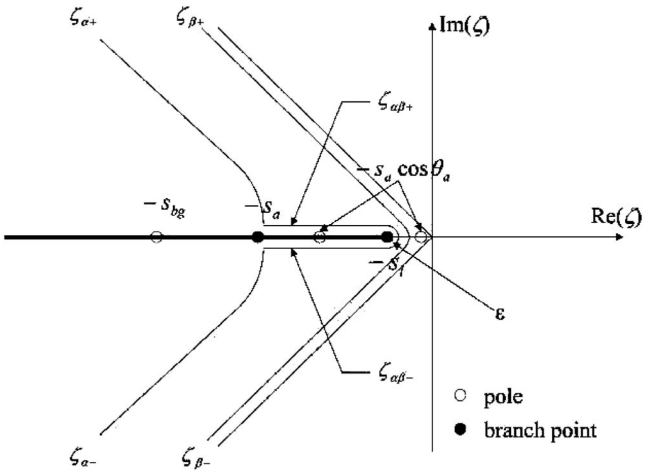

Fig. 2 The Cagniard-deHoop inversion paths Γ_α, Γ_β, and $\Gamma_{\alpha\beta}$ for acoustic excitation

$$\psi^*(x,y,p)=\frac{1}{2\pi ip}\int_{\zeta_\beta-i\infty}^{\zeta_\beta+i\infty}\left[\left(\frac{e_{15}}{\epsilon_{11}}C_f\sigma_0+\operatorname{sgn}(y)\frac{\tilde{c}_{44}\sqrt{s_a+\zeta}\sqrt{s_a+s_h}\sqrt{s_\ell+s_h}}{\sqrt{s_\ell-\zeta}}\phi_0\right)\cdot K(\zeta)\right]\times\exp[-p(\beta(\zeta)\operatorname{sgn}(y)y-\zeta x)]d\zeta. \tag{82}$$

4 Scattering Fields

4.1 Cagniard-deHoop Inversion. Having carried out the Wiener-Hopf decomposition, we are now in a position to invert the integrals in Eqs. (81) and (82) to obtain explicit solutions in the physical domain. The exact inversion can be achieved by the Cagniard-de Hoop scheme [32,33]. First, the scattered displacement and the pseudo-electric potential fields for an incident acoustic wave are considered so that $s_h=s_a\cos(\theta_a)$ in the integrals. We proceed by replacing the original Bromwich path by a deformed Cagniard contour such that the one-sided Laplace transform can be obtained by inspection. In the following, the inversion procedure is presented only for $y>0$; the inversion procedure for $y<0$ is identical and is omitted.

Shown in Fig. 2, the following inversion paths are chosen: Γ_α, $\Gamma_{\alpha\beta}$, and Γ_β, in which

$$\begin{aligned}\alpha(\zeta)y-\zeta x=t,\quad &\zeta\in\Gamma_\alpha,\Gamma_{\alpha\beta}\\ \beta(\zeta)y-\zeta x=t,\quad &\zeta\in\Gamma_\beta.\end{aligned}\tag{83}$$

Let $x=r\cos\theta$ and $y=r\sin\theta$. One then has

$$\zeta_{\alpha\pm}=\frac{1}{r}\left(-t\cos\theta\pm i\sin\theta\sqrt{t^2-s_a^2r^2}\right),\quad s_ar\leqslant t<\infty \tag{84}$$

$$\zeta_{\alpha\beta\pm}=\frac{1}{r}\left(-t\cos\theta\pm\sin\theta\sqrt{s_a^2r^2-t^2}\right)\pm i\epsilon,\quad t_{\alpha0}\leqslant t<s_ar \tag{85}$$

$$\zeta_{\beta\pm}=\frac{1}{r}\left(-t\cos\theta\pm i\sin\theta\sqrt{t^2-s_\ell^2r^2}\right),\quad s_\ell r\leqslant t\leqslant\infty \tag{86}$$

where $t_{\alpha0}=\sqrt{s_a^2-s_\ell^2}y+s_\ell x$.

It should be noted that at $\zeta=-s_a\cos\theta$, the path Γ_α intercepts the real axis Re(ζ). Thus, a supplement path $\Gamma_{\alpha\beta}$ is needed to circumvent the branch cut of multivalued function $\beta(\zeta)=\sqrt{s_\ell^2-\zeta^2}$. This leads to the occurrence of the electroacoustic head wave (see discussions in [13] as well as [15]). Along path $\Gamma_{\alpha\beta}$, the parameter θ varies in the range

$$0\geqslant\theta\geqslant\theta_{cr}^{a\ell} \tag{87}$$

where $\theta_{cr}^{a\ell}:=|\cos^{-1}(s_\ell/s_a)|$.

Following de Hoop [33], one may show that

$$\frac{\partial\zeta_{\alpha\pm}}{\partial t}=\frac{\pm i\alpha(\zeta_{\alpha\pm})}{\sqrt{t^2-s_a^2r^2}};\quad \alpha(\zeta_{\alpha\pm})=\frac{\sin\theta}{r}t\pm i\frac{\cos\theta}{r}\sqrt{t^2-s_a^2r^2}; \tag{88}$$

$$\frac{\partial\zeta_{\alpha\beta\pm}}{\partial t}=\frac{\mp\alpha(\zeta_{\alpha\beta\pm})}{\sqrt{s_a^2r^2-t^2}};\quad \alpha(\zeta_{\alpha\beta\pm})=\frac{\sin\theta}{r}t\pm\frac{\cos\theta}{r}\sqrt{s_a^2r^2-t^2}; \tag{89}$$

$$\frac{\partial\zeta_{\beta\pm}}{\partial t}=\frac{\pm i\beta(\zeta_{\beta\pm})}{\sqrt{t^2-s_\ell^2r^2}};\quad \beta(\zeta_{\beta\pm})=\frac{\sin\theta}{r}t\pm i\frac{\cos\theta}{r}\sqrt{t^2-s_\ell^2r^2}; \tag{90}$$

and subsequently exact inversions are found:

$$\begin{aligned}w^{(s)}(x,y,t)&=\int_0^t G(t-\tau)w_\delta^{(s)}(x,y,\tau)d\tau+w_r^{(s)}(x,y,t)\\ \psi^{(s)}(x,y,t)&=\int_0^t G(t-\tau)\psi_\delta^{(s)}(x,y,\tau)d\tau+\psi_r^{(s)}(x,y,t)\end{aligned}\tag{91}$$

where the subscript "δ" represents the scattering fields due to the impulsive incident wave, and $w_r^{(s)}$, $\psi_r^{(s)}$ are reflected/refracted displacement and pseudo-electric fields.

$$\begin{aligned}w_\delta^{(s)}(x,y,t)=-\frac{1}{\pi}\Bigg\{&\Re\left[\left(\sigma_0+\operatorname{sgn}(y)\frac{e_{15}\sqrt{s_\ell+\zeta_{\alpha+}}\sqrt{s_a+s_h}\sqrt{s_\ell+s_h}}{\sqrt{s_a-\zeta_{\alpha+}}}\phi_0\right)\cdot\left(\frac{(s_{bg}-\zeta_{\alpha+})\sqrt{s_a+s_h}\mathcal{T}_-(\zeta_{\alpha+})}{(\zeta_{\alpha+}+s_h)\sqrt{s_a-\zeta_{\alpha+}}(s_{bg}+s_h)\mathcal{T}_-(-s_h)BG(\zeta_{\alpha+})}\right)\frac{\alpha(\zeta_{\alpha+})}{\sqrt{t^2-s_a^2r^2}}\right]\\ &\cdot H(t-s_ar)-\Im\left[\left(\sigma_0+\operatorname{sgn}(y)\frac{e_{15}\sqrt{s_\ell+\zeta_{\alpha\beta+}}\sqrt{s_a+s_h}\sqrt{s_\ell+s_h}}{\sqrt{s_a-\zeta_{\alpha\beta+}}}\phi_0\right)\cdot\left(\frac{(s_{bg}-\zeta_{\alpha\beta+})\sqrt{s_a+s_h}\mathcal{T}_-(\zeta_{\alpha\beta+})}{(\zeta_{\alpha\beta+}+s_h)\sqrt{s_a-\zeta_{\alpha\beta+}}(s_{bg}+s_h)\mathcal{T}_-(-s_h)BG(\zeta_{\alpha\beta+})}\right)\right.\\ &\left.\times\frac{\alpha(\zeta_{\alpha\beta+})}{\sqrt{t^2-s_a^2r^2}}\right]\cdot[H(t-t_{\alpha0})-H(t-s_ar)]\Bigg\},\end{aligned}\tag{92}$$

$$\psi_\delta^{(s)}(x,y,t)=\frac{1}{\pi}\left[\left(\frac{e_{15}}{\epsilon_{11}}C_f\sigma_0+\operatorname{sgn}(y)\frac{\tilde{c}_{44}\sqrt{s_a+\zeta_{\beta+}}\sqrt{s_a+s_h}\sqrt{s_\ell+s_h}}{\sqrt{s_\ell-\zeta_{\beta+}}}\phi_0\right)\left(\frac{(s_{bg}-\zeta_{\beta+})\sqrt{s_a+s_h}\mathcal{T}_-(\zeta_{\beta+})}{(\zeta_{\beta+}+s_h)\sqrt{s_a-\zeta_{\beta+}}(s_{bg}+s_h)\mathcal{T}_-(-s_h)BG(\zeta_{\beta+})}\right)\frac{\beta(\zeta_{\beta+})}{\sqrt{t^2-s_\ell^2r^2}}\right]\cdot H(t-s_\ell r). \tag{93}$$

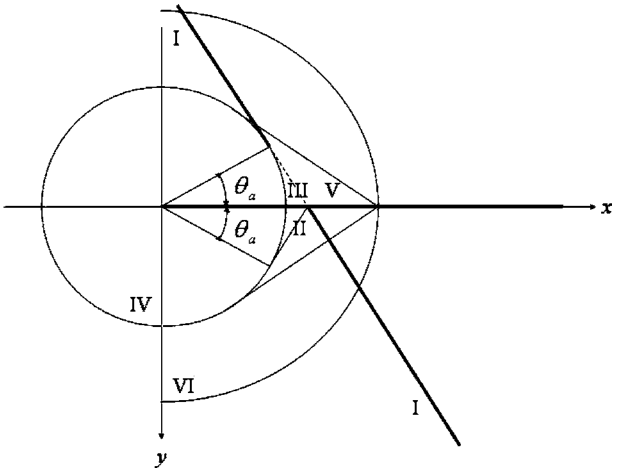

Fig. 3 The scattering patterns excited by an acoustic source: case (1)

4.2 Scattering Fields in Front of the Crack Tip. Scattering fields due to different incident waves in front of the crack tip are discussed as follows:

4.2.1 Incident Acoustic Plane Wave. In diffraction theory, both the acoustic and the electromagnetic, the simple pole that represents the incident source determines the geometrical reflection/refraction patterns. These geometrical scattering patterns induced by acoustic excitation depend on the incident angle of the acoustic wave, because the position of simple pole relies on the angle of incident acoustic wave. Figure 2 shows that there are two different positions of the simple pole, $\zeta=-s_h=-s_a\cos(\theta_a)$, and the positions of $-s_h$ in the ζ plane will directly affect the outcome of the reflection and refraction fields. There are basically two cases:

(1) $s_a\cos(\theta_a)>s_\ell$

In this case, the pole always lies to the right of Γ_α but to the left of Γ_β and $\Gamma_{\beta'}$. This means that there are pole contributions to the paths Γ_α, but no contributions to the paths Γ_β. After evaluating the residues of the poles for the corresponding integral in (81) and (82), we have

$$w_r^{(s)}(x,y,t)=\begin{cases}\mathfrak{R}\left(\dfrac{s_a\sin(\theta_a)+\tilde{k}_e^2\sqrt{s_\ell^2-[s_a\cos(\theta_a)]^2}}{s_a\sin(\theta_a)-\tilde{k}_e^2\sqrt{s_\ell^2-[s_a\cos(\theta_a)]^2}}\right)\cdot w_o^{(i)}G(t-s_a[\cos(\theta_a)x+\sin(\theta_a)y]) & \\ -\mathfrak{I}\left(\dfrac{s_a\sin(\theta_a)+\tilde{k}_e^2\sqrt{s_\ell^2-[s_a\cos(\theta_a)]^2}}{s_a\sin(\theta_a)-\tilde{k}_e^2\sqrt{s_\ell^2-[s_a\cos(\theta_a)]^2}}\right)\cdot w_o^{(i)}\mathcal{H}\{G(t-s_a[\cos(\theta_a)x+\sin(\theta_a)y])\}, & 0\leqslant\theta<\theta_a;\\ 0, & \theta_a\leqslant\theta<\pi;\\ 0, & \pi\leqslant\theta<2\pi-\theta_a;\\ -w_o^{(i)}G(t-s_a[\cos(\theta_a)x-\sin(\theta_a)y]), & 2\pi-\theta_a\leqslant\theta<2\pi,\end{cases} \tag{94}$$

$$\psi_r^{(s)}(x,y,t)=\begin{cases}0, & 0\leqslant\theta<\pi;\\ 0, & \pi\leqslant\theta<2\pi;\end{cases} \tag{95}$$

where the Hilbert transform $\mathcal{H}\{\cdot\}$ is defined as

$$\mathcal{H}\{f(t)\}=\frac{1}{\pi}PV\int_{-\infty}^{\infty}\frac{f(\tau)}{\tau-t}d\tau, \tag{96}$$

where *PV* denotes the Cauchy principal value.

The complete scattering pattern is shown in Fig. 3. Note that the refracted acoustic wave (dashed line in the figure) completely cancels the incident acoustic wave.

(2) $s_\ell\geqslant s_a\cos(\theta_a)$

In this case, the pole lies to the right of all the paths, and, therefore, after evaluating the residues of the poles for all the corresponding integrals, we have

$$w_r^{(s)}(x,y,t)=\begin{cases}\left(\dfrac{s_a\sin(\theta_a)+\tilde{k}_e^2s_\ell\sin(\theta_\ell)}{s_a\sin(\theta_a)-\tilde{k}_e^2s_\ell\sin(\theta_\ell)}\right)\cdot w_o^{(i)}G(t-s_a[\cos(\theta_a)x+\sin(\theta_a)y]), & 0\leqslant\theta<\theta_a;\\ 0, & \theta_a\leqslant\theta<\pi;\\ 0, & \pi\leqslant\theta<2\pi-\theta_a;\\ -w_o^{(i)}G(t-s_a[\cos(\theta_a)x-\sin(\theta_a)y]), & 2\pi-\theta_a\leqslant\theta<2\pi,\end{cases} \tag{97}$$

$$\psi_r^{(s)}(x,y,t)=\begin{cases}\left(\dfrac{-2e_{15}C_f s_a\sin(\theta_a)}{\epsilon_{11}(s_a\sin(\theta_a)-\tilde{k}_e^2 s_\ell\sin(\theta_\ell))}\right)\cdot w_o^{(i)}G(t-[s_a\cos(\theta_a)x+s_\ell\sin(\theta_\ell)y]), & 0\leqslant\theta<\theta_\ell;\\ 0, & \theta_\ell\leqslant\theta<\pi;\\ 0, & \pi\leqslant\theta<2\pi-\theta_\ell;\\ 0, & 2\pi-\theta_\ell\leqslant\theta<2\pi.\end{cases}\tag{98}$$

The complete scattering pattern is shown in Fig. 4. Again, the refracted acoustic wave (dashed line in the figure) completely cancels the incident acoustic wave.

In both cases, one can observe that a refracted acoustic wave is passing through the slit, which will not happen in purely elastic media.

4.2.2 Incident Electric Plane Wave. As shown in Fig. 5, the simple pole $\zeta=-s_h=-s_\ell\cos(\theta_\ell)$ always lies to the right of all the integration paths, and thus the residue of the pole due to the corresponding integral needs to be evaluated. Therefore, the reflection and refraction fields due to an incident pseudo-electric source are

$$w_r^{(s)}(x,y,t)=\begin{cases}\left(\dfrac{2e_{15}s_\ell\sin(\theta_\ell)}{\tilde{c}_{44}(s_a\sin(\theta_a)-\tilde{k}_e^2 s_\ell\sin(\theta_\ell))}\right)\cdot\psi_o^{(i)}G(t-[s_\ell\cos(\theta_\ell)x+s_a\sin(\theta_a)y]), & 0\leqslant\theta<\theta_a;\\ 0, & \theta_a\leqslant\theta<\pi;\\ 0, & \pi\leqslant\theta<2\pi-\theta_a;\\ 0, & 2\pi-\theta_a\leqslant\theta<2\pi,\end{cases}\tag{99}$$

$$\psi_r^{(s)}(x,y,t)=\begin{cases}-\left(\dfrac{s_a\sin(\theta_a)+\tilde{k}_e^2 s_\ell\sin(\theta_\ell)}{s_a\sin(\theta_a)-\tilde{k}_e^2 s_\ell\sin(\theta_\ell)}\right)\cdot\psi_o^{(i)}G(t-s_\ell[\cos(\theta_\ell)x+\sin(\theta_\ell)y]), & 0\leqslant\theta<\theta_\ell;\\ 0, & \theta_\ell\leqslant\theta<\pi;\\ 0, & \pi\leqslant\theta<2\pi-\theta_\ell;\\ -\psi_o^{(i)}G(t-s_\ell[\cos(\theta_\ell)x-\sin(\theta_\ell)y]), & 2\pi-\theta_\ell\leqslant\theta<2\pi.\end{cases}\tag{100}$$

The complete scattering pattern is shown in Fig. 6. Note that the refracted electric wave (dashed line in the figure) completely cancels the incident electric wave.

5 Discussions

5.1 Displacement Time History. With the analytical expressions of the diffracted waves, the displacement time history at a fixed point can be traced and calculated during the electroacoustic scattering so that we may be able to compare them with the measurements obtained in the nondestructive testing. Figures 7 and 8 show the displacement time histories at various θ with fixed y in the upper half space due to an impulsive incident acoustic source and an electric source, respectively, with Fig. 7 corresponding to acoustic source case (1) in the previous section. Recall that θ is measured clockwise beginning from the x axis, so that with y fixed, $\theta=-90$ deg in both figures is closest to the crack tip while $\theta=-10$ deg is the farthest. A distinctive feature of scattering by a conducting crack is the ability of the head wave to tunnel through the crack, a phenomenon which is not observed in the purely elastic case in [34]. Note that in Figs. 7 and 8 the head wave arrives at almost identical times at each θ in both figures. Since the speed of light is much larger than the acoustic wave speed, the head wave wavefront is almost parallel to the crack. (Imagine the

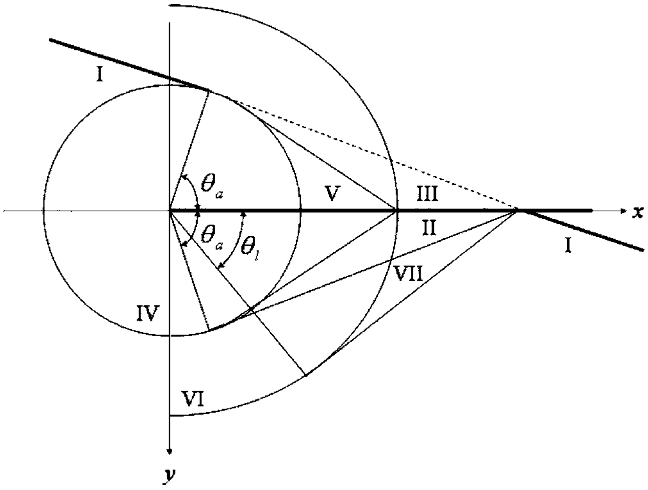

Fig. 4 The scattering patterns excited by an acoustic source: case (2)

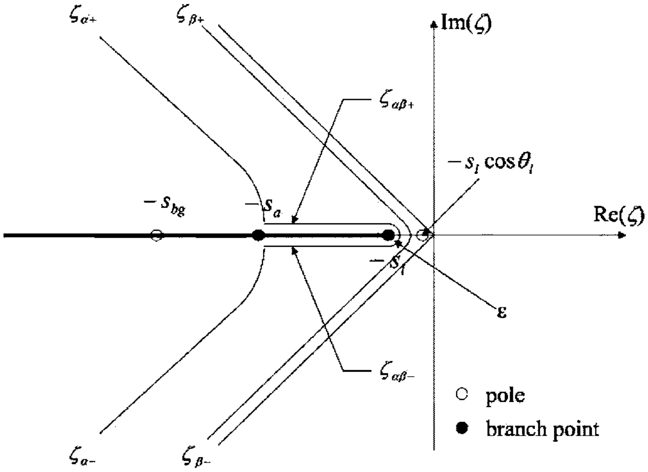

Fig. 5 The Cagniard-deHoop inversion paths for pseudo-electric excitation

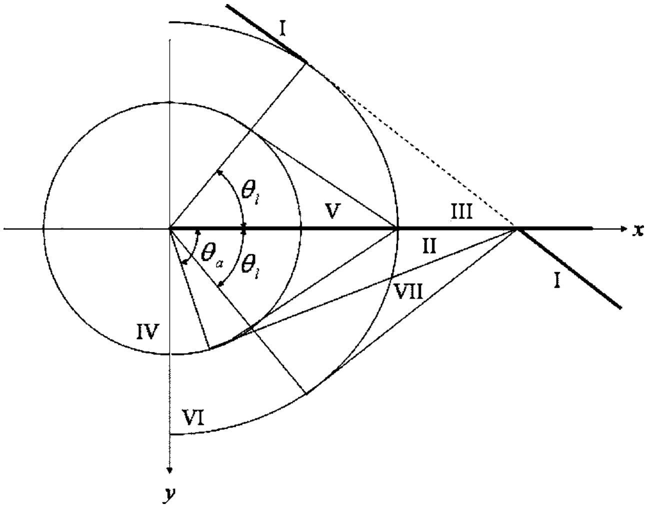

Fig. 6 The scattering patterns excited by an electric source

arc next to "**V**" in Figs. 3–6 is much larger. Then the electroacoustic head wave line connecting the arc would be more parallel to the crack.). This electromagnetic acoustic head wave has also been observed in experiments, e.g., [35]. Another distinctive feature of the scattering field is the cancellation of the refracted acoustic wave by the incident acoustic wave as seen in equations (95) and (98) and, thus, no diffracted acoustic wave or incident acoustic wave exists in the displacement time histories for $|\theta| < |\theta_a|$. Also, the scattered acoustic wave originating from the crack tip can be observed in both time histories as decreasing in magnitude as the observation point is moving farther away from the crack tip.

5.2 Mode Conversion and Reflection/Refraction Coefficients. As shown above, in a piezoelectric medium an acoustic incident wave can trigger both acoustic and electric scattering fields, and vice versa an electric incident wave can generate both acoustic and electric scattering fields as well. It would be interesting to examine the possible mode conversion between these geometrical reflection/refraction waves. To do so, similar convention used by Aki and Richards [36] for purely elastic wave reflection conversion is adopted here. The ratios of all possible mode conversions are defined and calculated as follows,

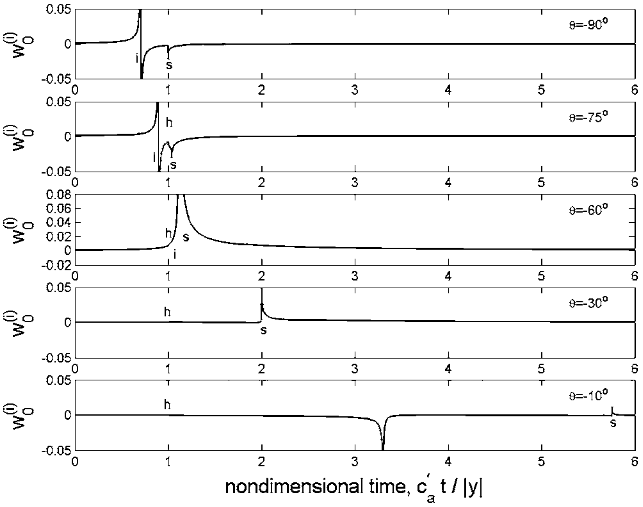

Fig. 7 Displacement-time histories at various θ with fixed y due to an impulsive acoustic source incident at θ_a=45°. Labels: i=incident wave, h=head wave, and s=scattered wave.

$$\acute{A}\acute{A} := \frac{w_r^{(s)}}{w^{(i)}} = -1, \quad \pi \leq \theta < 2\pi \tag{101}$$

$$\acute{A}\acute{E} := \frac{\psi_r^{(s)}}{w^{(i)}} = 0, \quad \pi \leq \theta < 2\pi \tag{102}$$

$$\acute{E}\acute{A} := \frac{w_r^{(s)}}{\psi^{(i)}} = 0, \quad \pi \leq \theta < 2\pi \tag{103}$$

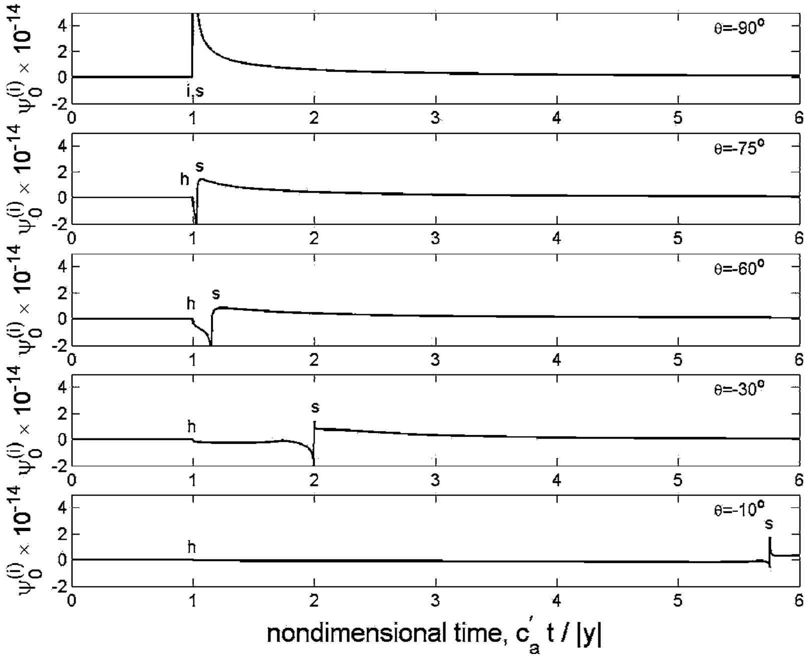

Fig. 8 Displacement time histories at various θ with fixed y due to an impulsive electric source incident at θ_ℓ=45°. Labels: i=incident wave, h=head wave, and s=scattered wave.

$$\acute{E}\acute{E} := \frac{\psi_r^{(s)}}{\psi^{(i)}} = -1, \quad \pi \leqslant \theta < 2\pi \tag{104}$$

$$\acute{A}\grave{A} := \frac{\omega_r^{(s)}}{w^{(i)}} = \frac{s_a \sin(\theta_a) + \tilde{k}_e^2 s_\ell \sin(\theta_\ell)}{s_a \sin(\theta_a) - \tilde{k}_e^2 s_\ell \sin(\theta_\ell)}, \quad 0 \leqslant \theta < \pi \tag{105}$$

$$\acute{A}\grave{E} := \frac{\psi_r^{(s)}}{w^{(i)}} = \frac{-2e_{15}C_f s_a \sin(\theta_a)}{\epsilon_{11}(s_a \sin(\theta_a) - \tilde{k}_e^2 s_\ell \sin(\theta_\ell))}, \quad 0 \leqslant \theta < \pi \tag{106}$$

$$\acute{E}\grave{A} := \frac{w_r^{(s)}}{\psi^{(i)}} = \frac{2e_{15}s_\ell \sin(\theta_\ell)}{\tilde{c}_{44}(s_a \sin(\theta_a) - \tilde{k}_e^2 s_\ell \sin(\theta_\ell))}, \quad 0 \leqslant \theta < \pi \tag{107}$$

$$\acute{E}\grave{E} := \frac{\psi_r^{(s)}}{\psi^{(i)}} = -\frac{s_a \sin(\theta_a) + \tilde{k}_e^2 s_\ell \sin(\theta_\ell)}{s_a \sin(\theta_a) - \tilde{k}_e^2 s_\ell \sin(\theta_\ell)}, \quad 0 \leqslant \theta < \pi \tag{108}$$

5.3 Dynamic Intensity Factors. At the tip of the screen or the crack, scattering fields will become singular, which is of great importance for material strength. In what follows, the intensity factors of the singular fields generated by the antisymmetry solutions are calculated. Define

$$K_\sigma(t) := \lim_{x \to 0^-} \sqrt{2\pi|x|}\,\sigma_{yz}^{(s)}(x,0,t), \tag{109}$$

$$K_D(t) := \lim_{x \to 0^-} \sqrt{2\pi|x|}\,D_y^{(s)}(x,0,t), \tag{110}$$

$$K_E(t) := \lim_{x \to 0^-} \sqrt{2\pi|x|}\,E_y^{(s)}(x,0,t). \tag{111}$$

Considering the asymptotic relations [37],

$$\lim_{x \to 0^-} (\pi|x|)^{1/2}\sigma_{yz}^*(x,0,p) = \lim_{\zeta \to -\infty} |p\zeta|^{1/2}\frac{\Sigma_-(\zeta,p)}{p} \tag{112}$$

$$\lim_{x \to 0^-} (\pi|x|)^{1/2}D_y^*(x,0,p) = \lim_{\zeta \to -\infty} |p\zeta|^{1/2}\hat{D}_y^*(\zeta,p) \tag{113}$$

$$\lim_{x \to 0^-} (\pi|x|)^{1/2}E_y^*(x,0,p) = \lim_{\zeta \to -\infty} |p\zeta|^{1/2}\hat{E}_y^*(\zeta,p), \tag{114}$$

one can derive that

$$K_\sigma^*(p) = \sqrt{2}\frac{\sigma_0\sqrt{s_a + s_h}}{\mathcal{T}_-(-s_h)(s_{bg} + s_h)}\left(\frac{-g^*(p)}{\sqrt{p}}\right) \tag{115}$$

After performing inverse Laplace transform, one may obtain

$$K_\sigma(t) = -\frac{\sigma_0\sqrt{s_a + s_h}}{\mathcal{T}_-(-s_h)(s_{bg} + s_h)}\chi(t) \tag{116}$$

where

$$\chi(t) := \sqrt{\frac{2}{\pi}}\int_{+0}^{t} \frac{1}{\sqrt{\tau}}g(t-\tau)d\tau \tag{117}$$

Similarly, based on the definition

$$\hat{D}_y^*(\zeta,p) = [-e_{15}(1-C_f)\alpha(\zeta)A(\zeta) + \epsilon_{11}\beta(\zeta)B(\zeta)]/p, \tag{118}$$

$$\hat{E}_y^*(\zeta,p) = \left(\alpha(\zeta)A(\zeta) + \frac{e_{15}}{\epsilon_{11}}C_f\beta(\zeta)B(\zeta)\right)/p, \tag{119}$$

one can then show that

$$\begin{aligned} K_D(t) = &-[e_{15}\sigma_0\chi(t) + (e_{15}^2(1-C_f) \\ &+ \tilde{c}_{44}\epsilon_{11})\sqrt{s_a + s_h}\sqrt{s_\ell + s_h}\phi_0\mathcal{H}\{\chi(t)\}] \\ &\cdot \frac{\sqrt{s_a + s_h}}{\tilde{c}_{44}(1-\tilde{k}_e^2)\mathcal{T}_-(-s_h)(s_{bg} + s_h)}, \end{aligned} \tag{120}$$

$$\begin{aligned} K_E(t) = &-\left[\left(1 + \frac{e_{15}^2}{\epsilon_{11}^2}C_f^2\right)\sigma_0\chi(t) + \left(e_{15} + \frac{e_{15}}{\epsilon_{11}}C_f\tilde{c}_{44}\right)\right. \\ &\left.\times\sqrt{s_a + s_h}\sqrt{s_\ell + s_h}\phi_0\mathcal{H}\{\chi(t)\}\right] \\ &\cdot \frac{\sqrt{s_a + s_h}}{\tilde{c}_{44}(1-\tilde{k}_c^2)\mathcal{T}_-(-s_h)(s_{bg} + s_h)}. \end{aligned} \tag{121}$$

Define the following stress, electric displacement, and electric field phase functions in the Laplace transform domain as

$$G_\sigma(s_h) := \frac{K_\sigma^*(p)}{\chi^*(p)} = -\frac{\sigma_0\sqrt{s_a + s_h}}{\mathcal{T}_-(-s_h)(s_{bg} + s_h)} \tag{122}$$

$$\begin{aligned} G_D(s_h) := \frac{K_D^*(p)}{\chi^*(p)} = &-\{e_{15}\sigma_0 + i\,\mathrm{sgn}(p)[e_{15}^2(1-C_f) + \tilde{c}_{44}\epsilon_{11}] \\ &\cdot \sqrt{s_a + s_h}\sqrt{s_\ell + s_h}\phi_0\}\frac{\sqrt{s_a + s_h}}{\tilde{c}_{44}(1-\tilde{k}_e^2)\mathcal{T}_-(-s_h)(s_{bg} + s_h)} \end{aligned} \tag{123}$$

$$\begin{aligned} G_E(s_h) := \frac{K_E^*(p)}{\chi^*(p)} = &-\left[\left(1 + \frac{e_{15}^2}{\epsilon_{11}^2}C_f^2\right)\sigma_0 + i\,\mathrm{sgn}(p)\left(e_{15} + \frac{e_{15}}{\epsilon_{11}}C_f\tilde{c}_{44}\right)\right. \\ &\left.\cdot \sqrt{s_a + s_h}\sqrt{s_\ell + s_h}\phi_0\right]\frac{\sqrt{s_a + s_h}}{\tilde{c}_{44}(1-\tilde{k}_e^2)\mathcal{T}_-(-s_h)(s_{bg} + s_h)} \end{aligned} \tag{124}$$

Apparently, the electric displacement and electric field are functions of the frequency of the incident shape function.

Figures 9–11 display the phase functions G_σ, G_D, and G_E, which are normalized by the incident acoustic wave amplitude w_0 or the incident electric wave amplitude ψ_0 at its respective incident angle for a broad range of electromechanical coupling coefficients ($\tilde{k}_e$). In general, the amplitude of the normalized phase function increases with increasing electromechanical coupling coefficient. Examining the normalized stress phase functions G_σ in Figs. 9(*a*) and 9(*b*), the amplitude increases with the increase of incident angle, because more work is done on the crack tip by incident waves at large angles. Also, the amplitude of the normalized stress phase function due to an incident acoustic source is much larger than that due to an electric source. The amplitude of the electric displacement and electric field phase functions G_D and G_E due to an incident acoustic wave and an incident electric wave are plotted in Figs. 10 and 11, respectively. In general, the amplitudes of both functions decrease with the increase of incident angles. There are two competing effects here: as incident angle increases, the incident wave is more focused on opening the crack; on the other hand, when the horizontal slowness of the wave decreases, the wave has less time to do work on the crack. The former effect is much more significant in mechanical stress analysis, but the latter effect is more pronounced for the electric displacement and electric field. The most striking fact is that the amplitudes for both phase functions are significantly larger for an incident acoustic source than for that of an electric source, and thus the large electromechanical coupling plays an important role in the increase of electric displacement and electric field intensities.

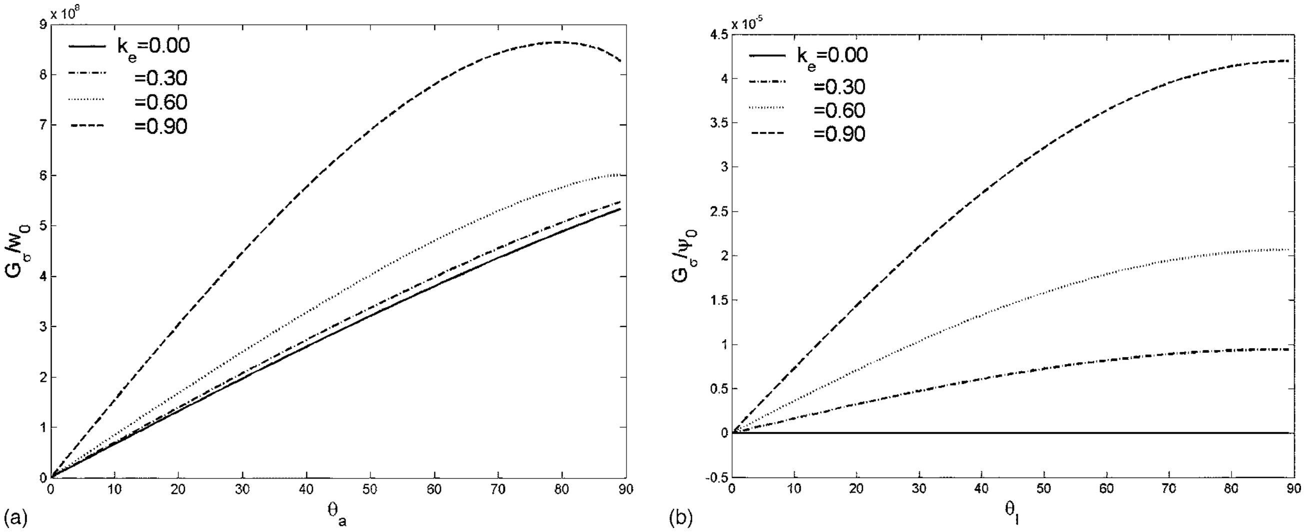

Fig. 9 Amplitude of the normalized stress phase function for various electro-mechanical coupling coefficients ($\tilde{k}_e$) (*a*) versus incident angle for an incident acoustic source G_σ/w_0 and (*b*) versus incident angle for an incident electric source G_σ/ψ_0

6 Conclusions

In this work, a complete solution of a Kirchhoff diffraction problem in a piezoelectric medium is obtained. It is not possible to obtain such solution by employing the quasi-static approximation that has been used traditionally in the design of ferroelectric sensors. Under the quasi-static approximation, the initial boundary value problem becomes ill-posed, because the corresponding wave equations are not hyperbolic anymore.

As shown in [15], the characteristics of the scattering patterns in piezoelectric media have major differences from that in elastic media. For instance, considering the scattering field generated by an SH acoustic incident wave, there is no "shadow zone" behind the half-plane slit in a piezoelectric media, which is in contrast with the similar case in a purely elastic media [38]. In other words, the crack is somewhat "transparent" to incident waves. This is because in a piezoelectric medium the incident acoustic/electric wave interacts with the crack to produce the electro-acoustic head wave that can penetrate the crack surface as shown in Figs. 3, 4, and 6.

Another interesting feature of the scattering fields is that the different head waves exist in many different scenarios, which is a much richer physical phenomenon than the scattering field in a purely elastic medium.

Moreover, it may be observed that the critical angle $\theta_{cr}^{a\ell}$ dictates the reflection pattern. For example, when the incident acoustic angle is smaller than the critical angle, there will be no reflected electric wave as shown in Fig. 3.

To the best of the authors' knowledge, up to this date, there is no systematic experimental study on the Kirchhoff diffraction in piezoelectric/ferroelectric materials. We have not found any experimental data of the Kirchhoff diffraction in piezoelectric materials in open literature. Nevertheless, some of the scattered wave modes and head wave modes predicted in this paper are in good agreement with the experimental data obtained from an experiment of the transient surface excitation of a piezoelectric material (see [35,39]), which cannot be predicted by the commonly used quasi-static approximation theory at all.

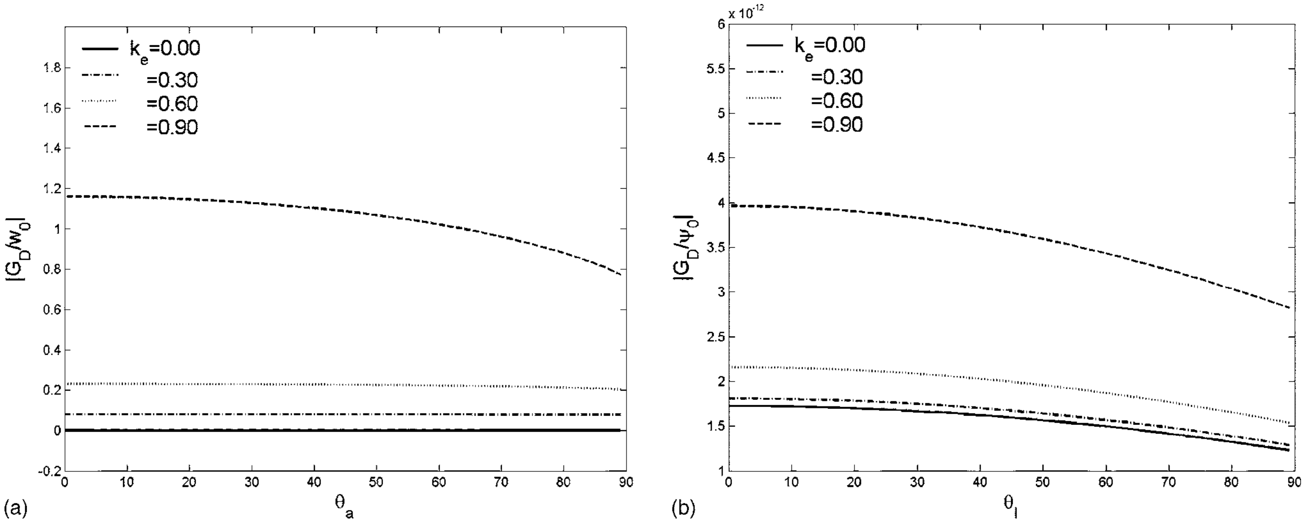

Fig. 10 Amplitude of the normalized electric displacement phase function for various electro-mechanical coupling coefficients ($\tilde{k}_e$) (a) versus an incident acoustic source G_D/w_0 and (b) versus an incident electric source G_D/ψ_0

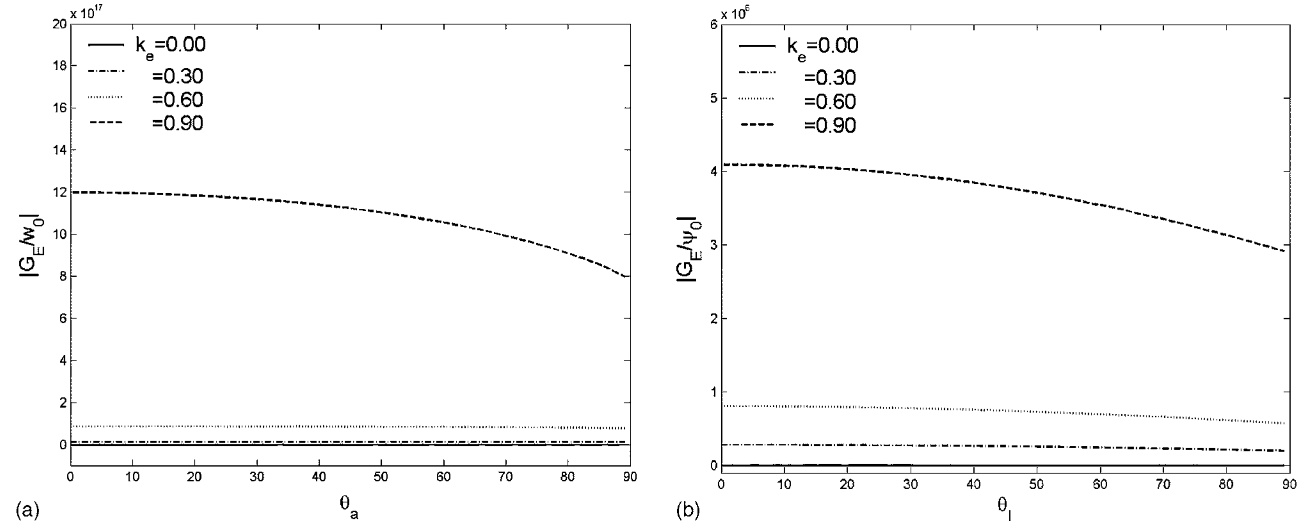

Fig. 11 Amplitude of the normalized electric field phase function for various electro-mechanical coupling coefficients ($\tilde{k}_e$) (a) versus an incident acoustic source G_E/w_0 and (b) versus an incident electric source G_E/ψ_0

Acknowledgments

This research is supported by a grant from NSF (Grant No. CMS-0239130) (SL), and by Jane Lewis Fellowship from University of California, Berkeley (ACT), and another grant from NSF (Grant No. CMS-9908218) (SDG), which are gratefully acknowledged.

Appendix: Solution of the Wiener-Hopf Equations

The key to solving the two Wiener-Hopf equations (58) and (59) is how to factorize the Bleustein-Gulyaev function $BG(\zeta)$ into sectionally analytic functions in the left and right half complex-ζ planes, respectively. This has been done by Li and Mataga [40] and by Li [13],

$$BG(\zeta)=\frac{(s_{bg}+\zeta)(s_{bg}-\zeta)}{\sqrt{\ s_a+\zeta)(s_a-\zeta)}}\mathcal{T}_+(\zeta)\mathcal{T}_-(\zeta)D_s \tag{A1}$$

where

$$D_s:=\bar{c}_{44}(1-\tilde{k}_e^2), \tag{A2}$$

and

$$\mathcal{T}_\pm(\zeta):=\exp\left[-\frac{1}{\pi}\int_{s_\ell}^{s_a}\arctan\left(\frac{-\tilde{k}_e^2\bar{\beta}(\eta)}{\alpha(\eta)}\right)\frac{d\eta}{\eta\pm\zeta}\right], \tag{A3}$$

where $\bar{\beta}(\eta):=\sqrt{\eta^2-s_\ell^2}$.

We first proceed to solve the stress-displacement Wiener-Hopf equation (44). Substituting Eq. (A1) into the Wiener-Hopf equation (58) yields

$$-D_s\frac{s_{bg}+\zeta}{\sqrt{s_a+\zeta}}\Delta U_+(\zeta)\mathcal{T}_+(\zeta)=\Sigma_-(\zeta)R_-(\zeta)+\frac{\sigma_0 g^*(p)R_-(\zeta)}{\zeta+s_h} \tag{A4}$$

where

$$R_-(\zeta):=\frac{\sqrt{s_a-\zeta}}{(s_{bg}-\zeta)\mathcal{T}_-(\zeta)} \tag{A5}$$

In order to separate the second term on the right side of Eq. (A4) into two sectionally analytic functions, additive factorization is performed. By inspection, a possible additive decomposition is

$$\frac{R_-(\zeta)}{\zeta+s_h}=\left(\frac{R_-(\zeta)-R_-(-s_h)}{\zeta+s_h}\right)_-+\left(\frac{R_-(-s_h)}{\zeta+s_h}\right)_+, \tag{A6}$$

where the constant $R_-(-s_h)$ is evaluated as

$$R_-(-s_h)=\frac{\sqrt{s_a+s_h}}{(s_{bg}+s_h)\mathcal{T}_-(-s_h)}. \tag{A7}$$

The Wiener-Hopf equation can then be rearranged into the desired form

$$-D_s\frac{s_{bg}+\zeta}{\sqrt{s_a+\zeta}}\Delta U_+(\zeta)\mathcal{T}_+(\zeta)-\frac{\sigma_0 g^*(p)R_-(-s_h)}{\zeta+s_h}=\Sigma_-(\zeta)R_-(\zeta)+\frac{\sigma_0 g^*(p)[R_-(\zeta)-R_-(-s_h)]}{\zeta+s_h}. \tag{A8}$$

Equating both left- and right-hand sides of (A8) to an entire function, say $ET(\zeta)$,

$$ET(\zeta)=\Sigma_-(\zeta)R_-(\zeta)+\frac{\sigma_0 g^*(p)(R_-(\zeta)-R_-(-s_h))}{\zeta+s_h} \tag{A9}$$

$$-ET(\zeta)=D_s\frac{s_{bg}+\zeta}{\sqrt{s_a+\zeta}}\Delta U_+(\zeta)\mathcal{T}_+(\zeta)+\frac{\sigma_0 g^*(p)R_-(-s_h)}{\zeta+s_h}. \tag{A10}$$

By the Abel theorem [41] and the extended Liouville's theorem [42], the entire function $ET(\zeta)$ must be identically zero. Hence,

$$\Sigma_-(\zeta)=\frac{\sigma_0 g^*(p)}{\zeta+s_h}\left(\frac{R_-(-s_h)}{R_-(\zeta)}-1\right) \tag{A11}$$

$$\Delta U_+(\zeta)=-\frac{\sigma_0 g^*(p)\sqrt{s_a+\zeta}R_-(-s_h)}{(\zeta+s_h)(s_{bg}+\zeta)D_s\mathcal{T}_+(\zeta)}. \tag{A12}$$

By substituting (A12) into Eqs. (53) and (54), one can obtain both $A_{sy}(\zeta)$ and $B_{sy}(\zeta)$,

$$A_{sy}(\zeta)=-\frac{\sigma_0 g^*(p)\sqrt{s_a+\zeta}R_-(-s_h)}{(\zeta+s_h)(s_{bg}+\zeta)D_s\mathcal{T}_+(\zeta)}, \tag{A13}$$

$$B_{sy}(\zeta)=\frac{e_{15}C_f\sigma_0 g^*(p)\sqrt{s_a+\zeta}R_-(-s_h)}{\epsilon_{11}(\zeta+s_h)(s_{bg}+\zeta)D_s\mathcal{T}_+(\zeta)}. \tag{A14}$$

The procedure of solving the electric potential-displacement Wiener-Hopf equation (59) is almost identical. Substituting Eq. (A1) into (59) yields

$$\frac{D_s(s_{bg}+\zeta)}{e_{15}^2(1-C_f)+\epsilon_{11}\tilde{c}_{44}}\frac{\Delta D_+(\zeta)\mathcal{T}_+(\zeta)}{(s_a+\zeta)\sqrt{s_\ell+\zeta}}=\Phi_-(\zeta)S_-(\zeta)+\frac{\phi_0 g^*(p)S_-(\zeta)}{\zeta+s_h} \tag{A15}$$

where

$$S_-(\zeta):=\frac{(s_a+\zeta)\sqrt{s_\ell+\zeta}}{(s_{bg}+\zeta)\mathcal{T}_-(\zeta)} \tag{A16}$$

By using the additive decomposition mentioned above, the Wiener-Hopf equation can then be rearranged into the desired form

$$\begin{aligned}\frac{D_s(s_{bg}+\zeta)}{e_{15}^2(1-C_f)+\epsilon_{11}\tilde{c}_{44}}\frac{\Delta D_+(\zeta)\mathcal{T}_+(\zeta)}{(s_a+\zeta)\sqrt{s_\ell+\zeta}}-\frac{\phi_0 g^*(p)S_-(-s_h)}{\zeta+s_h}\\=\Phi_-(\zeta)S_-(\zeta)+\frac{\phi_0 g^*(p)[S_-(\zeta)-S_-(-s_h)]}{\zeta+s_h}\end{aligned} \tag{A17}$$

where the constant $S_-(-s_h)$ is evaluated as

$$S_-(-s_h)=\frac{(s_a+s_h)\sqrt{s_\ell+s_h}}{(s_{bg}+s_h)\mathcal{T}_-(-s_h)}. \tag{A18}$$

Equating both the left- and right-hand sides of (A17) to an entire function, say $ET(\zeta)$,

$$ET(\zeta)=\Phi_-(\zeta)S_-(\zeta)+\frac{\phi_0 g^*(p)(S_-(\zeta)-S_-(-s_h))}{\zeta+s_h} \tag{A19}$$

$$ET(\zeta)=\frac{D_s(s_{bg}+\zeta)\Delta D_+(\zeta)\mathcal{T}_+(\zeta)}{[e_{15}^2(1-C_f)+\epsilon_{11}\tilde{c}_{44}](s_a+\zeta)\sqrt{s_\ell+\zeta}}-\frac{\phi_0 g^*(p)S_-(-s_h)}{\zeta+s_h}. \tag{A20}$$

Application of the Abel theorem [41] and the extended Liouville's theorem [42] reveals that the entire function $ET(\zeta)$ must be identically zero. Hence,

$$\Phi_-(\zeta)=\frac{\phi_0 g^*(p)}{\zeta+s_h}\left(\frac{S_-(-s_h)}{S_-(\zeta)}-1\right) \tag{A21}$$

$$\Delta D_+(\zeta)=-\frac{\phi_0 g^*(p)(s_a+\zeta)\sqrt{s_\ell+\zeta}S_-(-s_h)(e_{15}^2(1-C_f)+\epsilon_{11}\tilde{c}_{44})}{(\zeta+s_h)(s_{bg}+\zeta)\mathcal{T}_+(\zeta)D_s} \tag{A22}$$

The antisymmetry solution, $A_{an}(\zeta)$ and $B_{an}(\zeta)$, can then be obtained by substituting (A22) into Eqs. (56) and (57),

$$A_{an}(\zeta)=-\frac{\phi_0 g^*(p)\sqrt{s_a+\zeta}\sqrt{s_\ell+\zeta}S_-(-s_h)e_{15}}{\sqrt{s_a-\zeta}(s_{bg}+\zeta)\mathcal{T}_+(\zeta)D_s}, \tag{A23}$$

$$B_{an}(\zeta)=\frac{\phi_0 g^*(p)(s_a+\zeta)S_-(-s_h)\tilde{c}_{44}}{\sqrt{s_\ell-\zeta}(s_{bg}+\zeta)\mathcal{T}_+(\zeta)D_s}. \tag{A24}$$

References

[1] Auld, B. A., 1990, *Acoustic Fields and Waves in Solids*, 2nd ed., Krieger, Malabar, FL (two volumes).

[2] Berlincourt, D., 1981, "Piezoelectric Ceramics: Characteristics and Applications," J. Am. Ceram. Soc., **70**, pp. 1506–1595.

[3] Suo, Z., Kuo, C.-M., Barnett, D. M., and Willis, J. R., 1992, "Fracture Mechanics for Piezoelectric Ceramics," J. Mech. Phys. Solids, **40**, pp. 739–765.

[4] Cao, H. C., and Evans, A. G., 1994, "Electric-Field Induced Fatigue Crack Growth in Piezoelectrics," J. Am. Ceram. Soc., **77**, pp. 1783–1786.

[5] Culshaw, B., 1996, *Smart Structures and Materials*, Artech House, Boston.

[6] Uchino, K., 1998, "Materials Issues in Design and Performance of Piezoelectric Actuators: An Overview," Acta Mater., **46**, pp. 3745–3753.

[7] Shindo, Y., Togawa, R., and Moribayashi, H., 1999, "Scattering of Antiplane Shear Waves in a Piezoelectric Fibrous Composite Medium With Slip at Interfaces," J. Intell. Mater. Syst. Struct., **10**, pp. 257–262.

[8] Narita, F., and Shindo, Y. Y., 1999, "Scattering of Antiplane Shear Waves by a Finite Crack in Piezoelectric Laminates," Acta Mech., **134**, pp. 27–43.

[9] Wang, J., Sottos, N. R., and Weaver, R. L., 2003, "Mixed-Mode Failure of Thin Films Using Laser-Generated Shear Waves," Exp. Mech., **43**, pp. 323–330.

[10] Daros, C. H., and Antes, H., 2000, "The Elastic Motion of a Transversely Isotropic Piezoelectric Solid Caused by Impulsive Loading," ZAMP, **51**, pp. 397–418.

[11] Daros, C. H., and Antes, H., 2000, "On Strong Ellipticity Conditions for Piezoelectric Material of the Crystal Classes 6 mm and 622," Wave Motion, **31**, pp. 237–253.

[12] Li, S., 1996, "The Electromagneto-Acoustic Surface Wave in a Piezoelectric Medium: The Bleustein-Gulyaev Mode," J. Appl. Phys., **80**, pp. 5264–5269.

[13] Li, S., 2000, "Transient Wave Propagation in a Transversely Isotropic Piezoelectric Half Space," ZAMP, **51**, pp. 236–266.

[14] Daros, C. H., 2002, "A Fundamental Solutions for Transversely Isotropic, Piezoelectric Solids Under Electrically Irrotational Approximation," Mech. Res. Commun., **29**, pp. 61–71.

[15] Li, S., 2001, "On Diffraction in a Piezoelectric Medium by Half-Plane: The Sommerfeld Problem," ZAMP, **52**, pp. 101–134.

[16] Kottler, F., 1923, "Theory of Inflection in Black Screens," Ann. Phys., **70**, pp. 405–456.

[17] Kottler, F., 1965, "Diffraction at a Black Screen, Part I: Kirchoff Theory," Prog. Opt., **4**, pp. 281–314.

[18] Suo, Z., 1993, "Models for Breakdown-Resistant Dielectric and Ferroelectric Ceramics," J. Mech. Phys. Solids, **41**, pp. 1155–1176.

[19] Yang, W., and Suo, Z., 1994, "Cracking in Ceramic Actuators Caused by Electrostriction," J. Mech. Phys. Solids, **42**, pp. 649–663.

[20] Ru, C., 2000, "Electrode-Ceramic Interfacial Cracks in Piezoelectric Multilayer Materials," ASME J. Appl. Mech., **67**, pp. 255–261.

[21] Ru, C. Q., Mao, X., and Epstein, M., 1998, "Electric-Field Induced Interfacial Cracking in Multilayer Electrostrictive Actuators," J. Mech. Phys. Solids, **46**, pp. 1301–1318.

[22] Winzer, S. R., Shakar, N., and Ritter, A., 1989, "Designing Cofired Multilayer Electrostrictive Actuators for Reliability," J. Am. Ceram. Soc., **72**, pp. 2246–2257.

[23] Furuta, A., and Uchino, K., 1993, "Dynamic Observation of Crack Propagation in Piezoelectric Multilayer Ceramic Actuators," J. Am. Ceram. Soc., **76**, pp. 1615–1617.

[24] Aburatani, H., Harada, S., Uchino, K., and Furuta, A., 1994, "Destruction Mechanism of Ceramic Multilayer Actuators," Jpn. J. Appl. Phys., Part 1, **33**, pp. 3091–3094.

[25] Freiman, S. W., and White, G. S., 1994, "Intelligent Ceramic Materials: Issues of Brittle Fracture," in *Proceedings of the 2nd International Conference for Intelligent Materials*, Technical Publisher, Lancaster, PA, pp. 52–62.

[26] Hao, T. H., Gong, X., and Suo, Z., 1996, "Fracture Mechanics for the Design of Ceramic Multilayer Actuators," J. Mech. Phys. Solids, **44**, pp. 23–48.

[27] McMeeking, R. M., 1989, "On Mechanical Stresses at Cracks in Dielectrics With Application to Dielectric Breakdown," J. Appl. Phys., **62**, pp. 3116–3122.

[28] McMeeking, R. M., 1989, "Electrostrictive Stress Near Crack-Like Flaws," ZAMP, **40**, pp. 615–627.

[29] Fulton, C. C., and Gao, H., 2001, "Effect of Local Polarization Switching on Piezoelectric Fracture," J. Mech. Phys. Solids, **49**, pp. 927–952.

[30] Bleustein, J. L., 1968, "A New Surface Wave in Piezoelectric Materials," Appl. Phys. Lett., **13**, pp. 412–413.

[31] Gulyaev, Y. V., 1969, "Electrocoustic Surface Waves in Solids," Sov. Phys. JETP, **9**, pp. 37–38.

[32] Cagniard, L., 1939, *Reflexion et Refraction des Ondes Seismiques Progressives*. Gauthier-Villars, Paris. English translation; *Reflection and Refraction of Progressive Seismic Waves*, 1962, by E. A. Flinn and C. H. Dix, McGraw-Hill, New York.

[33] de Hoop, A. T., 1960, "A Modification of Cagniard's Method for Solving Seismic Pulse Problems," Appl. Sci. Res., Sect. B, **8**, pp. 349–360.

[34] Achenbach, J. D., 1973, *Wave Propagation in Elastic Solids*, North-Holland, Amsterdam.

[35] Liu, Y., Wang, C. H., and Ying, C. F., 1989, "Electromagnetic Acoustic Head Waves in Piezoelectric Media," J. Appl. Phys., **55**, pp. 434–436.

[36] Aki, K., and Richards, P. G., 2000, *Quantitative Seismology*, 2nd ed., University Science Books, Sausalito, CA.

[37] Freund, L. B., 1990, *Dynamic Fracture Mechanics*, Cambridge University Press, Cambridge.

[38] Sommerfeld, A., 1949, *Optics: Lectures on Theoretical Physics Vol. IV*, Academic Press, New York.

[39] Liu, Y., Wang, C. H., and Ying, C. F., 1995, "Head Waves in Piezoelectric Half Space," IEEE Trans. Ultrason. Ferroelectr. Freq. Control, **42**, pp. 66–72.

[40] Li, S., and Mataga, P. A., 1996, "Dynamic Crack Propagation in Piezoelectric Materials, Part I: Electrode Solution," J. Mech. Phys. Solids, **44**, pp. 1799–1830.

[41] van der Pol, B., and Bremer, H., 1955, *Operational Calculus*, 2nd ed., Cambridge University Press, Cambridge.

[42] Noble, B., 1958, *Methods Based on the Wiener-Hopf Technique*, Pergamon Press, New York.

Evolution of Wrinkles in Elastic-Viscoelastic Bilayer Thin Films

S. H. Im

R. Huang
e-mail: ruihuang@mail.utexas.edu

Center for Mechanics of Solids, Structures and Materials,
Department of Aerospace Engineering and Engineering Mechanics,
The University of Texas,
Austin, TX 78712

This paper develops a model for evolving wrinkles in a bilayer thin film consisting of an elastic layer and a viscoelastic layer. The elastic layer is subjected to a compressive residual stress and is modeled by the nonlinear von Karman plate theory. A thin-layer approximation is developed for the viscoelastic layer. The stability of the bilayer and the evolution of wrinkles are studied first by a linear perturbation analysis and then by numerical simulations. Three stages of the wrinkle evolution are identified: initial growth of the fastest growing mode, intermediate growth with mode transition, and, finally, an equilibrium wrinkle state. [DOI: 10.1115/1.2043191]

1 Introduction

Complex wrinkle patterns have been observed in various thin-film systems, typically with integrated hard and soft materials. The wrinkles are a nuisance in some applications [1,2], but may be used as stretchable interconnects for flexible electronics [3,4] or biological assays [5]. Diverse wrinkle patterns can be generated by engineering the surface structures or chemistry with potential applications for micro- and nanoscale fabrication [6,7]. It is also possible to extract mechanical properties (e.g., elastic modulus and residual stress) of both organic and inorganic thin-film materials from wrinkle patterns [8,9]. Quantitative understanding of the wrinkling behavior is essential for these applications.

The underlying mechanism of wrinkling has been generally understood as a stress-driven instability, similar to Euler buckling of an elastic column under compression. For a solid film bonded to a substrate, however, the instability is constrained. If the substrate is elastic, there exists a critical compressive stress beyond which the film wrinkles with a particular wavelength selected by minimizing the total elastic energy in the film and the substrate [10–12]. Under a typical compressive stress, a wrinkle forms when the substrate is considerably softer than the film. If the substrate is viscous (e.g., glasses and polymers at high temperatures), wrinkling becomes a kinetic process [13,14]. Since the viscous substrate does not store elastic energy, a compressed blanket film on top is always energetically unstable. The viscous flow in the substrate controls the kinetics of wrinkle growth, selecting a fastest growing wavelength. More generally, if the substrate is viscoelastic (e.g., cross-linked polymers), both energetics and kinetics play important roles. A spectrum of evolving wrinkle patterns has been observed, experimentally, in metal/polymer bilayers [15], exhibiting a peculiar kinetic process. A linear perturbation analysis has shown that the viscoelastic property of the substrate has a profound effect on the stability and kinetics of the wrinkling process [16]. This paper develops a model that allows direct simulation of wrinkle evolution in thin elastic-viscoelastic bilayers beyond the limit of linear perturbation analysis.

The plan of the paper is as follows. Section 2 presents the model formulation, which consists of a summary of the nonlinear von Karman plate theory for the elastic layer and the development of a thin-layer approximation for the viscoelastic layer. Although the model is applicable for two-dimensional wrinkle patterns, the remainder of this study focuses on one-dimensional wrinkles under the plane-strain condition. Section 3 performs a linear perturbation analysis. Section 4 reviews a solution for the equilibrium state at the elastic limit. In Sec. 5, numerical simulations are conducted, showing the transient evolution process. Section 6 concludes with a summary of results.

2 Model Formulation

Figure 1 shows the model structure considered in this study: an elastic layer of thickness h_f lying on a viscoelastic layer of thickness H, which, in turn, lies on a rigid substrate. At the reference state (Fig. 1(*a*)), both layers are flat, and the elastic layer is subjected to an in-plane biaxial compressive stress σ_0 (i.e., $\sigma_0 < 0$). The surface of the bilayer is free of tractions. Upon wrinkling (Fig. 1(*b*)), the elastic layer undergoes both in-plane and out-of-plane displacements to relax the residual stress, and the viscoelastic layer deforms concomitantly. Both the upper and lower interfaces of the viscoelastic layer are assumed to remain bonded. This section develops a model that couples the elastic and viscoelastic deformation in the bilayer. For convenience, a Cartesian coordinate system is set up with the x_1-x_2 plane coinciding with the interface between the two layers, as shown in Fig. 1(*a*).

2.1 Deformation of the Elastic Layer. We employ the nonlinear von Karman plate theory [17] to model the elastic layer. Let w be the lateral deflection, u_α the in-plane displacement ($\alpha = 1, 2$), q the normal traction at the interface with the viscoelastic layer, and τ_α the shear tractions at the same interface. Equilibrium requires that

$$q = -D_f \frac{\partial^4 w}{\partial x_\alpha \partial x_\alpha \partial x_\beta \partial x_\beta} + N_{\alpha\beta} \frac{\partial^2 w}{\partial x_\alpha \partial x_\beta} + \tau_\alpha \frac{\partial w}{\partial x_\alpha} \tag{1}$$

$$\tau_\alpha = \frac{\partial N_{\alpha\beta}}{\partial x_\beta} \tag{2}$$

where

$$D_f = \frac{E_f h_f^3}{12(1 - \nu_f^2)} \tag{3}$$

$$N_{\alpha\beta} = \sigma_0 h_f \delta_{\alpha\beta} + \frac{E_f h_f}{1 - \nu_f^2}[(1 - \nu_f)\varepsilon_{\alpha\beta} + \nu_f \varepsilon_{\gamma\gamma}\delta_{\alpha\beta}] \tag{4}$$

Contributed by the Applied Mechanics Division of THE AMERICAN SOCIETY OF MECHANICAL ENGINEERS for publication in the ASME JOURNAL OF APPLIED MECHANICS. Manuscript received by the Applied Mechanics Division, May 23, 2003; final revision; March 24, 2005. Associate Editor: A. A. Ferri. Discussion on the paper should be addressed to the Editor, Prof. Robert M. McMeeking, Journal of Applied Mechanics, Department of Mechanical and Environmental Engineering, University of California—Santa Barbara, Santa Barbara, CA 93106-5070, and will be accepted until four months after final publication in the paper itself in the ASME JOURNAL OF APPLIED MECHANICS.

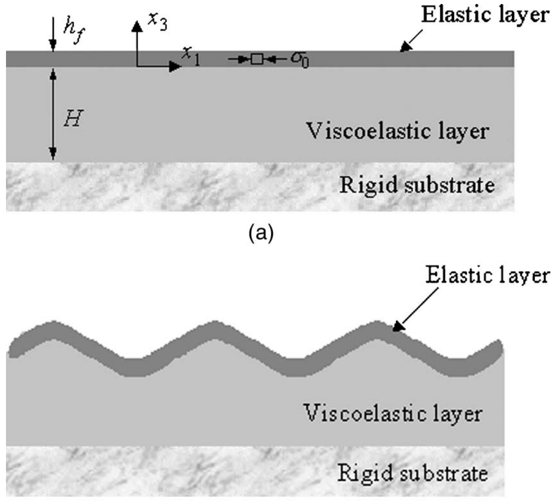

(a)

(b)

Fig. 1 Schematic of an elastic-viscoelastic bilayer on a rigid substrate: (*a*) the reference state and (*b*) a wrinkled state

$$\varepsilon_{\alpha\beta} = \frac{1}{2}\left(\frac{\partial u_\alpha}{\partial x_\beta} + \frac{\partial u_\beta}{\partial x_\alpha}\right) + \frac{1}{2}\frac{\partial w}{\partial x_\alpha}\frac{\partial w}{\partial x_\beta} \tag{5}$$

Here E_f is the Young's modulus of the elastic layer, ν_f the Poisson's ratio, D_f the flexural rigidity, $N_{\alpha\beta}$ the in-plane membrane force, $\varepsilon_{\alpha\beta}$ the in-plane strain, and $\delta_{\alpha\beta}$ the Kronecker delta. The Greek subscripts α and β take on the values of the in-plane coordinates 1 and 2, and a repeated Greek subscript implies summation over 1 and 2.

Note that, a nonlinear term is included in Eq. (5) to account for moderately large deflections of the elastic layer. In addition, the coupling between the in-plane deformation and the lateral deflection in Eq. (1) introduces further nonlinearity. The nonlinear equations have been widely used for analyses of buckle-delamination in thin films [18].

2.2 Deformation of a Viscoelastic Thin-Layer. Next consider the viscoelastic layer. The linear theory of viscoelasticity [19] is adopted, where the stress-strain relation is described in an integral form with a shear relaxation modulus $\mu(t)$ and Poisson's ratio $\nu(t)$, both time dependent, in general. The Laplace transform of the stress-strain relation has a form identical to that of linear elasticity with the elastic shear modulus μ and Poisson's ratio ν replaced by $s\bar{\mu}(s)$ and $s\bar{\nu}(s)$, respectively, where a bar over a variable designates its Laplace transform with respect to time t and s is the transform variable. Therefore, the Laplace transformed solution of a viscoelastic problem can be obtained directly from the solution of a corresponding elastic problem, namely, the correspondence principle. The final solution for the viscoelastic problem can then be realized upon inverting the transformed solution.

For the present study, the viscoelastic layer is stress free initially ($t=0$) and subjected to normal and shear tractions at the top surface for $t>0$, namely,

$$\sigma_{33} = S_3(x_1,x_2,t) \quad \text{and} \quad \sigma_{3\alpha} = S_\alpha(x_1,x_2,t) \text{ at } x_3 = 0 \tag{6}$$

At the lower interface, the displacement is fixed

$$u_\alpha = u_3 = 0 \text{ at } x_3 = -H \tag{7}$$

In the following, a thin-layer approximation is developed to solve for the response of the viscoelastic layer subjected to arbitrary tractions.

A previous study by Huang [16] solved a similar problem, but under the plane-strain condition, where $S_2=u_2=0$, and the tractions at the top surface take the form

$$S_1 = A(t)\sin kx_1 \tag{8}$$

$$S_3 = B(t)\cos kx_1 \tag{9}$$

with a constant wave number k and arbitrarily time-dependent amplitudes $A(t)$ and $B(t)$. The Laplace transform of the displacements at the top surface was obtained as follows:

$$\bar{u}_1(x_1,s) = \frac{1}{2ks\bar{\mu}(s)}[\gamma_{11}(s\bar{\nu},kH)\bar{A}(s) + \gamma_{12}(s\bar{\nu},kH)\bar{B}(s)]\sin(kx_1) \tag{10}$$

$$\bar{u}_3(x_1,s) = \frac{1}{2ks\bar{\mu}(s)}[\gamma_{21}(s\bar{\nu},kH)\bar{A}(s) + \gamma_{22}(s\bar{\nu},kH)\bar{B}(s)]\cos(kx_1) \tag{11}$$

where

$$\gamma_{11} = \frac{1+\kappa}{4}\,\frac{\kappa\sinh(2kH)+2kH}{\kappa\cosh^2(kH)+(kH)^2+\left(\dfrac{1-\kappa}{2}\right)^2} \tag{12}$$

$$\gamma_{22} = \frac{1+\kappa}{4}\,\frac{\kappa\sinh(2kH)-2kH}{\kappa\cosh^2(kH)+(kH)^2+\left(\dfrac{1-\kappa}{2}\right)^2} \tag{13}$$

$$\gamma_{12} = \gamma_{21} = -\frac{\dfrac{\kappa(1-\kappa)}{2}\sinh^2(kH)+(kH)^2}{\kappa\cosh^2(kH)+(kH)^2+\left(\dfrac{1-\kappa}{2}\right)^2} \tag{14}$$

and $\kappa=3-4s\bar{\nu}(s)$.

The above solution shows that, in general, the surface of the viscoelastic layer undergoes both out-of-plane and in-plane displacements and they are coupled. However, in two special cases, the two displacements can be decoupled. In the first case, the viscoelastic layer is infinitely thick ($kH\to\infty$) and incompressible ($\nu=0.5$), which has been considered in the previous study [16]. In the other case, as will be considered in the present study, the viscoelastic layer is very thin ($kH\to 0$), for which Eqs. (10) and (11) reduce to

$$\bar{u}_1(x_1,s) = \frac{1}{2ks\bar{\mu}(s)}\left[2kH\bar{A}(s) - \frac{1-4\nu}{2(1-\nu)}(kH)^2\bar{B}(s)\right]\sin(kx_1) \tag{15}$$

$$\bar{u}_3(x_1,s) = \frac{1}{2ks\bar{\mu}(s)}\left[\frac{1-2\nu}{1-\nu}(kH)\bar{B}(s) - \frac{1-4\nu}{2(1-\nu)}(kH)^2\bar{A}(s)\right]\cos(kx_1) \tag{16}$$

By the thin-layer approximation, only the leading terms in kH are retained in Eqs. (15) and (16). In addition, the Poisson's ratio has been assumed to be a constant independent of time, considering the factor that the Poisson's ratio is typically a weak function of time. If the viscoelastic layer is incompressible (i.e., $\nu=0.5$), however, Eq. (16) takes a different form

$$\bar{u}_3(x_1,s) = \frac{1}{2ks\bar{\mu}(s)}\left[\frac{2}{3}(kH)^3\bar{B}(s) + (kH)^2\bar{A}(s)\right]\cos(kx_1) \tag{17}$$

where the first term in the brackets scales with $(kH)^3$ instead of kH in Eq. (16). On the other hand, Eq. (15) remains valid. As will be shown later, this leads to different kinetics of wrinkling for compressible and incompressible viscoelastic layers.

To be specific, consider the Kelvin model of linear viscoelasticity, modeled by a mechanical analog consisting of a spring and a dashpot in parallel, for which the relaxation modulus is

$$\mu(t) = \mu_\infty + \eta\delta(t) \tag{18}$$

where μ_∞ is the stiffness of the spring, representing the elastic shear modulus at the rubbery limit, and η is the viscosity. The Laplace transform of the relaxation modulus is

$$\bar{\mu}(s) = \frac{\mu_\infty}{s} + \eta \tag{19}$$

After substituting (19) into Eqs. (15) and (16), inverse Laplace transform leads to

$$\frac{\partial u_1}{\partial t} = \frac{H}{\eta}S_1 - \frac{1-4\nu}{4(1-\nu)}\frac{H^2}{\eta}\frac{\partial S_3}{\partial x_1} - \frac{\mu_\infty}{\eta}u_1 \tag{20}$$

$$\frac{\partial u_3}{\partial t} = \frac{1-2\nu}{2(1-\nu)}\frac{H}{\eta}S_3 + \frac{1-4\nu}{4(1-\nu)}\frac{H^2}{\eta}\frac{\partial S_1}{\partial x_1} - \frac{\mu_\infty}{\eta}u_3 \tag{21}$$

Similarly, for an incompressible viscoelastic layer ($\nu=0.5$), the inverse transform of Eq. (17) leads to

$$\frac{\partial u_3}{\partial t} = -\frac{H^3}{3\eta}\frac{\partial^2 S_3}{\partial x_1^2} - \frac{H^2}{2\eta}\frac{\partial S_1}{\partial x_1} - \frac{\mu_\infty}{\eta}u_3 \tag{22}$$

Equations (20) and (22) have the similar form as the Reynold's lubrication theory for nearly parallel flow of a thin liquid layer [14,20], but with an additional term accounting for the elastic limit of the viscoelastic layer.

For the present study, we assume a compressible viscoelastic layer (i.e., $\nu \neq 0.5$) and further neglect the H^2 terms in Eqs. (20) and (21) for thin-layer approximation, which leads to

$$\frac{\partial u_1}{\partial t} = \frac{H}{\eta}S_1 - \frac{\mu_\infty}{\eta}u_1, \tag{23}$$

$$\frac{\partial u_3}{\partial t} = \frac{1-2\nu}{2(1-\nu)}\frac{H}{\eta}S_3 - \frac{\mu_\infty}{\eta}u_3 \tag{24}$$

Here the two traction components are assumed to have comparable magnitudes and the thickness of the viscoelastic layer is assumed to be small compared to the wavelength ($L=2\pi/k$). Equation (23) is equivalent to a shear lag model, which assumes uniform shear stress across the thin layer. Similar models have been used for both elastic and viscous layers [21,22]. Equation (24) is similar to the Winkler model for elastic foundation [23] but includes a time derivative term due to the viscous effect. The two equations are uncoupled under the thin-layer approximation.

In the above development, plane-strain deformation and periodic surface tractions have been assumed. The restriction of periodic tractions has been relaxed by using differentiation of the surface tractions with respect to x_1 in places of the particular wave number after inverse Laplace transform. The resulting equations, (20) and (21), are apparently independent of wave number and can be used for arbitrary tractions by linear superposition of their Fourier components. At the end, the in-plane and out-of-plane responses are decoupled by the thin-layer approximation. Therefore, the restriction of plane-strain deformation can be relaxed by generalizing the in-plane response, Eq. (23), for both x_1 and x_2 directions, which leads to

$$\frac{\partial u_\alpha}{\partial t} = \frac{H}{\eta}S_\alpha - \frac{\mu_\infty}{\eta}u_\alpha \tag{25}$$

for $\alpha=1,2$. Equations (24) and (25) then represent the approximate solution for the three-dimensional response of a thin viscoelastic layer subjected to the boundary conditions in Eqs. (6) and (7).

In the case of an incompressible viscoelastic layer, however, the Winkler-type equation for the out-of-plane displacement (Eq. (24)) breaks down and the decoupling is not applicable. The coupled equations, (20) and (22), must be used in this case. Generalization of the plane-strain response to the three-dimensional would take the similar form as the lubrication theory [14], but will not be further pursued in the present study.

2.3 Coupled Evolution Equations. The interface between the elastic and viscoelastic layers is assumed to remain bonded during deformation. Consequently, the displacements and tractions are continuous across the interface, which couples the equilibrium equations of the elastic layer, Eqs. (1) and (2), with the time-dependent responses of the viscoelastic layer, Eqs. (24) and (25), and leads to

$$\frac{\partial w}{\partial t} = \frac{1-2\nu}{2(1-\nu)}\frac{H}{\eta}\left(-D_f\frac{\partial^4 w}{\partial x_\alpha\partial x_\alpha\partial x_\beta\partial x_\beta} + N_{\alpha\beta}\frac{\partial^2 w}{\partial x_\alpha\partial x_\beta} + \frac{\partial N_{\alpha\beta}}{\partial x_\beta}\frac{\partial w}{\partial x_\alpha}\right) - \frac{\mu_\infty}{\eta}w \tag{26}$$

$$\frac{\partial u_\alpha}{\partial t} = \frac{H}{\eta}\frac{\partial N_{\alpha\beta}}{\partial x_\beta} - \frac{\mu_\infty}{\eta}u_\alpha \tag{27}$$

Equations (26) and (27) are coupled, nonlinear evolution equations, which may be solved numerically to simulate three-dimensional deformation of an elastic-viscoelastic bilayer and evolution of the resulting two-dimensional wrinkle patterns. In the remainder of this paper, however, we focus our attention on plane-strain deformation and one-dimensional wrinkles only, leaving the two-dimensional wrinkles for a subsequent study. The reduced equations for the plane-strain wrinkles are summarized as follows:

$$\frac{\partial w}{\partial t} = \frac{1-2\nu}{2(1-\nu)}\frac{H}{\eta}\left(-D_f\frac{\partial^4 w}{\partial x^4} + N\frac{\partial^2 w}{\partial x^2} + \frac{\partial N}{\partial x}\frac{\partial w}{\partial x}\right) - \frac{\mu_\infty}{\eta}w \tag{28}$$

$$\frac{\partial u}{\partial t} = \frac{H}{\eta}\frac{\partial N}{\partial x} - \frac{\mu_\infty}{\eta}u \tag{29}$$

$$N = \sigma_0 h_f + \frac{E_f h_f}{1-\nu_f^2}\left[\frac{\partial u}{\partial x} + \frac{1}{2}\left(\frac{\partial w}{\partial x}\right)^2\right] \tag{30}$$

Recently, Huang et al. [24] developed a similar model to simulate the evolution of two-dimensional wrinkle patterns in elastic films on soft substrates, where the viscoelastic Kelvin model was used to relate the lateral deflection and the normal traction, similar to Eq. (24), but the relation between the in-plane displacement and the shear traction was taken to be linear elastic. While the attention there was focused on various equilibrium wrinkle patterns, the interest of the present study is the temporal evolution of wrinkles.

3 Linear Perturbation Analysis

Assume a small deflection of the elastic layer in the form of

$$w(x,t) = A(t)\cos kx \tag{31}$$

For the linear perturbation analysis, the evolution of the in-plane displacement is uncoupled from the lateral deflection and, therefore, ignored. Inserting (31) into Eq. (28) and retaining only the leading-order terms in A, we obtain that

$$\frac{dA}{dt} = \frac{\alpha E_f - \mu_\infty}{\eta}A(t) \tag{32}$$

where

$$\alpha = \frac{(1-2\nu)k^2 H h_f}{24(1-\nu)(1-\nu_f^2)}\left[-k^2 h_f^2 - \frac{12(1-\nu_f^2)\sigma_0}{E_f}\right] \tag{33}$$

Solving Eq. (32) leads to

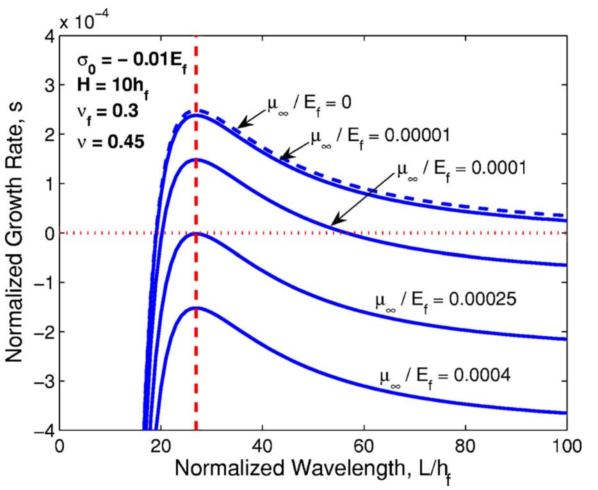

Fig. 2 Initial growth rate as a function of wavelength by the linear perturbation analysis, for various ratios between the rubbery modulus of the viscoelastic layer and the Young's modulus of the elastic layer

$$A(t) = A_0 \exp\left(s\frac{t}{\tau}\right) \tag{34}$$

where A_0 is the initial perturbation amplitude, $\tau=\eta/E_f$ is a characteristic time scale, and $s=\alpha-\mu_\infty/E_f$ is the dimensionless growth rate of the perturbation. The stability of the bilayer therefore depends on the sign of the growth rate. If $s<0$ for all wave numbers k, the bilayer is stable and remains flat. Otherwise, if $s>0$ for any permissible wave numbers, the bilayer is unstable and perturbations grow to form wrinkles. In this case, the amplitude grows exponentially with time at the initial stage. A more sophisticated analysis [16] has shown that the initial growth can be nonexponential if the viscoelastic layer has a finite elastic modulus at the glassy state (elastic limit as $t\to 0$).

Figure 2 plots the growth rate as a function of the perturbation wavelength ($L=2\pi/k$) for different ratios between the rubbery modulus of the viscoelastic layer and the elastic modulus of the elastic layer. At the limiting case when $\mu_\infty=0$, $s=\alpha$ and the growth rate is positive (recall that $\sigma_0<0$) for long wave perturbations, as shown by the dashed line in Fig. 2. Consequently, the bilayer is always unstable. The critical wavelength is

$$L_c = \pi h_f \sqrt{-\frac{E_f}{3(1-\nu_f^2)\sigma_0}} \tag{35}$$

which is identical to the critical length of Euler buckling. The growth rate is positive when $L>L_c$ and peaks at the wavelength

$$L_m = \pi h_f \sqrt{-\frac{2E_f}{3(1-\nu_f^2)\sigma_0}} \tag{36}$$

Similar results were obtained for an elastic film on a viscous layer [14,25], where the fastest growing wavelength L_m is, however, shorter by 13.4% due to the incompressibility of the viscous layer. Using typical values for a thin aluminum layer: $E_f=70$ GPa, $\nu_f=0.35$, $h_f=40$ nm, and $\sigma_0=-100$ MPa, we obtain $L_c=2.05$ μm and $L_m=2.90$ μm. The latter compares closely to the initial wavelengths observed in experiments by Yoo and Lee [15] despite the rough estimate of the stress.

As the ratio μ_∞/E_f increases, the growth rate decreases; the curve in Fig. 2 shifts down, but without any change in the shape. As a result, the critical wavelength increases, and a second critical wavelength emerges at the long wave end. The growth rate is now positive within a window bounded by the two critical wavelengths. On the other hand, the fastest growing wavelength does not change, but the corresponding growth rate decreases. The fastest growth rate reduces to zero at a critical ratio

$$\left(\frac{\mu_\infty}{E_f}\right)_c = \frac{3(1-\nu_f^2)(1-2\nu)}{2(1-\nu)}\frac{H}{h_f}\left(\frac{\sigma_0}{E_f}\right)^2 \tag{37}$$

The bilayer becomes stable when μ_∞/E_f is greater than the critical ratio. Alternatively, Eq. (37) may be rewritten to give the critical compressive stress, below which a bilayer with the given thickness ratio and moduli ratio is stable. The critical condition is identical to that for an elastic film on a thin elastic substrate with the shear modulus $\mu=\mu_\infty$ [12,16].

It is noted that, by the critical condition in Eq. (37), the stability of an elastic-viscoelastic bilayer depends on the rubbery modulus (i.e., the long-term limit of the relaxation modulus) of the viscoelastic layer, but independent of the initial modulus (e.g., the glassy state). In other words, despite that the viscoelastic layer is initially stiff or even rigid, the bilayer "foresees" the subsequent softening of the layer and becomes unstable spontaneously. The time scale of wrinkle growth is proportional to the viscosity, and the growth rate increases as the rubbery modulus decreases. The wavelength of the fastest growing mode, however, is independent of the viscoelastic layer, as given in Eq. (36). Our previous study [16] showed that the fastest growing wavelength weakly depends on the thickness ratio and Poisson's ratio. The thin-layer approximation in the present study leads to a reasonably accurate wavelength, but underestimates the growth rate for the fastest growing mode when the thickness ratio H/h_f is larger than 2.

4 Equilibrium Wrinkles

Setting $\partial/\partial t=0$ in Eqs. (28) and (29) leads to two coupled nonlinear ordinary differential equations, from which one can solve for equilibrium states. The solution is identical to that for an elastic film on a thin elastic substrate with the shear modulus $\mu=\mu_\infty$. The latter has been obtained by an energy minimization procedure [12,16], as summarized below. First, the equilibrium amplitude of a sinusoidal wrinkle with a wave number k is given by

$$A_{eq} = \frac{2\sqrt{1-\nu_f^2}}{k}\left[-\frac{\sigma_0}{E_f} - \frac{(kh_f)^2}{12(1-\nu_f^2)} - \frac{2(1-\nu)}{1-2\nu}\frac{\mu_\infty}{E_f}\frac{1}{k^2Hh_f}\right]^{1/2} \tag{38}$$

It can be confirmed that only when the bilayer is unstable does there exist nonzero, real-valued equilibrium wrinkle amplitudes. Furthermore, minimization of the elastic strain energy in the bilayer with respect to the wave number selects an equilibrium wrinkle wavelength

$$L_{eq} = \pi h_f\left[\frac{2(1-2\nu)}{3(1-\nu)(1-\nu_f^2)}\frac{E_f}{\mu_\infty}\frac{H}{h_f}\right]^{1/4} \tag{39}$$

The corresponding wrinkle amplitude can be obtained from Eq. (38) with $k=2\pi/L_{eq}$. Again, using typical values: $E_f=70$ GPa, $\nu_f=0.35$, $h_f=40$ nm, $\mu_\infty=0.01$ MPa, $\nu=0.45$, $H=400$ nm, and $\sigma_0=-100$ MPa, we obtain $L_{eq}=7.00$ μm and $A_{eq}=71.9$ nm. It is noted that Eq. (39) underestimates the equilibrium wavelength when the thickness ratio H/h_f is larger than 2.

Comparing the equilibrium wrinkle wavelength to the initially fastest growing wavelength given by Eq. (36), we note that the two wavelengths can be totally independent. The fastest growing wavelength, which dominates the initial growth, is determined by the kinetics and depends on the compressive stress in the elastic layer, but independent of the viscoelastic layer. The equilibrium wavelength, on the other hand, is determined by energetics and depends on the thickness and rubbery modulus of the viscoelastic layer, but independent of the stress in the elastic layer. Such independence may enable simultaneous determination of the residual stress and rubbery modulus from the initial and final wrinkle wavelengths, respectively.

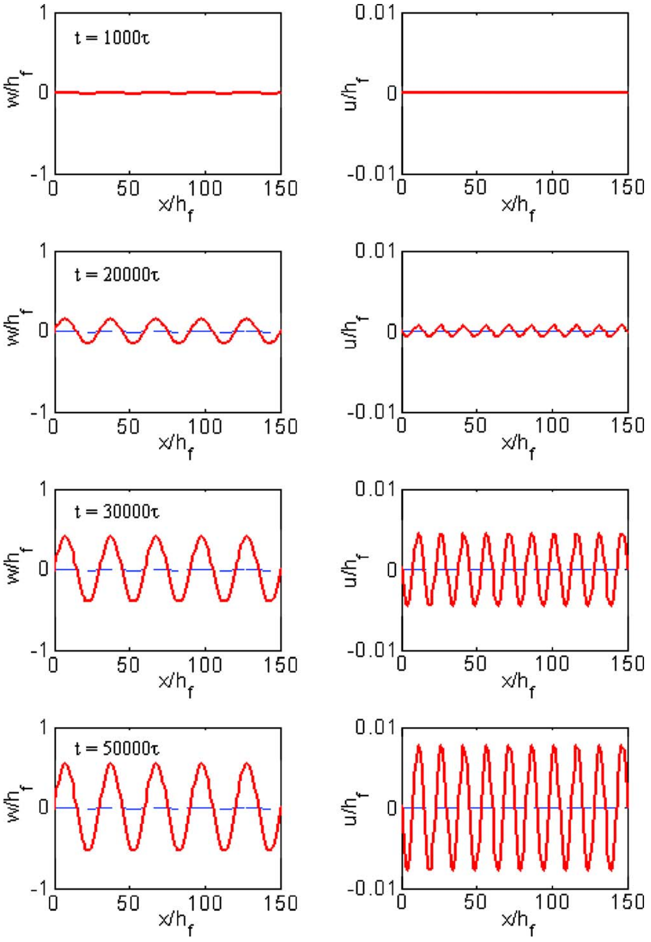

Fig. 3 Evolution of the lateral deflection *w* and the in-plane displacement *u* by numerical simulation with a sinusoidal initial perturbation

At the equilibrium state, the shear traction at the interface is nearly zero and the lateral displacement approximately takes the form [12,14]

$$u = \frac{1}{8}kA_{eq}^2 \sin(2kx) \tag{40}$$

where $k=2\pi/L_{eq}$. The wavelength of the in-plane displacement is half of the wrinkle wavelength at the equilibrium state.

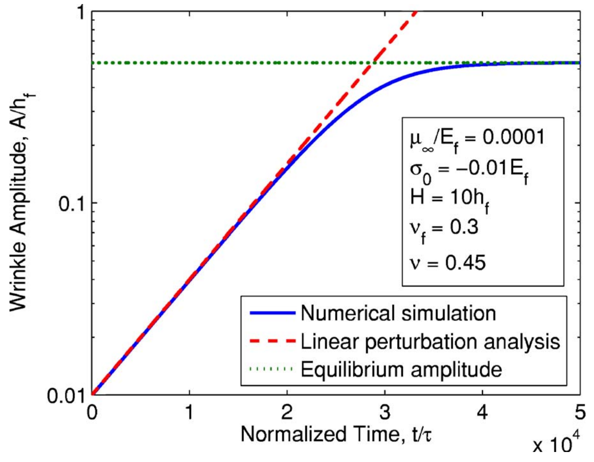

Fig. 4 Amplitude of a sinusoidal wrinkle as a function of time

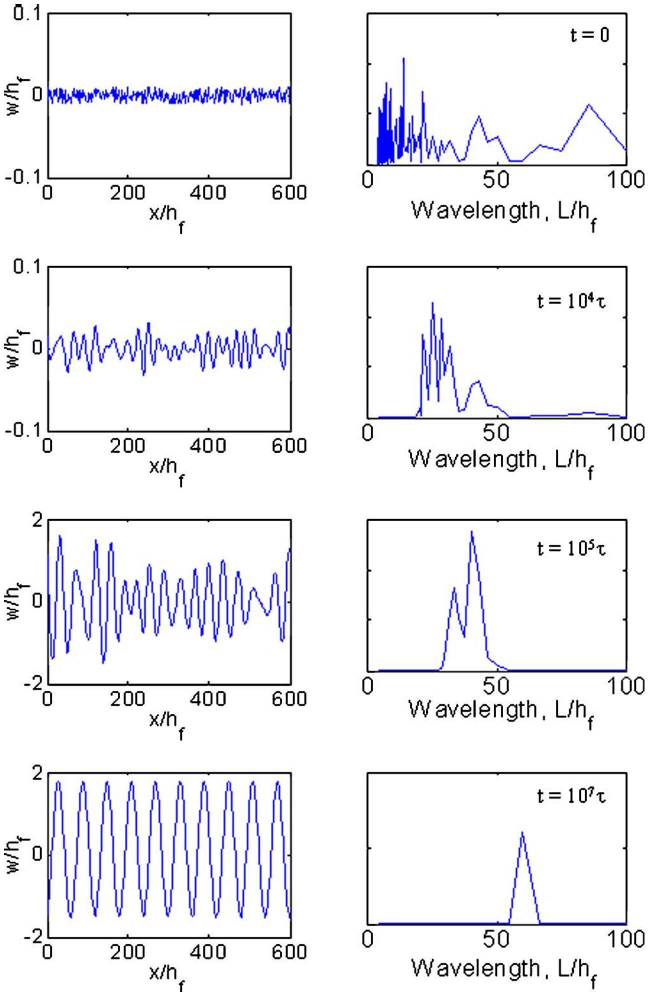

Fig. 5 Numerical simulation of evolving wrinkles with a random initial perturbation. The left column shows the deflection of the elastic layer, and the right column shows the corresponding Fourier spectra.

5 Numerical Simulations

In this section, we simulate the evolution of wrinkles by numerically integrating the nonlinear equations, (28) and (29). For simplicity, we use the explicit forward-time-center-space (FTCS) finite difference method. The algorithm is conditionally stable. To achieve sufficient accuracy, a small space step Δx is first specified. Next, the time step Δt is determined by the stability and convergence of the numerical results. In the following simulations, we use $\Delta x=1.0h_f$ and $\Delta t=0.1\eta/E_f$. The time is normalized by the time scale $\tau=\eta/E_f$, which ranges widely from 1 μs to 1 s, depending on the material of the viscoelastic layer and the temperature. In all simulations, the periodic boundary condition is assumed.

The bilayer is in equilibrium at the reference state (Fig. 1(*a*)) with no tractions at the interface. By introducing a small perturbation displacement to the reference state as the initial condition, the system evolves until it reaches another equilibrium state. First, we start with a sinusoidal deflection of amplitude $A_0=0.01h_f$ and zero in-plane displacement at $t=0$. The wavelength $L=30h_f$ was selected to be close to the fastest growing wavelength ($L_m=26.9h_f$) to save the computational time. Other parameters are $\sigma_0=-0.01E_f$, $\mu_\infty=0.0001E_f$, $H=10h_f$, $\nu_f=0.3$, and $\nu=0.45$. As noted before, the present model underestimates the growth rate and the equilibrium wavelength for thick viscoelastic layers ($H>2h_f$). Nevertheless, the wrinkling kinetics should be similar, and

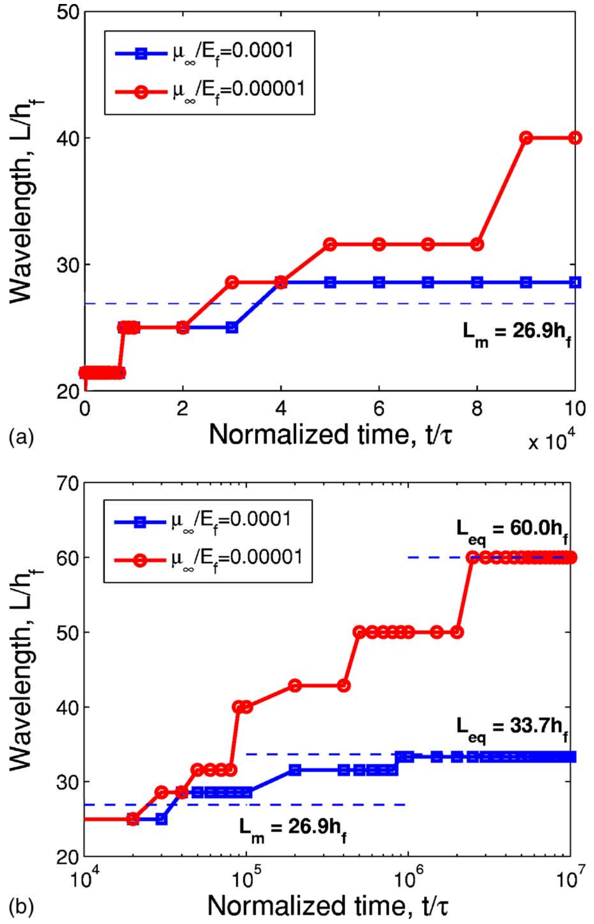

Fig. 6 Evolution of the dominant wrinkle wavelength by numerical simulation: (a) short time evolution and (b) long time evolution

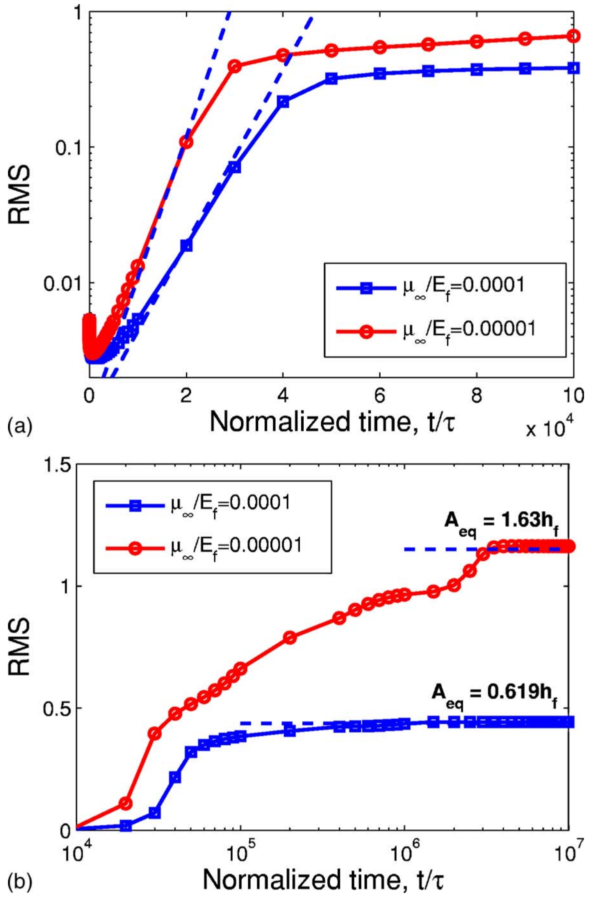

Fig. 7 The root mean square (RMS) of the wrinkle as a function of time: (*a*) short-time evolution and (*b*) long-time evolution

in the numerical simulations, we use $H=10h_f$ as in the metal/polymer bilayer experiments by Yoo and Lee [15]. Figure 3 shows snapshots of the evolving displacements. The amplitude of the lateral deflection grows with time, but the wavelength remains constant for the entire period of the simulation up to $t=50{,}000\tau$. Meanwhile, relatively small in-plane displacement evolves concomitantly, but with a wavelength half of the wrinkle wavelength, as predicted by the equilibrium solution in Eq. (40). Figure 4 shows the wrinkle amplitude as a function of time. The amplitude first grows exponentially, as predicted by the linear perturbation analysis (shown as the straight dashed line). Starting at about $t=20{,}000\tau$, the growth rate deviates from the linear behavior and gradually approaches a plateau. The amplitude essentially remains constant after $t=40{,}000\tau$, indicating that an equilibrium state has been reached. The equilibrium amplitude given by Eq. (38) for the selected wavelength ($L=30h_f$) is $A_{eq}=0.537h_f$, as indicated by the horizontal dotted line in Fig. 4. The result from the numerical simulation agrees closely with the analytical solutions by the linear perturbation analysis at the initial stage and by the energetic analysis for the equilibrium amplitude.

In the above simulation, the wrinkle wavelength is arbitrarily selected *a priori* and the evolution stops when the corresponding equilibrium state is reached. However, the wavelength is not necessarily the equilibrium wavelength selected by energy minimization, as given in Eq. (39). In other words, the equilibrium state reached in the previous simulation is energetically unstable. To further relax the strain energy, continual evolution is possible once the equilibrium state is perturbed with different wavelengths [14]. In real situations, various sources (e.g., thermal fluctuation and surface defects) may induce the initial perturbation, which is random, in general. Figure 5 shows a numerical simulation of evolving wrinkles that starts from a random initial perturbation. The in-plane displacement is again zero initially (not shown). Other parameters are $\sigma_0=-0.01E_f$, $\mu_\infty=0.00001E_f$, $H=10h_f$, $\nu_f=0.3$, and $\nu=0.45$. For each snapshot of the wrinkle, the corresponding Fourier spectrum is shown to the right. Although many wavelengths coexist in the initial perturbation, only those of intermediate wavelengths grow and the fastest growing wavelength dominates at the initial stage. Consequently, an increasingly regular wrinkle emerges from the initially random perturbation. As the evolution continues, the amplitude grows and the wavelength increases. After a sufficiently long time, only one wavelength remains and the wrinkle reaches an equilibrium state. Figure 6 plots the evolution of the dominant wavelength (maximum intensity in the Fourier spectrum), and Fig. 7 shows the root-mean square (rms) of the wrinkle as a function of time. Also plotted in Figs. 6 and 7 are the simulation results with a larger rubbery modulus, $\mu_\infty=0.0001E_f$, for comparison.

From the numerical simulations, three stages of wrinkle evolution can be identified: initial growth of the fastest growing mode, intermediate growth with mode transition, and, finally, an equilibrium wrinkle state. Such behavior qualitatively agrees with the experimental observations in a metal/polymer bilayer film [15]. At the initial stage, the wavelength of the fastest growing mode predicted by the linear perturbation analysis is $L_m=26.9h_f$, which is independent of the rubbery modulus. Figure 6(*a*) shows that the dominant wavelengths in the two simulations are indistinguishable up to $t=2\times10^4\tau$, and the wavelength is close to the predicted value. During this stage, the wrinkle amplitude grows exponentially, but the growth rate depends on the rubbery modulus. In Figure 7(*a*), the two dashed lines indicate the exponential growth predicted by the linear perturbation analysis, where the larger modulus leads to slower growth. At the intermediate stage, both the amplitude and wavelength of the wrinkle evolve toward the equilibrium state. The analytical solutions for the equilibrium state are indicated as dashed lines in Figs. 6(*b*) and 7(*b*). For $\mu_\infty = 0.00001E_f$, the equilibrium wrinkle has a wavelength $L_{eq} = 60.0h_f$ and an amplitude $A_{eq} = 1.63h_f$ (rms$=1.15h_f$). For $\mu_\infty = 0.0001E_f$, the equilibrium wrinkle has a wavelength $L_{eq} = 33.7h_f$ and an amplitude $A_{eq} = 0.619h_f$ (rms$=0.438h_f$). The equilibrium states agree closely with the numerical results. It is noted that, although the initial growth is slower, the time to reach the equilibrium state is significantly shorter with the larger rubbery modulus for the viscoelastic layer.

6 Summary

We have developed a nonlinear model for temporal evolution of wrinkles in elastic-viscoelastic bilayer thin films. The model couples a nonlinear theory of elastic plates with a thin-layer approximation of linear viscoelastic responses. Although the model is three-dimensional in nature, the analyses and numerical simulations of the present study have focused on plane-strain deformation. Analytical solutions are obtained for the linear perturbation analysis and the equilibrium state. Numerical simulations illustrate the evolution process from the initial growth to the equilibrium state. The results show that the kinetics of wrinkling strongly depend on the viscoelastic layer.

Acknowledgment

The authors are grateful for the support by NSF Grant No. CMS-0412851 and by the Texas Advanced Technology Program.

References

[1] Iacopi, F., Brongersma, S. H., and Maex, K., 2003, "Compressive Stress Relaxation Through Buckling of a Low-k Polymer-Thin Cap Layer System," Appl. Phys. Lett., **82**, pp. 1380–1382.

[2] Yin, H., Huang, R., Hobart, K. D., Liang, J., Suo, Z., Shieh, S. R., Duffy, T. S., Kub, F. J., and Sturm, J. C., 2003, "Buckling Suppression of SiGe Islands on Compliant Substrates," J. Appl. Phys., **94**, pp. 6875–6888.

[3] Watanabe, M., Shirai, H., and Hirai, T., 2002, "Wrinkled Polypyrrole Electrode for Electroactive Polymer Actuators," J. Appl. Phys., **92**, pp. 4631–4637.

[4] Lacour, S. P., Wagner, S., Huang, Z. Y., and Suo, Z., 2003, "Stretchable Gold Conductors on Elastomeric Substrates," Appl. Phys. Lett., **82**, pp. 2404–2406.

[5] Cerda, E., and Mahadevan, L., 2003, "Geometry and Physics of Wrinkling," Phys. Rev. Lett., **90**, 074302.

[6] Bowden, N., Brittain, S., Evans, A. G., Hutchinson, J. W., and Whitesides, G. M., 1998, "Spontaneous Formation of Ordered Structures in Thin Films of Metals Supported on an Elastomeric Polymer," Nature (London), **393**, pp. 146–149.

[7] Chua, D. B. H., Ng, H. T., and Li, S. F. Y., 2000, "Spontaneous Formation of Complex and Ordered Structures on Oxygen-Plasma-Treated Elastometric Polydimenthylsiloxane," Appl. Phys. Lett., **76**, pp. 721–723.

[8] Martin, S. J., Godschalx, J. P., Mills, M. E., Shaffer II, E. O., and Townsend, P. H., 2000, "Development of a Low-Dielectric-Constant Polymer for the Fabrication of Integrated Circuit Interconnect," Adv. Mater. (Weinheim, Ger.), **12**, pp. 1769–1778.

[9] Stafford, C. M., Harrison, C., Beers, K. L., Karim, A., Amis, E. J., Vanlandingham, M. R., and Kim, H.-C., Volksen, W., Miller, R. D., and Simonyi, E. E., 2004, "A Buckling-Based Metrology for Measuring the Elastic Moduli of Polymeric Thin Films," Nat. Mater., **3**, pp. 545–550.

[10] Groenewold, J., 2001, "Wrinkling of Plates Coupled With Soft Elastic Media," Physica A, **298**, pp. 32–45.

[11] Chen, X., and Hutchinson, J. W., 2004, "Herringbone Buckling Patterns of Compressed Thin Films on Compliant Substrates," J. Appl. Mech., **72**, pp. 597–603.

[12] Huang, Z. Y., Hong, W., and Suo, Z., 2005, "Nonlinear Analysis of Wrinkles in Films on Soft Elastic Substrates," J. Mech. Phys. Solids, **53**, pp. 2101–2118.

[13] Sridhar, N., Srolovitz, D. J., and Suo, Z., 2001, "Kinetics of Buckling of a Compressed Film on a Viscous Substrate," Appl. Phys. Lett., **78**, pp. 2482–2484.

[14] Huang, R., and Suo, Z., 2002, "Wrinkling of an Elastic Film on a Viscous Layer," J. Appl. Phys., **91**, pp. 1135–1142.

[15] Yoo, P. J., and Lee, H. H., 2003, "Evolution of a Stress-Driven Pattern in Thin Bilayer Films: Spinodal Wrinkling," Phys. Rev. Lett., **91**, 154502.

[16] Huang, R., 2005, "Kinetic Wrinkling of an Elastic Film on a Viscoelastic Substrate," J. Mech. Phys. Solids, **53**, pp. 63–89.

[17] Timoshenko, S., and Woinowsky-Krieger, S., 1987, *Theory of Plates and Shells*, 2nd Edition, McGraw-Hill, New York.

[18] Freund, L. B., and Suresh, S., 2003, *Thin Film Materials*, Cambridge University Press, Cambridge.

[19] Christensen, R. M. 1982, *Theory of Viscoelasticity*, Academic Press, New York.

[20] Reynolds, O., 1886, "On the Theory of Lubrication and its Applications to Mr. Beauchamp Tower's Experiments, Including an Experimental Determination of the Viscosity of Olive Oil," Philos. Trans. R. Soc. London, **177**, pp. 157–234.

[21] Xia, Z. C., and Hutchinson, J. W., 2000, "Crack Patterns in Thin Films," J. Mech. Phys. Solids, **48**, pp. 1107–1131.

[22] Huang, R., Prevost, J. H., and Suo, Z., 2002, "Loss of Constraint on Fracture in Thin Film Structures Due to Creep," Acta Mater., **50**, pp. 4137–4148.

[23] Allen, H. G., 1969, *Analysis and Design of Structural Sandwich Panels*, Pergamon, New York.

[24] Huang, Z. Y., Hong, W., and Suo, Z., 2004, "Evolution of Wrinkles in Hard Films on Soft Substrates," Phys. Rev. E, **70**, 030601(R).

[25] Huang, R., and Suo, Z., 2002, "Instability of a Compressed Elastic Film on a Viscous Layer," Int. J. Solids Struct., **39**, pp. 1791–1802.

Journal of Applied Mechanics

Technical Briefs

Three-Dimensional Contact Boundary Element Method for Roller Bearing

Guangxian Shen
College of Mechanical Engineering, Yanshan University,
Hebei 066004, China

Xuedao Shu
College of Mechanical Engineering, University of Science
and Technology, Beijing 100083, China

Ming Li
College of Mechanical Engineering, Yanshan University,
Hebei 066004, China

The analysis of the forces and the rigidity of roller bearings is a multi-body contact problem, so it cannot be solved by contact boundary element method (BEM) for two elastic bodies. Based on the three-dimensional elastic contact BEM, according to the character of roller bearing, the new solution given in this paper replaces the roller body with a plate element and traction subelement. Linear elements are used in non-contact areas and a quadratic element is used in the contact area. The load distribution among the roller bodies and the load status in the inner rolling body can be extracted. [DOI: 10.1115/1.2041662]

Introduction

Roller bearings are critical parts of rolling mills. Four-row roller bearings are normally used because of heavy loads and high speed. How long a roller bearing is used will affect the productivity of the rolling mill and the manufacturing cost (Shaowei, [1]). It is very important to consider the peculiar load distribution when choosing correct bearings and calculating bearing life. However, up to now, calculations are still based on ideal conditions (Harris, [2], Xuanhuai [3]). In fact, the assumed ideal conditions do not exist because the shape of the roller bearing and the external loading are very complicated. In addition, the distributed three-dimensional (3D) contact pressure on each row of the roller bearings is not uniform. It is improper to calculate contact pressure by assuming ideal conditions. Presently, many scholars have adopted mathematical methods to calculate the distribution of contact pressure on roller bearings (Jian [4], Honeygosky [7], and Jianxin, [10]), but their calculations assume only a two-dimensional distribution.

This paper is based on a three-dimensional elastic contact boundary element method (BEM). This new method adopts traction subelements (Xuedao [5], Yujin [12]) and utilizes plate elements, so the roller bearing contact problem changes into a two-body elastic contact problem without friction. The radial displacement of the rollers is calculated by the Hertz contact formula and is considered as a gap to be placed into the matrix equation (Chang'an [8] and Chang'an [9]). Thereby, the three-dimensional distribution of contact pressure on the roller bearing can be solved.

This method is suitable for multi-row tapered-roller bearings and other combinations of tapered cylindrical roller bearings.

Three-Dimensional Contact BEM for Roller Bearings

The special conditions for roller bearings follow:

(1) There are many contact bodies (Chang'an [9]).

(2) The dimensions of the inner and outer rings are much larger than the rollers, so all the rollers are considered to be the same.

(3) The rollers are assumed to have line contact with both the inner and outer rings of the roller bearing.

(4) The rolling friction coefficient is so small that the friction force may be neglected.

Based on these conditions, the authors adopted the traction subelement method to divide meshes on the contact surface of the roller bearing and have substituted a plate element to replace the middle rollers.

Traction Subelement Method. Figure 1 shows that the roller bearing can be divided into boundary elements according to the arrangement shown in Fig. 2. Assume that element i is in contact with the roller. The contact traction of this element is equal to the contact pressure on the roller. Therefore, on this element, its displacement is continuous, but its traction is discontinuous.

According to the contact condition of the roller bearing and the arrangement of meshes dividing the contact surface, this element may be divided into three subelements (shown in Fig. 3). On subelement Γ_i^1 and Γ_i^2, the traction is continuous, and on subelement Γ_i^3, the traction is equal to zero. Hence, the traction influence on coefficient is only calculated for Γ_i^1 and Γ_i^2. Because the displacement distribution is continuous, the displacement influence coefficient can be calculated directly for the whole element.

Since the traction distribution on the subelement Γ_i^1 and Γ_i^2 is unknown, a quadratic distribution along the length and width of the two subelements (shown in Fig. 3) is chosen as an approximation. So the traction t_i on the subelement can be expressed as follows:

Contributed by the Applied Mechanics Division of THE AMERICAN SOCIETY OF MECHANICAL ENGINEERS for publication in the ASME JOURNAL OF APPLIED MECHANICS. Manuscript received by the ASME Applied Mechanics Division, November 18, 2002; final revision, June 14, 2005. Review conducted by D. A. Siginer.

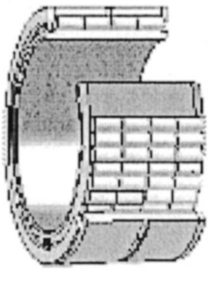

Fig. 1 Four row short cylinder roller bearing

$$\left\{\begin{aligned} t_i^1 &= \sum_{j=1}^{2} f_1(\xi_1) f_1(\xi_2) t_i^j \\ t_i^2 &= \sum_{j=3}^{4} f_2(\xi_1) f_2(\xi_2) t_i^j \end{aligned}\right. \tag{1}$$

By calculating Γ_i^1 and Γ_i^2, respectively, and adding them, the traction influence coefficient for the whole element can be obtained. Since the ratio of length to width on Γ_i^1 and Γ_i^2 is much larger (usually no less than 20), the elements of Γ_i^1 and Γ_i^2 must be divided further until the ratio of length to width is not more than 3, otherwise a singularity will occur when the traction influence coefficient is calculated.

Plate Element. A roller bearing is made up of an inner ring, an outer ring and several rollers (Fig. 1). The contact condition of one of these rollers is shown in Fig. 4 (Yujin [11], Brebbia [13])

$$\left.\begin{aligned} & t_{\xi 1}^{Q_0^A} = t_{\xi 1}^{Q_0^B} = 0, t_{\xi 2}^{Q_0^A} = t_{\xi 2}^{Q_0^B} = 0 \\ & t_{\xi 3}^{Q_0^A} - t_{\xi 3}^{Q_0^B} = 0, t_{\xi 3}^{Q_0^A} < 0 \\ & u_{\xi 3}^{Q_0^A} + u_{\xi 3}^{Q_0^B} = u_p^0 \end{aligned}\right\} Q_0^k \in \Gamma_{CC}, \quad k = A,B \tag{2}$$

$$\left.\begin{aligned} & t_{\xi j}^{Q_0^A} = t_{\xi j}^{Q_0^B} = 0, \quad j = 1,2,3 \\ & u_{\xi 3}^{Q_0^A} + u_{\xi 3}^{Q_0^B} < u_p^0 \end{aligned}\right\} Q_0^k \in \Gamma_{CF}, \quad k = A,B \tag{3}$$

$$\Gamma_C = \Gamma_{CC} + \Gamma_{CF} \tag{4}$$

where Γ_C, Γ_{CC}, Γ_{CF} are assumed to be the contact zone, the contact zone in fact, and the non-contact zone in Γ_C, respectively.

From Eqs. (2)–(4) and Fig. 4, we know that all the rollers are assumed to have only their radial displacements $u_{\xi 3}^{Q_i}$ and $u_{\xi 3}^{Q_i'}$ affecting the contact conditions, then the displacements in the other two directions are equal to zero. With the radial displacements $u_{\xi 3}^{Q_i}$ and $u_{\xi 3}^{Q_i'}$ being substituted into the system matrix equation incorporating the calculated gap information, further calculating precision will not be affected when the system equation is solved iteratively. So, in this paper, plate elements, having only radial displacements (the displacements in the other two directions are equal to zero) may replace the middle rollers. And the plate elements are fixed on the inner ring. The contact pairs are Q_i' and $Q_0^{B(i)}$. Then the multi-body contact problem can be transformed into a two-body contact problem.

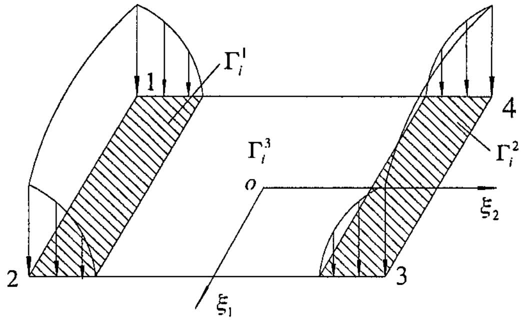

Fig. 3 Distribution of traction on the subelement

Plate element radial displacements $u_{\xi 3}^{Q_i}$ and $u_{\xi 3}^{Q_i'}$ can be calculated by the following Hertz contact formula. For cylindrical and tapered roller bearings, the radial displacement is:

$$\begin{bmatrix} u_{\xi 3}^{Q_i} \\ u_{\xi 3}^{Q_i'} \end{bmatrix} = \begin{bmatrix} \dfrac{0.580\left[\ln\left(\dfrac{4R_1R_2}{b_1^2}\right) + 0.814\right]}{E\ell} & 0 \\ 0 & \dfrac{1.82(1 - \ln b_2)}{E\ell} \end{bmatrix} \times \begin{bmatrix} t_{\xi 3}^{Q_0^A} \\ t_{\xi 3}^{Q_0^B} \end{bmatrix} \tag{5}$$

where

$$b_1 = 1.522\sqrt{\frac{PR_1R_2}{E\ell(R_2 + R_1)}}$$

$$b_2 = 1.522\sqrt{\frac{PR_1R_3}{E\ell(R_3 - R_1)}}$$

R_1 °TMRadius of short cylinder roller (mm)
R_2 °TMRadius of bearing internal ring (mm)
R_3 °TMRadius of bearing external ring (mm)
ℓ °TMLength of short cylinder roll (mm)

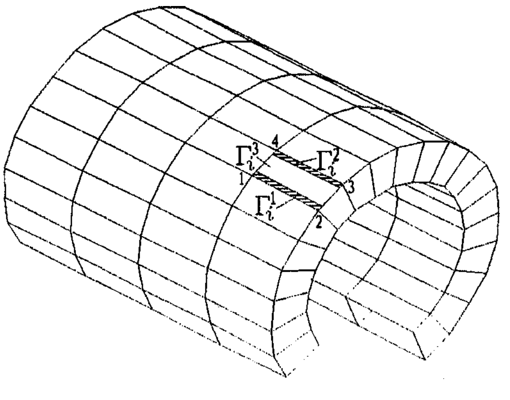

Fig. 2 Boundary discrete model

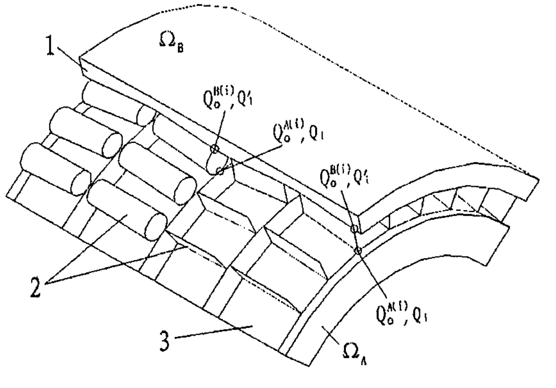

Fig. 4 Contact conditions described by plate element. 1. Outer ring 2. Middle rollers (plate element) 3. Inner ring

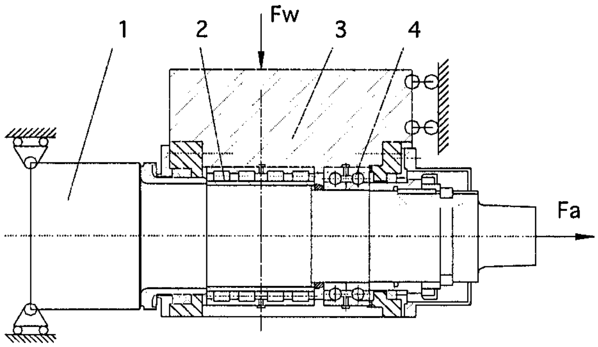

Fig. 5 Roller bearings mounted on the work roll. 1. Roll 2. Four row short cylindrical roller bearing 3. Chock 4. Double row angular contact ball bearing.

E °™Modulus of elasticity (GPa)

Therefore, when rollers are replaced by plate elements, the total radial gap is

$$u_p^0 = u_{\xi 3}^0 - u_{\xi 3}^{Q_i} - u_{\xi 3}^{Q_i'} \tag{6}$$

Three-Dimensional Contact BEM for Roller Bearing. A pair of contact points (Q_0^A, Q_0^B) is chosen arbitrarily from the roller bearing, and the physical strength is not considered. The Somigliana equation is expressed in the following form (Guangxian [15]):

$$u_j(P_0^A) = u_{\xi k}(P_0^A)\alpha_{jk}(P_0^A), \quad P_0^A \in \Gamma_C^A \tag{7}$$

$$\left.\begin{aligned} u_j(P_0^B) &= u_{\xi k}(P_0^B)\alpha_{jk}(P_0^B) \\ u_{\xi 3}(P_0^B) &= u_p^0 - u_{\xi 3}(Q_0^A) \end{aligned}\right\} P_0^B \in \Gamma_C^B \tag{8}$$

where α_{jk} is the direction cosine for the local coordinate ξ_j with respect to the coordinate x_k.

The matrix equation for the discrete boundary of the inner and outer rings of the roller bearing is

$$[H]^k[u]^k = [G]^k[t]^k \quad k = \text{A,B} \tag{9}$$

where $[H]^k$, $[G]^k$ are displacement and traction influence coefficients matrix of body k, $[u]^k$, $[t]^k$ are displacement and traction row matrices of body k.

According to the contact boundary condition of Eqs. (2)–(8), linking the matrix equation of body A and body B, leads to the system matrix Eq. (10).

$$C\Delta X = \Delta F \tag{10}$$

where

C °™influence coefficients matrix.

ΔX °™increments of unknown displacement and traction.

ΔF °™increments of known displacement and traction.

The three-dimensional distribution of contact pressure on the roller bearing can be obtained by solving the system matrix equations iteratively.

This method has a high precision because the elastic deformations of the inner and outer rings of the roller bearing and rollers are taken into consideration.

Example

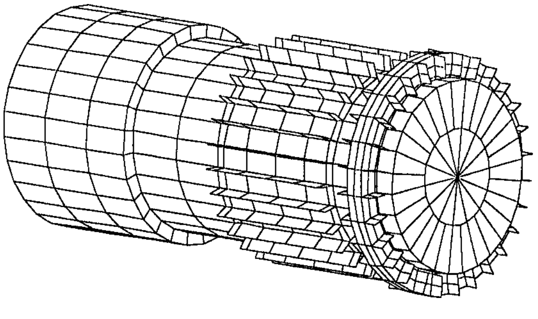

Fig. 6 Boundary element model of the roll

The intermediate mill for rolling 2350 alloy aluminum foil is used as an example for modeling a particular loading of the work roll. Four short cylindrical roller bearings are mounted on the work roll shown in Fig. 5. Boundary element models for the roll and for the chock are shown in Figs. 6 and 7. The roll is divided into 700 elements with 702 nodes, and the chock is divided into 1296 elements with 1296 nodes. Both of them have 364 node pairs in possible contact. In the assumed contact zone, the boundary surface is divided into quadratic elements by the rule of traction subelement method. The elements of rest boundary surface are linear elements, and satisfy the rule that the ratio of length to width is not more than 3. The calculating parameters are shown in Table 1.

A peculiar load is shown in Figs. 8 and 9 when the roller is simulated by the plate element. Through the calculations described above, we can say that the load on the cylindrical roller bearings is seriously uneven. The coefficient of unevenness is about 3.5. The distribution of the load on the end thrust bearing is also uneven along the circle. About 60% of the rollers bear the

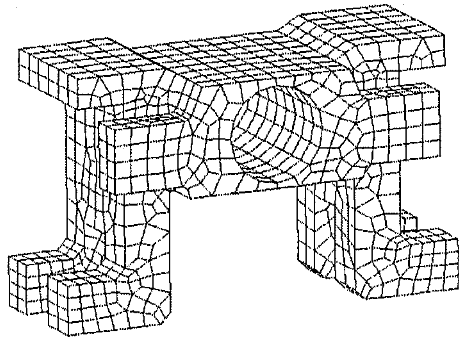

Fig. 7 Boundary element model of the chock

Table 1 2350 aluminum foil mill roller bearing load peculiarity calculating parameters

Diameter of roll neck	Length of roll body	Initial gap	Modulus of elasticity	Bend force	Thrust force
d/mm	L/mm	u_R/mm	E/GPa	F_W/KN	F_a/KN
165	2350	0.035	210	50	40

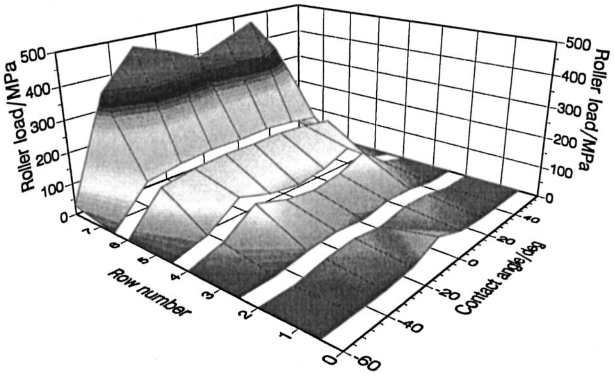

Fig. 8 3D distribution of the load on four-row cylinder roller bearing under open restrain conditions

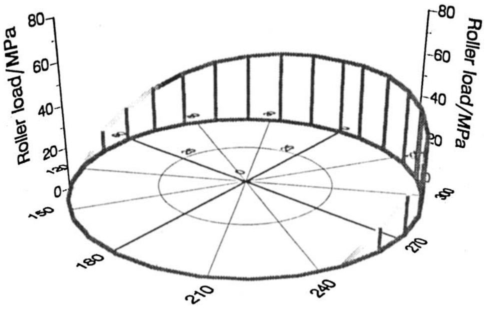

Fig. 9 Circumferential distributions of the load on thrust bearing under open restrain conditions

total load (Zhanfu [6], Honeygosky [7]). Compared with the known result by FEM, the rule of load radial distribution is accordant (Honeygosky [7], Jianxin [10]). Therefore, the method is effective for calculating 3D load distribution of roller bearing.

Conclusions

1. Based on the BEM for the three-dimensional elastic contact problem, a new BEM has been used to calculate the particular 3D load on the roller bearing. The traction subelements are connected by the plate element that is used to simulate the roller. Deformation of roller is calculated by the Hertz contact formula. This method has utilized a simple calculating model and provides an effective method.
2. This method can also be used to calculate particular loads for multi-row tapered-roller bearings and other combinations of tapered cylindrical roller bearings.
3. This method is a valid computational tool for the life of roller bearing and analyzing particular roller bearing loads.

Acknowledgment

The National Natural Science Foundation of China sponsors this research work (No. 50075075).

References

[1] Shaowei, Z., et al., 1998, "Retrospect and Prospect of Large Scale Bearing Longevity Pre-estimate," China Engineer, **3**, p. 9.
[2] Harris, T. A., and Jiwei, L., et al., 1997, *Translating Analysis of Roller Bearing*, Luoyang Bearing Research Institute, pp. 129–188.
[3] Xuanhuai, Q., 1997, *Mechanical Design*, Higher Education, pp. 369–388.
[4] Jian, L., 1998, "Analysis of Mechanic Peculiarity of SY Type High Rigid Mill," Metall. Equip., (1), pp. 16–22.
[5] Shu, Xuedao, Zhangfu, C., and Guangxian, S., 1999, "Numerical Calculation of Special Load of Mill Bearing," Heavy Machine, (1), pp. 31–34.
[6] Zhanfu, C., 2000, "Characteristics of Heavy-duty Mechanism Synthesis and Multi-column Rolling Self-aligning Principle," Metall. Equip., **2**, pp. 5–8.
[7] Honeygosky, M. A., Gracia, J. A., and Butine, J. A., 1993, "Finite Element Analysis of Work Roll Chock and Bearing Equipment," Iron Steel Eng., **1**, pp. 46–49.
[8] Chang'an, I., and Xiaowen, Z., 1996, "Deformation Characteristics of Tapered Roller Bearing With Load," Bearing, **7**, pp. 6–11.
[9] Chang'an, D., and Jianyu, Z., 1996, "Deformation of Roller Bearing With Load," Bearing, **9**, pp. 6–9.
[10] Jianxin, H., and Jianyu, Z., 1994, "Analysis of the Bearing Lifetime on GY-Type Short-Stress Path Mill," Iron Steel Eng., **29**, pp. 69–70.
[11] Yujin, H., and Yunke, L., 1994, "Application of BEM in Rolling Bearing Load Distribution Calculation," Bearing, **6**, pp. 5–8.
[12] Yujin, H., and Yunke, L., 1992, "Sub-structure Method of Rolling Bearing 3-D Finite Element Analysis," Bearing, **3**, pp. 2–7.
[13] Brebbia, C. A., Telles, T. C., and Worbel, L. C., 1984, *Boundary Element Method Techniques*, Springer, New York.
[14] Guangxian, S., et al., 1992, "Test and Study About Radial Load Distribution of Four-Rows Roller Bearing," Exp. Mech., **4**, pp. 16–19.
[15] Guangxian, S., and Xingchang, L., 1990, "Computation of Three-dimensional Contact Pressure Distribution on Multi-Row Roller Bearing by BEM," Comput. Struct. Mech. Appl., **7**, pp. 9–16.

Stability of Second-Order Asymmetric Linear Mechanical Systems With Application to Robot Grasping

Amir Shapiro
Department of Mechanical Engineering,
Ben Gurion University of the Negev,
P. O. B. 653, Beer Sheva 84105, Israel

This technical correspondence presents a surprisingly simple analytical criterion for the stability of general second-order asymmetric linear systems. The criterion is based on the fact that if a symmetric system is stable, adding a small amount of asymmetry would not cause instability. We compute analytically an upper bound on the allowed asymmetry such that the overall linear system is stable. This stability criterion is then applied to robot grasping arrangements which, due to physical effects at the contacts, are asymmetric mechanical systems. We present an application of the stability criterion to a 2D grasp arrangement.
[DOI: 10.1115/1.2042484]

Introduction

This technical correspondence is concerned with the stability of second-order linear systems that have an asymmetric stiffness matrix. Our goal is to provide an analytical criterion for the stability of systems of the form

$$M\ddot{p} + K_d\dot{p} + K_p p = 0, \tag{1}$$

where $M \in \mathbb{R}^{n\times n}$ and $K_d \in \mathbb{R}^{n\times n}$ are symmetric positive definite, and $K_p \in \mathbb{R}^{n\times n}$ is *asymmetric*. Such systems arise in the linearized dynamics of robot grasping arrangements [1], and in other applications such as feedback control. See, for instance, [2] and [3, p. 36].

Researchers have taken the following approach to the investigation of general asymmetric systems, where M, K_d, and K_p are asymmetric. Their approach is based on transforming the asymmetric system into a symmetric one. The subclass of asymmetric systems that can be transformed into symmetric systems is called symmetrizable systems. Inman has introduced necessary and sufficient conditions for a subclass of such systems to be symmetrizable via similarity transformation [4]. Ahmadian and Chou have developed a systematic technique for computing the coordinate system in which the symmetrizable system is symmetric [5]. Coghey and Ma have given a condition for transforming the system into a decoupled diagonal system [6]. Utilizing equivalence transformation rather than similarity transformation enables the subclass of symmetrizable systems to be enlarged [7,8]. All these results are exact and give conditions for the stability of the original asymmetric system. However, only subclasses of asymmetric systems can be treated in these ways, and the application of stability criteria based on transformation to symmetric systems is cumbersome.

In this technical correspondence we develop a simple criterion for the stability of asymmetric systems of the form (1). In the context of robot grasping applications, this stability criterion leads to a synthesis rule that indicates which contact points and what preloading profile guarantee stable grasp.

We make the following two assumptions, which are motivated by consideration of the grasping application. First, as in many mechanical systems, we assume that the inertia and damping matrices, M and K_d, are symmetric positive definite matrices. Second, we assume that the symmetric part of the stiffness matrix, $(K_p)_s = \frac{1}{2}(K_p + K_p^T)$, is positive definite. This assumption has been shown to hold true for almost every robot grasping application [1].

The stability criterion is based on the idea that if the symmetric system is asymptotically stable, one can add a bounded amount of asymmetry and the system will remain stable. In our solution we compute an upper bound on the norm of $(K_p)_{as} = \frac{1}{2}(K_p - K_p^T)$ such that the eigenvalues of the first-order equation recast from Eq. (1) are located in the open left half-plane. After establishing the stability criterion for such systems, we illustrate the applicability of the result for analyzing the stability of robot grasping arrangements.

Stability of Second-Order Asymmetric Systems

For simplicity we begin with the following system:

$$\ddot{p} + K_d\dot{p} + K_p p = 0, \tag{2}$$

which is identical to (1), except that here M is the identity matrix. The following theorem states that if the skew-symmetric part of K_p, $(K_p)_{as}$, is sufficiently small, the system (2) is globally asymptotically stable.

THEOREM 1 *(global asymptotic stability). Consider the system (2). Let $\beta \in \mathbb{R}$ be the minimal eigenvalue of K_d. Let $\alpha \in \mathbb{R}$ be the minimal eigenvalue of $(K_p)_s$, and let $\gamma \in \mathbb{R}$ be the matrix norm[1] of the skew-symmetric part of K_p. If*

$$|\gamma| < \sqrt{\alpha}\beta,$$

the system (2) is globally asymptotically stable.

Proof: The system (2) can be written as

$$\frac{d}{dt}\begin{pmatrix} p \\ \dot{p} \end{pmatrix} = \underbrace{\begin{bmatrix} 0 & I \\ -K_p & -K_d \end{bmatrix}}_{A}\begin{pmatrix} p \\ \dot{p} \end{pmatrix}.$$

For global asymptotic stability, it suffices to show that the real part of the eigenvalues of A is negative. Let $\lambda \in \mathbb{C}$ be an eigenvalue of A with corresponding nonzero eigenvector $\nu = (\nu_1, \nu_2) \in \mathbb{C}^{2n}$. Note that each ν_i is a complex vector in $\mathbb{C}^n$. Then

$$\begin{bmatrix} 0 & I \\ -K_p & -K_d \end{bmatrix}\begin{pmatrix} \nu_1 \\ \nu_2 \end{pmatrix} = \begin{pmatrix} \nu_2 \\ -K_p\nu_1 - K_d\nu_2 \end{pmatrix} = \lambda\begin{pmatrix} \nu_1 \\ \nu_2 \end{pmatrix}.$$

Since $(K_p)_s > 0$, K_p is nonsingular. This implies that $\lambda = 0$ cannot be an eigenvalue of A. Since $\lambda \neq 0$, it follows that $\nu_1 \neq \vec{0}$ and $\nu_2 \neq \vec{0}$. Hence, we may assume without loss of generality that $\nu_1^* \cdot \nu_1 = 1$, where $*$ denotes complex conjugate transpose. Based on this choice, we can write $\lambda^2 = \nu_1^*\lambda^2\nu_1 = \nu_1^*\lambda\nu_2 = \nu_1^*(-K_p\nu_1 - K_d\nu_2) = -\nu_1^*K_p\nu_1 - \lambda\nu_1^*K_d\nu_1$, where we used the relations $\lambda\nu_1 = \nu_2$ and $\lambda\nu_2 = -K_p\nu_1 - K_d\nu_2$. Since $K_d > 0$, the scalar $\tilde{\beta} = \nu_1^*K_d\nu_1$ is positive real. Similarly, the scalar $\tilde{\alpha} = \nu_1^*(K_p)_s\nu_1$ is also positive real. Since $(K_p)_{as}$ is skew-symmetric, we can write $j\tilde{\gamma} = \nu_1^*(K_p)_{as}\nu_1$, where $j = \sqrt{-1}$ and $\tilde{\gamma}$ is real. Substituting these scalars into the quadratic equation in λ gives

$$\lambda^2 + \tilde{\beta}\lambda + \tilde{\alpha} + j\tilde{\gamma} = 0. \tag{3}$$

Note that every eigenvalue of A satisfies this equation. The solution of (3) is

---

Contributed by the Applied Mechanics Division of THE AMERICAN SOCIETY OF MECHANICAL ENGINEERS for publication in the ASME JOURNAL OF APPLIED MECHANICS. Manuscript received by the ASME Applied Mechanics Division, July 18, 2004; final revision, March 3, 2005. Review conducted by N. Sri Namachchivaya.

[1] The matrix norm is defined as $\|E\| = \max\{\|Eu\|\}$ over all vectors $\|u\| \leq 1$.

$$\lambda_{1,2} = \tfrac{1}{2}(-\tilde{\beta} \pm \sqrt{\tilde{\beta}^2 - 4(\tilde{\alpha} + j\tilde{\gamma})}). \tag{4}$$

Let us pause to recall how one computes the square root of a complex number. Consider a complex number $z = a + jb$ with a norm $|z| = \sqrt{a^2 + b^2}$ and argument $\theta = \arctan(b/a)$. Then $\sqrt{z} = \pm(a^2 + b^2)^{1/4} \angle \theta/2$, and in Cartesian coordinates $\sqrt{z} = \pm(a^2 + b^2)^{1/4}[\cos(\theta/2) + j\sin(\theta/2)]$. Since $\cos(\theta) = a/\sqrt{a^2+b^2}$, we use the trigonometric identity $\cos(\theta/2) = \sqrt{[1 + \cos(\theta)]/2}$ to obtain

$$\mathrm{Re}\{\sqrt{z}\} = \pm \frac{(a^2+b^2)^{1/4}}{\sqrt{2}}\left(1 + \frac{a}{\sqrt{a^2+b^2}}\right)^{1/2}.$$

In our case $a = \tilde{\beta}^2 - 4\tilde{\alpha}$ and $b = -4\tilde{\gamma}$, and (4) implies that

$$\mathrm{Re}\{\lambda_{1,2}\} = -\frac{\tilde{\beta}}{2} \pm \frac{[(\tilde{\beta}^2 - 4\tilde{\alpha})^2 + 16\tilde{\gamma}^2]^{1/4}}{2\sqrt{2}} \times \left(1 + \frac{\tilde{\beta}^2 - 4\tilde{\alpha}}{\sqrt{(\tilde{\beta}^2 - 4\tilde{\alpha})^2 + 16\tilde{\gamma}^2}}\right)^{1/2}.$$

The requirement $\mathrm{Re}\{\lambda_{1,2}\} < 0$ introduces an inequality in $\tilde{\alpha}$, $\tilde{\beta}$, and $\tilde{\gamma}$. Rearranging terms in this inequality gives the equivalent inequality,

$$(4\tilde{\alpha} + \tilde{\beta}^2)^2 > (\tilde{\beta}^2 - 4\tilde{\alpha})^2 + 16\tilde{\gamma}^2.$$

Cancelling similar terms yields the inequality

$$|\tilde{\gamma}| < \sqrt{\tilde{\alpha}}\tilde{\beta}. \tag{5}$$

For stability we must ensure that (5) holds for every $\tilde{\alpha}$, $\tilde{\beta}$, and $\tilde{\gamma}$. In other words, (5) must hold for every eigenvalue λ and every associated eigenvector ν of A. Therefore we bound $\tilde{\alpha}$, $\tilde{\beta}$, and $\tilde{\gamma}$ as follows. First, $0 < \alpha = \lambda_{min}((K_p)_s) \leqslant \nu_1^*(K_p)_s\nu_1 = \tilde{\alpha}$. Second, $0 < \beta = \lambda_{min}(K_d) \leqslant \nu_1^* K_d \nu_1 = \tilde{\beta}$. Third, $|\gamma| = \|(K_p)_{as}\| \geqslant |\nu_1^*(K_p)_{as}\nu_1| = |j\tilde{\gamma}| = |\tilde{\gamma}|$. Using these bounds, $\gamma < \sqrt{\alpha}\beta$ implies that $|\tilde{\gamma}| < \sqrt{\tilde{\alpha}}\tilde{\beta}$ for every $\tilde{\alpha}$, $\tilde{\beta}$, and $\tilde{\gamma}$. □

Note that the theorem gives only sufficient stability condition, and the proof does not indicate what should be the necessary condition for global asymptotic stability. Next, we present a corollary that adapts the theorem to a global asymptotic stability criterion for systems that contain a nonunit inertia matrix.

COROLLARY 2.1. *Consider the following system*

$$M\ddot{p} + K_d\dot{p} + K_p p = 0, \tag{6}$$

where all parameters are as above, except for the matrix M which is symmetric positive definite. Let $\beta > 0$ *be the minimal eigenvalue of* $M^{-1/2}K_dM^{-1/2}$. *Let* $\alpha > 0$ *be the minimal eigenvalue of* $M^{-1/2}(K_p)_sM^{-1/2}$, *and let* $\gamma \in \mathbb{R}$ *be the matrix norm of* $M^{-1/2}(K_p)_{as}M^{-1/2}$. *If*

$$|\gamma| < \sqrt{\alpha}\beta$$

the system (6) is globally asymptotically stable.

Proof. We define the coordinate transformation $\tilde{p} = M^{1/2}p$ or $p = M^{-1/2}\tilde{p}$. (A similar transformation appeared in [3, p. 87].) Note that the matrices $M^{1/2}$ and $M^{-1/2}$ are symmetric positive definite. Moreover, we have that $M = M^{1/2}M^{1/2}$ and $M^{-1} = M^{-1/2}M^{-1/2}$. Substituting the new coordinates into (1) and premultiplying by $M^{-1/2}$ gives

$$\ddot{\tilde{p}} + \underbrace{M^{-1/2}K_dM^{-1/2}}_{\tilde{K}_d}\dot{\tilde{p}} + \underbrace{M^{-1/2}K_pM^{-1/2}}_{\tilde{K}_p}\tilde{p} = 0.$$

This system is exactly of the form used for Theorem 1, but instead of K_d and K_p we now have $\tilde{K}_d$ and $\tilde{K}_p$, respectively. If the latter system is asymptotically stable, it entails that (1) is asymptotically stable, since the two systems differ only by coordinate transformation. The global asymptotic stability of (6) therefore follows from Theorem 1. □

We conclude this section with a simple numerical example that shows the applicability of the stability criterion.

Example. Consider the dynamical system

$$\begin{bmatrix} 10 & 0 \\ 0 & 11 \end{bmatrix}\ddot{p} + \begin{bmatrix} 4 & 1 \\ 1 & 5 \end{bmatrix}\dot{p} + \begin{bmatrix} 8 & s \\ -s & 9 \end{bmatrix}p = 0, \tag{7}$$

where s is a free parameter. The matrices M, K_d, and the symmetric part of K_p are all symmetric positive definite. Hence, when $s = 0$ the system is symmetric and asymptotically stable. Qualitatively, increasing the value of s increases the asymmetric part of the stiffness matrix. Calculation of α, β, and γ yields $\alpha = \frac{4}{5}$, $\beta = 0.328$, and $\gamma = s/\sqrt{110}$. Therefore, the stability condition of Corollary 2.1 becomes the condition $|s| < 3.078$. For comparison we numerically calculated the eigenvalues of the 4×4 matrix A. It turns out that for $0 \leqslant s < 3.920$ the system (7) is asymptotically stable (A's eigenvalues are in the left half-plane). We can see that apart from being conservative, our stability condition correctly predicts the system's global asymptotic stability.

Application to Grasp Synthesis

In this section our objective is to determine the stability of frictional grasps or fixtures. We consider a grasp, or fixture, arrangement where a 2D object B is held by stationary 2D bodies $A_1, \ldots, A_k$ that represent fingertips or fixturing elements. We assume frictional contacts between the stationary bodies $A_1, \ldots, A_k$ and B. The usual assumption made in the solid mechanics literature is that the contacting bodies are *quasi-rigid*, which means that their deformations due to compliance effects are localized to the vicinity of the contacts [9]. This assumption is always valid for all bodies that are not made of exceptionally soft material and do not contain slender substructures [10]. The quasi-rigidity assumption allows us to describe the overall motion of B relative to the stationary bodies $A_1, \ldots, A_k$ using rigid body kinematics. Since the grasping bodies are stationary, we focus on B's *configuration space* (c-space). The c-space of a planar object is parametrized by $q = (d, \theta) \in \mathbb{R}^2 \times \mathbb{R}$, where d is B's position and θ is a parametrization of B's orientation.

We have derived the following linearized dynamics of a quasi-rigid object B held in equilibrium grasp by stationary quasi-rigid bodies $A_1, \ldots, A_k$ [1]:

$$M(q_0)\Delta\ddot{q} + K_d(q_0)\Delta\dot{q} + K_p(q_0)\Delta q = 0, \tag{8}$$

where q_0 is the grasped object equilibrium configuration and Δq is the deviation of the actual configuration from the equilibrium.

In grasping applications $M(q_0)$ is the inertia matrix, and $K_d(q_0)$ is the damping matrix. Both matrices are symmetric and positive definite. The matrix $K_p(q_0)$ is the grasp stiffness matrix associated with the mechanics of quasi-rigid frictional contacts. This matrix is composed of the individual contact stiffness matrices, which are asymmetric. See [1] for more details.

The asymmetry of K_p strongly depends on the direction of the contact forces, which in some cases can be selected during grasp synthesis. The magnitude of the matrix norm of $(K_p)_{as}$ increases as the angle between the contact force and the normal at the contacts increases.

For example, consider the two-finger frictional grasp shown in Fig. 1. The example shows a grasp of a wedge-like object, which has a head angle ϕ and base angle $90° - \phi$ as shown in the figure. Hence, the example is actually a grasp of a family of wedge-like objects with different head angles. In this example we assume that the friction is sufficiently large that the fingers do not slide. Of course, the two-finger grasp forms an equilibrium grasp. However, the stiffness matrix K_p is asymmetric and local deformations at the contacts can cause instability. In the example, if the contact forces F_1 and F_2 are collinear with the normals at the contacts n_1 and n_2, then K_p is symmetric. When the contact forces rotate away from

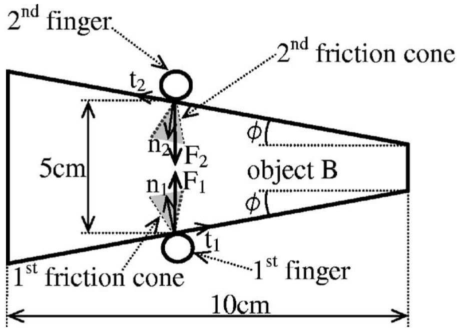

Fig. 1 A two-finger grasp of a family of wedge-like objects

the normal directions the matrix norm $\|(K_p)_{as}\|$ increases. The rotation of the contact forces with respect to the normal is due to the grasping of different objects with varying ϕ angles. The stability condition of Corollary 2.1 places a limit on the amount of asymmetry allowed. Consequently, it bounds the value of the allowed angle ϕ. Computation of the maximal ϕ angle reveals that the grasp is stable for $\phi < 12.68°$.

Conclusion

Adding an asymmetric matrix to a stable symmetric second-order system has the potential to cause instability. In order to avoid such instability, we establish an analytic upper bound on the amount of asymmetry that is guaranteed to keep the asymmetric system globally asymptotically stable. It should be emphasized that the simple criterion presented here is sufficient for stability, but it is not the necessary stability condition. Hence, if the criterion is satisfied, it predicts the system stability, but, if it is not satisfied, it cannot definitely predict if the system is unstable.

Recent results show that a frictional contact stiffness matrix is asymmetric. As a result, the grasp stiffness matrix of the entire grasp is asymmetric. We obtained a concise condition for the global asymptotic stability of the grasp linearized dynamics and therefore a local asymptotic stability for the nonlinear system.

Acknowledgment

I would like to thank Elon Rimon for his valuable comments and for helping me in preparing this technical correspondence item. I would also like to gratefully acknowledge many fruitful discussions with Yizhar Or.

References

[1] Shapiro, A., and Rimon, E., 2004, "On the Mechanics of Natural Compliance in Frictional Contacts and Its Effect on Grasp Stiffness and Stability," IEEE Int. Conference on Robotics and Automation, pp. 1264–1269.

[2] Kliem, W. R., 1992, "Symmetrizable Systems in Mechanics and Control Theory," ASME J. Appl. Mech., **59**, pp. 454–456.

[3] Inman, D. J., 1989, *Vibration With Control Measurement and Stability*, Prentice-Hall, Englewood Cliffs, NJ.

[4] Inman, D. J., 1983, "Dynamics of Asymmetric Nonconservative Systems," ASME J. Appl. Mech., **50**, pp. 199–203.

[5] Ahmadian, M., and Chou, S.-H., 1987, "A New Method for Finding Symmetric Form of Asymmetric Finite-Dimensional Dynamic Systems," ASME J. Appl. Mech., **54**, pp. 700–705.

[6] Caughey, T. K., and Ma, F., 1993, "Complex Modes and Solvability of Nonclassical Linear Systems," ASME J. Appl. Mech., **60**, pp. 26–28.

[7] Ma, F., and Caughey, T. K., 1995, "Analysis of Linear Nonconservative Vibrations," ASME J. Appl. Mech., **62**, pp. 685–691.

[8] Adhikari, S., 2000, "On Symmetrizable Systems of Second Kind," ASME J. Appl. Mech., **67**, pp. 797–802.

[9] Johnson, K. L., 1985, *Contact Mechanics*, Cambridge University Press, Cambridge, UK.

[10] Xydas, N., and Kao, I., 1999, "Modeling of Contact Mechanics and Friction-Limit-Surfaces for Soft Fingers in Robotics, With Experimental Results," Int. J. Robot. Res., **18**(8), pp. 941–950.

On the Modified Virtual Internal Bond Method

K. Y. Volokh
Faculty of Civil and Environmental Engineering,
Technion, Haifa 32000, Israel
e-mail: cvolokh@tx.technion.ac.il

H. Gao
Max Planck Institute for Metals Research,
Heisenbergstrasse 3, Stuttgart 70569, Germany
e-mail: hjgao@mf.mpg.de

The virtual internal bond (VIB) method was developed for the numerical simulation of fracture processes. In contrast to the traditional approach of fracture mechanics where stress analysis is separated from a description of the actual process of material failure, the VIB method naturally allows for crack nucleation, branching, kinking, and arrest. The idea of the method is to use atomic-like bond potentials in combination with the Cauchy-Born rule for establishing continuum constitutive equations which allow for the material separation–strain localization. While the conventional VIB formulation stimulated successful computational studies with applications to structural and biological materials, it suffers from the following theoretical inconsistency. When the constitutive relations of the VIB model are linearized for an isotropic homogeneous material, the Poisson ratio is found equal to $1/4$ *so that there is only one independent elastic constant—Young's modulus. Such restriction is not suitable for many materials. In this paper, we propose a modified VIB (MVIB) formulation, which allows for two independent linear elastic constants. It is also argued that the discrepancy of the conventional formulation is a result of using only two-body interaction potentials in the microstructural setting of the VIB method. When many-body interactions in "bond bending" are accounted for, as in the MVIB approach, the resulting formulation becomes consistent with the classical theory of isotropic linear elasticity.*
[DOI: 10.1115/1.2047628]

1 Introduction

As a possible alternative to the Griffith-Orowan-Irwin approach to fracture mechanics, multiscale material considerations may be used to formulate continuum models allowing for material separation–strain localization. Based on the so-called Cauchy-Born rule, a virtual internal bond approach to modeling material failure has been proposed by Gao and Klein [1]. This approach differs from atomistic methods in that a phenomenological "cohesive force law" is assumed to act between "material particles" which are not necessarily atoms; it also differs from the "cohesive surface" models in that, rather than imposing a cohesive law along a prescribed set of discrete surfaces, a network of cohesive bonds is statistically incorporated into a constitutive law via the Cauchy-Born rule, i.e., by equating the strain energy density on the continuum level to the potential energy stored in the cohesive bonds due to the imposed deformation.

Although the conventional formulation of the VIB model can be successfully used in simulations of crack nucleation, growth, kinking, and branching, it suffers from the following inconsistency. When the constitutive relations of the VIB model are linearized for an isotropic homogeneous material, they allow for only one independent material constant—Young's modulus—while the second constant—Poisson ratio—is not independent and it is equal to $1/4$. Since such restriction is not suitable for many materials, it is desirable to modify the conventional VIB formulation. This is done in the present work. The modified formulation allows for two independent material constants in the case of the linearized isotropic elasticity. The conventional formulation of VIB is based on two-body interaction potentials in the microstructural setting. The modified VIB approach accounts for many-body interactions associated with "bond bending" and the resulting formulation appears to be more consistent with the classical theory of isotropic linear elasticity.

2 Conventional VIB Formulation and its Deficiency

Consider a solid body comprising microparticles, for example, atoms, placed at $\mathbf{r}_i$ in the 3D space. Generally, the volumetric density of the total potential energy of the body is a function of the particle positions: $\Phi(\mathbf{r}_1,\mathbf{r}_2,\ldots,\mathbf{r}_n)$, where n is the number of particles. More specifically, the potential energy can be written in terms of two-particle interactions as

$$\Phi=\frac{1}{2\Omega}\sum_{i,j}U(r_{ij}),\quad r_{ij}=|\mathbf{r}_{ij}|=|\mathbf{r}_i-\mathbf{r}_j|,\tag{2.1}$$

where Ω is the volume occupied by the system.

According to the Cauchy-Born rule, originally applied to the crystal elasticity, the current $\mathbf{r}_{ij}$ and initial (reference) $\mathbf{R}_{ij}=\mathbf{R}_i-\mathbf{R}_j$ relative positions of the same two particles can be related by the deformation gradient $\mathbf{F}=\mathrm{Grad}\boldsymbol{\chi}(\mathbf{X})$:

$$\mathbf{r}_{ij}=\mathbf{F}\mathbf{R}_{ij},\tag{2.2}$$

It is assumed above that particles are in the vicinity of point $\mathbf{X}$ at the reference state. This point is placed at $\boldsymbol{\chi}(\mathbf{X})$ after the deformation.

Substituting Eq. (2.2) in Eq. (2.1) yields

$$\Phi=\frac{1}{2\Omega}\sum_{i,j}U(r_{ij})=\Phi(\mathbf{C}),\quad \mathbf{C}=\mathbf{F}^T\mathbf{F}.\tag{2.3}$$

Now the second Piola-Kirchhoff stress tensor and the tangent stiffness, moduli can be derived in the usual way: $S_{IJ}=2\partial\Phi/\partial C_{IJ}$; $K_{IJMN}=2\partial S_{IJ}/\partial C_{MN}$. Evidently, the microstructural approach is as phenomenological as continuum mechanics. The phenomenology, however, is moved to the microlevel in the former case to allow for more flexible analysis.

Direct application of Eq. (2.3) to analysis of material behavior seems to be difficult because of the large amount of microparticles. Gao and Klein [1] and Klein and Gao [2,3] proposed the following averaging procedure:

$$\Phi=\frac{1}{\Omega_0}\int_{\Omega_0^*}U(l)D_\Omega d\Omega.\tag{2.4}$$

Here Ω_0 is the reference representative volume; $U(l)$ is the bond potential; $l=r_{ij}=L\sqrt{\xi_I C_{IJ}\xi_J}$ is the current virtual bond length; $\boldsymbol{\xi}=(\mathbf{R}_i-\mathbf{R}_j)/L$; $L=R_{ij}=|\mathbf{R}_i-\mathbf{R}_j|$; D_Ω is the volumetric bond density function; and Ω_0^* is the integration volume defined by the range of influence of U.

Considerations being limited to centrosymmetric bond density functions, where spherical coordinates are used: $\xi_1=\sin\theta\cos\varphi$; $\xi_2=\sin\theta\sin\varphi$; $\xi_3=\cos\theta$, it is possible to express an average as

$$\langle\bullet\rangle=\frac{1}{\Omega_0}\int_{-\pi}^{\pi}\int_0^{\pi}\int_0^{L^*}(\bullet)D(L,\theta,\varphi)L^2\sin\theta dLd\theta d\varphi,\tag{2.5}$$

where L^* presents the maximum distance over which particles interact. Then the elastic moduli take the form

---

Contributed by the Applied Mechanics division of THE AMERICAN SOCIETY OF MECHANICAL ENGINEERS for publication in the ASME JOURNAL OF APPLIED MECHANICS. Manuscript received by the ASME Applied mechanics Division, November 2, 2004; final revision, April 5, 2005. Review conducted by R. M. McMeeking.

$$K_{IJMN}=4\partial\Phi/\partial C_{IJ}\partial C_{MN}=\langle (U''(l)/l^2-U'(l)/l^3)L^4\xi_I\xi_J\xi_M\xi_N\rangle . \tag{2.6}$$

The precise definition of $D(L,\theta,\varphi)$ is that $D(L,\theta,\varphi)L^2\sin\theta dLd\theta d\varphi$ presents the number of bonds in the undeformed solid with bond length between L and $L+dL$ and orientation between $\{\theta,\varphi\}$ and $\{\theta+d\theta,\varphi+d\varphi\}$.

So far, most reported analyses based on the VIB model use the simple two-parameter phenomenological cohesive force law: $U'(l)=A(l-L)\exp[-B(l-L)]$, where A is the slope of $U'(l)$ for the unstretched bond and $1/B$ is the critical stretch at which the maximum bond strength is reached.

The deficiency of the conventional formulation appears under the assumption of homogeneity and isotropy of material, i.e., $D(L,\theta,\varphi)=D_L(L)$. In this case, the linearized elastic moduli take the form

$$K_{IJMN}=\langle U''(L)L^2\rangle_L\int_{-\pi}^{\pi}\int_{0}^{\pi}\xi_I\xi_J\xi_M\xi_N\sin\theta d\theta d\varphi$$

$$=\mu(\delta_{IJ}\delta_{MN}+\delta_{IM}\delta_{JN}+\delta_{IN}\delta_{JM}). \tag{2.7}$$

Here $\mu=4\pi\langle L^2U''(L)\rangle_L/15$ is the only elastic (Lame) constant. The latter is in contradiction with the continuum mechanics result for isotropic linear materials, which should have two independent material constants. We can compare this tensor of elastic moduli to the classical isotropic linear elasticity. In the latter case, the elastic moduli tensor takes the following form,

$$H_{IJMN}=\lambda\delta_{IJ}\delta_{MN}+\mu(\delta_{IM}\delta_{JN}+\delta_{IN}\delta_{JM}), \tag{2.8}$$

where $\lambda=2\mu\nu/(1-2\nu)$ is the second Lame constant and ν is the Poisson ratio. By setting $\nu=1/4$ we obtain $\lambda=\mu$ and $H_{IJMN}=K_{IJMN}$. Thus the VIB formulation allows for the linear isotropic elasticity as a special case where the Poisson ratio equals 1/4. Since this restriction is not suitable for the description of many materials, we propose a modification of the VIB method to be fully consistent with the classical linear elasticity.

3 Modified VIB Formulation

The simple pair (two-body) potential used within the Cauchy-Born approach is a good candidate to be responsible for the inconsistencies of the conventional VIB model[1] pointed out above. It seems that the role of the averaging procedure is fairly subsidiary in the inconsistencies of the whole approach. Modification of the cohesive law and the use of a different analytical expression instead of the exponential law, say the Lennard-Jones potential, will not help if the cohesive law does not change qualitatively. We discuss one way to revise and modify the conventional VIB approach below.

From the microstructural point of view, the simple pair potential does not allow for considering simultaneous multiple (multi-body) particle interactions.[2] It may be said, instead, following Phillips and Ortiz [4], that the pair potential excludes "bending" of the bonds between the particles. A way to circumvent this problem and to include bending of the bonds in analysis is to extend Eq. (2.1) to the three-body terms, for example,

$$\Phi=\frac{1}{2\Omega}\sum_{i,j}U(r_{ij})+\frac{1}{3!\Omega}\sum_{i,j,k}V(r_{ij},r_{jk},\vartheta_{ijk}), \tag{3.1}$$

where ϑ_{ijk} is an angle between $\mathbf{r}_k-\mathbf{r}_j$ and $\mathbf{r}_i-\mathbf{r}_j$, and V is, say, the Stillinger-Weber [5] potential. The number of simultaneously interacting particles can be further increased, of course. In the latter case, it is not entirely clear where this process should be truncated and what the multi-body potentials should look like. We proceed with a different plan (see [6]), which should be preceded by the following methodological remark.

The Cauchy-Born approach is a mixture of atomistic, or particulate, and continuum concepts. The weight of the atomistic concepts in setting the approximate material model is dominant when one plays with the number of interacting particles and the character of their interaction. The concept of continuum deformation appears only at the last stage of the model formulation when Eq. (2.2) is used. Below, we propose a different strategy where the character of continuum deformation—dilatation/distortion—is essentially involved in the model formulation while the potential energy includes only two-body interactions, in which the pair-bonds enjoy both stretching and bending.

From the point of view of continuum mechanics, we begin with replacing the interatomic distance r_{ij} in the total potential energy by a more convenient quadratic measure of the interatomic distance change

$$\Delta=l^2-L^2=L^2(C_{IJ}-\delta_{IJ})\xi_I\xi_J=2L^2E_{IJ}\xi_I\xi_J, \tag{3.2}$$

where $\mathbf{E}=(\mathbf{C}-\mathbf{1})/2$ is the Green strain tensor. Let this tensor be decomposed into spherical and deviatoric parts accordingly:

$$E_{IJ}=E_{KK}\delta_{IJ}/3+\hat{E}_{IJ}. \tag{3.3}$$

Substituting Eq. (3.3) in Eq. (3.2) we have

$$\Delta=\psi+\hat{\Delta},\quad \psi=2L^2E_{KK}/3,\quad \hat{\Delta}=2L^2\hat{E}_{IJ}\xi_I\xi_J. \tag{3.4}$$

Here ψ is the bond length change due to spherical dilatational deformation and $\hat{\Delta}$ is the bond length change due to the devitoric deformation.

Now the stored energy can be written in the following form:

$$U(\Delta)=U(\psi,\hat{\Delta})=A-A(1+\psi\sqrt{B/A})\exp[-\psi\sqrt{B/A}-\hat{\Delta}^2C/(2A)]. \tag{3.5}$$

The physical meaning of the introduced potential can be clarified with the help of the "stretching" and "shearing" forces which are derived by differentiating the potential with respect to ψ and $\hat{\Delta}$ accordingly:

$$U_{\psi}=\frac{\partial U(\psi,\hat{\Delta})}{\partial\psi}=B\psi\exp[-\psi\sqrt{B/A}-\hat{\Delta}^2C/(2A)], \tag{3.6}$$

$$U_{\hat{\Delta}}=\frac{\partial U(\psi,\hat{\Delta})}{\partial\hat{\Delta}}=C(1+\psi\sqrt{B/A})\hat{\Delta}\exp[-\psi\sqrt{B/A}-\hat{\Delta}^2C/(2A)]. \tag{3.7}$$

These forces are presented in Fig. 1. The maximum of U_{ψ} occurs at $\psi=\sqrt{A/B}$, where $\hat{\Delta}=0$. B is the slope of U_{ψ} at $\psi=0$. The maximum of $U_{\hat{\Delta}}$ occurs at $\hat{\Delta}=\pm\sqrt{A/C}$, where $\psi=0$. C is the slope of $U_{\hat{\Delta}}$ at $\hat{\Delta}=0$.

In order to examine consistency of the modified VIB formulation with the linear elasticity, we compute the linearized tensor of elastic moduli for isotropic materials. Omitting tedious intermediate transformations we get finally

$$K_{IJMN}=\langle L^4\rangle_L\pi\left(\tfrac{16}{9}B-\tfrac{32}{45}C\right)\delta_{IJ}\delta_{MN}+\langle L^4\rangle_L\pi\tfrac{16}{15}C(\delta_{IM}\delta_{JN}+\delta_{IN}\delta_{JM}), \tag{3.8}$$

Comparing Eq. (3.8) with the elastic moduli of the classical linear theory [Eq. (2.8)] we obtain for the Lame parameters

$$\lambda=\pi\langle L^4\rangle_L\left(\tfrac{16}{9}B-\tfrac{32}{45}C\right),\quad \mu=\pi\langle L^4\rangle_L\tfrac{16}{15}C. \tag{3.9}$$

These two formulas present the relations between the macroscopic Lame parameters and the microscopic parameters of the bond potential.

---

[1] Klein and Gao [2] extended the VIB method to directionally bonded lattices such as Si by introducing an internal degree of freedom. This approach is not applicable to the isotropic case.

[2] Here we mean a simultaneous interaction of many particles, which cannot be described by a sum of the pair potentials of every two particles involved in the interaction as it is often done in the literature.

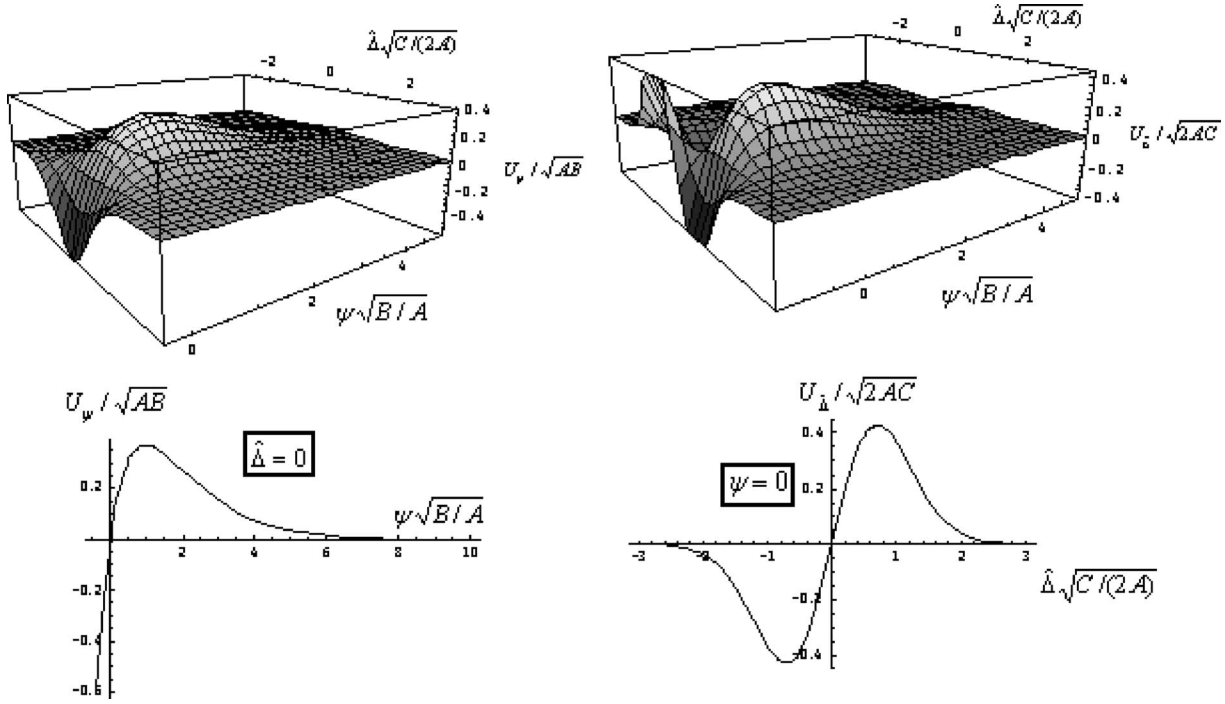

Fig. 1 “Stretching” (left) and “shearing” (right) forces in the modified VIB formulation

4 Concluding Remarks

A modified formulation of the virtual internal bond method has been proposed in the present work. At the level of material particles or atoms, this formulation still considers two-body (pair) bonds. However, these bonds possess both stretching and bending stiffness. The stretching stiffness corresponds to the classical interaction of two particles along the line connecting them. The bending stiffness of the bond is a more subtle subject. It is supposed to account for the simultaneous interactions between the given two particles and other particles (multi-body interaction) without explicitly introducing the latter ones. The modified VIB (MVIB) formulation resolves the discrepancy between the conventional VIB formulation and the classical linear elasticity because the MVIB formulation leads to two independent material parameters. The latter is in contrast to the conventional VIB formulation which leads to only one independent material parameter when it is linearized. Thus the conventional VIB formulation is not in peace with the well-established classical theory of isotropic elasticity which requires two independent material parameters.

The modified VIB formulation is a marriage of the conventional VIB formulation and the purely phenomenological approach of Volokh [6]. While the differences between the conventional and modified VIB formulations are clear from the present work, the qualitative comparison between MVIB and the phenomenological approach is worth performing. The advantages of the MVIB method come from its intrinsic consideration of the material microstructure. Particularly, the MVIB approach naturally allows for considering material anisotropy and introducing the characteristic length scale. These features make the MVIB method physically desirable and more flexible than the phenomenological framework of Volokh [6]. On the other hand, the MVIB formulation is more involved computationally and this is the expected price for its generality.

References

[1] Gao, H., and Klein, P., 1998, “Numerical Simulation of Crack Growth in an Isotropic Solid With Randomized Internal Cohesive Bonds,” J. Mech. Phys. Solids, **46**, pp. 187–218.

[2] Klein, P., and Gao, H., 1998, “Crack Nucleation and Growth as Strain Localization in a Virtual-Bond Continuum,” Eng. Fract. Mech., **61**, pp. 21–48.

[3] Klein, P., and Gao, H., 2000, “Study of Crack Dynamics Using the Virtual Internal Bond Method,” in *Multiscale Deformation and Fracture in Materials and Structures*, Kluwer, Dodrecht, pp. 275–309.

[4] Phillips, R., and Ortiz, M., 1999, “Nanomechanics of Defects in Solids,” Adv. Appl. Mech., **36**, pp. 1–79.

[5] Stillinger, F. H., and Weber, T. A., 1985, “Computer-Simulation of Local Order in Condensed Phases of Silicon,” Phys. Rev. B, **31**(8), pp. 5262–5271.

[6] Volokh, K. Y., 2004, “Nonlinear Elasticity for Modeling Fracture of Isotropic Brittle Solids,” ASME J. Appl. Mech., **71**, pp. 141–143.

Effects of Thermal Contact Resistance on Transient Thermoelastic Contacts for an Elastic Foundation

---

Yong Hoon Jang
School of Mechanical Engineering,
Yonsei University,
Shincheon-Dong 134, Seodaemun-Gu, Seoul, Korea
e-mail: jyh@yonsei.ac.kr

The paper presents a numerical solution to the problem of a hot rigid indenter sliding over a thermoelastic Winkler foundation with a thermal contact resistance at constant speed. It is shown analytically that no steady-state solution can exist for sufficiently high temperature or sufficiently small normal load or speed, regardless of the thermal contact resistance. However, the steady-state solution may exist in the same situation if the thermal contact resistance is considered. This means that the effect of the large values of temperature difference and small value of force or velocity which occur at no steady state can be lessened due to the thermal contact resistance. When there is no steady state, the predicted transient behavior involves regions of transient stationary contact interspersed with regions of separation regardless of the thermal contact resistance. Initially, the system typically exhibits a small number of relatively large contact and separation regions, but after the initial transient, the trailing edge of the contact area is only established and the leading edge loses contact, reducing the total extent of contact considerably. As time progresses, larger and larger numbers of small contact areas are established, until eventually the accuracy of the algorithm is limited by the discretization used. [DOI: 10.1115/1.2042485]

1 Introduction

When two bodies slide against each other, frictional heating at the interface causes thermoelastic deformation which modifies the contact pressure distribution. Hills and Barber [1] gave an analytical solution for sliding Hertzian contact, using a thermoelastic Green's function to reduce the problem to the solution of an integral equation with a Bessel function kernel. A remarkable feature of their results was that no steady-state solution could be found in certain ranges of the applied load and sliding speed without violation of the unilateral contact constraints. Similar results were demonstrated by Yevtushenko and Ukhanska [2] for a problem with interfacial thermal contact resistance, which was not a function of pressure. Jang [3] showed that similar problems arise in the simpler case in which the contacting bodies are replaced by elastic foundation. He developed a numerical algorithm for the transient problem in this case and showed that the contact area tends to break down into a number of smaller regions as sliding progresses. Even more surprising is the fact that this process appears to continue without limit, leading to larger and larger numbers of smaller contact areas. Existence theorems can be proved for the corresponding transient problem, so we must conclude that in these parameter ranges the system must undergo periodic or random transient variations in contact conditions.

In this study, Jang's analysis is extended to the sliding without friction of a hot, rigid, perfectly conducting indenter over a linear thermoelastic Winkler foundation with a thermal contact resistance, which is not a function of pressure. We will investigate the effects of the thermal contact resistance on the transient thermoelastic contact problems.

2 Statement of the Problem

Consider the problem illustrated in Fig. 1, where an indenter at temperature T_0 is pressed into the foundation with a force F and moves to the right at constant speed V. The mechanical behavior of the foundation is defined by the statement that, the local contact pressure p is proportional to the local indentation u—i.e., $u(x,t)=cp(x,t)$, where c is the elastic foundation compliance. We also assume that lateral thermal conduction in the foundation can be neglected so that it behaves likes a set of parallel one-dimensional rods oriented normal to the interface and each rod acts independently of its neighbors.[1]

If the indenter contacts with a surface at time $t=t_0$ with a thermal resistance $1/hA$ where A is the contact area, the temperature for $y<0,\ t>t_0$ is given by Schneider [4] such as

$$T = T_0\left[\operatorname{erfc}\left(\frac{y}{2\sqrt{\kappa(t-t_0)}}\right) - e^{h\sqrt{\kappa(t-t_0)}/k[y/\sqrt{\kappa(t-t_0)}+h\sqrt{\kappa(t-t_0)}/k]} \times \operatorname{erfc}\left(\frac{y}{2\sqrt{\kappa(t-t_0)}} + \frac{h}{k}\sqrt{\kappa(t-t_0)}\right)\right] \quad (1)$$

where κ and k are the thermal diffusivity and the thermal conductivity, respectively. The corresponding thermal displacement on the surface can be shown to be

$$\delta(x,t) = T_0\left[\frac{2\alpha\sqrt{\kappa(t-t_0)}}{\sqrt{\pi}} + \frac{\alpha k}{h}e^{h^2\kappa(t-t_0)/k^2} \times \operatorname{erfc}\left(\sqrt{\frac{h^2\kappa(t-t_0)}{k^2}}\right) - \frac{\alpha k}{h}\right] \quad (2)$$

where α is the coefficient of the thermal expansion. If contact at x ends at $t=t_1$, the thermal displacement will remain constant at the value $\delta(x,t_1)$ for $t>t_1$.

Using these results, the gap function can be defined as follows,

$$g(x,t) = g_0(x,t) - d(t) - \delta(x,t) + u(x,t), \quad (3)$$

where

$$g_0(x,t) = (x-Vt)^2/2R \quad (4)$$

is the gap between the indenter and an un-deformed foundation and d is an unknown rigid body displacement which will generally vary with time.

The boundary condition for contact and separation regions can be written

$$\begin{aligned} &\text{separation } p(x,t)=0; \quad g(x,t)>0; \\ &\text{contact } p(x,t)>0; \quad g(x,t)=0 \end{aligned} \quad (5)$$

and equilibrium requires that

$$F = \int_C p(x,t)\,dx, \quad (6)$$

where C is the contact region.

3 Dimensionless Formulation

The number of independent parameters can be reduced by utilizing the self-similarity of the punch profile. There are two length scales in the problem—the radius R and a force-related quantity $L=\sqrt[3]{cFR}$. We define the dimensionless coordinates $\hat{x}=x/L$, $\hat{t}$

Contributed by the Applied Mechanics Division of THE AMERICAN SOCIETY OF MECHANICAL ENGINEERS for publication in the ASME JOURNAL OF APPLIED MECHANICS. Manuscript received by the ASME Applied Mechanics Division, November 18, 2004; final revision, March 2, 2005. Review conducted by S. Mukherjee.

[1] This is quite a good approximation for the thermal behavior of a half-space if the Peclet number is sufficiently high.

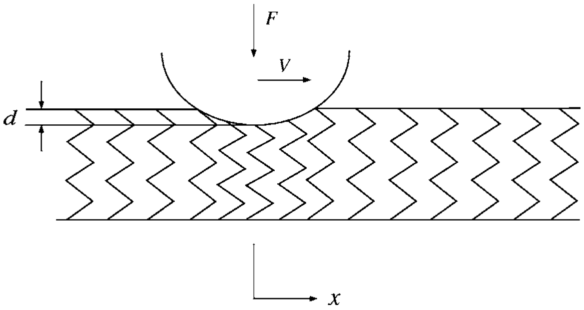

Fig. 1 Geometry configuration of transient thermal contact

$=Vt/L$, and other dimensionless quantities through $\hat{\delta}=R\delta/L^2$, $\hat{g}=Rg/L^2$, $\hat{d}=Rd/L^2$, $\hat{p}=cRp/L^2$, and $\hat{H}=k/h\sqrt{V/(\kappa L)}$. Introducing these definitions into Eqs. (2)–(4) and (6) yields

$$\hat{\delta}(\hat{x},\hat{t}) = \sqrt{\frac{3\pi\lambda}{8}}\left[2\sqrt{\frac{\hat{t}-\hat{t}_0(\hat{x})}{\pi}} - \hat{H} + \hat{H}e^{[\hat{t}-\hat{t}_0(\hat{x})/\hat{H}^2]}\operatorname{erfc}\left(\frac{\sqrt{\hat{t}-\hat{t}_0(\hat{x})}}{\hat{H}}\right)\right]; \quad \hat{t}_0(\hat{x}) < \hat{t} < \hat{t}_1(\hat{x}), \tag{7}$$

$$\hat{g}(\hat{x},\hat{t}) - \hat{p}(\hat{x},\hat{t}) = \frac{(\hat{x}-\hat{t})^2}{2} - \hat{d}(\hat{t}) - \hat{\delta}(\hat{x},\hat{t}), \tag{8}$$

and

$$\int_{\hat{C}} \hat{p}(\hat{x},\hat{t})d\hat{x} = 1, \tag{9}$$

where $\lambda \equiv 8\alpha^2 T_0^2 \kappa R/(3\pi cFV)$.

Notice that with this formulation, the dimensionless parameters governing the evolution of the process are λ which can be seen as a ratio between thermoelastic and elastic effects and $\hat{H}$.

The contact boundary conditions (5) show that at least one of $\hat{g},\hat{p}$ must be zero for all $\hat{x}$ and that the other cannot be negative. Thus, if the right-hand side of Eq. (8) can be calculated, a positive value will indicate a state of separation and will be equal to the local value of $\hat{g}$, whereas a negative value will correspond to contact and will be equal to the local value of $(-\hat{p})$.

4 Steady-State Solution

Since the contacting body moves at a constant speed, it is natural to expect the long-time behavior to become invariant in a frame of reference moving with the body. In particular, the indentation $\hat{d}$ would then be independent of $\hat{t}$. Denoting the value of this constant by d_0, we can then find the leading edge $\hat{a}(\hat{t})$ of the contact area by enforcing $\hat{g}=0$, $\hat{p}=0$ in Eq. (8), with the result

$$\frac{(\hat{a}-\hat{t})^2}{2} = d_0, \tag{10}$$

since the thermal expansion must be zero before contact starts. It follows that $\hat{a}(\hat{t})=\sqrt{2d_0}+\hat{t}$ or alternatively that $\hat{t}_0(\hat{x})=\hat{x}-\sqrt{2d_0}$.

The expansion in the contact area can now be calculated from Eq. (7) and the contact pressure from (8), with the result

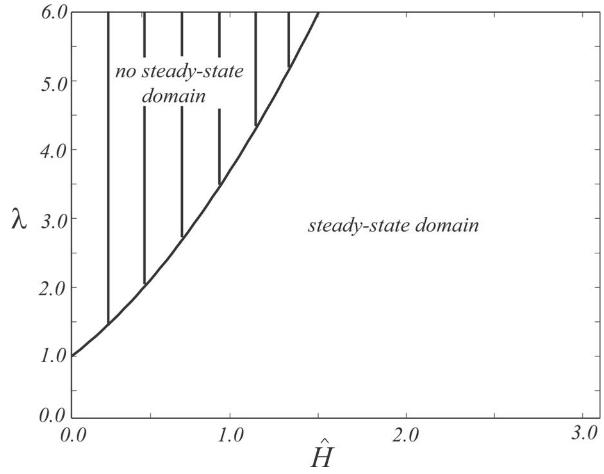

Fig. 2 Stability diagram for λ and $\hat{H}$

$$\hat{p}(\hat{x},\hat{t}) = -\frac{(\hat{x}-\hat{t})^2}{2} + d_0 + \sqrt{\frac{3\pi\lambda}{8}}\left[2\sqrt{\frac{\hat{t}-\hat{x}+\sqrt{2d_0}}{\pi}} - \hat{H} + \hat{H}e^{[(\hat{t}-\hat{x}+\sqrt{2d_0})/\hat{H}^2]}\operatorname{erfc}\left(\frac{\sqrt{\hat{t}-\hat{x}+\sqrt{2d_0}}}{\hat{H}}\right)\right]. \tag{11}$$

The trailing edge of the contact area $\hat{b}(\hat{x})$ is defined by the condition that the contact pressure goes to zero. One solution of the resulting equation is clearly $\hat{a}(\hat{t})$ and the other is the one real root which comes from Eq. (11) with $\hat{p}(\hat{x},\hat{t})=0$. Once $\hat{a},\hat{b}$ have been determined, the corresponding value of λ can be obtained from Eq. (9).

For the special case where $d_0=0$, we then have $\hat{a}(\hat{t})=\hat{t}$ from (10) and $\hat{b}(\hat{t})$ from Eq. (11). The corresponding pressure distribution is

$$\hat{p}(\hat{x},\hat{t}) = -\frac{(\hat{x}-\hat{t})^2}{2} + \sqrt{\frac{3\pi\lambda}{8}}\left[2\sqrt{\frac{\hat{t}-\hat{x}}{\pi}} - \hat{H} + \hat{H}e^{(\hat{t}-\hat{x})/\hat{H}^2}\operatorname{erfc}\left(\frac{\sqrt{\hat{t}-\hat{x}}}{\hat{H}}\right)\right], \tag{12}$$

and Eq. (9) then yields

$$1 = \int_{\hat{b}}^{\hat{a}} \hat{p}(\hat{x},\hat{t})d\hat{x} \tag{13}$$

$$= \frac{-\xi}{12}[2\xi^2 + \sqrt{6\lambda}(3\hat{H}\sqrt{\pi} - 4\sqrt{\xi})] + \frac{\hat{H}}{2}\sqrt{\frac{3\pi\lambda}{2}}\left[\frac{2\hat{H}}{\sqrt{\pi}}\sqrt{\xi} + e^{(\xi)/\hat{H}^2}\hat{H}^2 \times \operatorname{erfc}\left(\frac{\sqrt{\xi}}{\hat{H}}\right) - \hat{H}^2\right], \tag{14}$$

where $\xi=\hat{t}-\hat{x}$.

Only positive values of d_0 are admissible and it can be shown that the integral in (9) is a monotonically increasing function of d_0 in the range $d_0 > 0$. Thus, there is no steady-state solution of the assumed form if the value of the right-hand side in Eq. (14) is greater than 1. Notice that the integral in Eq. (14) has two parameters, λ and $\hat{H}$, to identify the steady-state solution. Figure 2 shows the stability diagram in which the thermal contact resistance is included. The steady-state solutions are obtained when λ is less than 1 regardless of the value of $\hat{H}$. However, even when λ is greater than 1 and $\hat{H}$ is above a certain value, the steady-state solution can exist.

In general, steady solutions do not exist at sufficiently large values of temperature difference or sufficiently small values of force or velocity. But the effect of the large values of temperature difference and small value of force or velocity which occur at no steady state can be lessened due to the thermal contact resistance.

To determine how the system behaves at large values of time for $\lambda > 1$ and $\hat{H} > 0$, a numerical solution of the problem has been developed, which is described in the next section.

5 Numerical Implementation

The contact problem can be discretized in space and time by dividing the elastic foundation into discrete strips of width $\Delta\hat{x}$ and proceeding in increments of time $\Delta\hat{t}$. The numerical algorithm explained below was developed by Jang [3].

It is convenient to take the vertical rigid body displacement $\hat{d}(\hat{t}_j)$ as a fundamental variable defining the evolution of the process, where $\hat{t}_j$ is the time after the jth time increment. If $\hat{d}(\hat{t}_j)$ were known for all j, the trajectory of all points on the moving body would also be known and hence we would be able to determine the time $\hat{t}_0(\hat{x}_i)$ at which any given element at $\hat{x}_i$ comes into contact. The subsequent thermal expansion could then be determined for each $\hat{x}_i$ from Eq. (7) and the contact pressure $\hat{p}(\hat{x}_i,\hat{t}_j)$ from Eq. (8). A negative value of $\hat{p}(\hat{x}_i,\hat{t}_j)$ at any contacting element indicates loss of contact and could be used to set the value for $\hat{t}_1(\hat{x}_i)$.

Of course, $\hat{d}(\hat{t}_j)$ is not known a priori. Instead, it must take whatever value is required to satisfy the equilibrium condition (9), which in discretized form can be written

$$S \equiv \sum_{i \in \hat{C}} \hat{p}(\hat{x}_i,\hat{t}_j)\Delta\hat{x} = 1, \tag{15}$$

where $\hat{C}$ is the set of nodes in contact. The relation between S and $\hat{d}$ is nonlinear because the contact area $\hat{C}$ varies with $\hat{d}$. In the numerical solution, we must therefore determine $\hat{d}$ at each time step by iteration. We take the value of $\hat{d}$ at the previous time step as an initial guess for this process. The right-hand side of (8) can then be calculated for all nodes and those in which negative values are obtained correspond to contact nodes, which make a contribution to the sum in Eq. (15). The value of S so calculated will generally differ from unity and we therefore make a correction to $\hat{d}$ using the algorithm

$$\hat{d}_{\text{new}} = \hat{d}_{\text{old}} + \frac{1-S}{N_C\Delta\hat{x}}, \tag{16}$$

where N_C is the number of elements in $\hat{C}$ at the previous iteration.

Equation (15) shows that this would yield the correct value of $\hat{d}$ in one iteration if the elements of $\hat{C}$ were unchanged after the iteration. Of course, this is not generally the case, but convergence is found to be very rapid and terminates completely once the increment in $\hat{d}$ is small enough to have no further effect on the set of contact nodes.

When the value of $\hat{d}(\hat{t}_j)$ has been established, the elements are scanned to determine which, if any, change state from separation to contact or vice versa during the jth time step, in order to set the corresponding values of $\hat{t}_0,\hat{t}_1$ in Eq. (7). The time can now be updated through

$$\hat{t}_{j+1} = \hat{t}_j + \Delta\hat{t} \tag{17}$$

and the process repeats indefinitely.

Note that in the numerical simulation, the discrete strips of width $\Delta\hat{x}=0.001$ and the increments of time $\Delta\hat{t}=0.001$.

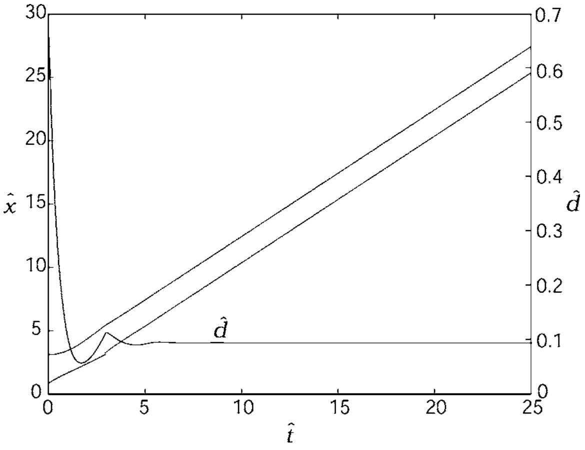

Fig. 3 Extent of contact area and rigid body penetration $\hat{d}$ as a function of time $\hat{t}$ for $\lambda=0.9$ and $\hat{H}=0.5$

6 Results

6.1 Contact Area and Rigid Body Penetration. The results confirm that for $\lambda < 1$, the system always settles into a steady state from the initial period even if $\hat{H}$ is any value. This demonstrates that the steady-state solution is stable under transient perturbations. Figure 3 shows the extent of the contact area and the rigid body penetration. The indenter is assumed to be pressed against the foundation at $\hat{t}=0$ and to start moving immediately at speed V. In the initial transient, the leading edge moves parabolically with time while the trailing edge of the contact area moves linearly with time, but the total extent of contact changes a little. During this period, thermal expansion forces the bodies apart, causing $\hat{d}$ to decrease. Eventually the expansion levels off and the additional elastic displacement associated with the reduction in contact area (and consequent increase in contact pressure) allows $\hat{d}$ to increase again, until a steady contact area is established. A steady state, with a single contact area, both boundaries of which move at speed V, is established after $\hat{t}=3$.

When $\lambda > 1$, the transient behavior of the system depends upon the values of $\hat{H}$. Figure 4 shows the extent of the contact area and the rigid body penetration $\hat{d}$ as functions of time $\hat{t}$ for $\lambda=6.0$ and

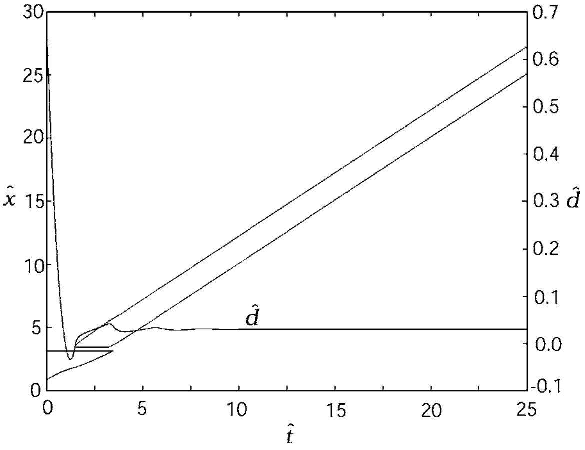

Fig. 4 Extent of contact area and rigid body penetration $\hat{d}$ as a function of time $\hat{t}$ for $\lambda=6.0$ and $\hat{H}=2.0$

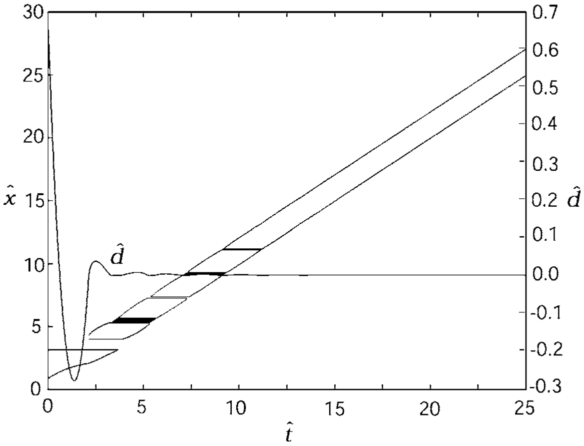

Fig. 5 Extent of contact area and rigid body penetration $\hat{d}$ as a function of time $\hat{t}$ for $\lambda=6.0$ and $\hat{H}=1.5$

$\hat{H}=2.0$. In the initial transient, the leading edge of the contact area remains unchanged, while the trailing edge moves, reducing the total extent of contact. During this period, a similar transient contact behavior like the case of Fig. 3 is shown, until a new separated contact area is established. A steady state, with a single contact area, both boundaries of which move at speed V, is established after about $\hat{t}=3$.

As $\hat{H}$ decreases, the duration of the initial transient increases and involves a succession of separated contact areas and oscillations in the value of $\hat{d}$. However, the transient contact behavior is still affected by $\hat{H}$. Figure 5 shows the extent of the contact area and the rigid body penetration $\hat{d}$ as functions of time $\hat{t}$ for $\lambda=6.0$ and $\hat{H}=1.5$. It shows that a steady state with a single contact area is established after about $\hat{t}=12$, confirming that the system settles into a steady state as already expected in the map of steady state shown in Fig. 2.

When $\hat{H}$ decreases more and the system settles into no steady state, the duration of the initial transient increases and involves a succession of separated contact areas and oscillations in the value of $\hat{d}$ incessantly. In addition, regions of alternating contact and separation occur for all time and the size of the typical contact area appears to decrease continually as the state evolves. After the initial transient, only the trailing edge of the contact area at the initial transient is established and the leading edge loses contact, reducing the total extent of contact considerably. Figures 6 and 7 show the results for $\lambda=6.0$ and $\hat{H}=1.0$, and $\lambda=6.0$ and $\hat{H}=0.5$, respectively. For Fig. 6, it shows that the system has no steady state and its state is characterized as contact with numerous small intervening regions of separation after about $\hat{t}=4$. A corresponding small oscillation occurs in the rigid body penetration $\hat{d}$. For Fig. 7, in the early stage, the same explanation given for Fig. 6 can be used and then the larger total extent of contact is established and varies. The penetration $\hat{d}$ increases more for a new contact area to form, compared with the case of Fig. 6.

For $\lambda=6.0$ and $\hat{H}=0.1$, larger separation zones alternate with relatively small zones of contact (Fig. 8). Periodically the penetration $\hat{d}$ increases sufficiently for a new contact area to form (and hence expand) or lateral motion permits the trailing contact zone to be lost.

This transient state does not tend to appear to a steady periodic state (e.g., one with equal-spaced contact areas). Also, the typical contact area size decreases as time progresses, ultimately approaching the level of discretization of the algorithm.

6.2 Dynamic Behavior of Rigid Body Penetration. This investigation presents that the rigid body penetration $\hat{d}$ oscillates continuously after the initial transient, being small or large according to λ and $\hat{H}$ in the no-steady-state domain. We can pre-

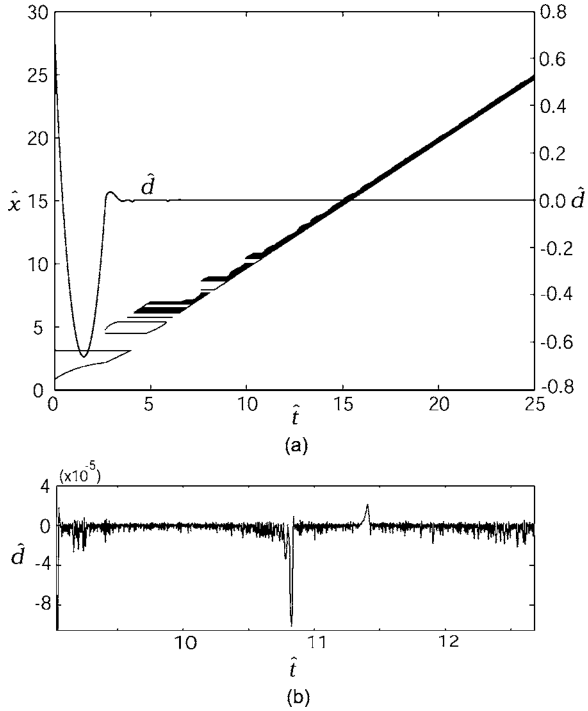

Fig. 6 Extent of contact area and rigid body penetration $\hat{d}$ as a function of time $\hat{t}$ for $\lambda=6.0$ and $\hat{H}=1.0$

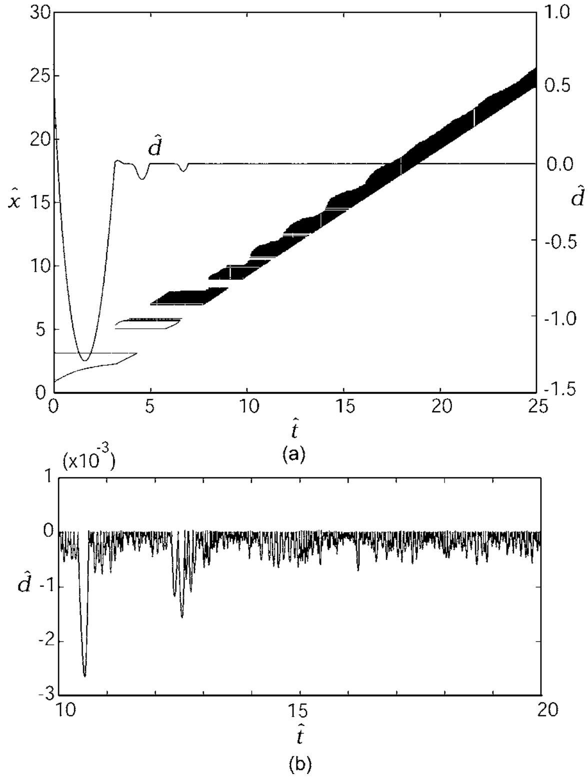

Fig. 7 Extent of contact area and rigid body penetration $\hat{d}$ as a function of time $\hat{t}$ for $\lambda=6.0$ and $\hat{H}=0.5$

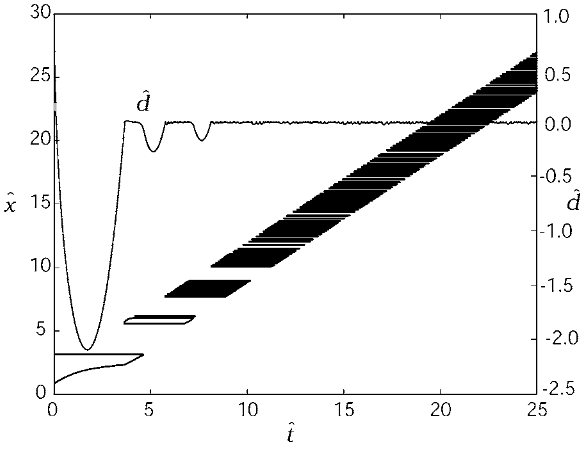

Fig. 8 Extent of contact area and rigid body penetration $\hat{d}$ as a function of time $\hat{t}$ for $\lambda=6.0$ and $\hat{H}=0.1$

cisely identify the state of the system, steady or no steady state, by considering the long-term dynamic behavior of the rigid body penetration. A phase diagram, representing the two dimensional relationship between $\hat{d}$ and $\dot{\hat{d}}$, is used to investigate the stability of the system.

When the system has a steady state solution, the motion of the rigid body penetration is stable, while the system has a chaotic solution when there is no steady state solution. Figures 9 and 10 show the phase diagram for $\lambda=6.0$ and $\hat{H}=2.0$, and $\lambda=6.0$ and $\hat{H}=1.5$, respectively. It shows that the state trajectories converge to a point, meaning that the systems are stable. Thus we can confirm that the system is stable since the systems settle into a steady state as explained in the above results.

When the system undergoes no steady state, the state trajectories have a large locus at the initial transient and then converge to a certain amount of locus, finally deviating from the locus. As time progresses, the locus of the trajectory grows and the motion after the initial transient is repeated. Even though the locis of trajectories are small, however, we can confirm that the system is unstable since the locus of the state trajectory after the initial transient increases further. Figures 11–13 show the phase diagram for $\lambda=6.0$ and $\hat{H}=1.0$, $\lambda=6.0$ and $\hat{H}=0.5$, and $\lambda=6.0$ and $\hat{H}=0.1$, respectively. The locus of the state trajectories after the initial transient grows larger as $\hat{H}$ decreases, implying that the oscillation of the rigid body penetration $\hat{d}$ increases.

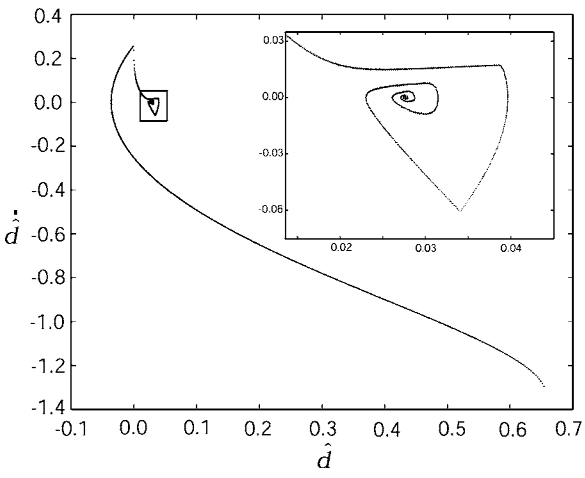

Fig. 9 Phase diagram for $\lambda=6.0$ and $\hat{H}=2.0$

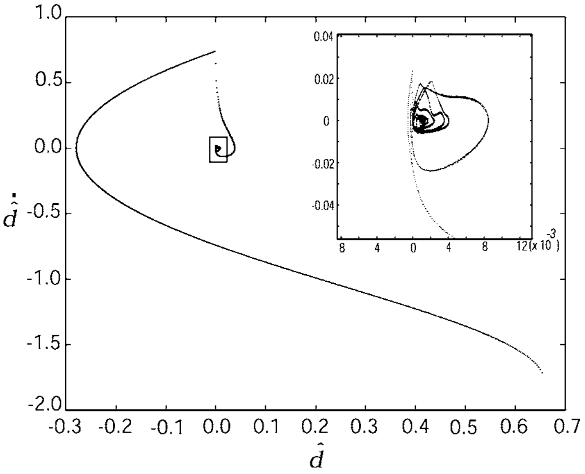

Fig. 10 Phase diagram for $\lambda=6.0$ and $\hat{H}=1.5$

7 Discussion and Conclusions

The investigation presents a numerical solution to the problem of a hot rigid indenter sliding over a thermoelastic Winkler foundation with a thermal resistance at a constant speed. The numeri-

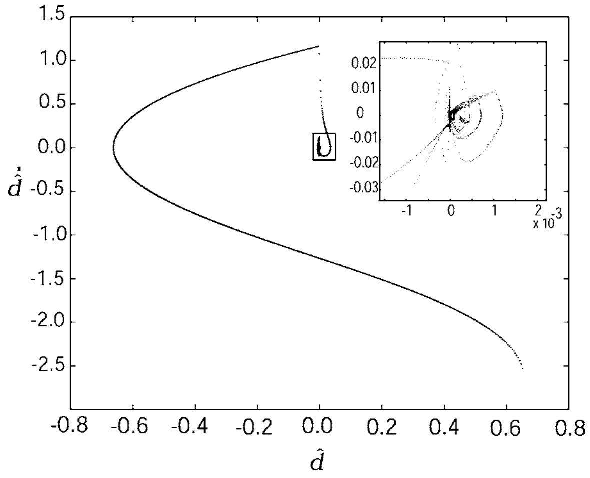

Fig. 11 Phase diagram for $\lambda=6.0$ and $\hat{H}=1.0$

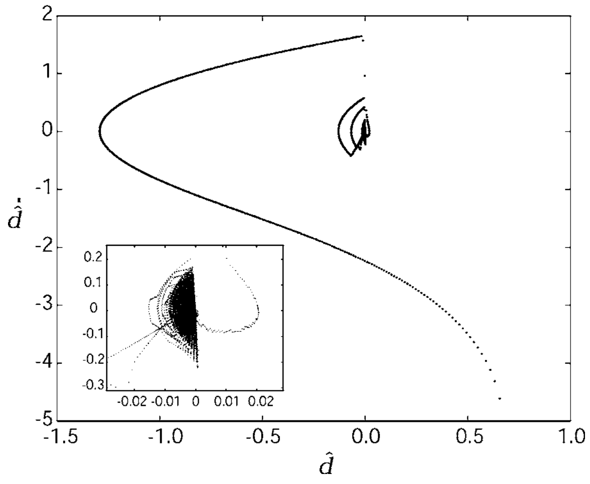

Fig. 12 Phase diagram for $\lambda=6.0$ and $\hat{H}=0.5$

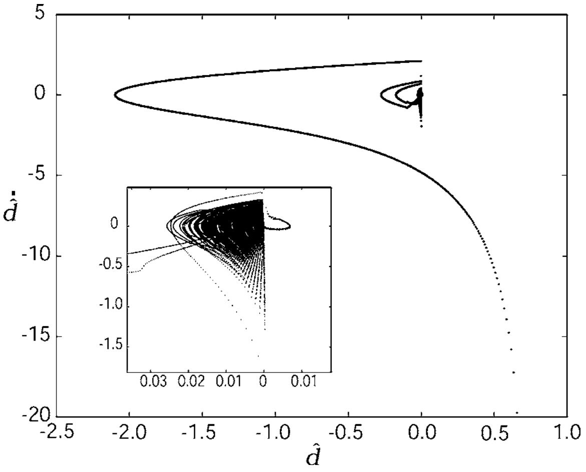

Fig. 13 Phase diagram for $\lambda=6.0$ and $\hat{H}=0.1$

cal solution shows that the steady-state solution, when it exists, is the final condition regardless of the initial conditions imposed. This suggests that the steady state is also stable. When there is no steady state the predicted transient behavior involves regions of transient stationary contact interspersed with regions of separation. Initially, the system typically exhibits a small number of relatively large contact and separation regions, but as time progresses, larger and larger numbers of small contact areas are established, until eventually the accuracy of the algorithm is limited by the discretization used.

The results also show that the thermal contact resistance affects the long-term behavior of the system along with the parameter λ, a ratio between thermoelastic and elastic effects. Regardless of the thermal contact resistance, the steady-state solutions are obtained when λ is less than 1. However, when λ is greater than 1, the steady-state solution can exist according to the thermal contact resistance. This means that the effect of the large values of temperature difference and the small value of force or velocity which occur at no steady state can be lessened due to the thermal contact resistance. Furthermore, after the initial transient, the trailing edge of the contact area is only established and the leading edge loses contact, reducing the total extent of contact considerably. This contact behavior was not seen in the system without the thermal contact resistance.

A question still exists as to how much the Winkler foundation assumption, which states that the local contact pressure is proportional to the local indentation, may affect the predicted contact behavior. One of the limitations of the Winkler foundation assumption is that it does not consider the shear effect. Our calculations may not predict the exact transient behavior of real thermoelastic surfaces, but the calculations provide an indication that the periodic or random contact will occur under a certain range of applied load, sliding speed, temperature, and particularly thermal contact resistance.

References

[1] Hills, D. A., and Barber, J. R., 1986, "Steady Sliding of a Circular Cylinder Over a Dissimilar Thermally Conducting Half-Plane," Int. J. Mech. Sci., **28**, pp. 613–622.

[2] Yevtushenko, A. A., and Ukhanska, O. M., 1993, "Plane Contact Problem of Thermoelasticity With Quasi-steady Frictional Heating," Int. J. Eng. Sci., **31**, pp. 1565–1573.

[3] Jang, Y. H., 2000, "Transient Thermoelastic Contact Problems for an Elastic Foundation," Int. J. Solids Struct., **37**, pp. 1997–2004.

[4] Schneider, P. J., 1955, *Conduction Heat Transfer*, Addison-Wesley, Reading, MA.

Journal of
Applied
Mechanics

Discussion

Discussion: "The Resistance of Clamped Sandwich Beams to Shock Loading" (Fleck, N. A., and Deshpande, V. S., 2004, ASME J. Appl. Mech., 71, pp. 386–401)

P. J. Tan

S. R. Reid[1]
Fellow ASME
e-mail: steve.reid@manchester.ac.uk

J. J. Harrigan

School of Mechanical, Aerospace and Civil Engineering,
The University of Manchester, P. O. Box 88,
Sackville Street, Manchester M60 1QD, UK

Fleck and Deshpande (FD) proposed an analytical model to encapsulate the response of clamped sandwich beams to blast loadings in air and under water. Four pertinent issues, viz., (1) application of Taylor's model [1] to air blast loadings, (2) the limiting impulse transferable to a stationary rigid face in an air blast, (3) inconsistencies in the proposed shock model, and (4) application of the shock theory to certain micro-architectured core materials, require clarification. Detailed comments are as follows:

(1) The net pressure acting on the front face of the sandwich beam [Eq. (15) of FD] was proposed to be the superposition of the incoming and reflected blast wave pulses. This is acceptable for the typically *weak* shock (or sound) waves generated in underwater explosions because water is nearly incompressible. However, by using the results of the *weak* shock analysis to estimate typical impulses delivered to the front face of the sandwich beam by *strong* shock waves in air blasts (pages 389 and 397 of FD), FD imply that their modified Taylor's model [1] is also applicable to *non-linear*, finite amplitude disturbances propagating in a compressible medium. This needs to be justified or qualified.

(2) For air blast loadings, FD rightly propose that full transmission of the blast impulse to the sandwich beam, assuming a stationary rigid front face, be considered for safe design. However, the limiting impulse transmitted is based on a *weak* shock in water, where the reflected overpressure (peak pressure) is twice the incident overpressure, given by FD to be

$$I = \int_0^\infty 2p_o e^{-t/\theta} dt = 2p_o \theta, \tag{1}$$

where p_o is the overpressure and θ the decay constant. By contrast, the Rankine-Hugoniot relations predict a reflected overpressure of eight times the incident overpressure for a *strong* shock propagating in an ideal gas, giving a limiting impulse of $8p_o\theta$ from momentum considerations, a classical result well known to fluid mechanicists [2–4]. The actual reflected overpressure could reach a factor of 20, or even higher, if real gas effects, such as dissociation and ionization of the air molecules, are taken into consideration [4]. Therefore, it is questionable whether the performance charts constructed based on Eq. (1) provide a safe guide for the design of *air-blast* resistant sandwich beams.

(3) Instead of establishing a local balance of energy across the shock wave[2] front, FD presents a global energy balance of the sandwich beam where the following two inconsistencies arise from the use of the term $\sigma_{nY}\varepsilon_D X$ [Eq. (28) in FD]:

(i) That the energy absorbed per unit volume of core material ($\sigma_{nY}\varepsilon_D$) is independent of the initial front face velocity v_o. For an aluminium alloy foam core, this is not consistent with FD's own recent studies reported in [5], nor with the authors' experimental data [6].

(ii) That the change in the internal energy[3] density of the core material $[\rho_c U]$ ($=\sigma_{nY}\varepsilon_D$ by FD) is *independent* of the particle velocity jump $[v]$ across the shock front, where $[\,] \equiv (\,)_d - (\,)_u$, U is the internal energy per unit mass, ρ_c is the core density and the symbols used by FD also apply here. By contrast, the basic jump conditions predict that [7]

$$[\rho_c U] = \sigma_u[\varepsilon] + \rho_c[v]^2/2. \tag{2}$$

This can also be confirmed with an idealized example using ABAQUS explicit. Figure 1 shows a two-dimensional honeycomb (comprised of 21×74 regular cells of 4 mm edge length and 0.34 mm wall thickness) with a relative density of 0.1, which is fixed at the right end and compressed at a constant velocity from the left. The aluminium alloy cell walls have rate-independent, elastic, perfectly plastic properties identical to those used by Chen et al. [8]. Each cell wall is modeled using four general-purpose shell elements (S4R of ABAQUS) and self-contact simulations have been incorporated. Figure 2 shows the internal energy density (using "ALLIE" in ABAQUS) of the honey-

---

[1] To whom correspondence should be addressed.

[2] Note that the term "shock wave" is used to describe a progressive cell-crushing phenomenon (see Fig. 1). This is an inertial phenomenon often associated with the high velocity compression of cellular materials and structures [9,10]. In a sense, it is not the classical shock wave described by fluid mechanicists and shock physicists. Rather, the deformation response exhibits "shock-type" characteristics and the field variables appear to obey the basic jump conditions [6,7]. Terms such as compaction or consolidation waves could equally be used.

[3] Since all forms of non-mechanical energies and the energy dissipated by viscous effects and by time-dependent deformation are neglected, the contributions to the internal energy of a fixed body of material are the recoverable elastic strain energy and the energy dissipated by plasticity [11].

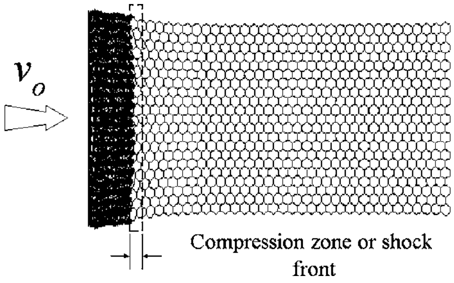

Fig. 1 In-plane compression of a honeycomb at up to $\delta/L \approx 50\%$, where δ is the displacement of the left end measured from its initial configuration and L is the initial length of the structure

comb at three velocity levels. The upturn at the end of each curve shows an increased absorption of energy by the honeycomb at full locking with impact velocity. In all cases, the energy dissipated by rate-independent plastic deformation occurs mostly within the compression zone highlighted in Fig. 1, and accounts for more than 95% of the internal energy density plotted. Since $[v] \approx v_o$, Fig. 2 shows that $[\rho_c U]$ is *dependent* upon $[v]$ at every stage of the compression process. Therefore, it is questionable whether energy conservation has been achieved by Eq. (28) of FD.

(4) Two of the core topologies depicted in Figs. 2(*d*) and 2(*e*) of FD are likely to exhibit strong "Type-II" inertial effect where the shock analysis is known to be unsatisfactory [9,10]. Previous studies of the dynamic compression of wood along the grain and of the out-of-plane compression of honeycombs have shown that a shock model based upon their respective quasi-static stress-strain curve consistently under-predicts their dynamic strength, and this is particularly evident at the higher impact velocities where a shock is expected to form. The reasons for this have been identified and explained by Reid et al. [9,10].

An important conclusion of FD's analysis is the apparent advantage of sandwich construction over solid plates of the same mass per unit area to blast loadings. However, despite the good agreement between the predictions of the model and the results of FE simulations by Xue and Hutchinson [12], which also assumes that the limiting reflected overpressure is *twice* the incident overpressure for air blast loadings, the efficacy of FD's model should be treated with caution for the above reasons and requires further validation.

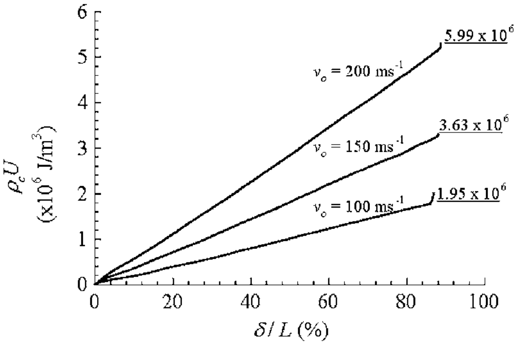

Fig. 2 Internal energy density of the honeycomb vs impact-end displacement at three velocity levels. The overall energy absorbed at full locking predicted by Eq. (2) is given by the underscored values. Parameters used in their calculations were $[\varepsilon]=\varepsilon_D$=0.85, σ_u=0.7 MPa, and $[v]=v_o$. The stress measured at the fixed end (σ_u) remains almost constant during compression and varies little with impact velocity.

Acknowledgment

The authors are grateful to the EPSRC (U.K.) for their financial support under Grant No. GR/R26542/01.

References

[1] Taylor, G. I., 1963, "The Pressure and Impulse of Submarine Explosion Waves on Plates," *The Scientific Papers of G. I. Taylor*, Vol. III, Cambridge University Press, Cambridge, U.K., pp. 287–303.

[2] Taylor, G. I., 1963, "Pressures on Solid Bodies Near an Explosion," *The Scientific Papers of G. I. Taylor*, Vol. III, Cambridge University Press, Cambridge, U.K., pp. 260–267.

[3] Billingham, J., and King, A. C., 2000, *Wave Motion*, Cambridge University Press, Cambridge, Chap. 7.

[4] Baker, W. E., 1973, *Explosions in Air*, University of Texas Press, Austin, Chap. 1.

[5] Radford, D. D., Deshpande, V. S., and Fleck, N. A., 2005, "The Use of Metal Foam Projectiles to Simulate Shock Loading on a Structure," Int. J. Impact Eng., **31**, pp. 1152–1171.

[6] Tan, P. J., Harrigan, J. J., and Reid, S. R., 2002, "Inertia Effects in the Uniaxial Dynamic Compression of a Closed-Cell Aluminium Alloy Foam," Mater. Sci. Technol., **18**, pp. 480–488.

[7] Tan, P. J., Reid, S. R., Harrigan, J. J., Zou, Z., and Li, S., 2005, "Dynamic Compressive Strength Properties of Aluminium Foams. Part II—'Shock' model and Comparison with Experimental Data," J. Mech. Phys. Solids, **53**, pp. 2206–2230.

[8] Chen, C., Lu, T. J., and Fleck, N. A., 1999, "Effect of Imperfections on the Yielding of Two-Dimensional Foams," J. Mech. Phys. Solids, **47**, pp. 2235–2272.

[9] Reid, S. R., Reddy, T. Y., and Peng, C., 1993, "Dynamic Compression of Cellular Structures and Materials," *Structural Crashworthiness and Failure*, N. Jones and T. Wierzbicki, eds., Elsevier, Amsterdam, pp. 295–340.

[10] Reid, S. R., and Peng, C., 1997, "Dynamic Uniaxial Crushing of Wood," Int. J. Impact Eng., **19**, pp. 531–570.

[11] *Abaqus Theory Manual*, 2002, Version 6.3, Hibbitt, Karlsson & Sorensen, Providence, RI.

[12] Xue, Z., and Hutchinson, J. W., 2004, "A Comparative Study of Impulse-Resistant Metal Sandwich Plates," Int. J. Impact Eng., **30**, pp. 1283–1305.

Closure to "Discussion of 'The Resistance of Clamped Sandwich Beams to Shock Loading'" (2005, ASME J. Appl. Mech., 72, pp. 978–979)

N. A. Fleck
e-mail: naf1@eng.cam.ac.uk

V. S. Deshpande

Department of Engineering, Cambridge University,
Trumpington Street, Cambridge CB1 1PZ, UK

The authors, Fleck and Deshpande (FD), are grateful for the interest shown in their work [1] by Tan et al. [2].

The aim of the FD study [1] was to present a simple analytical framework in order to understand the sequence of deformation events in shock-loaded sandwich beams. The analytical framework, although limited in accuracy, provides physical insight and allows for the interpretation of full numerical simulations and experiments. We reply to the comments of Tan et al. [2] point by point.

Points 1 and 2: We agree with Tan et al. [2] that the Taylor [3] analysis is of limited accuracy for strong air shocks. However, the FD analysis can handle strong air shocks provided one takes the transmitted impulse as an input to the model. This was done in the paper.

Point 3: (i) A global energy balance is a possible assumption for the core compression phase, leading to an internally self-consistent theory. FD used it in order to obtain simple analytical expressions for the degree of core compression. Recently, the accuracy of this assumption in predicting the sandwich panel shock response has been assessed by Deshpande and Fleck [4] for the case of a foam core. For such a core, shock wave effects and rate effects are important. The simple energy balance then overpredicts the degree of core compression as it neglects additional mechanisms of dissipation (largely viscous we believe).

Recall that the FD model was developed for lattice cores such as the corrugated core. The application of shock theory to those cores remains in open topic and hence FD used a simple energy balance argument to develop an initial understanding of the sandwich beam response.

Point 3: (ii) Tan et al. [2] argue that large internal energy can accrue in a metallic foam made from a rate independent plastic solid material by a switch in the deformation mode from bending to stretching of the cell walls. It is difficult to see how this mechanism switch can explain increases in plastic work by an order of magnitude or more at high velocities. This can argued as follows. An ideal work calculation can be performed by equating the change in internal energy shown in the FE calculations of Tan et al. [2] to the degree of axial stretch of the cell walls of the foam in the extreme case of all the cell walls equally sharing this energy change. In the case of an impact velocity $v_o = 200\ \mathrm{ms}^{-1}$, each cell wall would need to undergo a nominal compressive strain of 0.99[1] or equivalently the cell walls thickening by more than a factor of 100. This is physically unrealistic and not borne out by experiment [5]. It is the opinion of FD that a major component to the internal work in the simulations of Tan et al. [2] (Figs. 1 and 2) is from the artificial viscosity inherent in the explicit FE simulations using ABAQUS.

Point 4: We agree that the dynamic strength of lattice cores can exceed the static strength. This can be due to rate sensitivity and/or inertial effects. The FD analysis neglects both effects. Despite these simplifications (not inconsistencies) the model is remarkably robust.

Comparison of the FD analysis with more sophisticated calculations and experiments remains an active research topic, and FD welcome such activity.

References

[1] Fleck, N. A., and Deshpande, V. S., 2004, "The Resistance of Clamped Sandwich Beams to Shock Loading," J. Appl. Mech., **71**(3), 386.

[2] Tan, P. J., Reid, S. R., and Harrigan, J. J., 2004, Discussion: "The Resistance of Clamped Sandwich Beams to Shock Loading" (Fleck, N.A., Deshpande, V.S., 2004, ASME J. Appl. Mech., **71**, pp. 386–401), this issue.

[3] Taylor, G. I., 1963, *The Scientific Papers of G. I. Taylor*, Cambridge University Press, Cambridge, Vol III, pp. 287–303.

[4] Deshpande, V. S., and Fleck, N. A., 2004, "One-Dimensional Shock Response of Sandwich Plates," submitted to J. Mech. Phys. Solids 2004.

[5] Radford, D. D., Deshpande, V. S., and Fleck, N. A., 2005, "The Use of Metal Foam Projectiles to Simulate Shock Loading on a Structure," Int. J. Impact Eng., **31**, 1152.

---

[1] Here we assumed a solid material yield strength of 70 MPa which is consistent with the choice $\sigma_u = 0.7$ MPa by Tan et al. [2].

Discussion: "Applicability and Limitations of Simplified Elastic Shell Equations for Carbon Nanotubes" (Wang, C. Y., Ru, C. Q., and Mioduchowski, A., 2004, ASME J. Appl. Mech., 71, pp. 622–631)

J. G. Simmonds
Fellow ASME
Department of Civil Engineering, University of Virginia,
Charlottesville, VA 22904
e-mail: jgs@virginia.edu

I wish to point out that there are equations for the vibration ([1], pp. 259–261) and buckling [2] of elastically isotropic circular cylindrical shells that are as accurate as, but much simpler than, the so-called Exact Flügge Equations (Model III) that the authors use as their standard of comparison for the two sets of approximate equations they analyze, namely, the (simplified) Donnell Equations (Model I) and the Simplified Flügge Equations (Model II). (I use the adjective "so-called" because there is no set of two-dimensional shell equations that is "exact.") On pp. 225–230 of [1] Niordson presents one possible derivation of the Morley-Koiter equations in terms of midsurface displacements in which the two equations of tangential equilibrium (or motion) are *identical* to the simplified Donnell equations—that is, the first two of the authors' Flügge equations (3) with the coefficients of the small parameter $(1-\nu^2)(D/EhR^2)$ set to zero—whereas the equation of normal equilibrium (or motion) may be obtained from the third Flügge equation by replacing the coefficient of $(1-\nu^2)(D/EhR^2)$ in brackets by $2R^2\nabla^2 w + w$, where $\nabla^2 = \partial^2/\partial x^2 + R^{-2}\partial^2/\partial\theta^2$.

A simplified set of buckling equations for an elastically isotropic circular cylindrical shell under uniform axial, torsional, and internal pressure loads may be found in [2] where, as may be seen there from Eqs. (3.25)–(3.29), the equations for buckling of a simply supported cylinder under a uniform axial load or a uniform internal pressure are considerably simpler than the analogous Flügge equations yet free of the defects of the simplified Donnell equations. (A notable feature of these equations is that Poisson's ratio ν appears only in the combined parameter D/EhR^2.)

It is also important to point out that these simple, accurate equations have been shown *rigorously* [3,4] to be as accurate as the Flügge equations for *any* problem that can be formulated as a variational principle using the Rayleigh quotient. The key is the demonstration that the modified strain-energy density that leads to the Morley-Koiter equations (and their analog for buckling) differs from the strain-energy density of the Flügge equations by terms of relative order h/R—terms that are of the same order as the intrinsic errors in the Flügge equations.

References

[1] Niordson, F. I., 1985, *Shell Theory*, North-Holland, Amsterdam.
[2] Danielson, D. A., and Simmonds, J. G., 1969, "Accurate Buckling Equations for Arbitrary and Cylindrical Elastic Shells," Int. J. Eng. Sci., **7**, pp. 459–468.
[3] Danielson, D. A., and Simmonds, J. G., 1971, "A Proof of the Accuracy of a Set of Simplified Buckling Equations for Circular Cylindrical Shells," *Developments in Theoretical and Applied Mechanics*, Vol. 5, University of North Carolina Press, pp. 1015–1028.
[4] Simmonds, J. G., 1974, "Comments on the Paper 'On an Accurate Theory for Circular Cylindrical Shells' by S. Cheng," ASME J. Appl. Mech., **41**, pp. 541–542.

Discussion: "Boundary Element Analysis of Multiple Scattering Waves in High Performance Concretes" (Sato, Hirotaka, Kitahara, Michihiro, and Shoji, Tetsuo, 2005, ASME J. Appl. Mech., 72, pp. 165–171)

Jin-Yeon Kim
George W. Woodruff School of Mechanical Engineering,
Georgia Institute of Technology, 801 Ferst Dr.,
Altanta, GA 30332

This discussion intends to make comments on the recent article of Sato et al. [1] regarding their descriptions of self-consistency conditions for the effective medium in the multiple scattering theory. Equations (13) and (14) in Ref. [1] were obtained originally by Yang and Mal [2] by extending the static generalized self-consistent method (GSCM) with recourse to Waterman and Truell's theory [3]. Recently, the dynamic GSCM was recast [4] based on a simple consideration of wave energy in the model applying the energy theorem for the scattering in absorbing media [5], and also the equivalence between Eqs. (13) and (14) and

$$A_1^*(K_p,\mathbf{e}_1)=B_1^*(K_{\text{sv}},\mathbf{e}_1)=0$$

was shown. In the dynamic GSCM, the self-consistency condition of the effective medium (or the dispersion relation) reduces to vanishing of the wave energy extinction in the model. It should be noted that this can be further generalized to different self-consistent-type formulations of the multiple scattering problem. A simple but fairly general way to show this might be to express the Ewald formula [3] in the self-consistent form

$$K=K+\left(\frac{2\pi n_o}{K}\right)F(\mathbf{e}_1)$$

or therefore

$$F(\mathbf{e}_1)=0$$

where n_o is the scatter number density and $F(\mathbf{e}_1)$ denotes the forward scattering amplitude defined in the effective medium with consideration of multiple scattering effect. Note that subscript denoting the wave mode is suppressed for brevity.

In the article by Sato et al. [1], several logical and conceptual problems are found (Eqs. (16)–(19)). For example, it is obvious that Eq. (16) is just a sufficient condition to Eqs. (13) and (14), thus the equivalence cannot be so asserted. So it is again with Eq. (19) to Eqs. (17) and (18). Moreover, Eq. (19)

$$A_\alpha^*(K_p,\hat{\mathbf{x}})=B_\alpha^*(K_{\text{sv}},\hat{\mathbf{x}})=0 \text{ for } \forall\,\hat{\mathbf{x}}\neq\pm\mathbf{e}_1$$

can be brought up more reasonably from the known physical fact, "the absence of coherence in non-propagation directions," than from Eqs. (17) and (18) which appear to be rather trivial when reminding that the Waterman and Truell formula is meaningful only in the propagation direction. All this awkwardness seems to arise because the dynamic GSCM was formulated in the framework of the Waterman and Truell theory, which is not necessary at all. Even though the paper [4] provides a theoretically simple proof for a physically conceivable fact, the result takes away all those problems in the above caused in the constraint of Waterman and Truell formalism.

References

[1] Sato, H., Kitahara, M., and Shoji, T., 2005, "Boundary Element Analysis of Multiple Scattering Waves in High Performance Concretes," ASME J. Appl. Mech., **72**, pp. 165–171.

[2] Yang, R. B., and Mal, A. K., 1994, "Multiple Scattering of Elastic Waves in a Fiber-Reinforced Composites," J. Mech. Phys. Solids, **42**, pp.1945–1968.

[3] Waterman, P. C., and Truell, R., 1961, "Multiple Scattering of Waves," J. Math. Phys., **2**, pp. 512–537.

[4] Kim, J.-Y., 2004, "On the Generalized Self-Consistent Model for Wave Propagation in Composite Materials," Int. J. Solids Struct., **41**, pp. 4349–4360.

[5] Kim, J.-Y., 2003, "Extinction of Elastic Wave Energy Due to Scattering in a Viscoelastic Medium," Int. J. Solids Struct., **40**, pp. 4319–4329.